Computational Models of Nanostructured Materials for Energy Storage and Conversion

by

Brett Robert Henderson
B.A., Harvard University, 2017

A Dissertation Submitted in Partial Fulfillment of the
Requirements for the Degree of

DOCTOR OF PHILOSOPHY

in the Department of Chemistry

We acknowledge and respect the Lək̓ʷəŋən (Songhees and Xʷsepsəm/Esquimalt) Peoples on whose territory the university stands, and the Lək̓ʷəŋən and W̱SÁNEĆ Peoples whose historical relationships with the land continue to this day.

Computational Models of Nanostructured Materials for Energy Storage and Conversion

by

Brett Robert Henderson
B.A., Harvard University, 2017

Supervisory Committee

Dr. Irina Paci, Supervisor
(Department of Chemistry)

Dr. Thomas Baker, Departmental Member
(Department of Chemistry)

Dr. Ulrike Stege, Outside Member
(Department of Computer Science)

ABSTRACT

This dissertation develops and benchmarks computational methods for the rational design of materials for energy storage and conversion. The first portion of the text presents three projects aimed at introducing computationally efficient methods for studying the mechanisms of capacitive energy storage in nanocomposite dielectric materials. Studying model systems consisting of alkaline earth metal oxides with nanoscopic silver inclusions using Density Functional Theory reveals that manipulating the composition and morphology of a nanocomposite's components permits large increases in electric permittivity. A continuum model for such composites is introduced and shown to reproduce many of the effects of inclusion morphology on permittivity. Finally, a model based on inducible atomic dipoles is studied for several types of inorganic cluster, and its accuracy is shown to be dependent in part upon the degree of charge transfer within the clusters. Together, these projects advance the understanding of the mechanisms underlying capacitive energy storage in nanostructured dielectrics and add efficient new methodologies to the simulation toolkit for designing novel dielectrics for energy storage. The second portion of the dissertation benchmarks the performance of various Density Functional Approximations in the prediction of the activity of metal–nitrogen–carbon (M–N–C) catalysts for the oxygen reduction reaction. The calculated activity trends of M–N–C catalysts—specifically metalloporphyrins—are found to by highly method-dependent. The primary drivers of this dependence are explored, and best practices for similar systems are suggested while also highlighting the importance of benchmarking for new systems. This work is necessary for advancing the field of single-atom catalysts, since it helps practitioners avoid common pitfalls in the computational protocols used to design and screen catalysts.

Contents

List of Tables

List of Figures

ACKNOWLEDGEMENTS

I would like to thank:

my partner, Sofia, who inspires me daily and believes in me when I do not believe in myself.

James McFarlane, for his timely invitations to pottery classes.

Irina Paci, for her patience, trust, guidance, and thoughtfulness. It has been incredibly rewarding to have a supervisor who expects so much yet demands so little. Her trust in me has made me a better scientist, and her deep care helped me persevere.

Natural Sciences and Engineering Research Council of Canada, for its support through the CREATE in Quantum Computing program.

The Estate of Norah and Mark de Goutiere, for its generous scholarship that allowed me to pursue my academic interests more freely.

And this I believe: that the free, exploring mind of the individual human is the most valuable thing in the world. And this I would fight for: the freedom of the mind to take any direction it wishes, undirected. And this I must fight against: any idea, religion, or government which limits or destroys the individual. This is what I am and what I am about.

John Steinbeck, East of Eden

DEDICATION

To Mom and Dad.

Chapter 1

Introduction

1.1 Materials Demands for a Clean Energy Future

In order to combat anthropogenic climate change and secure a sustainable future, an increasing proportion of global energy demands must be met using clean and renewable sources.[1] The integration of new energy sources in the electrical grid and high-energy sectors like transportation and heavy industry has lead to an explosion in the types of devices needed to effectively store, convert, and ultimately use that energy.

One area of intense effort has been improving the availability of renewable energy, both in terms of managing intermittency and increasing portability. Some renewable energy sources are inherently intermittent, creating a demand for energy storage. For example, the widespread adoption of wind and solar energy calls for ever improving battery technology to store the intermittently generated electricity for use when demand is high and generating capacity low.[2] At the same time, stable, long-term energy storage needs to be improved to fill in the remaining gaps from intermittent sources. Fuel cells offer one way to utilize the energy stored in clean chemical fuels, which can be stored indefinitely, without harmful emissions. Hydrogen fuel cells, for instance, offer the promise of clean electricity via the conversion of hydrogen gas into water vapor, with a portability that makes them a potential boon for the transportation sector provided their cost can be reduced.[3] Applications with much smaller timescales of energy storage also exist—capacitors store and release energy quickly to smooth the electrical energy delivered in power electronics systems such as those in electric vehicles.[4] These examples illustrate that an increasingly diverse energy

portfolio comprising sources both intermittent and stable, stationary and portable, coupled with variable-duration storage capacity, is required to supplement and eventually supplant fossil fuels.

Beyond these storage and availability requirements, a sustainable energy ecosystem necessitates technologies that can meet various power and energy density demands. That is, some applications require delivery of large amounts of energy over very short time periods, while others require more sustained delivery over large amounts of time. While batteries and fuel cells provide the energy density needed for the latter application, capacitors exhibit the power density required for the former.[5] As such, capacitors are critical for storing and delivering in pulsed power systems, such as pulsed lasers and microwave sources.[6] In addition, high-energy density capacitors are increasingly important in the power electronics used to convert and deliver energy in the grid and in electric vehicles.[7, 8] In these capacities, they are often required to operate under high voltage, temperature, and even mechanical stress, necessitating materials innovations in order to maintain high performance and durability.[7] Of course, some applications have intermediate demands or simultaneously large energy and power requirements. Regenerative braking in electric vehicles, for example, relies on supercapacitors, which have energy and power densities between batteries and traditional capacitors.[9] All told, there is no one-size-fits-all or universally optimal technology for delivering energy. Thus, it is crucial to continue to develop both high-energy density devices like fuel cells (while simultaneously pushing power density) and high-power density devices such as capacitors (while pushing their energy density).

The diversification of energy sources and the explosion of energy demand, combined with the need to deliver that energy over a variety of time and power scales, calls for improved devices that can be tailored to specific applications. From a chemistry perspective, the need for improved devices entails the need for rational and efficient material design to optimize device performance while minimizing the environmental footprint of those devices over their life cycle. This means that the materials should be easily synthesized from abundant and non-toxic elements while being durable and long-lasting. In addition, the materials design process itself should be rapid and sustainable to reduce costs that could be transferred to consumers and also allow quick and iterative improvements to be made to meet the demands of a rapidly evolving energy landscape. In the past several decades, computational tools have become invaluable in the materials development pipeline. Accurate computer simulations allow

researchers to predict the properties of novel materials before synthesizing them in the lab. Moreover, these simulations can be used to derive mechanistic explanations for properties observed in the lab. Armed with a mechanistic understanding of the relationship between material composition and observable properties is understood, one can rationally design a material with the desired properties.

1.2 Problem Statement

In this dissertation, we develop and evaluate simulation methodologies for the rational design of materials for two distinct energy storage and conversion applications: dielectrics for high energy-density capacitors and catalysts for the oxygen reduction reaction (ORR) in hydrogen fuel cells. In the context of capacitive energy storage, we focus on the behavior of nanocomposite dielectrics using model systems composed of alkaline earth metal oxides with nanoscopic silver inclusions. As we will see, manipulation of the composition and morphology of a nanocomposite's components permits the optimization of material properties while also introducing additional simulation complexity. In the context of the ORR, we benchmark the performance of the ubiquitous quantum mechanical simulation method Density Functional Theory (DFT) in the prediction of the activity of a specific class of catalyst. Dubbed metal–nitrogen–carbon (M–N–C) catalysts, these materials are composed of single-metal-atom catalytic sites coordinated by nitrogen atoms within a carbon scaffold. While they are a promising alternative to the current state-of-the-art platinum catalysts, M–N–C catalysts have complicated electronic structures which can produce misleading results when using the DFT methods that have been commonly applied to older-generation catalyst materials. The primary thrust of this work for both capacitor and fuel cell applications is the selection of simulation methodologies that yield a favorable trade-off between simulation cost and the accuracy of the obtained material properties.

This dissertation focuses on obtaining accurate material properties and linking them to specific structural characteristics—it does not deal with the integration of those materials into the design of devices. In the design of the devices themselves, these materials properties could constitute inputs into multiphysics models of device performance. Or, working in the opposite direction, device modeling might define a range of desirable materials properties that can be optimized for in the materials modeling process.

With the generalities of what this dissertation does and does not set out to do

established, the remainder of this chapter introduces some of the principal considerations involved in materials design for capacitive energy storage and ORR catalysis. The promise that nanostructured materials hold in both contexts is then highlighted before noting the challenges associated with studying such materials computationally. Finally, an outline of the rest of the dissertation highlights the various ways that this disseration attempts to address these challenges.

1.3 Capacitive Energy Storage

A capacitor is a device that stores energy electrostatically in the form of physically separated charge. The simplest capacitor variant is a parallel-plate capacitor, consisting of two parallel metal plates separated by some small distance.[5] Between these plates lies an insulating material, called a dielectric, which prevents current flow between the plates unless they are connected by an external circuit. When an external potential is applied across the capacitor plates in a closed circuit, current flows between them until there is a build up of positive charge on one and negative charge on the other. If the external potential is removed and the circuit broken, the charges remain separated on the capacitor plates (indefinitely if the plates are perfectly isolated from their environment). The capacitor is said to be charged, and the separated charges establish an electric field across the dielectric layer and represent a form of stored potential energy. When the circuit is completed, the capacitor discharges. The separated charges flow back through the circuit as current, able to drive an external load until there are no charges left to do work. Figure 1.1 illustrates the governing principles of energy storage in a capacitor and the impact of dielectric structure.

The amount of charge that a capacitor is able to store for a given applied voltage is quantified by its *capacitance*. On the one hand, the capacitance depends on the geometry of the capacitor, being directly proportional to the area of the capacitor plates A and inversely proportional to the distance d between them. However, the capacitance is also directly proportional to a property of the dielectric called the *electric permittivity* (sometimes referred to as the dielectric constant), ϵ.[5, 7] The electric permittivity is related to the ability of bound charges in the dielectric to polarize—that is, the ability of positive and negative charges in the dielectric to separate—in the presence of an electric field such as that created by charged capacitor plates.[10]

In an external field with a direction orthogonal to the capacitor plates, the po-

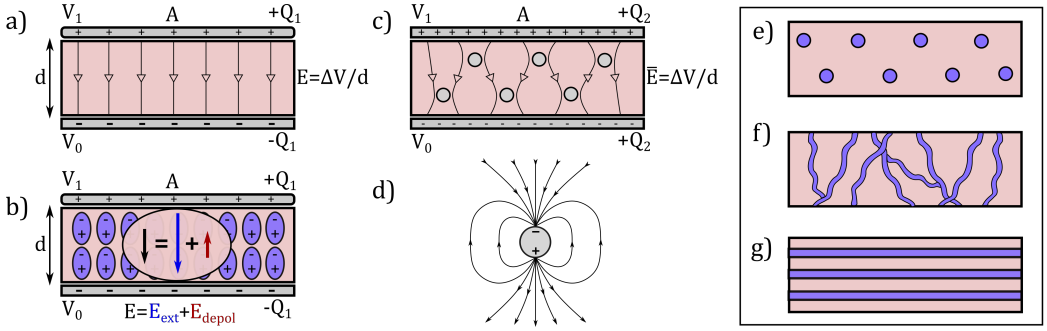

Figure 1.1: Introduction to capacitor operation. Panel **a)** depicts a charged parallel plate capacitor with macroscopically uniform dielectric layer (salmon), plate area A, and dielectric thickness d. A potential difference of $\Delta V = V_1 - V_0$ is established across the plates corresponding to stored charge Q_1 and a uniform electric field (open arrows). Panel **b)** depicts a model for the microscopic operation of such a capacitor. Microscopic dipoles (purple ellipses) are induced by the external field E_{ext} and establish a depolarizing field E_{depol}. The direction of these fields and the total field E is shown as an inset. **c)** Shows the same capacitor with a matrix-inclusion composite dielectric. The total field varies strongly on length scales similar to the inclusion size. When inclusions are more polarizable than the surrounding matrix, the charge stored on the plates increases. Panel **d)** shows the induced electric field around a polarizable inclusion. Panels **e)**-**g)** show three types of composite structures: matrix-inclusion, matrix-fiber, and laminar (respectively). Each type can potentially confer different improvements in dielectric properties,[7], though the focus of this dissertation is matrix-inclusion structures.

larization of the dielectric produces an induced electric field in the opposite direction within the dielectric. Because of its superposition with the external field, the induced field reduces the total electric field between the capacitor plates for a given charge density on them.[11] Thus, for a given applied potential, a capacitor with a dielectric layer will accumulate more charge on its plates than a capacitor in which the dielectric is replaced with unpolarizable vacuum. Similarly, the greater the ability of the dielectric to polarize (and hence the greater its electric permittivity), the greater the accumulation of charge on the capacitor plates, and the greater the amount of potential energy stored to drive external loads.[5, 7] Thus, high-permittivity dielectrics are important for capacitive energy storage applications.

Another application requiring high-permittivity dielectrics are gate dielectrics for modern metal-oxide-semiconductor field-effect transistors (MOSFETs), which form the basis of computer logic circuits, flash memory, and dynamic random-access memory (DRAM).[12, 13] MOSFETS rely on a capacitive coupling between their gate

electrode and semiconductor body via a dielectric oxide layer. The amount of current that can be driven between the source and drain terminals of the MOSFET is directly related to the capacitance of the oxide layer.[14] As the footprint of transistors has shrunk exponentially in modern integrated circuits, oxide thicknesses have been decreased in order to maintain gate capacitances.[15] However, as gate thicknesses approach the nanometer scale, unwanted electron tunneling can occur between the gate electrode and the conducting channel between source and drain. High-permittivity (also called high-κ) gate dielectrics allow high gate capacitances even with thicker dielectric layers that limit tunneling.[14] DRAM cells also rely on capacitors (in addition to MOSFETs) for charge-based memory storage. Similar to MOSFET trends, the drive toward increasing DRAM cell density has led to a shrinking of these capacitors and demand for high-κ dielectrics in order to reduce leakage currents.[16]

While high permittivity is a figure of merit for both capacitive energy storage and gate dielectric applications, effective devices have other important material requirements. For energy storage, the recoverable energy from a capacitor depends not only on the dielectric's permittivity but also on the strength of the applied voltage. Thus, in high-energy density applications, a dielectric must have a high breakdown strength, or the ability to withstand large electric fields without material degradation or conduction.[5] Other important properties for both applications include large band gaps, low dielectric loss (energy dissipation due to dielectric relaxation processes), low leakage currents, heat tolerance, processability, and—particularly for gate dielectrics—easy deposition on other semiconductors and the formation of a stable interface with them.[5, 14, 17, 7, 4] Within the rapidly growing field of flexible and stretchable electronics, mechanical properties such as flexibility and durability (i.e. through self-healing polymers) also become paramount.[7, 18]

Although these auxiliary material properties are essential considerations for device design, this dissertation will focus almost exclusively on the calculation of electric permittivity. In doing so, the intent is not to directly design the next generation of materials for high-energy density capacitors or high-κ gate oxides. Rather, the emphasis will be on developing methods for calculating the permittivity of nanostructured materials and developing a quantitative understanding of the relationship between structure and permittivity. We expect these methodological advancements to be useful in practical materials design when used in combination with additional approaches for optimizing material properties beyond permittivity.

1.4 Oxygen Reduction Reaction Catalysts

Hydrogen fuel cells produce electrical current via the electrochemical reaction of hydrogen gas with ambient oxygen gas, yielding water as the only product. While there are many implementations of hydrogen fuel cells, the most popular design for transportation applications, and the design of interest in this dissertation, is a proton-exchange membrane fuel cell (PEMFC). PEMFCs consist of two electrodes separated by an insulating polymer electrolyte that is permeable to protons. At the anode, hydrogen gas is oxidized to yield two protons and two electrons. While the electrons travel through an external circuit to drive a an electrical load such as a motor, the protons diffuse through the membrane to the cathode. At the cathode, these protons react with oxygen and the energy-depleted electrons to form water.[3] The overall reaction involves the transfer of four electrons and is called the four-electron oxygen reduction reaction (ORR):[19]

$$2H_2 + O_2 \longrightarrow 2H_2O. \tag{1.1}$$

While the ORR is thermodynamically favorable, with a standard potential of 1.23 V,[19] it proceeds slowly, meaning it must be catalyzed in fuel cells to produce the currents needed for practical applications. The cathode reaction $4H^+ + O_2 + 4e^- \longrightarrow 2H_2O$ is particularly sluggish and demands careful catalyst design for commercially viable devices. Most commercial PEMFCs employ a thick cathode catalyst layer consisting of carbon-supported platinum nanoparticle catalysts.[20, 21] However, the past decade has seen a concerted effort to replace these catalysts for several reasons. On the economic front, reducing the amount of platinum or removing it entirely would bring down the cost of PEMFCs, propelling them toward a wider market.[20, 22] Commercialization is also hindered by the limited durability of catalysts layers, which experience the aggregation of platinum nanoparticles and reduction of electrochemical surface area as cell voltage is cycled.[23] Moreover, platinum catalysts are also susceptible to poisoning, especially by carbon monoxide, though this is largely an issue for hydrogen oxidation catalysts at PEMFC anodes, which are exposed to impurities in the H_2 fuel source.[24] Finally, theoretical modeling suggests that it should be possible to increase the activities of ORR catalysts with more sophisticated materials design—that is to say that while platinum catalyzes the ORR, it is not optimal.[19] In order to meet power density targets and make PEMFCs competitive in the transportation sector, both intrinsic catalyst activity and the density of catalytic sites

must be improved.[20, 25]

In the design of ORR catalysts with improved activities, the figure of merit is the catalyst's *overpotential*. This overpotential is the difference between the theoretical cell potential for the ORR (1.23 V) and the lower measured potential, or *limiting potential*, of the catalyzed cell.[19] Minimizing the overpotential results in more thermodynamically efficient fuel cells. Furthermore, this overpotential is directly related to how strongly a catalyst binds oxygen, as well as the other intermediates in the ORR.[26] According to the Sabatier principle, the optimal catalyst should neither bind these intermediates too strongly nor two weakly.[27] Put another way, the catalyst needs to bind the intermediates tightly enough so that they do not desorb before the formation of water, yet weakly enough so that the product can be easily desorbed to free up the catalytic site. Because of this relationship, catalyst limiting potentials, when plotted against the binding energy of an intermediate, yield a volcano-shaped plot, called simply a "volcano plot" (Figure 1.2). Fortunately, thermodynamic volcano plots (i.e. those plotting limiting potential on the y-axis) for the ORR demonstrate a striking similarity in shape and peak position to volcano plots of ORR kinetics, meaning catalysts producing the lowest overpotentials also tend to produce the fastest reactions and largest currents.[19, 28]

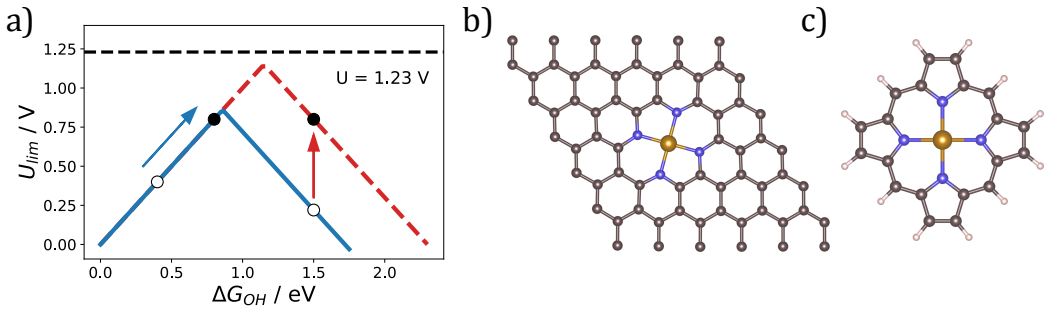

Figure 1.2: ORR catalyst design. Panel **a)** depicts a theoretical volcano plot for the ORR. Solid blue lines represent data fit to actual ORR catalysts (Ref [19]). Red dashed lines represent a hypothetical alternative volcano for a novel class of catalysts that circumvent traditional scaling relationships. ΔG_{OH} is the energy of a hydroxyl intermediate relative to the ORR products, such that the left side of the volcano consists of catalysts that bind the intermediate too tightly, and the right side too weakly. Circles and arrows represent two possible modes of catalyst optimization: 1) optimizing binding strength to climb the volcano (blue arrow) and 2) circumventing traditional scaling (red arrow). Panel **b)** depicts a graphene flake with a pyridinic FeNC catalytical site, and panel **c)** depicts an iron porphyrin, which contains a pyrollic FeNC catalytic site.

Computational chemistry allows volcano plots to be constructed *in-silico*. The calculation of the binding energies of intermediates is standard practice in computational chemistry, and work by Nørskov and co-workers in the early 2000s elucidated how intermediate binding energies could be used to derive theoretical overpotentials.[26] Finally, among the many different types of catalysts studied for the ORR, almost all of them obey strict linear scaling relationships between the binding energies of their various intermediates.[29, 19] These relationships can be used to define a theoretical volcano along which the activities of almost all catalysts seem to lie. As a consequence, the peak of this theoretical volcano defines a theoretical maximum limiting potential (minimum overpotential). Platinum lies near, but not at, the peak of this volcano, suggesting two avenues for improving catalysts, which are depicted in Figure 1.2.[19] The more conservative approach is to iteratively improve the design of materials which follow the traditional scaling relationships so as to inch them nearer to the volcano peak.[30] Alternatively, one could try to circumvent traditional scaling relationships altogether, as by designing a catalyst which selectively strengthens the binding of some intermediates while weakening the binding of others.[30, 31, 32]

It is worth noting that though the focus in this dissertation will be the accurate calculation of overpotentials, other factors are crucial to the design of PEMFCs. In particular, a good catalyst layer exhibits both a high density and stability of catalytic sites, efficient mass transport, and selectivity for the 4-electron over the 2-electron ORR.[21, 33, 25, 19] While mass transport and site density depend largely on the synthetic pathway used, the stability and selectivity of catalytic sites can be evaluated at least to some degree via simulation. Assessing selectivity typically necessitates thermodynamic calculations of the competing 2-electron ORR, which produces hydrogen peroxide and leads to device degradation via oxidation of the carbon substrate.[34] Fortunately, methods that produce accurate overpotentials for the 4-electron ORR should also be well suited to evaluate the thermodynamics of the 2-electron ORR. Thus, the refinement of computational methods for determining the overpotentials of the 4-electron ORR should have spillover benefits into the other objectives of catalyst design.

1.5 The Promise of Nanostructured Materials

Modern fabrication techniques allow ever increasing control of material structure at the nanoscale, which allows the precise engineering of atomic and electronic struc-

ture.[35, 36] The ability to control material nanostructure provides many additional handles that can be tweaked in order to design materials with optimal electronic properties for use in energy storage and conversion technologies. This may involve engineering specific morphologies and facets of nanoparticles, defect sites in bulk materials, nanocomposite materials, or specific coordination environments on catalytic surfaces. These latter two applications of nanostructure will be the focus of much of this dissertation.[35]

In a nanocomposite, two or more materials, at least one of which has dimensions on the order of nanometers, are interfaced in order to create a new material with distinct properties.[35, 7] As with traditional composites, nanocomposites combine the beneficial properties of their constituent phases. By controlling the composition, morphology, and relative proportions of these phases, the composite's properties can be optimally tuned for a given application. However, unlike traditional composites, nanocomposites utilize small length scales to avail themselves of quantum mechanical effects.[37, 38] Furthermore, as composite domains approach the nanometer and even sub-nanometer scale, the interfaces between domains comprise an ever greater proportion of the material, and the unique properties of these interfaces become extremely influential to material properties and important to understand.[7, 39]

Nanocomposites constitute a promising class of materials for high-permittivity dielectrics. In energy storage applications, composites consisting of a low-permittivity polymer bulk phase with metallic or ceramic inclusions combine the flexibility, easy processing, and high breakdown strength of the polymer with the high polarizability of the inclusions to maximize energy density.[18, 4, 7] Additionally, inorganic composites consisting of metal-oxide bulk phases with nanoscale metallic inclusions take advantage of the large band-gap insulating oxides and polarizable inclusions to yield composites that remain insulating while having drastically increased permittivities relative to the parent oxide.[40, 41, 42, 43, 44, 45, 46] Inclusions can either be locally conducting or insulating—in either case their polarizability and resulting effect on composite permittivity is closely tied to inclusion shape and size.[4, 47] The development of polymer versus inorganic matrix materials largely depends on the target application, with heat tolerance, flexibility, interface quality with other device materials, and integrability into device fabrication pipelines being potential differentiating factors.[5, 7, 18]

Beyond nanostructured dielectrics, engineering of nanostructure is an extremely powerful tool in designing surfaces for ORR electrocatalysis. In order to improve upon

the catalytic activity of platinum catalysts, researchers have extensively investigated the impact of nanoparticle morphology and composition. High-index facets, cage and frame structures, and even molecule-sized "fluxional" nanoparticles (i.e. nanoparticles capable of rapid atomic reordering) offer large surface areas and improved activities over Pt (111) surfaces.[48, 3, 49] Alloyed nanoparticles and core-shell nanoparticles with a non-precious core and platinum surface have also been fabricated as a means to reduce the total volume of platinum used in catalyst layers while maintaining or even improving activity.[49, 20, 3]

Single-atom catalysts (SACs) are an alternative to metallic nanoparticle catalysts, wherein the catalytic sites are single (often non-precious) metal atoms embedded in a typically carbon scaffold. M–N–C catalysts are a subclass of SACs wherein the catalytic sites occur in a nitrogen-doped carbon scaffold.[33] One approach to synthesizing M–N–C catalysts is to pyrolyze macrocyclic precursors, such as metalloporphyrins, metallophthalocyanines, or metallocorroles, leading to a variety of catalytic sites with different activities embedded in graphene sheets.[50, 33] Alternatively, the coordination environment of catalytic sites can be precisely engineered using chemical synthesis to functionalize such macrocycles, which can either act as homogeneous catalysts or be covalently anchored to a carbon framework.[51, 52] Metal-organic frameworks with M–N–C sites are also the subject of intense investigation, both as precursors for pyrolysis and as ORR catalysts themselves, with finely tuned three-dimensional coordination environments.[53, 54, 55, 56] Functionalized macrocycles and 3D frameworks allow the electronic and steric environment of each bound intermediate to be fine tuned.[57, 56] The holy grail of such a design is to selectively stabilize intermediates, as by introducing indermediate-dependent hydrogen bonding in order to circumvent linear scaling relations and reduce theoretical minimum overpotentials.[19, 58]

1.6 Nanostructure Modeling Challenges

Despite their advantages, nanostructured materials present distinct challenges to the computational methods that could otherwise be used to expedite their design. To understand why, it is important to consider that materials simulation can generally be organized into a hierarchy based on the level of theory, with each rung of the hierarchy encompassing a different trade-off between transferability (the ability to treat chemically different systems accurately) and computational efficiency (Figure

1.3.[59, 60] At the bottom of the hierarchy in terms of complexity and transferability lie classical continuum methods, which treat materials properties via constitutive relationships that ignore the intricacies of atomic and electronic structure altogether. Such methods allow materials and even entire devices to be modeled at the macroscopic level.[10] At the next rung of the hierarchy lie force field methods. Including molecular mechanics and molecular dynamics, these methods consider atomic structure explicitly but either ignore electronic structure completely or include its effects it in a simplified classical manner. Interatomic forces are treated via classical force fields, and in some cases, the atomic structure is coarse grained to allow the treatment of larger systems.[61] In the most efficient implementations, force field methods allow access to simulations of up to roughly a billion atoms.[62, 63] At the top of the hierarchy lie methods based on quantum mechanics, often called first-principles or *ab initio* methods. These approaches consider the atomic and electronic structure of materials based on expensive solutions of the Schrödinger equation. Even within the realm of *ab initio* methods, various approximations can be introduced, which affect accuracy, transferrability, and efficiency.[64] The most efficient of these approximations allow the simulation of systems with up to thousands of atoms,[60, 65] while benchmarking level accuracy often requires methods that can only treat tens of atoms.[64]

The computational study of nanostructured materials makes the judicious choice of simulation methodology uniquely challenging on the basis of both *scalability* and *transferability*. On the one hand, large simulation domains—typically on the order of hundreds to thousands of atoms—are required to encompass nanometer-scale structural elements.[65] While classical force field methods are more than capable of treating such system sizes, the twin thrusts of this dissertation—dielectric permittivity and catalyst activity—require a rigorous treatment of the electronic structure of materials. At the very least, an *ab initio* treatment is required initially to parameterize more efficient and scalable classical methods, and such a treatment becomes prohibitive for systems composed of more than about a thousand atoms.

Besides large length scales, nanostructures with different chemical domains strain the transferability of methods to different chemical environments, as an accurate treatment is required of all subsystems and the interfaces between them. While calculations based on first principles should in theory exhibit excellent transferability across these domains, in practice the approximations introduced end up being more accurate for some types of systems (e.g. bulk metallic surfaces) than others (e.g. single metal atoms).[60, 64] Later chapters in this dissertation employ a variety of

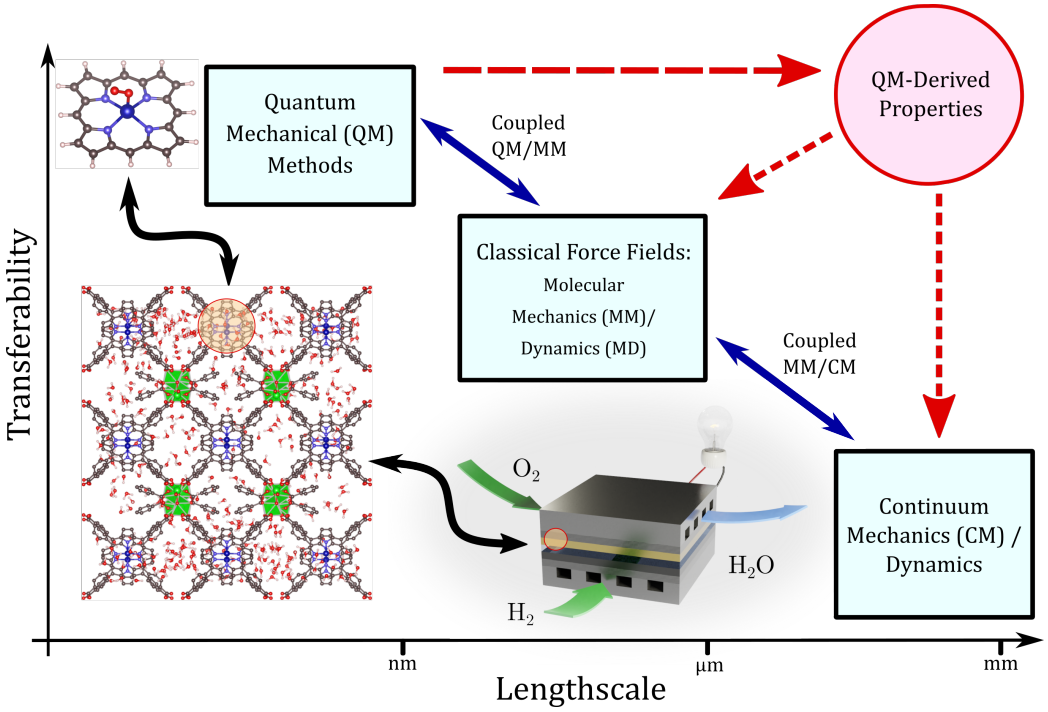

Figure 1.3: Computational method hierarchy, adapted from Refs [59] and [60] Broad (and non-exhaustive) method classes are depicted as boxes. Blue arrows denote methods that couple multiple scales, and red arrows indicate that the direction of information flow when using small quantum mechanical models to derive parameters for less foundational methods. Axes show approximate length and time scales accessible by each method. Three systems are shown as examples of what is accessible with each method class within the context of ORR catalysis: a cobalt porphyrin binding ORR intermediates (quantum), a metal organic framework with cobalt porphyrin moieties[55] and explicit aqueous solvation (classical force fields), and a model PEMFC (continuum).

methods aiming to address both of these challenges, with scalability being a primary subject of method development for the dielectric response of nanocomposites and transferrability the focus of method benchmarking for single-atom ORR catalyst. Across these two primary thrusts, this dissertation wields a broad arsenal of computational methods, ranging from quantum mechanical approaches to treat electronic structure with varying degrees of approximation to classical continuum treatments of electrostatics.

1.7 Preview of Following Chapters

The remainder of this dissertation encapsulates the work undertaken by the present author and collaborators to advance the theoretical understanding of dielectric polarization in nanocomposites and a pragmatic understanding of the selection of best-practice methods in the study of modern ORR catalysts.

The chapters pertaining to dielectric polarization use and expand upon a recently developed first-principles approach to decompose the dielectric response of alkaline earth oxide / silver nanocomposites into contributions from their various structural elements. This characterization technique reveals the complex behavior at the interface between inclusions and the surrounding matrix, which may either enhance or diminish permittivity, thus enabling more rational design of nanocomposites for capacitive energy storage. Additionally, these chapters present new coarse-grained models for the same class of nanocomposites, based on both classical continuum and inducible dipole approaches. These models allow the simulation of much larger material length scales than quantum mechanical approaches. With further development, they can be a potent tool in the materials design toolkit, allowing the simulation of materials with large inclusions or multiple domains which cannot be studied with more computationally demanding methods.

In the chapter pertaining to the ORR, a significant benchmarking work is undertaken to understand the origins and consequences of discrepancies between different DFT approximations when simulating 3d metalloporphyrin catalysts. This work informs best practices in the computational study of M–N–C catalysts, and in an even broader context, single-atom catalysts. In this rapidly expanding field, the work presented herein is important for guiding accurate and thoughtful computational approaches to electronically complicated materials, which is necessary for effective computational catalyst design. By highlighting the challenges these materials pose to DFT, the work also motivates the development of efficient multiconfigurational methods which can treat the electronic structure of these materials in a more consistent and transferrable manner.

Aside from a chapter devoted to introducing the methodological threads that run through the entire work, each chapter focuses on a different *project* undertaken as part of the larger PhD work. While thematically distinct, these chapters are interdependent and often cross-referential, specifically those expanding on dielectric polarization. Thus, an attempt has been made to order these chapters such that

they build on each other conceptually, even though this order does not necessarily reflect the chronological order in which the projects were completed. Each chapter begins with an introduction which situates its contents into the larger context of the dissertation.

Chapters 4 and **6** contain articles that have been published in peer-reviewed journals. The present author is the primary author of each of these articles—thus, they have been reformatted to conform to the style of this dissertation but otherwise only minimally edited. The introductions of each of these chapters clearly outline the contributions of all collaborators to these works. The remaining chapters represent the original work of the present author and have not yet appeared as either pre-print or peer-reviewed articles. With this background in mind, the rest of this dissertation is organized as follows.

Chapter 2 introduces the computational methods that are used repeatedly throughout this dissertation. A brief introduction to DFT and the wave function theories used in later chapters leads into a description of the modern theory of polarization within the context of density functional theory.

Chapter 3 describes the use of maximally localized Wannier functions (MLWFs) to spatially map the polarization response of matrix-inclusion nanocomposites. A method developed by Hally and Paci[39] is applied to a variety of alkaline earth metal oxides with nanoscopic silver inclusions in order to decompose their dielectic response into matrix and inclusion contributions. The effects of inclusion loading, inclusion shape, and matrix composition are investigated.

Chapter 4 develops a continuum model for MgO/Ag nanocomposites using a procedure for fitting the continuum response to the quantum one. The model is evaluated on nanocomposites with rod- and disk-like silver inclusions, and applied to inclusions that are too large to treat with DFT.

Chapter 5 explores a classical inducible dipole model of polarization for inorganic oxides and nanocomposites. The model is based on an empirical volume scaling law of atomic polarizability that is commonly used in the development of semi-empirical dispersion corrections to DFT. The ability of the model to handle anisotropic polarization and to be transferrable between oxides with different levels of ionic bonding

is a particular focus.

Chapter 6 benchmarks the performance of various density functional approximations in the calculation of metalloporphyrin catalyst activities for the oxygen reduction reaction. Activities from DFT are compared with those from local coupled cluster calculations. The effects of spin contamination and moderate multiconfigurational character are analyzed and lead to actionable recommendations for functional selection in similar systems.

Chapter 7 summarizes the conclusions that can be drawn from the present dissertation and provides an outlook for future research directions.

Some of the work undertaken during the author's time as a PhD student did not fit well into any of the above chapters. This work was either supplemental to the more important message of a chapter or constituted a short-term project that fell outside the larger scope of this dissertation. Work of both varieties has been included in appendices at the end of this document.

Appendix A summarizes a coupled finite well model for optically trapped quantum dots. The model was developed in Matlab in order to support the work of collaborators who had trapped and characterized the optical properties of such dots. While the complete work was eventually published as the letter "Coupling Perovskite Quantum Dot Pairs in Solution using a Nanoplasmonic Assembly" in ACS Nanoletters,[66] the present author's contribution represented only a small part. **Appendix B** includes supporting information for Chapter 3, such as convergence studies for the computational methods used. **Appendix D** provides additional mathematical background for the methods in Chapter 5. **Appendices C** and **E** provide supporting information for Chapters 4, and 6, respectively. These appendices are minimally edited versions of the supporting information documents published along with the articles these two Chapters include. **Appendix F** includes a summary of three other software development projects the present author contributed to during his PhD. These projects include a web tool for producing catalytic cycle drawings with encoded kinetic information, a web tool for kinetic analysis using the CAKE method, and a web tool for kinetic analysis using the VTNA method. The first two tools have been made public along with associated journal publications.[67, 68] Finally, **Appendix G** includes the primary scripts and programs that were developed to perform the

analysis throughout this dissertation.

Bibliography

[1] UN. Secretary-General. Report of the secretary-general on the 2019 climate action summit and the way forward in 2020. Report, United Nations, 2019. "https://digitallibrary.un.org/record/3850027?ln=en&v=pdf".

[2] Jason Rugolo and Michael J Aziz. Electricity storage for intermittent renewable sources. *Energy Environ. Sci.*, 5(5):7151, 2012.

[3] Kui Jiao, Jin Xuan, Qing Du, Zhiming Bao, Biao Xie, Bowen Wang, Yan Zhao, Linhao Fan, Huizhi Wang, Zhongjun Hou, Sen Huo, Nigel P. Brandon, Yan Yin, and Michael D. Guiver. Designing the next generation of proton-exchange membrane fuel cells. *Nature*, 595(7867):361–369, July 2021.

[4] Guoqiang Zhang, Qiong Li, Elshad Allahyarov, Yue Li, and Lei Zhu. Challenges and opportunities of polymer nanodielectrics for capacitive energy storage. *ACS Applied Materials & Interfaces*, 13(32):37939–37960, August 2021.

[5] Ge Wang, Zhilun Lu, Yong Li, Linhao Li, Hongfen Ji, Antonio Feteira, Di Zhou, Dawei Wang, Shujun Zhang, and Ian M Reaney. Electroceramics for high-energy density capacitors: Current status and future perspectives. *Chemical Reviews*, 121(10):6124–6172, April 2021.

[6] Ian R. McNab. Large-scale pulsed power opportunities and challenges. *IEEE Transactions on Plasma Science*, 42(5):1118–1127, May 2014.

[7] Minzheng Yang, Mengfan Guo, Erxiang Xu, Weibin Ren, Danyang Wang, Sean Li, Shujun Zhang, Ce-Wen Nan, and Yang Shen. Polymer nanocomposite dielectrics for capacitive energy storage. *Nature Nanotechnology*, 19(5):588–603, January 2024.

[8] Knowles Capacitors. Multilayer ceramic capacitors in automotive. *Power Electronics Europe*, 36(2), May 2017.

[9] Ravindranath Tagore Yadlapalli, RamaKoteswara Rao Alla, Rajani Kandipati, and Anuradha Kotapati. Super capacitors for energy storage: Progress, applications and challenges. *Journal of Energy Storage*, 49:104194, May 2022.

[10] John David Jackson. *Classical Electrodynamics*. John Wiley & Sons, Nashville, TN, 3 edition, July 1998.

[11] Charles Kittel. *Introduction to solid state physics*. John Wiley & Sons, Nashville, TN, 8 edition, October 2004.

[12] Robert Clark. Emerging applications for high k materials in vlsi technology. *Materials*, 7(4):2913–2944, April 2014.

[13] Chun Zhao, Ce Zhao, Stephen Taylor, and Paul Chalker. Review on non-volatile memory with high-k dielectrics: Flash for generation beyond 32 nm. *Materials*, 7(7):5117–5145, July 2014.

[14] John Robertson. High dielectric constant gate oxides for metal oxide si transistors. *Reports on Progress in Physics*, 69(2):327–396, December 2005.

[15] K. Mistry, R. Chau, C.-H. Choi, G. Ding, K. Fischer, T. Ghani, R. Grover, W. Han, D. Hanken, M. Hattendorf, J. He, C. Allen, J. Hicks, R. Huessner, D. Ingerly, P. Jain, R. James, L. Jong, S. Joshi, C. Kenyon, K. Kuhn, K. Lee, C. Auth, H. Liu, J. Maiz, B. McIntyre, P. Moon, J. Neirynck, S. Pae, C. Parker, D. Parsons, C. Prasad, L. Pipes, B. Beattie, M. Prince, P. Ranade, T. Reynolds, J. Sandford, L. Shifren, J. Sebastian, J. Seiple, D. Simon, S. Sivakumar, P. Smith, D. Bergstrom, C. Thomas, T. Troeger, P. Vandervoorn, S. Williams, K. Zawadzki, M. Bost, M. Brazier, M. Buehler, and A. Cappellani. A 45nm logic technology with high-k+metal gate transistors, strained silicon, 9 cu interconnect layers, 193nm dry patterning, and 100packaging. In *2007 IEEE International Electron Devices Meeting*. IEEE, December 2007.

[16] Se Eun Kim, Ju Young Sung, Yewon Yun, Byeongjun Jeon, Sang Mo Moon, Han Bin Lee, Chae Hyun Lee, Hae Jun Jung, Jae-Ung Lee, and Sang Woon Lee. Atomic layer deposition of high-k and metal thin films for high-performance dram capacitors: A brief review. *Current Applied Physics*, 64:8–15, August 2024.

[17] Kanghoon Yim, Youn Yong, Joohee Lee, Kyuhyun Lee, Ho-Hyun Nahm, Jiho Yoo, Chanhee Lee, Cheol Seong Hwang, and Seungwu Han. Novel high-κ dielectrics for next-generation electronic devices screened by automated ab initio calculations. *NPG Asia Materials*, 7(6):e190–e190, June 2015.

[18] Binghao Wang, Wei Huang, Lifeng Chi, Mohammed Al-Hashimi, Tobin J. Marks, and Antonio Facchetti. High-kgate dielectrics for emerging flexible and stretchable electronics. *Chemical Reviews*, 118(11):5690–5754, May 2018.

[19] Ambarish Kulkarni, Samira Siahrostami, Anjli Patel, and Jens K. Nørskov. Understanding catalytic activity trends in the oxygen reduction reaction. *Chemical Reviews*, 118(5):2302–2312, February 2018.

[20] Xiao Xia Wang, Mark T. Swihart, and Gang Wu. Achievements, challenges and perspectives on cathode catalysts in proton exchange membrane fuel cells for transportation. *Nature Catalysis*, 2(7):578–589, July 2019.

[21] Yanyan Sun, Shlomi Polani, Fang Luo, Sebastian Ott, Peter Strasser, and Fabio Dionigi. Advancements in cathode catalyst and cathode layer design for proton exchange membrane fuel cells. *Nature Communications*, 12(1), October 2021.

[22] Michael M. Whiston, Inês L. Azevedo, Shawn Litster, Kate S. Whitefoot, Constantine Samaras, and Jay F. Whitacre. Expert assessments of the cost and expected future performance of proton exchange membrane fuel cells for vehicles. *Proceedings of the National Academy of Sciences*, 116(11):4899–4904, February 2019.

[23] Mohammed Jourdan, Hamid Mounir, and Abdellatif El Marjani. Compilation of factors affecting durability of proton exchange membrane fuel cell (pemfc). In *2014 International Renewable and Sustainable Energy Conference (IRSEC)*, page 542–547. IEEE, October 2014.

[24] Velia Fabiola Valdés-López, Tom Mason, Paul R. Shearing, and Dan J.L. Brett. Carbon monoxide poisoning and mitigation strategies for polymer electrolyte membrane fuel cells – a review. *Progress in Energy and Combustion Science*, 79:100842, July 2020.

[25] Yanghua He, Shengwen Liu, Cameron Priest, Qiurong Shi, and Gang Wu. Atomically dispersed metal–nitrogen–carbon catalysts for fuel cells: advances in catalyst design, electrode performance, and durability improvement. *Chemical Society Reviews*, 49(11):3484–3524, 2020.

[26] J. K. Nørskov, J. Rossmeisl, A. Logadottir, L. Lindqvist, J. R. Kitchin, T. Bligaard, and H. Jónsson. Origin of the overpotential for oxygen reduction at a

fuel-cell cathode. *The Journal of Physical Chemistry B*, 108(46):17886–17892, October 2004.

[27] Hideshi Ooka, Jun Huang, and Kai S. Exner. The sabatier principle in electrocatalysis: Basics, limitations, and extensions. *Frontiers in Energy Research*, 9, May 2021.

[28] T. Bligaard, J.K. Nørskov, S. Dahl, J. Matthiesen, C.H. Christensen, and J. Sehested. The brønsted–evans–polanyi relation and the volcano curve in heterogeneous catalysis. *Journal of Catalysis*, 224(1):206–217, May 2004.

[29] F. Abild-Pedersen, J. Greeley, F. Studt, J. Rossmeisl, T. R. Munter, P. G. Moses, E. Skúlason, T. Bligaard, and J. K. Nørskov. Scaling properties of adsorption energies for hydrogen-containing molecules on transition-metal surfaces. *Physical Review Letters*, 99(1):016105, July 2007.

[30] Nitish Govindarajan, Marc T. M. Koper, Evert Jan Meijer, and Federico Calle-Vallejo. Outlining the scaling-based and scaling-free optimization of electrocatalysts. *ACS Catalysis*, 9(5):4218–4225, March 2019.

[31] Aleksandra Vojvodic and Jens K. Nørskov. New design paradigm for heterogeneous catalysts. *National Science Review*, 2(2):140–143, April 2015.

[32] Javier Pérez-Ramírez and Núria López. Strategies to break linear scaling relationships. *Nature Catalysis*, 2(11):971–976, October 2019.

[33] Xiang Ao, Haoran Wang, Xia Zhang, and Chundong Wang. Atomically dispersed metal–nitrogen–carbon catalysts for acidic oxygen reduction reaction. *ACS Applied Materials & Interfaces*, January 2025.

[34] Yuyan Shao, Jean-Pol Dodelet, Gang Wu, and Piotr Zelenay. Pgm-free cathode catalysts for pem fuel cells: A mini-review on stability challenges. *Advanced Materials*, 31(31), February 2019.

[35] Nadeem Baig, Irshad Kammakakam, and Wail Falath. Nanomaterials: a review of synthesis methods, properties, recent progress, and challenges. *Materials Advances*, 2(6):1821–1871, 2021.

[36] Xiangbo Meng, Xinwei Wang, Dongsheng Geng, Cagla Ozgit-Akgun, Nathanaelle Schneider, and Jeffrey W. Elam. Atomic layer deposition for nanomaterial synthesis and functionalization in energy technology. *Materials Horizons*, 4(2):133–154, 2017.

[37] Luke D. Geoffrion and Grégory Guisbiers. Quantum confinement: Size on the grill! *Journal of Physics and Chemistry of Solids*, 140:109320, May 2020.

[38] Mingcong Yang, Shaojie Wang, Jing Fu, Yujie Zhu, Jiajie Liang, Sang Cheng, Shixun Hu, Jun Hu, Jinliang He, and Qi Li. Quantum size effect to induce colossal high-temperature energy storage density and efficiency in polymer/inorganic cluster composites. *Advanced Materials*, 35(30), June 2023.

[39] David J.T. Hally and Irina Paci. Low-frequency polarization in molecular-scale noble-metal/metal-oxide nanocomposites. *Nanoscale*, 10(20):9583–9593, 2018.

[40] T. K. Kundu and D. Chakravorty. Nanocomposites of lead-zirconate-titanate glass ceramics and metallic silver. *Applied Physics Letters*, 67(18):2732–2734, October 1995.

[41] G.C. Vezzoli, M.F. Chen, and J. Caslavsky. New high dielectric strength materials: Micro/nanocomposites of suspended au clusters in sio2/sio2 al2o3 li2o gels. *Ceramics International*, 23(2):105–108, January 1997.

[42] Ramasamy Ravindran, Maslina Othman, Minseong Yun, Nivedita Biswas, Narendra Mehta, Suchi Guha, Keshab Gangopadhyay, and Shubhra Gangopadhyay. Enhanced dielectric constant of hfo2 and al2o3 thin-films with silver nanoparticles. *ECS Transactions*, 3(3):535–544, October 2006.

[43] R. Ravindran, K. Gangopadhyay, S. Gangopadhyay, N. Mehta, and N. Biswas. Permittivity enhancement of aluminum oxide thin films with the addition of silver nanoparticles. *Applied Physics Letters*, 89(26), December 2006.

[44] Mohsin Saleem, Muhammad Shoaib Butt, Adnan Maqbool, Malik Adeel Umer, Muhammad Shahid, Farhan Javaid, Rizwan Ahmed Malik, Hamid Jabbar, Hafiz Muhammad Waseem Khalil, Lim Dong Hwan, Minsoo Kim, Bo-Kun Koo, and Soon Jong Jeong. Percolation phenomena of dielectric permittivity of a microwave-sintered batio3–ag nanocomposite for high energy capacitor. *Journal of Alloys and Compounds*, 822:153525, May 2020.

[45] Alexander I. Sidorov, Alexey V. Nashchekin, Rene A. Castro, Irina N. Anfimova, and Tatiana V. Antropova. Optical and dielectric properties of nanocomposites on base nanoporous glasses with silver and silver iodide nanowires. *Physica B: Condensed Matter*, 603:412764, February 2021.

[46] Zongrong Wang, Tao Hu, Xiaoge Li, Gaorong Han, Wenjian Weng, Ning Ma, and Piyi Du. Nano conductive particle dispersed percolative thin film ceramics with high permittivity and high tunability. *Applied Physics Letters*, 100(13), March 2012.

[47] Archita N. S. Adluri, Brett Henderson, and Irina Paci. Tuning the dielectric response in a nanocomposite material through nanoparticle morphology. *RSC Advances*, 12(17):10778–10787, 2022.

[48] Zisheng Zhang, Borna Zandkarimi, Julen Munarriz, Claire E. Dickerson, and Anastassia N. Alexandrova. Fluxionality of subnano clusters reshapes the activity volcano of electrocatalysis. *ChemCatChem*, 14(15), June 2022.

[49] Jianbo Wu and Hong Yang. Platinum-based oxygen reduction electrocatalysts. *Accounts of Chemical Research*, 46(8):1848–1857, June 2013.

[50] Zhen Zhang, Xiyi Dong, Tingting Gu, Qilong Li, Mengyu Liu, Minzhi Li, Weihua Zhu, and Xu Liang. How the macrocyclic precursors influence the m-n-c catalysts? preparation and their applications on the electrochemically catalyzed hydrogen evolutions. *Journal of Alloys and Compounds*, 991:174518, July 2024.

[51] Xialiang Li, Haitao Lei, Lisi Xie, Ni Wang, Wei Zhang, and Rui Cao. Metalloporphyrins as catalytic models for studying hydrogen and oxygen evolution and oxygen reduction reactions. *Accounts of Chemical Research*, 55(6):878–892, February 2022.

[52] Zuozhong Liang, Hongbo Guo, Guojun Zhou, Kai Guo, Bin Wang, Haitao Lei, Wei Zhang, Haoquan Zheng, Ulf-Peter Apfel, and Rui Cao. Metal–organic-framework-supported molecular electrocatalysis for the oxygen reduction reaction. *Angewandte Chemie International Edition*, 60(15):8472–8476, March 2021.

[53] Siqi Wu, Xinyue Qu, Jiawei Zhu, Xiaobin Liu, Huimin Mao, Ketao Wang, Guizhong Zhou, Jingqi Chi, and Lei Wang. Recent advances in metal-organic

frameworks derived electrocatalysts for oxygen reduction reaction. *Journal of Alloys and Compounds*, 970:172518, January 2024.

[54] Pavel M. Usov, Brittany Huffman, Charity C. Epley, Matthew C. Kessinger, Jie Zhu, William A. Maza, and Amanda J. Morris. Study of electrocatalytic properties of metal–organic framework pcn-223 for the oxygen reduction reaction. *ACS Applied Materials & Interfaces*, 9(39):33539–33543, April 2017.

[55] Magdalena Ola Cichocka, Zuozhong Liang, Dawei Feng, Seoin Back, Samira Siahrostami, Xia Wang, Laura Samperisi, Yujia Sun, Hongyi Xu, Niklas Hedin, Haoquan Zheng, Xiaodong Zou, Hong-Cai Zhou, and Zhehao Huang. A porphyrinic zirconium metal–organic framework for oxygen reduction reaction: Tailoring the spacing between active-sites through chain-based inorganic building units. *Journal of the American Chemical Society*, 142(36):15386–15395, August 2020.

[56] Tyler Sours, Anjli Patel, Jens Nørskov, Samira Siahrostami, and Ambarish Kulkarni. Circumventing scaling relations in oxygen electrochemistry using metal–organic frameworks. *The Journal of Physical Chemistry Letters*, 11(23):10029–10036, November 2020.

[57] Jakub D. Baran, Henrik Grönbeck, and Anders Hellman. Analysis of porphyrines as catalysts for electrochemical reduction of o2 and oxidation of h2o. *Journal of the American Chemical Society*, 136(4):1320–1326, January 2014.

[58] Joseph H. Montoya, Linsey C. Seitz, Pongkarn Chakthranont, Aleksandra Vojvodic, Thomas F. Jaramillo, and Jens K. Nørskov. Materials for solar fuels and chemicals. *Nature Materials*, 16(1):70–81, December 2016.

[59] Ashwin Ramasubramaniam and Emily A. Carter. Coupled quantum–atomistic and quantum–continuum mechanics methods in materials research. *MRS Bulletin*, 32(11):913–918, November 2007.

[60] Laura E. Ratcliff, Stephan Mohr, Georg Huhs, Thierry Deutsch, Michel Masella, and Luigi Genovese. Challenges in large scale quantum mechanical calculations. *WIREs Computational Molecular Science*, 7(1), November 2016.

[61] W. G. Noid. Perspective: Advances, challenges, and insight for predictive coarse-grained models. *The Journal of Physical Chemistry B*, 127(19):4174–4207, May 2023.

[62] Jaewoon Jung, Wataru Nishima, Marcus Daniels, Gavin Bascom, Chigusa Kobayashi, Adetokunbo Adedoyin, Michael Wall, Anna Lappala, Dominic Phillips, William Fischer, Chang-Shung Tung, Tamar Schlick, Yuji Sugita, and Karissa Y. Sanbonmatsu. Scaling molecular dynamics beyond 100, 000 processor cores for large-scale biophysical simulations. *Journal of Computational Chemistry*, 40(21):1919–1930, April 2019.

[63] Jaewoon Jung, Chigusa Kobayashi, Kento Kasahara, Cheng Tan, Akiyoshi Kuroda, Kazuo Minami, Shigeru Ishiduki, Tatsuo Nishiki, Hikaru Inoue, Yutaka Ishikawa, Michael Feig, and Yuji Sugita. New parallel computing algorithm of molecular dynamics for extremely huge scale biological systems. *Journal of Computational Chemistry*, 42(4):231–241, November 2020.

[64] Frank Jensen. *Introduction to Computational Chemistry 3rd. ed.* Wiley, 3rd ed. edition, 2017.

[65] William Dawson, Augustin Degomme, Martina Stella, Takahito Nakajima, Laura E. Ratcliff, and Luigi Genovese. Density functional theory calculations of large systems: Interplay between fragments, observables, and computational complexity. *WIREs Computational Molecular Science*, 12(3), October 2021.

[66] Hao Zhang, Parinaz Moazzezi, Juanjuan Ren, Brett Henderson, Cristina Cordoba, Vishal Yeddu, Arthur M. Blackburn, Makhsud I. Saidaminov, Irina Paci, Stephen Hughes, and Reuven Gordon. Coupling perovskite quantum dot pairs in solution using a nanoplasmonic assembly. *Nano Letters*, 22(13):5287–5293, June 2022.

[67] James McFarlane, Brett Henderson, Sofia Donnecke, and J. Scott McIndoe. An information-rich graphical representation of catalytic cycles. *Organometallics*, 38(21):4051–4053, October 2019.

[68] Peter J. H. Williams, Charles Killeen, Ian C. Chagunda, Brett Henderson, Sofia Donnecke, Wil Munro, Jaspreet Sidhu, Denaisha Kraft, David A. Harrington, and J. Scott McIndoe. Continuous addition kinetic elucidation: catalyst and

reactant order, rate constant, and poisoning from a single experiment. *Chemical Science*, 14(36):9970–9977, 2023.

Chapter 2

Overview of Methods

As discussed in Chapter 1, this dissertation applies a variety of computational methods to the study of nanostructured materials with the goal of balancing the complex trade-offs that these materials pose between scalability and transferrability. The point of the present chapter is not to provide an exhaustive exposition of each of these methods—for the most part, excellent descriptions already exist in textbooks. Rather, this chapter aims to contextualize the methods, providing brief theoretical introductions and definitions that motivate the use of each approach for its respective application later in the dissertation. After a brief definition of notation (Section 2.1), the chapter proceeds with an introduction to the electronic structure problem defined by the electronic Schrödinger equation (Section 2.2). Next, we review the electronic structure methods that this dissertation employs to solve this problem, which include both wave function and density functional theories (Section 2.3). Particular emphasis is placed on the trade-off between computational scaling and accuracy for each approach and the numerical parameters like basis set size that affect these trade-offs. The considerations explored in this section are thus echoed throughout all subsequent chapters. Next, Section 2.4 introduces both classical and quantum theories of electronic polarization in molecules and solids. By allowing the calculation of the effective permittivities of nanocomposites and polarizabilities of clusters, these theories underpin Chapters 3, 4, and 5.

2.1 Notation and Units

An effort is made to adopt a consistent and readable notation for equations throughout the present and all subsequent chapters. As a general rule, *vectors*, *tensors*, and *matrices* will all be written in **boldface** type, whereas normal font weight is used for scalars. Table 2.1 list other symbols used commonly throughout the text.

Table 2.1: Mathematical notation.

Notation	Definition
$\hat{\mathbf{O}}$	A general linear operator.
∇	The gradient. In 3D Cartesian coordinates $\nabla = \left(\frac{\partial}{\partial x}, \frac{\partial}{\partial y}, \frac{\partial}{\partial z}\right)$.
∇^2	The Laplacian. In 3D Cartesian coordinates $\nabla^2 = \left(\frac{\partial^2}{\partial x^2} + \frac{\partial^2}{\partial y^2} + \frac{\partial^2}{\partial z^2}\right)$.
Δ	Finite difference. $\Delta x = x_1 - x_0$.
v_i	The i^{th} element of vector $\mathbf{v}$.
A_{ij}	The element in the i^{th} row and j^{th} column of matrix $\mathbf{A}$ or the i, j component of a second-order Cartesian tensor $\mathbf{A}$.
$\mathbf{I}$	The identity matrix.
δ_{ij}	The Kronecker delta. $\delta_{ij} = 1$ if $i = j$. Else, $\delta_{ij} = 0$.
$\delta(x)$	The Dirac delta function. $\delta(x) = 0$ for all $x \neq 0$, and $\int_{a-\epsilon}^{a+\epsilon} f(x)\delta(x-a)dx = f(a)$ for $\epsilon > 0$.
$F[f(\mathbf{x})]$	Denotes that F is a functional of the function $f(\mathbf{x})$.
$\langle f \vert g \rangle$	$\int_{-\infty}^{\infty} f^*(\mathbf{x}) g(\mathbf{x}) d\mathbf{x}$, where f^* is the complex conjugate of f.
$\langle f \vert \hat{\mathbf{O}} \vert g \rangle$	$\int_{-\infty}^{\infty} f^*(\mathbf{x}) \hat{\mathbf{O}} g(\mathbf{x}) d\mathbf{x}$.

Continued on next page

Notation	Definition
$\langle\hat{\mathbf{O}}\rangle$	Expectation value of $\hat{\mathbf{O}}$ for a given state. For state Ψ, $\langle\hat{\mathbf{O}}\rangle = \langle\Psi\|\hat{\mathbf{O}}\|\Psi\rangle$.
$\|\mathbf{x}\|$	Norm of vector $\mathbf{x}$. Equal to $\sqrt{\langle\mathbf{x}\|\mathbf{x}\rangle}$ in general, or $\sqrt{x^2+y^2+z^2}$ for a 3D Cartesian vector.
$\|x\|$	Absolute value of a scalar x.
$\Psi(\{\mathbf{x}_i\})$	Multi-determinant wave function, where $\mathbf{x}_i$ are the spatial and spin coordinates of the i^{th} electron and i runs from 1 to N.
$\Phi(\{\mathbf{x}_i\})$	Single-determinant wave function, with $\mathbf{x}_i$ defined as above for Ψ.
ψ	Independent-particle wave function, or spatial orbital. Occupied by up to 2 electrons.
ϕ	Single-particle spin-orbital. Consists of a spatial orbital multiplied by an α or β spin function.
$\boldsymbol{\epsilon}^0$	Low-frequency permittivity tensor.
$\boldsymbol{\epsilon}^\infty$	High-frequency, or optical, permittivity tensor.

2.1.1 Atomic Units

Unless otherwise stated, all of the equations in this chapter are written using Hartree atomic units, or a.u., with fundamental constants equal to unity omitted. Under this system of units, the reduced Planck constant $\hbar$, electron mass m_e, and magnitude of the electron charge e are defined to be 1, and the permittivity of free space ϵ_0 is defined to be $1/4\pi$.[1] This simplifies the expressions for the electronic Hamiltonian and results in numerical quantities that vary on scales relevant to atoms and molecules. We will occasionally reference specific atomic units by name—in particular the unit for length is the *Bohr*, and the unit of energy is the *Hartree*.

2.2 The Electronic Structure Problem

Repeatedly throughout this dissertation, we will find ourselves concerned with the evaluating the energies of chemical systems. On their own, these energies allow us to compare the stability of different atomic structures or electronic states and—when combined with statistical thermodynamics—evaluate the thermodynamics of reaction mechanisms. Furthermore, the derivatives of these energies allow access to geometry optimizations and dynamics (derivatives with respect to nuclear coordinates) as well as various properties, such as vibrational modes (second derivatives with respect to nuclear coordinates), dipole moments (derivative with respect to external field) and responses to external perturbations like electric fields (higher order and mixed derivatives with respect to different perturbations). Thus, accessing the energy and its various derivatives for molecules, clusters, and unit cells of materials is the essential goal of this dissertation.

The allowable energies of a chemical system can be obtained by solving the Time-Independent Schrödinger Equation (TISE):

$$\hat{\mathbf{H}}\Psi = E\Psi. \tag{2.1}$$

This amounts to finding the eigenfunctions Ψ and corresponding eigenenergies E of the chemical Hamiltonian $\hat{\mathbf{H}}$. Almost all of this dissertation deals specifically with the *ground state* of the studied system, which is the overall lowest energy TISE solution (E_{GS}, Ψ_{GS}). In specific cases, we will also concern ourselves with the lowest energy solution that satisfies certain symmetry requirements, such as when we compute adiabatic spin-splitting energies in Chapter 6.

For a chemical system, the Hamiltonian may be written as a sum of terms expressing the kinetic energy of the constituent nuclei and electrons as well as the potential energy due to the Coulombic interactions between them.[1] We first express this Hamiltonian as it is written in S.I. units, so that all of the involved physical constants are explicit:

$$\hat{\mathbf{H}} = \hat{\mathbf{T}}_{\mathrm{n}} + \hat{\mathbf{T}}_{\mathrm{e}} + \hat{\mathbf{V}}_{\mathrm{nn}} + \hat{\mathbf{V}}_{\mathrm{ne}} + \hat{\mathbf{V}}_{\mathrm{ee}} \tag{2.2}$$

$$= -\sum_{A=1}^{M} \frac{\hbar^2}{2m_A}\nabla_A^2 - \sum_{i=1}^{N} \frac{\hbar^2}{2m_e}\nabla_i^2 + \sum_{A=1}^{M}\sum_{B>A}^{M} \frac{Z_A Z_B e^2}{4\pi\epsilon_0 r_{AB}} - \sum_{i=1}^{N}\sum_{A=1}^{M} \frac{Z_A e^2}{4\pi\epsilon_0 r_{iA}} + \sum_{i=1}^{N}\sum_{j>i}^{N} \frac{e^2}{4\pi\epsilon_0 r_{ij}}. \tag{2.3}$$

The terms on the right hand side of these expressions are, respectively, the nuclear kinetic energy, electronic kinetic energy, the nuclear-nuclear repulsion, nuclear-electronic attraction, and electron-electron repulsion. A and B are used as nuclear indices while i, j are used as electron indices, such that this system is composed of M atoms with a total of N electrons. Furthermore, Z_A is the atomic number of atom A and m_A is its nuclear mass. The notation r_{pq} is a shorthand denoting the distance between particles p and q ($r_{pq} = \|\mathbf{r_p} - \mathbf{r_q}\|$), and ∇_p^2 is the Laplace operator with respect to the Cartesian coordinates of particle p. The remaining constants are the electron mass m_e, the reduced Planck constant $\hbar$, the magnitude of the electron charge e, and the permittivity of free space ϵ_0. Re-writing the Hamiltonian in atomic units using the identities from Section 2.1.1 produces the simpler form

$$\hat{\mathbf{H}} = -\sum_{A=1}^{M} \frac{1}{2m_A}\nabla_A^2 - \frac{1}{2}\sum_{i=1}^{N} \nabla_i^2 + \sum_{A=1}^{M}\sum_{B>A}^{M} \frac{Z_A Z_B}{r_{AB}} - \sum_{i=1}^{N}\sum_{A=1}^{M} \frac{Z_A}{r_{iA}} + \sum_{i=1}^{N}\sum_{j>i}^{N} \frac{1}{r_{ij}}. \tag{2.4}$$

In the present work, we universally adopt the *Born-Oppenheimer (BO) Approximation*, which assumes that the nuclear and electronic motion can be decoupled due to the significantly larger mass and slower motion of the nuclei.[1] That is, the nuclei are taken to be fixed when solving for the electronic motion. This allows the total wave function to be written as a product of electronic and nuclear wave functions. The electronic wave function and energy can then be obtained by solving the electronic Schrödinger equation,

$$\hat{\mathbf{H}}_{\mathrm{elec}}\Psi = E_{\mathrm{elec}}\Psi \tag{2.5}$$

$$\hat{\mathbf{H}}_{\mathrm{elec}} = \hat{\mathbf{T}}_{\mathrm{e}} + \hat{\mathbf{V}}_{\mathrm{nn}} + \hat{\mathbf{V}}_{\mathrm{ne}} + \hat{\mathbf{V}}_{\mathrm{ee}}. \tag{2.6}$$

The nuclear kinetic energy term has been dropped, and with fixed nuclei, $\hat{\mathbf{V}}_{\mathrm{nn}}$ is now simply a constant.[†] The nuclear motion is calculated after solving for the electronic wave function, with the electronic energy at different nuclear configurations constructing a *potential energy surface* on which the nuclei are said to move.[1] Despite the BO approximation, solving the *electronic structure problem* of Equation (2.5) is very demanding since the electron-electron repulsion term $\hat{\mathbf{V}}_{\mathrm{ee}}$ prevents separation of the Hamiltonian into terms involving only individual electronic degrees of freedom. The motions of electrons are thus coupled, or *correlated*. In fact, analytical solutions to Equation (2.5) only exist for single-electron systems.

All multi-electron systems require a numerical approach to the electronic structure problem, which in turn demands an inevitable trade-off between accuracy and resource requirements brought about by various approximations. In the present dissertation, these approximations take the form of 1) discretization, as all wave functions are expanded in a finite basis set, and 2) modifications of the Hamiltonian and/or restrictions on the form of the wave function that make solving Equation (2.5) less laborious. We first discuss discretization, which in this thesis refers to the expansion of electronic wavefunctions in finite basis sets. Afterwards, we turn our attention to the second point, which refers to the selection of a particular *electronic structure method*.

2.2.1 Basis Sets

In calculations on finite systems, molecular orbitals were expanded in a set of atom-centered Gaussian basis functions. Generally, increasing the number of basis set functions increases computational demand, with scaling dependent on the particular electronic structure method (Section 2.3.5). With this in mind, we strove to use the largest basis sets that were computationally feasible for each application. The Ahlrichs (Def2) basis sets were employed for nearly all DFT calculations for finite systems.[2] These functions consist of a relatively small number of primitive Gaussian functions (i.e. they are loosely contracted), which makes them quite efficient, and they also demonstrate consistent accuracy across different electronic structure methods. Def2 basis sets were designed to be used with effective core potentials (ECPs) for atoms heavier than Kr. Thus, while almost all molecular calculations were performed

[†]this term is sometimes omitted from $\hat{\mathbf{H}}_{\mathrm{elec}}$ and added to the energy after solution of the electronic Schrödinger equation

with an all-electron basis, in Chapter 5, we used ECPs for silver clusters.[3]

Basis sets with extra polarization and diffuse basis functions were used in particular contexts. In the porphyrin calculations of Chapter 6, we considered it important to use basis sets with an extra set of polarization functions on the metal atoms (denoted Def2-TZVPP and Def2-QZVPP). These functions are important for describing the metal-centered orbitals in a complex environment, especially for the correlated wavefunction theory calculations performed in that chapter. Meanwhile, diffuse functions can be important for describing noncovalent interactions,[4, 5, 6] anions,[7] and polarizability.[8] Thus, both augmented polarization-consistent (aug-pc-3) sets[9] and augmented Karlsrhue basis sets (def2-XZVPD)[8] were used for calculating the polarizabilities of small molecules and clusters, respectively, in Chapter 5. Meanwhile, augmented correlation-consistent basis sets (aug-cc-pVXZ)[10, 11, 12] were used for calculating binding energies to porphyrins using correlated wave function theory in Chapter 6. In addition to possessing diffuse functions, these basis sets were optimized specifically for correlated calculations.[13]

Basis sets take a different form for the periodic calculations in this dissertation. While we briefly use a basis of finite pseudoatomic orbitals for treating silver clusters in Chapter 4, the remaining calculations are performed using plane-wave basis sets. These basis sets are systematically improvable—one only needs to include increasingly high-frequency plane waves to yield better and better results. Compared to the number of basis functions in molecular calculations, many more plane waves are typically required to expand the wavefunction of a unit cell of material, but the computational efficiency of plane wave algorithms mean this trade-off is generally worth it for periodic calculations. More detail about the size and convergence properties of plane wave basis sets is given in Section 2.3.3.

2.3 Electronic Structure Methods

We now discuss various approximations to the electronic Hamiltonian and forms of the electronic wave function that were used throughout this dissertation. We introduce these methods mostly at a conceptual level, only providing mathematical detail insofar as it clarifies points made in later chapters. Detailed descriptions of these methods abound elsewhere—in particular, the work of Szabo and Ostlund[14], Jensen[1], Atkins and Friedman,[15] Martin [16] were used extensively by the present author to gain more understanding. The electronic structure methods in this dis-

sertation can be grouped into the broad classes of wave function theory (WFT) and Density Functional Theory (DFT) methods. Figure 2.1 presents a tree diagram of the electronic structure methods used throughout this dissertation.

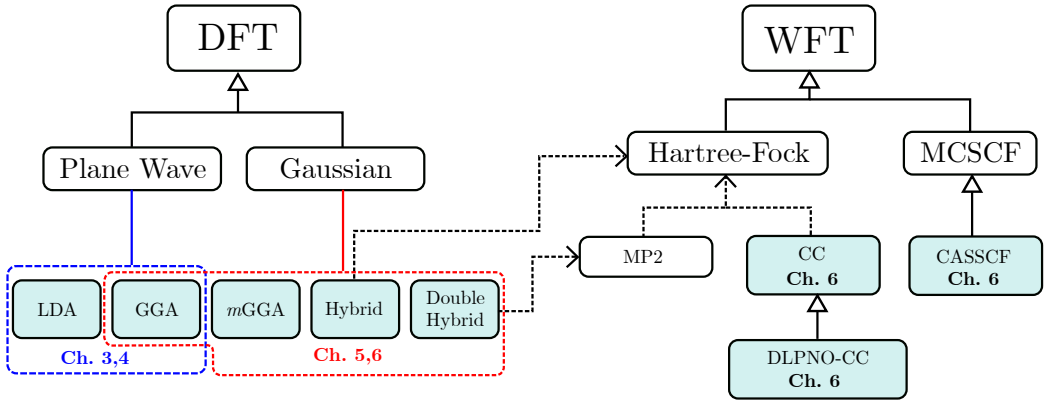

Figure 2.1: Overview of the electronic structure methods used throughout this dissertation. Dashed arrows indicate that the method at the arrow's tail depends on the method at its head. Solid arrows indicate that the method at the arrow's tail is a specific variety of the more general method at the arrow's head. Blue and red lines group the levels of density functional approximation used with either Plane Wave or Gaussian DFT in this dissertation. Light blue boxes indicate that these are the specific methods used in the dissertation, with chapters where the methods are used indicated (e.g. Plane Wave LDA and GGA appear in Chapters 3 and 4) All acronyms are defined in the text.

2.3.1 Wave Function Theories

Hartree-Fock

The Hartree-Fock (HF) method[17, 18, 19] serves as the foundation for several the wave function methods used in Chapter 6 for studying metalloporphyrins. In the HF approach, the wave function is formulated as a Slater determinant of one-electron orbitals, which is antisymmetric with respect to exchange of electrons as demanded by the Pauli exclusion principle.[18] Electron-electron repulsion is only accounted for in a *mean field* way—that is, each electron is treated as experiencing the average, smeared-out potential created by all other electrons. Because this potential depends on orbitals of those other electrons, and hence on the Slater determinant, the Hartree-Fock equations must be solved iteratively until self-consistency is achieved. Thus, it is often referred to as a Self-Consistent Field (SCF) method.[14]

As a mean-field method, the HF approach neglects some of the correlations between electrons, which in reality experience a potential that depends on the exact coordinates of all other electrons. In fact, *correlation energy* is defined as the difference between the energy of the exact ground state wave function and the HF one in the basis set limit.[15] Due to the enforced antisymmetry of the HF wave function, HF theory does include the *exchange energy*, also called Fermi correlation, a stabilizing effect that accounts only for correlations between electrons of the same spin.[15, 1] As a result, HF is known to overstabilize electronic states with many unpaired electron spins (high-spin states),[20, 21, 22] a crucial consideration when determining ground states of organometallic complexes in Chapter 6.

Many post-HF methods have been developed to recover at least some of the correlation energy that is missing from HF theory. In general, they do so by expanding the full wave function in a basis of Slater determinants. The HF determinant is formally the lowest-energy single-determinant wave function, and in many cases it represents a good first-order approximation to the wave function. Thus, post-HF methods generally begin with the HF determinant Φ_{HF} as a *reference*, called Φ_0, and additional determinants are constructed as excitations of one or more electrons from occupied to virtual HF orbitals.[1] Thus, the full wave function can be expressed as

$$\Psi = a_0\Phi_0 + \sum_{i=1} a_i\Phi_i. \tag{2.7}$$

Inclusion of all possible excited determinants yields the Full Configuration Interaction wave function, which is the exact wave function in a given basis set.[14] However, this is intractable for all but the smallest chemical systems, so post-HF methods truncate the sum in Equation 2.7, attempting to include only the most important excited determinants in order to most economically recover correlation energy. Different post-HF methods vary in their approach to this truncation, each offering a specific trade-off between accuracy and computational efficiency. In particular, coupled-cluster (CC) has become incredibly popular for both main group and transition metal chemistry because of its favorable trade-off in this regard.

Coupled Cluster

In coupled cluster, the wave function is assumed to have the following form, or *ansatz*:[23, 24]

$$\Psi_{\mathrm{CC}} = e^{\hat{\mathbf{T}}}\Phi_0. \tag{2.8}$$

The reference wave function Φ_0 is often taken to be the HF determinant. However, for transition metal and open-shell systems, it can be beneficial to use a determinant constructed from occupied orbitals from a DFT calculation,[25, 26, 27] which we do in Chapter 6. The *cluster operator* $\hat{\mathbf{T}}$ is defined as

$$\hat{\mathbf{T}} = \hat{\mathbf{T}}_1 + \hat{\mathbf{T}}_2 + \hat{\mathbf{T}}_3 + ... + \hat{\mathbf{T}}_{N_{\mathrm{elec}}}, \tag{2.9}$$

where $\hat{\mathbf{T}}_i$ is an operator that generates all i-electron excitations from a reference determinant. For instance, $\hat{\mathbf{T}}_2$ generates all double excitations, as in

$$\hat{\mathbf{T}}_2\Phi = \sum_{ab}\sum_{ij} t_{ij}^{ab}\Phi_{ij}^{ab}, \tag{2.10}$$

where Φ_{ij}^{ab} is the determinant formed by promoting electrons from occupied orbitals i and j to virtual orbitals a and b. The coefficients t_{ij}^{ab} are called the *double excitation amplitudes*.

In Chapter 6, we utilize Coupled Cluster with explicit Singles and Doubles plus perturbative Triples excitations [CCSD(T)]. This means that the cluster operator is truncated to only include single and double excitations ($\hat{\mathbf{T}} = \hat{\mathbf{T}}_1 + \hat{\mathbf{T}}_2$). By expanding the exponential in Equation (2.8) as a Taylor series, one can show that the resulting wave function will contain all single and double excitations, plus higher-order excitations from repeated application of the two lower-order excitation operators $\hat{\mathbf{T}}_1$ and $\hat{\mathbf{T}}_2$.[1] Obtaining the coupled cluster wave function and energy requires solving for the single and double excitation amplitudes t_i^a and t_{ij}^{ab}. Inclusion of triples in the cluster operator is generally too expensive for systems with more than several atoms. Thus, in the CCSD(T) approach, the approximate effect of triples on the energy is obtained more economically via perturbation theory.[28, 29] This approach is often touted as the "gold-standard" for main group molecules, yielding accurate geometries, electronic properties, and energies to comparable to experimental accuracy.[30, 31, 32, 33] In many cases it is also capable of providing reference-level accuracy for transition metal complexes.[34, 26, 35]

Local Coupled Cluster

In Chapter 6, we used Domain-Based Local Pair Natural Orbital CCSD(T) [DLPNO-CCSD(T)] to compute ORR pathway energetics that serve as a benchmark for DFT methods. Like other "local" coupled cluster variants, DLPNO-CCSD(T) takes advantage of the rapid drop-off in the correlation energy of and electron pair with distance—electrons that are far apart in a molecule are only weakly correlated. To make use of this, DLPNO-CCSD(T) localizes the occupied orbitals with the Foster-Boys method.[36] A set of Projected Atomic Orbitals (PAOs), which are also local in nature, is used to expand the virtual orbitals, and correlation domains of atoms neighboring the electrons in a pair are defined such that PAOs can be restricted to this domain when calculating pair correlation energies.[36] For the electron pairs that are admitted into the CCSD procedure, the virtual space is constructed from Pair Natural Orbitals (PNOs) expanded in the basis of PAOs, which make a rapidly converging basis set for correlated calculations.[37] Finally, a linear-scaling iterative algorithm is used to compute the triples correction.[38]

From the user's perspective, the accuracy of DLPNO-CCSD(T) is controlled via the definition of several cutoff parameters, with the final energy converging to the canonical CCSD(T) value as these parameters are pushed toward their most stringent values. For the CCSD portion of the calculation, the most important parameters are T_{CutDO}, which determines the size of the correlation domains, T_{CutPairs}, which determines the number of electron pairs that enter the CCSD iterations, and T_{CutPNO}, which determines the number of PNOs for each electron pair. The most important of these parameters, both in terms of accuracy and compute time, is T_{CutPNO}. Altun and colleagues have shown that the CCSD(T) energy converges smoothly as the parameter is decreased and suggested an extrapolation procedure for estimating the DLPNO-CCSD(T) energy in the Complete PNO Space (CPS) limit.[39] CPS extrapolation allows DLPNO-CCSD(T) energies to be calculated at a level much closer to canonical CCSD(T) for a given computational cost. This is useful for medium to large systems when high accuracy is required, but tightening the T_{CutPNO} threshold to the level required for that accuracy makes a calculation prohibitively expensive.

The CPS procedure works as follows. By calculating the DLPNO-CCSD(T) energy using two different values of T_{CutPNO} ($T_{\mathrm{CutPNO}} = 10^{-x}$ and $T_{\mathrm{CutPNO}} = 10^{-y}$, with $x < y$) the CPS energy can be calculated as

$$E_{\mathrm{CPS}} = E_x + F(E_y - E_x). \tag{2.11}$$

E_x and E_y are the energies calculated using each threshold, and F is a value that can be fit by minimizing the error with respect to canonical CCSD(T). In Chapter 6, we use the CPS procedure to calculate both spin-splitting and reaction energies for metalloporphyrins. In particular, we use the variant of the CPS procedure from Drosou and colleagues (specifically the method called CPS1).[40] In this variant, $F = 2.38$, $x = 1.0 \times 10^{-6}$, and $y = 3.33 \times 10^{-7}$. The remaining thresholds in both DLPNO-CCSD(T) calculations are set to the values defined by the NormalPNO setting in ORCA 5.0.4. In particular, $T_{\mathrm{CutPairs}} = 10^{-4}$ and $T_{\mathrm{CutDO}} = 10^{-2}$.

Basis Set Extrapolation for DLPNO-CCSD(T)

For DLPNO-CCSD(T) calculations, special attention was given to the size of basis set needed to produce converged correlation energies. All calculations suffer from some degree of basis set incompleteness error—the difference between the calculated result and the value that would be obtained with a theoretically infinite, or complete basis set (CBS). For HF and DFT calculations with pure functionals, calculations converge relatively quickly to the CBS limit, but correlated wave function calculations converge much more slowly. In fact, the convergence in HF and DFT theory is often fit to an exponential[41] ($E^X_{\mathrm{SCF}} = E^{\mathrm{CBS}} + A\exp(-\alpha X)$) or root-exponential[42, 43, 44] ($E^X_{\mathrm{SCF}} = E^{\mathrm{CBS}} + A\exp(-\alpha\sqrt{X})$) function of the basis set size X (equal to the zeta-value).[†] On the other hand, the slower convergence of the correlation energy can be shown theoretically to converge asymptotically in an inverse cubic relationship with X ($E^X_{\mathrm{corr}} = E^{\mathrm{CBS}}_{\mathrm{corr}} + BX^{-3}$).[47] Therefore, even though a triple-zeta basis with appropriate polarization functions may yield relative energies (e.g. reaction energies) close to the CBS limit for DFT, the same basis would be insufficient for quantitative results with CCSD(T).

Extrapolation to the CBS limit is important for correlated treatments of medium to large molecules which are too large to treat with a large basis set. We thus extrapolate both reaction energies and spin-splitting energies for metalloporphyrins to the CBS limit in Chapter 6 when using DLPNO-CCSD(T). In the extrapolation,

[†]The convergence behavior of HF and DFT is not established on the same theoretical footing as the convergence of correlated WFT. Thus, multiple expressions are used in the literature, including power laws rather than exponentials.[45] The performance of a given expression is dependent on the basis-set family and particular treatment of exchange and correlation.[46]

distinct schemes are used to extrapolate the SCF and correlation energies due to their different convergence properties with respect to the basis set size. Furthermore, this is a two-point extrapolation, meaning a calculation is performed with a smaller basis set of size X (e.g. for a TZ basis, $X = 3$), followed by a calculation with larger basis of size Y. Such an extrapolation is called an X/Y extrapolation.

Under this scheme, the extrapolated SCF energy assumes root exponential scaling and is given by

$$E_{\mathrm{SCF}}^{\mathrm{CBS}} = \frac{e^{\alpha\sqrt{X}} E_{\mathrm{SCF}}^{(X)} - e^{\alpha\sqrt{Y}} E_{\mathrm{SCF}}^{(Y)}}{e^{\alpha\sqrt{X}} - e^{\alpha\sqrt{Y}}}. \tag{2.12}$$

Meanwhile, the extrapolated correlation energy assumes a general inverse power scaling and is given by

$$E_{\mathrm{corr}}^{\mathrm{CBS}} = \frac{X^{\beta} E_{\mathrm{corr}}^{(X)} - Y^{\beta} E_{\mathrm{corr}}^{(Y)}}{X^{\beta} - Y^{\beta}}. \tag{2.13}$$

Benchmarking by Neese et al. produced standard α and β values for several basis set families, which we use in our extrapolations.[44] It should be noted that for large X and Y, β converges to 3 as predicted by the theoretical inverse cubic scaling law.[44] It is also important to note that in DLPNO-CCSD(T) extrapolations, E_{SCF} is always the HF energy of the single determinant wave function defined by whichever orbitals are used as input to the correlation procedure. In Chapter 6, these orbitals were from a prior DFT calculation, but the energy from DFT is not used anywhere in the extrapolation. Figure 2.2 illustrates CBS extrapolations for the O_2 molecule using different X/Y values. Note that the correlation energies are about twice as far from the CBS limit as HF energies for double- and triple-zeta basis sets, and that larger values of X and Y produce more reliable extrapolations.

When using DLPNO-CCSD(T), it is important to combine both CBS and CPS extrapolation when computing the energies of metalloporphyrins. In the combined procedure, three calculations are required.[40] Using one value of TCutPNO, two calculations are performed with basis sets X and Y to obtain $E^{(X)}$ and $E^{(Y)}$, which extrapolate to E^{CBS}. Then a CBS extrapolation contribution to the energy is defined as

$$\delta^{\mathrm{CBS}} = E^{\mathrm{CBS}} - E^{(X)}. \tag{2.14}$$

Next, a calculation is performed with basis set X, but a looser TCutPNO thresh-

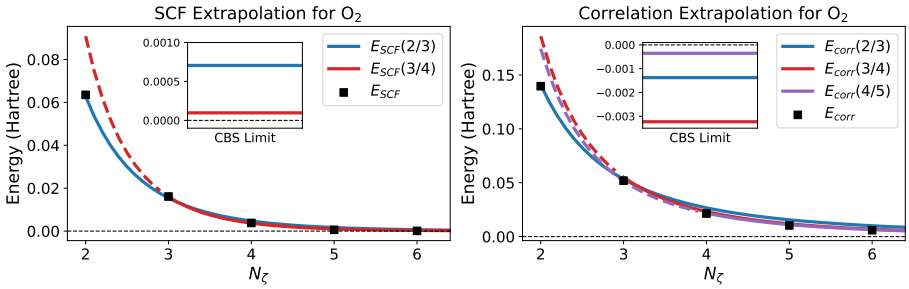

Figure 2.2: Two-point extrapolations to the CBS limit using the cc-pVNZ basis set family. The left panel shows extrapolations of the HF energy of O_2 using Equation (2.12). The right panel shows the extrapolations of the correlation energy of O_2 from CCSD calculations using Equation (2.13). In both panels, points show the calculated energy for each individual basis set, and lines show the convergence behavior assumed by the respective extrapolation formulas, with parameters for extrapolations taken from Ref [44]. Insets show the deviations of the extrapolations from the CBS limit, which was taken to be the energy using the decontracted aug-cc-pV6Z basis set for HF and the energy of a 5/6 extrapolation with deconstracted aug-cc-pVNZ basis sets for correlation. Energies are zeroed at the CBS limit.

old, to give $E_x^{(X)}$. Now, with the earlier $E^{(X)}$, calculated with the default (tighter) TCutPNO threshold relabeled as $E_y^{(X)}$, we calculate the CPS energy $E_{\text{CPS}}^{(X)}$ using $E_x^{(X)}$ and $E_y^{(X)}$ with Equation (2.11). Finally, the total energy incorporating both extrapolations is given by:

$$E_{\text{CPS}}^{\text{CBS}} = E_{\text{CPS}}^{(X)} + \delta^{\text{CBS}}. \tag{2.15}$$

Coupled Cluster and Multireference Character

One important caveat to the accuracy of both CCSD(T) and DLPNO-CCSD(T) is that all excitations are generated from a single reference determinant—hence, CCSD(T) is called a *single reference* method. As a result, CCSD(T) results can become unreliable when the reference determinant does not have a large overlap with the full wave function. In such cases, one or more other determinants may have significant coefficients in the full wave function, which is said to have *multireference* character. One method for evaluating the extent of multireference character in a system, and thus the appropriateness of applying single reference CCSD(T), is to compute the weights of the most important electron *configurations*[†] in a Complete Active Space-SCF (CASSCF) wave function.[48] When multiple configurations have

[†]A configuration describes the occupation pattern of spatial orbitals

significant weight, CCSD(T) should be avoided in favor of multireference methods like Multireference Configuration Interaction (MRCI). More tools for diagnosing multireference character will be discussed in Chapter 6

CASSCF as a Diagnostic Tool for Multireference Character

As a Complete Active Space method, CASSCF truncates the sum over all possible determinants in Equation (2.7) by restricting the occupation numbers of certain orbitals.[49, 50, 51] In particular, some number of chemically relevant orbitals are selected to be an *active space*, and their occupations are allowed to vary between different determinants. In contrast, low-lying orbitals are taken to be inactive, with occupations fixed at 2 in all determinants, and high-energy virtual orbitals are precluded from entering any determinants. The coefficients of all determinants that can be created by different occupations within the active space are determined (a full configuration interaction calculation within the active space). Additionally, in an iterative SCF loop, the molecular orbitals entering the determinants are also optimized in order to minimize the total energy. The resulting wave function is a linear combination of determinants.[†] Because the number of possible determinants in CASSCF scales factorially with the number of active orbitals, active spaces are generally limited to about 15 orbitals.

Upon convergence of the CASSCF procedure, the sum of the squared coefficients of all determinants belonging to a given configuration is the *weight* of that configuration. A generally accepted rule of thumb is that for a system to be considered single reference, the most important CASSCF (reference) configuration should have a weight > 0.9 and no other single configuration should have a weight > 0.02.[48] While CCSD(T) should provide excellent results when these thresholds are met, it has also been shown to produce accurate energetics even when more significant multiconfigurational character is present, so long as the electronic structure is dominated by a single configuration.[52, 53]. The critical point is that important configurations should be accessible by single and double excitations for CCSD(T) to be reliable. One caveat about the usefulness of CASSCF configuration weights is that they only reflect excited determinants accessible with the chosen CAS size, which should therefore contain all chemically relevant orbitals in order to reliably assess multireference character. In the metalloporphyrin systems we examine in Chapter 6, however, a judicious choice of

[†]Practically, the wave function is expanded in a basis of Configuration State Functions, which are themselves symmetry-adapted linear combinations of determinants

CAS includes metal and some important porphyrin orbitals while inevitably excluding many other valence orbitals. In this context, configuration weights are still a very useful indicator of the extent of multireference character when the CAS is carefully chosen. However, simply meeting the weight thresholds above cannot unequivocally rule out the importance of excitations from inactive (porphyrin macrocycle) orbitals.

2.3.2 Density Functional Theory

Having covered the wave function methods that will be used in Chapter 6, we now introduce Density Functional Theory (DFT), which is used extensively throughout this dissertation. DFT is enabled by the Hohenberg-Kohn theorems[54], one of which showed that the ground state properties, including energy, of a system were unambiguously defined by the electron density.[54, 15] Thus, the energy of the system can be defined as a functional[†] of the electron density $E[\rho(\mathbf{r})]$. The second Hohenberg-Kohn theorem showed that this energy functional was variational.[54, 15] That is, the functional reaches a minimum at the ground state density. Practically speaking, these two theories together mean that the ground state density of a system, and hence the ground state properties of the system, can be determined by minimizing the energy functional above over some trial electron density.[15] Nevertheless, while the exact energy functional exists in theory, in practice it has only been approximated, and to various degrees of sophistication.[1]

In general terms, the DFT energy functional can be written as follows:[15]

$$E[\rho] = T_0[\rho] + E_{\text{ne}}[\rho] + J[\rho] + E_{\text{xc}}[\rho]. \tag{2.16}$$

The first 3 terms on the RHS of the equation are the electron kinetic energy (computed for non-interacting electrons), the nuclear-electron attraction, and the Coulomb (mean-field) electronic repulsion, all defined equivalently to HF theory. The final term in (2.16), E_{xc}, is called the *exchange-correlation* functional, and for the exact total energy functional, it includes all of the energy due to electron-electron interactions that is not included in the remaining terms.[15] In practice, the exact form of E_{xc} is not known, and various approximations are made based on the basis of physical arguments and potentially empirical fitting.[1] We note that from now on, any mentions of *density functional approximations* refer specifically to the approximation made for E_{xc}.

[†]A function of a function.

In Kohn-Sham DFT, which is the most common form of DFT today, the electron density is defined in terms of singly-occupied spin oribitals ϕ_i[†].[55] The equivalence $\rho = \sum_i |\phi_i|^2$ means that all terms of (2.16) can be written as functionals of either single determinant wavefunctions or the density directly.

While the variety of density functional approximations can be overwhelming, they can be broadly classified into a hierarchy based on the assumptions and mathematical form of their construction. This hierarchy also corresponds with the computational complexity and often (but not always) the accuracy of an approximation when used to compute chemical energies and properties.[1] Thus, the hierarchy has been dubbed "Jacob's ladder" of density functional approximations,[56] a Biblical allusion suggesting that each successive rung of brings one closer to heaven—or in this case, the universal functional (Figure 2.3). Selection of an appropriate functional was a consideration in all of the projects of this dissertation. In particular, the performance of functionals on different rungs of Jacob's ladder was scrutinized when computing energies for metalloporphyrins in Chapter 6. Thus, we now include a brief introduction to each of these rungs.

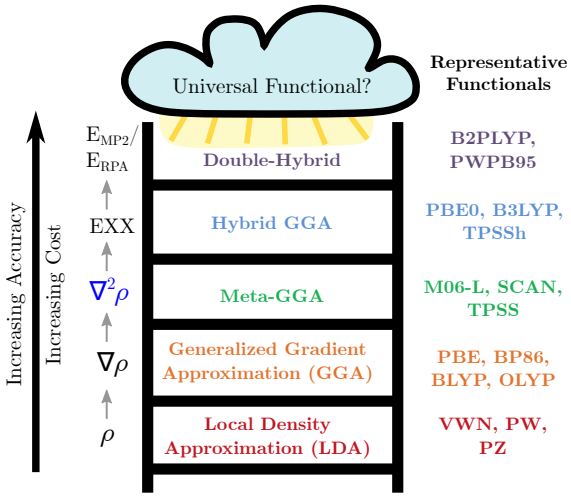

Figure 2.3: Jacob's Ladder of Density Functionals. A conceptual organization of E_{xc} functionals in an order that corresponds to increasing complexity and *general* trends in accuracy across diverse benchmarks. The left hand side of the ladder denotes additional dependencies of E_{xc} at each rung, where ρ is the electron density and EXX is exact exchange from HF theory.

[†]Non spin-polarized calculations can also be employed with doubly-occupied orbitals

Rung 1: The Local Density Approximation

In the Local (Spin) Density Approximation (LDA), the density of a system is assumed to be slowly varying. Thus the expressions for exchange and correlation energy densities at a given point in space are derived from a uniform electron gas with the same electron density.[1] The LDA is known to perform poorly for the energetics of molecular systems, though it does often produce adequate results for solid state materials.[57, 1] In Chapter 4, we use the Perdew-Wang parameterization of the LDA[58] to calculate electronic densities in MgO/Ag nanocomposites.

Rung 2: The Generalized Gradient Approximation

In the Generalized Gradient Approximation (GGA), the local density and its gradient are both included in the expression for E_{xc}. Expressions are often constructed as a correction to LDA energies. We use two very popular GGA functionals, PBE[59] and BP86,[60, 61] to study metalloporphyrins in Chapter 6. Both of these functionals produce good geometries for broad classes of molecules, including notoriously finicky transition metal systems. In Chapter 3, we also employ PBESol, a variant of PBE that has been reparameterized to produced better equilibrium properties for solids.[62] While GGA functionals offer a large improvement over the LDA,[57] they still tend to overestimate binding strengths and atomization energies,[63] predict overly-delocalized electron densities,[64] and overstabilize low-spin states.[65] Furthermore, both GGA and LDA functionals significantly underestimate band gaps in insulating solids, which we will see can lead to systematic errors in electric permittivities.[66, 57]

Rung 3: Meta-GGA

The next rung encompasses the meta-GGA (m-GGA) functionals. In practice, such functionals include either a kinetic energy density term or the physically related Laplacian of the electron density.[1] By including information related to the Laplacian of the density in addition to its gradient, m-GGAs represent a logical extension of GGA functionals. We do not use any pure m-GGA functionals directly in this dissertation (as discussed next, the hybrid m-GGA functional TPSSh is used).

Rung 4: Hybrid DFT

In the next rung of Jacob's Ladder, a significant jump is made by writing the exchange part of the E_{xc} functional as a linear combination of an approximate exchange functional and the exchange energy calculated from HF theory.[1] The incorporation of HF theory distinguishes these so called *hybrid functionals* from the *pure functionals* of the previous three rungs. We will hereafter refer to the exchange energy used in hybrid DFT as *exact exchange*, rather than HF exchange, because it is calculated using DFT orbitals and not the canonical HF ones. In Chapters 5 and 6, we extensively use the PBE0 hybrid functional,[67] which has no empirical parameters and whose form is

$$E_{\text{xc}}^{\text{PBE0}} = 0.25E_x^{\text{HF}} + 0.75E_x^{\text{PBE}} + E_c^{\text{PBE}}. \tag{2.17}$$

That is, its exchange part consists of 25% exact exchange and 75% PBE exchange, and its correlation part is simply PBE correlation. In Chapter 6, we also evaluate the extremely popular B3LYP functional,[68] which has three empirically fit parameters, including 20% exact exchange. Finally, we test TPSSh,[69] which is built around the m-GGA TPSS[70] and an empirically-fit 10% exact exchange.

Hybrid functionals improve many of the shortcomings of GGA functionals and perform well on benchmarking across a wide range of systems.[57, 71, 72] However, their performance for particular properties and systems can be highly dependent on the percentage of exact exchange. For example, the amount of exact exchange tunes the preference for low-spin (less exact exchange) and high-spin (more exact exchange) states.[20] Thus, hybrid functionals optimized for a specific system or property type may underperform in a different context. Moreover, hybrid functionals are not widely used in solid state calculations due to the expense of computing exact exchange in periodic boundary conditions, though they are noted to improve on the LDA/GGA band gap problem.[73]

Rung 5: Double-Hybrid DFT

Lastly, *double-hybrid functionals* include both a portion of HF exchange and correlation energy from a method that explicitly considers unoccupied orbitals. Most frequently, this method is second order Moller-Plessett perturbation theory (MP2), but another common approach is to include correlation from the Random Phase Approximation.[1] The general form of a double-hybrid functional with MP2 correla-

tion is given by

$$E_{\mathrm{xc}}^{\mathrm{DH}} = (1-a)E_x^{\mathrm{DFT}} + aE_x^{\mathrm{HF}} + (1-b)E_c^{\mathrm{DFT}} + bE_c^{\mathrm{MP2}}. \tag{2.18}$$

We examine the performance of two MP2-based double-hybrid functionals on metalloporphyrins in Chapter 6—B2PLYP and PWPB95. B2PLYP takes the above form with a and b fit empirically to 0.53 and 0.27.[74] PWPB95 uses $a = 0.50$ and $b = 0.269$ while using different flavors of E_x^{DFT} and E_c^{DFT}, including a m-GGA formulation for E_c^{DFT}.[75] In addition, PWPB95 uses a variant of MP2 called Spin-Opposite Scaled MP2, which only includes the correlation energy from electron pairs of opposite spins. We note that in both of these functionals, the MP2 energy is calculated using the orbitals computed self-consistently from a typical hybrid-DFT calculation—that is, using only first three terms on the RHS of Equation (2.18).[74, 75] Both B2PLYP and PWPB95 perform very well on many thermochemistry benchmarks, demonstrating a marked improvement over hybrid functionals even for many transition metal systems.[72, 76, 77] However, they are quite computationally expensive compared to other functionals and not generally available for solid state calculations.

Dispersion Corrections

Many density functionals, especially pure functionals, struggle to accurately capture attractive long-range dispersion interactions, often also called van der Waals interactions.[78] Thus, throughout this dissertation, we make use of semi-classical dispersion corrections to the DFT energy. Specifically, we use Grimme's D3 approach with Becke-Johnson damping[79] in Chapter 6 and the D4 approach[80, 81] in Chapter 5. In both of these approaches, the dispersion energy is expressed as a sum over classical pairwise interactions, which include dipole-dipole and dipole-quadropole terms. In the D4 model, an additional three-body term (dipole-dipole-dipole) is included.[80] Moreover, the D4 model uses a more sophisticated model for the atom-in-material polarizabilities that are used to compute these interactions, wherein atom polarizabilities are scaled by partial charges that account for the local chemical environment. Nevertheless, the chemical environment is taken into account to a large extent in *both* D3 and D4 approaches by an interpolation of atom-in-material polarizabilities from reference calculations using an atomic coordination number descriptor.[82, 80] The D3(BJ) and D4 dispersion corrections have a set of functional-specific parameters that are fit to reference CCSD(T) energies of non-covalent interactions.[82, 80] Their

use alongside DFT functionals from all rungs of Jacob's ladder significantly improves binding and reaction energies for both main group and transition metal systems, though their impact tends to be smaller for double hybrid functionals that already include dispersion via MP2.[72, 76, 77]

2.3.3 Periodic DFT

Chapters 3 and 4 deal almost exclusively with solid materials. In some cases, these materials are crystalline bulk oxides, while in other cases the consist of oxides surrounding molecular scale metal inclusions. However, in all cases a single unit of the material, which could be a primitive unit cell or a supercell containing defects or inclusions, is simulated as if it infinitely repeats along all the three vectors ($\mathbf{a}_1$, $\mathbf{a}_2$, $\mathbf{a}_3$) defining the cell. *Bloch's Theorem* states that for a periodic external potential such as this, the eigenfunctions of the Hamiltonian can be written as[16]

$$\psi_{n,\mathbf{k}}(\mathbf{r}) = e^{i\mathbf{k}\cdot\mathbf{r}} u_{n,\mathbf{k}}(\mathbf{r}), \tag{2.19}$$

where a plane wave $e^{i\mathbf{k}\cdot\mathbf{r}}$ with wavevector $\mathbf{k}$ is multiplied by a function $u_{n,\mathbf{k}}(\mathbf{r})$ that shares the periodicity of the cell. The index n labels a distinct electronic *band*, an electron state that contain a single electron per cell (or two electrons in the case of non-spin-polarized DFT). Bloch functions $\psi_{n,\mathbf{k}}$ are the delocalized analogs of molecular orbitals in the solid state, and the energy of a given band $\varepsilon_n(\mathbf{k})$ varies smoothly with $\mathbf{k}$.[16] .

Plane-Wave Energy Cutoffs

Due to the periodicity of the lattice, it is useful to expand the lattice-periodic part of Bloch functions in a basis of plane waves for numerical calculations:

$$u_{n,\mathbf{k}}(\mathbf{r}) = \sum_m c_{n,m}(\mathbf{k}) e^{i\mathbf{G}_m\cdot\mathbf{r}}. \tag{2.20}$$

Here $c_{n,m}$ are the expansion coefficients for a given band n, and $\mathbf{G}_m$ are reciprocal lattice vectors, defined as follows. $\mathbf{G}_m$ are restricted to produce plane waves that match the periodicity of the lattice. This can be ensured by constructing $\mathbf{G}_m$ such that $\mathbf{G}_m \cdot \mathbf{a}_i = 2\pi x$ for integer x and all lattice vectors $\mathbf{a}_i$.[16] With such a plane wave expansion of $u_{n,\mathbf{k}}(\mathbf{r})$, the entire Bloch function is now also a sum of plane waves:

$$\psi_{n,\mathbf{k}}(\mathbf{r}) = \sum_m c_{n,m}(\mathbf{k}) e^{i(\mathbf{k}+\mathbf{G}_m)\cdot\mathbf{r}}. \tag{2.21}$$

In Chapters 3 and 4, we use such plane wave basis sets in our periodic calculations. The number of plane waves included in the expansions were determined by a maximum cutoff for the energy of a given plane wave:

$$E_m^{\mathrm{PW}} = \frac{1}{2}\|\mathbf{k}+\mathbf{G}_m\|^2 < E_{\mathrm{cut}}. \tag{2.22}$$

A higher energy cutoff (usually 4–12× larger) is typically needed to accurately expand the charge density $\rho(\mathbf{r})$ in a plane wave basis, which is required for computing the DFT potential.[16] The chosen values for these cutoffs for different calculations were determined through inspection of the convergence of the desired properties being calculated—usually lattice vectors and permittivities—and are reported in the corresponding chapters. An example showing the convergence of the energy and electric permittivity of magnesium oxide with the number of plane waves is shown in Figure 2.4.

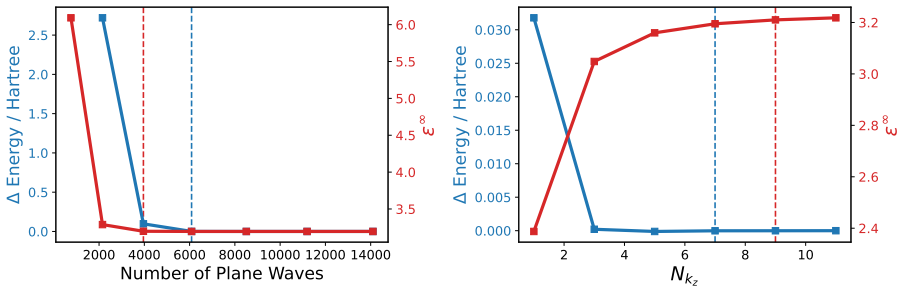

Figure 2.4: Convergence of plane-wave DFT properties. The left panel shows the convergence of the energy and high-frequency electric permittivity with the number of plane waves in a calculation of a single conventional unit cell of MgO with a 3x3x7 k-point grid. The right panel shows the convergence of the same properties with the number of k-points in the z-direction. For both panels, permittivity was calculated using a finite field in the z-direction. Blue and red dashed lines indicate where the energy first came within 0.001 Ha and the permittivity within 0.01 of the most converged values, respectively.

Sampling of the Brillouin Zone

A consequence of Bloch's Theorem is that the Kohn-Sham equations must be solved separately for different values of $\mathbf{k}$ to determine the wave function of the system. In

practice, all **k** can be chosen to come from a single primitive cell of the *reciprocal lattice*, called the *Brillouin Zone* (BZ).[16] This is because Bloch functions are invariant to translations by reciprocal lattice vectors ($\psi_{n,\mathbf{k}} = \psi_{n,\mathbf{k}+\mathbf{G}}$). Many quantities, including the DFT energy, are determined by integrations over the BZ, which in practice are accomplished by summation over a discrete grid of **k**-vectors, also called k-points.[16] Throughout this disseration, we define these k-points using a Monkhorst-Pack grid, a uniform grid with a specified number of points along each primitive reciprocal lattice vector.[83] For example, a $4 \times 4 \times 4$ grid would contain 4 k-points along each direction of the BZ (though this can usually be reduced by symmetry).

In general, increasing the number of k-points improves accuracy and computational cost. However, the size of the BZ, and hence the number of k-points required for a given accuracy, also decreases with the size of the real-space simulation cell. In our calculations of nanocomposites, the cell sizes are quite large, spanning several lengths of the conventional oxide lattices from which they were constructed in each direction. As a result, few k-points are generally required for these calculations, and we typically only performed nanocomposite calculations at a single k-point in the center of the BZ, called the Gamma-point. In fact, the particular implementation of DFT that we used for many of those calculations (the Car-Parrinello module of Quantum Espresso, described in more detail shortly) only allows calculations at the Gamma point. For calculations of smaller cells of pure materials and in calculations validating the accuracy of the Gamma-point-only calculations, we used more substantial k-point grids, which are defined at the relevant places in the text. Figure 2.4 shows how the energy and electric permittivity converge with the k-point grid for a conventional unit cell of magnesium oxide.

Effective Core Potentials

Part and parcel with the plane wave approach is the use of effective core potentials (ECPs), which are also commonly referred to as pseudopotentials. All-electron calculations contain rapid oscillations in the electron density near nuclei due to the strong nuclear Coulomb potential. ECPs replace this strong potential with a weaker one combining the effects of the nuclei and core electrons. The resulting valence-only calculations contain a relatively smooth pseudo-density which lacks high frequency components near nuclei while accurately representing the valence electron density outside of the core region.[16] Thus, ECPs reduce both the number of electrons that

need to be explicitly calculated and the number of plane waves needed to describe the electronic wave functions (and density), yielding important computational savings.

The ECP for a given element is not unique—in fact ECPs come in many flavors that vary in manners such as the assumed mathematical form of the potential in the "core" region, the cutoff radius of this core, and the enforcement of certain physical constraints such as norm conservation. Throughout this dissertation, we use both norm-conserving and ultrasoft ECPs, some of which are also scalar-relativistic. The precise flavors of ECPs used are indicated within the relevant chapters. In some cases, ECPs were chosen for continuity with previous work. In Chapter 4, for example, we used the specific ECPs that were employed in modeling the same nanocomposites in the earlier work of Hally[84] and Adluri[85], since we were comparing our results directly to these earlier reports. The remaining ECPs were taken from the Pseudo Dojo repository of Optimized Norm-Conserving Vanderbilt potentials.[86, 87] This particular type of ECP is quite *soft*, meaning that smooth wave functions require relatively low plane wave cutoffs, which results in efficient calculations.

Iterative Minimization Methods

Throughout this dissertation, two primary approaches are used for finding the Kohn-Sham solutions in plane wave DFT. In the first approach, which is more commonly employed in the study of dielectrics, the electronic energy is fully minimized over the set of plane wave coefficients for each set of nuclear coordinates in a geometry optimization. In such simulations, we use the Davidson iterative diagonalization method in the PWSCF module of Quantum Espresso,[88] and we can speak of the nuclear coordinates being propagating along the Born-Oppenheimer potential energy surface.

In the alternative approach, we use the Car-Parrinello method, also called Car-Parrinello Molecular Dynamics (CPMD),[89] to propagate both the electronic wave functions and nuclear coordinates in tandem. In CPMD, the electronic degrees of freedom, namely the plane wave coefficients, are treated as dynamical variables in the same sense as nuclear coordinates.[89, 90] This leads to a set of constrained equations of motion for each electronic band

$$\mu \frac{d^2}{dt^2}\psi_i = -\left[\hat{\mathbf{H}}_{\mathrm{KS}} - \gamma\frac{d}{dt} - \lambda_i\right]\psi_i. \tag{2.23}$$

Here μ is a fictitious electronic *mass* and λ_i is a Lagrange multiplier given by $\lambda_i =$

$\langle\psi_i|H_{\mathrm{KS}}|\psi_i\rangle$ that ensures normalization of the state as it is propagated.[90] The middle term on the right hand side is a *damping* term with damping coefficient γ, which gradually removes kinetic energy from the electrons when $\gamma > 0$. The above expression shows the acceleration of the electronic states reaches zero when they are eigenfunctions of H_{KS} and their velocity has reached zero through damping. Therefore, the ground state wave function can be determined by initializing ψ_i with some amount of kinetic energy and integrating Equation (2.23) numerically, as with a Verlet algorithm, to gradually bring the plane wave coefficients to their ground state values.[90] This process is illustrated schematically in Figure 2.5(a).

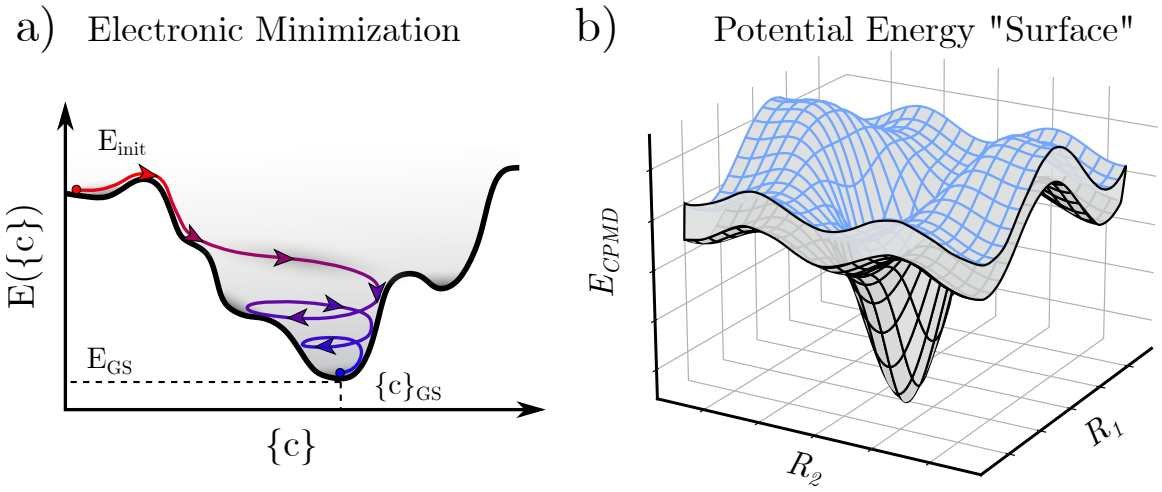

Figure 2.5: Diagrams adapted from [90] showing the iterative minimization approach developed by Car and Parrinello. Panel (a) shows the damped dynamics of the electronic degrees of freedom. (b) Ionic relaxation in CPMD amounts to system evolution on a potential energy surface with thickness corresponding to the kinetic energy of the electronic degrees of freedom.

After reaching the ground state, the nuclear coordinates can be propagated along the potential energy surface. However, unlike the Davidson approach described above, in CPMD the electronic wave functions need not be optimized at each time step. Instead, if the electrons are appropriately damped, they remain close to their ground state as the nuclei are propagated, and alternating steps of nuclear and electronic propagation results in a trajectory along a Born-Oppenheimer-like potential energy surface. In CPMD, however, this surface has some finite thickness corresponding to the kinetic energy of the electronic states (Figure 2.5(b)).[89] Nuclear coordinates can be optimized by preforming damped dynamics, or else a molecular dynamics trajectory can be generated if damping is removed. By circumventing the repeated diag-

onalization of the Kohn-Sham Hamiltonian, CPMD offers substantial speed-ups for large systems in our calculations of dielectric properties of nanocomposites. Chapter 3 offers some performance comparisons between CPMD and traditional Born-Oppenheimer DFT in computing these properties. CPMD is used exclusively for the DFT results for nanocomposites in Chapter 4.

2.3.4 Unrestricted Calculations and Spin Contamination

For open-shell calculations throughout this work, we utilize the *unrestricted* variants of HF and DFT, in which the spatial components of spin-up (α) and spin-down orbitals are allowed to optimize separately. This extra freedom allows improved energies for many systems, but the resulting wave function is not an eigenfunction of the $\hat{\mathbf{S}}^2$ operator as it should be. *Spin contamination* is the difference between the expectation value of $\langle \hat{\mathbf{S}}^2 \rangle$ and its ideal value of $S(S+1)$. The unrestricted wave function can be expanded in terms of restricted determinants, which shows that this spin contamination arises from admixture of higher spin determinants into the wave function.[1] For example, an open-shell singlet wave function with severe spin contamination could have contributions from triplet and possibly quintet determinants. Because of the tendency of HF to overstabilize high-spin states, HF and hybrid DFT (especially with a high percentage of exact exchange) are more prone to spin contamination than pure DFT functionals.[91]

On the one hand, by effectively including additional restricted determinants, this spin-symmetry breaking can capture some amount of correlation within a single-determinant approach. Conceptually, the orbitals have more freedom to optimize such that electrons of opposite spin more effectively avoid each other.[1] However, this admixture of high-spin states is not always desirable. Because it occurs more in systems with multireference character, significant spin contamination (roughly speaking when $\frac{|\langle \hat{\mathbf{S}}^2 \rangle - S(S+1)|}{S(S+1)} > 0.1$) can indicate that one should move away from single reference approaches like DFT or even CCSD(T).[92] However, it is also possible to observe *artificial* spin-symmetry breaking, which does not represent multireference character and will be removed with a more accurate treatment of correlation.[93] Transition metal systems in particular often have multiple low-lying spin states and are prone to spin-contamination.[92] Special care must be taken to ascertain whether this represents artificial symmetry breaking or an actual indication of multireference character.

It is useful here to note two caveats that pertain to calculations of spin contamination, which occur frequently in Chapter 6. First, there is some debate about the meaning of spin contamination in unrestricted DFT, with some arguing that some spin contamination is an expected feature of unrestricted DFT required for producing accurate spin densities.[94, 95] Still, others have found $\langle \hat{\mathbf{S}}^2 \rangle_{\mathrm{DFT}}$ a useful tool for identifying strongly correlated systems, since such contamination tends to disappear when moving from UHF to UKS calculations if correlation is treated sufficiently well by DFT.[92] Thus, we generally do put stock in $\langle \hat{\mathbf{S}}^2 \rangle_{\mathrm{DFT}}$, using it to identify biradicals and other sources of strong correlation. Second, the DLPNO-CCSD(T) method removes all spin contamination from the reference determinant by the construction of *Quasi-Restricted Orbitals*[96] from the unrestricted orbitals generated by the SCF procedure. This is usually beneficial for the resulting CCSD convergence and energy. However, in cases where the SCF calculation produced severe spin contamination, the generation of QROs can change the reference significantly by removing important multireference character. Such systems could in theory be treated with fully unrestricted CCSD(T),[97] but should not be treated with the current DLPNO-CCSD(T) implementation.

2.3.5 Computational Scaling Considerations

As we have already alluded to, the choice of both electronic structure method and basis set involves a trade-off between computational efficiency and accuracy. The computational efficiency can be described in terms of the asymptotic scaling of a method with the size of the basis set (and thus effectively with the number of electrons). For N_o basis functions, HF formally scales as $O(N_o^4)$ due to the expensive calculation of 2-electron integrals.[1] Meanwhile, DFT scales as $O(N_o^3)$, with the bottleneck being the cost of diagonalizing the Kohn-Sham Hamiltonian.[1]† The scaling of both HF and DFT can be improved by the use of accurate Resolution of Identity (RI) approximations for calculating Coulomb and exchange integrals, which is used throughout this dissertation.[1]

It should be noted that under the umbrella of DFT, further approximations based on localized orbitals or orbital-free methods can achieve linear scaling in the number of atoms.[98, 99, 100, 101, 102, 103] These implementations allow routine treatment of

†When the Coulomb term in DFT is calculated directly from 2-electron integrals, DFT also scales formally as $O(N_o^4)$, but in practice the Coulomb term is evaluated via reduced-scaling methods.[1]

tens of thousands of atoms, with systems consisting of million atoms within reach in highly parallel computing environments.[101, 99] While we do not use any linear scaling methods in this dissertation, they represent a promising avenue of further research for some of the nanostructures studied herein, especially nanocomposite dielectrics like those examined in Chapters 3 and 4.

Within DFT, the computational effort generally increases with increasing rungs of Jacob's ladder, even if the asymptotic scaling is unchanged. The one exception is double-hybrid DFT, whose MP2 component results in $O(N_o^5)$ scaling that can become prohibitive for large systems.[1] These scalings can also be compounded by basis set dependence. MP2 converges slower to the basis set limit than pure DFT[47]—thus the computational expense of hybrid and double-hybrid DFT is compounded by the need to use more basis functions. Periodic plane-wave DFT requires slightly different scaling considerations than Gaussian calculations. In periodic calculations, computational times scale linearly with the number of independent k-points.[90] However, for each k-point, the asymptotic scaling for each solution of the Kohn-Sham equations in the self-consistent loop has several terms that differ in their dependence on the number of plane waves N_{pw}, number of occupied bands N_{band}, and the number of ECP projectors N_{ecpp}. Thus, some calculations with very high plane wave cutoffs[†] and tight charge density grids may be dominated by the time required for Fast Fourier Transforms ($\propto N_{\mathrm{band}} N_{\mathrm{pw}} ln(N_{\mathrm{pw}})$), whereas other calculations may be slowed significantly by the time for orthogonalization ($\propto N_{\mathrm{band}}^2 N_{\mathrm{pw}}$) or the time for computing the contributions of nonlocal pseudopotentials to the energy ($\propto N_{\mathrm{band}} N_{\mathrm{pw}} N_{\mathrm{ecpp}}$).[90, 88] Since N_{band}, N_{pw}, and N_{ecpp} all scale roughly linearly with the number of atoms in the system for a solid state calculation, the upshot of this all is that the scaling is essentially cubic with that number of atoms.

As we will discuss, many of the periodic DFT calculations we employ also require the application of a finite electric field. While this field does not change the asymptotic scaling of the calculations, it introduces a large scaling pre-factor and additional computational overhead that makes calculations on large nanostructured unit cells that much more difficult. This computational complexity drives the search for classical approaches to the dielectric response of nanostructured materials in Chapters 4 and 5. Figure 2.6 illustrates the scaling of a plane wave DFT calculations with the number of k-pts, plane waves, and electronic bands for pure MgO. It should be noted that as the number of atoms in the unit cell increases (and hence unit cell dimensions),

[†] N_{pw} is often about two orders of magnitude larger than N_{band}.[90]

computation times increase quite rapidly due to the increase in both the number of plane waves and electronic bands. Furthermore, calculations performed under a finite electric field require roughly four times the compute time per self-consistent cycle as a calculation without an electric field.

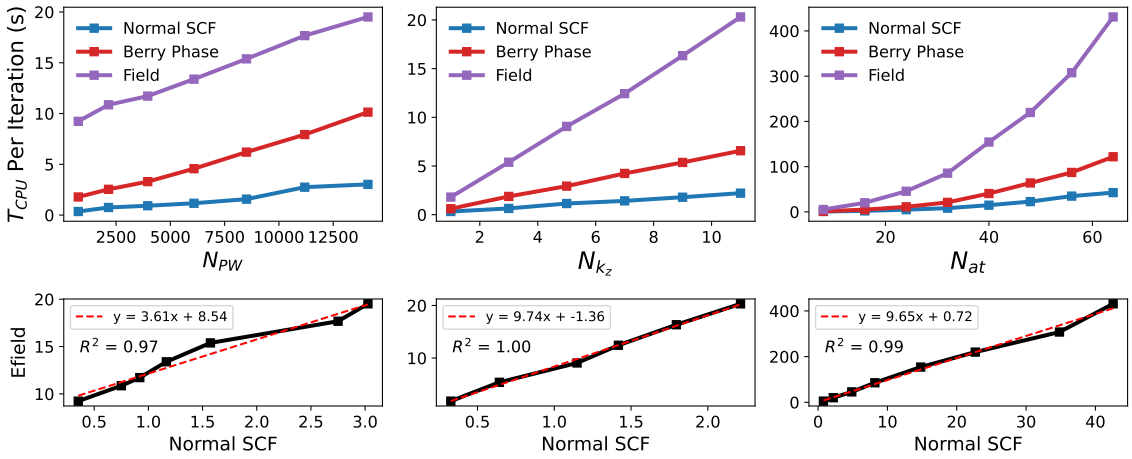

Figure 2.6: Plane-Wave DFT time scaling for simulations of MgO with and without an applied electric field. "Berry Phase" indicates the calculation of the polarization via the Berry Phase in the absence of an external electric field. The left panel shows how the CPU time per SCF iteration increases with the number of plane waves used for a calculation single conventional unit cell. The middle panel shows how the CPU time per SCF iteration varies with the number of k-points along the applied field direction. The right panel shows the how the CPU time per SCF iteration varies as the number of atoms in the simulation cell is increased. Increasingly larger cells were generated by copying the conventional unit cell along the z-direction, without changing the k-point sampling or plane-wave cutoff. The bottom row plots the CPU time per iteration when an electric field is applied against the CPU time per iteration when no field is applied for the corresponding plots above. In each case, the relationship is essentially linear, demonstrating that the application of the efield does not change the leading term in the asymptotic scaling but merely changes the prefactor.

For all of its accuracy, CCSD(T) is computationally expensive, with $O(N^6)$ scaling for the CCSD portion and $O(N^7)$ scaling for (T).[1] This expense is prohibitive for systems beyond a few dozen correlated electrons. The requirement for large basis sets due to the slow convergence of the correlation energy further raises computational demands, meaning basis set extrapolations with moderately sized basis sets are usually necessary. Incredibly, closed shell DLPNO-CCSD(T) formally expresses linear $O(N)$ scaling in compute time, memory, and disk requirements due to the local correlation treatment.[104] Its open-shell variant scales slightly worse due to

some quadratically scaling steps that become important for large systems,[105], and it should be noted that DLPNO-CCSD(T) requires orbitals from an SCF calculation with cubic scaling. In theory, this means that DLPNO-CCSD(T) should be applicable to all systems that can be treated with DFT, bringing molecules like porphyrins (or even small proteins!) into the realm of computational feasibility. However, the near-linear scaling only refers to the asymptotic limit and by no means results in computational times lower than or even on par with DFT for porphyrin systems in our experience. Moreover, the iterative triples portion of the calculation requires many read/write operations to disk, as well as ample local disk space available (on the order of 1 TB for the porphyrins we examined at the TZ level).[38] Thus, such calculations required a special allocation within our compute clusters and should not be considered a panacea for treating correlation in all research environments.

2.3.6 Software

A relatively small set of software platforms were used for executing the electronic structure methods described above. All Gaussian basis DFT calculations, along with all WFT calculations, were performed with the ORCA program.[106, 107] Almost all plane wave DFT was performed using the Quantum Espresso suite of programs.[88, 108] Within this suite, the CP.x program was used to perform CPMD, and the PW.x was used for the remaining calculations. A small number of plane wave calculations in Chapter 5 were performed using the GPAW program.[109] Finally, a small number of calculations using pseudoatomic orbitals for silver clusters in Chapter 4 were performed with the SIESTA program[102]

2.4 Polarization and Homogeneous Electric Fields

Capacitive energy storage relies on the polarization of bound charges in a dielectric layer. In bulk materials, the macroscopic property of electric susceptibility relates this polarization to the macroscopic electric field in the material. However, fundamentally the response of a material to applied fields is determined by its electronic structure and the microscopic rearrangement of charge (i.e. flow of current) that occurs when a field is turned on. In this section, we review the principles of polarization from both classical and quantum perspectives. We begin with polarization in finite systems, such as isolated molecules, which is readily described in terms of

the classical expression for the dipole moment. Next we turn to bulk dielectrics, reviewing the macroscopic definition of polarization and how it can be calculated in the context of quantum chemical calculations in periodic boundary conditions via the Modern Theory of Polarization. We show how this polarization can be mapped back onto a simple dipole moment expression using Wannier Functions, which will prove extremely useful in the study of nanostructures. The application of finite fields in electronic structure calculations is discussed for both finite and bulk systems.

2.4.1 Polarization in Finite Systems

For a finite system composed of point charges q_i at locations $\mathbf{r}_i$, the dipole moment μ can be calculated by a simple sum[110]:

$$\boldsymbol{\mu} = \sum_i q_i \mathbf{r}_i. \tag{2.24}$$

As long as the total system is charge neutral, this expression is not dependent on the choice of origin for the coordinate system and is thus uniquely defined. For a continuous, though still finite, charge distribution with charge density $\rho(r)$, the sum above becomes an integral over all space:[110]

$$\boldsymbol{\mu} = \int \mathbf{r}\rho(\mathbf{r})d\mathbf{r}. \tag{2.25}$$

This integral can be used to calculate the dipole moment of a molecule, cluster, or otherwise isolated chemical system, where the charge density includes both nuclear (ρ_n) and electronic (ρ_e) contributions:

$$\rho_{\text{mol}}(\mathbf{r}) = \rho_n(\mathbf{r}) + \rho_e(\mathbf{r}) \tag{2.26}$$

$$\rho_n(\mathbf{r}) = \sum_n Z_n \delta(\mathbf{r} - \mathbf{R}_n). \tag{2.27}$$

In the latter equation, Z_n is the charge of nucleus n at site $\mathbf{R}_n$, and δ is the Dirac delta function. Plugging these expressions into Equation (2.25), the dipole moment of an isolated chemical system can be evaluated as an integral over the electrons and a sum over nuclei:

$$\boldsymbol{\mu}_{\text{mol}} = \int \mathbf{r}\rho_e(\mathbf{r})d\mathbf{r} + \sum_n Z_n \mathbf{R}_n. \tag{2.28}$$

As before, this entire expression is origin-independent so long as the molecule is charge neutral.

The response of the energy of an isolated charge distribution (e.g. a molecule) to a homogeneous external electric field $\boldsymbol{\mathcal{E}}$ is given by following Taylor series expansion of the energy[1]

$$E(\boldsymbol{\mathcal{E}}) = E(0) + \frac{\partial E}{\partial \boldsymbol{\mathcal{E}}}\boldsymbol{\mathcal{E}} + \frac{1}{2}\frac{\partial^2 E}{\partial \boldsymbol{\mathcal{E}}^2}\boldsymbol{\mathcal{E}}^2 + \frac{1}{6}\frac{\partial^3 E}{\partial \boldsymbol{\mathcal{E}}^3}\boldsymbol{\mathcal{E}}^3 + ... \tag{2.29}$$

$$= E(\mathbf{0}) - \boldsymbol{\mu}_0\boldsymbol{\mathcal{E}} - \frac{1}{2}\boldsymbol{\alpha}\boldsymbol{\mathcal{E}}^2 - \frac{1}{6}\boldsymbol{\beta}\boldsymbol{\mathcal{E}}^3 + ..., \tag{2.30}$$

where all derivatives are understood to be evaluated with a vanishing electric field. The resultant dipole moment of the perturbed distribution can be written as a similar series[1]

$$\boldsymbol{\mu}(\boldsymbol{\mathcal{E}}) = \boldsymbol{\mu}_0 + \boldsymbol{\alpha}\boldsymbol{\mathcal{E}} + \frac{1}{2}\boldsymbol{\beta}\boldsymbol{\mathcal{E}}^2 + ..., \tag{2.31}$$

where $\boldsymbol{\alpha}$ and $\boldsymbol{\beta}$ are called the *polarizability* and *hyperpolarizability* tensors. In this dissertation, we work strictly in the realm of *linear response*, where the applied fields remain small enough that contributions from hyperpolarizability and higher-order terms are small, and the dipole moment can be approximated as

$$\boldsymbol{\mu}(\boldsymbol{\mathcal{E}}) \approx \boldsymbol{\mu}_0 + \boldsymbol{\alpha}\boldsymbol{\mathcal{E}}. \tag{2.32}$$

Thus, the polarizability tensor $\boldsymbol{\alpha}$ is of principal importance in the linear response of finite systems. From Equations (2.29), (2.30), and (2.31), we see that $\boldsymbol{\alpha}$ can alternately be evaluated as the first derivative of the dipole moment or the second derivative of the energy with respect to the applied field. Written explicitly for the individual tensor components, this is[1]

$$\alpha_{ij} = -\frac{\partial^2 E}{\partial \mathcal{E}_i \mathcal{E}_j} = \frac{\partial \mu_i}{\partial \mathcal{E}_j}. \tag{2.33}$$

The latter expression leads to the intuitive definition of polarizability α_{ij} as the rate of change in the system's dipole moment in direction i induced by an applied field

in direction j. In practice, this expression can be evaluated perturbatively by solution of coupled-perturbed SCF equations,[111, 112, 113, 114] or by a finite difference calculation using different values of an applied electric field.

Applying a homogeneous electric field to a finite system such as a molecule in electronic structure calculations is straightforward. The Hamiltonian of the system need only be augmented by the interaction between the external field and the system's dipole moment. In atomic units, this additional term is simply[1]

$$\hat{\mathbf{H}}_{\boldsymbol{\mathcal{E}}} = -\boldsymbol{\mathcal{E}} \cdot \boldsymbol{\mu}_{\text{mol}}, \tag{2.34}$$

where $\boldsymbol{\mu}_{\text{mol}}$ is calculated for the system as in Equation (2.28). The resulting ground state under this perturbed Hamiltonian will exhibit a polarized electronic density relative to the zero-field calculations.

For systems with polar or ionic bonding, the atomic structure will change in the presence of an external field if the nuclei are given time to respond to the field. Thus, one can speak of the electronic polarizability of a system, which corresponds to the induced electronic dipole when the nuclei are clamped, and the relaxed-ion polarizability, which includes the effects of geometric relaxation. This relaxed-ion polarizability usually is further decomposed into a low-frequency rotational component that occurs when the system has a permanent dipole and the component that comes from the compression or stretching of ionic bonds.[115] Because the nuclear motion is typically much slower than electronic (as assumed by the BO approximation), the electronic polarizability is sometimes referred to as the high-frequency polarizability. In all cases in this dissertation, however, we compute these values with time-invariant external fields, and so we speak of the polarizabilities as static polarizabilities.

2.4.2 Polarization in Bulk Systems

For finite systems, it was relatively straightforward to describe the linear response to external fields with a polarizability tensor $\boldsymbol{\alpha}$ that could be calculated from first principles. In this section, we outline the analogous proportionality between polarization and electric field in linear dielectric media, which is described by the material property of electric permittivity $\boldsymbol{\epsilon}$. The section describes the classical theory of $\boldsymbol{\epsilon}$ and how it can be calculated from first principles using the Modern Theory of Polarization.

Classical Theory of Polarization

The classical theory of polarization in dielectrics was developed as a phenomenological model relating the *macroscopic* fields and charge distributions in a material to the empirical properties of that material. Before proceeding it is worth defining what precisely is meant by *macroscopic* from here on out. In his treatise on Classical Electrodynamics, Jackson notes that in bulk materials, fields and charge densities vary rapidly near individual atoms, whereas these oscillations are irrelevant for a phenomenolgical description of material behavior.[110] Macroscopic thus refers to an average of microscopic quantities over a volume much larger than a single atom.[110] All of the fields and charge densities that enter the equations in this section are understood to be averaged as such, and hence quite smooth. An example of a macroscopically averaged potential and charge density from a 12-layer slab of MgO in an external electric field is shown in Figure 2.7

By considering macroscopic fields, the classical theory of dielectrics neglects the atomic and electronic structure of a dielectric, instead regarding it as a polarizable continuum. In such a material, the electric polarization can be obtained from the macroscopic form of Gauss's Law[110]

$$\nabla \cdot \mathbf{D}(\mathbf{r}) = 4\pi\rho(\mathbf{r}), \tag{2.35}$$

where ρ is the density of free charge and $\mathbf{D}$ is called the *electric displacement*, a field that includes the effects of both the electric field and the polarization of *bound* charges. The electric displacement can be defined as

$$\mathbf{D} = \boldsymbol{\mathcal{E}} + 4\pi\mathbf{P}, \tag{2.36}$$

where $\boldsymbol{\mathcal{E}}$ is the macroscopic electric field, and $\mathbf{P}$ is the *polarization density*, or the dipole moment per unit volume.[110] Note that from now on, we will refer to $\mathbf{P}$ simply as the *polarization*, which is synonymous with polarization density in the context of bulk materials. For *linear* dielectric—that is, those whose induced polarization varies linearly with the applied field—the electric displacement is related to the electric field by the simple constitutive relationship

$$\mathbf{D} = \boldsymbol{\epsilon}\boldsymbol{\mathcal{E}}, \tag{2.37}$$

where $\boldsymbol{\epsilon}$ is a second order tensor called the *electric permittivity*. By combining Equa-

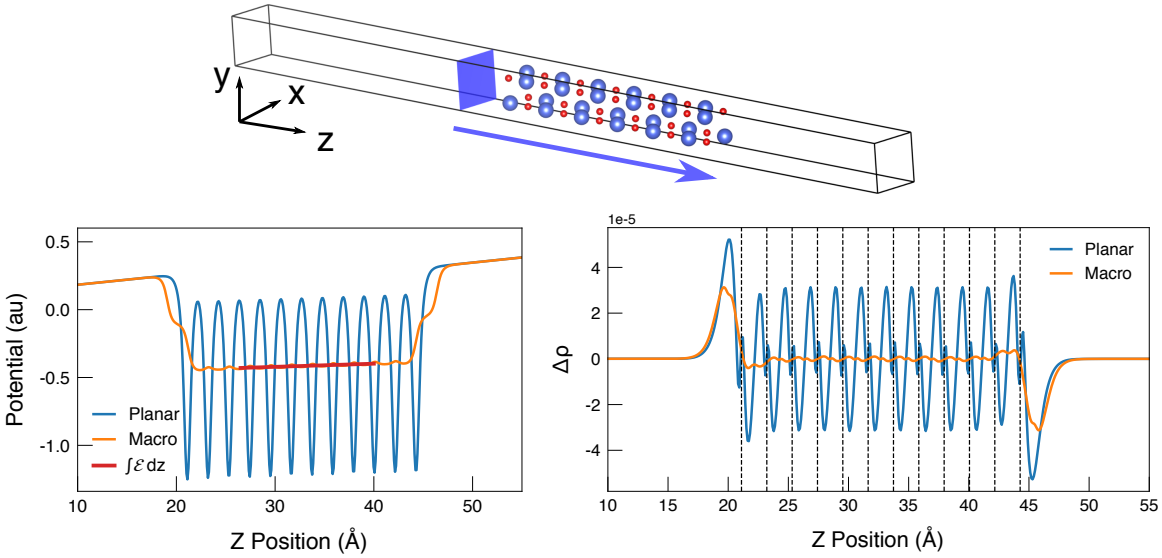

Figure 2.7: Macroscopic averaging of the potential and charge density of an MgO slab in an sawtooth potential. The top panel depicts the geometry of the slab and a plane in the xy-plane over which planar averages of the potential and charge density can be taken as it is translated over the width of the slab. The lower left panel shows the planar average of the electrostatic potential in and around the slab, with troughs in the potential aligning with the atomic layers of the slab. The macroscopic average is obtained by convoluting this planar average with a smoothing function with a width equal to the lattice constant.[116, 117] The macroscopic electric field is equal to the slope of this macroscopically averaged potential. Note that the field (slope) inside the slab is smaller than the field outside the slab due to the polarization of the slab. The ratio of the external to internal macroscopic fields yields the electric permittivity of the slab ϵ.[118, 119] The lower right panel shows the planar and macroscopic averages of the induced electron density, which is the difference in electron density between the applied-field and zero-field states. Note that electrons "pile up" at the lower surface of the slab when the field is applied, and similar dipolar charge rearrangements appear at each atomic layer.

tions (2.37) and (2.36), we obtain the linear relationship between polarization and electric field

$$\mathbf{P} = \boldsymbol{\chi}_e \boldsymbol{\mathcal{E}}. \tag{2.38}$$

The components of the *electric susceptibility* $\boldsymbol{\chi}_e$ are related to those of the electric permittivity $\boldsymbol{\epsilon}$ by

$$(\chi_e)_{ij} = (\epsilon_{ij} - \delta_{ij})/4\pi, \tag{2.39}$$

where δ_{ij} is the Kronecker delta. From Equation (2.38), we can see that $\boldsymbol{\chi}_e$ is analogous to the polarizability tensor of an isolated system $\boldsymbol{\alpha}$, but for continuous dielectrics. Like $\boldsymbol{\alpha}$, $\boldsymbol{\chi}_e$ as a derivative of the polarization with respect to the applied field (in this case the macroscopic field), a formulation which we will find particularly useful in the *ab initio* treatment:

$$\chi_{ij} = \frac{\partial P_i}{\partial \mathcal{E}_j}. \tag{2.40}$$

Continuum Calculations of Electric Permittivity

Many problems in classical electrostatics require the solution of Equation (2.35) with a specific set of boundary conditions. Aside from some idealized cases that allow an analytical solution, Equation (2.35) is typically solved using numerical methods, such as the Finite Element Method (FEM).[120, 121, 122] The FEM is our chosen method for calculating the effective electric permittivity of continuum models for composite materials in Chapter 4, which involves solving Equation (2.35) over potentially complicated geometries.

The FEM is commonly used to solve differential equations in the engineering sciences, but it has also found application in chemistry as a real-space DFT solver.[123, 124] In Appendix A, we use the FEM to solve the independent particle Schrödinger equation for electrons in finite wells, highlighting the versatility of the approach. FEM works by discretizing the spatial domain of a problem into smaller domains called elements, each of which is associated with with piece-wise polynomial functions.[125] These so-called shape functions are only non-zero inside of their associated element and form a basis set for expanding the solution to the differential equation. Thus, solving an equation like (2.35) using the FEM involves finding the optimal coefficients for these basis functions.[125] The introduction of Chapter 4 provides some additional technical details about this procedure, including the definition of appropriate boundary conditions for nanocomposite simulations.

Quantum Calculations of Electric Permittivity

As we have stressed, the classical treatment of polarization—and hence electric permittivity—in linear dielectrics describes the behavior of macroscopically averaged fields in continuous media, with no assumed relation to a more fundamental atomic description of matter. Shortly, we will discuss how the polarization can be calculated

from a quantum treatment of atomic and electronic structure. However, it is useful to first sketch an outline of how we calculate electric permittivity for periodic atomic systems, under the assumption that we are able to calculate the polarization $\mathbf{P}$ for a given set of nuclear coordinates, under an applied homogeneous (still macroscopic) electric field $\boldsymbol{\mathcal{E}}$. In such a scenario, the easiest way to calculate $\boldsymbol{\epsilon}$ is to use Equation (2.40) to evaluate $\boldsymbol{\chi}_e$ by finite differences and then calculate $\boldsymbol{\epsilon}$ with Equation (2.39).

Practically speaking, this strategy involves a four step process.

1. **Zero Field Optimization**: Optimization of the cell and atomic coordinates of the structure in the absence of an external field. calculate the polarization.

2. **Zero Field Polarization**: Perform a Berry Phase calculation of the polarization at zero field on the optimized structure.

3. **Clamped Ion Polarization**: Apply a small homogeneous electric field $\boldsymbol{\mathcal{E}}$. Calculate the electronic ground state and corresponding polarization.

4. **Relaxed Ion Polarization**: Optimize the nuclear coordinates in the presence of the same field and calculate the polarization.

Using the polarization values calculated in steps 2–4, the electric permittivity, ϵ, of a material is calculated with

$$\epsilon_{ij} = 1 + 4\pi \frac{\Delta P_i}{\mathcal{E}_j}, \tag{2.41}$$

where i and j are Cartesian directions. When ΔP is taken to be the polarization difference between steps 2 and 3 above, the result is the electron-only, or *clamped-ion*, permittivity ϵ^{∞}, indicated by the green arrow in Figure 2.8. Conversely, taking the difference between steps 2 and 4 gives the combined electronic and ionic contributions, known as the *relaxed-ion* permittivity ϵ^{0}. For isotropic materials, steps 3 and 4 need to be performed for only one direction of the applied field, whereas anisotropic materials require these steps to be repeated for all three field directions in order to obtain the full permittivity tensor.

Frequency-Dependence of Electric Permittivity

Before proceeding with the quantum description of polarization, we note that as with molecular calculations, all calculations of bulk materials in external fields in this

dissertation consider only static, or time-invariant, fields. In more general terms, the electric permittivity is a function of the frequency ω of the applied electric field and can be written

$$\boldsymbol{\epsilon}(\omega) = \boldsymbol{\epsilon}'(\omega) + i\boldsymbol{\epsilon}''(\omega). \tag{2.42}$$

The real part $\boldsymbol{\epsilon}'$ describes the dielectric polarization of bound charges, and the imaginary part $\boldsymbol{\epsilon}''$ corresponds to energy dissipation via absorption and is directly proportional to the conductivity of the material at a given frequency.[110] The frequency dependence of $\boldsymbol{\epsilon}'$ arises from the same three physical mechanisms that determine molecular polarizability—namely dipolar, ionic, and electronic polarization, which operate at different timescales. Figure 2.8 depicts these mechanisms and their effect on the frequency dependence of $\boldsymbol{\epsilon}$.

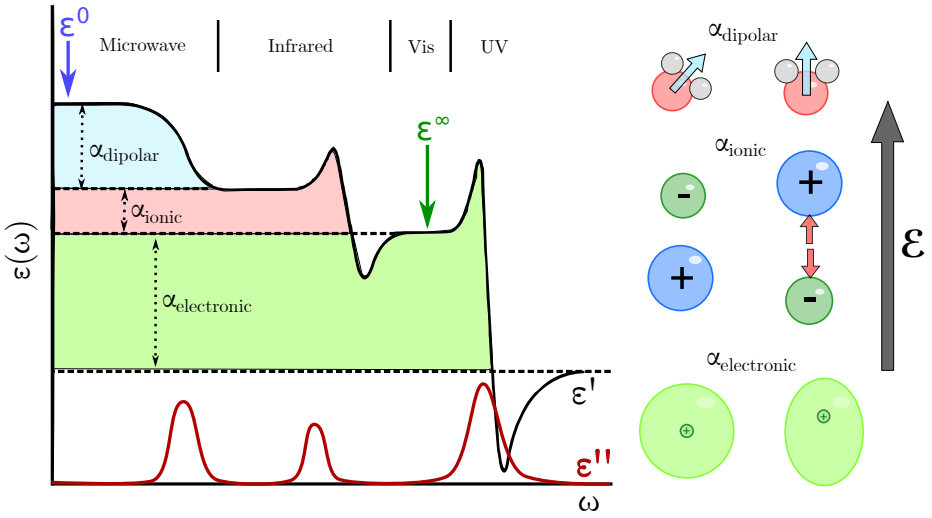

Figure 2.8: The relationship between the real and imaginary permittivity and the electric field frequency ω, adapted from [115]. The contributions of different types of microscopic polarizabilities, α, are labeled in their corresponding frequency domain.

Because of the frequency dependence of these mechanisms, it might seem that only considering only time-invariant fields imposes quite a severe limitation on the usefulness of the obtained material properties. However, as described in Section 2.4.2, by constraining or relaxing the positions of atomic nuclei, we are able to calculate a permittivity that includes either the electronic polarization alone or both electronic and ionic contributions. The different physical origins of polarization in these two values correspond to two important frequency domains in Figure 2.8. The relaxed-ion permittivity $\boldsymbol{\epsilon}^0$, in which all modes of polarization are able to respond to the applied

field, is also known as the *low-frequency permittivity*. This quantity corresponds to the application of DC fields and is the relevant regime for capacitive energy storage applications. Furthermore, as shown in Figure 2.8, $\boldsymbol{\epsilon}^0$ is generally a good approximation for permittivity at frequencies up to at least the microwave regime. Additionally, the clamped-ion permittivity $\boldsymbol{\epsilon}^\infty$ is also called the *high-frequency permittivity*, since it corresponds to a frequency that is high enough that nuclei are unable to respond, but at which the electrons are still able to polarize fully.[†] Its place in the frequency domain is indicated by a green arrow in Figure 2.8. Because this regime lies in the visible region for many materials, $\boldsymbol{\epsilon}^\infty$ is called the optical permittivity and is a quite useful quantity for optical applications—note in particular that the complex optical permittivity is equal to the square of that material's complex refractive index.[115] Thus, while we cannot access the full spectrum of $\boldsymbol{\epsilon}$ with static fields, we are still able to evaluate both low-frequency and optical permittivities, which are important for many applications. Furthermore, since we only calculate the permittivity of finite band-gap insulators, where $\boldsymbol{\epsilon}''$ is negligible for static fields, we only deal with the real permittivity $\boldsymbol{\epsilon}'$ from here on and drop the apostrophe.

Modern Theory of Polarization

When discussing calculating $\boldsymbol{\epsilon}$ from atomistic simulations above, we assumed that we could calculate the polarization for a given set of nuclear coordinates. We now discuss just how this is done. Despite the ubiquitous intuition that macroscopic polarization results from the collective polarization of the atoms or molecules comprising a material, it turns out that obtaining the macroscopic polarization of a material from its microscopic behavior is no trivial endeavor. In fact even the definition of polarization as the dipole moment per unit volume becomes problematic when considering continuous charge distributions in a periodic unit cell due to the position operator being ill-defined,[126] an inability to partition the density into discrete dipole contributions,[127] and a dependence on the unit cell definition. [128] Fortunately, work in the early 1990s by Resta, King-Smith, and Vanderbilt worked out these difficulties and established the Modern Theory of Polarization (MTP), by which we are able to compute the polarization of bulk.[129, 130, 131, 132] We now sketch the major results of this theory.

[†]The notation $\boldsymbol{\epsilon}^\infty$ can sometimes cause confusion. It does not indicate the permittivity as the frequency tends toward ∞. Rather, it indicates the permittivity at a frequency much higher than the frequency of nuclear motion.

Although the charge density alone cannot be used to derive a meaningful definition of polarization as a bulk property,[129] the change in polarization of a unit cell during some adiabatic process of material can be defined as the integrated average current density in the cell:[127]

$$\Delta\mathbf{P} = \int_0^{\Delta t} dt\mathbf{j}(t), \tag{2.43}$$

where $\mathbf{j}$ is the average current density in the cell. In the context of the response of a material to an electric field, one can imagine that slowly turning on the field causes the electrons in the bulk to reorganize, producing a momentary current that can be integrated over time to yield the induced polarization. Inherent in this approach is the idea that the *change* in polarization is the quantity of interest, rather than the polarization itself.[129]

King-Smith and Vanderbilt showed that in an insulator, the electronic polarization at any point along an adiabatic transition could be calculated using an expression that depends only on the occupied electronic bands:[131]

$$\mathbf{P}_{\text{elec}} = \frac{-if}{(2\pi)^3} \sum_n \int_{\text{BZ}} d\mathbf{k} \langle u_{n\mathbf{k}} | \nabla_{\mathbf{k}} | u_{n\mathbf{k}} \rangle. \tag{2.44}$$

In the above equation, f is the occupation of each band (2 for non-spin-polarized calculations), $u_{n\mathbf{k}}$ is the lattice-periodic part of the Bloch functions, and $\nabla_{\mathbf{k}}$ is the gradient operator with respect to the k-point. The integral over the BZ provides the contribution from the n-th electronic band and is related to a quantity called the Berry Phase.

The expression for $\mathbf{P}_{\text{elec}}$ can be more intuitively understood by re-writing it in terms of the centers of charge of so-called *Wannier functions*. Wannier functions are a transformation of the delocalized Bloch states $\psi_{n\mathbf{k}}$ that *localizes* them in a real-space cell.[133] The Wannier function for band n in the cell labeled by the lattice vector $\mathbf{R}$ is obtained by

$$w_{n\mathbf{R}} = \frac{\Omega}{(2\pi)^3} \int_{\text{BZ}} d\mathbf{k} e^{i\mathbf{k}\cdot\mathbf{R}} \psi_{n\mathbf{k}}. \tag{2.45}$$

The expectation value of the position of an electron occupying a Wannier function is given by $\mathbf{r}_{n\mathbf{R}} = \langle w_{n\mathbf{R}} | \mathbf{r} | w_{n\mathbf{R}} \rangle$. This *Wannier center* defines the locus of charge for that Wannier function, and summation over the Wannier centers from all electronic bands, times the occupation and electronic charge, yields the electronic dipole moment of the cell, analogously to the point dipole expression in Equation (2.24). In fact, the

Berry Phase expression for the electronic polarization can be rewritten in just this way, as[131]

$$\mathbf{P}_{\text{elec}} = -\frac{f}{\Omega}\sum_{n}\mathbf{r}_{n\mathbf{R}}. \tag{2.46}$$

As we will see in chapter 3, Wannier functions can be further localized to yield Maximally Localized Wannier Functions (MLWFs), which are especially useful for studying polarization in nanostructures.[134] In particular, their localization means that MLWF centers can be assigned to individual atoms or groups of atoms in the system, allowing the total polarization response to be partitioned into site-specific contributions.[84, 134] Figure 2.9 briefly introduces the Wannier transformation and its application to polarization induced by an electric field.

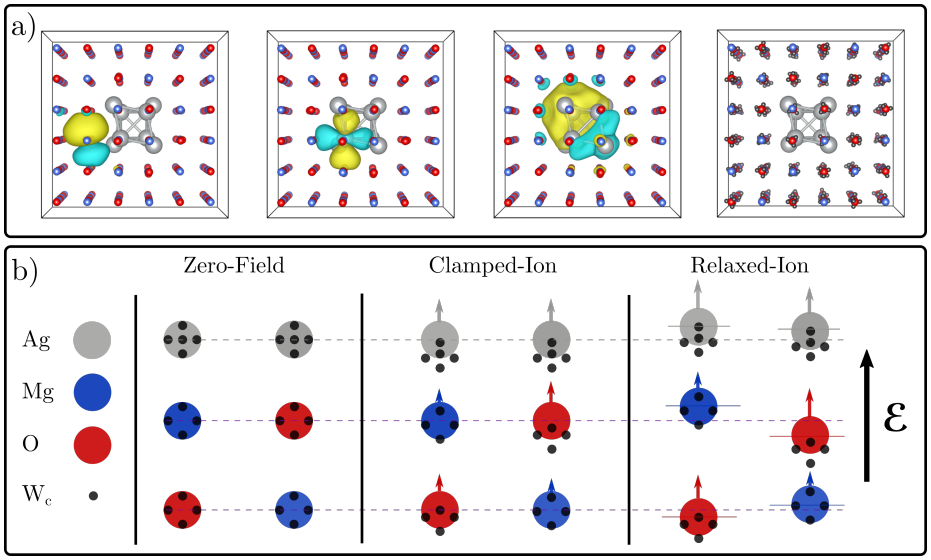

Figure 2.9: Wannier functions and bulk polarization. Panel **a)** shows, from left to right, representative O sp^3-like, Ag $4d$-like, and Ag pseudoatomic $5s$-like Wannier functions in an MgO/Ag nanocomposite unit cell. The rightmost image shows the Wannier centers W_c superimposed on the atomic positions. Panel **b)** shows schematically how bulk polarization results from Wannier center displacement. From left to right, the frames show a portion of the MgO/Ag nanocomposite under zero-field, clamped-ion, and relaxed-ion conditions. Arrows on atoms show the total induced dipole moment that is associated with each atom. The left-hand legend applies to both Panels **a)** and **b)**.

When calculating the electric permittivity, we are after the *change* in polarization upon application of a field. Furthermore, the MTP shows us that the polarization will not generally be zero in the zero-field case.[127] Thus, we must calculate the

polarization for both the zero-field and applied field cases and take their difference to obtain the useful quantity $\Delta\mathbf{P}$. The electronic contribution can either be calculated as the change in Berry phases or the displacement of Wannier functions, using Equations (2.44) or (2.46). For polar and ionic materials, the ionic contribution is calculated using the displacements of the nuclear positions ($\Delta\mathbf{r}_I$), times the charge of the bare ion cores (Z_I).[†] Combining this with the Wannier center expression for electrons, the total polarization change is

$$\begin{aligned}\Delta\mathbf{P} &= \Delta\mathbf{P}_{\text{elec}} + \Delta\mathbf{P}_{\text{ion}} \\ &= \frac{1}{\Omega}\left[\sum_n f\Delta\mathbf{r}_{n\mathbf{R}} + \sum_I Z_I\Delta\mathbf{r}_I\right],\end{aligned} \tag{2.47}$$

where the indices n and I run over all Wannier centers and ion cores, respectively.

Importantly, as a phase, the Berry phase is only defined up to a factor of 2π. Similarly, Wannier centers are only defined modulo a lattice vector $\mathbf{R}$, since under periodic boundary conditions, translating an electron by a lattice vector returns it to its original location.[127] This leads to the polarization being multi-valued, only defined modulo the *quantum of polarization* $\mathbf{P}_q = \frac{\mathbf{R}}{\Omega}$, or the polarization change resulting from translating an electron (with unit charge in atomic units) by a lattice vector.[127] The calculated change in polarization, too, is only defined modulo $\mathbf{P}_q$. Thus, while current flow—and hence the true polarization induced by a perturbation—is single-valued, its calculation via the MTP is not. Using this result, we can define the true polarization change ΔP as[127]

$$\Delta\mathbf{P} = (\mathbf{P}_1 - \mathbf{P}_0) + c\mathbf{P}_q, \tag{2.48}$$

where c is some integer. For the electric field perturbations we apply, $\Delta\mathbf{P}$ is usually smaller than the quantum of polarization, making it easy to determine c in the above equation. Additionally, while relaxing ions in the presence of a field, we compute the polarization at each step along a damped dynamics trajectory, allowing us to plot the polarization at each step to easily identify any jumps by a quantum of polarization. Figure 2.10 shows the polarization in such a trajectory.

[†]In pseudopotential calculations, Z_I is equal to the charge of the pseudopotential for atom I.

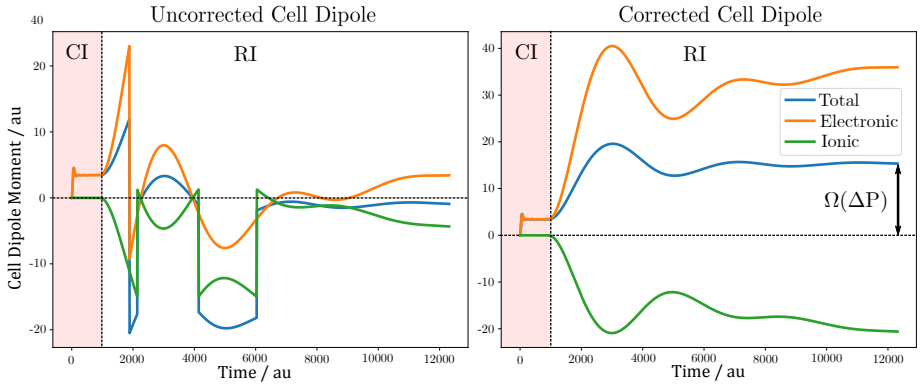

Figure 2.10: Removing discontinuities in the polarization curve. In the left hand plot, several jumps by integer multiples of the quantum of polarization occur during ionic relaxation. In the right hand plot, these jumps are corrected on the right to yield the correct change in polarization, ΔP. CI denotes the clamped-ion, or electron-only polarization, while RI denotes the relaxed-ion polarization. The trajectory was computed for an MgO/Ag nanocomposite using CPMD.

Finite Homogeneous Electric Fields in Bulk Calculations

Armed with the ability to calculate the change in polarization of a bulk material, we now discuss the application of a finite electric field within periodic DFT. The effects of a homogeneous macroscopic field $\boldsymbol{\mathcal{E}}$ can be simulated by minimizing the *electric enthalpy functional* below

$$F[\psi_{n\mathbf{k}};\boldsymbol{\mathcal{E}}] = E_{\mathrm{KS}}[\{\psi_{n\mathbf{k}}\}] - \Omega\boldsymbol{\mathcal{E}}\cdot\mathbf{P}[\{\psi_{n\mathbf{k}}\}], \tag{2.49}$$

where Ω is the unit cell volume, E_{KS} is the usual Kohn-Sham energy functional, $\mathbf{P}$ is the polarization computed with the MTP, and $\psi_{n\mathbf{k}}$ are the field-modified Bloch functions.[135, 136, 137]

Importantly, the application of such a field removes the periodicity of the external potential and the minima of the electric enthalpy will vanish if the applied electric field is too large (Figure 2.11). Physically, this effect can be interpreted as the Zener tunneling of electrons from the valence bands of one cell to the conduction bands of periodic image cells (Figure 2.11(a)).[136] To avoid this tunneling, the applied field in a given direction should be chosen such that it is below a critical value approximated by $\mathcal{E}_c \approx E_{\mathrm{gap}}/(RN_k)$, where E_{gap} is the material band gap, R is the length of the primitive lattice vector in the field direction, and N_k is the number of k-points.[136] As mentioned above, we often perform Gamma-point calculations on large cells using CPMD. For such a cell with length L in the direction of the applied field, the critical

field strength is $\mathcal{E}_c \approx E_{\text{gap}}/L$. Thus, avoiding large fields, we can use the finite field approach to calculate the electrical permittivity in bulk materials. Specifically, we used the Gamma point implementation of this approach from Umari and Pasquarello when using the CPMD module of Quantum Espresso,[137] and the more general implementation of Souza, Iñiguez, and Vanderbilt when using the PW module.[138]

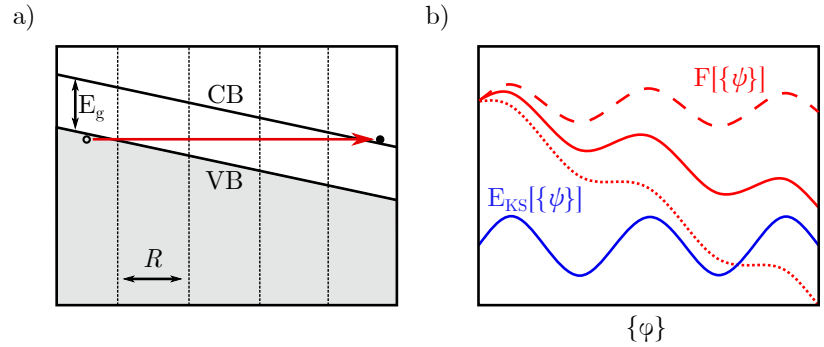

Figure 2.11: Quirks of the Modern Theory of Polarization. Panel a) shows the bending of the valence bands (VB) and conduction bands (CB) due to an applied electric field. Zener tunneling of an electron is illustrated by the red arrow. Panel b) shows the electric enthalpy functional in Equation (2.49). The periodic Kohn-Sham part of the functional is shown in blue, while the overall functional is shown in red for small (dashes), medium (solid), and large (dotted) external field. Note that local minima in $F[\{\phi\}]$ are metastable states that disappear when $\mathcal{E}$ is too large.

Alternative Approach: Density Functional Perturbation Theory

It is worth noting that Density Functional Perturbation Theory (DFPT) offers an alternative way to calculate the first-order response of materials to electric fields.[139, 140, 141, 142] Such methods predate the MTP and do not rely on the understanding of the polarization itself as a multi-valued quantity, and thus in some sense they offer a simpler approach to permittivity. However, DFPT suffers from serious computational scaling issues that make it incompatible with our interest in nanostructured materials. On the one hand, DFPT displays an efficiency competitive with finite field Berry Phase calculations for calculating the clamped ion electric permittivity ϵ^{∞} and Born Effective Charges, which require the response to a single perturbation (though a denser k-grid may be required for accurate results in DFPT).[139, 142, 143] However, calculation of the ionic contribution to permittivity under DFPT requires the calculation of the phonon modes of the material, which requires 3 perturbations per atom (one displacement in each direction).[142] Thus, for the large unit cells

required for nanostructured materials, a geometry relaxation under a finite field is much more computationally attractive.[137] This, combined with the spatial resolution of contributions to the dielectric response afforded by the MLWF approach, makes the application of MTP in finite electric fields a natural choice over DFPT for our applications.

2.5 Summary

The current chapter provided a theoretical introduction to several different electronic structure methods that are used to study the dielectric and catalytic properties of nanostructured materials in this dissertation. In particular, we highlighted the important trade-off between computational cost and simulation accuracy and how balancing these factors can be especially challenging for nanostructures given the large length scales and heterogeneity involved. This challenge motivates the occasional use of well-informed approximations over theoretically more sophisticated methods in order to widen the range of materials that can be studied. Developing computationally inexpensive approximations to polarization is the subject of Chapters 4 and 5, while Chapter 6 investigates the accuracy limits of relatively cheap DFT for nanostructured ORR catalysts. Beyond an intruduction to DFT and WFT, this chapter also described the theory of polarization of both finite and periodic systems. The methodology used to calculate the macroscopic permittivity of materials from DFT was described, and a brief preview of how Wannier functions could be used to spatially resolve polarization behavior was offered. The current chapter is not exhaustive—additional theory will be presented at the beginning of subsequent chapters. However, for the most part, these later theoretical incursions build on the groundwork established to this point.

Bibliography

[1] Frank Jensen. *Introduction to Computational Chemistry 3rd. ed.* Wiley, 3rd ed. edition, 2017.

[2] Florian Weigend and Reinhart Ahlrichs. Balanced basis sets of split valence, triple zeta valence and quadruple zeta valence quality for h to rn: Design and assessment of accuracy. *Physical Chemistry Chemical Physics*, 7(18):3297, 2005.

[3] D. Andrae, U. Häußermann, M. Dolg, H. Stoll, and H. Preuß. Energy-adjusted ab initio pseudopotentials for the second and third row transition elements. *Theoretica Chimica Acta*, 77(2):123–141, 1990.

[4] Ewa Papajak and Donald G. Truhlar. Efficient diffuse basis sets for density functional theory. *Journal of Chemical Theory and Computation*, 6(3):597–601, February 2010.

[5] Antonio Bauzá, David Quiñonero, Pere M. Deyà, and Antonio Frontera. Is the use of diffuse functions essential for the properly description of noncovalent interactions involving anions? *The Journal of Physical Chemistry A*, 117(12):2651–2655, March 2013.

[6] Erin R. Johnson, Alberto Otero-de-la Roza, Stephen G. Dale, and Gino A. DiLabio. Efficient basis sets for non-covalent interactions in xdm-corrected density-functional theory. *The Journal of Chemical Physics*, 139(21), December 2013.

[7] Jayaraman Chandrasekhar, Juan G. Andrade, and Paul von Rague Schleyer. Efficient and accurate calculation of anion proton affinities. *Journal of the American Chemical Society*, 103(18):5609–5612, September 1981.

[8] Dmitrij Rappoport and Filipp Furche. Property-optimized gaussian basis sets for molecular response calculations. *The Journal of Chemical Physics*, 133(13), October 2010.

[9] Frank Jensen. Polarization consistent basis sets. iii. the importance of diffuse functions. *The Journal of Chemical Physics*, 117(20):9234–9240, November 2002.

[10] Rick A. Kendall, Thom H. Dunning, and Robert J. Harrison. Electron affinities of the first-row atoms revisited. systematic basis sets and wave functions. *The Journal of Chemical Physics*, 96(9):6796–6806, May 1992.

[11] Nikolai B. Balabanov and Kirk A. Peterson. Systematically convergent basis sets for transition metals. i. all-electron correlation consistent basis sets for the 3d elements sc–zn. *The Journal of Chemical Physics*, 123(6):064107, August 2005.

[12] Nikolai B. Balabanov and Kirk A. Peterson. Basis set limit electronic excitation energies, ionization potentials, and electron affinities for the 3d transition metal atoms: Coupled cluster and multireference methods. *The Journal of Chemical Physics*, 125(7):074110, August 2006.

[13] Thom H. Dunning. Gaussian basis sets for use in correlated molecular calculations. i. the atoms boron through neon and hydrogen. *The Journal of Chemical Physics*, 90(2):1007–1023, January 1989.

[14] Attila Szabo and Neil S. Ostlund. *Modern Quantum Chemistry: Introduction to Advanced Electronic Structure Theory*. Dover Publications, Inc., Mineola, first edition, 1996.

[15] Peter W Atkins and Ronald S Friedman. *Molecular Quantum Mechanics*. Oxford University Press, London, England, 5th edition, November 2010.

[16] Richard M. Martin. *Electronic Structure: Basic Theory and Practical Methods*. Cambridge University Press, 2nd edition, August 2020.

[17] J. C. Slater. Note on hartree's method. *Physical Review*, 35(2):210–211, January 1930.

[18] V. Fock. Näherungsmethode zur lösung des quantenmechanischen mehrkörperproblems. *Zeitschrift für Physik*, 61(1–2):126–148, January 1930.

[19] D R Hartree and W Hartree. Self-consistent field, with exchange, for beryllium. *Proc. R. Soc. Lond.*, 150(869):9–33, May 1935.

[20] Markus Reiher, Oliver Salomon, and Bernd Artur Hess. Reparameterization of hybrid functionals based on energy differences of states of different multiplicity. *Theoretical Chemistry Accounts: Theory, Computation, and Modeling (Theoretica Chimica Acta)*, 107(1):48–55, December 2001.

[21] Damián A. Scherlis and Darío A. Estrin. Structure and spin-state energetics of an iron porphyrin model: An assessment of theoretical methods. *International Journal of Quantum Chemistry*, 87(3):158–166, January 2002.

[22] Marcel Swart and Maja Gruden. Spinning around in transition-metal chemistry. *Accounts of Chemical Research*, 49(12):2690–2697, November 2016.

[23] Jiří Čížek. On the correlation problem in atomic and molecular systems. calculation of wavefunction components in ursell-type expansion using quantum-field theoretical methods. *The Journal of Chemical Physics*, 45(11):4256–4266, December 1966.

[24] Rodney J. Bartlett and Monika Musiał. Coupled-cluster theory in quantum chemistry. *Reviews of Modern Physics*, 79(1):291–352, February 2007.

[25] Zongtang Fang, Zachary Lee, Kirk A. Peterson, and David A. Dixon. Use of improved orbitals for ccsd(t) calculations for predicting heats of formation of group iv and group vi metal oxide monomers and dimers and ucl6. *Journal of Chemical Theory and Computation*, 12(8):3583–3592, July 2016.

[26] Zongtang Fang, Monica Vasiliu, Kirk A. Peterson, and David A. Dixon. Prediction of bond dissociation energies/heats of formation for diatomic transition metal compounds: Ccsd(t) works. *Journal of Chemical Theory and Computation*, 13(3):1057–1066, January 2017.

[27] Luke W. Bertels, Joonho Lee, and Martin Head-Gordon. Polishing the gold standard: The role of orbital choice in ccsd(t) vibrational frequency prediction. *Journal of Chemical Theory and Computation*, 17(2):742–755, January 2021.

[28] Krishnan Raghavachari, Gary W. Trucks, John A. Pople, and Martin Head-Gordon. A fifth-order perturbation comparison of electron correlation theories. *Chemical Physics Letters*, 157(6):479–483, May 1989.

[29] John D. Watts, Jürgen Gauss, and Rodney J. Bartlett. Coupled-cluster methods with noniterative triple excitations for restricted open-shell hartree–fock and other general single determinant reference functions. energies and analytical gradients. *The Journal of Chemical Physics*, 98(11):8718–8733, June 1993.

[30] J. Russell Thomas, Bradley J. DeLeeuw, George Vacek, T. Daniel Crawford, Yukio Yamaguchi, and Henry F. Schaefer. The balance between theoretical method and basis set quality: A systematic study of equilibrium geometries, dipole moments, harmonic vibrational frequencies, and infrared intensities. *The Journal of Chemical Physics*, 99(1):403–416, July 1993.

[31] Trygve Helgaker, Jürgen Gauss, Poul Jo/rgensen, and Jeppe Olsen. The prediction of molecular equilibrium structures by the standard electronic wave functions. *The Journal of Chemical Physics*, 106(15):6430–6440, April 1997.

[32] Keld L. Bak, Jürgen Gauss, Poul Jørgensen, Jeppe Olsen, Trygve Helgaker, and John F. Stanton. The accurate determination of molecular equilibrium structures. *The Journal of Chemical Physics*, 114(15):6548–6556, April 2001.

[33] Pavel Hobza. Calculations on noncovalent interactions and databases of benchmark interaction energies. *Accounts of Chemical Research*, 45(4):663–672, January 2012.

[34] Latévi Max Lawson Daku, Francesco Aquilante, Timothy W. Robinson, and Andreas Hauser. Accurate spin-state energetics of transition metal complexes. 1. ccsd(t), caspt2, and dft study of [m(nch)6]2+(m = fe, co). *Journal of Chemical Theory and Computation*, 8(11):4216–4231, October 2012.

[35] Yuri A. Aoto, Ana Paula de Lima Batista, Andreas Köhn, and Antonio G. S. de Oliveira-Filho. How to arrive at accurate benchmark values for transition metal compounds: Computation or experiment? *Journal of Chemical Theory and Computation*, 13(11):5291–5316, October 2017.

[36] Christoph Riplinger and Frank Neese. An efficient and near linear scaling pair natural orbital based local coupled cluster method. *The Journal of Chemical Physics*, 138(3), January 2013.

[37] Frank Neese, Frank Wennmohs, and Andreas Hansen. Efficient and accurate local approximations to coupled-electron pair approaches: An attempt to revive the pair natural orbital method. *The Journal of Chemical Physics*, 130(11), March 2009.

[38] Yang Guo, Christoph Riplinger, Ute Becker, Dimitrios G. Liakos, Yury Minenkov, Luigi Cavallo, and Frank Neese. Communication: An improved linear scaling perturbative triples correction for the domain based local pair-natural orbital based singles and doubles coupled cluster method [dlpno-ccsd(t)]. *The Journal of Chemical Physics*, 148(1), January 2018.

[39] Ahmet Altun, Frank Neese, and Giovanni Bistoni. Extrapolation to the limit of a complete pair natural orbital space in local coupled-cluster calculations.

Journal of Chemical Theory and Computation, 16(10):6142–6149, September 2020.

[40] Maria Drosou, Christiana A. Mitsopoulou, and Dimitrios A. Pantazis. Reconciling local coupled cluster with multireference approaches for transition metal spin-state energetics. *Journal of Chemical Theory and Computation*, 18(6):3538–3548, May 2022.

[41] Asger Halkier, Trygve Helgaker, Poul Jørgensen, Wim Klopper, and Jeppe Olsen. Basis-set convergence of the energy in molecular hartree–fock calculations. *Chemical Physics Letters*, 302(5–6):437–446, March 1999.

[42] Frank Jensen. Estimating the hartree—fock limit from finite basis set calculations. *Theoretical Chemistry Accounts*, 113(5):267–273, June 2005.

[43] Shijun Zhong, Ericka C. Barnes, and George A. Petersson. Uniformly convergent n-tuple-ζ augmented polarized (nzap) basis sets for complete basis set extrapolations. i. self-consistent field energies. *The Journal of Chemical Physics*, 129(18), November 2008.

[44] Frank Neese and Edward F. Valeev. Revisiting the atomic natural orbital approach for basis sets: Robust systematic basis sets for explicitly correlated and conventional correlated ab initio methods? *Journal of Chemical Theory and Computation*, 7(1):33–43, December 2010.

[45] Donald G. Truhlar. Basis-set extrapolation. *Chemical Physics Letters*, 294(1–3):45–48, September 1998.

[46] Peter Kraus. Basis set extrapolations for density functional theory. *Journal of Chemical Theory and Computation*, 16(9):5712–5722, August 2020.

[47] Trygve Helgaker, Wim Klopper, Henrik Koch, and Jozef Noga. Basis-set convergence of correlated calculations on water. *The Journal of Chemical Physics*, 106(23):9639–9646, June 1997.

[48] Wanyi Jiang, Nathan J. DeYonker, and Angela K. Wilson. Multireference character for 3d transition-metal-containing molecules. *Journal of Chemical Theory and Computation*, 8(2):460–468, January 2012.

[49] Per Siegbahn, Anders Heiberg, Björn Roos, and Bernard Levy. A comparison of the super-ci and the newton-raphson scheme in the complete active space scf method. *Physica Scripta*, 21(3–4):323–327, January 1980.

[50] Björn O. Roos, Peter R. Taylor, and Per E.M. Sigbahn. A complete active space scf method (casscf) using a density matrix formulated super-ci approach. *Chemical Physics*, 48(2):157–173, May 1980.

[51] Per E. M. Siegbahn, Jan Almlöf, Anders Heiberg, and Björn O. Roos. The complete active space scf (casscf) method in a newton–raphson formulation with application to the hno molecule. *The Journal of Chemical Physics*, 74(4):2384–2396, February 1981.

[52] Milica Feldt and Quan Manh Phung. Ab initio methods in first-row transition metal chemistry. *European Journal of Inorganic Chemistry*, 2022(15):e202200014, April 2022.

[53] Hagen Neugebauer, Hung T. Vuong, John L. Weber, Richard A. Friesner, James Shee, and Andreas Hansen. Toward benchmark-quality ab initio predictions for 3d transition metal electrocatalysts: A comparison of ccsd(t) and ph-afqmc. *Journal of Chemical Theory and Computation*, 19(18):6208–6225, September 2023.

[54] P. Hohenberg and W. Kohn. Inhomogeneous electron gas. *Physical Review*, 136(3B):B864–B871, November 1964.

[55] W. Kohn and L. J. Sham. Self-consistent equations including exchange and correlation effects. *Physical Review*, 140(4A):A1133–A1138, November 1965.

[56] John P. Perdew and Karla Schmidt. Jacob's ladder of density functional approximations for the exchange-correlation energy. *AIP Conference Proceedings*, 577(1):1–20, 07 2001.

[57] Roberto Peverati and Donald G. Truhlar. Quest for a universal density functional: the accuracy of density functionals across a broad spectrum of databases in chemistry and physics. *Philosophical Transactions of the Royal Society A: Mathematical, Physical and Engineering Sciences*, 372(2011):20120476, March 2014.

[58] J. P. Perdew and Alex Zunger. Self-interaction correction to density-functional approximations for many-electron systems. *Physical Review B*, 23(10):5048–5079, May 1981.

[59] John P. Perdew, Kieron Burke, and Matthias Ernzerhof. Generalized gradient approximation made simple. *Physical Review Letters*, 77(18):3865–3868, October 1996.

[60] A. D. Becke. Density-functional exchange-energy approximation with correct asymptotic behavior. *Physical Review A*, 38(6):3098–3100, September 1988.

[61] John P. Perdew. Density-functional approximation for the correlation energy of the inhomogeneous electron gas. *Physical Review B*, 33(12):8822–8824, June 1986.

[62] John P. Perdew, Adrienn Ruzsinszky, Gábor I. Csonka, Oleg A. Vydrov, Gustavo E. Scuseria, Lucian A. Constantin, Xiaolan Zhou, and Kieron Burke. Restoring the density-gradient expansion for exchange in solids and surfaces. *Physical Review Letters*, 100(13), April 2008.

[63] Stefan Kurth, John P. Perdew, and Peter Blaha. Molecular and solid-state tests of density functional approximations: Lsd, ggas, and meta-ggas. *International Journal of Quantum Chemistry*, 75(4–5):889–909, 1999.

[64] Kyle R. Bryenton, Adebayo A. Adeleke, Stephen G. Dale, and Erin R. Johnson. Delocalization error: The greatest outstanding challenge in density-functional theory. *WIREs Computational Molecular Science*, 13(2), July 2022.

[65] Frank Neese. Prediction of molecular properties and molecular spectroscopy with density functional theory: From fundamental theory to exchange-coupling. *Coordination Chemistry Reviews*, 253(5–6):526–563, March 2009.

[66] John P. Perdew. Density functional theory and the band gap problem. *International Journal of Quantum Chemistry*, 28(S19):497–523, 1985.

[67] Carlo Adamo and Vincenzo Barone. Toward reliable density functional methods without adjustable parameters: The pbe0 model. *The Journal of Chemical Physics*, 110(13):6158–6170, April 1999.

[68] Axel D. Becke. Density-functional thermochemistry. iii. the role of exact exchange. *The Journal of Chemical Physics*, 98(7):5648–5652, April 1993.

[69] Viktor N. Staroverov, Gustavo E. Scuseria, Jianmin Tao, and John P. Perdew. Comparative assessment of a new nonempirical density functional: Molecules and hydrogen-bonded complexes. *The Journal of Chemical Physics*, 119(23):12129–12137, December 2003.

[70] Jianmin Tao, John P. Perdew, Viktor N. Staroverov, and Gustavo E. Scuseria. Climbing the density functional ladder: Nonempirical meta–generalized gradient approximation designed for molecules and solids. *Physical Review Letters*, 91(14), September 2003.

[71] Lars Goerigk and Stefan Grimme. A thorough benchmark of density functional methods for general main group thermochemistry, kinetics, and noncovalent interactions. *Physical Chemistry Chemical Physics*, 13(14):6670, 2011.

[72] Lars Goerigk, Andreas Hansen, Christoph Bauer, Stephan Ehrlich, Asim Najibi, and Stefan Grimme. A look at the density functional theory zoo with the advanced gmtkn55 database for general main group thermochemistry, kinetics and noncovalent interactions. *Physical Chemistry Chemical Physics*, 19(48):32184–32215, 2017.

[73] Jing Yang, Stefano Falletta, and Alfredo Pasquarello. Range-separated hybrid functionals for accurate prediction of band gaps of extended systems. *npj Computational Materials*, 9(1), June 2023.

[74] Stefan Grimme. Semiempirical hybrid density functional with perturbative second-order correlation. *The Journal of Chemical Physics*, 124(3), January 2006.

[75] Lars Goerigk and Stefan Grimme. Efficient and accurate double-hybrid-meta-gga density functionals—evaluation with the extended gmtkn30 database for general main group thermochemistry, kinetics, and noncovalent interactions. *Journal of Chemical Theory and Computation*, 7(2):291–309, December 2010.

[76] Sebastian Dohm, Andreas Hansen, Marc Steinmetz, Stefan Grimme, and Marek P. Checinski. Comprehensive thermochemical benchmark set of realistic

closed-shell metal organic reactions. *Journal of Chemical Theory and Computation*, 14(5):2596–2608, March 2018.

[77] Leonard R. Maurer, Markus Bursch, Stefan Grimme, and Andreas Hansen. Assessing density functional theory for chemically relevant open-shell transition metal reactions. *Journal of Chemical Theory and Computation*, 17(10):6134–6151, September 2021.

[78] Stefan Grimme, Andreas Hansen, Jan Gerit Brandenburg, and Christoph Bannwarth. Dispersion-corrected mean-field electronic structure methods. *Chemical Reviews*, 116(9):5105–5154, April 2016.

[79] Stefan Grimme, Stephan Ehrlich, and Lars Goerigk. Effect of the damping function in dispersion corrected density functional theory. *Journal of Computational Chemistry*, 32(7):1456–1465, March 2011.

[80] Eike Caldeweyher, Sebastian Ehlert, Andreas Hansen, Hagen Neugebauer, Sebastian Spicher, Christoph Bannwarth, and Stefan Grimme. A generally applicable atomic-charge dependent london dispersion correction. *The Journal of Chemical Physics*, 150(15), April 2019.

[81] Eike Caldeweyher, Jan-Michael Mewes, Sebastian Ehlert, and Stefan Grimme. Extension and evaluation of the d4 london-dispersion model for periodic systems. *Physical Chemistry Chemical Physics*, 22(16):8499–8512, 2020.

[82] Stefan Grimme, Jens Antony, Stephan Ehrlich, and Helge Krieg. A consistent and accurate ab initio parametrization of density functional dispersion correction (dft-d) for the 94 elements h-pu. *The Journal of Chemical Physics*, 132(15), April 2010.

[83] Hendrik J. Monkhorst and James D. Pack. Special points for brillouin-zone integrations. *Physical Review B*, 13(12):5188–5192, June 1976.

[84] David J.T. Hally and Irina Paci. Low-frequency polarization in molecular-scale noble-metal/metal-oxide nanocomposites. *Nanoscale*, 10(20):9583–9593, 2018.

[85] Archita N. S. Adluri, Brett Henderson, and Irina Paci. Tuning the dielectric response in a nanocomposite material through nanoparticle morphology. *RSC Advances*, 12(17):10778–10787, 2022.

[86] D. R. Hamann. Optimized norm-conserving vanderbilt pseudopotentials. *Physical Review B*, 88(8), August 2013.

[87] M.J. van Setten, M. Giantomassi, E. Bousquet, M.J. Verstraete, D.R. Hamann, X. Gonze, and G.-M. Rignanese. The pseudodojo: Training and grading a 85 element optimized norm-conserving pseudopotential table. *Computer Physics Communications*, 226:39–54, May 2018.

[88] Paolo Giannozzi, Stefano Baroni, Nicola Bonini, Matteo Calandra, Roberto Car, Carlo Cavazzoni, Davide Ceresoli, Guido L Chiarotti, Matteo Cococcioni, Ismaila Dabo, Andrea Dal Corso, Stefano de Gironcoli, Stefano Fabris, Guido Fratesi, Ralph Gebauer, Uwe Gerstmann, Christos Gougoussis, Anton Kokalj, Michele Lazzeri, Layla Martin-Samos, Nicola Marzari, Francesco Mauri, Riccardo Mazzarello, Stefano Paolini, Alfredo Pasquarello, Lorenzo Paulatto, Carlo Sbraccia, Sandro Scandolo, Gabriele Sclauzero, Ari P Seitsonen, Alexander Smogunov, Paolo Umari, and Renata M Wentzcovitch. Quantum espresso: a modular and open-source software project for quantum simulations of materials. *Journal of Physics: Condensed Matter*, 21(39):395502, September 2009.

[89] R Car and M Parrinello. Unified approach for molecular dynamics and density-functional theory. *Physical Review Letters*, 55(22):2471–2474, 1985.

[90] M C Payne, M P Teter, D. C. Allan, T A Arias, and J. D. Joannopoulos. Iterative minimization techniques for ab initio total-energy calculations: Molecular dynamics and conjugate gradients. *Reviews of Modern Physics*, 64(4):1045–1097, 1992.

[91] Jon Baker, Andrew Scheiner, and Jan Andzelm. Spin contamination in density functional theory. *Chemical Physics Letters*, 216(3–6):380–388, December 1993.

[92] James Shee, Matthias Loipersberger, Diptarka Hait, Joonho Lee, and Martin Head-Gordon. Revealing the nature of electron correlation in transition metal complexes with symmetry breaking and chemical intuition. *The Journal of Chemical Physics*, 154(19), May 2021.

[93] Joonho Lee and Martin Head-Gordon. Distinguishing artificial and essential symmetry breaking in a single determinant: approach and application to the c60, c36, and c20 fullerenes. *Physical Chemistry Chemical Physics*, 21(9):4763–4778, 2019.

[94] John A. Pople, Peter M. W. Gill, and Nicholas C. Handy. Spin-unrestricted character of kohn-sham orbitals for open-shell systems. *International Journal of Quantum Chemistry*, 56(4):303–305, November 1995.

[95] Christoph R. Jacob and Markus Reiher. Spin in density-functional theory. *International Journal of Quantum Chemistry*, 112(23):3661–3684, August 2012.

[96] Frank Neese. Importance of direct spin-spin coupling and spin-flip excitations for the zero-field splittings of transition metal complexes: A case study. *Journal of the American Chemical Society*, 128(31):10213–10222, July 2006.

[97] Johannes T. Margraf, Ajith Perera, Jesse J. Lutz, and Rodney J. Bartlett. Single-reference coupled cluster theory for multi-reference problems. *The Journal of Chemical Physics*, 147(18), November 2017.

[98] José M Soler, Emilio Artacho, Julian D Gale, Alberto García, Javier Junquera, Pablo Ordejón, and Daniel Sánchez-Portal. The siesta method for ab initio order-n materials simulation. *Journal of Physics: Condensed Matter*, 14(11):2745–2779, March 2002.

[99] Linda Hung and Emily A. Carter. Accurate simulations of metals at the mesoscale: Explicit treatment of 1 million atoms with quantum mechanics. *Chemical Physics Letters*, 475(4–6):163–170, June 2009.

[100] Stephan Mohr, Laura E. Ratcliff, Luigi Genovese, Damien Caliste, Paul Boulanger, Stefan Goedecker, and Thierry Deutsch. Accurate and efficient linear scaling dft calculations with universal applicability. *Physical Chemistry Chemical Physics*, 17(47):31360–31370, 2015.

[101] Ayako Nakata, Jack S. Baker, Shereif Y. Mujahed, Jack T. L. Poulton, Sergiu Arapan, Jianbo Lin, Zamaan Raza, Sushma Yadav, Lionel Truflandier, Tsuyoshi Miyazaki, and David R. Bowler. Large scale and linear scaling dft with the conquest code. *The Journal of Chemical Physics*, 152(16), April 2020.

[102] Alberto García, Nick Papior, Arsalan Akhtar, Emilio Artacho, Volker Blum, Emanuele Bosoni, Pedro Brandimarte, Mads Brandbyge, J. I. Cerdá, Fabiano Corsetti, Ramón Cuadrado, Vladimir Dikan, Jaime Ferrer, Julian Gale, Pablo García-Fernández, V. M. García-Suárez, Sandra García, Georg Huhs, Sergio

Illera, Richard Korytár, Peter Koval, Irina Lebedeva, Lin Lin, Pablo López-Tarifa, Sara G. Mayo, Stephan Mohr, Pablo Ordejón, Andrei Postnikov, Yann Pouillon, Miguel Pruneda, Roberto Robles, Daniel Sánchez-Portal, Jose M. Soler, Rafi Ullah, Victor Wen-zhe Yu, and Javier Junquera. Siesta: Recent developments and applications. *The Journal of Chemical Physics*, 152(20), May 2020.

[103] Joseph C. A. Prentice, Jolyon Aarons, James C. Womack, Alice E. A. Allen, Lampros Andrinopoulos, Lucian Anton, Robert A. Bell, Arihant Bhandari, Gabriel A. Bramley, Robert J. Charlton, Rebecca J. Clements, Daniel J. Cole, Gabriel Constantinescu, Fabiano Corsetti, Simon M.-M. Dubois, Kevin K. B. Duff, José María Escartín, Andrea Greco, Quintin Hill, Louis P. Lee, Edward Linscott, David D. O'Regan, Maximillian J. S. Phipps, Laura E. Ratcliff, Álvaro Ruiz Serrano, Edward W. Tait, Gilberto Teobaldi, Valerio Vitale, Nelson Yeung, Tim J. Zuehlsdorff, Jacek Dziedzic, Peter D. Haynes, Nicholas D. M. Hine, Arash A. Mostofi, Mike C. Payne, and Chris-Kriton Skylaris. The ¡scp¿onetep¡/scp¿ linear-scaling density functional theory program. *The Journal of Chemical Physics*, 152(17), May 2020.

[104] Christoph Riplinger, Peter Pinski, Ute Becker, Edward F. Valeev, and Frank Neese. Sparse maps—a systematic infrastructure for reduced-scaling electronic structure methods. ii. linear scaling domain based pair natural orbital coupled cluster theory. *The Journal of Chemical Physics*, 144(2), January 2016.

[105] Masaaki Saitow, Ute Becker, Christoph Riplinger, Edward F. Valeev, and Frank Neese. A new near-linear scaling, efficient and accurate, open-shell domain-based local pair natural orbital coupled cluster singles and doubles theory. *The Journal of Chemical Physics*, 146(16), April 2017.

[106] F. Neese. The orca program system. *WIRES Comput. Molec. Sci.*, 2(1):73–78, 2012.

[107] F. Neese. Software update: the orca program system, version 5.0. *WIRES Comput. Molec. Sci.*, 12(1):e1606, 2022.

[108] P Giannozzi, O Andreussi, T Brumme, O Bunau, M Buongiorno Nardelli, M Calandra, R Car, C Cavazzoni, D Ceresoli, M Cococcioni, N Colonna,

I Carnimeo, A Dal Corso, S de Gironcoli, P Delugas, R A DiStasio, A Ferretti, A Floris, G Fratesi, G Fugallo, R Gebauer, U Gerstmann, F Giustino, T Gorni, J Jia, M Kawamura, H-Y Ko, A Kokalj, E Küçükbenli, M Lazzeri, M Marsili, N Marzari, F Mauri, N L Nguyen, H-V Nguyen, A Otero-de-la Roza, L Paulatto, S Poncé, D Rocca, R Sabatini, B Santra, M Schlipf, A P Seitsonen, A Smogunov, I Timrov, T Thonhauser, P Umari, N Vast, X Wu, and S Baroni. Advanced capabilities for materials modelling with quantum espresso. *Journal of Physics: Condensed Matter*, 29(46):465901, October 2017.

[109] Jens Jørgen Mortensen, Ask Hjorth Larsen, Mikael Kuisma, Aleksei V. Ivanov, Alireza Taghizadeh, Andrew Peterson, Anubhab Haldar, Asmus Ougaard Dohn, Christian Schäfer, Elvar Örn Jónsson, Eric D. Hermes, Fredrik Andreas Nilsson, Georg Kastlunger, Gianluca Levi, Hannes Jónsson, Hannu Häkkinen, Jakub Fojt, Jiban Kangsabanik, Joachim Sødequist, Jouko Lehtomäki, Julian Heske, Jussi Enkovaara, Kirsten Trøstrup Winther, Marcin Dulak, Marko M. Melander, Martin Ovesen, Martti Louhivuori, Michael Walter, Morten Gjerding, Olga Lopez-Acevedo, Paul Erhart, Robert Warmbier, Rolf Würdemann, Sami Kaappa, Simone Latini, Tara Maria Boland, Thomas Bligaard, Thorbjørn Skovhus, Toma Susi, Tristan Maxson, Tuomas Rossi, Xi Chen, Yorick Leonard A. Schmerwitz, Jakob Schiøtz, Thomas Olsen, Karsten Wedel Jacobsen, and Kristian Sommer Thygesen. Gpaw: An open python package for electronic structure calculations. *The Journal of Chemical Physics*, 160(9), March 2024.

[110] John David Jackson. *Classical Electrodynamics*. John Wiley & Sons, Nashville, TN, 3 edition, July 1998.

[111] J. Gerratt and I. M. Mills. Force constants and dipole-moment derivatives of molecules from perturbed hartree–fock calculations. i. *The Journal of Chemical Physics*, 49(4):1719–1729, August 1968.

[112] S. P. Karna and M. Dupuis. Frequency dependent nonlinear optical properties of molecules: Formulation and implementation in the hondo program. *Journal of Computational Chemistry*, 12(4):487–504, May 1991.

[113] Horst Weiss, Reinhart Ahlrichs, and Marco Häser. A direct algorithm for self-consistent-field linear response theory and application to c60: Excitation ener-

gies, oscillator strengths, and frequency-dependent polarizabilities. *The Journal of Chemical Physics*, 99(2):1262–1270, July 1993.

[114] Shaopeng Li, Linping Hu, Liang Peng, Weitao Yang, and Feng Long Gu. Coupled-perturbed scf approach for calculating static polarizabilities and hyperpolarizabilities with nonorthogonal localized molecular orbitals. *Journal of Chemical Theory and Computation*, 11(3):923–931, February 2015.

[115] Charles Kittel. *Introduction to solid state physics*. John Wiley & Sons, Nashville, TN, 8 edition, October 2004.

[116] Alfonso Baldereschi, Stefano Baroni, and Raffaele Resta. Band offsets in lattice-matched heterojunctions: A model and first-principles calculations for gaas/alas. *Physical Review Letters*, 61(6):734–737, August 1988.

[117] Javier Junquera, Morrel H Cohen, and Karin M Rabe. Nanoscale smoothing and the analysis of interfacial charge and dipolar densities. *Journal of Physics: Condensed Matter*, 19(21):213203, May 2007.

[118] R. Ramprasad and N. Shi. Dielectric properties of nanoscale hfo_2 slabs. *Physical Review B*, 72(5), August 2005.

[119] Massimiliano Stengel and Nicola A. Spaldin. Ab initiotheory of metal-insulator interfaces in a finite electric field. *Physical Review B*, 75(20), May 2007.

[120] Viktor Myroshnychenko and Christian Brosseau. Finite-element method for calculation of the effective permittivity of random inhomogeneous media. *Physical Review E - Statistical, Nonlinear, and Soft Matter Physics*, 71(1):1–16, 2005.

[121] Nawfal Jebbor and Seddik Bri. Effective permittivity of periodic composite materials: Numerical modeling by the finite element method. *Journal of Electrostatics*, 2012.

[122] Xiangyu Xu, Boming Zhang, Kai Liu, Dawei Liu, Ming Bai, and Yun Li. Finite element simulation and analysis of the dielectric properties of unidirectional aramid/epoxy composites. *Polymer Composites*, 39:E2226–E2233, 2018.

[123] P. Motamarri, M.R. Nowak, K. Leiter, J. Knap, and V. Gavini. Higher-order adaptive finite-element methods for kohn–sham density functional theory. *Journal of Computational Physics*, 253:308–343, November 2013.

[124] Phani Motamarri, Sambit Das, Shiva Rudraraju, Krishnendu Ghosh, Denis Davydov, and Vikram Gavini. Dft-fe – a massively parallel adaptive finite-element code for large-scale density functional theory calculations. *Computer Physics Communications*, 246:106853, January 2020.

[125] Anastasis C. Polycarpou. *Introduction to the Finite Element Method in Electromagnetics*. Springer International Publishing, 2006.

[126] Raffaele Resta. Quantum-mechanical position operator in extended systems. *Physical Review Letters*, 80(9):1800–1803, March 1998.

[127] Raffaele Resta and David Vanderbilt. *Theory of Polarization: A Modern Approach*, page 31–68. Springer Berlin Heidelberg, 2007.

[128] Nicola A. Spaldin. A beginners guide to the modern theory of polarization. *Journal of Solid State Chemistry*, 195:2–10, 2012.

[129] R Resta. Theory of the electric polarization in crystals. *Ferroelectrics*, 136(1):51–55, November 1992.

[130] Raffaele Resta. Macroscopic polarization in crystalline dielectrics: the geometric phase approach. *Rev. Mod. Phys.*, 66(3):899–915, July 1994.

[131] R D King-Smith and D Vanderbilt. Theory of polarization of crystalline solids. *Phys. Rev. B Condens. Matter*, 47(3):1651–1654, January 1993.

[132] D Vanderbilt and R D King-Smith. Electric polarization as a bulk quantity and its relation to surface charge. *Phys. Rev. B Condens. Matter*, 48(7):4442–4455, August 1993.

[133] Gregory H. Wannier. The structure of electronic excitation levels in insulating crystals. *Physical Review*, 52(3):191–197, August 1937.

[134] Nicola Marzari, Arash A Mostofi, Jonathan R Yates, Ivo Souza, and David Vanderbilt. Maximally localized wannier functions: Theory and applications. *Rev. Mod. Phys.*, 84(4):1419–1475, October 2012.

[135] R. W. Nunes and Xavier Gonze. Berry-phase treatment of the homogeneous electric field perturbation in insulators. *Physical Review B*, 63(15), March 2001.

[136] Ivo Souza, Jorge Íñiguez, and David Vanderbilt. First-principles approach to insulators in finite electric fields. *Physical Review Letters*, 89(11), August 2002.

[137] P. Umari and Alfredo Pasquarello. Ab initiomolecular dynamics in a finite homogeneous electric field. *Physical Review Letters*, 89(15), September 2002.

[138] Ivo Souza, Jorge Íñiguez, and David Vanderbilt. Dynamics of berry-phase polarization in time-dependent electric fields. *Physical Review B*, 69(8), February 2004.

[139] Stefano Baroni and Raffaele Resta. Ab initio calculation of the macroscopic dielectric constant in silicon. *Physical Review B*, 33(10):7017–7021, May 1986.

[140] Stefano Baroni, Paolo Giannozzi, and Andrea Testa. Green's-function approach to linear response in solids. *Physical Review Letters*, 58(18):1861–1864, May 1987.

[141] Paolo Giannozzi, Stefano de Gironcoli, Pasquale Pavone, and Stefano Baroni. Ab initio calculation of phonon dispersions in semiconductors. *Physical Review B*, 43(9):7231–7242, March 1991.

[142] Stefano Baroni, Stefano de Gironcoli, Andrea Dal Corso, and Paolo Giannozzi. Phonons and related crystal properties from density-functional perturbation theory. *Reviews of Modern Physics*, 73(2):515–562, July 2001.

[143] Xavier Gonze and Changyol Lee. Dynamical matrices, born effective charges, dielectric permittivity tensors, and interatomic force constants from density-functional perturbation theory. *Physical Review B*, 55(16):10355–10368, April 1997.

Chapter 3

Ab Initio Studies of Nanocomposite Dielectric Oxides: Decomposing the Local Polarization Response Using Wannier Centers

3.1 Introduction

Nanocomposite and otherwise nanostructured materials can be designed to have tailored dielectric response properties. Because of their inhomogeneous composition, their dielectric response will also contain spatially localized components. In the present dissertation, we are primarlily concerned with matrix-inclusion type nanocomposites. In such systems, inclusions will have a localized nanoparticle response, which in turn interacts with the matrix response in the surrounding area. Similarly, cavities, thin films, grain boundaries, and other nanoscopic structural deviations from the pure material will perturb the local polarization field in the material. Therefore, it is important to have theoretical tools to probe the local polarization of materials in the presence of external fields. Such tools would allow us to decompose the overall material response into different structural units. This decomposition, in turn, affords a greater understanding of how to tailor the response properties by precise tuning of the nanoscopic environment.

One way to spatially resolve the dielectric response is to compute of the full *non-local* dielectric susceptibility matrix $\chi(\mathbf{r}, \mathbf{r'})$. Accessible via the Random Phase Approximation[1] or DFPT,[2] $\boldsymbol{\chi}(\mathbf{r}, \mathbf{r'})$ relates the local polarization $\mathbf{p}(\mathbf{r})$ to the local electric field $\mathbf{e}(\mathbf{r})$ via[3]

$$p_i(\mathbf{r}) = \int d\mathbf{r'} \chi_{ij}(\mathbf{r}, \mathbf{r'}) e_j(\mathbf{r}). \tag{3.1}$$

Galli and co-workers have shown that for layered periodic heterostructures, this dielectric matrix can be partitioned into the responses of each subsystem, plus the response of an interfacial layer.[4] However, the method is computationally demanding. Although relatively efficient methods have been developed to compute this matrix approximately[5, 6], it is still quite expensive to do so for nanocomposites with large simulation cells. Thus, a non-perturbational finite-field approach is desirable.

Finite field approaches to local permittivities generally avail themselves of transforming the electronic bands into localized Wannier functions. As discussed in Chapter 2.4, the polarization of a periodic material can be described by the displacement of Wannier centers over the course of an adiabatically applied external perturbation. When Wannier functions are localized, their centers can be assigned to nearby atoms, atom groups, atomic layers, or even bonds. The displacements of the centers assigned to a local region of the structure can then be used to define the local polarization response for that region.

One possible end goal in this decomposition of the nanocomposite response is to derive polarizabilities of distinct structural units in the material or a local position-dependent electric susceptibility. In one of the earliest such methods, Giustino, Umari, and Pasquarello define local 1D electric permittivity profiles across planar interfaces.[7, 3] In this method, the induced charge density in a finite electric field is used to define a local electric susceptibility, and a Wannier function representation is used to compute contributions to this susceptibility from atomic layers and the polarizability of atomic groups.[7, 3] Shi and Ramprasad have applied this method to a variety of slabs and stacked insulator heterostructures,[8, 9] and Spaldin and Stengel expanded the approach to study the permittivity profiles of insulator-metal planar heterostructures[10] More recently, Galli and coworkers have used a very similar approach to define hybrid density functionals wherein the proportion of exact exchange is dependent on the local permittivity in a heterostructure.[4, 11] In this approach, the local permittivity is determined from the Wannier function displacements of in-

dividual atoms, smoothed by a Gaussian function.

The above approaches have some downsides in the context of matrix-inclusion nanocomposites. For one, there is an inherent arbitrariness in how the local electric and polarization fields are defined. In particular, they are based on averaging induced charge densities and local electric fields. Although averaging or otherwise smoothing the rapidly varying nanoscopic local fields is required, the particular averaging or smoothing method used is essentially arbitrary. The above strategies work well for planar interfaces and slab geometries, in which the macroscopic averaging technique[12] is a logical choice for defining these smoothed fields. The resulting locally averaged electric field and permittivity profiles are smooth functions of the atomic layer. However, for matrix-inclusion heterostructures, it is more useful to understand the permittivity profile as a function of the radial distance from the inclusion. In other words, it is useful to consider the permittivity profile in concentric shells of matrix atoms surrounding the inclusion. However, because of the dipolar induced field around the inclusion, the average local field varies significantly within a given shell, and a shell-indexed permittivity defined according to the method of Giustino, Umari, and Pasquarello is more difficult to define, requiring a careful reconsideration of the averaging procedure and definition of the local field.

Within our lab, Hally has developed an alternative methodology for decomposing the dielectric response of matrix-inclusion nanocomposites that circumvents these difficulties.[13] As with the above methods, Hally's approach relies on the partitioning of MLWFs between atoms of the simulation cell based on the location of the Wannier centers. However, instead of defining atomic polarizabilities or local susceptibilities based on a definition of the local electric field, Hally's approach instead quantifies the contribution of the inclusion to the nanocomposite's macroscopic permittivity by making reference to a simulation of the bulk matrix. The result is a permittivity enhancement factor α_{enh}, which is in turn composed of contributions from the inclusion, the vacancy in the matrix that is filled by the inclusion, and the matrix itself. The last term incorporates changes in the interfacial layer of matrix nearest to the inclusion, which behaves differently from the bulk. All of these quantities are defined in terms of the macroscopic electric field and do not require any volume averaging to determine the smooth induced field.

Hally and Paci used this method to decompose the response of an MgO / Ag nanocomposite. In this chapter, we apply the same method to study the effects of inclusion shape and volume loading within the same types of composites. In addition,

three other rock-salt structured oxide matrix materials are investigated to see the sensitivity of the inclusion permittivity enhancement to the matrix identity.

The chapter is organized as follows. Section 3.2 details the methodology developed by Hally and Paci. Next, Section 3.3 presents a practical example of how the method can be applied through a series of Quantum Espresso input files and python post-processing. In the following sections, the method is applied to several different oxide / Ag systems, to investigate the impact of inclusion volume loading (Section 3.4), inclusion shape (Section 3.5), and matrix identity (Section 3.6) on the resulting permittivity enhancement. Finally, Section 3.7 revisits the approaches of Giustino *et al.*[7, 3] and Galli *et al.*[4, 11] to defining local permittivities and polarizabilities. The section is mostly discussion-based, positing how such methods might be extended to matrix-inclusion composites in future work. Much of the work to benchmark the methods presented herein and a description of an alternative practical approach to calculating the Wannier functions needed is offered in Appendix B.

3.2 Methods

First and foremost, the method of Hally and Paci relies on the ability to unambiguously assign Wannier centers to specific atoms, or at least atom types. For an ionic solid, this is trivial. All centers of MLWFs will be located relatively close to a given atomic nucleus and far from others, and we can assign each center to the closest nucleus. With a metallic nanoparticle inclusion, matters are not changed significantly. Generally, some of the metal's MLWFs will be localized on individual metal atoms, and their centers are easily assigned to those nuclei. Other MLWFs may be delocalized over all or part of the nanoparticle. Nevertheless, the center of such MLWFs should still reside unambiguously within the inclusion (somewhere near its center of mass if the MLWF is delocalized over the whole particle. Thus, if our goal is to partition the Wannier centers into those belonging to the matrix and those belonging to the inclusion, we can generally do so easily for an ionic matrix and metallic inclusion.

It is worth noting that materials with significant covalent bonding interactions between an inclusion and matrix will not be readily decomposed as above. In such a case, Wannier centers will reside somewhere along the bonding axes, as the electron density is shared between multiple nuclei. While we will not explore different approaches to partitioning bond-centered orbitals, we note that the simplest protocol, which has been adopted previously by Giustino and Pasquarello, is to simply split

the contributions from such Wannier centers evenly between the bonded atoms.[3]

With Wannier centers assigned to inclusion and matrix, the change in the dipole moment of the inclusion Δp_{inc} can be defined as a sum over its ionic charges and assigned Wannier centers, each of which has either a 1– or 2–electron charge. Assuming all Wannier functions are doubly occupied, with Wannier centers $\mathbf{r}_i$, nuclear positions $\mathbf{R}_i$, and nuclear charges Z_I:

$$\Delta \mathbf{p}_{\text{inc}} = -2 \sum_{\text{inc}} \Delta \mathbf{r}_i + \sum_{\text{inc}} Z_I \Delta \mathbf{R}_I. \tag{3.2}$$

So long as the nanoparticle inclusion is charge neutral, this change in dipole is unambiguously defined and does not depend on the choice of origin. Note that for the clamped-ion case, all ionic displacements are zero, and the ionic sum in Equation (3.2) is dropped.

Armed with the partition of Wannier centers and resulting definition of inclusion dipole, Hally and Paci lay out a framework for assessing the contribution of each component of the material unit cell to the overall polarizability of the cell, that is, the change in the cell's dipole moment per unit of applied field. First, recall that the relative permittivity of a solid can be defined in terms of the change in dipole moment of a unit cell Δp under an applied field $\mathscr{E}$ for unit cell volume Ω as

$$\epsilon_r = 1 + 4\pi \frac{\Delta p}{\mathscr{E}\Omega} \tag{3.3}$$

$$\epsilon_r = 1 + 4\pi \frac{\alpha}{\Omega}. \tag{3.4}$$

In the second expression, we've simply defined a cell polarizability $\alpha = \frac{\Delta p}{\mathscr{E}}$. Hally and Paci then separate the polarizability of the unadulterated matrix (bulk) from the enhanced polarizability contributed by the addition of an inclusion to the cell:

$$\epsilon_{\text{comp}} = 1 + 4\pi \frac{\alpha_{\text{bulk},\Omega_{\text{comp}}}}{\Omega_{\text{comp}}} + n_{\text{inc}} \alpha_{\text{enh}}. \tag{3.5}$$

Here, n_{inc} is the number density of the inclusions added to the matrix—that is, the number of nanoparticles per unit volume. For all of the systems considered in this chapter, the simulation cell contains *one* nanoparticle inclusion, meaning that n_{inc} is simply the inverse of the simulation cell volume. Moreover, $\alpha_{\text{bulk},\Omega_{\text{comp}}}$ is the polarizability of the bulk material, obtained from another calculation but then scaled

to the volume of the unit cell for the composite. It can be derived from Equation (3.4) to be $\alpha_{\text{bulk},\Omega_{\text{comp}}} = \Omega_{\text{comp}}(\epsilon_{\text{bulk}} - 1)/4\pi$. Going one step further, Hally and Paci define an expression relating the permittivity of the composite material ϵ_{comp} to that of the bulk ϵ_{bulk} via a polarizability enhancement term α_{enh}:

$$\epsilon_{\text{comp}} = \epsilon_{\text{bulk}} + 4\pi n_{\text{inc}} \alpha_{\text{enh}} \tag{3.6}$$

$$\alpha_{\text{enh}} = \alpha_{\text{inc}} + \alpha_{\text{cav}} + \alpha_{\text{mat}}. \tag{3.7}$$

Equation (3.7) then decomposes the polarizability enhancement into contributions from (1) the inclusion α_{inc}, (2) the cavity occupied by the inclusion α_{cav}, and (3) the matrix α_{mat}. These contributions to polarizability are defined relative to the applied electric field $\mathscr{E}$ as follows:

1) **The polarizability of the inclusion**, α_{inc} As a polarizability, it is defined as a change in dipole moment per unit of applied field:

$$\alpha_{\text{inc}} = \frac{\Delta p_{\text{inc}}}{\mathscr{E}}. \tag{3.8}$$

2) **The polarizability of the cavity in the matrix in which the inclusion sits**, α_{cav}. This component represents the polarizabilty lost by removing matrix ions to make room for an inclusion and is thus defined as a negative contribution:

$$\alpha_{\text{cav}} = -\frac{N_{\text{cav}}}{N_{\text{cell}}} \frac{\Delta p_{\text{bulk}}}{\mathscr{E}}. \tag{3.9}$$

3) **The polarizability of the matrix**, α_{mat}:

$$\alpha_{\text{mat}} = \frac{\Delta p_{\text{comp}}}{\mathscr{E}} - \frac{\Omega_{\text{comp}}}{4\pi}(\epsilon_{\text{bulk}} - 1) - \alpha_{\text{cav}} - \alpha_{\text{inc}}. \tag{3.10}$$

This last equation is derived from Equations (3.5)–(3.9). Essentially, α_{mat} is taken to be everything left over after α_{inc} and α_{cav}.

3.2.1 Model Systems

We study the permittivity enhancement for systems consisting of an alkaline-earth oxide matrix with silver inclusions. MgO / Ag matrix-inclusion composites have previously been investigated by both Hally,[13] in the original publication of the premittivity enhancement protocol, and Adluri,[14] who investigated the effect of inclusion aspect ratio on composite permittivities. We validate the current implementation of the approach on the system from Ref [13], which has an 8-atom Ag inclusion and then apply the approach to several of the systems from Ref [14] with 12-, 16-, and 18-atom inclusions. Finally, the same 8-atom inclusion as above is examined in CaO, SrO, and BaO matrices, all of which have the same rocksalt structure as MgO.

Following the procedure of Hally and Adluri, the geometries were generated by first creating a suitable supercell of the matrix material. Supercells were generated so that neighboring inclusion images would have at least two atomic layers of matrix separating them in every direction. In all but one geometry, this separation is at least four atomic layers. From the initial supercell, a number of matrix ions equal to the number of inclusion atoms is substituted with inclusion atoms according to the templates illustrated in Figure 3.1(b). The resulting composite geometry is then optimized by allowing both ionic positions and lattice parameters to relax using damped dynamics. For MgO in particular, the relaxation results in a notable expansion of the lattice parameters and a relaxation of the ions around the inclusion to allow more room for Ag, as illustrated in Figure 3.1(a).[†] Nevertheless, all cells remained orthorhombic during cell optimization.

Nearly all geometries were obtained at the LDA level of theory with the PZ functional, using the same simulation parameters as in Refs [13] and [14]. Specifically, Rappe–Rabe–Kaxiras–Joannopoulos ultrasoft pseudopotentials[15] were used for O and Ag while a Bachelet–Hamann–Schluter norm-conserving pseudopotential[16] was used for Mg. In this approach, the pseudopotentials include 11, 6, and 2 valence electrons for Ag, O, and Mg, respectively. This means that Mg in particular, which is essentially fully ionized in the bulk structure, has zero Wannier functions associated with it. In order to obtain an improved mapping of the polarization to Wannier center displacement on all elements, including Mg, we performed single-point

[†]While Ag and MgO have similar lattice constants, in this process we are substituting Ag for both the anionic and cationic sites in the lattice, which results in significantly smaller interatomic distances for Ag than in bulk metal. As noted by Hally, even after structural relaxation these distances are still somewhat smaller than the bondlengths of the same Ag nanocluster optimized in vacuum.[13]

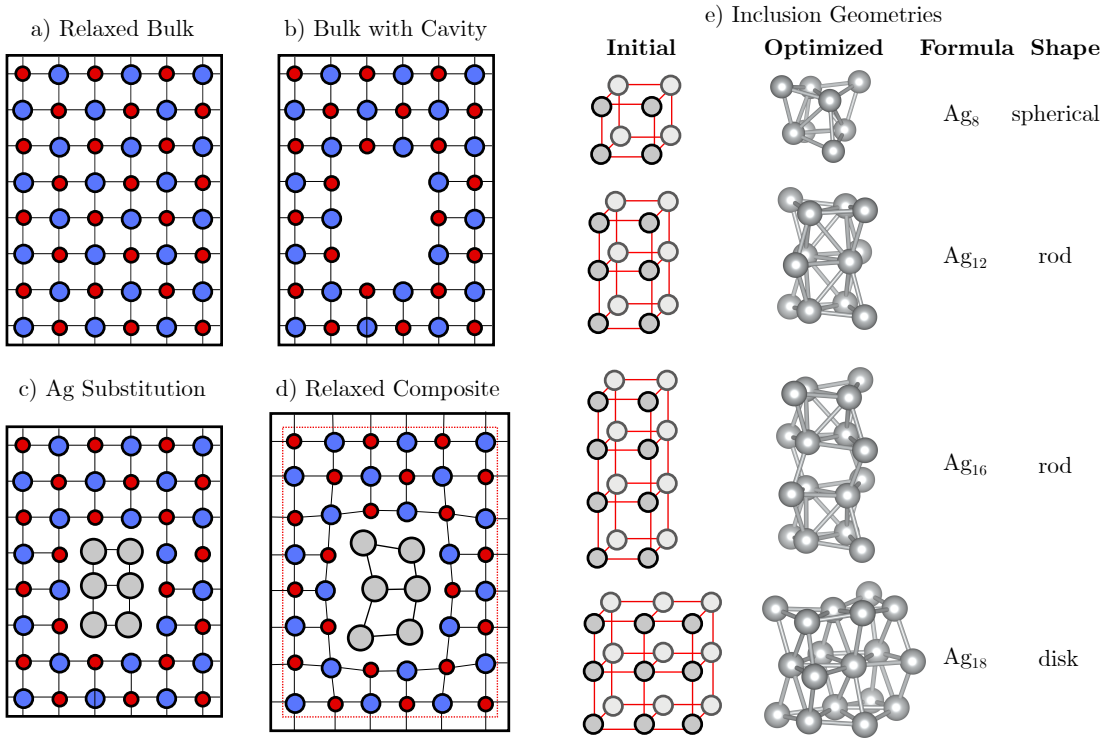

Figure 3.1: Procedure for Generating Composite Geometries. **a)** through **d)** show the ordered process of generating a composite geometry from a bulk supercell. The 2D lattice shown represents a single atomic layer of the rod-like Ag_{12} geometry in later sections. Note that while the vacancy geometry in **b)** is not evaluated computationally, it is conceptually important in the calculation of α_{enh} via equation (3.9). **e)** Depicts the inclusion geometries both before and after optimization along with inclusion formulas and shape descriptors.

calculations and obtained MLWFs at the PBE level of theory using optimized norm-conserving Vanderbilt pseudopotentials[17] from PseudoDojo.[18] These pseudopotentials included semicore electrons for both Ag and Mg, meaning 19, 6, and 10 electrons were ultimately included for each atom of Ag, O, and Mg, respectively. The only exception to this procedure are in Section 3.6, where the effects of different matrices are investigated. Therein, the entire calculations were performed at the PBESol level using optimized norm-conserving Vanderbilt pseudopotentials from PseudoDojo using the same computational parameters as the PBE single-point calculations on other geometries.

We note that three single-point calculations are needed to obtain PBE permittivities: one in zero-field on the optimized geometry, one in finite field on the same geometry, and a final one with finite field on the geometry that has been relaxed in

the same field strength. These single-point calculations were performed using wavefunction and charge density energy cutoffs of 70 Ry and 280 Ry, respectively, whereas the geometry optimizations were performed with the respective cutoffs of 50 Ry and 400 Ry. For all finite field calculations, an external field of 0.001 au was applied, and in relaxed-ion optimizations, ions were relaxed while keeping cell vectors fixed. Thus, any piezoelectric contributions to the relaxed-ion permittivity are ignored. Benchmarking in Appendix B demonstrates that the permittivities calculated either entirely at the PZ level or using single-point PBE calculations on the PZ geometries are very similar.

3.2.2 Born Effective Charges

An atom's Born effective charge (BEC) quantifies the change in force experienced by that atom for a change in the macroscopic electric field—or equivalently, the change in polarization of the system that accompanies a displacement of that atom. Thus, if the presence of an inclusion increases the magnitude of the BECs for interfacial matrix ions, it contributes to a net enhancement of the ionic permittivity of the matrix.[13] As a result, BECs can help describe the spatial distribution of the ionic contributions to α_{mat}. In addition, BECs acquired by the inclusion atoms in the composite indicate the ability of the inclusion to contribute directly to ionic polarization.

Mathematically, the BEC Z^* of an atom is a rank two tensor:[19]

$$Z^*_{ij} = \Omega \frac{\partial P_i}{\partial R_j} = \frac{\partial F_i}{\partial \mathcal{E}_j}, \tag{3.11}$$

where Ω is the unit cell volume, P is the polarization, R is the position of the atom, F is the force on the atom, $\mathcal{E}$ is the macroscopic electric field, and i and j are Cartesian directions. We calculated the zz component of the BECs for different materials using a discretized version of the second equality above:[20]

$$Z^*_{zz} = \frac{F_z(\mathcal{E}_1) - F_z(\mathcal{E}_0)}{\mathcal{E}_1 - \mathcal{E}_0}. \tag{3.12}$$

The two field states used were $\mathcal{E}_0 = 0$ and $\mathcal{E}_1 = 0.001$ au, and the ions were clamped in the same geometry for both states of the field.

3.2.3 Brillouin Zone Sampling Convergence

In this chapter, we exclusively use the CPMD code of Quantum Espresso to perform electronic structure calculations. This code performs calculations at the Gamma-point only, meaning the BZ sampling will be finer for larger simulation cells due to the inverse relationship between the size of the BZ and real-space cell. Finite field Berry phase calculations of the electric permittivity exhibit a an L_z^-2 convergence with the length of the simulation cell along the polarization direction L_z. Consideration of this convergence behavior is important in the calculation of permittivity enhancement factors because the factors are computed with reference to bulk permittivities. Thus, bulk permittivities should be calculated with a supercell roughly the same size as the composite cell to minimize discrepancies in BZ sampling.

In the following sections, we perform calculations on composites with cell lengths ranging from approximately 9 Å to 17 Å in both the direction parallel to the applied field and those orthogonal to it. The geometries are created by starting from a supercell of the matrix material and then substituting matrix ions with Ag before relaxing the ions and lattice parameters. Thus, the protocol that we adopted was to generate a separate bulk reference permittivity for each composite system, using the initial matrix supercell from which the composite was generated. Importantly, we use the optimal matrix lattice constant for these supercells, rather than scaling them to match the composite cell size exactly.[†] Linear effects from changes in the cell size upon introduction of the inclusion are accounted for by scaling α_{bulk} to $\alpha_{\text{bulk, comp}}$ in Equation (3.5) and do not affect α_{enh}, whereas non-linear inclusion-induced strain effects appear in α_{mat}.

3.2.4 Wannier Center Polarization Convergence

The polarization computed from Wannier center displacements presents the same L_z^{-2} convergence as the Berry phase polarization.[21] Furthermore, the Wannier center polarization is formally equivalent to the Berry phase expression for polarization only in the large supercell limit for Gamma-point calculations (or in the limit of dense k-point sampling otherwise).[22] Thus, in our calculations, we notice a slight discrepancy between the electric permittivities calculated with these methods. To minimize computational work, reference bulk calculations were only performed with

[†]Artificially straining the bulk supercell to match the composite cell can result in large changes in the permittivity.

the Berry phase formalism. Thus, Δp_{bulk} and ϵ_{bulk} in Equations (3.9) and (3.10) were calculated with the Berry phase formalism. For consistency across the methodology, we also computed Δp_{comp} in Equation (3.10) with the Berry phase approach. Finally, Δp_{inc} in Equation (3.8) is necessarily computed from the Wannier centers. However, we scaled this Wannier center polarization by the factor $\Delta P_{\text{comp}}/\Delta P_{\text{comp, WC}}$, where $\Delta P_{\text{comp, WC}}$ is the total polarization change of the composite calculated using Wannier centers, so that all of the polarization changes in Equations (3.8)–(3.10) are consistent with a Berry phase approach to the polarization.[†]

3.3 Ag_8 Inclusion in 216-Atom Cell

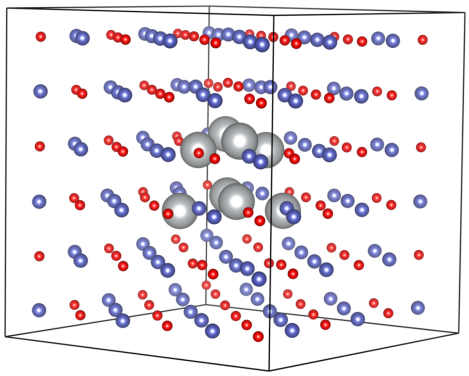

Figure 3.2: Model system. 8–atom silver inclusion surrounded by 104 Mg and 104 O atoms.

With the methodological foundation for the permittivity enhancement via Wannier decomposition in place, we illustrate practically how such calculations are performed. To do so, we perform the analysis on the same system used by Hally and Paci in their presentation of the method and shown in Figure 3.2. The system consists of a cubic 216-atom supercell of MgO, wherein the central 4 formula units of MgO have been replaced by 8 silver atoms.

[†]In the original proposal of this method, Δp_{inc} is calculated only from the Wannier centers and not scaled. We noted that in general, the Wannier center polarization was slightly smaller than the Berry phase polarization. In these cases, our calculations will generally result in slightly higher α_{inc} and slightly lower α_{mat} values than the original method.

3.3.1 Quantum Espresso Procedure

We now briefly describe how to obtain Wannier centers for both ionic configurations and different states of the external field. We will need to compute these centers for three states of the system: (1) zero-field, (2) clamped-ion, and (3) relaxed-ion. Figure 3.3 illustrates the process for calculating Wannier functions for the three states above under the Car-Parrinello approach within Quantum Espresso.

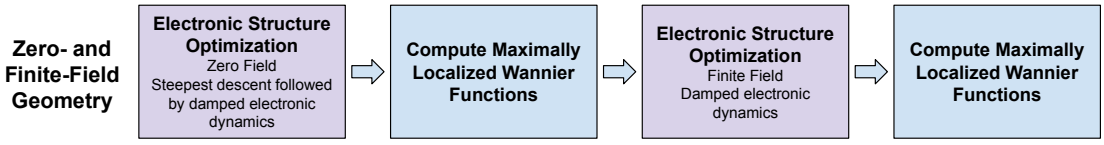

Figure 3.3: Process for calculating MLWFs for the zero-field, clamped-ion, and relaxed-ion states. We note that the first two steps in the procedure are only necessary for the clamped-ion geometry in order to perform the analysis that follows. However, obtaining the zero-field wavefunction before turning on the finite field can aid in convergence.

All of the input files for Quantum Espresso, as well as a Python script for generating the scripts for a given system and analyzing the results are contained in Appendix B. Here we simply note that we used the Jacobi rotation procedure in Quantum Espresso for minimizing the spread of the Wannier functions. We found that between 100 and 300 iterations were sufficient to produce localized Wannier functions with centers close to atomic nuclei. Testing showed that damped dynamics also produced well-localized Wannier functions, provided sufficiently many steps were performed, but the Jacobi rotation proved more robust and we use it throughout the following.

3.3.2 Results

Table 3.1 shows the results calculated by Hally and Paci compared with our own. Despite the difference in functional and our use of a scaled version of the Wannier displacements, the results between the two methods agree very well. Notably, the permittivities, which are derived solely from a Berry phase calculation, are identical to the first decimal. Furthermore, the discrepancies between α_{inc} for the two methods, which are based solely on the displacements of Wannier centers, are under 5% for both the clamped- and relaxed-ion states. With this test case out of the way, we now turn our attention to the behavior of α_{enh} as the percent loading of inclusions changes.

Table 3.1: Comparison of results from Ref [13] with the present work.

Polarization Type	Source	ϵ_{bulk}	ϵ_{comp}	α_{inc}	α_{mat}	α_{cav}	α_{enh}
Clamped-ion	Hally	3.04	3.66	588	217	-83	722
	Present Work	3.03	3.62	563	199	-83	679
Relaxed-ion	Hally	9.26	11.94	1221	2233	-338	3116
	Present Work	9.31	11.97	1197	2229	-340	3085

3.4 Inclusion Loading Effects

The partitioning proposed by Hally and Paci aims to quantify the polarization enhancement of a particular combination of matrix identity, inclusion identity, inclusion size, and inclusion shape. In doing so, the method assumes a linear relationship between loading expressed as number density of inclusions, n_{inc} and the effective permittivity of the nanocomposite. That is, α_{enh} should be a constant for a given combination of inclusion and matrix, and the nanocomposite permittivity is increased linearly with the number density of those inclusions. In the next two sections, we show how this assumption holds up for the Ag_8 inclusion in MgO matrix. For the remainder of this analysis, we will switch from speaking of the number density of inclusions to the more intuitive descriptor of the atomic percentage of silver, or %At. Ag, which is simply the percentage of atoms in the unit cell which are Ag. For a given inclusion, this property has essentially a 1:1 correspondence with number density.

We examine three different loadings of the Ag_8 inclusion: a low-loading case of 1.6 %At. silver, which is created from a 512-atom MgO supercell, and a high-loading case of 12.5 %At. silver, which is created from a 64-atom supercell. Both of these are compared to the system from the previous section, which has 3.7 %At. silver. Under a linear regime, we would expect α_{enh} and its various components to be constant between different inclusion loadings. We will see that linearity is essentially preserved while loading remains small, but that interactions between inclusions and with the surrounding matrix cause a stark breakdown of linearity as loading increases.

The results of all three systems are collected in Table 3.2, where the 216-atom cell results are reproduced from our results in Table 3.1 above. In order to draw conclusions from these results, we begin by drawing comparisons between the 216- and 512-atom cells—that is, the systems in the low loading regime. First, we note that the permittivity of the bulk MgO is not perfectly converged with respect to the supercell size at for the intermediate cell, as both the clamped- and relaxed-ion

permittivities increase slightly between the 216-atom and 512-atom cells. Thus, it is important to use reference bulk permittivities from the corresponding supercell when calculating α_{enh} for each composite. With this accounted for, α_{enh} and its decomposition into inclusion and matrix components are very similar between the two loadings in the clamped-ion case. While there is a slight increase in α_{inc} and concomitant decrease in α_{mat} and α_{enh} in going to the lowest loading case, we believe much of this is accounted for by numerical noise, which will be discussed more below. In the relaxed-ion case, on the other hand, we notice a roughly 17% decrease in α_{enh} due to significant drops in inclusion (-9%) and matrix (-19%) contributions in going to the lowest loading.

Table 3.2: Effect of Ag_8 loading in MgO matrix.

Pol. Type	%At. Ag	Cell Size	ϵ_{bulk}	ϵ_{comp}	α_{inc}	α_{mat}	α_{cav}	α_{enh}
Clamped-ion	12.5	64-Atom	2.87	5.25	768	218	-77	909
	3.7	216-Atom	3.03	3.62	563	199	-83	679
	1.6	512-Atom	3.11	3.35	599	138	-86	651
Relaxed-ion	12.5	64-Atom	9.29	34.02	4588	5208	-339	9457
	3.7	216-Atom	9.31	11.97	1197	2229	-340	3085
	1.6	512-Atom	9.38	10.33	1088	1807	-343	2553

One interpretation of this finding is that the effects that an inclusion has on ion dynamics converge more slowly with supercell size than its electrostatic effects. The induced dipole field of the inclusion appears to be effectively screened by just the four layers of MgO separating inclusions in the 216-atom cell (and 6 layers in the 512-atom cell), leading to minimal mutual polarization between images that would result in non-linearity of the clamped-ion partitioning. On the other hand the coupling of the inclusion to the ionic response extends slightly beyond the bounds of the 216-atom cell, resulting in some constructive interaction between neighboring inclusions and a small degree of non-linearity. Indeed, Hally posited that this might be the case, as the Born effective charges, the deviations of which from bulk values quantify the coupling between the inclusion and ionic polarization, are still anomalous even at the cell boundaries in the direction parallel to the finite field for the 216-atom cell.

An alternative, though related, interpretation of the relaxed-ion results is that the discrepancy could be a strain-effect. For the larger supercell, the strain due to lattice mismatch around the nanoparticle has more surrounding layers of MgO over which it can dissipate within the simulation cell and will be essentially fully dissipated at the

cell boundaries. Indeed, the lattice dimensions of the 512-atom composite are only 0.6% larger than the corresponding bulk supercell,[†] whereas the 216-atom composite has lattice dimensions 1.6% larger than bulk. Furthermore, the interatomic spacing in the layers furthest from the inclusion in the larger supercell have essentially returned to bulk values.

Regardless of whether one prefers to interpret the nonlinearity in relaxed-ion polarization as stemming from the extent of strain or anomolous Born effective charges, there is still some resulting interaction between neighboring inclusions, mediated by the surrounding matrix.[‡] Nevertheless, the nonlinearity is rather small, which comes more into focus when we consider the high loading case of the 64-atom supercell.

Viewing the 64-atom supercell results in comparison with the two larger cells, it is clear that the system is well outside the linear regime for α_{enh}. Notably, the effect is much smaller in the clamped-ion case. With ions clamped, α_{inc} is significantly increased by over 30% relative to the baseline 216-atom system, presumably due to strong mutual polarization of closely-spaced neighboring inclusion images. However, there is essentially no change in the matrix contribution to the polarizability enhancement.

In contrast, the relaxed-ion polarizability enhancement is more than three times higher than in the lower-loading systems. There are significant increases in both the matrix and inclusion contributions, indicating large ionic relaxation of both components. This likely stems from a destabilization of the interface ions around silver inclusions, which is explored further in the next chapter. Interestingly, this severe nonlinearity corroborates the above finding that the ionic contributions to non-linearity are more severe than the electrostatic ones.

By examining different inclusion loadings, we have observed the limits of the linear regime assumed Hally and Paci. In high-loading cases, both coupling between neighboring inclusions and ionic relaxation seem to increase substantially and contribute to non-linearity. At low-loadings, these effects are greatly reduced, but it is still important to consider sources of nonlinearity that may creep in to such calculations before drawing conclusions about physically meaningful effects.

[†]With the bulk supercell lattice parameter calculated from a 216-atom bulk supercell.

[‡]Of course, the effect of different BZ sampling in the different supercell sizes due to using a Gamma-point code is not completely ruled out as a cause of the discrepancies, but testing with denser k-meshes in Appendix B suggest that it should not be a significant contributor for the 216-atom supercell and larger.

3.5 Shape Effects

3.5.1 System Description

In this section, we examine two composites with rod-like inclusions and a third with a disk-like inclusion and compare their permittivity enhancements to the low volume loading cases discussed above. The optimized inclusions are all illustrated in Figure 3.1, and further information about the supercells in which they are embedded is provided in Table 3.3. In particular, we note the %At. loading and number of matrix atomic layers separating neighboring inclusions along each direction. The corresponding values for the Ag_8 inclusion in a 216-atom cell are included as reference. Based on the similarities in loading and separation, we expect the composites with rod- and disk-like inclusions would fall in a similar regime to the Ag_8 inclusion, wherein non-linearity in α_{enh} is small but not completely absent.

Table 3.3: Supercell description for composites with rod- and disk-like inclusions.

Inclusion	Shape[a]	%At. Ag	MgO Layers $\parallel$[b]	MgO Layers $\perp$[c]
Ag_8	Sphere	3.7	4	4
Ag_{12}	Rod	4.2	5	4
Ag_{16}	Rod	5.6	4	4
Ag_{18}	Disk	4.7	5	4

[a] Sphere: all axes identical, Rod: two axes identical and the third longer, Disk: two axes identical and the third shorter.
[b] Number of layers between inclusions along the long inclusion axis/axes.
[c] Number of layers between inclusions along the shorter inclusion axis/axes.

With the anisotropy of these inclusions comes an anisotropy of their dielectric response. Thus, we examine each composite using two different directions of the applied field—one which is parallel to the longest axis of the inclusion and denoted as the *longitudinal* direction, and one which is orthogonal to this direction and denoted the *transverse* direction. For Ag_{18}, we choose a direction along one of the two long axes as the longitudinal direction, and the direction parallel to the short axis is the transverse one. We build most of the following discussion on comparison with the Ag_8 inclusion discussed above, which is built from two atomic layers of Ag along each axis. Relative to this reference inclusion, the interactions of other inclusions with an external field are modulated by an increased length of the inclusion along the field direction (rods with longitudinal field), an increased cross-sectional area orthogonal

to the field (rods and disk with transverse field), or both (disk with longitudinal field). We will refer to these modulations as changes in **polarization length** and **polarization cross-section**. We also note that for both changes, there is a corresponding modulation of the interfacial layer of matrix, which we define as the first atomic layer of MgO surrounding the inclusion.

Adluri *et al.* found that for rod-like inclusions, increasing polarization length drove large increases in relaxed-ion composite permittivity, while increases in polarization cross-section had a smaller effect.[14] In contrast, an interplay between the total number of inclusion electrons (which we will refer to as **polarization volume**), and inclusion cross-section seemed to explain trends in relaxed-ion permittivity for disk-like inclusions.[14] While these conclusions were drawn directly from the effective permittivities of the composites, the decomposed α_{enh} approach offers more granular insights into the mechanisms of polarization for different inclusions by localizing the effects onto either inclusion or surrounding matrix. Furthermore, under the assumption of linearity, α_{enh} offers a more direct comparison of the inclusions themselves by accounting for the loading of inclusions, whereas effective permittivities will indeed be affected by changes in the number density of inclusions which could skew interpretation. Thus, in the following discussion, we use α_{enh} to re-examine the above conclusions on inclusion shape effects, with the discussion being couched in the same concepts of polarization length, polarization cross-section, and polarization volume.

3.5.2 Results from Wannier Center Displacements

Table 3.4 shows the results for all oblong inclusions. Data from the Ag_8 inclusion in the 216-atom composite from Table 3.2 is also reproduced in Table 3.4 for convenient reference. From this collection of inclusions of varying aspect ratios, we can begin to draw conclusions about how the particle morphology affects the different contributions to α_{enh}. To facilitate comparisons between inclusions, we have included the ratio of each α_{inc} to the corresponding value for the Ag_8 inclusion in the column α^r_{inc}.

Increasing Polarization Length

In order to examine the effect of increasing polarization length, we inspect the results of two series of inclusion that represent this change: 1) $Ag_8 \longrightarrow Ag_{12}$ (longitudinal field) $\longrightarrow Ag_{16}$ (longitudinal field) and 2) Ag_{12} (transverse field) $\longrightarrow Ag_{18}$ (longitudinal field). In the clamped-ion regime, both series show a larger than linear increase

Table 3.4: Comparison of permittivity enhancement for different oblong Ag inclusions.

Pol Type[a]	Field[b]	Inclusion	ϵ_{bulk}	ϵ_{comp}	α_{inc}	α_{inc}^{r} [c]	α_{mat}	α_{cav}	α_{enh}
CI	L	Ag_8	3.03	3.62	563	1.0	199	-83	679
		Ag_{12}	3.11	4.22	1442	2.56	419	-129	1732
		Ag_{16}	3.11	5.89	3658	6.50	916	-172	4401
		Ag_{18}	3.11	4.24	1969	3.50	583	-194	2358
	T	Ag_8	3.03	3.62	563	1.0	199	-83	679
		Ag_{12}	3.04	3.67	826	1.47	289	-125	990
		Ag_{16}	3.04	3.85	1078	1.91	374	-167	1286
		Ag_{18}	3.04	3.68	1129	2.01	402	-187	1344
RI	L	Ag_8	9.31	11.97	1197	1.0	2229	-340	3085
		Ag_{12}	9.38	12.90	3415	2.85	2582	-514	5483
		Ag_{16}	9.38	17.65	9878	8.25	3915	-685	13108
		Ag_{18}	9.38	13.87	4352	3.64	5787	-771	9368
	T	Ag_8	9.31	11.97	1197	1.0	2229	-340	3085
		Ag_{12}	9.33	12.69	1666	1.39	4077	-511	5232
		Ag_{16}	9.33	13.93	2154	1.80	5812	-682	7284
		Ag_{18}	9.34	14.79	1650	1.38	10483	-768	11365

[a] CI = clamped-ion, RI = relaxed-ion.
[b] L = longitudinal, T = transverse.
[c] α_{inc}^{r} is the ratio of α_{inc} of the given inclusion to α_{inc} of the Ag_8 inclusion.

in α_{inc} as the particle is lengthened. In series 1, this manifests as α_{inc}^{r} of 2.56 and 6.50 for Ag_{12} and Ag_{16}, when the polarization lengths of these particles has only increased by 1.5× and 2× relative to Ag_8. For the second series, a 1.5× increase in polarization length results in a 2.48× increase in α_{inc}, very similar to the effect in rods. In addition to the inclusion itself, there is a larger than linear increase in α_{mat} with polarization length. However, the relative increases in α_{mat} when moving up in polarization length within each series are slightly smaller than the increase in α_{inc}. Furthermore, the absolute values of α_{inc} are several times larger than those of α_{mat} for all of the inclusions considered. Thus, the primary contributor to increasing α_{enh} with polarization length in the clamped-ion regime is the large electronic polarizability of the inclusion itself, and the rapid increase in this polarizability with inclusion length.

In the relaxed-ion regime, these two series follow essentially the same qualitative trends for α_{inc} but the effect on α_{mat} is significantly different. The relative increases in α_{inc} were super-linear and slightly greater than in the clamped-ion case. In contrast,

relative increases in α_{mat} were smaller than linear for both series. In going from the Ag_8 inclusion to the Ag_{16} inclusion, for example, α_{mat} increased by 1.76 times. This can be rationalized by the fact that α_{mat} is mainly driven by the increased polarizability of the ions closest to the inclusion—that is, the polarizability of interfacial matrix ions. Already in the Ag_8 composite, the first layer of matrix around the inclusion consists of 56 matrix ions, only increasing to 72 and then 88 for the Ag_{12} and Ag_{16} rods, and 82 for the Ag_{18} disk. In the second series, the number of interfacial atoms increases from 72 atoms for Ag_{12} to 82 for Ag_{18}. Thus, for these small inclusions, the number of interfacial matrix atoms does not increase proportionally with the size of the inclusion, and the relative increases in α_{mat} seem to be more in line with the relative increases in the number of interface ions. Unlike the clamped-ion regime, the overall α_{enh} is dominated by α_{mat} for smaller inclusions, where the number of interfacial ions is far greater than the number of inclusion atoms. However, the relative contribution of α_{inc} quickly catches up to α_{mat} with increasing polarization length.

Increasing Polarization Cross-Section

Next, we examine what the data set has to say about the effect of increasing the length of the particle in a direction orthogonal to the applied field. For this, we examine three series of inclusions: (1) $Ag_8 \longrightarrow Ag_{12}$ (transverse field) $\longrightarrow Ag_{16}$ (transverse field), (2) Ag_{12} (longitudinal field) $\longrightarrow Ag_{18}$ (longitudinal field), and (3) Ag_{12} (transverse field) $\longrightarrow Ag_{18}$ (transverse field). In the clamped-ion regime, these series all show a roughly linear increase in α_{inc} with the inclusion's cross-section. The relative increase in α_{inc} is slightly less than the relative increase in the number of inclusion atoms. As an example, within the first series increasing the number of cross-section atoms by 1.5× in going from Ag_8 to Ag_{12} results in a 1.47× increase in α_{inc}. Moreover, doubling the cross-section from Ag_8 to Ag_{16} results in a 1.91× increase in α_{inc}. There is also an approximately linear increase in α_{mat} as the particle is lengthened, with relative increases very similar to those in α_{inc}. Because α_{inc} dominates α_{enh} in the clamped-ion regime for all of the studied inclusions, we can again say that trends in α_{enh} are essentially explained by a near linear increase in the electronic polarizability of the inclusion with increasing cross-section.

In the relaxed-ion regime, the trend in α_{inc} is mostly similar to the clamped-ion regime, but the trend in α_{mat} is quite different. For the first two series of inclusions, the proportional increases in α_{inc} are still close to linear in the cross-section, yet

quantitatively smaller than in the clamped-ion regime. Using the same example as above, increasing the number of cross-section atoms by 1.5× in going from Ag_8 to Ag_{12} results in only a 1.39× increase in α_{inc}, while doubling the cross-section from Ag_8 to Ag_{16} results in a 1.80× increase in α_{inc}. Meanwhile, there is a more rapid increase in α_{mat}. For the same series, α_{mat} increased by 1.83× and 2.61×. For all of the inclusions across the three series, α_{mat} is either similar in magnitude to α_{inc} or dominates α_{enh} outright. Thus, the rapid increase in α_{mat} results in an increase in α_{enh} that is greater than the proportional increase in the number of inclusion atoms. It should be noted that the third series considered actually shows different α_{inc} behavior than the other two, with α_{inc} remaining virtually unchanged in going from Ag_{12} to Ag_{18}. Nevertheless, Ag_{18} shows a very large relative increase in α_{mat} that matches the picture from the other two series wherein there is a faster than linear increase in α_{enh} driven primarily by changes in the matrix.

Summary of Shape Effects on Wannier Partitioning

We glean three principles from these examinations of shape effects. First, increasing polarization length leads to rapid increases in α_{inc} in both the clamped- and relaxed-ion regimes, and these increases are the main contributors to an overall permittivity enhancement. Second, increasing polarization cross-section yields slower, roughly proportional increases in α_{inc}. While this principle mostly holds in both clamped- and relaxed-ion polarization, it is more consistent in the clamped-ion case. The third principle is obtained by comparing the trends of increasing inclusion cross-section with increasing polarization length. In both scenarios, changes in the clamped-ion enhancement are driven by changes in the inclusion polarizability. However, for the relaxed-ion regime, while changes in the inclusion polarizability are still the primary driver of changes in α_{enh} for increasing polarization length, changes in α_{mat} drive changes in α_{enh} for increasing polarization cross-section. Thus, we can say that the ionic contributions of the matrix take on an increasingly important role in polarization as the polarization cross-section is enlarged. Further work is of course necessary to determine the applicability of these principles to different matrices and different inclusion lengths outside the small range examined.

3.5.3 Classical Modeling

Classical models can be useful for conceptualizing the origins of permittivity enhancement with different shaped inclusions. As a point of comparison to the Wannier center results, we modeled the inclusions that we studied as both dielectric ellipsoids and cylinders embedded in an infinite uniform dielectric. Thus, we assume zero interaction between neighboring particles. In these models, we consider the ellipsoids to have an unknown electric permittivity of ϵ_i and the host matrix to have permittivity ϵ_h. The polarizability of an embedded ellipsoid with axes a_x, a_y, and a_z is a diagonal tensor whose j^{th} diagonal element is given by[23]

$$\alpha_j^{\text{ell}} = \frac{a_x a_y a_z}{3} \frac{\epsilon_h(\epsilon_i - \epsilon_h)}{\epsilon_h + N_j(\epsilon_i - \epsilon_h)}. \tag{3.13}$$

N_j is a depolarization factor that depends on the aspect ratio of the ellipsoid. For a sphere, $N = 1/3$ for all three directions, but in the general case N_j can be calculated with the integral

$$N_j = \frac{a_x a_y a_z}{2} \int_0^\infty \frac{ds}{(s + a_j^2)\sqrt{(s + a_x^2)(s + a_y^2)(s + a_z^2)}}. \tag{3.14}$$

The polarizability of embedded dielectric cylinders does not have such an analytical form. However, the problem has been treated numerically using the Method of Moments, and interpolation formulas are available for a range of aspect ratios and host–inclusion permittivity ratios.[24] Using these relationships, we first examine how such a classical model predicts the polarizability of an inclusion to change with increasing polarization length and cross-section for rod-like inclusions. These results can then be compared qualitatively to the trends observed above for the $Ag_8 \longrightarrow Ag_{12} \longrightarrow Ag_{16}$ series of inclusions. In the classical modeling, inclusions were either considered to be prolate spheroids or cylinders with a length greater than their diameter. The predicted polarizabilities of these inclusions can be expressed relative to the polarizability of the Ag_8 inclusion, modeled either as a sphere or a cylinder with a length equal to its diameter, to describe the enhancement in inclusion polarizability expected for an elongated particle relative to a short one. For both ellipsoid and cylindrical models, the rod diameter was held fixed as the length was increased. For prolate spheroids this ratio can be derived from Equation (3.13). Using the substitution $\tau = \epsilon_i/\epsilon_h$, the ratio is given by

$$\frac{\alpha_j^{\text{rod}}}{\alpha^{\text{sphere}}} = \left(\frac{a_l}{a_t}\right) \frac{1 + \frac{1}{3}(\tau - 1)}{1 + N_j^{\text{rod}}(\tau - 1)}, \tag{3.15}$$

where a_l and a_t are the longitudinal and transverse axis lengths for the rod (a_t is also the sphere radius). The analogous ratios for cylinder models are computed using the interpolation formulas from Ref [24]. It is worth noting that these ratios only depend on the aspect ratio of the particles and not on the absolute dimensions.

Figure 3.4 plots the expression in Equation (3.15) as a function of the long axis of the ellipsoidal rod a_l for both longitudinal and transverse polarization directions using several different values of τ. For all values of τ, the longitudinal polarization increases superlinearly, with the increase being faster as the permittivity contrast τ is increased. In contrast, the transverse polarization increases slower than linearly (though to the eye it may appear almost linear), and the increase is slower as the permittivity contrast is increased. Furthermore, transverse polarizability is predicted to be considerably smaller than longitudinal polarizability, with the differences increasing with τ and inclusion length. Cylindrical and ellipsoidal models show nearly the same evolution with rod length.

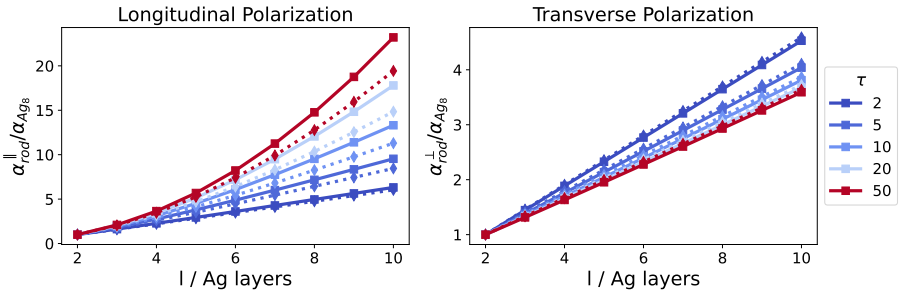

Figure 3.4: Polarizability enhancement as a function of rod length for classical ellipsoidal and cylindrical models. **a)** shows the enhancement in the longitudinal direction for various τ values, and **b)** shows the enhancement in the transverse direction. The x-axis is given as the hypothetical number of silver layers in the rod along its long axis. Thus, $x = 2$ corresponds to the Ag_8 model and $x = 10$ would correspond to an Ag_{40} rod. Solid lines with square markers depict the ellipsoidal model, and dashed lines with diamond markers depict the cylindrical model.

These trends are qualitatively similar to what we observed in the quantum simulations above. In those calculations, with a longitudinal field, α_{inc} increased faster than linearly with increasing polarization length. Meanwhile, as the rod length was increased in a transverse field so as to increase polarization cross-section, the relative increases in α_{inc} were slightly smaller than the relative increases in cross-section. Be-

cause we only examined a single disk in the quantum calculations, we did not include results for oblate spheroids or disk-like cylinders in Figure 3.4. However, we note that as with rods, the longitudinal polarizability for these shapes is larger than the transverse polarizability and increases more rapidly with inclusion aspect ratio.

Having examined polarizability enhancements as a function of rod length, we also use the ellipsoidal model to obtain more quantitative classical predictions of α_{inc} for Ag_{12}, Ag_{12}, and Ag_{12} inclusions relative to Ag_8. To do so, we considered the aspect ratios of Ag_{12}, Ag_{18}, and Ag_{16} to be 3:2, 3:2, and 4:2, respectively. Thus, we ignored subtle differences in lattice constants that arose in the optimization of atomic coordinates that would affect these ratios. We did, however, account for the differences in the composite permittivity between the different systems by setting ϵ_h to the corresponding composite permittivity (both clamped- and relaxed-ion permittivities are considered) for each inclusion in Equation (3.13). It is difficult to determine an appropriate value for the inclusion permittivity ϵ_i in these simulations, though we do assume that it will be significantly larger than the host permittivity. Thus, we calculated results using a wide range of values for ϵ_i. We looked at the ratios of the polarizabilities of these model rods to the polarizabilities of the model Ag_8 inclusion to compare against the same ratios of α_{inc} calculated quantum mechanically using Wannier center displacements.

The ratios plotted in Figure 3.5 can be thought of as predicted enhancements in the polarizability of a given rod relative to the Ag_8 inclusion. These enhancements vary rapidly with ϵ_i at first before leveling off, thus providing a range of possible enhancement values that depends on the actual value of the inclusion permittivity. Hereafter, we focus on the behavior for large ϵ_i, since these seem to agree more quantitatively with the quantum results. Longitudinal enhancements are greatest for the Ag_{16} rod. As ϵ_i becomes very large, this rod is predicted to be over $6\times$ more polarizable than Ag_8 for the clamped-ion case and well over $5\times$ more polarizable in the relaxed-ion case. Ag_{18} a distant second, at just over $3\times$ more polarizable than Ag_8 in both cases. Meanwhile, for a transverse field, the Ag_{16} rod is more polarizable than the Ag_{12} rod, and the Ag_{16} and Ag_{18} inclusions have quite similar polarizabilities. In fact, the Ag_{18} is slightly more polarizable than Ag_{16} for the relaxed-ion case and less polarizable in the clamped-ion case. Another notable feature is that due to the inclusion of the dependence on the change in composite permittivity, the longitudinal enhancements are all greater for the clamped-ion case than the relaxed-ion one, and the transverse enhancements are greater for the relaxed-ion case.

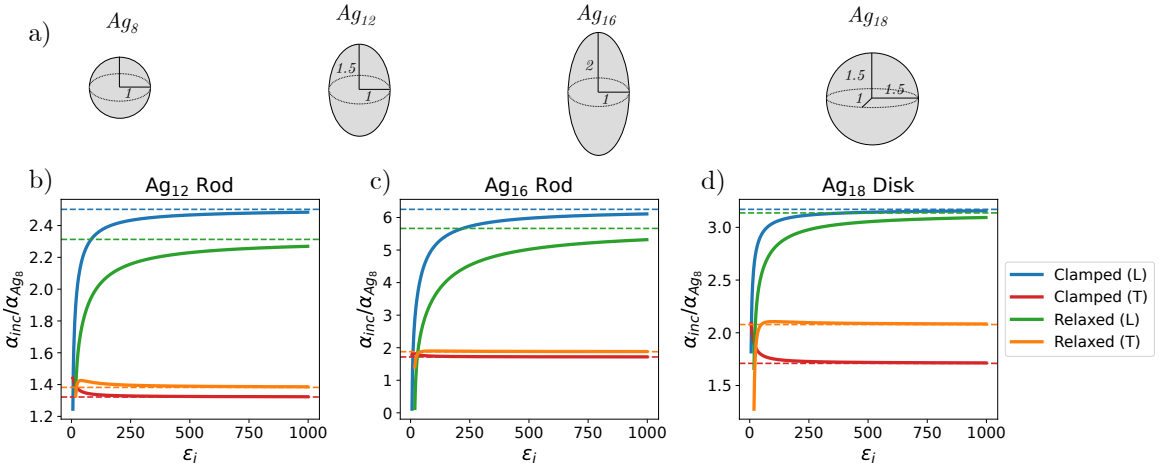

Figure 3.5: Classical models of Ag inclusions as dielectric solids in uniform dielectric background. **a)** shows the two models used for each inclusion, labeled with relative lengths. **b)**–**d)** show the ratio of the longitudinal (L) and transverse (T) polarizabilities of the ellipsoidal inclusion models to that of the Ag_8 sphere model, for Ag_{12}, Ag_{16}, and Ag_{18}, respectively. Clamped and Relaxed ion cases are handled with difference values of the matrix permittivity ϵ_h. Dashed horizontal lines indicate the values of the ratios in the limit of large ϵ_i

.

Table 3.5 provides the values of these polarizability enhancements in the limit as ϵ_i becomes very large—that is, as the inclusion is taken to become a conductor in an otherwise insulating composite. Additionally, the table includes the enhancement ratios calculated from the quantum calculations above (given also in the α^r_{inc} column in Table 3.4). These show that there is generally good qualitative agreement between the quantum results and classical predictions. Namely, both present longitudinal enhancements that increase in the order Ag_{12} <Ag_{18} <Ag_{16}. Both also indicate that the transverse enhancements of Ag_{16} are greater than Ag_{12} The quantitative agreement with the quantum results is also surprisingly good for most of the data points, considering the simplicity of the model used. However, it should be noted that the model vastly underestimates the relaxed-ion longitudinal polarizability enhancement of Ag_{16} and severely overestimates the relaxed-ion transverse polarizability enhancement of Ag_{18}. These two examples suggest the distinct difficulty of capturing the effects of ion dynamics in a classical continuum model.

While it is tempting to conclude that the studied inclusions can be reasonably well-modeled as conducting ellipsoids, several caveats should be noted. First, we directly compared the polarizability enhancements predicted by the classical model with the

Table 3.5: $\alpha/\alpha_{\mathrm{Ag_8}}$ in the $\tau \to \infty$ limit from classical ellipsoidal model.

Inclusion	Pol Type	Classical		Quantum	
		Longitudinal	Transverse	Longitudinal	Transverse
Ag_{12}	Clamped-Ion	2.50	1.32	2.56	1.47
	Relaxed-Ion	2.31	1.38	2.85	1.39
Ag_{16}	Clamped-Ion	6.25	1.72	6.50	1.91
	Relaxed-Ion	5.66	1.88	8.25	1.80
Ag_{18}	Clamped-Ion	3.17	1.71	3.50	2.01
	Relaxed-Ion	3.14	2.08	3.64	1.38

α_{inc} enhancements from the quantum calculations. However, it should be noted that α_{inc} is defined using the macroscopic applied field in the quantum calculation, which will in general differ from the the local field experienced by the inclusion. Thus, the direct quantitative comparisons with the classical model should be made with caution. Second, while the qualitative effects of changing the inclusion aspect ratio can be reconciled mostly with classical electrostatics, this is not necessarily true of the effects on the surrounding matrix. Any quantitative classical approach to modeling the permittivity of such composites will ultimately need to address not only the large permittivity of the inclusion but also the changes to the permittivity of the matrix at its interface with the inclusion.

3.6 Matrix Composition Effects

In addition to the nanoparticle-centered parameters of loading and shape, we can use the Wannier partitioning scheme to interrogate the effects of changing the matrix identity. To do so, we look at a series of alkaline earth metal oxides, where the cation identity is varied between Mg, Ca, Sr, and Ba. To these matrices, we substitute 8 central ions (4 cations and 4 anions) with Ag, resulting in the same form of nanocomposite as in Section 3.3. The bulk oxides in this series all have the same rocksalt crystal structure, strong ionic character, and similar high frequency relative permittivities between 3-4. Despite these similarities, the matrices exhibit a range of lattice constants and ionic radii. Table 3.6 shows the experimental lattice constants for these oxides as well as their calculated lattice constants and Born effective charges. Lattice constants increase with the size of the cationic radii, allowing more space for

an Ag inclusion and less strain in the layer of matrix adjacent to the inclusion. In fact, the prominent lattice expansion in the MgO composite is essentially gone for SrO, and BaO even experiences a slight contraction of its lattice when the inclusion is introduced.

Table 3.6: Lattice constants of bulk oxides (a_{bulk}) and Ag_8 nanocomposites (a_{bulk}).

Material	BEC[a]	a_{bulk} (Exp.)[b]	a_{bulk} (DFT)[c]	a_{comp}[d] (DFT)
MgO	±1.99[e]	4.213	4.167	4.258
CaO	±2.34	4.810	4.755	4.781
SrO	±2.43	5.160	5.111	5.121
BaO	±2.72	5.539	5.498	5.488

[a] Born Effective Charge.
[b] Computed from the densities in references [25, 26].
[c] Computed with 3x3x3 supercells of the conventional lattice with PBESol.
[d] Lattice constant of the composite, optimized with CPMD.
[e] Calculated with 100 Ry wavefunction cutoff to ensure converged BECs.

The series of alkaline earth oxides also demonstrates a trend of increasing permittivity with increasing cation radius. Table 3.7 provides our calculated clamped- and relaxed-ion permittivities for the different bulk oxides alongside experimental values. Theoretical values were obtained using CPMD with a 3x3x3 supercell of the bulk matrix. While the clamped-ion results are in quite good agreement with experiment, we note that the relaxed-ion results overestimate experimental values for all non-MgO matrices.

Table 3.7: Computed and experimental permittivities of alkaline earth oxides.

Material	$\epsilon^{\infty}_{\text{DFT}}$	$\epsilon^{\infty}_{\text{Exp.}}$	$\epsilon^{0}_{\text{DFT}}$	$\epsilon^{0}_{\text{Exp.}}$
MgO	3.00	3.00[a]	9.00	9.78[b]
CaO	3.47	3.33[c]	14.34	11.1[c]
SrO	3.47	3.46[c]	18.42	13.1[c]
BaO	3.81	3.90[d]	43.31	34[e]

[a] Calculated from a refractive index of 1.733345 at 656.3 nm and 296.15 K.[27]
[b] From Ref [28] at 50K and zero pressure.
[c] Values from Ref [29].
[d] Calculated from a refractive index of 1.97571 at 623.8 nm and 296.15 K.[30]
[e] Value from Ref [31].

Table 3.8 provides the calculated permittivities for composites and the partitioning of the resulting α_{enh} into inclusion and matrix contributions. Adding Ag_8 inclusions to these oxides universally increases their high-frequency permittivity, leading to positive values of α_{enh}. These enhancements are very similar for MgO, CaO, and SrO, but notably larger for BaO. However, it should be noted that the relative increases in permittivity (and susceptibility) upon introduction of the inclusion decrease monotonically in going from the MgO to BaO matrix. The low-frequency permittivities show the same trend of decreasing relative enhancement, this time with a concomittant monotonic decrease in α_{enh} from MgO to BaO. In fact, the relaxed-ion permittivity of BaO actually decreases slightly upon embedding silver nanoparticles, resulting in a negative α_{enh}. By partitioning α_{enh}, we can better understand the coupling between matrix and inclusion that leads to these results.

Table 3.8: Partitioning of α_{enh} for different oxide matrices.

Oxide	**Polarization Type**	ϵ_{comp}	α_{inc}	α_{mat}	α_{cav}	α_{enh}
MgO	Clamped-ion	3.61	543	221	-78	686
	Relaxed-ion	11.83	1033	2451	-311	3174
CaO	Clamped-ion	3.88	612	181	-142	651
	Relaxed-ion	15.86	1110	2080	-770	2420
SrO	Clamped-ion	3.83	655	232	-177	710
	Relaxed-ion	18.78	1436	500	-1250	686
BaO	Clamped-ion	4.16	730	340	-251	820
	Relaxed-ion	41.73	3001	-3005	-3777	-3780

Trends in Clamped-Ion Polarization

In the clamped-ion regime, α_{inc} increases steadily from MgO to BaO. However, this increase is almost exactly offset by the steadily more negative α_{cav} that results for the increasing permittivity of the bulk. Thus, the trend in α_{enh} is accounted for primarily by α_{mat}, which is relatively small for CaO and large for BaO.

The trend in α_{inc} can be accounted for by considering the increasing lattice constants as the oxide cationic radius increases, in addition to the variation in the spreads of Wannier functions near the inclusion. Increasing the lattice constant of the matrix creates more space around the inclusion in the composite, both allowing the Ag-Ag bonds to lengthen and reducing the confinement of the highly polarizable Ag

s-electrons. These two factors produce an inclusion with a larger volume, both in a structural and electronic sense. As volume is directly correlated with the polarizability of both isolated molecules[32, 33] and atoms in materials,[34] the increase in α_{inc} with lattice constant can be rationalized by the increasing volume of the inclusion. In the context of an MgO matrix, Hally rationalized the large polarizability of the inclusion as a balance between the polarizability-enhancing effect of electrons in the inclusion being polarized toward neighboring Mg cations and the polarizability-quenching effect of inclusion s-electrons being repelled (and thereby confined) by neighboring O^{2-} anions.[13] Increasing the lattice constant of the matrix has the effect of removing this latter effect. Indeed, the spreads of the s-like Ag Wannier functions are seen to increase steadily with the lattice constant (Figure 3.6).

To some extent, trends in α_{mat} should be expected to reflect α_{inc}. Since the matrix responds to the induced field of the inclusion, increasing inclusion polarizability enhances the local field experienced by the matrix ions, resulting in more polarization compared to the same ions in bulk. In the present case, α_{mat} does not directly mirror α_{inc}, requiring additional explanatory mechanisms that go beyond an electrostatic coupling to the inclusion.

Quantum mechanical effects related to the electronic delocalization at the interface can be investigated via the spreads of Wannier functions. Hally rationalized the enhancement in the matrix for the MgO composite by noting and increased delocalization of oxygen electrons in the vicinity of the inclusion relative to the bulk oxide[13]. Figure 3.6 shows the spreads of the Wannier functions as function of distance from the inclusion center for each matrix. All of the matrices exhibit a similar trend of increased spread in the oxygen Wannier centers close to the inclusion. This increase in spread is particularly great for the BaO matrix, which also has an additional large peak in the Wannier function spreads for the central oxygens in the second layer of matrix away from the inclusion that is much larger than the corresponding peak in the other matrices. In fact, this peak is completely absent for the CaO matrix, which may partly account for it having the lowest α_{mat}. Finally, it is worth noting that in MgO, the spreads of oxygen Wannier functions remain above bulk values even at the cell boundaries, whereas they return to bulk values a relatively short distance from the inclusion for all of the other matrices. Combining these observations appears to account for the variation in α_{mat} in the clamped-ion regime—namely, there being a sharp drop from MgO to CaO followed by a steady increase from CaO to BaO.

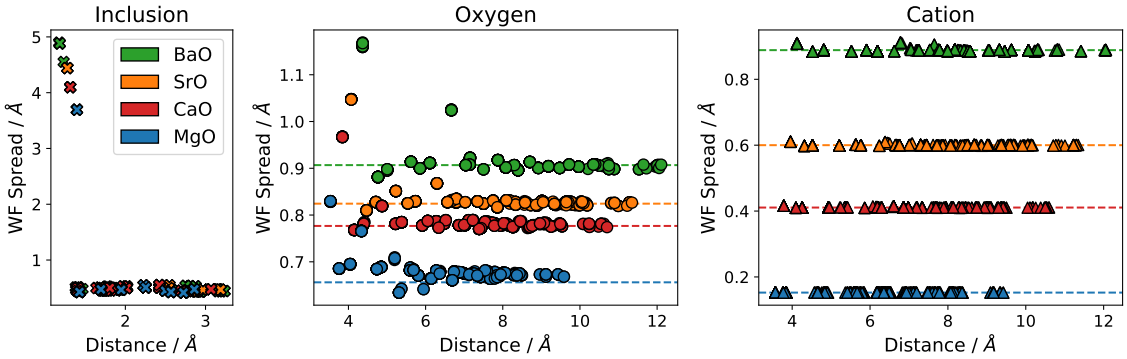

Figure 3.6: Wannier Function spreads as a function of distance from the center of the Ag_8 inclusion for different oxides. Horizontal lines in the oxygen and cation plots indicate the average Wannier function spread in the bulk.

Trends in Relaxed-Ion Polarization

We now return to Table 3.8 to examine the trends in the relaxed-ion regime. As with the clamped-ion case, α_{inc} increases monotonically from MgO to BaO (though the increase from MgO to CaO is minimal). However, in this case, α_{cav} decreases more rapidly than the increase in α_{inc}, reflecting the rapid increase in ionic polarizability in the bulk matrices. In the end, the increasing polarizability of the inclusion does not keep up with the polarizability lost from replacing matrix ions, and the sum of α_{inc} and α_{cav} is negative for and BaO. The matrix enhancement α_{mat} decreases rapidly from MgO to BaO as well, to the point where the polarizability of the matrix is actually significantly decreased in the BaO composite relative to bulk. Combining all of these factors results in the steadily declining α_{enh} for the series, including a negative α_{enh} for BaO.

These trends seem to be both an effect of the increasingly polarizable bulk, whose polarizability the inclusion must at least match to provide an enhancement and a diminished constructive effect of the inclusion on the surrounding ion dynamics, which can be quantified in the Born effective charges (BECs). Hally noted that the presence of an inclusion in MgO produced anomalous BECs in the vicinity of the inclusion, whose distribution reflected a strong induced dipole field around the inclusion.[13] In particular, deviations in the component of BECs collinear with the applied field from bulk values was seen to drop off with distance from the inclusion according to an approximately inverse cubic relationship, just as the field of a point dipole.

Figure 3.7 shows Z^*_{zz} in all composites plotted as a function of distance from the inclusion. This quantifies the change in force on an ion in the $z-$direction when a

field is also applied along the $z-$axis, as we have done in our simulations. Thus, BEC tensor components (which we will just refer to as BECs from now on) tell us about the response of ions colinear with an applied field. As the matrix is changed from MgO to BaO, the distribution of cationic BECs becomes progressively tighter about the bulk values, with the large enhancement in the BEC of the nearest axial cations in MgO all but gone in BaO. The distribution of oxygen BECs also becomes tighter on the whole, though there are still large deviations from bulk for the sites nearest to the inclusion and for the equivalent sites in the second layer of matrix from the inclusion. Since BEC deviations decay rapidly with distance, this likely reflects the fact that the shortest Ag–O bonds are significantly shorter than the shortest Ag–cation bonds, due to the nested tetrahedral structure of the inclusion.[13]. Furthermore, the Ag–cation bondlengths increase more rapidly than the Ag–O bondlengths as the matrix changes from MgO to BaO.

In fact, the changing distributions of BECs between different matrices can largely be explained by the variation in lattice constants and the inverse cubic drop-off of the BEC variation due to the inclusion dipole field. Panels **e)** and **f)** of Figure 3.7 show the BECs of all four composites overlaid. Regardless of the matrix, the anomalous BECs appear to decay according to the same inverse cubic envelope. As a result, when the lattice constant is increased, matrix ions are further from the inclusion center and the deviations of their BECs from bulk values fall further out along the inverse cubic envelope. In other words, they experience a lower induced field from the inclusion. The importance of this induced field is also noticeable in the mean BECs of the cations different atom types 3.9. In particular, while there is an average enhancement in the BECs for all matrix ions relative to bulk values, this enhancement is largest for MgO and steadily drops in going from MgO to BaO. Across all matrices, the mean BEC values for O in the composite are larger in magnitude than the cationic BECs, reflective of the positive charge acquired by the Ag atoms and demonstrating the tight dynamic coupling between these species. Note, however, that the Ag charges decrease steadily from MgO to BaO, indicating less coupling of the inclusion ion dynamics to the matrix.

Summary Of Matrix Effects

In the current section, we have seen that much of the variation between composites with different alkaline-earth metal oxide matrices could be understood by an appli-

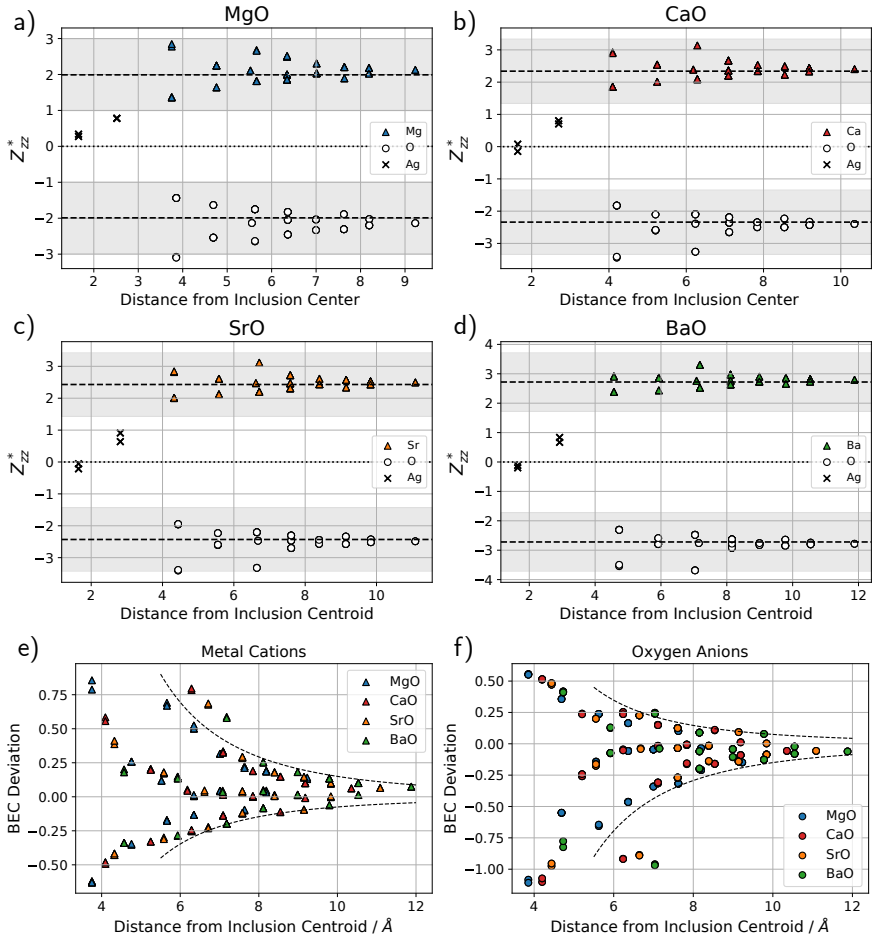

Figure 3.7: Born effective charges (BECs) for different matrices. Panels **a)-d)** plot Z^*_{zz} for each composite as a function of the distance to from the inclusion centroid (mean position of silver atoms). Dashed lines give the Z^* values of the bulk, and shaded areas highlight a deviation of 1 charge unit on either side of these bulk values. Panels **e)** and **f)** Show the BECs of all matrix ions, centered at their respective bulk values. Dashed lines show an inverse cubic envelope. For metal cations, these are $y = 150r^{-3}$ and $y = -75r^{-3}$, and for oxygen anions, they are $y = 75r^{-3}$ and $y = -150r^{-3}$. The factor of 2 difference in the positive and negative envelope comes from a dipolar model of the BEC distribution,[13] wherein the magnitude of deviation of BECs for equatorial ions is half that of axial ones.

cation of the methodology developed by Hally.[13] In particular, the decomposition of α_{enh} for these composites followed smooth trends as the matrix cation identity was changed. These trends reflected differences in the delocalization of electrons at the interface between matrix and inclusion, as well as differences in the dynamic coupling of the inclusion and matrix ions at this interface. Both of these effects showed a sharp drop-off with distance from the inclusion, which allowed us to propose a simple

Table 3.9: Mean Z^*_{zz} Values in Bulk and Composites.

Matrix	Bulk[a]	Composite[a]	Cation[b]	O[b]	Ag[b]
MgO	1.99	2.10	2.08	-2.12	0.54
CaO	2.34	2.39	2.38	-2.41	0.36
SrO	2.43	2.48	2.47	-2.49	0.32
BaO	2.72	2.76	2.75	-2.78	0.30

[a] The mean absolute value of all BECs of non-Ag atoms.
[b] In the composite.

mechanism for the observed trends. With symmetry being the same for all matrices, changes in the lattice constant and resulting interatomic spacing between matrices account for much of the observed variation. Increasing interatomic distances allows more room for the electronic polarization of the inclusion the inclusion. This in turn leads to a strong electrostatic coupling of the matrix to the induced field of the inclusion, which competes with a decrease in the delocalization of all but the closest matrix electrons to yield the observed trends in α_{mat} for clamped-ions. Increasing lattice constants also yield a reduction in the impact of the inclusion on the Born effective charges of surrounding matrix ions, resulting in a decrease in the relaxed-ion permittivity enhancement.

3.7 Discussion: Alternative Approaches

Thus far, we have adopted Hally's approach of computing inclusion-specific permittivity enhancement factors. The protocol establishes some degree of spatial localization of the polarization increase on either the inclusion or surrounding matrix, which can be linked to other spatially-resolved descriptors of the electronic structure such as Wannier function spreads and Born effective charges. However, as discussed earlier, an alternative approach is to determine a local position-dependent (nanoscopic) electric susceptibility. This inevitably involves a spatial averaging over the local polarization and electric field to produce a smoothly varying permittivity. Such an approach suggests distinct benefits in the study of nanocomposites. First, it would allow fine-grained spatial resolution of the physical and chemical mechanisms that affect permittivity, and second, it could be used to produce computationally cheap continuum models. Thus, in this section, we briefly discuss the method developed by Giustino, Umari, and Pasquarello[7, 3] to compute local permittivities within the

simulation cells of *ab initio* calculations, and our initial attempts to modify the approach for matrix inclusion composites. The work herein represents the beginning of a research direction and is by no means conclusive.

The method of Giustino and co-workers focuses specifically on resolving local electric permittivity $\epsilon_{\text{loc}}(x)$ profiles across planar interfaces (where the x-direction is normal to the interface).[7, 3] A finite field orthogonal to the interface is used to perturb the electronic structure, and the induced charge density is smoothed via planar averaging parallel to the interface followed by convolution with a Gaussian function to yield the smoothed induced charge density $\overline{\overline{\rho}}_{\text{ind}}(x)$. This smooth density is used to derive the smooth local electric field $\overline{\overline{E}}_{\text{loc}}(x)$ via Gauss's law as

$$\frac{d}{dx}\overline{\overline{E}}_{\text{loc}}(x) = 4\pi\overline{\overline{\rho}}_{\text{ind}}(x). \tag{3.16}$$

This equation gives $\overline{\overline{e}}(x)$ to within an additive constant, which is determined from the value applied macroscopic field. The local polarization can also be obtained from the induced density with the relationship

$$\frac{d}{dx}\overline{\overline{P}}_{\text{loc}}(x) = -\overline{\overline{\rho}}_{\text{ind}}(x), \tag{3.17}$$

which determines the local polarization to within an additive constant that can be obtained from the cell polarization via a Berry phase calculation. Finally, the local polarization and electric field can be used to define a local susceptibility as

$$\overline{\overline{P}}_{\text{loc}}(x) = \chi_{\text{loc}}(x)\overline{\overline{E}}_{\text{loc}}(x), \tag{3.18}$$

which is related to the local permittivity in the usual way:

$$\epsilon_{\text{loc}}(x) = 1 + 4\pi\chi_{\text{loc}}(x). \tag{3.19}$$

While the above procedure is applicable to planar stacked heterostructures and slabs, it would not work for the nanocomposites studied in this chapter. In particular, the planar averaging used to smooth the local fields does not match the symmetry of the inclusion-matrix interface. Instead, we propose that a method based on 3D Gaussian smoothing could be a path forward. This approach also utilizes finite field calcuations and involves 1) obtaining the local electric field via the gradient of the Gaussian-smoothed induced potential, 2) obtaining the local induced polarization via Gaussian-blurred Wannier center (and potentially ionic) displacements, and 3)

combining these two quantities to obtain the local permittivity.

In order to obtain the local electric field, we first calculate the electrostatic potential $V(\mathbf{r})$ throughout the simulation cell in both a zero field ($V^0(\mathbf{r})$) and finite field calculation ($V^{\text{field}}(\mathbf{r})$). Then, the induced potential is given by $V_{\text{ind}}(\mathbf{r}) = V^{\text{field}}(\mathbf{r}) - V^0(\mathbf{r})$. The smoothed induced potential $\overline{V}_{\text{ind}}(\mathbf{r})$ is obtained by convolution of V_{ind} with a Gaussian function of appropriate spread, and the smooth local electric field $\overline{\mathbf{E}}_{\text{loc}}(\mathbf{r})$ is given by

$$\overline{\mathbf{E}}_{\text{loc}}(\mathbf{r}) = -\nabla(\overline{V}_{\text{ind}}(\mathbf{r})) + \mathbf{E}_{\text{mac}}, \tag{3.20}$$

where the first term contains the induced electric field, and $\mathbf{E}_{\text{mac}}$ is the applied macroscopic electric field. Compared to beginning with the induced charge density, this approach preempts the need to solve the Poisson equation of Equation (3.16) in order to obtain the induced electric field.[35] Furthermore, the electrostatic potential is available via post-processing tools for most electronic structure codes, including Quantum Espresso.

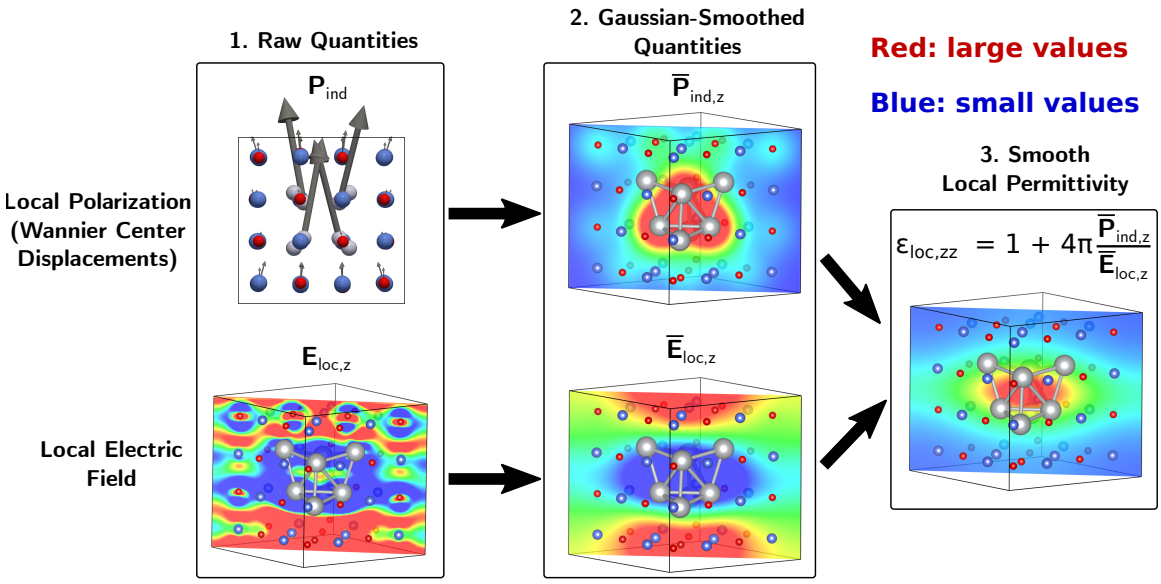

Figure 3.8: Procedure for calculating the local permittivity, shown for the highest volume loading system from Section 3.4. Note that the smoothed electric field is obtained from the negative gradient of the Gaussian-smoothed induced potential, not by direct smoothing of the raw electric field. Heat maps of the electric field and polarization show the $z-$components of the respective fields, for an applied field in the $z-$direction. Thus, The obtained permittivity is $\varepsilon_{zz}(\mathbf{r})$. For all heatmaps, red indicates relatively large values, and blue indicates relatively small values.

The local induced polarization is obtained in much the same way as the inclusion polarization in the α_{enh} procedure. MLWFs are obtained for both zero and finite field calculations, and their centers are assigned to the nearest atomic nuclei. The induced dipole moment for atom I is obtained as a sum over the Wannier center displacements $\Delta\mathbf{r}_i$, multiplied by the charge of each Wannier function ($-2e$ for doubly-occupied functions, or simply -2 in atomic units). When considering relaxed-ion polarization, an additional term including the ionic displacement ΔR and nuclear (pseudopotential) charge Z must also be included. Thus, the total induced dipole moment of atom I is given by

$$\Delta\mathbf{p}_I = -2\sum_i^{N_I} \Delta\mathbf{r}_i + Z_I \Delta\mathbf{R}_I. \tag{3.21}$$

In order to turn discrete atomic dipole moments into continuous polarization throughout the simulation cell, the value of the induced dipole moment at each atomic coordinate is multiplied by a Gaussian function of an appropriate spread. The superposition of all of these Gaussians yields the smooth induced polarization $\overline{\mathbf{P}}_{\text{ind}}(\mathbf{r})$. Note that this is indeed now the polarization *density*, and its integral over the simulation cell gives the total induced cell dipole moment. This definition of local polarization has been used by Galli and co-workers in their dielectric-dependent density functionals, where the spread of the smoothing Gaussians is taken to be the mean Wannier function spread for a given atom.[4]

The components of the local dielectric permittivity tensor are then given by

$$\epsilon_{\text{loc},ij}(\mathbf{r}) = 1 + 4\pi \frac{\overline{P}_{\text{ind},i}(\mathbf{r})}{\overline{E}_{\text{loc},j}(\mathbf{r})}. \tag{3.22}$$

We note that this quantity differs from the local dielectric constant in Galli's dielectric-dependent functionals. In their definition, the electric field in the denominator is taken to be the macroscopic applied field, rather than the local field.[4, 11] The proposed approach to local electric permittivity is illustrated in Figure 3.8.

We calculated $\epsilon_{\text{loc},zz}(\mathbf{r})$ using the newly proposed method for the model system studied by Hally. As with the higher volume loading composite shown in Figure 3.8, the induced electric field demonstrated a strong dipolar shape resulting from charge redistribution to either side of the inclusion. This was true for both the clamped- and relaxed-ion cases. This field is parallel with the applied field along the axis of the inclusion and antiparallel with the applied field within inclusion and along its

equator. In fact, the induced field was large enough that the total local field, which is the sum of the induced and applied fields, was negative in some regions of the cell and near zero in others unless a rather large Gaussian spread was used for smoothing out the induced potential. As negative fields produce negative local permittivities (the local polarization was strictly positive), and zero local fields produce divergent local permittivities, both should be avoided. Thus, we chose Gaussian spreads of 2.5 Å and 3.0 Å for the clamped- and relaxed-ion fields, respectively, which produced strictly positive local electric fields.

Figure 3.9 shows the resulting local permittivities, juxtaposed with the permittivities calculated using the macroscopic electric field instead of the local field in the definition of Equation (3.22). By examining the quantities calculated with the macroscopic field, we are seeing an effective map of the local polarization. In both the clamped-and relaxed-ion cases, these maps show a large polarization localized on the central four Ag atoms. When the ions are clamped, matrix atoms closest to the inclusion also exhibit larger-than-bulk polarization, with the increase extending further along the polarization axis through the inclusion than around its equator. In the relaxed-ion case, the polarization is also large in the shell of matrix ions around the inclusion, but there is a more pronounced increase in polarization for all matrix ions both above and below the inclusion, which experience an induced electric field aligned with the applied field. There is also a relatively low polarization (though still larger than bulk) for the matrix ions at the cell edges around the inclusion equator, where the induced field would oppose the applied field. Notably, the matrix ions directly above and below the inclusion experience a diminished polarization relative to their neighbors. It is also interesting that all values of the resulting permittivity fall in a relatively narrow range.

Using the smoothed local electric field to compute the local permittivity results in a different, physical picture of the polarization response, showing not which regions experience the largest polarization, but which are the most polarizable. Under this approach, the inclusion itself is still seen to have a large local permittivity–in fact, significantly larger than the surrounding matrix. This reflects a very small local electric field in the inclusion due to effective screening of the applied one. Moreover, the local permittivity of the matrix at the interface with the inclusion is actually calculated to be larger about the inclusion equator than along its polarization axis. This effect is particularly pronounced in the relaxed-ion permittivity. That is the ions along the inclusion equator polarize proportionally more for the local field they

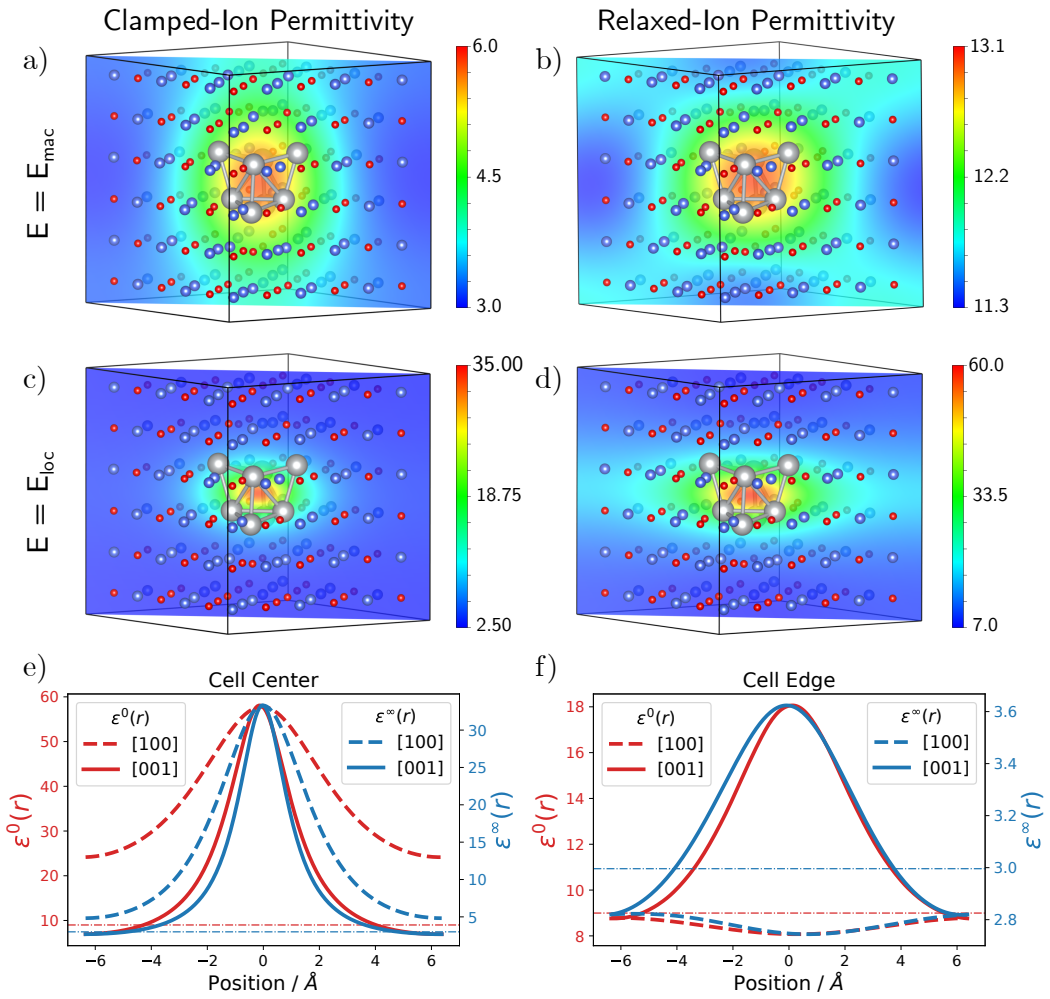

Figure 3.9: Local permittivity $\epsilon_{\mathrm{loc},zz}(\mathbf{r})$ of the 216-atom MgO/Ag_8 Nanocomposite. Panels **a)** and **b)** show the clamped- and relaxed-ion local permittivity calculated using the Galli's method (i.e. using the macroscopic electric field in Equation (3.22)). Panels **c)** and **d)** show the clamped- and relaxed-ion permittivities calculated using the local electric field. All of **a)**-**d)** show a (110) slice of the permittivity that passes through the inclusion. Panel **e)** shows traces of the local permittivity (as defined with the local electric field) through the center of the inclusion, following both the [100] and [001] directions. Panel **f)** shows traces along the same vectors, but along the cell edges far from the inclusion. Positions are relative to the inclusion center along the given direction. Dash-dot horizontal lines indicate bulk permittivities.

experience than the ions along the inclusion poles.

This angular distribution of ϵ_{zz} is emphasized by the 1D traces of the local permittivity in Figure 3.9(e) and (f). Passing from matrix through the inclusion and back to the matrix along the $z-$direction, the permittivity goes from the bulk value (in

fact, slightly below the bulk value), increases sharply at the inclusion interface, and then drops back to bulk values on the other side of the inclusion. In contrast, a trace through the inclusion along its equator remains significantly above bulk values even at the cell edges. Traces of the permittivity along the cell edges show essentially the same behavior—along the top- and bottom faces of the cell, both the clamped and relaxed-ion permittivities remain near bulk values, while along the equatorial plane, the permittivity still rises significantly with proximity to the inclusion.

3.7.1 Takeaways from Local Permittivity Mapping

Treating the local permittivity in this way has the potential to elucidate both the angular and radial (relative to the inclusion) dependence of the dielectric response in a way that is not done in the α_{enh} approach. Furthermore, the method produces a continuous local permittivity defined throughout the simulation cell. Thus, it could be used to produce classical continuum models of nanocomposites, since these classical models rely on the definition of a simulation cell with spatially-dependent permittivity. Such an approach would become useful if it could be shown that the permittivity profiles of different inclusions were transferable or generalizable in some way, allowing continuum models to be generated for new inclusions without the need to perform a quantum calculation.

However, several points need to be addressed before further application of the local permittivity method outlined here. Most importantly, the computed permittivities are very sensitive to the value of the Gaussian spread used in smoothing the induced potential and local polarization. While we found it necessary to use spreads of ≥ 2.5 Å in order to enforce the non-negativity of the local field, this spread is actually larger than the matrix interatomic distances in the studied composites. Thus, such smoothing perhaps excessively blurs the local electric field and local polarization. As a point of comparison, we note that Galli's method uses a spread equal to the mean Wannier spreads at a given atom, which in our composites are typically under 1 Å in the matrix.[4] Similarly, Giustino *et al.* use a 1 Å Gaussian filter in their macroscopic averaging. One potential path forward for our method would be to adopt the method of Wannier-spread-based smoothing for the polarization while continuing to use a wider Gaussian for smoothing the induced potential. Alternatively, the local permittivity could be defined only outside of some radial cutoff distance away from the inclusion center, effectively ignoring small or negative fields inside the inclusion

such that smaller smoothing Gaussians can be used.

In preliminary testing, we also performed the same methodology on both the low and high volume-loading composites studied above in Section 3.4. While the permittivity profiles demonstrated similar shapes for the three different loadings, the peak permittivities in the inclusion were quite different between geometries. It is likely that this is a consequence of the same issue in defining an appropriate local field smoothing. Essentially, because the local electric field in the inclusion is so small in the present method, the local permittivity is very sensitive to small changes in that field. Addressing these issues will be the subject of future work.

3.8 Conclusions

In this chapter, we have applied a method to decompose the dielectric response of matrix-inclusion composites to several systems composed of alkaline-earth metal oxide matrices with silver inclusions in order to investigate the effects of inclusion loading, inclusion shape, and matrix identity. The method requires simulating a supercell of the matrix alone, as well as the same cell where a single inclusion is present, using both zero and finite applied electric fields. We have seen that the method is sensitive to the percent loading of inclusions. However, this dependence effectively disappears at small loadings of a couple of percent silver, allowing one to calculate enhancement factors for the polarization of both the inclusion and surrounding matrix which are intrinsic to the identities of each. We showed that these enhancement factors were sensitive to the inclusion's polarization length and cross-section in ways that were qualitatively similar to classical models of ellipsoidal inclusions. Furthermore, the enhancement of the surrounding matrix was seen to be generally much larger when ions were allowed to relax than when they were clamped, with this ionic enhancement being quite sensitive to the geometry of the matrix-inclusion interface. Finally, different alkaline-earth oxide matrices exhibited robust trends in inclusion and matrix enhancement, which were tied to both the lattice constants and bulk matrix permittivities. In the last section of the chapter, we proposed an alternative means of spatially resolving the dielectric response of these composites via the calculation of a local nanoscopic permittivity. A proof-of-concept was presented using an MgO/Ag_8 composite, and directions for future improvement of the method were identified.

Bibliography

[1] Stephen L. Adler. Quantum theory of the dielectric constant in real solids. *Physical Review*, 126(2):413–420, April 1962.

[2] Stefano Baroni and Raffaele Resta. Ab initio calculation of the macroscopic dielectric constant in silicon. *Physical Review B*, 33(10):7017–7021, May 1986.

[3] Feliciano Giustino and Alfredo Pasquarello. Theory of atomic-scale dielectric permittivity at insulator interfaces. *Physical Review B*, 71(14), April 2005.

[4] Huihuo Zheng, Marco Govoni, and Giulia Galli. Dielectric-dependent hybrid functionals for heterogeneous materials. *Physical Review Materials*, 3(7), July 2019.

[5] Hugh F. Wilson, François Gygi, and Giulia Galli. Efficient iterative method for calculations of dielectric matrices. *Physical Review B*, 78(11), September 2008.

[6] Hugh F. Wilson, Deyu Lu, François Gygi, and Giulia Galli. Iterative calculations of dielectric eigenvalue spectra. *Physical Review B*, 79(24), June 2009.

[7] Feliciano Giustino, Paolo Umari, and Alfredo Pasquarello. Dielectric discontinuity at interfaces in the atomic-scale limit: Permittivity of ultrathin oxide films on silicon. *Physical Review Letters*, 91(26), December 2003.

[8] N. Shi and R. Ramprasad. Atomic-scale dielectric permittivity profiles in slabs and multilayers. *Physical Review B*, 74(4), July 2006.

[9] N. Shi and R. Ramprasad. Local dielectric permittivity of hfo2 based slabs and stacks: A first principles study. *Applied Physics Letters*, 91(24), December 2007.

[10] Massimiliano Stengel and Nicola A. Spaldin. Ab initiotheory of metal-insulator interfaces in a finite electric field. *Physical Review B*, 75(20), May 2007.

[11] Jiawei Zhan, Marco Govoni, and Giulia Galli. Nonempirical range-separated hybrid functional with spatially dependent screened exchange. *Journal of Chemical Theory and Computation*, 19(17):5851–5862, August 2023.

[12] Alfonso Baldereschi, Stefano Baroni, and Raffaele Resta. Band offsets in lattice-matched heterojunctions: A model and first-principles calculations for gaas/alas. *Physical Review Letters*, 61(6):734–737, August 1988.

[13] David J. T. Hally and Irina Paci. Low-frequency polarization in molecular-scale noble-metal/metal–oxide nanocomposites. *Nanoscale*, 10(20):9583–9593, 2018.

[14] Archita N. S. Adluri, Brett Henderson, and Irina Paci. Tuning the dielectric response in a nanocomposite material through nanoparticle morphology. *RSC Advances*, 12(17):10778–10787, 2022.

[15] Andrew M. Rappe, Karin M. Rabe, Efthimios Kaxiras, and J. D. Joannopoulos. Optimized pseudopotentials. *Physical Review B*, 41(2):1227–1230, January 1990.

[16] G. B. Bachelet, D. R. Hamann, and M. Schlüter. Pseudopotentials that work: From h to pu. *Physical Review B*, 26(8):4199–4228, October 1982.

[17] D. R. Hamann. Optimized norm-conserving vanderbilt pseudopotentials. *Physical Review B*, 88(8), August 2013.

[18] M.J. van Setten, M. Giantomassi, E. Bousquet, M.J. Verstraete, D.R. Hamann, X. Gonze, and G.-M. Rignanese. The pseudodojo: Training and grading a 85 element optimized norm-conserving pseudopotential table. *Computer Physics Communications*, 226:39–54, May 2018.

[19] Nicola A. Spaldin. A beginner's guide to the modern theory of polarization. *Journal of Solid State Chemistry*, 195:2–10, November 2012.

[20] P. Umari and Alfredo Pasquarello. Ab initiomolecular dynamics in a finite homogeneous electric field. *Physical Review Letters*, 89(15), September 2002.

[21] Massimiliano Stengel and Nicola A. Spaldin. Accurate polarization within a unified wannier function formalism. *Physical Review B*, 73(7), February 2006.

[22] Nicola Marzari and David Vanderbilt. Maximally localized generalized wannier functions for composite energy bands. *Physical Review B*, 56(20):12847–12865, November 1997.

[23] Vadim A. Markel. Introduction to the maxwell garnett approximation: tutorial. *Journal of the Optical Society of America A*, 33(7):1244, June 2016.

[24] Jukka Venermo and Ari Sihvola. Dielectric polarizability of circular cylinder. *J. Electrostat.*, 63(2):101–117, February 2005.

[25] Z P Chang and G R Barsch. Pressure dependence of the elastic constants of single-crystalline magnesium oxide. *J. Geophys. Res.*, 74(12):3291–3294, June 1969.

[26] Z.P. Chang and E.K. Graham. Elastic properties of oxides in the nacl-structure. *Journal of Physics and Chemistry of Solids*, 38(12):1355–1362, 1977.

[27] R.E. Stephens and I.H. Malitson. Index of refraction of magnesium oxide. *Journal of Research of the National Bureau of Standards*, 49(4):249, October 1952.

[28] R. A. Bartels and P. A. Smith. Pressure and temperature dependence of the static dielectric constants of kcl, nacl, lif, and mgo. *Physical Review B*, 7(8):3885–3892, April 1973.

[29] J.L. Jacobson and E.R. Nixon. Infrared dielectric response and lattice vibrations of calcium and strontium oxides. *Journal of Physics and Chemistry of Solids*, 29(6):967–976, June 1968.

[30] C. J. Anderson and E. B. Hensley. Index of refraction of barium oxide. *Journal of Applied Physics*, 46(1):443–443, January 1975.

[31] Renate S. Bever and Robert L. Sproull. The dielectric constant of barium oxide. *Physical Review*, 83(4):801–805, August 1951.

[32] Keith E. Laidig and Richard F. W. Bader. Properties of atoms in molecules: Atomic polarizabilities. *The Journal of Chemical Physics*, 93(10):7213–7224, November 1990.

[33] Tore Brinck, Jane S. Murray, and Peter Politzer. Polarizability and volume. *The Journal of Chemical Physics*, 98(5):4305–4306, March 1993.

[34] Alexandre Tkatchenko and Matthias Scheffler. Accurate molecular van der waals interactions from ground-state electron density and free-atom reference data. *Physical Review Letters*, 102(7), February 2009.

[35] T. Anh Pham, Tianshu Li, Sadasivan Shankar, Francois Gygi, and Giulia Galli. Microscopic modeling of the dielectric properties of silicon nitride. *Physical Review B*, 84(4), July 2011.

Chapter 4

Dielectric Metal/Metal Oxide Nanocomposites: Modeling Response Properties at Multiple Scales

Preface

The following chapter consists of a minimally edited version of an article of the same title published in the IOP journal *Modeling and Simulation in Materials Science and Engineering*.[1] Changes were made to the published work to match the format of the rest of this dissertation without altering the content of the article. The complete author byline from the article is reproduced below for transparency. I (BH) carried out all simulation work and prepared the initial manuscript. ANSA provided structures for nanocomposites with rod- and disk-like inclusions and contributed valuable discussions about the quantum origins of shape effects on permittivity, which helped to conceptually drive the design of the continuum model presented. JTP provided guidance on the use of FEM and also edited the manuscript thoroughly—in particular helping to shape the language used to refer to the quantum and continuum models. IP provided the initial concept for the project and extensive guidance during its execution, in addition to extensive editing of the manuscript.

Brett Henderson[1,2], Archita N S Adluri[1,2], Jeffrey T Paci[1], and Irina Paci[1,2]

[1] *Department of Chemistry and the Centre for Advanced Materials and Related Technology, University of Victoria, Victoria, British Columbia, Canada*

[2] *Quantum Algorithms Institute, Surrey, British Columbia, Canada*

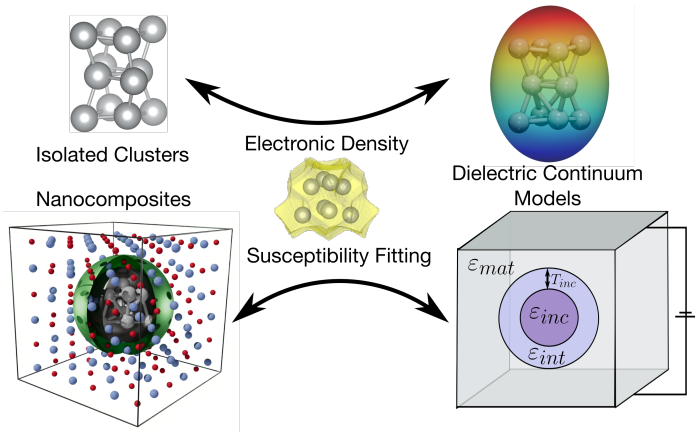

Abstract

Nanocomposites with metallic inclusions show great promise as tunable functional materials, particularly for applications where high permittivities are desirable, such as charge-storage. These applications strain quantum mechanical computational approaches, as any representative sample of the material includes hundreds if not thousands of atoms. Many continuum methods offer some predictive power for matrix-inclusion composites, but cannot be directly applied to composites with small inclusions, for which quantum and interfacial effects dominate. Here, we develop an adjustable finite element approach to calculate the permittivities of composites consisting of a metal-oxide matrix with nanometer-scale silver inclusions, by introducing an interfacial layer in the model. The approach involves solving the Laplace equation with Dirichlet and Neumann boundary conditions. We demonstrate that such a continuum model, when appropriately informed using quantum mechanical results, can capture many of the relevant polarization effects in a metal/metal oxide nanocomposite, including those that contain arbitrarily-small inclusions, at a fraction of the computational cost of performing the full quantum mechanics.

4.1 Introduction

Materials with high permittivities are important research and development targets, as gate components in metal-oxide semiconductor transistors [2, 3] and high energy density capacitors.[4, 5] Industry demands ever-increasing performance in these devices, with capacitance increased most often by decreasing dielectric layer thicknesses. However, the thicknesses of traditional SiO_2 gate layers can not be decreased below ~ 1 nm,[3] because increasing leakage currents negate capacitance improvements. Using thicker dielectrics with larger permittivities allows device footprints to continue to shrink while maintaining low leakage currents.

One way to increase the permittivity of a dielectric is to add highly polarizable inclusions.[4, 6] As with other composites, the properties of the mixed material are potentially tunable. By adjusting the composition, size, and loading of inclusions, materials with desired properties such as static dielectric permittivities, breakdown voltages, and dielectric losses can be fabricated. This can be accomplished while maintaining favorable properties of the matrix, such as processability and interfacial fit with other device components.

Matrix-inclusion composites have long been investigated for energy storage applications. Polymer matrices with ceramic inclusions, combine the high breakdown voltages and processability of polymers with the large polarizabilities of ceramics.[4, 7, 8] In addition, the inclusion of metallic nanoparticles has been shown to increase the permittivities of both polymer and metal oxide (ZnO, Al_2O_3, HfO_2, VO_2, etc.) thin films.[6, 9, 10, 11, 12, 7, 13, 14, 15] The latter combinations show potential for integrating dielectrically-enhanced composites with existing semiconductor technologies.

Several theoretical methods have been developed to model and explain the properties of dielectric composites. Effective medium theories such as the Maxwell-Garnett and Bruggeman models approximate the composite as dielectric spheres in a homogeneous medium.[16, 17, 18] The approximations lead to describing the composite's static dielectric response through a mixing formula of the component permittivities. Similar analytical models have been developed to treat general ellipsoidal inclusions.[19] However, experimental comparisons suggest that interfacial effects between the inclusions and matrix materials can cause significant deviations from these model predictions.[20, 21, 22] Researchers have attempted to address this issue by including parameters for capturing the interface structure and polarizability in the effective medium formalism.[23, 18]

Quantum mechanical electronic structure methods provide a means of exploring the behavior of nanocomposites without *a priori* knowledge. However, these methods scale poorly with the number of electrons, meaning they can only be applied to composites where the inclusions are sufficiently small to allow a unit cell on the order of a few hundred atoms. In two earlier publications from our group,[24, 25] Car-Parrinello quantum mechanical molecular dynamics (quantum dynamics) simulations were used to study nanocomposite dielectrics by optimizing electronic and nuclear coordinates under an applied electric field. The method was applied to modeling the dielectric response of metal-oxide matrix materials and noble metal nanoparticle inclusions.[24] The addition of 8-atom silver nanoparticles to the magnesium oxide matrix increased the permittivity by up to 30 % for atomic loadings of 3.7 % Ag. Larger, anisotropic inclusions led to further increases in permittivity, at similar loadings. These increases were attributed to both the high polarizabilities of the inclusions, and the increased polarizabilities of matrix ions near the inclusions, due to greater electron delocalization – a quantum effect. While elegant, this method is computationally expensive.

Among classical continuum approaches, the finite element method (FEM) and the finite difference method have been previously considered for describing the polarization response of mixed materials. Previous works have provided significant insight into the dielectric behavior of mixtures including elongated and irregularly-shaped microscale inclusions,[26, 27, 28] three-phase mixtures,[27] and random distributions of inclusions.[29, 30] These models often include an explicit interfacial layer, to account for the effects mentioned above.[27, 28] The results of these numerical calculations have prompted modifications to effective medium models, and helped elucidate the conditions under which those models lose their validity.

The applicability of the FEM to nanostructured materials has not been widely explored. In nanostructured systems, quantum effects due to small feature size and the electronic coupling between the inclusion and matrix can dominate the polarization response of the material.[24, 25] Although not directly addressing quantum effects, the FEM can be parameterized for these interactions as well as the shape effects that become important for non-trivial loading.

In the sections that follow, we explore such an FEM model (a term we use interchangeably with continuum model), parameterized based on quantum-level computational results. The set of parameters necessary to capture inclusion quantum mechanical size, shape and interfacial effects is considered in detail. We assess the transferability of these parameters to a range of inclusion types for mixtures of MgO

and nanoscale Ag inclusions. Along the way, we propose a definition of the continuum geometry based on Bader volumes calculated from quantum dynamics, define a procedure for fitting FEM parameters to quantum results, and validate the use of a continuum approach to the polarizability of isolated silver nanoparticles to motivate a similar approach for nanocomposites. Herein, the method devised by Hally and Paci [24] is used to generate quantum mechanical data for silver inclusions in MgO matrices. Based on this data, we parameterize a continuum model whose permittivity, ϵ, can be calculated via the FEM. The model is then used to investigate the effects of the shape and loading of inclusions on the permittivities of Ag/MgO nanocomposites.

4.2 Methods and Systems

4.2.1 Nanocomposite Systems

Models with "Spherical" Ag_8 Inclusions.

The methodology developed in this work is applied to a series of MgO nanocomposites with Ag inclusions. Using Car-Parrinello quantum mechanical molecular dynamics and the modern theory of polarization, Hally and Paci calculated the relative permittivity of bulk MgO to be $\epsilon_r = 9.3$.[24] $\epsilon_r = \epsilon/\epsilon_0$, where ϵ_0 is the permittivity of free space. The relative permittivity of an Ag_8/MgO nanocomposite was also determined, and was found to be 11.9, for an inclusion atomic loading of 3.7 %.[24] To explore the loading dependence of the permittivity, we examined two additional nanocomposites, comprised of MgO supercells of 64 and 512 atoms and Ag_8 inclusions. Additional details for these systems are provided in Appendix C.1.

Anisotropic Inclusions.

Nonspherical inclusions can provide desirable material properties, and various nanoparticle synthesis techniques can be used to finely control particle shape. Thus, there is the potential to use rod- and disk-like inclusions to introduce an anisotropic dielectric response. With this in mind, we considered five composites with rod- and disk-like inclusions from [25] to investigate shape effects. All geometries were created by substitution of Ag at adjacent MgO lattice sites followed by optimization of the lattice and atomic coordinates. Hereafter, we denote these inclusions by the number of atoms substituted in each direction ($2 \times 2 \times N$ for rods, and $N \times N \times 2$ for disks).

These composites are described in more detail in Appendix C.1.2, and the smallest two anisotropic inclusions are shown in Figure 4.1(d), alongside "spherical" Ag_8.

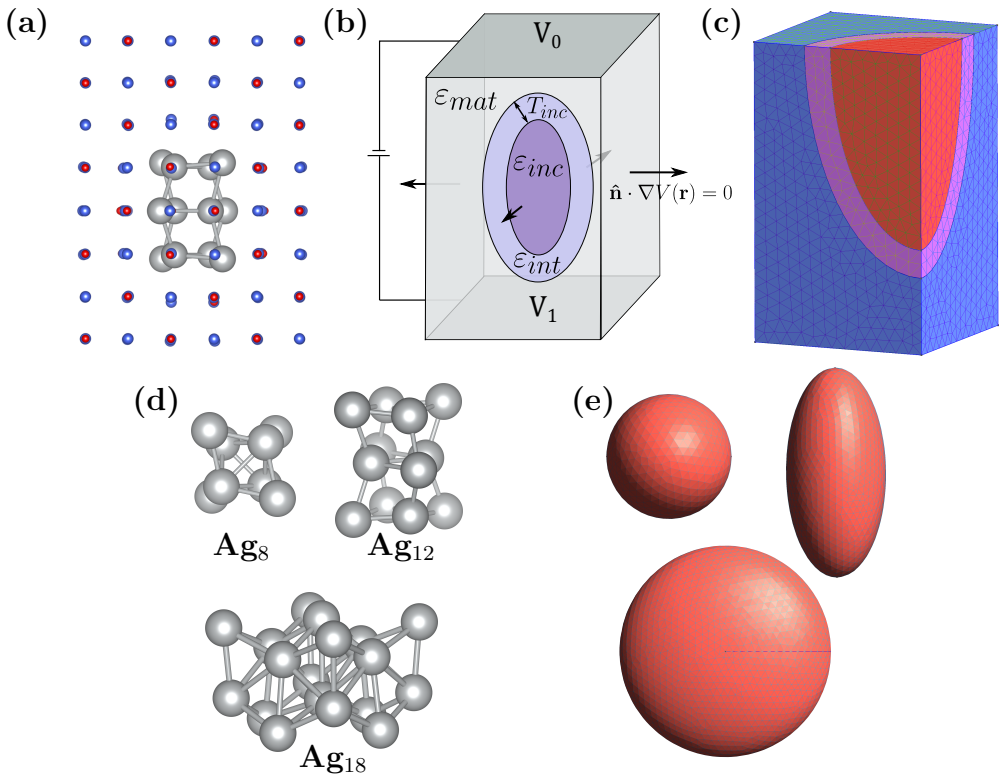

Figure 4.1: Quantum versus continuum models. (a) Ag_{12} is shown embedded in an MgO matrix containing 174 Mg and 174 O atoms. (b) The continuum model of an ellipsoid within a matrix with interfacial layer of thickness T_{int}. Matrix (ϵ_{mat}), inclusion (ϵ_{inc}), and interface (ϵ_{int}) permittivities are shown as well as boundary conditions for the potential. (c) The meshed and symmetry-reduced FEM representation of a composite with rod-like inclusuion. (d) The "spherical" Ag_8, rod-like Ag_{12} and disk-like Ag_{18} inclusions. (e) Discretized spherical, rod-like, and disk-like ellipsoids for the FEM.

4.2.2 Isolated Nanoparticles

To gain insight into the different contributions to the material's polarization response, we examine below a continuum model of the polarization of isolated nanoparticles. Quantum data used for the development of the model was generated as follows. Relaxed nanoparticle geometries were obtained using density functional theory by annealing in SIESTA,[31] using a PBE [32]/DZP approach and Troullier-Martins pseudopotentials [33, 34] obtained from the SIESTA Database. Polarizabilities α_{ii} along

Cartesian directions i were then calculated by applying an electric field E_i of 0.0001 a.u. (0.005 eV/Å), and calculating the change in dipole moment μ_i relative to the zero-field states:

$$\alpha_{ii} = \frac{\mu_i(E) - \mu_i(0)}{E_i}. \tag{4.1}$$

Unless otherwise noted, the reported polarizabilities are averaged over the diagonal elements of the polarizability tensor:

$$\overline{\alpha} = \frac{1}{3}(\alpha_{xx} + \alpha_{yy} + \alpha_{zz}). \tag{4.2}$$

The response was assumed to be linear due to the small size of the applied field,[35] and interactions with image particles were minimized by using a cubic cell with 100 Å side lengths. The electron delocalization volumes were calculated as the volumes of the 0.001 a.u. isosurfaces of the optimized electronic charge densities, as in previous work.[36]

4.2.3 Car-Parrinello Molecular Dynamics

Car-Parrinello quantum mechanical molecular dynamics were performed using plane wave basis sets in Quantum Espresso, version 6.6. After electronic minimization, both the ionic coordinates and cell size were relaxed using damped dynamics, with a force convergence threshold of $1.0 \times e^{-4}$ a.u. Next, the vanishing field polarization was calculated before applying a homogeneous electric field of 0.001 a.u.[37] Finally, the ionic and electronic degrees of freedom were relaxed using damping, until the polarization had converged.

The relative permittivity is calculated from

$$\epsilon_r = 1 + 4\pi\frac{\Delta p}{E\Omega}, \tag{4.3}$$

where E is the magnitude of the applied electric field, Δp is the change in simulation cell dipole moment relative to the vanishing field case, and Ω is the cell volume.

Car-Parrinello molecular dynamics was also used to investigate structural coupling of interfacial ions to inclusions in nanocomposites. All structures were equilibrated to 400 K using a Nosé-Hoover thermostat for a time of 4×10^4 a.u. before the thermostat was removed and the NVE ensemble sampled for a time of another 8×10^4 a.u. Mean square displacements of ions were calculated for the NVE ensemble using the python

wrapper of the Analisi code, version 0.5.0.[38]

4.2.4 Continuum Model and the FEM

In the continuum approach, a composite system is considered to be a union of matrix and inclusion materials, combined in the form of a representative volume element (RVE). Orthorhombic RVEs were generated (see Figure 4.1(b) and (c)), using optimized cell lengths from quantum dynamics simulations. The geometries of the inclusions were approximated by ellipsoids, with the same aspect ratios and volumes as the quantum inclusions. The ratios and volumes were determined using Bader analysis, as explained in Section 4.2.6. Symmetry allowed the simulation of just one-eighth of the full RVE (Figure 4.1(c)).

There are multiple options in choosing a shape for the nanoparticle inclusions in the FEM model: nanoparticles can be described by meshing the full Bader volume, or geometric shapes such as prisms, cylinders or ellipsoids may be used. In the following pages, we chose to implement the theory using ellipsoidal shapes for several reasons: 1) There are simple analytical expressions for their polarizability in vacuum that facilitate analysis of isolated particles. 2) They are commonly used as models for anisotropic inclusions in effective medium theory.[17] 3) There are available procedures for fitting ellipsoids to arbitrary shapes, such as Bader surfaces.[39] 4) It is simple to scale and extrapolate ellipsoidal shapes for larger inclusions that are not simulated quantum mechanically. Using Bader surfaces themselves as inclusion shapes, in contrast, would require a quantum simulation of each inclusion to be simulated prior to performing the FEM.

Nevertheless, the FEM is flexible. Since changing inclusion shape does not affect the boundary conditions employed but only the complexity of the mesh used, arbitrary shapes could be used to model inclusions where appropriate. However, the fitting for inclusion and interfacial permittivity must be done separately for each type of shape used. Aside from ellipsoids, we discuss analysis done with rounded prism inclusions in Appendix C.9.

In order to compute the permittivity, a uniform potential was simulated across the RVEs, and the electrostatic Laplace equation was solved using the methodology outlined in Appendix C.2 as in previous studies.[29, 27, 28] The RVEs were created and meshed in Gmsh, version 4.7.0.[40] First order tetrahedral meshes were used, and they were optimized using the Netgen extension. Meshes were further refined on the

surfaces of the inclusions, based on local curvature and until suitable convergence was obtained, as described in Appendix C.3. Finite element calculations were performed using the GetDP solver, version 3.3.1.[41]

4.2.5 Partitioning the Dielectric Response

The calculation of the permittivity of a composite via the FEM requires knowledge of the permittivity $\epsilon(\mathbf{r})$ at all points in the RVE. The bulk matrix response can be calculated via quantum dynamics or obtained by experiment. However, the response of the inclusions and that of the interface layers needs to be determined: the former may differ significantly from either bulk metal or nanoparticle-in-vacuum values, whereas the latter is completely unknown. We parameterize these values in a coarse-graining procedure discussed in sections 4.3.1 and 4.3.2, using quantum dynamics-calculated permittivities and the overall polarization, partitioned into inclusion and matrix contributions.

The response of a composite modeled using quantum dynamics can be partitioned using the polarization of Wannier centers within the composite as a heuristic mapping of the polarization strength of the inclusion, as distinct from the interface and matrix (see Appendix C.5.1 and [24] for a full description). Hally and Paci found that for the 216-atom Ag_8 nanocomposite under applied electric fields, the change in dipole moment relative to zero-field of the inclusion was 1.221 a.u., compared to a total change in the simulation cell dipole moment of 12.688 a.u. (calculated using Equation (4.3) and the values reported for ϵ_r, E, and Ω in [24]). Thus, the ratio of the inclusion dipole moment to the total cell dipole moment, which we call $P_{\mathrm{r,quant}}$, is 0.0926 for the 216-atom Ag_8 nanocomposite. We used this ratio as a point of comparison with the continuum model of the same 216-atom cell.

To obtain the corresponding dipole moment ratio for the continuum model, the polarization density $\mathbf{P}$ as defined by classical electrostatics can be integrated over the desired model component when the external field is applied. The projection of this density onto the applied field direction i takes the following form (in SI units):

$$P_i(\mathbf{r}) = \epsilon_0[\epsilon(\mathbf{r}) - 1]E_i(\mathbf{r}). \tag{4.4}$$

Here, we have used the linear relationship between polarization and the applied field ($\mathbf{P} = \epsilon_0\boldsymbol{\chi}\mathbf{E}$) and the relationship between the electric susceptibility $\boldsymbol{\chi}$ and relative permittivity $\boldsymbol{\epsilon}$ ($\chi_{ij} = \epsilon_{ij} - \delta_{ij}$).[42] Note that δ_{ij} is the Kronecker delta. Integrating

Equation (4.4) over the simulation cell yields the cell dipole moment. Similarly, the inclusion dipole moment is obtained by integrating the polarization density over the volume of the inclusion,

$$p_{\text{inc}} = \int_{\text{inc}} P_i(r) d^3\mathbf{r}. \tag{4.5}$$

Note that only the component of p_{inc} along the direction of the applied field is considered. Figure C.8 depicts the partitioning of dipole moments among different components of the composite in both the continuum and quantum models.

We call the ratio of the inclusion dipole moment p_{inc} to the total cell moment in the continuum model $P_{\text{r,FEM}}$. To directly compare the partitioning of the polarization between quantum and continuum models, we calculated the relative difference between $P_{\text{r,quant}}$ and $P_{\text{r,FEM}}$, denoted ω:

$$\omega = \frac{|P_{\text{r,FEM}} - P_{\text{r,quant}}|}{P_{\text{r,quant}}}. \tag{4.6}$$

The continuum model with both a low permittivity error and the lowest ω was deemed the "best-fit" model.

4.2.6 Volume Loading Definition

To draw parallels between quantum mechanical and FEM calculations of permittivity, it is necessary to rigorously define the inclusion volumes. The loading in quantum simulations is defined by atom volumes. Inclusion atoms replace matrix atoms in a one-to-one ratio. This suggests one option, which is to consider the percent atomic loading as a stand-in for volume loading.[24, 25] While this is a sufficient definition when loading is used only as a system descriptor, we find that a more rigorous definition of volume is necessary when developing inclusion shape, size and loading parameters for FEM.

A more precise description of electron delocalization volume in mixed materials requires the partition of electron density as done in Bader volume calculations.[43] Here, we define the inclusion volume as the summed Bader volumes of the inclusion atoms, calculated using the Henkelman Group code.[44]

This total volume envelopes the full inclusion (see Figure 4.2(a)). Furthermore, this treatment significantly improves the fit of a spherical inclusion model to the quantum results at low loadings, as shown in Figure 4.2(b), for which different volume loadings of spheres with permittivities 5, 10, and 1000 times larger than the matrix

permittivity ($\epsilon_r = 9.3$) were simulated using the FEM. Using a metallic sphere model does not significantly improve the fit to the quantum data relative to the most polarizable dielectric sphere shown at the volume loadings considered, and its curve would essentially overlay the $\epsilon_{\text{inc}}/\epsilon_{\text{mat}} = 1000$ curve. Higher loadings in quantum dynamics are not well treated with a single spherical inclusion model and require careful treatment of the local polarization of matrix near the inclusion, as discussed in Section 4.3.2.

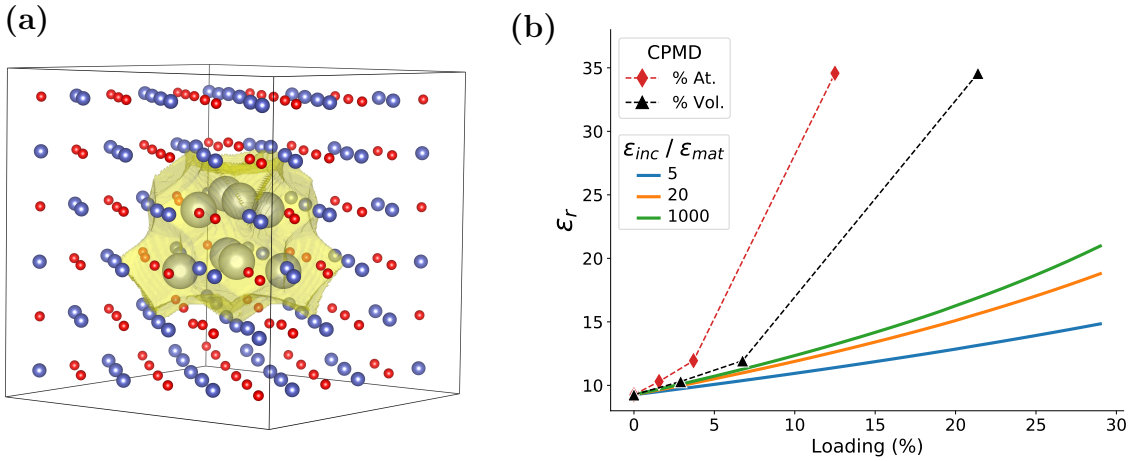

Figure 4.2: Discrepancy between atomic and volume loadings of silver. The Bader volume of a Ag_8 inclusion is plotted in panel (a), for the 3.7 % atomic loading / 6.8 % volume loading case. In panel (b), quantum dynamics-calculated permittivities are plotted using red diamonds and black triangles against the atomic and volume loading percent of silver, respectively. FEM-calculated permittivities are shown for different inclusion/matrix permittivity ratios.

4.3 Results and Discussion

4.3.1 Isolated Nanoparticles

The Spherical Continuum Model

Several density functional theory (DFT)-based studies have shown the static polarizability α of silver and gold nanoparticles to be directly proportional to the electron delocalization volume.[35, 36, 45] These analyses considered particles with up to several hundred atoms, and they are applicable to particles that include those with discrete energy levels. To confirm that this trend also holds for the responses considered

in our study, we examined the polarizabilities of thirteen silver particles containing from four to 55 atoms, using the process described in Section 4.2.2. For isolated silver nanoparticles of up to thirteen atoms, we found close agreement to the minimum energy structures and polarizabilites calculated by Pereiro and Baldomir.[35] Structures for larger nanoparticles were determined through a single annealing event and are expected to be local minima. The polarizability trends remain throughout the size range examined here, showing the expected linear volume dependence. The resulting relationship between volume and α is plotted in Figure 4.3(a). The proportionality

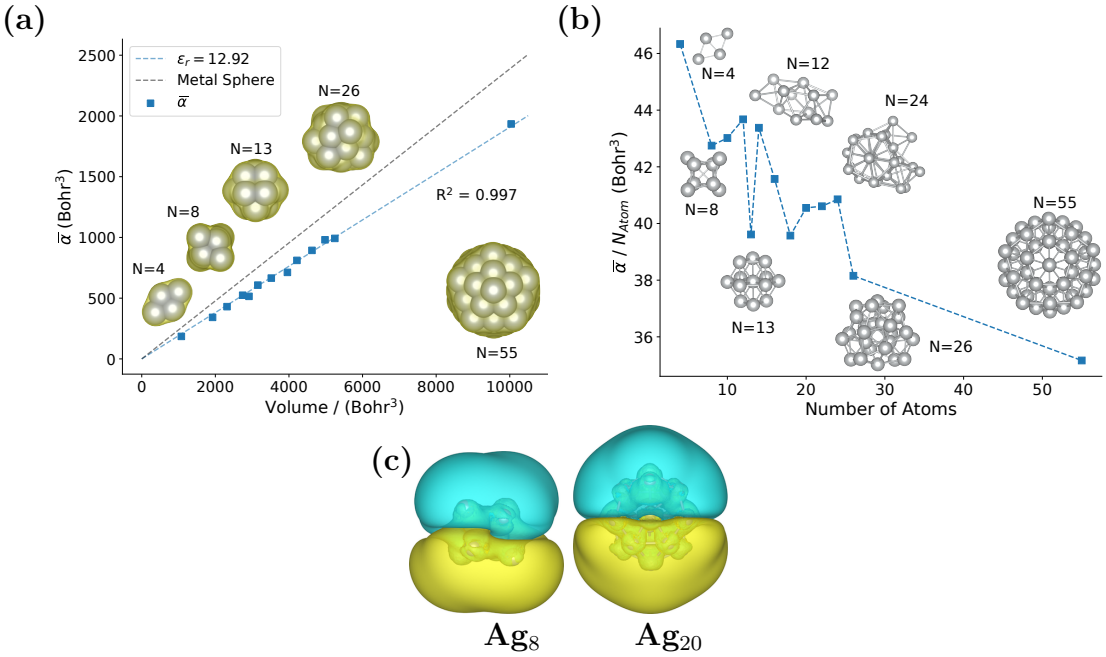

Figure 4.3: Polarizability α of isolated nanoparticles. The average polarizability of Ag particles composed of between four and 55 atoms is plotted as the total polarizability against particle volume in (a) and per atom against the number of atoms in the particle in (b). Representative particles are inset, with a 0.001 a.u. electron density isosurface added in (a). In (a), the blue dashed line shows the least squares fit of the polarizability. A metallic sphere model is included for reference in (a) (grey dashed line). Panel (c) shows the (1.34×10^{-6} a.u. isosurface value) change in electron density ($\Delta\rho$) with the application of a 0.001 a.u. electric field, for Ag_8 and Ag_{20}.

between particle polarizability and volume is similar to that of metallic spheres.[46] For a sphere of radius r, α is also directly proportional to its volume:[47, 48, 46]

$$\alpha = \frac{\epsilon_r - 1}{\epsilon_r + 2} r^3. \tag{4.7}$$

Note that in SI units, this expression would contain a factor of $4\pi\epsilon_0$, which we omit, reporting the polarizabilities in units of Bohr^3.

While nanoparticle polarizability increases linearly with volume, the polarizability per atom was found to, in general, decrease as particle size increases, as shown in Figure 4.3(b). This is due in part to the larger fraction of surface atoms in smaller particles, and the distinct contribution from surface and core atoms to properties such as α.[36, 49, 45] In addition to the downward trend, there are large fluctuations from particle to particle, with more elongated particles displaying larger polarizabilities than their higher-symmetry neighbors. We note that the elongated particles also tend to have a larger percentage of surface atoms. Thus, instead of considering only the number of atoms or electrons in a particle, we consider the electron delocalization volume. This volume depends on the electronic structure of the particle (see Figure 4.3(a)), and accounts for the distinction between surface (larger volume) and core (smaller volume) atoms. We used a least squares procedure to fit the data in Figure 4.3(a) to Equation (4.7), assuming spherical volumes. The fit assigned the particles a relative permittivity of 12.9. While dependent on the precise definition of particle volume, this value is a consistent characteristic of all particles surveyed when using our volume definition (Section 4.2.2), yielding $R^2 = 0.997$. Note, the polarizabilities of the particles are less than those of analogous metallic spheres, which are represented by the gray line in the figure panel. In most cases, the particle volume was roughly spherical, becoming more spherical as the number of atoms increased. The change in electron density with the application of an electric field closely resembles the polarization charge induced on a sphere, or in a coarser approximation, the charge separation of a point dipole (Figure 4.3(c)).

This analysis considers only the electronic polarizability, neglecting the ionic contribution that is present when particles are dispersed in a matrix. Still, the results provide a clear justification for using the volume model for describing polarizability. The following sections evaluate the suitability of such a model for treating anisotropic gas-phase particles and particles embedded in host matrices to determine the transferability of fitted permittivities, and the importance of particle shapes and volumes in the polarization behavior of each.

Particle Anisotropy

Not all particles are well approximated as spheres. In the analysis of Figure 4.3, we smoothed over anisotropy by considering the mean polarizability over the three principal axes. One way to capture the influence of non-sphericity is to fit an ellipsoidal model. As discussed in Section 4.2.6, defining the volume of a particle is nontrivial. Moreover, a Bader volume cannot be calculated for a particle in vacuum. One way to proceed is to consider a bounding box that encloses the electron delocalization volume of the inclusion. The principal axes of the ellipsoid are defined parallel in directions and proportional in lengths to the box. In this way, this approach incorporates aspect ratio and particle orientation information. Boxes were calculated to enclose the 0.001 a.u. electron density isosurfaces for the thirteen particles discussed in Section 4.3.1. The box sides were scaled so that the volumes of the ellipsoids were equal to those of the 0.001 a.u. isosurfaces.

The classical theory for a dielectric sphere can then be modified to treat ellipsoids oriented arbitrarily relative to an applied field, as described in Appendix C.6. This model accounts for most of the differences between the polarizability components calculated with quantum mechanics and the predictions of an analogous spherical model, as shown in Figure 4.4. The permittivity of the ellipsoidal model was determined by fitting the Cartesian projections of the particle polarizabilities to the quantum mechanical data. A least squares fit of Equation (C.16) to the polarizability data was used to obtain the relative permittivities $\epsilon_{XX} = 13.13$, $\epsilon_{YY} = 13.08$, and $\epsilon_{ZZ} = 11.78$, giving an average of 12.7, which is very close to that of the spherical model (12.9). Nevertheless, the ellipsoidal model produces a significantly better fit to the quantum data, because shape and orientation are included in the model (see Figure 4.4(b)). This indicates the importance of shape and orientation and provides justification for treating rod- and disk-like inclusions with an ellipsoidal model (Section 4.3.2).

Previous work on nanoparticle polarizability in vacuum used a classical mechanical cylindrical jellium model to account for shape effects, and showed a similar ability to reproduce quantum mechanical results.[50] The ellipsoidal model has the advantage that it is readily incorporated into FEM models for composite systems.

To develop such a FEM model, we began by testing the ellipsoid model on two rod- and disk-like particles from [25], $Ag_{12}(2 \times 2 \times 3)$ and $Ag_{18}(3 \times 3 \times 2)$ (see Figure 4.1(d)). Particles were re-optimized in vacuum using PBE/DZP using conjugate gradient minimization, which resulted in increased bond lengths, but little overall re-

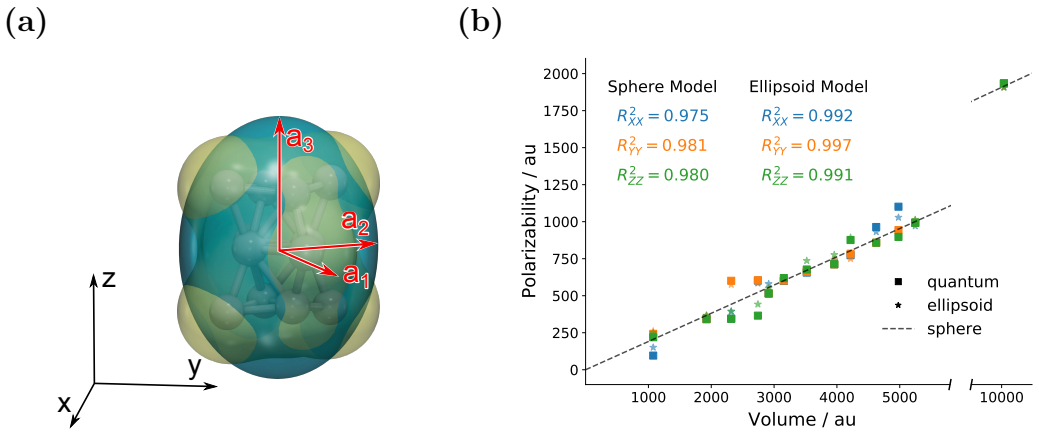

Figure 4.4: Ellipsoid model of isolated nanoparticles. Panel (a) shows the best-fit ellipsoid around the rod-like Ag_{12} particle of Figure 4.1(d), with principal axes shown in red. The predictions of the sphere (dashed line) and ellipsoid (stars) models compared to the results of quantum dynamics calculations (squares) for polarizability along each Cartesian direction are shown in (b).

configuration. The polarizabilities of the particles along each Cartesian axis were then calculated as in Section 4.3.1, for both the re-optimized particles and the geometries without re-optimization.

Ellipsoidal approximations for each particle were initially obtained using the bounding box procedure described above. However, for Ag_{12}, this produced an ellipsoid that was too wide. Using a least squares procedure,[39] followed by scaling the principal axes to attain an ellipsoid volume equal to the 0.001 a.u. isosurface volume (see Figure 4.4(b)) provided a better fit. The relative permittivity of the inclusions was set to 12.7, and the method outlined in Appendix C.6 was used to calculate polarizabilities.

Figure 4.5 shows the diagonal elements of the polarizability tensor, calculated using quantum dynamics and the two classical models. The spherical model reproduces the average polarizabilities with reasonable accuracy. The ellipsoidal model reproduces the quantum results well, including capturing the subtleties associated with anisotropy.

4.3.2 Nanocomposites

Quantum Modeling

Previous quantum mechanical investigations from our group of MgO/Ag nanocomposites have elucidated several mechanisms by which inclusions enhance permittivity.

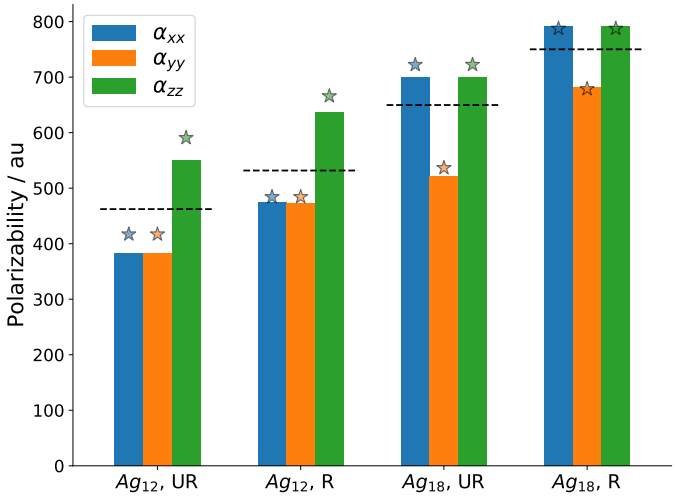

Figure 4.5: Polarization of anisotropic nanoparticles in vacuum. The diagonal elements of the polarizability tensor are presented, calculated with the electric field applied parallel to the corresponding axis. The Ag_{12} rod had its long axis along z and the Ag_{18} disk had long axes along x and z. Quantum mechanical (columns), spherical model (black dashed lines) and ellipsoidal model (stars) results, for particles with optimized composite inclusion geometries ("unrelaxed", UR) and particles structurally relaxed in vacuum ("relaxed", R) are shown. Spherical and ellipsoidal models had relative permittivities of 12.9 and 12.7, respectively.

First, Born effective charge analysis has shown that the large electronic polarizability of the embedded nanoparticles couples to both the electronic and ionic polarization of surrounding matrix atoms.[24, 25]. Second, Hally and Paci [24] explored the specific importance of the interface between matrix and nanoparticle using crystal orbital Hamiltonian population analysis. Stabilizing interactions were found between the O s-orbitals and the Ag atoms, Ag electrons and Mg ions, and between the O p-orbitals and Ag d-orbitals, all of which resulted in increased delocalization of electrons in the interfacial region. Third, the authors posited that the O-Ag p-d coupling could result in coupling of the ionic dynamics and low frequency polarization response of inclusion and matrix at the interface.

It is important to ascertain how a continuum model for these nanocomposites can capture these effects. The first phenomenon, that the polarizable nanoparticle generates an induced field which increases polarization in the surrounding matrix, is already qualitatively present in any continuum model with a dielectric ellipsoid with permittivity ϵ_{ell} in a polarized dielectric matrix with permittivity ϵ_{mat}, when $\epsilon_{\text{ell}} > \epsilon_{\text{mat}}$.[51] Nevertheless, there will be a quantitative difference in the screening

of this induced field by the surrounding ions in the atomic model and by a continuum dielectric. In addition, Figure 4.2 already shows that the continuum model of a dielectric sphere in matrix cannot reproduce the high polarization exhibited in quantum simulations. We believe this shortcoming is in large part explained by the greater electronic delocalization and coupling of the ionic dynamics of O and Ag at the interface. These quantum phenomena result in a layer of MgO atoms neighboring Ag that behave distinctly from bulk and are specifically more polarizable than bulk.

A distinct and more polarizable interfacial layer of MgO is supported by two additional analyses conducted in this work. First, Bader charge analysis (Figure C.1) shows a small transfer of electronic density from interfacial oxygen atoms to the inclusion, with a rapid return to bulk charges for subsequent layers. Second, we found significant increases in the mobilities of Mg and O ions neighboring Ag compared to bulk, furthering Hally's notion of ionic coupling. Mean squared displacements (MSD) of ions over the course of Car-Parrinello molecular dynamics are shown in Figure 4.6. The MSD for bare MgO shows comparable displacements of Mg and O ions, while nanocomposite MSD plots show that Ag has larger mobility within the unit cell. Furthermore, plots of the MSD of interfacial Mg and O ions, specifically those directly neighboring Ag atoms, show significantly larger displacement relative to other matrix ions. Thus, ionic mobility is enhanced at the interface, and this enhancement is localized.

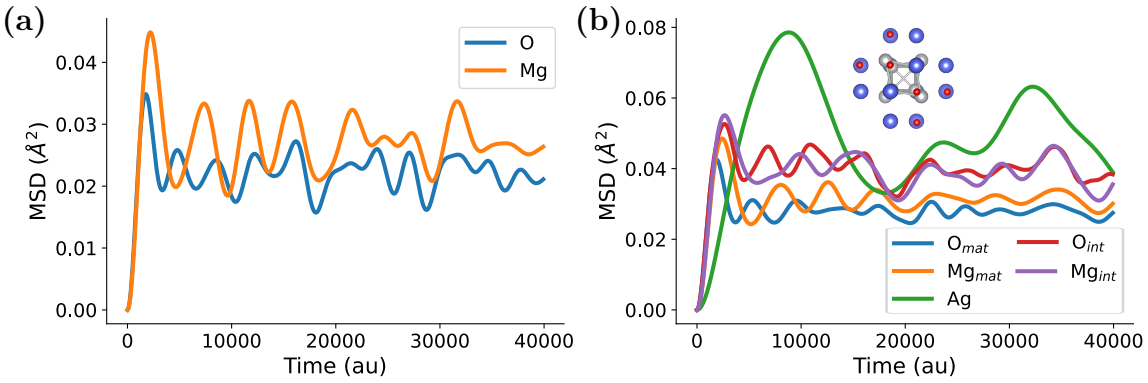

Figure 4.6: Mean squared displacement of ions during *ab initio* molecular dynamics. Panel (a) shows the MSD for Mg and O in the pure MgO matrix. Panel (b) shows the MSD of Mg, O, and Ag for a 216 atom nanocomposite cell with an Ag_8 inclusion. MSD for ions neighboring Ag atoms are denoted with the "int" subscript, and atoms further from the inclusion with the "mat" subscript. The inset shows the inclusion plus ions denoted as "int".

This structural coupling manifests as a large enhancement of the ionic polarization of nanocomposites relative to MgO bulk. Table C.1 shows that the enhancement of relaxed ion permittivity for nanocomposites relative to MgO is generally larger than the enhancement of electronic permittivity. This discrepancy is exaggerated as the percent loading of Ag increases, in which case the percent of interfacial Mg and O ions also increases, pointing to the importance of interfacial ionic coupling.

Continuum Modeling of the Interfacial Layer

Therefore, a continuum model must account for both the electronic coupling to the Ag inclusion and the increased ionic polarizability of the ions nearest the inclusion. To capture this coupling, we include an explicit interfacial layer, which is also ellipsoidal in shape, but with its axes all increased by a fixed thickness relative to the inclusion. This interface is assigned its own permittivity different than that of the bulk matrix by fitting the continuum model to quantum dynamics results as detailed in the following section. As expected, the best fit model includes a high-permittivity interface.

Fitting Procedure in Coarse-Graining the Quantum Response

Fitting of continuum to quantum dynamics permittivity was performed using a sweep over three parameters: The permittivities of the inclusion, that of the interfacial shell, and the interface thickness. The inclusion volume and matrix relative permittivity were fixed at the Bader value and 9.3, respectively. A 1 Å interface was selected to avoid encroachment on cell boundaries for high volume loadings (Appendix C.3.5). More importantly, this interface thickness also resulted in lower average errors than 2 or 3 Å interfaces, or no interface. Figure 4.7 depicts the parameter search space as well as the average permittivity errors τ for the three systems of Figure 4.2(b), where

$$\tau = \frac{\epsilon_{\mathrm{FEM}} - \epsilon_{\mathrm{QD}}}{\epsilon_{\mathrm{QD}}} \tag{4.8}$$

is the relative error. A region of this plot from the lower left to upper right shows relatively constant values of τ below 8%, which is within the error margins of the quantum dynamics method. This indicates that combinations with either (i) low inclusion and high interface permittivities or (ii) high inclusion and low interface permittivities, reproduced the quantum dynamics permittivity equally well.

The induced dipole moment was used as an additional parameter in defining our

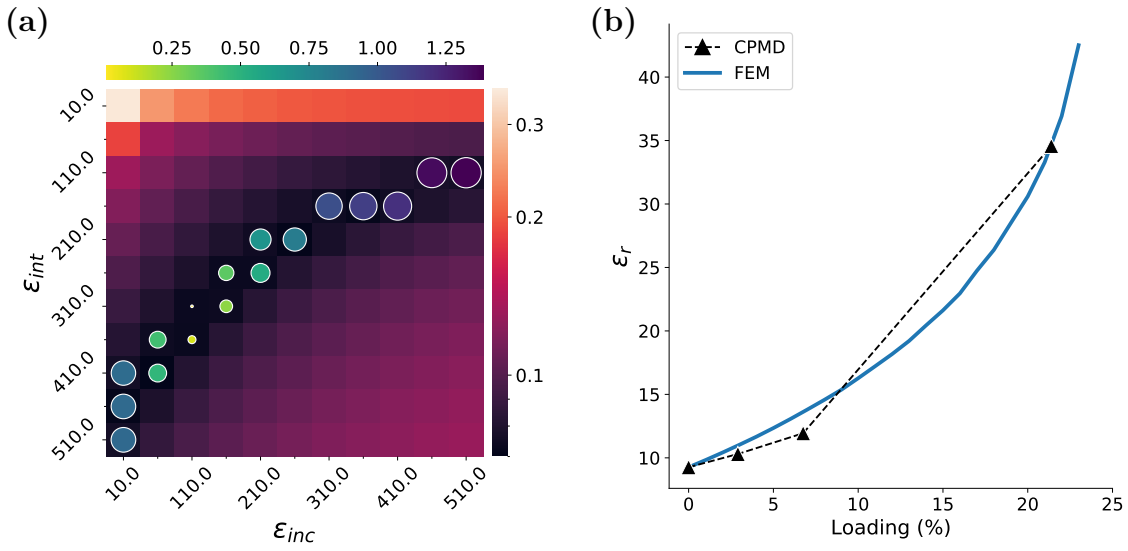

Figure 4.7: Optimal parameters for the FEM model. Panel (a) shows a heatmap of τ, the error in the composite permittivity, for an interface layer of 1 Å, at different values of the interface and inclusion permittivities. The color scale of τ is displayed on the right side of the panel. The values of errors in the inclusion dipole moment, ω, are overlaid as circles. Both the size of the circle and its color indicate the value of ω (colour scale displayed above the panel). Panel (b) shows the relative permittivities calculated using the FEM as a function of volume loadings (blue line) when the optimal parameters from panel (a) are used. Black triangles denote quantum dynamics-calculated permittivities.

FEM model. We calculated the optimal fit of the inclusion dipole by partitioning the polarization of the quantum dynamics model using the method described in Section 4.2.5, and determined the relative error of the FEM inclusion dipole (ω) from Equation (4.6). This procedure was performed for the 216-atom supercell using data from Hally and Paci [24] to obtain an ω for each tile in the heatmap of Figure 4.7. A pictorial representation and further details of the scheme are provided in Appendix C.5 and Figure C.8.

Along the constant-τ curve (the region of black shading in Figure 4.7(a)), the area of smallest discrepancy between the quantum dynamics- and FEM-calculated inclusion dipoles ($\omega \sim 1.0\%$, indicated by the smallest, yellow circles) corresponds to high permittivities for both the inclusion and interface relative to the matrix ($\epsilon_{\text{inc}} = 110$; $\epsilon_{\text{int}} = 310$; $\epsilon_{\text{mat}} = 9.3$). The dipole error increases significantly in both directions from this minimum. These values indicate that (i) The inclusion permittivity is significantly larger when embedded in a matrix relative to its permittivity in vacuum

($\epsilon_{\mathrm{NP}} \sim 13$, see Section 4.3.1 and Figure 4.3), and (ii) The interfacial MgO layer is much more polarizable than bulk MgO. The enhanced nanoparticle permittivity is largely due to an additional ionic polarizability component that is present in silver inclusions but absent in gas phase silver particles: When embedded in MgO, the silver atoms develop nontrivial positive Born Effective Charges [24], and the reorganization of these silvers and the interfacial MgO ions in the presence of an electric field contributes to the overall polarization of the system. In contrast, spherical silver particles in the gas phase only have an electronic component to their polarization.

While it may seem strange for the interface permittivity to be larger than the inclusion permittivity, this is an artifact of representing discrete atomic layers as a continuum. With the selected thickness of 1.0 Å and inner radius of 3.27 Å, the interface contains 24 atoms and an atomic density of 0.134 atoms/Å^3. The inclusion, however, contains only eight silver atoms and a density of 0.055 atoms/Å^3. Thus the high interface permittivity is largely explained by high atomic density in the continuum interface region. This effect could be mitigated by enforcing an interface shape that is consistent with the matrix crystal system (cubic here) and by constraining the interface thickness to be integer multiples of the matrix lattice spacing.

Rod- and Disk-Like Inclusions

The ellipsoid model was applied to the series of rod- and disk-like particles embedded in a MgO matrix from [25]. Two orientations were considered for each inclusion, with the long principal axes aligned either parallel ($\epsilon_{\parallel}$) or perpendicular ($\epsilon_{\perp}$) to the applied field. The continuum geometries of the $2 \times 2 \times 3$ and $3 \times 3 \times 2$ inclusions were generated using the bounding box method from Section (4.3.1). Ellipsoids for the remaining inclusions were extrapolated using the procedure in Appendix (C.10). Using the particle permittivity values derived in Section (4.3.2), we calculate the permittivities of composites with rod- and disk-shaped inclusions using the FEM. The relative permittivities thus obtained, as well as their quantum-dynamics-calculated counterparts, are listed in Table 4.1.

The ellipsoidal model displayed mixed performance in reproducing quantum dynamics results. The model correctly predicts the anisotropic response for rods and disks. However, while the error generally remains close to 10%, it is approximately double this for both the $2 \times 2 \times 4$ rod and the $4 \times 4 \times 2$ disk. Analysis of the physical basis for discrepancies between the continuum and quantum models can both

Table 4.1: Relative permittivities for rod- and disk-like silver nanoparticles embedded in MgO matrices, calculated with quantum dynamics (QD) and the FEM.

Inclusion[a]	% At.	% Vol.	$\epsilon_{\parallel,\,\mathrm{QD}}$[b]	$\epsilon_{\parallel,\,\mathrm{FEM}}$	$\tau_{\parallel}$	$\epsilon_{\perp,\,\mathrm{QD}}$[b]	$\epsilon_{\perp,\,\mathrm{FEM}}$	$\tau_{\perp}$
$2 \times 2 \times 3$	4.2	7.6	12.9	14.0	0.09	12.2	13.5	0.11
$2 \times 2 \times 4$	5.6	10.0	13.9	16.9	0.22	12.3	14.5	0.18
$2 \times 2 \times 5$	5.6	10.0	14.9	16.7	0.12	12.8	14.2	0.10
$3 \times 3 \times 2$	4.7	8.3	15.0	13.9	-0.07	13.3	13.4	0.01
$4 \times 4 \times 2$	4	6.9	16.9	13.0	-0.23	15.9	11.8	-0.26

[a] Symbols $\parallel$ and $\perp$ indicate whether the inclusion has its long axis oriented parallel to the applied field and perpendicular to it, respectively. The field is oriented along z in each case, thus the $\parallel$ notation indicates that the rod or disk long axis was along z, whereas the $\perp$ notation indicates that the long axis was in the xy plane. τ is the permittivity error defined in Equation (4.8).

[b] Values from [25].

suggest improvements to the continuum model and provide insights difficult to obtain from quantum dynamics alone. These insights may inform design principles for high-permittivity composites.

The continuum model performs best for the least anisotropic inclusions (such as the $2 \times 2 \times 3$ rod and the $3 \times 3 \times 2$ disk). The method can overestimate the permittivity of rod-based composites and underestimate that of disks. Several factors account for these discrepancies: (i) The anisotropy of inclusion polarization is only partially accounted for in a parameterization built on spherical inclusions; (ii) The ellipsoidal shape is an imperfect representation of rod- and disk-like inclusions, which do no exhibit sharp tips in the polarization direction, but may be better represented by cylindrical or rounded prism shapes; (iii) There is variability in the amount of padding between image inclusions in the different composites, restricted by volume loadings, that may not be fully captured by the interfacial region parameterized for the continuum model.

Notably, *ab initio* molecular dynamics simulations revealed differences in the ion mobilities of interfacial Mg and O ions between rod- and disk-like inclusions. Figure C.7 shows that interfacial ion mobility is significantly increased around an Ag_{18} disk relative to around an Ag_{12} rod, which shows an interfacial ion MSD more similar to that of the Ag_8 nanocomposite from Figure 4.6. This non-linear effect can help to account for the large ionic polarization in the studied disk-containing nanocomposites.

In turn, it may also account for some of the shortcomings of a continuum model with a single parameter for interfacial permittivity, notably its overestimation of rod-like polarization and underestimation of disk-based nanocomposite polarization.

Two first-order forays into alternate parameterization options are discussed in the SI. Appendix C.8 presents a parameterization that uses only low volume loading data to eliminate issues with interface and padding regions. The model significantly improves the fit for rod-like inclusions. The rounded-prism inclusion model discussed in Appendix C.9 underperforms the original ellipsoidal model.

Larger Anisotropic Inclusions

We also calculated the permittivites of composites with unit cells that were too large to simulate quantum mechanically. We focused on anisotropic inclusions, with rods containing up to 56 silver atoms and aspect ratios of 14:2 and disks containing up to 392 atoms (also with aspect ratio 14:2). Volume loadings were varied by starting with a cell with two layers of MgO around inclusions and then sequentially adding layers of matrix. We approximated the dimensions of the inclusions using multiples of the dimensions of the $2 \times 2 \times 3$ rod and $3 \times 3 \times 2$ disk studied above (details in Appendix C.10) and used an ellipsoidal model with the optimal parameters from Section 4.3.2. The dependence of relative permittivity on inclusion size and volume loading for these inclusions is presented in Figure 4.8.

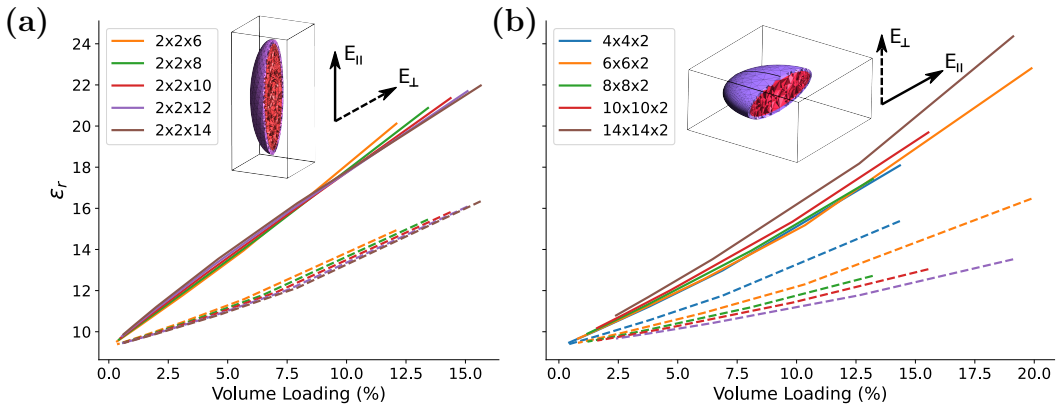

Figure 4.8: FEM simulation of large rods and disks. Rods with aspect ratios from 4:2 up to 14:2 are plotted in panel (a), and disks with aspect ratios 6:2 up to 14:2 are shown in panel (b). Solid and dashed lines indicate long axes orientation parallel and perpendicular to the incident field, respectively.

The volume ratio and anisotropy trends observed in quantum dynamics are conserved for the large inclusions in the FEM: The relative permittivity increases monotonically with the volume ratio. Small increases with axis ratios are seen for rod-like inclusions, when the inclusion is oriented parallel to the field, and small decreases are seen in perpendicular orientations (see Figure 4.8(a)). The aspect ratio dependence of the permittivity is stronger for disks, as seen in Figure 4.8(b), where each axis ratio represents a significantly larger number of atoms (and polarizable electrons) in the inclusion. It is worth noting the incipient saturation behaviour for larger rods in parallel orientation to the field, at higher volume loadings. The requirement of a dielectric interface presents an upper limit to the volume loading that can be treated with the present FEM, and the higher loadings presented here for large rods approach that limit.

4.4 Conclusions

We propose a finite element model for the dielectric response of nanocomposites of silver nanoparticles, described as polarizable dielectric spheres and ellipsoids, embedded in a dielectric matrix. A methodology for fitting the FEM to a quantum mechanical polarization model is also presented. When fit to a suitable quantum mechanical training set, an ellipsoidal model faithfully reproduces the polarizability of gas phase particles, including the anisotropy due to shape effects. For nanocomposite systems, the FEM requires the use of an accurate definition for the electron delocalization volume, as well as the addition of an interfacial layer to the model. A model containing ellipsoidal inclusions and an interfacial layer of high permittivity was found to reproduce the permittivities of nanocomposites with rod- and disk-like inclusions with reasonable fidelity, even though the interfacial permittivity was fitted on a set of nanocomposites with spherical inclusions. The FEM allows the estimation of permittivities for systems that cannot be treated quantum mechanically, such as systems with large anisotropic inclusions, over a large range of inclusion loadings. Furthermore, analysis of the FEM data provides insight into local field effects and the coupling of polarization between components, that is complementary to that obtained from quantum simulations.

To improve the FEM parameter set, further investigations are needed into other, non-ellipsoidal representations for anisotropic particles embedded in matrix. A more general mapping of the atomistic interface onto the interfacial layer of the FEM is

also being examined for model improvement. Additionally, a broader set of systems, including other matrix and inclusion materials, are currently being considered, in order to generalize the FEM implementation for an array of currently relevant dielectric ceramics with highly-polarizable inclusions.

Bibliography

[1] Brett Henderson, Archita N S Adluri, Jeffrey T Paci, and Irina Paci. Dielectric metal/metal oxide nanocomposites: modeling response properties at multiple scales. *Modelling and Simulation in Materials Science and Engineering*, 31(6):065015, July 2023.

[2] J. Robertson. High dielectric constant oxides. *The European Physical Journal Applied Physics*, 28(3):265–291, dec 2004.

[3] Jermey N.A. Matthews. Semiconductor industry switches to hafnium-based transistors. *Physics Today*, 61(2):25–26, 2008.

[4] Peter Barber, Shiva Balasubramanian, Yogesh Anguchamy, Shushan Gong, Arief Wibowo, Hongsheng Gao, Harry J. Ploehn, and Hans-Conrad Zur Loye. Polymer composite and nanocomposite dielectric materials for pulse power energy storage. *Materials*, 2(4):1697–1733, 2009.

[5] Yujuan Niu and Hong Wang. Dielectric Nanomaterials for Power Energy Storage: Surface Modification and Characterization. *ACS Applied Nano Materials*, 2(2):627–642, 2019.

[6] Ramasamy Ravindran, Maslina Othman, Minseong Yun, Nivedita Biswas, Narendra Mehta, Suchi Guha, Keshab Gangopadhyay, and Shubhra Gangopadhyay. Enhanced dielectric constant of HfO2 and al2o3 thin-films with silver nanoparticles. *ECS Transactions*, 3(3):535–544, December 2019.

[7] Pornsawan Kum-onsa, Narong Chanlek, Bundit Putasaeng, and Prasit Thongbai. Improvement in dielectric properties of poly(vinylidene fluoride) by incorporation of au–BiFeO3 hybrid nanoparticles. *Ceramics International*, 46(11):17272–17279, August 2020.

[8] Sunil Meti, Udaya K. Bhat, and M. Rizwanur Rahman. Colossal dielectric permittivity of nylon-6 matrix-based composites with nano-TiO2 fillers. *Applied Physics A*, 126(4), March 2020.

[9] Sung-Yub Ji, Han-Bo Jung, Min-Kyu Kim, Ji-Ho Lim, Jin-Young Kim, Jungho Ryu, and Dae-Yong Jeong. Enhanced energy storage performance of polymer/ceramic/metal composites by increase of thermal conductivity and coulomb-blockade effect. *ACS Applied Materials & Interfaces*, 13(23):27343–27352, June 2021.

[10] Alexander I. Sidorov, Alexey V. Nashchekin, Rene A. Castro, Irina N. Anfimova, and Tatiana V. Antropova. Optical and dielectric properties of nanocomposites on base nanoporous glasses with silver and silver iodide nanowires. *Physica B: Condensed Matter*, 603:412764, February 2021.

[11] Saliha Mutlu, Eyup Metin, Sureyya Aydin Yuksel, Ugur Bayrak, Cigdem Nuhoglu, and Nergis Arsu. In-situ photochemical synthesis and dielectric properties of nanocomposite thin films containing au, ag and MnO nanoparticles. *European Polymer Journal*, 144:110238, February 2021.

[12] Zihao He, Jie Jian, Shikhar Misra, Xingyao Gao, Xuejing Wang, Zhimin Qi, Bo Yang, Di Zhang, Xinghang Zhang, and Haiyan Wang. Bidirectional tuning of phase transition properties in pt : VO2 nanocomposite thin films. *Nanoscale*, 12(34):17886–17894, 2020.

[13] Anupam Maity, Subha Samanta, Shubham Roy, Debasish Biswas, and Dipankar Chakravorty. Giant dielectric constant of copper nanowires/amorphous SiO2 composite thin films for supercapacitor application. *ACS Omega*, 5(21):12421–12430, May 2020.

[14] Mohsin Saleem, Muhammad Shoaib Butt, Adnan Maqbool, Malik Adeel Umer, Muhammad Shahid, Farhan Javaid, Rizwan Ahmed Malik, Hamid Jabbar, Hafiz Muhammad Waseem Khalil, Lim Dong Hwan, Minsoo Kim, Bo-Kun Koo, and Soon Jong Jeong. Percolation phenomena of dielectric permittivity of a microwave-sintered BaTiO3–ag nanocomposite for high energy capacitor. *Journal of Alloys and Compounds*, 822:153525, May 2020.

[15] Matias Kalaswad, Bruce Zhang, Xuejing Wang, Han Wang, Xingyao Gao, and Haiyan Wang. Integration of highly anisotropic multiferroic BaTiO3–fe

nanocomposite thin films on si towards device applications. *Nanoscale Advances*, 2(9):4172–4178, 2020.

[16] Ari Sihvola. *Electromagnetic Mixing Formulas and Applications*. IET, January 1999.

[17] Ari Sihvola. Homogenization principles and effect of mixing on dielectric behavior. *Photonics and Nanostructures - Fundamentals and Applications*, 11(4):364–373, November 2013.

[18] Tien-Thinh Le. Probabilistic modeling of surface effects in nano-reinforced materials. *Computational Materials Science*, 186:109987, January 2021.

[19] Stefano Giordano. Effective medium theory for dispersions of dielectric ellipsoids. *Journal of Electrostatics*, 58(1-2):59–76, may 2003.

[20] Pandiyan Murugaraj, David Mainwaring, and Nelson Mora-Huertas. Dielectric enhancement in polymer-nanoparticle composites through interphase polarizability. *Journal of Applied Physics*, 98(5), September 2005.

[21] Frederick A. Pearsall, Julien Lombardi, and Stephen O'Brien. Monomer derived poly(furfuryl)/BaTiO3 0–3 nanocomposite capacitors: Maximization of the effective permittivity through control at the interface. *ACS Applied Materials & Interfaces*, 9(46):40324–40332, November 2017.

[22] Zhong-Hui Shen, Jian-Jun Wang, Xin Zhang, Yuanhua Lin, Ce-Wen Nan, Long-Qing Chen, and Yang Shen. Space charge effects on the dielectric response of polymer nanocomposites. *Applied Physics Letters*, 111(9):092901, August 2017.

[23] Hung T. Vo and Frank G. Shi. Towards model-based engineering of optoelectronic packaging materials: Dielectric constant modeling. *Microelectronics Journal*, 33(5-6):409–415, may 2002.

[24] David J.T. Hally and Irina Paci. Low-frequency polarization in molecular-scale noble-metal/metal-oxide nanocomposites. *Nanoscale*, 10(20):9583–9593, 2018.

[25] Archita N. S. Adluri, Brett Henderson, and Irina Paci. Tuning the dielectric response in a nanocomposite material through nanoparticle morphology. *RSC Adv.*, 12:10778–10787, 2022.

[26] J. P. Calame. Dielectric permittivity simulation of random irregularly shaped particle composites and approximation using modified dielectric mixing laws. *Journal of Applied Physics*, 104(11):114108, dec 2008.

[27] Nawfal Jebbor and Seddik Bri. Effective permittivity of periodic composite materials: Numerical modeling by the finite element method. *Journal of Electrostatics*, 2012.

[28] Xiangyu Xu, Boming Zhang, Kai Liu, Dawei Liu, Ming Bai, and Yun Li. Finite element simulation and analysis of the dielectric properties of unidirectional aramid/epoxy composites. *Polymer Composites*, 39:E2226–E2233, 2018.

[29] Viktor Myroshnychenko and Christian Brosseau. Finite-element method for calculation of the effective permittivity of random inhomogeneous media. *Physical Review E - Statistical, Nonlinear, and Soft Matter Physics*, 71(1):1–16, 2005.

[30] J. P. Calame. Finite difference simulations of permittivity and electric field statistics in ceramic-polymer composites for capacitor applications. *Journal of Applied Physics*, 99(8):084101, 2006.

[31] José M Soler, Emilio Artacho, Julian D Gale, Alberto García, Javier Junquera, Pablo Ordejón, and Daniel Sánchez-Portal. The SIESTA method for ab initio order-N materials simulation. *Journal of Physics: Condensed Matter*, 14(11):2745, mar 2002.

[32] John P. Perdew, Kieron Burke, and Matthias Ernzerhof. Generalized gradient approximation made simple. *Physical Review Letters*, 77(18):3865–3868, October 1996.

[33] N. Troullier and José Luís Martins. Efficient pseudopotentials for plane-wave calculations. *Phys. Rev. B*, 43:1993–2006, Jan 1991.

[34] N. Troullier and José Luís Martins. Efficient pseudopotentials for plane-wave calculations. ii. operators for fast iterative diagonalization. *Phys. Rev. B*, 43:8861–8869, Apr 1991.

[35] M. Pereiro and D. Baldomir. Structure of small silver clusters and static response to an external electric field. *Physical Review A*, 75(3), March 2007.

[36] Jinlan Wang, Mingli Yang, Julius Jellinek, and Guanghou Wang. Dipole polarizabilities of medium-sized gold clusters. *Physical Review A - Atomic, Molecular, and Optical Physics*, 74(2):1–5, 2006.

[37] P. Umari and Alfredo Pasquarello. Ab initio Molecular Dynamics in a Finite Homogeneous ElecNanotric Field. *Physical Review Letters*, 89(15):1–4, 2002.

[38] R. Bertossa and D. Tisi. analisi (https://github.com/rikigigi/analisi). Github.com, 2022. Compiled July 25, 2022.

[39] Yury. Ellipsoid fit (https://www.mathworks.com/matlabcentral/fileexchange/24693-ellipsoid-fit). MATLAB Central File Exchange, 2021. Retrieved September 5, 2021.

[40] Christophe Geuzaine and Jean-François Remacle. Gmsh: A 3-d finite element mesh generator with built-in pre- and post-processing facilities. *International Journal for Numerical Methods in Engineering*, 79(11):1309–1331, May 2009.

[41] Christophe Geuzaine. GetDP: a general finite-element solver for the de rham complex. *PAMM*, 7(1):1010603–1010604, December 2007.

[42] John David Jackson. *Classical Electrodynamics*. John Wiley & Sons, Nashville, TN, 3 edition, July 1998.

[43] Richard F.W. Bader, Marshall T. Carroll, James R. Cheeseman, and Cheng Chang. Properties of Atoms in Molecules: Atomic Volumes. *Journal of the American Chemical Society*, 109(26):7968–7979, 1987.

[44] W Tang, E Sanville, and G Henkelman. A grid-based bader analysis algorithm without lattice bias. *Journal of Physics: Condensed Matter*, 21(8):084204, January 2009.

[45] Rajarshi Sinha-Roy, Pablo García-González, and Hans Christian Weissker. How metallic are noble-metal clusters? Static screening and polarizability in quantum-sized silver and gold nanoparticles. *Nanoscale*, 12(7):4452–4458, 2020.

[46] Charles Kittel. *Introduction to solid state physics*. Wiley, 8 edition, 2004.

[47] Edward Purcell. *Electricity and Magnetism*. Cambridge University Press, 2 edition, 2011.

[48] Vadim A. Markel. Introduction to the Maxwell Garnett approximation: tutorial. *Journal of the Optical Society of America A*, 33(7):1244, 2016.

[49] K. Jackson, M. Yang, and J. Jellinek. Site-specific analysis of dielectric properties of finite systems. *Journal of Physical Chemistry C*, 111(48):17952–17960, dec 2007.

[50] K. A. Jackson, M. Yang, I. Chaudhuri, and Th. Frauenheim. Shape, polarizability, and metallicity in silicon clusters. *Phys. Rev. A*, 71:033205, Mar 2005.

[51] Richard Becker and Fritz Sauter. *Electromagnetic fields and interactions*. Dover, 1982.

Chapter 5

Inducible Atomic Dipole Model of Nanocomposite Polarization

5.1 Introduction

In the previous chapter, classical electrostatics were used to construct a phenomenological model of the static polarization in MgO/Ag nanocomposites. This approach benefited from simplicity. Inclusion shapes were defined as idealized ellipsoids, and the interfacial layer assumed to have a constant thickness. However, for all its gains in simplicity, the model neglected the atomic structure entirely. The inconsistent accuracy of the model for rod- and disk-like inclusions suggests that including this atomic structure is important for accurately capturing polarization at the interface.

The present chapter explores the notion of inducible atomic dipoles (IADs) as a model of polarization response in nanocomposites. More specifically, IADs are considered in both **predictive** and **descriptive** contexts. The predictive context refers to using a model of atom-centered classical inducible dipoles to *predict* the polarization of an atomic structure in response to applied fields. In the descriptive context, *ab initio* electronic densities are mapped to a picture of atomic dipoles using charge partitioning schemes as a way to *understand* atomic and group contributions to the collective response. In some cases, these two contexts are blurred. For example, the parameterization of a predictive model may begin with a mapping of the *ab initio* to atomic contributions.

As a predictive tool, we use IADs to model the dielectric response of small molecules, nanoclusters, and solids in a way that incorporates the details of atomic

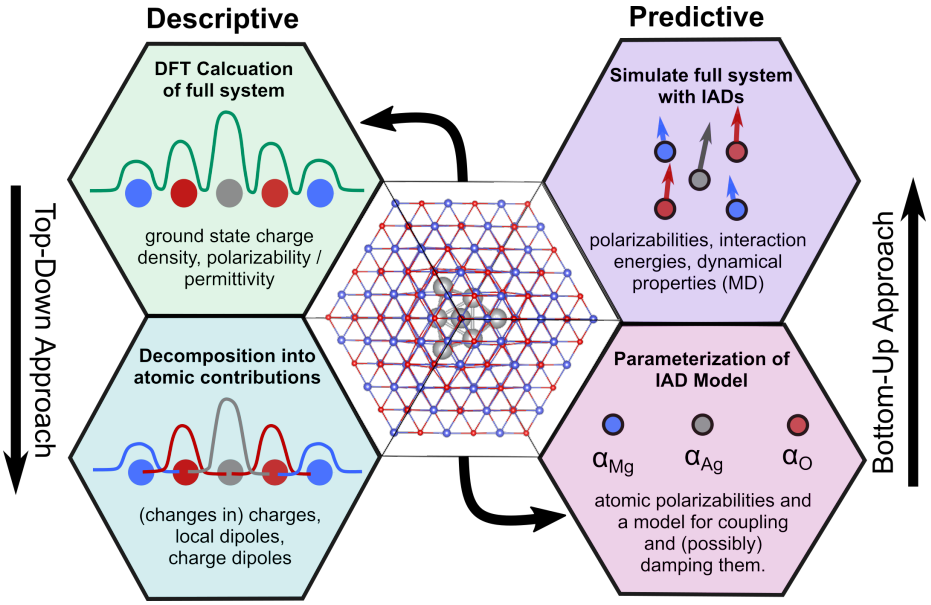

Figure 5.1: Overview of coarse-grained approaches to dielectric response. Ab initio response properties are used to parameterize either continuum or atomistic models. These approaches allow nanocomposites, like the MgO/Ag_8 matrix-inclusion system pictured center, to be modeled at minimal computational cost.

structure. Emphasis is placed on metal oxide and silver clusters, as well as cluster models of silver/metal oxide composites. Crucial to the utility of the IAD model, classical dipoles can be simulated much more efficiently than quantum atoms. On the other hand, the method only incorporates quantum effects very approximately and ignores higher order multipole polarizabilities and hyperpolarizabilities. Therefore the transferability of the method across different types of systems, and specifically its performance on heterogeneous systems that combine subsystems with different polarization mechanisms, is of primary concern.

As descriptive tool, we primarily use IADs to explore the site-specific contributions to polarization and to disentangle the physical mechanisms of polarization. Site-specific polarization is used to better understand the polarization of nanocomposites by quantifying the contributions of inclusion, interface, and matrix. In this way, the approach is related to the Maximally Localized Wannier Function analysis performed in Chapter 3, which can be considered a specific type of descriptive IAD approach. However, the present methodology also allows a decomposition of polarization into local atomic dipole contributions and charge transfer between atoms. Thus, we evaluate the varying role of charge transfer in different system types and explore the link between charge transfer and the anisotropy of the polarization response. Along the

way, we relate these physical descriptors to the performance of the aforementioned predictive IAD models to better understand why these models perform better for some systems than others.

Unlike the previous 2 chapters, the present restricts itself to the purely *electronic* response, wherein ions are clamped in an applied field (ϵ_∞ for solids). Empirically, this corresponds to the high frequency dielectric response. It would be possible to lump the electronic and ionic components of polarization into the definition of IADs, such as was done in the parameterization of the continuum model of the previous chapter. However, in the context of classical atomistic simulation, it is much more practical to treat both on equal footing via a polarizable force field. The "polarizable" part of such a force field can indeed be constructed using IADs, and so the lessons gleaned from this chapter could inform the future design of a polarizable force fields for nanocomposites with metallic inclusions.

The chapter is organized as follows. Section 5.2 introduces some background on IADs, including a description of alternative and related approaches. Next, Section 5.3 explains the methods and used throughout this chapter. Specifically, it outlines the particular predictive IAD model used which is based on a volume scaling of atomic polarizabilties. In addition, it introduces the local dipole and charge transfer contributions to polarizability, and defines the metrics used for evaluating models throughout the chapter. Following this, Section 5.4 evaluates the impact of the particular recipe used for volume-scaling in the predictive model as well as other model parameters. Section 5.5 quantifies the contribution of charge transfer to polarizabilty for a set of small molecules and several types of inorganic clusters and identifies it as a source of performance differences in the predictive IAD model. Section 5.6 pushes the limits of the predictive IAD model's ability to capture charge transfer and anisotropy in long silver nanorods. Finally, Section 5.7 proposes an embedded cluster model for an MgO/Ag nanocomostite and examines the performance of the IAD model on the system.

5.2 Background

Classical descriptions of the atoms as inducible dipoles can be traced back at least as far as the mid-19th century, when Ottaviano Mossotti (1847) and Rudolf Clausius (1879) independently derived the Clausius-Mossotti formula relating the macroscopic permittivity of a crystalline material to the polarizability of its lattice sites.[1] Even to-

day, classical descriptions of atomic polarizability are still incredibly important within the context of polarizable classical force fields. These force fields allow molecules to polarize in response to the electric field they experience, which can help improve the transferrability of force fields between different environments. The precise model of atomic polarization varies between three standard classes of implementations: the Drude oscillators (sometimes referred to as the Shell Model),[2, 3, 4, 5, 6] fluctuating charges,[7, 8, 9, 10, 11, 12] and inducible dipoles.[13, 14, 15] Though these approaches are the most common, they do not represent an exhaustive list. For instance, continuum dielectric models have also been proposed,[16, 17, 18] and some schemes involve combinations of inducible dipoles and fluctuating charges. Regarding notation, point dipoles will hereafter be referred to as IADs. While in principle these dipoles could be placed away from nuclear sites, in practice they are almost always associated with atomic nuclei.

The three primary approaches introduced above all have straightforward physical motivations and can reproduce the polarization of molecules. Both the Drude oscillator and inducible dipole approaches attempt to represent the charge redistribution in a molecule as the collective redistribution of charge around individual atomic nuclei. In the Drude picture, the charge distribution of an atom is modeled as a positively charged atomic core attached via a harmonic spring to a negatively charged particle (the Drude oscillator) that represents electronic charge. Thus, external fields induce a displacement between core and oscillator that results in an atomic dipole moment.[2, 3, 4, 5, 6] IADs model the same phenomenon of atomic charge redistribution, but instead of modeling a physical separation of charge, with IADs, the dipole moment is just a linear scaling of the external field by the atom's polarizability, α.[13, 14, 15] Under small fields, the Drude and point dipole schemes reduce to equivalent treatments.[19] In contrast to these two approaches, fluctuating charge models represent charge redistribution via changing atomic charges.[7, 8, 9, 10, 11, 12] Thus, polarization is the effect of charge flow along atomic bonds. This scheme can result in long range charge redistribution which can be important for metallic systems. However, unless non-nuclear charges are introduced to the model, fluctuating charges can only model polarization along bonding directions. In part because of these limitations, fluctuating charge models are less common than the other two approaches to polarizable force fields.[12]

Outside of classical force fields, atomic dipoles are also a foundational concept for semiclassical dispersion corrections to density functional theory. [20] In short,

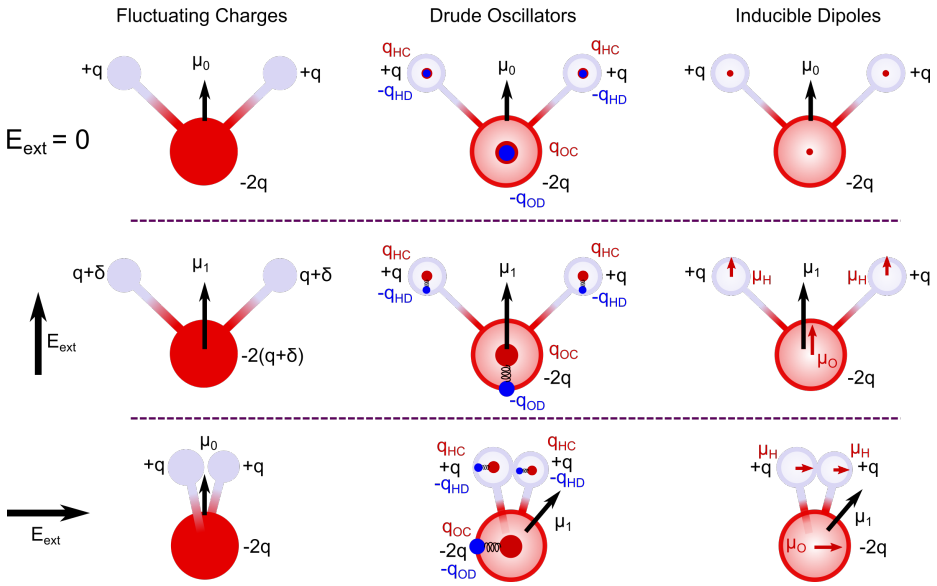

Figure 5.2: Illustration of fluctuating charge, Drude oscillator, and inducible dipole approaches to polarization in classical force fields. A water molecule is shown in three states of a homogeneous external field: no field, a field oriented parallel to the C_2 axis, and a field oriented orthogonal to the σ_v plane on which the molecular bonds lie. Net partial charges are labeled in black for all atoms. For the Drude model, atomic core charges are shown in red, and Drude charges in blue. The sum of these is equal to the the net partial charge. The molecular dipole moment is drawn with a black arrow and labeled μ_0 for the zero-field case and μ_1 in the where it differs from the zero-field value.

pairwise atomic contributions to the dispersion energy are related to the frequency-dependent atomic polarizabilities via the Casimir-Polder expression.[20] For some dispersion corrections, the polarizabilities are simply taken from free atoms or related references. However, in the popular Tkatchenko-Scheffler (TS) method, the chemical environment of the atoms is taken into account.[21] Furthermore, in TS with self-consistent screening (TS-SCS), the mutual polarization, or screening, of IADs in the molecular geometry is used to compute effective atomic polarizabilities.[22] This procedure is equivalent to the process of computing the self-consistent polarization of IADs in polarizable force fields like AMOEBA.[23]

In what follows, IADs, rather than Drude oscillators or fluctuating charges, are used to model the self-consistent polarization of clusters and materials. Specifically, the parameterization of these IADs is calculated using the method employed in TS dispersion corrections, and the self-consistent response model is taken from the TS-SCS method. Drude oscillators would likely produce very similar results, though

in the end IADs were chosen due to their wide use across the fields of both force field development and dispersion corrections and because of implementation ease. In the end of the chapter, potential advantages of adding in some degree of charge fluctuation are discussed. The lessons gleaned through this analysis can inform future development of polarizable force fields for nanocomposite materials with metallic inclusions. While only the static field electronic contributions to polarization are considered herein, such a force field would allow the low-frequency ionic contributions to be computed as well.

5.3 Methods

5.3.1 Predictive: Polarizability of a System of IADs

Applequist et al.[24] laid out the theory for calculating the molecular polarizability that results from a collection of IADs. Appendix D reviews the mathematics behind this theory, while here we simply present its foundational concepts.

When a uniform external electric field $\boldsymbol{\mathcal{E}}$ is applied to a collection of IADs, each site experiences a total electric field that is the superposition of the external field and the field generated self-consistently by all of the surrounding dipoles. Thus, the induced dipole moment $\boldsymbol{\mu}_i$ (a 3×1 column vector) of the i^{th} site can be calculated as [24]

$$\boldsymbol{\mu}_i = \boldsymbol{\alpha}_\mathbf{i} \left[\boldsymbol{\mathcal{E}} - \sum_{j \neq i} \mathbf{T}_{ij} \boldsymbol{\mu}_j \right]. \tag{5.1}$$

The term in square brackets on the RHS represents the total local electric field acting on the i^{th} site. In particular, $\mathbf{T}_{ij}$ is the (3×3) *dipole field tensor* describing the field at site i produced by the dipole at site j. Its mathematical form varies depending on the precise physical description used for the IADs and will be addressed later. Moreover, $\boldsymbol{\mu}_j$ is the induced dipole moment of site j, a 3×1 column vector, and the external field $\boldsymbol{\mathcal{E}}$ is also a 3×1 column vector. Finally, $\boldsymbol{\alpha}_\mathbf{i}$ is the (3×3) polarizability tensor of the i^{th} site. Appendix D gives a more detailed description of the quantities and mathematical notation appearing in Equation (5.1).

In some contexts, it can be useful to define an "effective", or "self-consistently screened" (SCS) polarizability of each IAD.[22] Unlike $\boldsymbol{\alpha}_i$, which defines the response to the local field, the SCS polarizability $\boldsymbol{\alpha}_i^{\text{SCS}}$ defines the response of the IAD at site

i to a uniform external field by implicitly encompassing the screening effects of all surrounding IADs. The mathematical construction of $\boldsymbol{\alpha}_i^{\mathrm{SCS}}$ is described in Appendix D. For now, we simply define it operationally as

$$\boldsymbol{\mu}_i = \boldsymbol{\alpha}_i^{\mathrm{SCS}} \boldsymbol{\mathcal{E}}, \tag{5.2}$$

where, again, $\boldsymbol{\mathcal{E}}$ is a uniform external field and $\boldsymbol{\mu}_i$ is the induced dipole moment on site i. Conveniently, these SCS polarizabilities are additive in that the molecular polarizability is obtained as a sum of SCS site polarizabilities:

$$\boldsymbol{\alpha}_{\mathrm{mol}} = \sum_i \boldsymbol{\alpha}_i^{\mathrm{SCS}}. \tag{5.3}$$

We used two programs, Tinker and libMBD, to solve for molecular polarizability of our IAD models. Tinker[25] is a molecular dynamics package that self-consistently solves Equation 5.1 using a conjugate gradient approach. On the other hand, libMBD [26] implements the Many Body Dispersion method with range-separated Self-Consistent Screening (MBD@rsSCS), an extension of the previously mentioned TS-SCS method. [27] The libMBD code solves for the SCS polarizability tensors $\boldsymbol{\alpha}_i^{\mathrm{SCS}}$, which are summed to yield the molecular polarizability. The libMBD code also implements periodic boundary conditions, in which the periodic dipole field tensor is evaluated via Ewald summation.[26]

5.3.2 Form of the Dipole Field Tensor

The mathematical form of the dipole field tensor $\mathbf{T}_{ij}$ depends on the physical description used for the IADs. The simplest description for an IAD is an idealized point dipole with no spatial extent. However, one can also represent IADs using various spherically symmetric charge distributions.[28] These different model charge densities can then be used to derive different dipole field tensors which take on the same general form, which for two IADs at sites i and j, can be written[29]:

$$\mathbf{T}_{ij} = \frac{f_e}{r_{ij}^3}\mathbf{I} - \frac{3f_t}{r_{ij}^5}\begin{bmatrix} x^2 & xy & xy \\ yx & y^2 & yz \\ zx & zy & z^2 \end{bmatrix}. \tag{5.4}$$

Here $\mathbf{I}$ is the 3×3 identity matrix, r_{ij} is the distance between the IADs, and x, y, and z are the Cartesian components of the vector pointing from site i to site j.

The terms f_e and f_t depend on the chosen charge distribution. For idealized point dipoles, $f_e = f_t = 1$.[24] However, when dipoles are aligned end-to-end at short range, this model can lead to infinite polarization.[28, 30]. When a physically "smeared out" charge distribution is used, f_e and f_t function as distance-dependent damping factors, which avoid this "polarization catastrophe".[28, 30]

Tinker Model

In Tinker, the charge distribution of each IAD is modeled with the following exponential form, originally defined by Thole:[28, 14]

$$\rho = \frac{3a}{4\pi} \exp(-au^3). \tag{5.5}$$

Here u is an effective distance calculated separately for different pairs of interacting dipoles as $u = r_{ij} / \left[(\alpha_i \alpha_j)^{1/6}\right]$, and a is an fitted damping parameter. This results in the following form for the damping factors:[31]

$$f_e = 1 - \exp(-au^3) \tag{5.6}$$

$$f_t = 1 - (1 + au^3) \exp(-au^3). \tag{5.7}$$

libMBD Model

The original many-body dispersion (MBD) and its range-separated variant MBD@rsSCS are laid out in detail in the works of Distasio *et al.* and Ambrosetti *et al.*, respectively. [32, 27] Details of the MBD@rsSCS implementation in libMBD are further described in Ref [26]. Here we review the details of MBD@rsSCS relevant to the present chapter—namely, the parts of the theory used to determine the effective polarizability of IADs. In the model, IADs are described as isotropic quantum harmonic oscillators with a Gaussian charge distribution. For a Gaussian IAD with spread σ, this charge distribution is given by [32]

$$\rho(r) = (\pi^{3/2}\sigma^3)^{-1} \exp\left[-r^2/(2\sigma^2)\right]. \tag{5.8}$$

Furthermore, the spread of an IAD's charge distribution is determined from its polarizability using the relation $\sigma_i = (\sqrt{2/\pi}\alpha_i/3)^{1/3}$.[32]

For Gaussians centered at $\mathbf{r}_i$ and $\mathbf{r}_j$, with spreads σ_i and σ_j, an effective width for

the pair can be defined as $\sigma_{ij} = \sqrt{\sigma_i^2 + \sigma_j^2}$,[32] and the damping functions in Equation (5.4) become

$$f_e = \mathrm{erf}(\zeta) - \frac{2}{\sqrt{\pi}}\zeta \exp(-\zeta^2) \tag{5.9}$$

$$f_t = f_e - \frac{4\zeta^2}{3\sqrt{pi}} \exp(\zeta^2), \tag{5.10}$$

where $\zeta = r_{ij}/\sigma_{ij}$ is a normalized distance from the IAD, and erf is the error function.

In the MBD@rsSCS method, the dipole field tensor is range-separated into short- and long-range coupling of dipoles.[27] The short-range interaction is described by the Gaussian-Gaussian interaction tensor–that is, Equation (5.4) with damping functions defined by Equation (5.9). We can the resulting tensor T_{ij}^{G}. On the other hand, the long-range interaction is chosen to be the point-dipole interaction, with damping functions $f_e = f_1 = 1$, which we call T_{ij}^{PD}. A Fermi-type damping function $f(r_{ij})$ is used to seamlessly transition between the two distance ranges. Including this Fermi damping, the final short-range (SR) and long-range (LR) dipole field tensors are, respectively[27]

$$T_{\mathrm{SR},ij} = (1 - f(r_{ij}))T_{ij}^{\mathrm{G}} \tag{5.11}$$

$$T_{\mathrm{LR},ij}^{ab} = f(r_{ij})T_{ij}^{\mathrm{PD}}. \tag{5.12}$$

The Fermi damping function has the form

$$\begin{aligned} f(r_{ij}) &= \frac{1}{1 + \exp\left[-a(r_{ij}/S_{\mathrm{vdW}} - 1)\right]} \\ S_{\mathrm{vdW}} &= \beta(R_{\mathrm{vdW}}^i + R_{\mathrm{vdW}}^j), \end{aligned} \tag{5.13}$$

where the MBD@rsSCS method, and therefore libMBD by default, fixes $a = 6$.[27] The parameter β determined separately for each density functional approximation by fitting to reference interaction energies, with tabulated values available for common functionals.[27] libMBD uses tabulated van der Waals radii for all elements.[26]

It is important to note that within the MBD@rsSCS method (and within the libMBD implentation of it that we use), only the short-range dipole field tensor

$T^{ab}_{\mathrm{SR},ij}$ is used to solve for the IAD effective polarizabilities and resulting molecular polarizability.[27] Therefore, in the work that follows, the mutual polarization of atom-centered dipoles is attenuated somewhat relative to the full Gaussian-Gaussian interaction, due to the Fermi damping of the response at medium to long range. We explore how this attenuation affects the performance of this IAD model.

5.3.3 Assignment of Isotropic Atomic Polarizabilities

In both the Tinker and libMBD approaches, isotropic polarizabilities α_i must be assigned to IADs before self-consistent IAD polarizabilities can be calculated using the methods described in the previous section. Myriad ways have been employed to fit polarizabilities for different atom types for polarizable force field development, including fitting to molecular polarizabilities from experiments or quantum calculations, theoretical interaction energies, or the changes in electrostatic potential in response to charge probes.[29] In Section 5.6, we fit atomic polarizabilities for the Tinker model by minimizing the error of IAD model isotropic cluster polarizabilities relative to DFT-calculated isotropic polarizabilities.

One the other hand, when using the libMBD model and not otherwise indicated, we adopt the approach of Tkatchenko and Scheffler (TS), whereby polarizabilities are determined from the *ab initio* electron density.[21] This approach attempts to incorporate quantum electronic structure effects related to the local environment of IADs into account via a long-recognized relationship between atomic volumes and polarizabilities [33]. For simplicity, we will hereafter refer to the volume-scaling approach to IADs, for which we use the short-range MBD@rsSCS dipole field tensor implemented in libMBD, simply as the TS model.

Under the volume-scaling TS model, the isotropic polarizability of an atom i in a molecule or material is defined relative to the polarizability of a free, or gas-phase, atom of the same element, α_i^{free}:

$$\alpha_i = \nu_i \alpha_i^{\mathrm{free}}. \tag{5.14}$$

Here ν_i, or the volume ratio, is defined as $\nu_i = \frac{\langle r^3 \rangle_i^{\mathrm{AIM}}}{\langle r^3 \rangle_i^{\mathrm{free}}}$. Strictly speaking, this is not a volume ratio, but a ratio of the third moment of the electronic density for the atom in the material (AIM) to that of the spherically averaged free atom density. We used the CCSD-calculated free atom densities and polarizabilities from Manz et al. for these reference values unless otherwise indicated.[34] In Section 5.5.4 and 5.6, we

also experiment with optimizing these free atom polarizabilities to best reproduce the DFT cluster polarizabilities. Figure 5.3 depicts the steps involved for computing the polarizability of a system via the TS model.

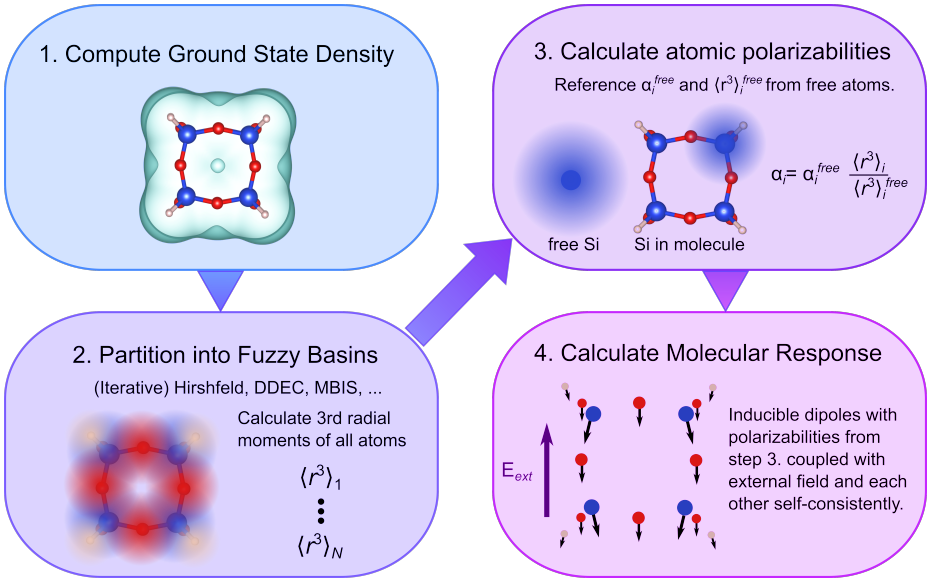

Figure 5.3: Procedure used for computing molecular response to external fields via the TS model. Steps 1-3 depict the process used to calculate IAD polarizabilities, and step 4 shows how these polarizabilities are used to compute molecular properties.

Defining Atoms in Materials

The definition of AIMs allows some flexibility. The original TS method used Hirshfeld partitioning to define AIM basins,[21] while more recent works have proposed using Iterative Hirshfeld (HI) partitioning for systems with more polar bonds.[35, 36] In what follows, we explore several additional flavors of atomic partitioning: Minimal Basis Iterative Stockholder (MBIS), and Density Derived Electrostatic and Chemical (DDEC6).

As its name suggests, the HI method builds off of the original Hirshfeld scheme in order to give more realistic charges and polarizabilities for both molecules and materials with ionic bonding, without compromising performance for species with non-polar bonding[37]. When integrated into the TS scheme, HI charges in turn improved dispersion energies for systems with ionic and highly polar bonds.[35, 36] The MBIS method is also iterative, but uses a different, computationally cheap basis for expanding the molecular charge density in terms of atomic contributions.[38] Like

HI, it generates more ionic charges than the original Hirshfeld method and is attractive due to its reasonable computational scaling. Finally, DDEC6 is the newest and most accurate in the family of DDEC charge density partitioning schemes, relying on an iterative procedure which produces reasonable charges for a broad range of chemical environments.[39, 40] We used the Chargemol package[41] to calculate DDEC6 charges and moments in this work. We used HORTON2[42] for HI charges and moments and both HORTON2 and the auxiliary DensPart[43] for MBIS.

Fractional Ion Reference Polarizabilities

In the traditional TS approach, only free *neutral* atom references are included in the volume-scaling procedure. The charge of AIMs thus only enters the calculation indirectly, insofar as it impacts the volume of the AIM. However, Gould and Bučko have suggested that this may be insufficient for highly ionic systems.[44], arguing that using reference free *ion* polarizabilities and radial moments can help account for significant differences in polarizability between different AIM charge states.

Thus, in combination with the different charge partitioning schemes mentioned above, we also tested Gould's fractional ion (FI) approach [44] for defining free ion reference polarizabilities α_i^{free} and radial moments $\langle r^3 \rangle_i^{\text{free}}$. Fractional ions are defined as a linear combination of the two integer charge states on either side of the atomic charge calculated for an AIM, and the FI radial moments and polarizabilities can be defined by a similar linear combination. Thus, for an AIM with nuclear charge Z and non-integer electronic population N from charge partitioning, we obtain α_i^{free} using [44]

$$\alpha_i^{\text{free}} = f\alpha_{Z,M+1}^{\text{free}}(\omega) + (1-f)\alpha_{Z,M}^{\text{free}}(\omega) \tag{5.15}$$

$$\langle r^3 \rangle_i^{\text{free}} = f\langle r^3 \rangle_{Z,M+1}^{\text{free}} + (1-f)\langle r^3 \rangle_{Z,M}^{\text{free}}(\omega). \tag{5.16}$$

Here M is the largest integer smaller than N and $f = N - M$. For the FI method, reference ionic polarizabilities were taken from the work of Gould and colleagues,[45] and reference ionic radial moments were extracted from the spherically averaged charge densities contained in the Chargemol program.[39]

5.3.4 Descriptive: Atomic Contributions to Polarizability

We used the method of Laidig and Bader[46] to partition the DFT polarizability of a system into atomic contributions. With this approach, the atomic polarizabilities can be further decomposed into a localized induced dipole contribution $\boldsymbol{\alpha}^p$ and a charge transfer contribution $\boldsymbol{\alpha}^q$. Similar methods developed by Jackson and colleagues have been used to study atomic polarizability in silicon and sodium clusters.[47, 48, 49] Each of these methods rely on partitioning the electronic density into atomic basins. We note that the specific definition of atomic basins is arbitrary, and the effect of different choices has been explored elsewhere.[50] In the original work of Bader and Laidig, and in the present work, Bader's Quantum Theory of Atoms in Molecules (QTAIM)[51] is used to generate atomic basins. Specifically, we use the Critic2 program to generate QTAIM basins and compute the charge moments.[52]

For a system partitioned into atomic basins Ω_A, the local dipole moment $\boldsymbol{\mu}_A$ of each atomic basin Ω_A is [46]

$$\boldsymbol{\mu}_A^p = \int_{\Omega_A} \rho(\mathbf{r})\,(\mathbf{r} - \mathbf{R}_A)\,d\mathbf{r}, \tag{5.17}$$

where $\mathbf{R}_A$ is the nuclear coordinate of atom A. In addition to the intrinsic dipole moment of a basin, each basin possesses a potentially non-zero net charge, which contributes to the dipole moment of the overall system. This contribution is called the charge transfer term. It can be written for each atom as [46]

$$\boldsymbol{\mu}_A^q = q_A \mathbf{R}_A, \tag{5.18}$$

where q_A is the net charge of atom A (nuclear charge minus the integrated electron charge in the basin). While $\boldsymbol{\mu}_A^p$ is not dependent on the choice of origin for the coordinate system, $\boldsymbol{\mu}_A^q$ is *origin-dependent*, since atomic basins are not necessarily charge neutral. Combining these two terms, the total dipole moment of an atom is given by [46]

$$\boldsymbol{\mu}_A = \boldsymbol{\mu}_A^p + \boldsymbol{\mu}_A^q. \tag{5.19}$$

Furthermore, the total system dipole moment $\boldsymbol{\mu}$ can be calculated as a sum over all atomic dipole moments $\boldsymbol{\mu}_A$. For a neutral system, $\boldsymbol{\mu}$, and hence the sum of all atomic charge transfer terms, is not dependent on the choice of origin.

Atomic polarizabilities can be computed by taking the derivative of these atomic

atomic dipole moments with respect to an external electric field. We do this numerically by applying an external field strength of $E_j = \pm 0.001$ au in each Cartesian direction j and computing the polarizability tensor as the finite difference

$$\alpha^c_{A,ij} = \frac{\mu^c_{A,i}(+E_j) - \mu^c_{A,i}(-E_j)}{2E_j}. \tag{5.20}$$

Here, c is the particular contribution to atomic polarizability being calculated, either intrinsic polarization (p) or charge transfer (q). Importantly for our implementation and in the original work of Bader and Laidig, atomic basins are generated separately for each state of the external field in the finite difference procedure, rather than reusing the basins from a zero-field calculation.[46] We found that this had an impact on the relative magnitudes of α^p and α^q, though the trends observed across all systems studied were essentially unchanged. It is important to note that like $\boldsymbol{\mu}^q_A$, the atomic charge transfer polarizabilities α^q_A are origin-dependent–thus, we have consistently defined the origin to be the center of mass to allow comparison between different systems.

As with the total atomic dipole moment, the total atomic polarizability is the sum of the intrinsic dipole and charge transfer components:[46]

$$\alpha_{A,ij} = \alpha^p_{A,ij} + \alpha^q_{A,ij}. \tag{5.21}$$

Furthermore, the total system polarizability can be recovered by summation of all atomic polarizabilities, and intrinsic dipole or charge transfer contributions to the total system polarizability can be obtained by summing those components over all atoms:[46]

$$\alpha^c_{ij} = \sum_A \alpha^c_{A,ij}. \tag{5.22}$$

Crucially, this sum is is independent of the chosen origin for both intrinsic dipole and charge transfer contributions, even for a system with net charge.[49] Thus, the partitioning of the total system polarizability into local polarization and charge transfer components is unique for a given charge partitioning method. At its core, the charge transfer polarizability quantifies the transfer of electrons between atoms as the external field is modulated, a phenomenon not accounted for by the dipolar redistribution of charge within atomic basins alone.[47]. Later, we discuss how the relative importance of charge transfer for a given system relates to the effectiveness of predictive

IAD models.

At this point, it is useful to note the connection between these descriptive atomic polarizabilities and the predictive ones discussed earlier. Because of their additivity, the descriptive polarizabilities resemble the self-consistently screened, or "effective" polarizabilities from the TS predictive IAD model. It would be interesting if these quantities could be directly compared, but the origin-dependence of descriptive atomic polarizabilities arising from the charge transfer term limits the usefulness of this comparison. Schemes for removing this origin dependence have been developed,[46, 53] and applying them to allow direct comparison with predictive IAD schemes is a potential future avenue of inquiry.

5.3.5 Metrics

Throughout this chapter, we report the errors of the polarizabilities predicted by the inducible dipole model. Since the polarizabilities we predict vary across several orders of magnitude, we often report *relative* errors in the form of Mean Relative Unsigned Errors (MRUE), and Mean Relative Signed Errors (MRSE) defined as

$$\text{MRUE} = \frac{1}{N}\sum_{i=0}^{N} |y_{\text{pred}} - y_{\text{ref}}|/y_{\text{ref}} \tag{5.23}$$

$$\text{MRSE} = \frac{1}{N}\sum_{i=0}^{N} (y_{\text{pred}} - y_{\text{ref}})/y_{\text{ref}}. \tag{5.24}$$

In other cases where the predicted values lie in a relatively small window of magnitudes, or where the reference values may be zero, we simply report Mean Unsigned Errors (MUE) and Mean Signed Errors (MSE) defined as

$$\text{MUE} = \frac{1}{N}\sum_{i=0}^{N} |y_{\text{pred}} - y_{\text{ref}}| \tag{5.25}$$

$$\text{MSE} = \frac{1}{N}\sum_{i=0}^{N} (y_{\text{pred}} - y_{\text{ref}}). \tag{5.26}$$

In addition, we use the approach of Cheng and Verstraelen[54] to analyze the anisotropy of the polarizability tensor and the contributions to this anisotropy, which

we now describe in some detail. This approach involves reformulating polarizability as the "recoupled" polarizability vector $\boldsymbol{\alpha}^{\mathbf{r}}$,[†] defined as [54]

$$\boldsymbol{\alpha}^{\mathbf{r}} = \begin{bmatrix} \alpha_{00} \\ \alpha_{20} \\ \alpha_{21c} \\ \alpha_{21s} \\ \alpha_{22c} \\ \alpha_{22s} \end{bmatrix} = \sqrt{\frac{2}{3}} \begin{bmatrix} -\frac{\sqrt{2}}{2} & 0 & 0 & -\frac{\sqrt{2}}{2} & 0 & -\frac{\sqrt{2}}{2} \\ -\frac{1}{2} & 0 & 0 & -\frac{1}{2} & 0 & 1 \\ 0 & 0 & \sqrt{3} & 0 & 0 & 0 \\ 0 & 0 & 0 & 0 & \sqrt{3} & 0 \\ \frac{\sqrt{3}}{2} & 0 & 0 & -\frac{\sqrt{3}}{2} & 0 & 0 \\ 0 & \sqrt{3} & 0 & 0 & 0 & 0 \end{bmatrix}. \tag{5.27}$$

The first term in $\boldsymbol{\alpha}^{\mathbf{r}}$ relates to the isotropic polarizability α^{iso} as [54]

$$\alpha^{\text{iso}} = -\frac{1}{\sqrt{3}}\alpha_{00} = \frac{1}{3}(\alpha_{xx} + \alpha_{yy} + \alpha_{zz}). \tag{5.28}$$

The remaining five entries define the *anisotropic polarizability vector*:[‡] [54]

$$\boldsymbol{\alpha}^{\text{aniso}} = \frac{1}{\sqrt{3}}(\alpha_{20}, \alpha_{21c}, \alpha_{21s}, \alpha_{22c}, \alpha_{22s}). \tag{5.29}$$

This definition allows the squared magnitude of the anisotropy to be defined as a scalar using a normal dot product: [54]

$$\|\boldsymbol{\alpha}^{\text{aniso}}\|^2 = \boldsymbol{\alpha}^{\text{aniso}} \cdot \boldsymbol{\alpha}^{\text{aniso}}. \tag{5.30}$$

When it comes to polarizability anisotropy, we would like to address two primary questions in our analysis. First, how much of this anisotropy is determined by charge transfer and how much by local dipole polarization? Second, how well can various IAD models reproduce this anisotropy? For these properties of interest, we can form the appropriate anisotropic polarizability vector ($\boldsymbol{\alpha}_q^{\text{aniso}}$, $\boldsymbol{\alpha}_p^{\text{aniso}}$, or $\boldsymbol{\alpha}_{\text{IAD}}^{\text{aniso}}$). Then, we compute the following scalar to answer the question of how closely aligned the anisotropy of the property of interest $\boldsymbol{\alpha}_c^{\text{aniso}}$ is with the reference anisotropic polarizability $\boldsymbol{\alpha}_{\text{ref}}^{\text{aniso}}$ (usually taken to be the DFT-computed vector):[54]

[†]Note that the recoupled polarizability is indeed a 6-element vector by definition, and not a rank two tensor.

[‡]Again, note that the anisotropic polarizability is a 5-element vector by definition, and not a rank two tensor.

$$u_c^{\parallel} = \frac{\boldsymbol{\alpha}_{\text{ref}}^{\text{aniso}} \cdot \boldsymbol{\alpha}_c^{\text{aniso}}}{\|\boldsymbol{\alpha}_{\text{ref}}^{\text{aniso}}\|^2 + (\alpha_{\text{ref}}^{\text{iso}})^2}. \tag{5.31}$$

When $\boldsymbol{\alpha}_c^{\text{aniso}}$ is taken to be $\boldsymbol{\alpha}_{\text{ref}}^{\text{aniso}}$ in the above equation, the result is called $u_{\text{ref}}^{\parallel}$ and gives the relative anisotropy of the reference polarizability. In cases where the property of interest reproduces the anisotropy of the reference well, $u_c^{\parallel}$ will be close to $u_{\text{ref}}^{\parallel}$.[54] Thus, we frequently utilize parity plots of $u_c^{\parallel}$ plotted against $u_{\text{ref}}^{\parallel}$ to visualize how well a property reproduces reference anisotropies over a large number of systems.

5.4 Impact of AIM Method on the TS Model

Under the TS model, the volume scaling relationship requires a choice of atomic partitioning scheme and a set of reference polarizabilities. We explored the impact of the partitioning scheme and the use of FI references on the accuracy of the TS model by comparing TS model polarizabilities against higher level calculations for two very different types of systems. First, we evaluated TS polarizabilities against a dataset of 118 CCSD(T) polarizabilities for small molecules computed by Hait *et al.*[55] We will hereafter refer to this molecule set as SM118.[†] The molecules in SM118 exhibit a range of bonding types and represent both open- and closed-shell species. Next, we calculated the TS cell polarizabilities for a dozen cubic crystal structures and compared against PBE reference values. These crystals spanned a range of ionicity, with DDEC6 charges on atoms ranging from 0 in the fully covalent crystals to ±1.52 in the most ionic (Table 5.1). Together, these two datasets offer a diverse test set for IAD models.

5.4.1 Small Molecule Polarizabilities

Electronic densities for AIM partitioning of small molecules were obtained from PBE0/aug-pc-3 single point DFT calculations with ORCA using equilibrium geometries from Ref [55]. PBE0/aug-pc-4 was previously shown to perform very well for computing both molecular dipole moments and polarizabilities.[55, 56] Moreover, the basis set dependence of computed dipole moments was found to be relatively small when using PBE0, so the PBE0/aug-pc-3 densities should be quite accurate. Indeed,

[†]We excluded all single atoms from the original dataset from Ref [55]. Additionally, we excluded CH_3O because of a large error in the PBE0 polarizability relative to CCSD(T) and Li_2, P_2, and NaLi because of difficulty computing QTAIM basins.

our testing showed a negligible difference between TS models based on aug-pc-3 and aug-pc-4 densities.

Figure 5.4 shows the isotropic TS model molecular polarizabilities plotted against reference values for the molecules in the dataset. The MRUEs of the various methods, inset in the Figure 5.4, demonstrate that the choice of charge partitioning can significantly impact calculated polarizabilities. When neutral reference atoms were employed (Figure 5.4(a)) iterative partitioning methods (HI, MBIS, DDEC6) performed significantly better than Hirshfeld partitioning. This improvement is most noticeable for a grouping of molecules with strong polar bonds in the lower left portion of the plot, which includes the molecules $LiBH_4$, LiCl, LiCN, LiH, NaCl, NaCN, and NaH. The polarizabilities of these molecules were all significantly overestimated when Hirshfeld partitioning was used. Improvements for such polar systems have previously been noted when using the HI method,[35, 36] and it seems that both MBIS and DDEC6 offer similar performance. Differences in MRUE between iterative schemes are rather small. However, based on its positive MRSE, HI exhibits a tendency to overestimate polarizability, while both MBIS and DDEC6 show MRSE values close to 0. Thus, while all iterative schemes produce relative errors below 10%, MBIS and DDEC6 appear to be particularly robust options.

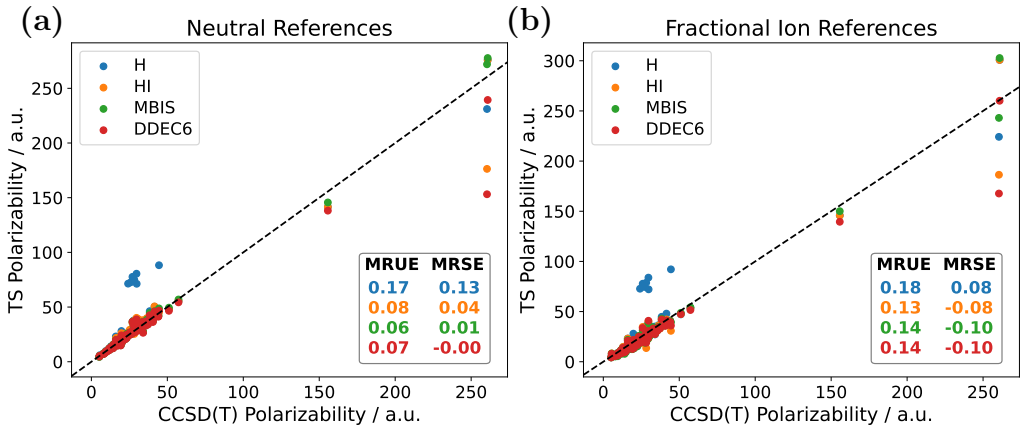

Figure 5.4: The isotropic polarizabilities of small molecules computed using the TS model with different charge partitioning schemes, compared to reference values. Reference values are CCSD(T) polarizabilities from Hait *et al.*[55]. Panel (a) shows the TS model with neutral atomic references, and Panel (b) shows the results from FI references

When FI references were used (Figure 5.4), the performance for all partitioning schemes degraded. For the iterative schemes in particular, this degradation was quite

significant. The smaller impact on the Hirshfeld method likely stems from the simple fact that this method predicts less ionic charges in the first place. In all cases, however, the FI approach reduced predicted polarizabilities on average, resulting in very negative MRSEs for all iterative schemes. By visually inspecting the plot, however, we can tell that this is not simply a systematic underestimation of polarizabilities. Scaling all TS model polarizabilities by a constant in order to eliminate MRSE resulted in a slight improvement in MRUE for the iterative schemes (MRUE(HI) = 0.11, MRUE(MBIS) = 0.11, MRUE(DDEC6) = 0.10), but the results were still worse than for when neutral reference atoms were used.

We also explored the anisotropic part of the polarizability, by computing $u_{\mathrm{TS}}^{\parallel}$ and $u_{\mathrm{ref}}^{\parallel}$ (Equation (5.31)). Because the reference CCSD(T) data from Ref [55] only contained the diagonal elements of the polarizability tensor, we calculated the full PBE0 polarizability tensors and used them as a reference. Figure 5.5 depicts $u_{\mathrm{TS}}^{\parallel}$ potted against $u_{\mathrm{ref}}^{\parallel}$ for each charge partitioning scheme, both with neutral and FI references. Recall that the values of $u_{\mathrm{TS}}^{\parallel}$ and $u_{\mathrm{ref}}^{\parallel}$ should be equal if the TS model perfectly reproduces the reference anisotropy, and that a negative $u_{\mathrm{TS}}^{\parallel}$ value indicates the anisotropy of the TS polarizability points in the opposite direction from the reference anisotropy.[54]

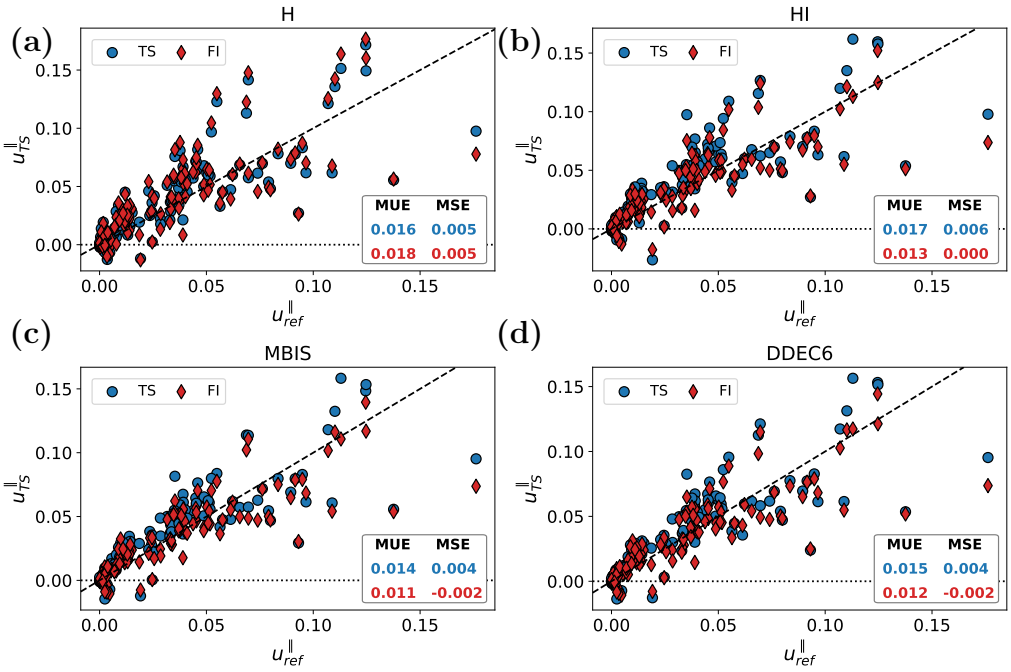

Figure 5.5: Anisotropy of the polarizability of small molecules computed using the TS-SCS method vs CCSD(T) reference values.[55]

MUE and MSE values are reported in the insets of the different panels of Figure 5.5. MSE values for all methods are quite small, supporting a visual assessment of the panels that the TS predictions are distributed fairly evenly about the line $y = x$. Thus, the TS approach does not seem to bias strongly toward over- or underestimating anisotropy, regardless of the charge partitioning or reference atoms used. Furthermore, the results for all charge partitioning schemes are rather similar, though there is a slight advantage to using either MBIS or DDEC6 in terms of MUE. Finally, the FI approach does improve the description of the anisotropy slightly when using any of the three iterative partitioning schemes. This makes some intuitive sense. For small molecules, anisotropy can come from structural effects (e.g. the planarity of the BH_3 molecule results in a smaller out-of-plane polarizability). But the polarity of single bonds can also play a role, such as in the case of BH_2Cl or CH_3Cl. An appropriately ionic treatment of the atomic references for atoms along those polar bonds likely contributes to the improvements when using FI references.

5.4.2 Cubic Crystal Cell Polarizabilities

For cubic crystals, electronic densities were calculated using the PBE functional in GPAW,[57] using structures for the primitive unit cells downloaded from Materials Project.[58] A plane wave cutoff of 600 eV was used, alongside a real-space grid point density of $1/(0.15\ \text{Å})^3$, and a $10 \times 10 \times 10$ k-point grid. Occupation numbers were smeared using the improved tetrahedron method. Reference values for cell polarizabilities were computed from the high frequency relative permittivity values of DFT calculations at the PBE level, obtained through Materials Project.[59, 60] For a cubic crystal, this permittivity can be related to the cell polarizability via the classical Clausius-Mossotti approximation:[61]

$$\alpha_{\text{cell}} = \frac{3\Omega}{4\pi}\frac{\epsilon^{\infty} - 1}{\epsilon^{\infty} + 2}. \tag{5.32}$$

Thus, cell polarizabilities from the TS model calculated using periodic boundary conditions were directly compared to these Clausius-Mossotti polarizabilites.

The crystals considered are listed in Table 5.1, alongside the atomic charges computed by both the DDEC6 and MBIS methods. For these systems, we limit ourselves to these two partitioning schemes based upon their good performance for the molecular systems above. Note that NaCl has not been included in the MBIS analysis, as the MBIS iterations did not converge in our use of DensPart. From Table 5.1, we see that the chosen crystals span a range of ionicities and that there are obvious differences between the charges predicted by the two partitioning methods. Furthermore while DDEC6 universally assigns less ionic charges, the differences between the two methods are larger in some systems (e.g. SiC) than others (e.g. CsCl). Thus, these systems offer a good test of the differences between two iterative charge partitioning methods and of the performance of the FI method.

Figure 5.6 shows the results obtained using both the MBIS and DDEC6 charge partitioning schemes, either with or without FI references. First, we note that the MRUE values for both partitioning methods (regardless of the type of reference atom used) are several times larger than for the small molecular systems. While significant, this is in line with previous reports for the HI method on similar systems.[36, 44] In one report, for example, HI partitioning with neutral atom references produced an MRUE of 0.44 for 18 cubic crystals, which is slightly smaller than our MRUEs of 0.55 and 0.54 for MBIS and DDEC6, respectively. Additionally, when neutral atom references are used, both charge partitioning methods almost exclusively overestimate

Table 5.1: Cubic crystalline solids used for validating the TS polarizability approach.

Material	Q_{DDEC6}	$\langle r^3 \rangle_{DDEC6}$	Q_{MBIS}	$\langle r^3 \rangle_{MBIS}$
C	0.00	28.3	0.00	30.9
Si	0.00	78.1	0.00	107.6
BN	±0.73	22.5/33.7	±1.35	13.2/43.5
SiC	±1.03	53.5/43.8	±2.21	31.3/88.6
MgO	±1.46	19.2/45.2	±1.94	5.5/50.1
MgS	±1.24	25.1/106.9	±1.92	5.7/157.5
AlN	±1.52	34.7/48.8	±2.55	12.7/77.7
AlP	±0.85	53.7/99.0	±1.48	40.5/160.5
ZnO	±0.90	49.4/35.0	±1.11	56.5/35.1
ZnS	±0.64	54.8/87.7	±1.26	37.7/128.4
CsCl	±0.83	120.5/87.5	±0.89	116.8/95.0
CsBr	±0.81	122.5/121.2	±0.87	118.8/130.4
NaCl	±0.84	14.5/87.8	–	

cell polarizabilities (note the large positive MRSE values).

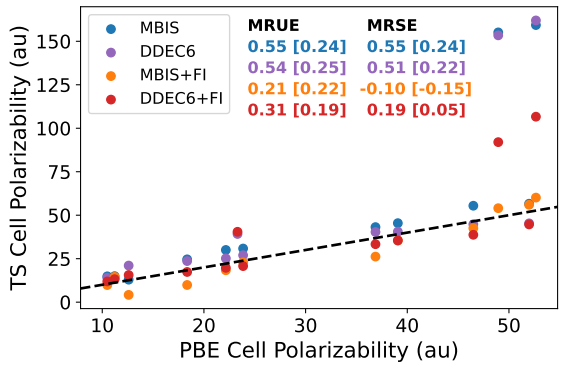

Figure 5.6: Cell polarizabilities for cubic crystals, calculated with DFT and the TS-SCS method. FI = Fractional Ions. Dashed line plots $y = x$. MR(U/S)E values in square brackets do not include CsCl and CsBr.

From Figure 5.6, we can see that using FI references significantly improves the performance of the TS model for both partitioning methods. This happens primarily through a large improvement in the predicted values for CsCl and CsBr, which are large outliers in the top right of the plot when FI references are not used (and even when they are used in the case of DDEC6 charges). Because of the significant influence of these two systems, Figure 5.6 also includes the MRUE and MRSE values when the two Cs systems are excluded from the data. In this subset of the data, FI references impart a more subtle improvement for both charge partitioning methods, as even

without fractional ions, all MRUEs are below 0.3.

In general, the FI approach reduces cell polarizabilities across the dataset, as evidenced by the decreased MRSEs for both charge partitioning schemes when FI references are used. When MBIS charges are used, the effect is an overcompensation that results in an underestimation of cell polarizabilities (MRSE = -0.1). The effect is smaller when DDEC6 charges are used, since these charges tend to be smaller in magnitude. The combination of DDEC6 charges with FI references produced the best results overall when Cs systems were excluded, with an MRUE of 0.19 and a small MRSE of 0.5. Thus, this combination seems to produce only a mild overestimation of cell polarizabilities, on average. When all systems are included, the combination of MBIS with FI references produces the best results. Furthermore, with FI references, both charge partitioning methods produced similar MRUEs to that reported elsewhere for HI charges and FI references (0.23).[44]

When working with such small sample sizes, it is difficult to conclude just which charge decomposition scheme is best. What we can say is that methods which tend to produce large ionic charges will be more strongly impacted by the use of FI references. In our limited test set, MBIS seems to be such a method. Furthermore, some systems seem particularly affected by the FI approach. In the case of CsCl and CsBr, this seems to be due to the Cs atom, which exhibits a very large drop in polarizability between its neutral and +1 state in the references we used.[45] It is difficult to generalize this phenomenon without further data, but it would seem likely that a similar sensitivity would apply to other heavy cations that are fully ionized.

5.4.3 Charge Partitioning Takeaways

In the previous two sections, we sought to better understand the sensitivity of the TS approach to the choice of charge partitioning scheme and reference atom type. From the application to small molecules, we corroborated previous reports of the importance of using an iterative charge partitioning scheme that can produce accurate partial charges for atoms involved in polar bonds. Moreover, we showed that the particular type of iterative scheme does not have a significant impact. In particular, both MBIS and DDEC6 schemes produced results of similar quality, and only slightly better than those from HI. When it comes to fractional ions, the merits of the approach seem to be system-dependent. Although the FI method has previously been shown to improve interaction energies in small molecules,[44] we found that it produced

worse molecular polarizabilities than the TS method with neutral atom references. In contrast, FI references did slightly improve the treatment of anisotropy in small molecules and the cell polarizability for cubic crystals. Thus, the merits of fractional ions should be evaluated on a case-by-case basis.

5.5 Charge Transfer-Anisotropy Correlation

In a recent work, Cheng and Verstraelen quantified the importance of charge transfer, or the fluctuations in atomic partial charges, for the polarizability of small molecules.[54] For the studied molecules, the charge transfer component of polarizability was seen to increase in importance with the number of non-hydrogen atoms and highly polarizable bonds and was also shown to be the dominant contributor to the anisotropy of the polarization response.[54] In suggesting that charge transfer be considered carefully in the development of future polarizable force fields, the authors join other works suggesting that IADs alone may not be able to fully capture polarization behavior, and especially the anisotropy of this polarization, in realistic systems.[16, 50] In the following section, we use the polarizability partitioning scheme described in Section 5.3.4 to further probe the link between anisotropy and charge transfer. We then explore the link between charge transfer and the accuracy of the TS model. Note that the partitioning scheme we adopt is different from that applied by Cheng. In particular, our definition of charge transfer includes both what Cheng refers to as "charge-flow" and "charge-dipole" contributions.[54] This difference affects the relationship between charge transfer and polarization anisotropy in ways that are discussed below.

Questions about the importance of charge transfer appear particularly relevant to the polarization behavior of nanocomposites. For matrix-inclusion type composites, a highly polarizable, potentially metallic, inclusion, is likely to exhibit significant electronic redistribution, or charge transfer, along its length in the presence of external fields. Furthermore, significantly anisotropic inclusions such as the silver rods studied in the previous chapter might display more significant charge transfer along some of the inclusion axes than others. Depending on the matrix type, the polarization behavior of the matrix might be quite different. For instance, in an ionic matrix like MgO, the lack of covalent bonding suggests a polarization picture more dominated by local dipole polarization, with electrons localized about oxygen anions polarizing within the ionic basin. Finally, there is the question of how charges redistribute

at the interface during polarization. Do they accumulate at the inclusion surfaces, or is there the potential for electrons to move to neighboring matrix atoms? Of course all of these questions will have potentially very different answers depending on the identities of the matrix and inclusion. But central to all of them is a need to understand the significance of charge transfer in various materials and to evaluate how well an IAD model without explicit fluctuating charges is able to model polarizability in the presence of these different physical mechanisms of polarization.

5.5.1 Models: Description and Characterization

In order to understand these questions, we studied the polarizabilities of Ag, MgO, SiO_2, and TiO_2 clusters and partitioned the responses into charge transfer and local dipole contributions using the scheme described in Section 5.3.4. For each cluster type, we evaluated a range of cluster sizes, depicted in Figure 5.7. These encompassed small-to-medium sized clusters, whose largest axis remained on the scale of roughly 1 nm. In particular, Ag clusters included up to 26 atoms, MgO up to 64, SiO_2 up to 48, and TiO_2 up to 30. Descriptive methods are used to quantify the role of charge transfer in each system type, and then the performance of the predictive TS model is evaluated for each of them. To round out the analysis, the same descriptive and predictive IAD approaches are also applied to the SM118 dataset of small molecules from the previous section.

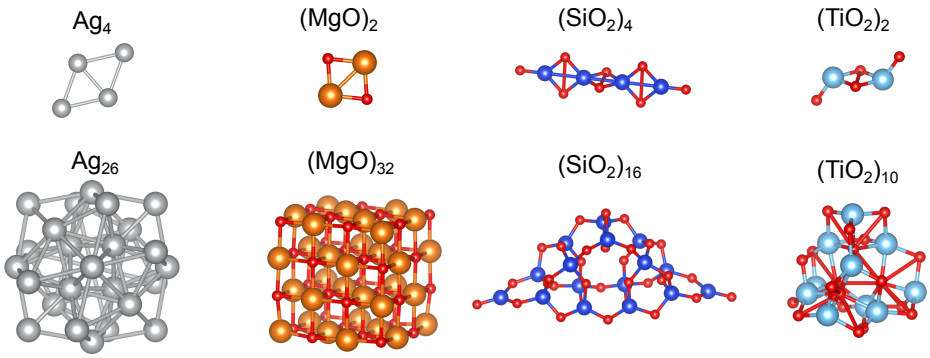

Figure 5.7: Structure of the smallest and largest of each cluster type.

The geometries for the different cluster types were obtained from various sources. Silver cluster geometries were reused from the previous chapter, where they were optimized in SIESTA at the PBE-D2 level. MgO geometries were obtained from the bulk MgO structure, by cutting along the 100, 010, and 001 planes to create

orthorhombic clusters. These were then optimized in ORCA 5 at the PBE-D4/Def2-SVP level. SiO_2 geometries were taken from Ref [62], where they were found via global optimization and refined at the B3LYP level. TiO_2 geometries were obtained from Ref [63], where they were also found through a global optimization and ultimately refined using the PBE0 functional. Figure 5.8 characterizes the trends in DDEC6 charges for each cluster type. In the ionic clusters, atom charges tend to increase in magnitude as cluster size increases, eventually leveling off for the largest studied clusters. Comparing between cluster types, the degree of negative charge on oxygen atoms increases in the order $SiO_2 < TiO_2 < MgO$. Note that the mean charges in neutral Ag clusters are very close to zero ($\sim 10^{-7}$) as they should be, indicating the accuracy of the DDEC6 integration scheme.

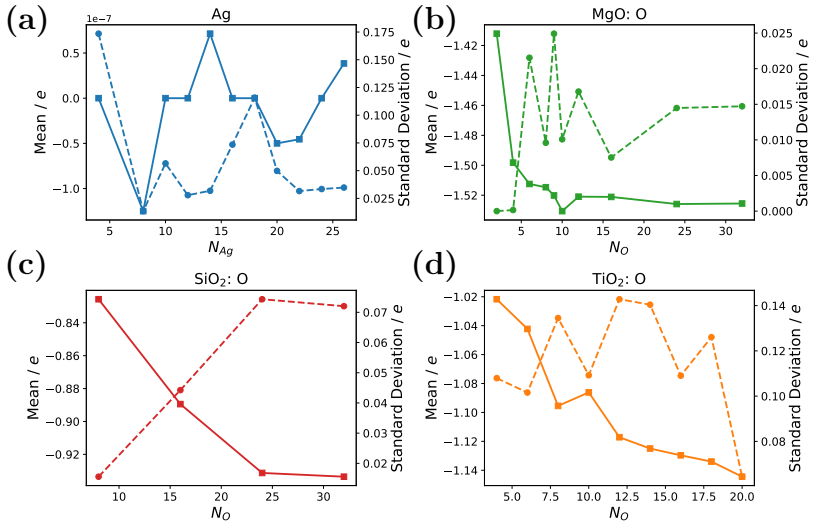

Figure 5.8: DDEC6 charge means and standard deviations for different cluster types as a function of cluster size. Solid lines depict means, and dashed lines standard deviations. Panel (a) shows the charges for Ag atoms in Ag clusters and panels (c)-(d) shows the charges of O anions in MgO, SiO_2, and TiO_2 clusters, respectively.

Single point calculations were performed on each cluster with the PBE0 functional with the RI approximation and Def2-TZVPPD basis, which was optimized for polarizability calculations.[64] The only exception to this methodology were the largest two MgO clusters [$(MgO)_24$ and $(MgO)_{32}$], for which we used the def2-TZVP basis set to avoid linear dependencies that were occurring in the RI basis when using diffuse functions. The polarizability tensor for each cluster was calculated analytically in ORCA. Figure 5.9 shows the analytically calculated isotropic polarizabilities for each

cluster. The cluster polarizabilities increase linearly with the cluster size, with silver clusters showing the steepest increase.

Polarizability tensors were also calculated numerically via finite differences with a 0.001 au field applied in the $\pm x$, $\pm y$, and $\pm z$ directions. The numerical polarizabilities were very similar to the analytical ones, with isotropic polarizabilities within 0.25% of the analytical values for all MgO clusters. In fact, this agreement was roughly 1-2 orders of magnitude better still for the Ag, TiO_2, and SiO_2 clusters. Thus, the chosen field value seems small enough to keep responses in the linear regime. The extra sensitivity to the external field in the MgO case is somewhat mysterious, though it may be related to the large negative charge of the roughly doubly charged surface oxygen anions, which are less stable in the gas phase than bulk.[45]

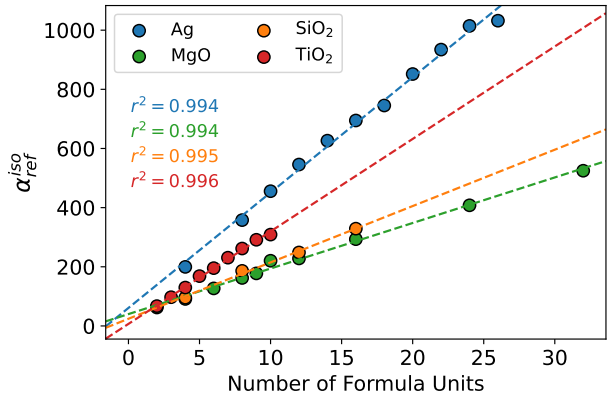

Figure 5.9: α^{iso} as a function of the number of formula units for each cluster type. The number of formula units is number of the smallest repeating net neutral units in each cluster type—that is the n in the cluster formulas Ag_n, $(MgO)_n$, $(SiO_2)_n$, (TiO_2). Dashed lines are least squares linear regression lines, with r^2 values inset.

5.5.2 Local Dipole and Charge Transfer Responses

Isotropic Polarizabilities

For each cluster and the molecules in the SM118 dataset, we computed the isotropic charge transfer polarizability α^q and local dipole polarizability α^p using the method outlined in Section 5.3.4. Figure 5.10 shows the magnitude of these two contributions relative to the total isotropic polarizability for all systems. Focusing first on the cluster response, two significant relationships are noted. First, the relative charge transfer contribution for all cluster types tends to increase with cluster size. This phenomenon has been noted previously in silicon clusters[47] and in small molecules[54].

As those previous works each used different decomposition methodologies, this trend appears to not be particularly sensitive to the specific definition of the charge transfer polarizability. Second, other than the general increase, different cluster types exhibit very different charge transfer patterns.

Qualitatively, the charge transfer patterns of Ag and TiO_2 clusters are quite similar, as are the patterns of MgO and SiO_2. Both Ag and TiO_2 show nearly equal contributions from charge transfer and local dipoles for the smallest cluster sizes. The charge transfer contribution then rapidly increases with cluster size before starting to level off, though the contribution is not actually able to converge to a constant level for the size of clusters studied. In contrast, both MgO and SiO_2 clusters exhibit mostly local dipole polarization across the entire range of clusters studied. The increase in the charge transfer contribution is much slower than for Ag and TiO_2. Thus, Ag and TiO_2 conform to a picture of having increasingly mobile charges as cluster size increases, while MgO and SiO_2 exhibit more tightly bound electrons that polarize mostly within ionic basins. The trends in charge transfer strength mirror those in the total isotropic polarizability, which increases more rapidly for Ag and TiO_2 than MgO and SiO_2 (Figure 5.9) It is worth noting that these trends do not strictly correlate with ionic charges. While MgO is the most ionic cluster type, TiO_2 is actually more ionic than SiO_2 by DDEC6 charge magnitudes (Figure 5.8) yet exhibits more charge transfer. Studying a larger selection of cluster types would be necessary to see the strength of any general correlations between ionicity and charge transfer.

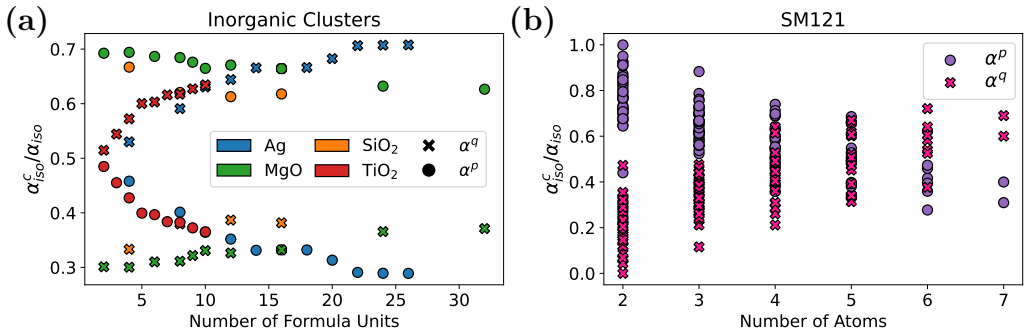

Figure 5.10: Ratio of charge transfer and local dipole contributions to total isotropic polarizability α_{iso} for (a) inorganic clusters, and (b) the SM118 dataset.

We now briefly turn our attention away from clusters and back to small molecules. As with the clusters, the SM118 dataset shows an increase in the charge transfer component as molecule size increases [Figure 5.10(b)]. Due to a diversity of atom types

across molecules, there is a significant spread in the charge transfer contribution for each molecular size. We suspect that if a dataset of small molecules were partitioned according to classes of molecules (e.g. alkanes of increasing chain length), the same clean increase in charge transfer contributions would be observed, and molecular classes could be compared by this rate of increase.[65] While we did not attempt such a partitioning, it is worth noting that we did explore the relationship between the relative charge transfer contribution and either ionicity (quantified by average DDEC6 atomic charge) or HOMO-LUMO gap. While there was a weak inverse relationship between the charge transfer contribution and ionicity ($r^2 = 0.153$), there was virtually no correlation between charge transfer and the HOMO-LUMO Gap ($r^2 = 0.003$).

Polarizability Anisotropy

We also inspected how well the anisotropy of both the charge transfer and local dipole responses aligned with the total anisotropy of the response. Cheng et al. recently demonstrated that charge transfer could qualitatively account for the anisotropy in small molecule polarizabilities.[54] Recall that the definition of charge transfer used in that work (and the method for calculating it), differs from our own. In particular, our definition of charge transfer includes what Cheng refers to as "charge-flow" and also part of what they refer to as "charge-dipole" contributions.[54] Cheng found that the charge-flow term on its own reproduced molecule anisotropy and that the charge-dipole term also pointed in the same direction but with about half the magnitude. Since our definition includes both terms, we might expect our calculated charge transfer contributions to overshoot the total anisotropy and be compensated by a local dipole contribution in the opposite direction.

Indeed, this is precisely what we see for the SM118 dataset. Table 5.2 shows the average values of $u^{\parallel}_{\text{ref}}$, $u^{\parallel}_{q}$, and $u^{\parallel}_{p}$ for the SM118 dataset and the different cluster types studied. Recall from the definition of these quantities in Equation (5.31) that if the value of $u^{\parallel}_{c}$ for a given contribution is close to $u^{\parallel}_{\text{ref}}$, this contribution's anisotropy reproduces the components of the total anisotropy. On the other hand, negative values indicate a contribution that opposes the total anisotropy. Thus, for the SM118 dataset, the charge transfer contribution does overshoot the total anisotropy by about 60% on average, but is compensated by the opposing local dipole contribution. This result indicates quite good agreement with Cheng *et al*,[54] which is significant given the different methods of calculating the response decomposition.

Table 5.2: Average charge transfer and local dipole contributions to anisotropy.

Cluster Type	$u^{\parallel}_{\text{ref}}$	$u^{\parallel}_{q}$	$u^{\parallel}_{p}$
SM118	0.037	0.059	-0.023
Ag	0.037	0.041	-0.005
MgO	0.009	0.007	0.003
SiO_2	0.033	0.029	0.005
TiO_2	0.056	0.060	-0.003

The situation is different in the inorganic clusters. For these systems, the charge transfer contribution alone tracks quite well with the total anisotropy, and the contribution from local dipole polarization is quite small across the board. This local dipole contribution generally points opposite to the total anisotropy for Ag and TiO_2 clusters but in the same direction for MgO and SiO_2. In this sense, the same pairing of cluster types appears here as we saw above for the isotropic response.

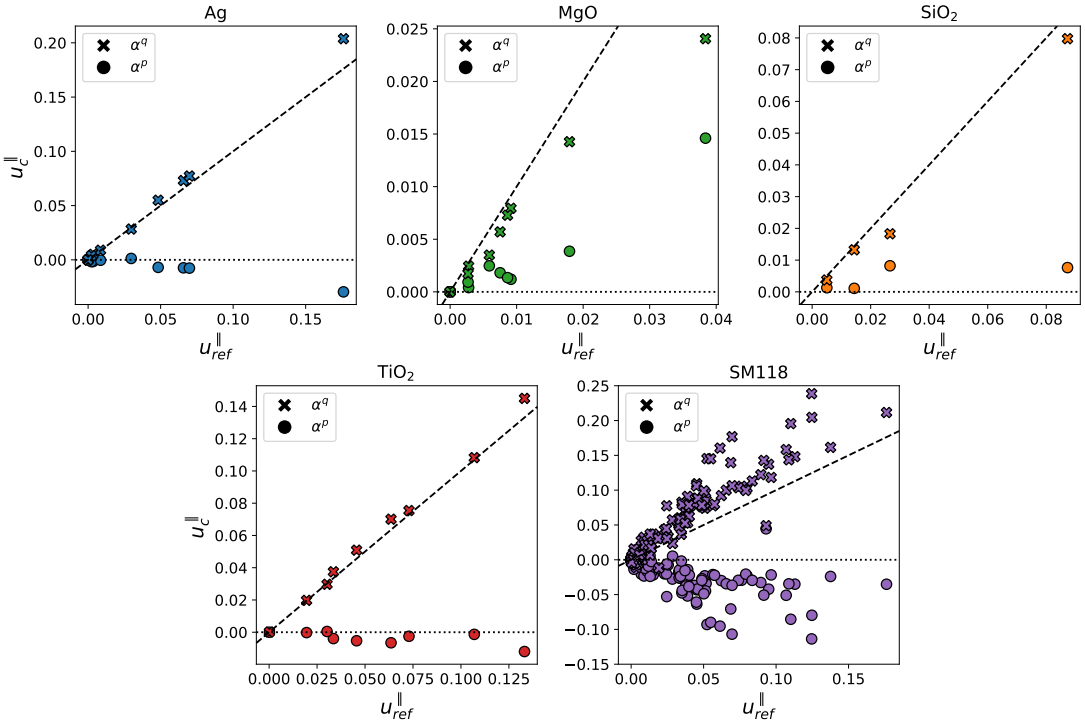

Figure 5.11: Charge transfer and local dipole contributions to anisotropy for all clusters and the SM118 dataset. The charge transfer anisotropy $u^{\parallel}_{q}$ and local dipole anisotropy $u^{\parallel}_{p}$ are plotted against the total relative anisotropy $u^{\parallel}_{\text{ref}}$. Dashed lines show $y = x$, and dotted lines show $y = 0$.

Figure 5.11 plots the $u^{\parallel}_{c}$ values against $u^{\parallel}_{\text{ref}}$ for all individual clusters and the

SM118 dataset. The results depict the same trends shown in aggregate in Table 5.2. Specifically, charge transfer anisotropy tends to align with the total relative anisotropy for all inorganic clusters and overshoots the total anisotropy for SM118. It is not immediately clear why the behavior within the SM118 dataset differs from the other clusters. The ionic nature of MgO and SiO_2 might be partly responsible for their distinct behavior, wherein the local dipole anisotropy aligns positively with the total anisotropy, but this does not account for the differences between the remaining cluster types and SM118. One possible explanation is that the clusters contain both surface and embedded atoms for all but the smallest systems, whereas the SM118 molecules contain only surface atoms. In fact, the most anisotropic Ag and TiO_2 systems at the right of their respective plots in Figure 5.11 are the smallest clusters with the fewest embedded atoms, and both show the same overshooting (though smaller in magnitude) of the total anisotropy by the charge transfer contribution as the SM118 dataset. How charge transfer is mediated by surface versus embedded atoms could be the subject of future investigation.

5.5.3 Performance of the TS Model

Isotropic Polarizabilities

We have already observed that the TS model performs quite well on the SM118 dataset, though perhaps better for predicting isotropic polarizabilities than anisotropy. Based on the above results from decomposing the response of clusters, it appears that accurately considering charge transfer effects will be important for modeling Ag and TiO_2 clusters, in particular. In addition, incorporating these effects should become increasingly important with cluster size. Since the TS model does not explicitly incorporate charge flow in the form of fluctuating atomic charges, one might predict that its performance would deteriorate for the larger clusters herein. Furthermore, since charge transfer, at least as we have defined it, accounts for much of the anisotropy of cluster response, one might also anticipate that the TS model would be inadequate for reproducing cluster anisotropy. Thus, we evaluated the performance of the TS model in these key regards.

Figure 5.12 depicts the performance of the TS model for isotropic polarizabilities when using both neutral atom and FI references. The neutral reference model performs well for both Ag and TiO_2 clusters, with mean relative errors below 5% (Table 5.3 and almost all individual errors below 5%. Interestingly, there is no noticeable

degradation in performance for these two cluster types as their size increases. Thus, the TS model appears to capture the increase in isotropic polarizability that was ascribed to increasing charge transfer in Figure 5.10. When applied to MgO and SiO_2 clusters, the TS model almost exclusively overestimates the polarizability, with relative errors of 14.3% and 19.1%, respectively.

The fractional ion approach worsens performance for all cluster types. In particular, it drastically reduces the predicted polarizability for MgO and SiO_2 clusters, reminiscent of its effect in cubic solids. However, it also results in an increase in the predicted values for TiO_2. The overall poor performance, coupled with the large effect on Ag clusters, which should not be significantly impacted by FI references, suggests that the values of the free ion polarizabilities, and not the fractional ion approach itself, may be partly to blame. For instance, the reference polarizability for neutral Ag from Ref [45] (which we use in the FI approach) is 46.2 $Bohr^3$, compared to a CCSD(T) value of 55 used in our neutral reference model.[34] A similar discrepancy exists for neutral Ti, where the value used in the FI approach (102.0 $Bohr^3$) is significantly larger than what is used in the neutral reference approach (86.9 $Bohr^3$). Thus, while reconsidering the reference values used in the FI approach would be beneficial, because of its poor performance with the current values, we restrict ourselves hereafter to the neutral reference approach.

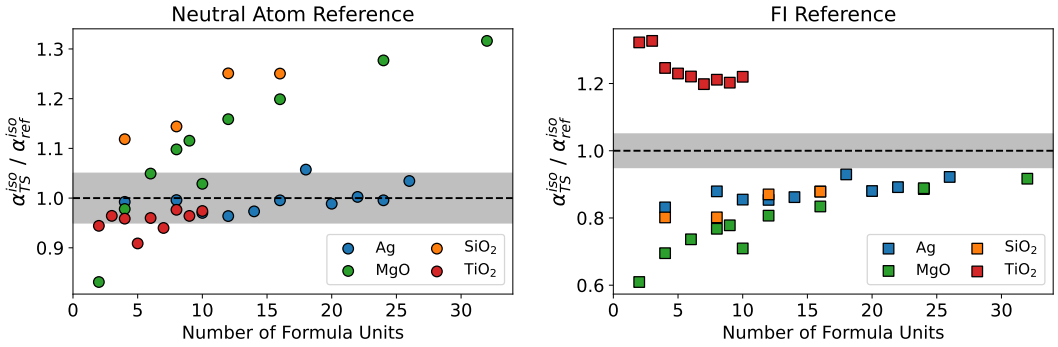

Figure 5.12: Performance of TS model with both neutral and FI references for different cluster types. Panel (a) shows the ratio of the TS-calculated isotropic polarizability to the reference istropic polarizability from DFT when neutral reference atoms are used. Panel (b) shows the same but for FI references. Grey areas highlight a ±5% margin of error for the TS model.

Polarizability Anisotropy

The relative alignment of the neutral reference TS model anisotropic polarizabilities with the reference DFT ones ($u^{\parallel}_{\mathrm{TS}}$) are depicted in Figure 5.13. In this case, the results are as anticipated based on the intuition regarding charge transfer. That is, the anisotropy is significantly underestimated in Ag and TiO_2 clusters, which were shown to be dominated by charge transfer effects. In contrast, the anisotropies of MgO and SiO_2 clusters appear to be captured reasonably well by the model (though it is worth noting that the reference anisotropies are generally smaller than for Ag and TiO_2). While there is a significant underestimation of the anisotropy of the smallest MgO cluster, there is no systematic underestimation as is observed in Ag and TiO_2.

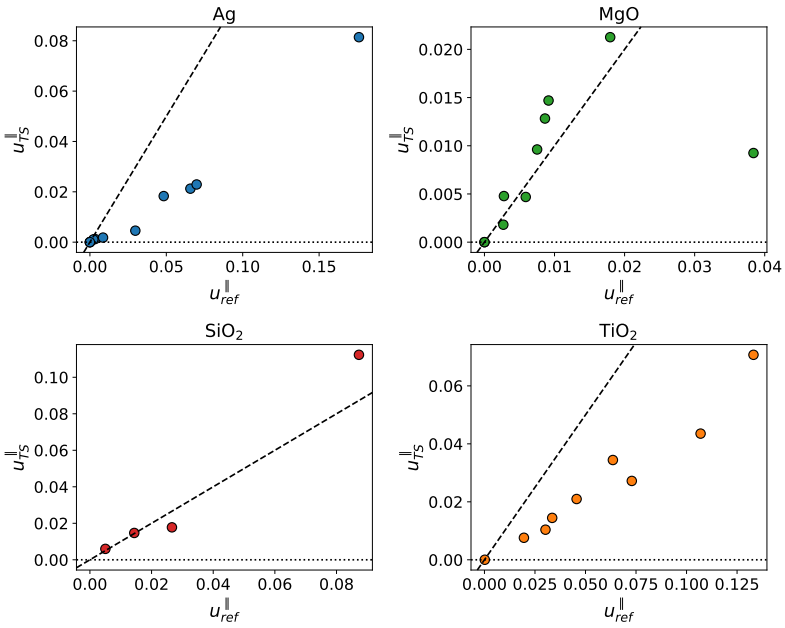

Figure 5.13: Anisotropy of the TS model. The relative alignment of the TS model anisotropy with the reference anisotropy is plotted against the reference anisotropy for each cluster type.

Taken together, the results of the TS model offer mixed support for the notion that the dipole-only model struggles to account for charge transfer effects in these clusters. The model is capable of modeling isotropic polarizabilities across the range of cluster sizes evaluated, even when charge transfer is deemed an important effect. However, the poor performance on anisotropies for the same systems suggests that by failing to model the complete mechanism of polarization (i.e. missing charge transfer), the TS model struggles to correctly model the shape of the response.

5.5.4 Optimization of Fermi Damping and α_i^{free}

Until now, we have relied on *ab initio* reference free atom polarizabilities α_i^{free} in the TS model. These references are assumed to be transferable between all systems, with the effects of differing environments accounted for by volume scaling (electronic structure effects) and self-consistent screening (geometric effects).[21, 22] As seen above, this approach yields better results for some systems than others, suggesting that volume scaling and self-consistent screening fall short in capturing some environmental effects. In these cases, using different reference polarizabilities could capture these missing effects. We note that in theory, the FI approach should accomplish some of this as well. In the following, however, we take a more direct approach by optimizing reference free atom polarizabilities for different systems.

The reference polarizabilities alone, however, cannot account for the shortcomings in the modeling of anisotropy described above. For instance, increasing the reference polarizability for Ag could potentially increase the predicted anisotropy through greater cooperative polarization along lengthened cluster axes, but this in turn would cause overestimated isotropic polarizabilities. Besides reference polarizabilities, one other handle for improving TS predictions is the Fermi function used to damp long-range interactions in the self-consistent screening procedure (Equation (5.13)). As shown in Figure 5.14, changing the parameters a and β in this function can be used to modify the onset of damping (dipole interactions are damped as this function approaches 1). Varying a changes how sharp the onset of damping is, and increasing β pushes the inflection point of this damping to further distances. β is typically optimized for different functionals (with $a = 6$ fixed) so as to improve the MBD@rsSCS dispersion energies, rather than the polarizabilities used as an input to this dispersion model. Thus, the β value optimal for computing polarizabilities is likely different than the literature values for computing dispersion energies.

Furthermore, one can imagine how this damping function might impact the anisotropy of the TS model polarizability. Since the function produces radially symmetric damping, it also has the effect of coercing the response to be more isotropic. Thus, the damping function used in the TS model offers a possible explanation for the underestimation of anisotropy in some clusters that does not rely on the concept of charge transfer. In the following, we reoptimize the reference free atom polarizabilities used for each cluster type using the Nelder-Mead optimizer in Scipy. We do this both with the standard β value for PBE0 and with a β value that is optimized concurrently.

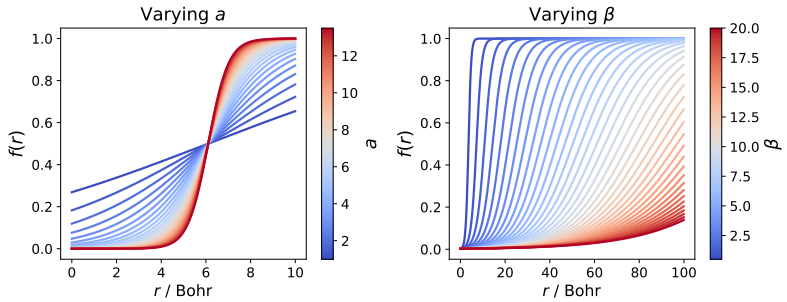

Figure 5.14: Effect of parameters in the Fermi damping function from Equation (5.13) Panel (a) shows the effect of varying the a parameter with β set to 0.85, and (b) shows the effect of varying β with a set to 6. For all plots, the sum of van der Waals radii ($R^i_{\text{vdW}} + R^j_{\text{vdW}}$) is set to 7.18 Bohr, the sum of two carbon radii in libMBD.

This optimization is performed separately for each system type, so as to minimize the MRUE in the isotropic polarizability relative to the DFT reference. When performing the optimization for the SM118 set, we removed all molecules containing elements that appeared less than five times in the dataset, to improve the robustness of the optimization. The resulting subset included 110 molecules and will hereafter be called SM110. The performance of the optimized models is displayed in Table 5.3.

Reoptimizing the reference polarizabilities alone significantly reduces the MRUE values for the isotropic polarizability of all cluster types and also brings the MRSEs closer to zero. In fact, for all cluster types except for MgO, the MRUE is brought below 5%, and all MRSEs are brought into the range ±1.5%. However, in terms of anisotropy, the performance of the optimized models are overall worse than before, with anisotropy now significantly underestimated for all system types except for SM110, where a slight overestimation using the original references has actually worsened. Also of note, for both the SiO_2 and MgO clusters, the polarizability of the oxygen anions was optimized to zero, with cation polarizabilities increasing dramatically to compensate.

Allowing the β parameter to optimize resulted in the value increasing dramatically (essentially eliminating Fermi damping) for the MgO, SiO_2, and TiO_2 clusters. As a result, we ended up fixing β to 1.0×10^6 for these three cluster types and then reoptimized the reference polarizabilities. For the Ag clusters, the optimal β value was found to be 8.52, also much higher than the original value of 0.85. As with the other cluster types, this large β value removed almost all Fermi damping, and we saw that there was only very minimal difference between using $\beta = 8.52$ or $\beta = 1.0 \times 10^6$ for the Ag clusters. For SM110, in contrast, β settled on an optimized value of 0.38

Table 5.3: Performance of TS model with different parameter sets.

Parameter Set	System	β	MPUE(α^{iso})[a]	MPSE(α^{iso})[b]	$\langle u^{\parallel}_{\text{ref}} \rangle$	$\langle u^{\parallel}_{\text{TS}} \rangle$
Original	Ag	0.85	1.99	-0.28	0.37	0.14
	MgO	0.85	14.33	10.51	0.009	0.008
	SiO_2	0.85	19.10	19.10	0.033	0.038
	TiO_2	0.85	4.55	-4.55	0.56	0.25
	SM110	0.85	6.64	-3.25	0.037	0.040
Reopt α^{free}	Ag	0.85	1.79	0.19	0.37	0.14
	MgO	0.85	9.08	-0.77	0.009	0.002
	SiO_2	0.85	1.96	-1.43	0.033	0.026
	TiO_2	0.85	1.29	-0.51	0.56	0.22
	SM110	0.85	4.68	-1.05	0.037	0.044
Reopt α^{free} and β	Ag	8.52	1.06	-0.08	0.037	0.031
	MgO	10^6	8.71	-0.26	0.009	0.012
	SiO_2	10^6	0.97	0.43	0.033	0.053
	TiO_2	10^6	0.68	-0.01	0.56	0.50
	SM110	0.38	4.40	-0.35	0.037	0.019

[q] Mean Percent Unsigned Error. Equal to MRUE $\times$ 100.
[b] Mean Percent Signed Error. Equal to MRSE $\times$ 100.

(increased damping relative to the original).

Using optimized β values combined with reoptimized reference polarizabilities further improved the performance for the isotropic response for each system. Examining Table 5.3, we see that the MRUEs for both SiO_2 and TiO_2 are reduced to below 1% and the MRUE for Ag to 1.06%. MRSEs are also universally small in magnitude. Moreover, the reoptimization of β had a significant effect on the anisotropic responses of all system types. In particular, the anisotropies of Ag and TiO2 clusters were brought considerably more in line with the reference values, while also allowing a slight improvement in the isotropic response. This is remarkable, considering only the MRUE of the isotropic polarizability was minimized in the optimization procedure. For SiO_2, the anisotropy did increase with β, but it overshot that of the reference significantly, whereas for for SM110 the anisotropy was overshot in the opposite direction with the decrease in β.

The reoptimized reference polarizabilities from these adjusted-β models are given in Table 5.4, alongside the original values. Because β is a damping parameter, opti-

mizing it alongside a reference polarizability will generally result in the two moving in opposite directions. For both Ag and SiO_2, the increase in β (effective removal of damping) resulted in a drop in the optimal reference polarizabilities for all atoms. For TiO_2, there was also a drop in $\alpha_{\mathrm{Ti}}^{\mathrm{free}}$, but it was accompanied by a slight increase in relatively smaller $\alpha_{O}^{\mathrm{free}}$. For the SM110 dataset, most polarizabilities increased slightly to counteract the decrease in β. For MgO, the optimization still produced an essentially null reference polarizability for O.

Table 5.4: Reoptimized reference atomic polarizabilities (Bohr^3).

Element	Original	Optimized Values				
		Ag	MgO	SiO_2	TiO_2	SM110
H	4.50					4.04
Li	164.78					188.43
B	20.42					18.68
C	11.63					11.82
N	7.21					8.35
O	5.15		9×10^{-6}	3.81	5.61	6.11
F	3.62					4.10
Mg	72.06		109.97			
Si	37.16			28.03		32.92
P	24.88					26.95
S	19.22					20.62
Cl	14.43					15.56
Ti	86.92				75.97	
Ag	55.00	52.96				

Figures 5.15 and 5.16 show the performance of the models with co-optimized reference polarizabilities and β for isotropic and anisotropic polarizability, respectively. While these mostly are summed up well by the mean value descriptors in Table 5.3, the poor performance for the isotropic polarizability of MgO is particularly glaring in Figure 5.15(a). Even after optimization, the TS model underestimates polarizability for small clusters and overestimates it for large ones. One interpretation is that the TS model is simply not able to account for the rapidly changing environmental effects as these clusters increase in size. However, further investigation should also be done to understand the reliability of the reference polarizabilities for these clusters in gas phase. For instance, special charge compensation methods are often used to calculated the polarizability of doubly-charged anions in the gas phase,[36] and it is

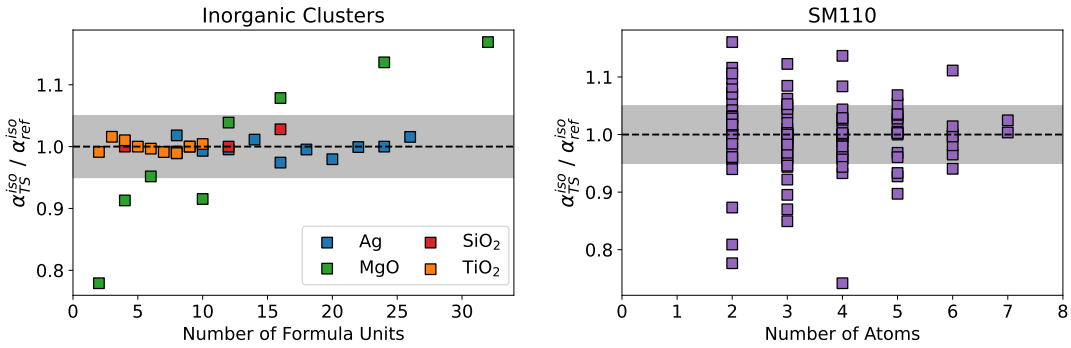

Figure 5.15: Performance of TS models for isotropic polarizabilities using reoptimized neutral reference polarizabilities. Panel (a) shows the ratio of the TS-calculated isotropic polarizability to the DFT reference for different inorganic clusters. Panel (b) shows the same for the SM110 dataset. Grey areas highlight a ±5% margin of error for the TS model. For inorganic clusters, β was set to 10^6, whereas for SM118, β was optimized to 0.37.

possible these MgO clusters may also require such special attention.

5.5.5 Takeaways About Charge Transfer and the TS Model

In the above section, we scrutinized the link between charge transfer, captured via descriptive IAD partitioning of the *ab initio* response, and the performance of the predictive TS model. Examination of four classes of inorganic clusters and the SM118 database demonstrated that charge transfer plays an increasingly important role as clusters—or molecules—increase in size. Moreover, charge transfer seemed to largely account for the anisotropy of the response in all cluster types, though its effect is matched with a compensatory local dipole response in the SM118 dataset.

The relative importance of charge transfer in different cluster types also seems to correlate well with performance of the TS model. For Ag and TiO_2, where charge transfer dominates, the "out-of-the-box" TS model performed well for isotropic polarizabilities but underestimated anisotropy. The opposite occurred for the local-dipole-dominated MgO and SiO_2, for which isotropic polarizabilities were significantly overestimated while reference anisotropy was generally reproduced.

Reoptimization of TS reference polarizabilities and the β damping parameter highlighted the crucial role of long-range damping on the anisotropic response of the TS model. By effectively removing this damping, the anisotropy of charge transfer dominated clusters was recovered. While anisotropy was still not well-reproduced in the SiO_2 and SM110 datasets, we note that we only optimized for performance on

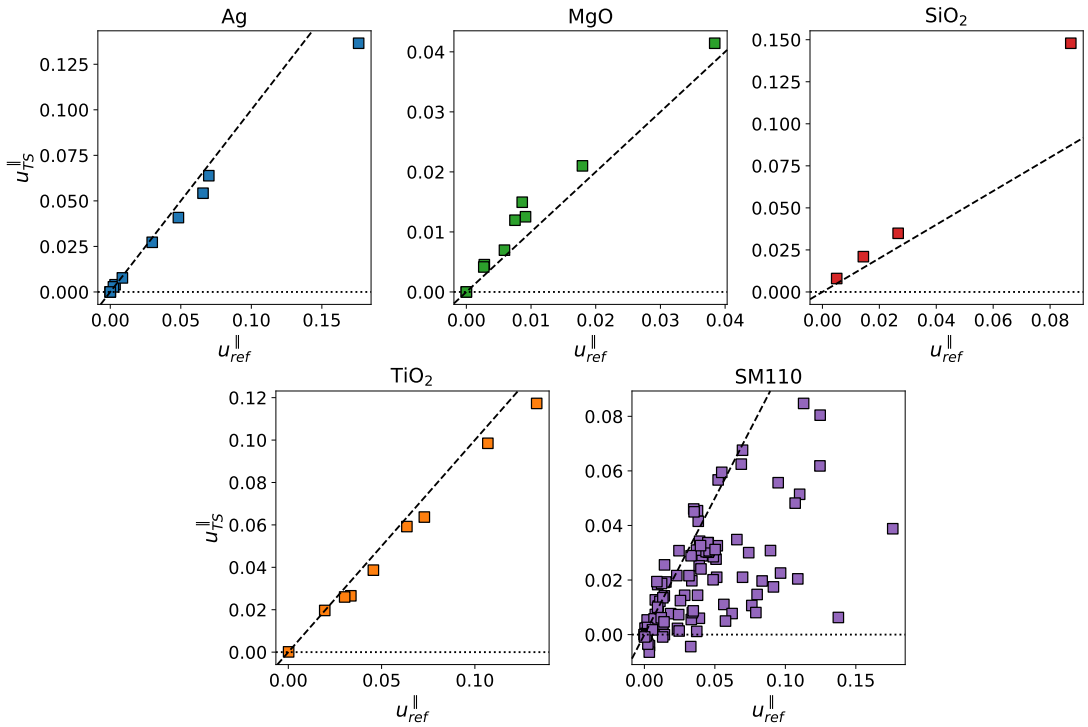

Figure 5.16: Anisotropy of the reoptimized TS model. The projection of the TS model anisotropy onto the reference anisotropy is plotted against the reference anisotropy for each cluster type and for the SM118 dataset after optimization of reference polarizabilities.

isotropic polarizabilities. Optimization for correct reproduction of the entire polarizability tensor would result in some degree of compromise between isotropic and anisotropic response, though this compromise might well be quite small. It is interesting to note that the cluster types more dominated by charge transfer (Ag and TiO_2) seem to require no such compromise, which is somewhat surprising given the lack of charge transfer in the TS model. Thus, for the cluster sizes considered, charge transfer effects appear to be mostly treatable under the TS approach to inducible dipoles, provided long-range damping is eliminated. Finally, it is worth noting that the TS model performed rather poorly for MgO clusters compared to the other systems, which warrants further investigation.

A brief discussion about the meaning of charge transfer polarizability as we have defined it is warranted. The charge transfer dipole moment, and therefore the charge transfer polarizability, contain information about the geometry of the system via their dependence on the atomic positions (Equation (5.18)).[66] Thus, the increasing importance of charge transfer with cluster size or the number of atoms in small molecules is

not altogether surprising. Even if the actual charges being transferred between atoms are small and remain so for increasing system sizes, increasing the average distance of the atoms from the centroid of the system will increase the relative contribution of charge transfer polarizability.[46, 65] Similarly, the strong correlation between the charge transfer polarizability anisotropy and the total polarizability anisotropy can be largely explained by geometric dependence of the charge transfer dipole. Essentially, the charge transfer dipole moment encodes the structural anisotropy of the system via its dependence on atomic positions, and the structural anisotropy is unsurprisingly a determining factor of the polarizability anisotropy.[66]

Thus, directly comparing the importance of charge transfer polarizability between two systems takes on a more precise meaning when the two systems have approximately the same dimensions. In such a case, the geometric dependence is removed and what is being assessed is more akin to the magnitude of charge flowing between atoms. In this sense, the comparisons above between cluster types do seem to indicate actual differences in the tendency of electrons to transfer between atoms as opposed to remaining tightly bound, in that TiO_2 and Ag clusters have larger contributions from charge transfer than SiO_2 and MgO clusters of similar sizes.

This understanding of the geometric contributions to charge transfer dipole moments provides some justification for why the TS model still seems to perform well for systems with large charge transfer polarizabilities. Specifically, for geometries that are long in the direction of polarization, the total charge transfer dipole may be large even if the changes in individual atomic charges are quite small. Indeed, the magnitude of the changes in atomic charge should be the more important factor than a global charge transfer descriptor when determining whether a polarizability model that neglects explicit charge transfer is appropriate. Thus, there is an argument to be made that it may be more instructive to simply compare the magnitude of the charges transferred rather than the charge transfer dipole moment or polarizability when assessing the importance of charge transfer in polarizable force fields.

5.6 Pentagonal Silver Nanorods

Based on the above results with inorganic clusters and SM110, it is clear that systems with static responses dominated by charge transfer can still be effectively modeled with the TS model. Even the anisotropic part of α can be reproduced when the TS model and associated damping functions are appropriately parameterized. However,

it is reasonable to assume that there would still be a threshold for charge transfer above which the IAD picture breaks down. For instance, metallic nanoparticles, where free charges can oscillate over the entire lengthscale of the nanoparticle, polarize in a manner physically distinct from molecules and molecular-scale nanoparticles with charges bound to nuclei.[67] It follows that an IAD model parameterized for the latter would struggle in simulating the former. In this section, we investigate systems in between these two regimes.

Silver nanorods display useful anisotropic optical properties that can be tuned by carefully engineering rod dimensions. In particular, pentagonal nanorods have absorption wavelengths and intensities that depend linearly on the rod length.[68, 69] As we will show, increasing the rod-length also leads to a super-linear increase in the isotropic and longitudinal static polarizabilities for these rods. Thus, these systems provide a good chance to assess of the TS model's ability to reproduce cluster polarizability over a broad range of anisotropy and, as will be seen, charge transfer values. In particular, we will see that the magnitude of charge accumulated at the ends of these rods when they are polarized increases with rod length and affects the performance of the TS model.

We simulated pentagonal Ag nanorods with 13, 19, 25, 31, 37, 43, 49, and 55 atoms, which have between 3 and 10 core Ag atoms. In past studies, the absorption spectra of these rods have been evaluated with a +1 charge (among other charge states), to allow a closed-shell treatment and avoid Jahn-Teller distortion that arises in the 31-, 37-, 49-, and 55-atom rods.[68, 69] Here, we studied both neutral (doublet) and +1 (singlet) charge states for all rods. The geometries of these rods were optimized at the BP86-D3(BJ)/def2-SVP level, and polarizabilities were calculated by solving coupled-perturbed SCF equations in ORCA at the PBE0/def2-SVPD level. The polarizabilities at the PBE0 level showed only very mild basis set dependence, with the def2-SVPD α^{iso} values differing from def2-TZVPPD α^{iso} values by less than 1 percent for the clusters with up to 25 atoms.

The response of both neutral and charged rods is dominated by charge transfer. Figure 5.17(a) shows the longitudinal polarizability (field oriented along the long axis) of these nanorods decomposed into charge transfer and local dipole components. For all but the shortest rod in each charge state, the relative contribution of the charge transfer component α^q sits above 80%, rising as high as 94% for the longest rods.

Because our definition of charge transfer dipoles is origin-dependent, changes in the charge of atoms toward the ends of rods will contribute increasingly to α^q for

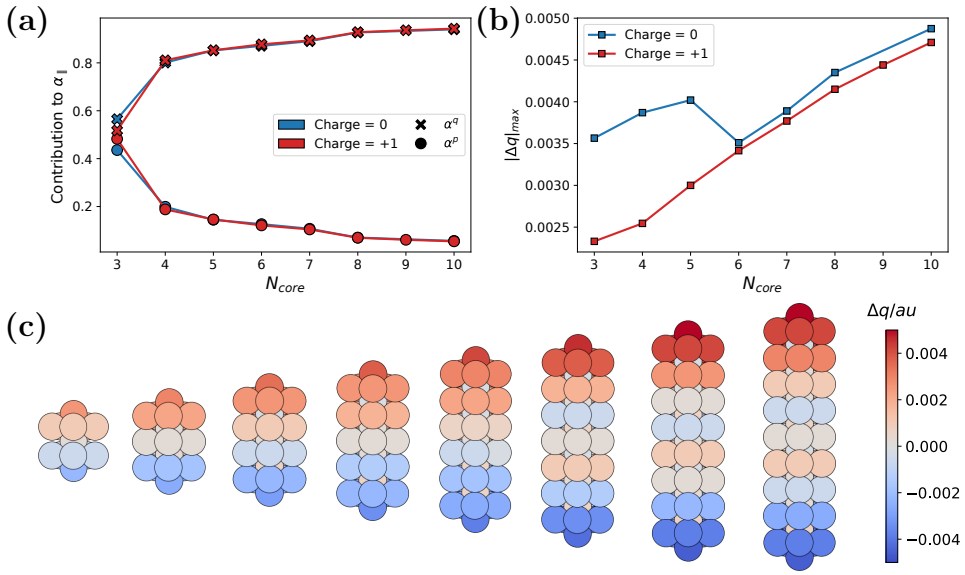

Figure 5.17: Charge transfer contributions to longitudinal rod polarizability. Panel (a) shows the longitudinal polarizability $\alpha_{\parallel}$ decomposed into charge transfer α^q and local dipole α^p contributions for both neutral and positively charged rods as a function of the number of core Ag atoms in a rod. The neutral Ag_{49} rod ($N_{\text{core}} = 9$) is omitted due to difficulies converging SCF procedure in an external field. Panel (b) shows heatmaps of the change in QTAIM charge on each atom between external field states of $\pm 1.0 \times 10^{-4}$ au for the positively charged rods.

longer rods due to their large distance from our chosen origin at the nanorod center of mass. However, the magnitude of charge transfer in end atoms also increases for longer rods. Figure 5.17(b) shows the maximum change in the QTAIM charge of atoms ($|\Delta q|_{\text{max}}$) between external fields of $\pm 1.0 \times 10^{-4}$ au along the long nanorod axis. These maximum changes correspond to the two end atoms of each rod. $|\Delta q|_{\text{max}}$ increases monotonically for positively charged rods as rod length increases. On the other hand, neutral rods show a sharp decrease in $|\Delta q|_{\text{max}}$ for the Ag_{31} rod, perhaps related to the symmetry-breaking Jahn-Teller distortion which first appears at this rod length in the neutral rod series.

It is worth noting that while charge transfer is important to the response of these rods, the actual magnitude of charge that builds up on either end of the rods is quite small, rising only to about 0.005 e for the longest rods studied. Furthermore, charge is not necessarily transferred uniformly along the rod length. As shown in Figure 5.17(c), although charge does accumulate primarily at rod ends, application of an external fields results in oscillations of the electron density along the rod length for rods with greater than 7 core electrons. This quantum effect would not be captured

by an IAD model. However, it does not appear to have a significant effect on the polarizability of these longer rods, as the rod polarizability and α^q increase smoothly throughout this transition in charge transfer behavior.

The TS model was tested on these rods, using the reference free Ag polarizability (52.86 Bohr^3) that was optimized for the small silver clusters in the previous section and a large β value of 10^6, Thus, long-range damping was effectively removed. Figure 5.18(a) shows the the ratio of isotropic polarization of the rods calculated by the TS model ($\alpha^{\text{iso}}_{\text{IAD}}$) to that calculated by DFT ($\alpha^{\text{iso}}_{\text{ref}}$). There is a monotonic decrease in this ratio with rod length for both neutral and positively charged rods. In the case of neutral rods, the smallest three rods in the series are treated adequately by the TS model, but for all longer rods the TS model underestimates α^{iso} by more than 5%. On the other hand, the TS model overestimates the polarizabilty of short, positively charged rods, but still underestimates the polarizability of all rods with more six or more core atoms. These results demonstrate that the TS model is incapable of capturing the isotropic polarizability across a broad range of particle anisotropies, which is likely attributable to the neglect increasing charge transfer effects across this range. Furthermore, they show that the TS model performance is sensitive to the charge state of the rods. Reference free atom polarzabilities that account for charge state, such as the FI approach, could be used to ameliorate this dependence.

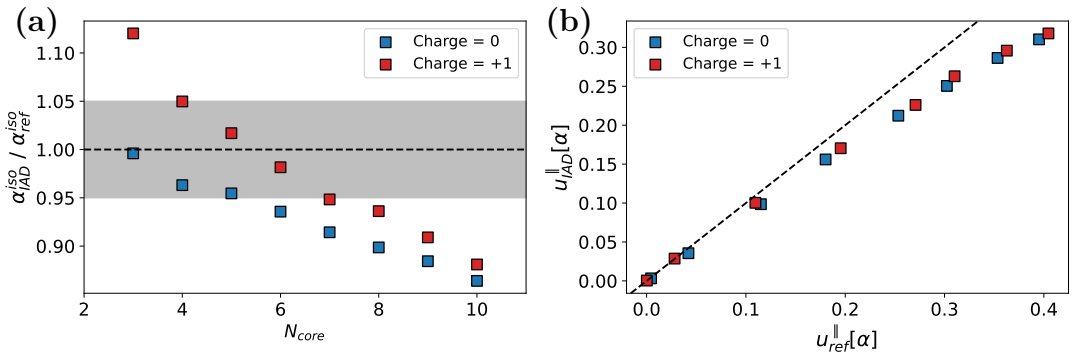

Figure 5.18: Comparison of DFT and TS models of polarizability for both neutral and positively charged pentagonal Ag rods. Panel (a) shows the ratio of isotropic polarization of the rods calculated by the TS model ($\alpha^{\text{iso}}_{\text{IAD}}$) to that calculated by DFT ($\alpha^{\text{iso}}_{\text{ref}}$). A 5% margin of error is highlighted in grey. Panel (b) shows $u^{\parallel}_{\text{IAD}}[\alpha]$ plotted against the DFT anisotropy $u^{\parallel}_{\text{ref}}[\alpha]$. The dashed line shows perfect parity ($y = x$). This shows the degree to which the TS model captures the anisotropy of the DFT response. Both panels include two charge states for each rod, neutral and +1.

Figure 5.18(b) shows how well IADs model the anisotropy of nanorod polarizability by plotting $u^{\parallel}_{\mathrm{IAD}}[\alpha]$ against $u^{\parallel}_{\mathrm{ref}}[\alpha]$. Because the rods increase in anisotropy of α as they increase in length, the data points going from left to right move from shorter to longer rods. Thus, we can see that for the three shortest rods, up to Ag_{25}, the TS model anisotropy aligns quite well with the DFT reference. However, the TS model performs increasingly poorly as rod length increases beyond this, with the TS anisotropy falling short of the reference. Interestingly, the charge state did not seem to significantly affect the performance of the TS model for this property.

To better understand the shortcomings of the anisotropic TS model response, we can inspect how well it separately reproduces the longitudinal and transverse polarizabilities of these rods–$\alpha^{\parallel}$ and $\alpha^{\perp}$, respectively. Figure 5.19 shows α^{iso} alongside these two components of the polarizability, as calculated by DFT and the TS model. In addition, we reoptimized the free atom reference polarizability for Ag (while keeping $\beta = 10^6$) to minimize the MRUE of α^{iso} for all rods. Values of 60.48 and 54.76 Bohr^3 were found to be optimal for neutral and positive rods, respectively. These results are displayed in Figure 5.19 as α_{IADr}. Reoptimizing this parameter significantly reduced the MRUE for $\alpha^{\parallel}$ and α^{iso} for neutral rods and to a smaller degree for positively charged ones, though it increased the error for $\alpha^{\perp}$ for both charge states. Regardless of which parameters were used, however, the TS models increasingly underestimated $\alpha^{\parallel}$ for longer rods. Furthermore, while reoptimizing the free atom polarizability improved this fit somewhat, it resulted in an overestimation of $\alpha^{\perp}$. Finally, the reoptimized TS model underestimates α^{iso} for large rods and overestimates it for short ones.

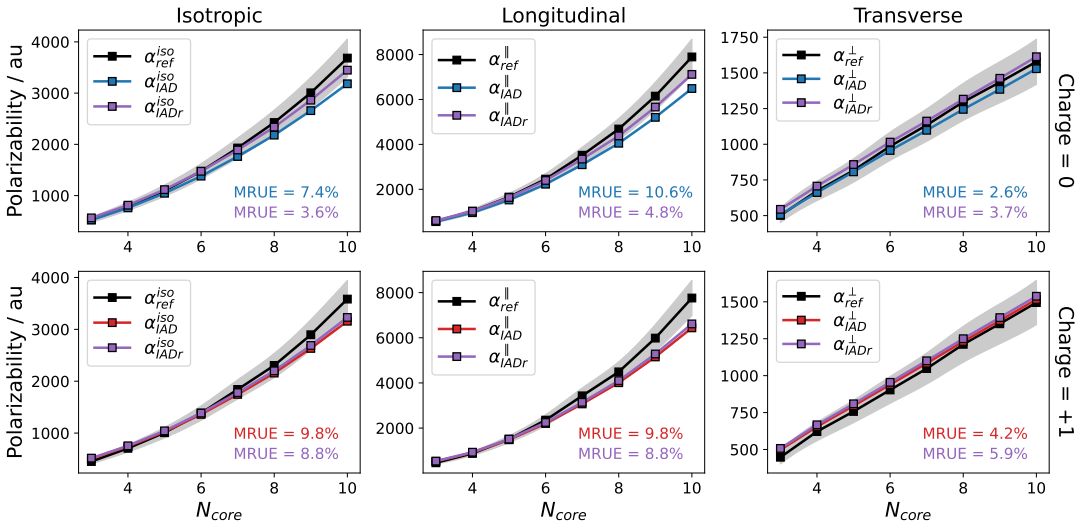

Figure 5.19: TS model performance for the different polarizability directions of Ag rods. Top and bottom rows show neutral and charged rods, respectively. Left, middle, and right columns show α^{iso}, $\alpha^{\parallel}$, and $\alpha^{\perp}$, respectively. TS model (IAD) and reoptimized reference TS model (IADr) models are both shown and their MRUEs are inlaid for each component of α. Grey areas show the region of $le10\%$ error about the reference polarizabilities.

The above results demonstrate that the TS model does a poor job generalizing across large ranges of charge transfer and/or anisotropy. However, one may still question whether this is an effect of the particular damping function employed in the TS model, rather than an invalidation of IAD models in general for systems with large charge transfer components. Indeed, changing to a different damping function does allow us to greatly improve upon the TS model results for these Ag nanorods. In Figure 5.20, we show the results for the Tinker Thole-style IAD model (denoted IADt) described in Section 5.3.2 applied to positively charged Ag nanorods. We fit two model parameters–the polarizability of Ag atoms α_{Ag}, and the damping parameter a–to minimize the MRUE of $\alpha^{\text{iso}}_{\text{IADt}}$. The optimized values were found to be $\alpha_{\text{Ag}} = 44.719$ Bohr^3 and $a = 0.753$. It is worth noting that this model requires no volume scaling of the atomic polarizability based on charge density or other properties of the chemical environment. Nevertheless, the optimized IADt model yields significantly lower MRUE values than the IADr model above. Furthermore, the model demonstrates consistently low relative errors across both longitudinal and transverse polarizability modes and across all nanorod lengths. As a result, we conclude that with the right approach to damping, even very anisotropic polarizabilities with large

charge transfer contributions can be modeled with IADs.

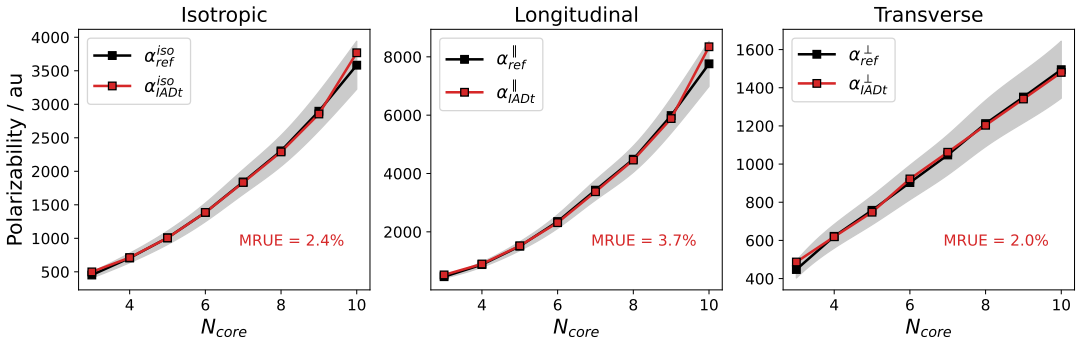

Figure 5.20: IADt performance for the different polarizability modes of positively charged Ag rods. MRUEs are inlaid for each component of α. Grey areas show the region of $\leq 10\%$ error about the reference polarizabilities.

It is important to note that we did not explore a reoptimization of the a parameter in the TS damping function, which is set to 6.0 for TS-SCS dispersion corrections but need not be fixed for our application. This parameter would provide another handle for optimization within the TS scheme that might bring the IADr results in line with the IADt model. Thus, we cannot say definitively that the volume scaling TS approach underperforms fixed-polarizabity alternatives. However, we can say that the fixed-polarizability Thole scheme offers impressive accuracy (MRUE $< 3\%$) over a broad range of particle anisotropies when properly parameterized.

5.6.1 Takeaways from Ag Nanorods

The studied Ag nanorods highlighted the sensitivity of TS model performance to both cluster charge and charge transfer effects. In particular, the TS model had a single fit parameter, the free atom polarizability of neutral Ag, fit to isotropic polarizabilities of relatively isotropic clusters with up to 26 Ag atoms. This model performed well for neutral rods of up to 25 atoms while overestimating the polarizability of positively charged rods of the same small size. The same model underestimated both the isotropic and anisotropic polarizabilities of larger rods regardless of charge. Reoptimizing the single fit parameter to reproduce rod polarizability improves overall accuracy but leads to an imbalanced treatment of the polarizability for short and long rods. The inability of an TS model to accurately treat the entire range of rod sizes is ascribed to the increasing charge transfer contribution to polarizability as rod length increases, which is neglected in the TS approach, combined with the specific charge

distribution model that leads to short-range damping. As others have mentioned, charge transfer contributions can be incorporated into IAD models via fluctuating charges,[12] or the anisotropy of the response can be modeled more directly by incorporating anisotropic atomic polarizabilities.[50]

5.7 Embedded Cluster Model of Nanocomposite Oxide

In this final section, we explore how the tools of descriptive and predictive IADs can be applied to composites through the use of embedded cluster models. To some extent, these approaches can also be used directly in periodic calculations—charge density partitioning and the mutual polarization of classical IADs are still valid under periodic boundary conditions. However, our approach to decomposing the response into atomic dipole and charge transfer contributions would require modification to treat atomic basin boundaries and charge transfer that cross periodic cell boundaries (Bader[70] gives a discussion of how this might be accomplished). In the following section, we examine an embedded cluster model of the MgO matrix with molecular Ag_8 inclusion that has been treated extensively in previous chapters. We note that the development of the embedded cluster approach is still ongoing, and the work presented here represents the first stages of investigation.

5.7.1 Finite Field Calculations

One of the goals of an embedded cluster model is to reproduce the behavior of a periodic nanocomposite model while allowing different computational approaches and facilitating different ways to analyze the electronic structure.[71] To better understand the correspondence between the embedded cluster and periodic models, we performed finite-field polarizability calculations on three types of models: embedded cluster models, gas phase cluster models, and full periodic boundary models. For each model type, we performed a calculation for both pure MgO and the now familiar $(MgO)_{104}Ag_8$ composite.

The polarizabilities of cluster models were calculated in Orca 5 at the PBE/def2-SVP level. A Stuttgart effective core potential (28 core electrons) was used for Ag, while all electrons were treated explicitly for Mg and O. We determined the polarizability using a finite difference calculation with a ± 0.001 au external field. As

all systems were isotropic, the finite difference calculations were performed only for the z-direction for each cluster. The resulting cluster polarizabilities are labeled α^{iso}. The cluster response was partitioned into local dipole and charge transfer components according to the method described in Section 5.3.4.

For periodic calculations, we used the CPMD module of Quantum Espresso. The PBESol functional was employed because of its accurate prediction of equilibrium structures of solids.[72] Furthermore, we used optimized norm-conserving Vanderbilt effective core potentials for all elements, which replaced the inner 2, 2, and 28 core electrons of O, Mg, and Ag respectively. The plane wave cutoff was set to 70 Ry for the wavefunction and 280 Ry for the charge density. The cell polarization was calculated under the conditions of no applied field and with a 0.001 au homogeneous macroscopic electric field applied in the z-direction. The cell polarizability was calculated from the resulting permittivity via the Clausius-Mossotti relation (Equation (5.32)).

5.7.2 Defining the Embedding Model

Figure 5.21(a) shows the scheme that we followed for building the embedding model. The scheme is inspired by an approach by Puchin *et al.* to incorporate environmental polarization into embedding models[73] and that described by Shi *et al.* to model oxygen vacancies in metal oxides.[74] The primary goals of this model are to mimic the electrostatics of the crystal environment and eliminate charge leakage into the vacuum from oxygen anions at the cluster surface, thus reducing surface effects from a finite model. To accomplish this, we employed a three layer approach, whereby a core of fully quantum mechanical atoms is surrounded by a layer of "capped" Effective Core Potentials (cECPs) and then further layers of Point Charges (PCs) to model the crystal environment.[74] In our model, a 216-atom quantum core was surrounded by a single layer of cECPs, where Mg and O ECPs were "capped" with ionic charges of ± 2 for Mg and O, and then three layers of point charges with ± 2 charge. The coordinates of the quantum core were taken from a periodic structure optimized with a CPMD (PBESol) calculation, and sites of cECPs and PCs were determined by adding layers at spacings of the average inter-layer spacing present in the quantum core. In order to allow the cluster environment to polarize consistently with the cluster itself, we added a polarizable continuum background outside of the cECP layer (overlapping the PCs) using the CPCM model, with $\epsilon = 3.61$, the value obtained from the CPMD calculation of ϵ^{∞} for the composite. In addition to the MgO/Ag composite, we also performed

calculations on an embedded cluster of pure MgO, in which ϵ for the surrounding CPCM region was set to 3.0.

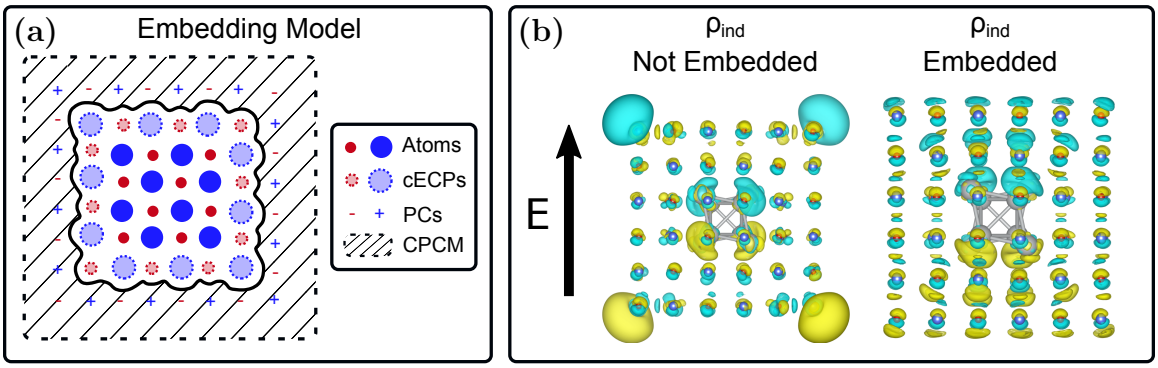

Figure 5.21: Embedded cluster model in an external electric field. Panel **(a)** schematically shows an embedded cluster. Panel **(b)** shows the electron density change ρ_{ind} induced by an external field for gas phase (left) and embedded (right) cluster models. The 0.0002 e isosurfaces are plotted, with yellow showing accumulation of electrons and blue depletion.

To contrast with the embedded model, we also examined the same structures in gas phase. Figure 5.21(b) depicts the change in electronic density ($\rho_{\text{ind}} = \rho(E_+) - \rho(E_-)$) between the $E_- = -0.001$ au and $E_+ = 0.001$ au applied field states for both the gas phase and embedded MgO/Ag clusters. In the gas phase cluster, there is some buildup of charge at the interface between Ag and MgO. More importantly there is a very large redistribution of electrons, or charge transfer, between the cluster's corner Mg cations. This phenomenon is effectively damped by the cECP shell in the embedded model, leading to more typical dipole-like charge redistribution about each ion with some larger charge buildup at the surface Ag atoms.

5.7.3 Comparing the Embedded Cluster and Other Models

Before examining the polarization behavior of the embedded cluster, let us first consider how well the different cluster models reproduce the periodic model's electronic structure by examining the charge distribution in each model. To do so, we calculated the DDEC6 charges and third radial moments for all atoms in both the periodic and cluster models. Table 5.5 shows the MRUEs for the cluster model atomic charges and radial moments relative to the periodic ones. Interestingly, the embedded composite model shows larger deviations from periodic model values than its gas-phase counterpart for both charges and moments. Note that the charges for the pure MgO

Table 5.5: Characterization of Models for MgO and MgO / Ag_8 Composite.

System	Model[a]	MRUE Q	MRUE $\langle r^3 \rangle$	$\alpha^{\mathrm{iso},p}$	$\alpha^{\mathrm{iso},q}$	α^{iso}
Pure	GP	0.07	0.08	1510	378	1888
	EC	–	–	1269	188	1457
	PBC	–	–	–	–	1259
Comp	GP	0.05	0.07	1375	2528	3903
	EC	0.15	0.16	1353	558	1911
	PBC	–	–	–	–	1563

[a] GP: Gas Phase, EC: Embedded Cluster, PBC: Periodic Boundary Conditions.

embedded model could not be obtained, as the DDEC6 procedure did not achieve its required integration accuracy for this system. However, the MRUEs for the gas phase cluster are comparable to the composite.

Embedded Clusters vs. Gas Phase Clusters

Table 5.5 also shows the calculated polarizability and, for the clusters, the contributions from local dipoles and charge transfer. For both embedded and gas-phase calculations, pure MgO clusters have responses dominated by local dipoles, which is consistent with our earlier analysis on smaller systems in Section 5.5.2. Furthermore, the effect of embedding is significant, causing both the overall polarizability to decrease by about 23% and the relative contribution of charge transfer to drop by about 7%. The decrease in overall polarizability can be rationalized by the increased confinement of the cluster by the cECP shell, which restricts polarization into the vacuum region. It is also worth noting that the total embedded cluster polarizability α^{iso} falls closer to the periodic cell polarizability than the gas phase cluster value.

When comparing pure MgO to composite clusters, introduction of the Ag inclusion causes the relative contribution of charge transfer to increase. This increase is unsurprising given that earlier, we found Ag cluster response to be dominated by charge transfer (Section 5.5.2). Moreover, the effect of embedding is much more dramatic for the composite clusters than for pure MgO. For the composite clusters, the polarizability of the embedded model is over 50% lower than the polarizability of the gas phase model. This suppression of polarizability in the embedded model comes almost entirely from reducing the charge transfer portion of the response. In fact, it seems that the large polarizability of the gas phase composite cluster is due primarily to the spurious charge buildup occurring at its corner Mg ions and depicted in Figure

5.21(b). By eliminating this charge buildup, the embedding model reduces both the total charge transfer and the resulting polarizability of the composite cluster.

Embedded Cluster vs. Periodic Model of the Composite

With surface charge buildup damped in the composite embedded cluster, the induced charge density in the embedded model qualitatively resembles that in the periodic calculation. As shown in Figure 5.22, both composite models exhibit significant accumulation of charge on the edges of the "inner" Ag atoms. These atoms are bordered by nearest neighbor Mg cations and have a larger area between them and these cations than between the outer Ag atoms and their neighboring oxygen anions. As a result, there is room for charge to build up at their surfaces. Both models also show strong dipole-shaped induced charge densities about the oxygen anions, which generally orient away from the the center of the inclusion and decrease in magnitude with distance from the inclusion. We note that these comparisons are merely qualitative. Since the field definitions in the periodic and cluster calculations differ—in particular the field in the periodic calculations is a *macroscopic* one—quantitative comparison of the induced charge densities was not considered.

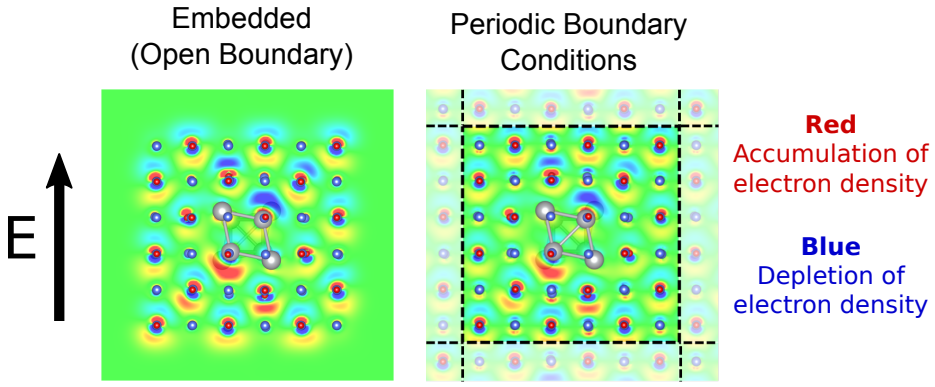

Figure 5.22: Polarization in embedded cluster and periodic solid models. The two panels shows slices in the YZ plane of the change in electron density induced by a field in the direction shown for an embedded cluster model (left) and periodic model (right) of the MgO/Ag_8 composite. Note that the applied field for the two cases differs, and the colormaps are intended for *qualitative* comparisons between models.

5.7.4 Charge Transfer in the Embedded Cluster Composite Model

We have established that the embedding procedure dampens spurious charge transfer and produces a polarization picture that is qualitatively similar to that observed in a fully periodic model. Now, we turn to examining what the embedded cluster model of the composite can tell us about the polarization mechanisms at play in the MgO/Ag composite. Specifically, we focus on the charge transfer processes occurring within the Ag inclusion and between the inclusion and neighboring matrix ions. In this section, we consider charge transfer differently than in the decomposition scheme described in Section 5.3.4 and used throughout the rest of the chapter for one primary reason. We noticed that the QTAIM charges used in that scheme, which are calculated from a real-space grid of the electronic density, exhibited a lot of numerical noise for these large systems. As an alternative, we computed DDEC6 atomic charges and considered the changes in these charges with different field states. Thus, we simply looked at fluctuations in atomic charges and did not compute the charge transfer polarizability in Equation (5.20).

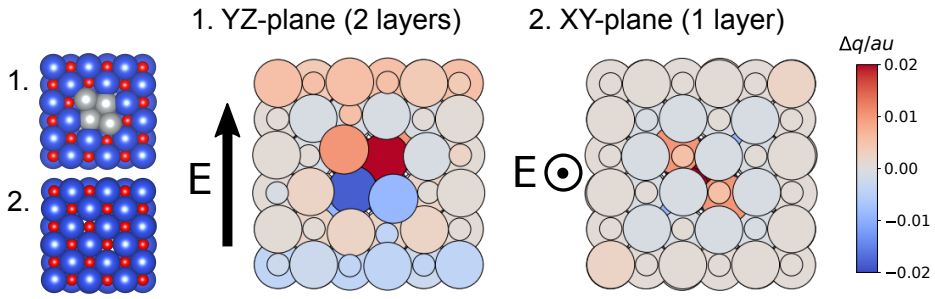

Figure 5.23: Charge transfer in the MgO/Ag_8 embedded cluster model. Colormaps shows the change in DDEC6 atomic charges induced by an external field. Induced charges are calculated as $\Delta q = q(E_+) - q(E_-)$, where the positive field direction is indicated by the arrows. In the YZ-plane view, the nearest 2 layers of MgO have been removed, and in the XY-plane view, the nearest layer has been removed. Structures on the left provide a key for atoms types, with Mg = Blue, O = Red, and Ag = Silver.

Figure 5.23 shows the change in DDEC6 atomic charges between the $E_- = -0.001$ au and $E_+ = +0.001$ au applied field states. The DDEC6 charge fluctuations support the notion that the increase in charge transfer relative to pure MgO is driven primarily by the fluctuating charges within the Ag cluster, rather than transfer across the interface. Specifically, the inner four Ag atoms show the largest changes in charges of all atoms. There is a smaller interfacial contribution as well, though. Most atoms

Table 5.6: Characterization of Models for MgO and MgO / Ag_8 Composite.

System	Model[a]	α^{iso}	$\alpha^{\mathrm{iso}}_{\mathrm{TS}}$	$\alpha^{\mathrm{iso}}_{\mathrm{TS,FI}}$
Pure	GP	1888	2432	1671
	EC	1457	–	–
	PBC	1259	2234	1715
Comp	GP	3903	2678	1985
	EC	1911	2317	1597
	PBC	1563	2502	1988

[a] GP: Gas Phase, EC: Embedded Cluster, PBC: Periodic Boundary Conditions.

in the first layer about the inclusion actually display small magnitude changes in charge opposite in sign to the Ag atoms they border. However, the interfacial oxygen anions nearest the outer Ag atoms seem to accumulate charge in the same way as the inclusion, appearing to act as an extension of the inclusion over which charge is able to move. This phenomenon is not simply an artifact from embedding, as it is observed in the charge fluctuations of the periodic model as well. Finally, despite the embedding model damping some surface effects, there is still clearly an accumulation of charge at opposing surfaces of the cluster, which is an artifact of the finite size of the model.

5.7.5 Applying the TS Model to the Composites

Finally, we applied the TS model to both the cluster and periodic models of the composite. For both gas-phase and embedded cluster models, the TS model polarizability was evaluated without periodic boundaries. This means that when simulating the embedded cluster in particular, the TS model neglects the mutual polarization between the cluster and its CPCM environment. Periodic boundary conditions as implemented in libMBD were used to simulate the periodic systems. The results of the TS model calculations are given in Table 5.6.

For gas phase clusters, the TS model overestimated the polarizability of pure MgO by 29%. Using FI references improves the result to an 11.5% underestimation. In contrast, the TS model significantly underestimated the polarizability of the gas phase composite cluster. This is not surprising given the aforementioned charge leakage at corner MgO atoms in this cluster, and so this poor performance can be considered more an artifact of a poorly behaved reference system than a poor-performing TS

model.

Now we turn to the embedded cluster model. As mentioned above, DDEC6 partitioning could not be performed for the pure MgO embedded cluster, so that cluster is omitted from the analysis. For the embedded composite cluster, the TS model overestimated the polarizability by 21%. When using FI reference polarizabilities, the TS model underestimated the embedded cluster polarizability by 16.5%.

The TS model performed much worse for the periodic models, overestimating the cell polarizability by 77% and 60% for the pure and composite systems, respectively. The performance improved when FI references were used, but the TS model still overestimated the pure MgO and composite cell polarizabilities by 36% and 27%, respectively. This result is in keeping with the better performance for FI references in cubic crystals that we noted earlier due to the tendency of neutral atoms to overestimate cell polarizabilities. In summation, the performance of the TS model for these systems was rather poor compared to our earlier results for inorganic clusters in section 5.5. However, the performance is more in line with that observed in cubic crystals in Section 5.4.2. Moreover, this performance appears to be a continuation of the trends observed earlier in smaller MgO clusters, for which the TS model progressively increased its overestimation of polarizability as cluster size increased.

5.7.6 Takeaways About the Embedded Cluster Model

This section proposed a methodology for studying the polarization of composites in finite cluster models and evaluated the performance of the TS models on these systems. Embedding an MgO/Ag composite cluster in shells of cECPs and point charges reduced some spurious surface effects compared to the gas phase cluster, and qualitatively reproduced the polarization behavior observed in periodic calculations. From the embedded cluster models, we could ascertain that the largest increase in polarization in the composite relative to bulk comes from charge transfer within the Ag inclusion, with smaller contributions coming from interfacial O anions. Nevertheless, the embedding model requires refinement in several respects. First, it was not able to quantitatively reproduce the atomic charges and volumes from periodic results. Second, the polarizabilities from embedded cluster calculations still overestimate periodic cell polarizabilites.

TS models performed poorly for both cluster and periodic models. The primary causes for this appear to be related to the poor performance of the model for MgO

clusters noted earlier. In fact, introducing an Ag inclusion actually improved the results somewhat. Thus, it is difficult to draw any general conclusions about how an interface of two materials with different polarization mechanisms impacts the performance of inducible dipole models. By working with a composite of two materials where the TS model was earlier shown to perform well (such as between SiO_2 and Ag), more concrete lessons might be gleaned.

5.8 Conclusions

Throughout this chapter, we have taken an atom-centered view of polarization, with the ultimate goal of being able to better model the response properties of heterogeneous systems. We began by studying the sensitivity of the predictive TS model to different charge partitioning schemes and the definition of reference atoms. In agreement with earlier work, we found that iterative charge partitioning schemes better capture the effects of atomic environment and result in more accurate polarizabilities. But we also found that the TS scheme was not strongly affected by the specific flavor of iterative scheme used. Moreover, we found that replacing neutral reference atoms with fractional ions produced an average decrease in the predicted polarizabilities, regardless of the type of charge partitioning used. This proved detrimental to the predictions for small molecules but improved results for cubic solids. The use of FI references did increase the sensitivity of the TS model to the charge partitioning method used for some ionic solids.

Next, we employed what we have termed a descriptive IAD approach, decomposing the polarizability of small molecules and clusters into atomic contributions. These atomic contributions were further partitioned into local dipole and charge transfer components. This analysis revealed that different systems showed significant differences in the relative importance of charge transfer in their polarizabilities. However, all systems showed an increase in charge transfer importance with increasing size, which we rationalized based on the inclusion of atomic coordinates in the definition of the charge transfer polarizability. Furthermore, the anisotropy of the system's polarizability was generally accounted for by the anisotropy of the charge transfer response. We found that although the TS model does not incorporate charge transfer explicitly, it could accurately predict isotropic polarizabilities for systems dominated by charge transfer. On the other hand, the TS model underestimated the anisotropy of the polarizability of these same systems.

Reoptimization of the TS model pointed to long range damping as a powerful handle for tuning the anisotropy of the response. The reoptimized TS model exhibited a more balanced balanced prediction of isotropic and anisotropic polarization. Application of the TS model to very anisotropic Ag nanorods bolstered this hypothesis, up to a point. Nevertheless, for the longest rods, even an effectively undamped TS model underestimated anisotropy. This ultimately appears to be a shortcoming of the TS model itself, as the Tinker implementation of the dipole field tensor without volume scaling performed much better across the range of rod lengths studied.

Finally, we took an atom-centered approach to the polarization of a composite MgO/Ag material using the lessons derived from the rest of this chapter. The cluster model developed for this system showed promise in being able to reproduce the mechanisms of polarization found in the periodic material while also facilitating the use of the descriptive IAD tools used to partition the response. Increased charge transfer in the composite could thus be linked to charge fluctuations within the inclusion and at the interface. In particular, we noted that during the polarization of the composite, some charge is transferred between the outer inclusion atoms and the nearest oxide ions of the matrix along the polarization axis. This mechanism enhances the polarizability of the composite by effectively increasing the polarization length of the inclusion.

While further investigation is warranted before drawing definitive conclusions from the embedded cluster model, the observed charge transfer suggests that the lattice match and nature of the chemical bonding between the inclusion and interface is a critical factor in electronic polarization and could be used as a design principle. For dielectrics, it is important to ensure that the charge transfer remains short-range in order to keep the material insulating. However, one may still imagine engineering the inclusion-matrix interface to ensure both spatial proximity and energetic overlap between inclusion and matrix orbitals to increase charge transfer at the interface. Furthermore, it seems likely that designing interfaces with covalent bonds between an insulating matrix and highly polarizable inclusion could increase interfacial charge transfer and the polarizability of the material.

Bibliography

[1] Helge Kragh. The lorenz-lorentz formula: Origin and early history. *Substantia*, page Vol 2 No 2 (2018), 2018.

[2] B. G. Dick and A. W. Overhauser. Theory of the dielectric constants of alkali halide crystals. *Physical Review*, 112(1):90–103, October 1958.

[3] P J Mitchell and D Fincham. Shell model simulations by adiabatic dynamics. *Journal of Physics: Condensed Matter*, 5(8):1031–1038, February 1993.

[4] Paul J. van Maaren and David van der Spoel. Molecular dynamics simulations of water with novel shell-model potentials. *The Journal of Physical Chemistry B*, 105(13):2618–2626, March 2001.

[5] Anna-Pitschna E. Kunz and Wilfred F. van Gunsteren. Development of a nonlinear classical polarization model for liquid water and aqueous solutions: Cos/d. *The Journal of Physical Chemistry A*, 113(43):11570–11579, August 2009.

[6] Justin A. Lemkul, Jing Huang, Benoît Roux, and Alexander D. MacKerell. An empirical polarizable force field based on the classical drude oscillator model: Development history and recent applications. *Chemical Reviews*, 116(9):4983–5013, January 2016.

[7] Steven W. Rick, Steven J. Stuart, and B. J. Berne. Dynamical fluctuating charge force fields: Application to liquid water. *The Journal of Chemical Physics*, 101(7):6141–6156, October 1994.

[8] Steven W Rick and B J Berne. Dynamical fluctuating charge force fields: The aqueous solvation of amides. *J. Am. Chem. Soc.*, 118(3):672–679, January 1996.

[9] Harry A. Stern, F. Rittner, B. J. Berne, and Richard A. Friesner. Combined fluctuating charge and polarizable dipole models: Application to a five-site water potential function. *The Journal of Chemical Physics*, 115(5):2237–2251, August 2001.

[10] Sandeep Patel and Charles L. Brooks. Charmm fluctuating charge force field for proteins: I parameterization and application to bulk organic liquid simulations. *Journal of Computational Chemistry*, 25(1):1–16, October 2003.

[11] Sandeep Patel, Alexander D. Mackerell, and Charles L. Brooks. Charmm fluctuating charge force field for proteins: Ii protein/solvent properties from molecular dynamics simulations using a nonadditive electrostatic model. *Journal of Computational Chemistry*, 25(12):1504–1514, June 2004.

[12] Frank Jensen. Using atomic charges to model molecular polarization. *Physical Chemistry Chemical Physics*, 24(4):1926–1943, 2022.

[13] George A. Kaminski, Harry A. Stern, B. J. Berne, Richard A. Friesner, Yixiang X. Cao, Robert B. Murphy, Ruhong Zhou, and Thomas A. Halgren. Development of a polarizable force field for proteins via ab initio quantum chemistry: First generation model and gas phase tests. *Journal of Computational Chemistry*, 23(16):1515–1531, October 2002.

[14] Pengyu Ren and Jay W. Ponder. Consistent treatment of inter- and intramolecular polarization in molecular mechanics calculations. *Journal of Computational Chemistry*, 23(16):1497–1506, October 2002.

[15] William L. Jorgensen, Kasper P. Jensen, and Anastassia N. Alexandrova. Polarization effects for hydrogen-bonded complexes of substituted phenols with water and chloride ion. *Journal of Chemical Theory and Computation*, 3(6):1987–1992, October 2007.

[16] Jean-François Truchon, Anthony Nicholls, Radu I. Iftimie, Benoît Roux, and Christopher I. Bayly. Accurate molecular polarizabilities based on continuum electrostatics. *Journal of Chemical Theory and Computation*, 4(9):1480–1493, August 2008.

[17] Jean-François Truchon, Anthony Nicholls, Benoît Roux, Radu I. Iftimie, and Christopher I. Bayly. Integrated continuum dielectric approaches to treat molecular polarizability and the condensed phase: Refractive index and implicit solvation. *Journal of Chemical Theory and Computation*, 5(7):1785–1802, June 2009.

[18] Jean-François Truchon, Anthony Nicholl's, J. Andrew Grant, Radu I. Iftimie, Benoît Roux, and Christopher I. Bayly. Using electronic polarization from the internal continuum (epic) for intermolecular interactions. *Journal of Computational Chemistry*, 31(4):811–824, July 2009.

[19] Michael Schmollngruber, Volker Lesch, Christian Schröder, Andreas Heuer, and Othmar Steinhauser. Comparing induced point-dipoles and drude oscillators. *Physical Chemistry Chemical Physics*, 17(22):14297–14306, 2015.

[20] Stefan Grimme, Andreas Hansen, Jan Gerit Brandenburg, and Christoph Bannwarth. Dispersion-Corrected Mean-Field Electronic Structure Methods. *Chemical Reviews*, 116(9):5105–5154, 2016.

[21] Alexandre Tkatchenko and Matthias Scheffler. Accurate molecular van der waals interactions from ground-state electron density and free-atom reference data. *Phys. Rev. Lett.*, 102:073005, Feb 2009.

[22] Alexandre Tkatchenko, Robert A Distasio, Roberto Car, and Matthias Scheffler. Accurate and efficient method for many-body van der Waals interactions. *Physical Review Letters*, 108(23):1–5, 2012.

[23] Jay W. Ponder, Chuanjie Wu, Pengyu Ren, Vijay S. Pande, John D. Chodera, Michael J. Schnieders, Imran Haque, David L. Mobley, Daniel S. Lambrecht, Robert A. DiStasio, Martin Head-Gordon, Gary N. I. Clark, Margaret E. Johnson, and Teresa Head-Gordon. Current status of the AMOEBA polarizable force field. *The Journal of Physical Chemistry B*, 114(8):2549–2564, February 2010.

[24] Jon Applequist, James R. Carl, and Kwok-Kueng Fung. Atom dipole interaction model for molecular polarizability. application to polyatomic molecules and determination of atom polarizabilities. *Journal of the American Chemical Society*, 94(9):2952–2960, May 1972.

[25] Joshua A. Rackers, Zhi Wang, Chao Lu, Marie L. Laury, Louis Lagardère, Michael J. Schnieders, Jean-Philip Piquemal, Pengyu Ren, and Jay W. Ponder. Tinker 8: Software tools for molecular design. *Journal of Chemical Theory and Computation*, 14(10):5273–5289, September 2018.

[26] Jan Hermann, Martin Stöhr, Szabolcs Góger, Shayantan Chaudhuri, Bálint Aradi, Reinhard J. Maurer, and Alexandre Tkatchenko. libmbd: A general-purpose package for scalable quantum many-body dispersion calculations. *The Journal of Chemical Physics*, 159(17), November 2023.

[27] Alberto Ambrosetti, Anthony M. Reilly, Robert A. Distasio, and Alexandre Tkatchenko. Long-range correlation energy calculated from coupled atomic response functions. *Journal of Chemical Physics*, 140(18), 2014.

[28] B.T. Thole. Molecular polarizabilities calculated with a modified dipole interaction. *Chemical Physics*, 59(3):341–350, August 1981.

[29] Junmei Wang, Piotr Cieplak, Jie Li, Tingjun Hou, Ray Luo, and Yong Duan. Development of polarizable models for molecular mechanical calculations i: Parameterization of atomic polarizability. *The Journal of Physical Chemistry B*, 115(12):3091–3099, March 2011.

[30] Piet Th. van Duijnen and Marcel Swart. Molecular and atomic polarizabilities: Thole's model revisited. *The Journal of Physical Chemistry A*, 102(14):2399–2407, March 1998.

[31] Pengyu Ren and Jay W. Ponder. Polarizable atomic multipole water model for molecular mechanics simulation. *The Journal of Physical Chemistry B*, 107(24):5933–5947, May 2003.

[32] Robert A. Distasio, Vivekanand V. Gobre, and Alexandre Tkatchenko. Many-body van der Waals interactions in molecules and condensed matter. *Journal of Physics Condensed Matter*, 26(21), 2014.

[33] Tore Brinck, Jane S Murray, and Peter Politzer. Polarizability and volume. *The Journal of Chemical Physics*, 98(5):4305–4306, 1993.

[34] Thomas A Manz, Taoyi Chen, Daniel J Cole, Nidia Gabaldon Limas, and Benjamin Fiszbein. New scaling relations to compute atom-in-material polarizabilities and dispersion coefficients: Part 1. Theory and accuracy. *RSC Advances*, 9(34):19297–19324, 2019.

[35] Tomáš Bučko, Sébastien Lebègue, Jürgen Hafner, and János G. Ángyán. Improved density dependent correction for the description of London dispersion forces. *Journal of Chemical Theory and Computation*, 9(10):4293–4299, 2013.

[36] Tomáš Bučko, Sébastien Lebègue, János G. Ángyán, and Jürgen Hafner. Extending the applicability of the Tkatchenko-Scheffler dispersion correction via iterative Hirshfeld partitioning. *Journal of Chemical Physics*, 141(3), 2014.

[37] Patrick Bultinck, Christian Van Alsenoy, Paul W. Ayers, and Ramon Carbó-Dorca. Critical analysis and extension of the hirshfeld atoms in molecules. *The Journal of Chemical Physics*, 126(14), April 2007.

[38] Toon Verstraelen, Steven Vandenbrande, Farnaz Heidar-Zadeh, Louis Vanduyfhuys, Veronique Van Speybroeck, Michel Waroquier, and Paul W. Ayers.

Minimal basis iterative stockholder: Atoms in molecules for force-field development. *Journal of Chemical Theory and Computation*, 12(8):3894–3912, July 2016.

[39] Thomas A. Manz and Nidia Gabaldon Limas. Introducing ddec6 atomic population analysis: part 1. charge partitioning theory and methodology. *RSC Advances*, 6(53):47771–47801, 2016.

[40] Nidia Gabaldon Limas and Thomas A. Manz. Introducing ddec6 atomic population analysis: part 2. computed results for a wide range of periodic and non-periodic materials. *RSC Advances*, 6(51):45727–45747, 2016.

[41] Nidia Gabaldon Limas and Thomas A. Manz. Introducing ddec6 atomic population analysis: part 4. efficient parallel computation of net atomic charges, atomic spin moments, bond orders, and more. *RSC Advances*, 8(5):2678–2707, 2018.

[42] Matthew Chan, Toon Verstraelen, Alireza Tehrani, Michelle Richer, Xiaotian Derrick Yang, Taewon David Kim, Esteban Vöhringer-Martinez, Farnaz Heidar-Zadeh, and Paul W. Ayers. The tale of horton: Lessons learned in a decade of scientific software development. *The Journal of Chemical Physics*, 160(16), April 2024.

[43] Toon Verstraelen. Denspart. https://github.com/theochem/denspart.

[44] Tim Gould, Sébastien Lebègue, János G. Ángyán, and Tomáš Bučko. A Fractionally Ionic Approach to Polarizability and van der Waals Many-Body Dispersion Calculations. *Journal of Chemical Theory and Computation*, 12(12):5920–5930, 2016.

[45] Tim Gould and Tomáš Bučko. C6 Coefficients and Dipole Polarizabilities for All Atoms and Many Ions in Rows 1-6 of the Periodic Table. *Journal of Chemical Theory and Computation*, 12(8):3603–3613, 2016.

[46] Keith E. Laidig and Richard F. W. Bader. Properties of atoms in molecules: Atomic polarizabilities. *The Journal of Chemical Physics*, 93(10):7213–7224, November 1990.

[47] K. Jackson, M. Yang, and J. Jellinek. Site-specific analysis of dielectric properties of finite systems. *The Journal of Physical Chemistry C*, 111(48):17952–17960, July 2007.

[48] Juan E. Peralta, Veronica Barone, and Koblar A. Jackson. Site-specific polarizabilities from analytic linear-response theory. *Chemical Physics Letters*, 608:24–27, July 2014.

[49] Koblar Jackson and Julius Jellinek. Si clusters are more metallic than bulk si. *The Journal of Chemical Physics*, 145(24), December 2016.

[50] Ye Mei, Andrew C. Simmonett, Frank C. Pickard, Robert A. DiStasio, Bernard R. Brooks, and Yihan Shao. Numerical study on the partitioning of the molecular polarizability into fluctuating charge and induced atomic dipole contributions. *The Journal of Physical Chemistry A*, 119(22):5865–5882, May 2015.

[51] Richard F. W. Bader. A quantum theory of molecular structure and its applications. *Chemical Reviews*, 91(5):893–928, July 1991.

[52] A. Otero-de-la Roza, Erin R. Johnson, and Víctor Luaña. Critic2: A program for real-space analysis of quantum chemical interactions in solids. *Computer Physics Communications*, 185(3):1007–1018, March 2014.

[53] Marc Montilla, Josep M. Luis, and Pedro Salvador. Origin-independent decomposition of the static polarizability. *Journal of Chemical Theory and Computation*, 17(2):1098–1105, January 2021.

[54] YingXing Cheng and Toon Verstraelen. The significance of fluctuating charges for molecular polarizability and dispersion coefficients. *The Journal of Chemical Physics*, 159(9), September 2023.

[55] Diptarka Hait and Martin Head-Gordon. How accurate are static polarizability predictions from density functional theory? an assessment over 132 species at equilibrium geometry. *Physical Chemistry Chemical Physics*, 20(30):19800–19810, 2018.

[56] Diptarka Hait and Martin Head-Gordon. How accurate is density functional theory at predicting dipole moments? an assessment using a new database of 200 benchmark values. *Journal of Chemical Theory and Computation*, 14(4):1969–1981, March 2018.

[57] Jens Jørgen Mortensen, Ask Hjorth Larsen, Mikael Kuisma, Aleksei V. Ivanov, Alireza Taghizadeh, Andrew Peterson, Anubhab Haldar, Asmus Ougaard Dohn, Christian Schäfer, Elvar Örn Jónsson, Eric D. Hermes, Fredrik Andreas Nilsson, Georg Kastlunger, Gianluca Levi, Hannes Jónsson, Hannu Häkkinen, Jakub Fojt, Jiban Kangsabanik, Joachim Sødequist, Jouko Lehtomäki, Julian Heske, Jussi Enkovaara, Kirsten Trøstrup Winther, Marcin Dulak, Marko M. Melander, Martin Ovesen, Martti Louhivuori, Michael Walter, Morten Gjerding, Olga Lopez-Acevedo, Paul Erhart, Robert Warmbier, Rolf Würdemann, Sami Kaappa, Simone Latini, Tara Maria Boland, Thomas Bligaard, Thorbjørn Skovhus, Toma Susi, Tristan Maxson, Tuomas Rossi, Xi Chen, Yorick Leonard A. Schmerwitz, Jakob Schiøtz, Thomas Olsen, Karsten Wedel Jacobsen, and Kristian Sommer Thygesen. Gpaw: An open python package for electronic structure calculations. *The Journal of Chemical Physics*, 160(9), March 2024.

[58] Anubhav Jain, Shyue Ping Ong, Geoffroy Hautier, Wei Chen, William Davidson Richards, Stephen Dacek, Shreyas Cholia, Dan Gunter, David Skinner, Gerbrand Ceder, and Kristin A. Persson. Commentary: The materials project: A materials genome approach to accelerating materials innovation. *APL Materials*, 1(1), July 2013.

[59] Ioannis Petousis, Wei Chen, Geoffroy Hautier, Tanja Graf, Thomas D. Schladt, Kristin A. Persson, and Fritz B. Prinz. Benchmarking density functional perturbation theory to enable high-throughput screening of materials for dielectric constant and refractive index. *Physical Review B*, 93(11), March 2016.

[60] Ioannis Petousis, David Mrdjenovich, Eric Ballouz, Miao Liu, Donald Winston, Wei Chen, Tanja Graf, Thomas D. Schladt, Kristin A. Persson, and Fritz B. Prinz. High-throughput screening of inorganic compounds for the discovery of novel dielectric and optical materials. *Scientific Data*, 4(1), January 2017.

[61] R. Clausius. *Die Mechanische Behandlung der Electricität*. Vieweg+Teubner Verlag, 1879.

[62] Andi Cuko, Antoni Macià Escatllar, Monica Calatayud, and Stefan T. Bromley. Properties of hydrated tio2and sio2nanoclusters: dependence on size, temperature and water vapour pressure. *Nanoscale*, 10(45):21518–21532, 2018.

[63] Oriol Lamiel-Garcia, Andi Cuko, Monica Calatayud, Francesc Illas, and Stefan T. Bromley. Predicting size-dependent emergence of crystallinity in nanomaterials: titania nanoclusters versus nanocrystals. *Nanoscale*, 9(3):1049–1058, 2017.

[64] Dmitrij Rappoport and Filipp Furche. Property-optimized gaussian basis sets for molecular response calculations. *The Journal of Chemical Physics*, 133(13), October 2010.

[65] R.F.W. Bader, T.A. Keith, K.M. Gough, and K.E. Laidig. Properties of atoms in molecules: additivity and transferability of group polarizabilities. *Molecular Physics*, 75(5):1167–1189, April 1992.

[66] Li Ma, Koblar Alan Jackson, Jianguang Wang, Mihai Horoi, and Julius Jellinek. Investigating the metallic behavior of na clusters using site-specific polarizabilities. *Physical Review B*, 89(3), January 2014.

[67] Rajarshi Sinha-Roy, Pablo García-González, and Hans Christian Weissker. How metallic are noble-metal clusters? Static screening and polarizability in quantum-sized silver and gold nanoparticles. *Nanoscale*, 12(7):4452–4458, 2020.

[68] Hannah E. Johnson and Christine M. Aikens. Electronic structure and tddft optical absorption spectra of silver nanorods. *The Journal of Physical Chemistry A*, 113(16):4445–4450, March 2009.

[69] Fahri Alkan and Christine M. Aikens. Td-dft and td-dftb investigation of the optical properties and electronic structure of silver nanorods and nanorod dimers. *The Journal of Physical Chemistry C*, 122(41):23639–23650, June 2018.

[70] R. F. W. Bader. Dielectric polarization: a problem in the physics of an open system. *Molecular Physics*, 100(21):3333–3344, November 2002.

[71] Paul S. Bagus, Michel J. Sassi, and Kevin M. Rosso. Cluster embedding of ionic systems: Point charges and extended ions. *The Journal of Chemical Physics*, 151(4), July 2019.

[72] John P. Perdew, Adrienn Ruzsinszky, Gábor I. Csonka, Oleg A. Vydrov, Gustavo E. Scuseria, Lucian A. Constantin, Xiaolan Zhou, and Kieron Burke. Restoring the density-gradient expansion for exchange in solids and surfaces. *Physical Review Letters*, 100(13), April 2008.

[73] Vladimir E. Puchin, Eugene V. Stefanovich, and Thanh N. Truong. An approach for inclusion of crystal polarization in embedded cluster calculations: application to caf2. *Chemical Physics Letters*, 304(3–4):258–264, April 1999.

[74] Benjamin X. Shi, Venkat Kapil, Andrea Zen, Ji Chen, Ali Alavi, and Angelos Michaelides. General embedded cluster protocol for accurate modeling of oxygen vacancies in metal-oxides. *The Journal of Chemical Physics*, 156(12), March 2022.

Chapter 6

Key Role of Density Functional Approximation in Predicting M–N–C Catalyst Activities for Oxygen Reduction

Preface

The following chapter consists of a minimally edited version of an article of the same title published in *The Journal of Physical Chemistry C*.[1] Changes were made to the published work to match the format of the rest of this dissertation without altering the content of the article. The complete author byline from the article is reproduced below for transparency. SD provided extensive insights used to refine the theory and methodology used in the article, performed initial geometry optimizations for metalloporphyrin intermediates, and collaborated with myself (BH) on an initial draft of the article, which was subsequently heavily re-worked. I (BH) refined geometries and added the TPSSh and PWPB95 functionals to the analysis, which were not included in the original set. I also performed all single-point DFT, DLPNO-CCSD(T), and CASSCF calculations, performed the data analysis, and prepared the final draft of the manuscript. SNG and IGR helped to guide the original idea for the manuscript, provided theoretical guidance on the selection of active spaces for correlated calculations. SNG engaged in biweekly discussions with myself and SD early on in the project. In this initial phase, we attempted to develop a reduced model for the cata-

lysts using single metal atoms, and SNG and IGR performed iterative qubit coupled cluster calculations on these systems using active spaces electronic integrals that I provided. Ultimately, that work did not enter into the article explicitly, but it did inform the methodological approach to the final article. IP helped conceive the project, provided extensive guidance along the way, and edited the manuscript.

Brett Henderson[1,2], Sofia Donnecke[1,2], Scott N. Genin[3], Ilya G. Ryabinkin[3], Irina Paci[1,2]

[1] *Department of Chemistry and the Centre for Advanced Materials and Related Technology, University of Victoria, Victoria, British Columbia, Canada*

[2] *Quantum Algorithms Institute, Surrey, British Columbia, Canada*

[3] *OTI Lumionics Inc., Toronto, Ontario, Canada*

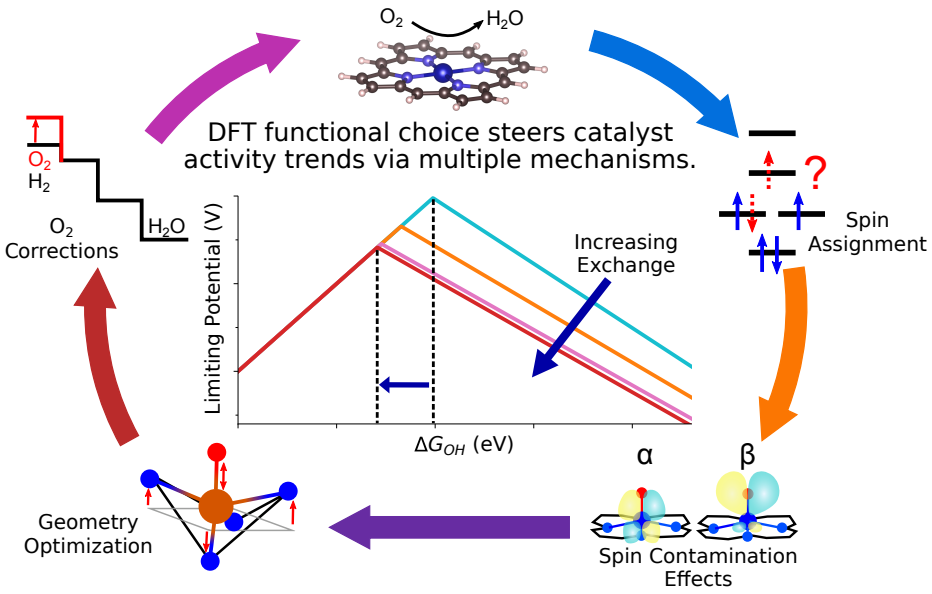

Abstract

Metal-Nitrogen-Carbon motifs present intriguing structural and electronic properties for a number of applications, including as oxygen reduction catalysts. However, computational investigations of M-N-C-catalyzed reactions must grapple with their complex electronic structures. In the present study, we evaluate the impact of the density functional approximation on calculated M-N-C catalyst activities for oxygen reduction. Using

metalloporphyrins as model catalysts, we find a significant split between pure (GGA) and hybrid functionals, with hybrid functionals, in particular B3LYP, showing greater agreement with DLPNO-CCSD(T) reaction energies. Notably, double-hybrids offered no noticeable improvement over the much more computationally efficient B3LYP and PBE0. Other discrepancies between functionals, as well as an in-depth analysis of ground state spin and geometry, are also considered in this work. Finally, both hybrid and double-hybrid functionals greatly reduced the gas phase errors associated with the main group molecules in the oxygen reduction reaction relative to GGA calculations, leading us to question the application of widely used empirical corrections to O_2.

6.1 Introduction

The oxygen reduction reaction (ORR) is a crucial biological process and a critical component of developing technologies such as metal-air batteries and hydrogen fuel cells. For hydrogen fuel cells, the ORR is current-limiting, and cathodes generally contain platinum catalysts to produce the current needed for industrial applications.[2] The broader commercialization of these devices relies on developing catalysts that are cheap, abundant, and active relative to the current state of the art.

Computational studies aid the design of novel catalysts in part by defining the factors that limit theoretical catalyst activity. Density functional theory has shown that most ORR catalysts are constrained by linear free energy scaling relationships (LFESRs) between the binding energies of reaction intermediates.[3, 4] These scaling relationships can be used to derive characteristic volcano plots that relate catalyst activities to the binding energy of a single ORR intermediate.[5, 6] Such plots show that Pt is near, but not at, the theoretical peak activity of metallic surfaces, and that a significant overpotential will remain unless these LFESRs can be circumvented by a novel class of catalyst.[4] As a result, new catalytic materials are sought to push catalyst activity past typical volcano plot scaling and provide alternatives to Pt.[7, 8, 9] Strategies to circumvent LFESRs have been explored for many catalytic processes including and beyond the ORR, with the guiding principle being to increase catalyst complexity.[10, 11] Defect engineering on surfaces,[12, 13, 14, 15, 16] precise control of nanoparticle catalyst size,[17, 18, 19] structural modification of active sites with ligands,[20, 21] and the introduction of external strains and electromagnetic

fields[22, 23, 24] all represent possible paths forward.

M-N-C single atom catalysts combine the principles of defect engineering and ligand modification to produce non-platinum group ORR catalysts with high theoretical limiting potentials[4] and experimentally demonstrated activities competitive with Pt-based catalysts.[25] Metalloporphyrins represent a flexible subclass of M-N-C catalysts. By varying functional groups on porphyrins, their electronic structure and sterics can be tuned to optimize activity and selectivity toward either the two-electron or four-electron ORR.[20, 26, 27, 28] In particular, bifunctional materials based on porphyrins are expected to circumvent typical scaling relationships through differentiating interactions between adsorbed intermediates and nearby functional groups.[8, 9] In addition, porphyrins can be covalently anchored to materials, such as carbon nanotubes and metal-organic frameworks, to build scalable heterogeneous catalysts.[29, 28]

In addition to serving as models for this broader class of functionalized porphyrin catalysts, bare metalloporphyrins also have a similar structure to the pyrrolic catalytic sites in graphitic M-N-C materials.[30, 31, 32] These materials have been widely studied using plane wave density functional theory,[33, 34, 25, 35] but it can be challenging to verify the accuracy of these simulations, since theoretically more accurate hybrid DFT or yet more accurate wavefunction theories can be costly to apply or unavailable for periodic materials. Several approaches to accurately treating correlation in periodic materials have emerged in recent years. Density Matrix Embedding Theory[36, 37] and similar schemes[38, 39] allow the use of accurate wavefunction theories to treat adsorption or catalytic active sites embedded in a periodic material that is simulated with a mean field treatment.[40] Embedded cluster models[41, 42, 43] and local coupled cluster and MP2 approaches[44, 45, 46, 47] have also become tractable ways to simulate active sites in periodic materials. An alternative approach is to use finite models, such as graphene flakes or porphyrins,[48, 30] upon which well-established methods like coupled cluster or complete active space theories and the local orbital picture common in homogeneous catalysis can be brought to bear for understanding catalytic mechanisms. A cycle depicting possible mechanisms for both the two-and four-electron ORR pathways on a metalloporphyrin catalyst is shown in Figure 6.1.

Despite their promise, describing the electronic structure of transition metal porphyrins is no trivial endeavor. These molecules possess complicated electronic structures which make the determination of ground spin states[49] and binding energies[50,

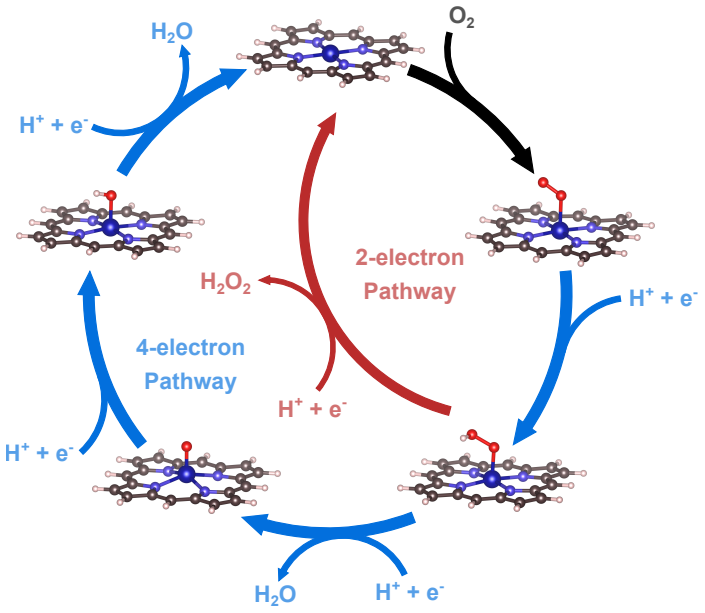

Figure 6.1: Catalytic cycle for oxygen reduction on a metalloporphyrin catalyst. Outer loop shows the associative 4-electron pathway studied herein, while the inner loop shows the 2-electron pathway producing H_2O_2.

51] challenging and highly dependent on the particular density functional approximation employed.[50, 52, 38] Studies aimed at related molecules have indicated that single hybrid functionals with small amounts of exact exchange perform well relative to wavefunction theories[53, 52] and experiment.[9] The recommendation of these low-exchange hybrids is consistent with generalized benchmarking efforts on transition metal complexes[54, 55, 56]. Nevertheless, others have suggested that as much as 40% exact exchange is required to best reproduce CASPT2 spin-state splittings in octahedral 3d transition metal complexes[57] and that the dependence on exact exchange seems to differ from metal to metal[30] (Table E.1 provides more detail on these benchmarking efforts). Thus, the question of the best functional for computing ORR reaction energies remains largely open and system-dependent.

In the present work, we aim to understand the impact of density functional on the predicted ORR activity of 3d-metalloporphyrin catalysts. We calculate scaling relationships and theoretical overpotentials using popular functionals that span different levels of approximation and compare results against the efficient coupled cluster variant DLPNO-CCSD(T) (Domain-Based Local Pair Natural Orbital Coupled Cluster with explicit Singles and Doubles excitations and a perturbative Triples correction).[58, 59, 60] In doing so, we expand upon the work in Ref [52] by using large

basis sets (and/or basis set extrapolation) and dispersion corrections throughout, investigating the double-hybrid B2PLYP, and focusing on metals relevant for the ORR. In addition, we scrutinize the sources of discrepancy between the functionals considered here, including the identification of ground spin states, geometry optimizations, and empirical gas-phase corrections.

6.2 Methods

6.2.1 Model Catalysts

We investigate four metalloporphyrin (MP) catalysts containing manganese (MnP), iron (FeP), cobalt (CoP) and nickel (NiP). Manganese, iron, and cobalt porphyrins, including functionalized variants, have been explored extensively for the ORR.[20, 26, 8, 61, 9, 62, 63] Nickel porphyrin has received only minimal attention as ORR catalysts due to its weak binding of O_2,[20, 64] yet its inclusion herein is useful as a way to cover the weak binding regime in the construction of LFESRs. Since MPs closely resemble pyrrolic MN_4 catalytic sites in M-N-C catalysts, we expect the conclusions drawn about the performance of different functionals to be relevant for this broader class of catalysts. Thus, the MPs considered herein comprise a valuable test set because they represent a class of notoriously complicated but widely studied 3d complexes spanning a range of ORR activities.

6.2.2 Reaction Mechanism

The ORR catalytic activity of metalloporphyrins was assessed for the 4-electron associative pathway depicted in Figure 6.1 and in the reaction scheme in Equations (6.1)(a)-(e). The reaction proceeds through the intermediate complexes MP(O_2), MP(OOH), MP(O), MP(OH). It is worth noting that many ORR studies neglect the initial step of this pathway, the binding of O_2 to the catalyst. However, we have included this step because 1) it shows a large dependence on functional choice and 2) the oxygen binding geometry and energetics are correlated with molecular catalyst activity for the ORR.[65, 26] As the goal of this work is to assess the variability and accuracy of various functionals rather than a direct comparison to experiment, the porphyrins were kept unfunctionalized to minimize computational complexity in the application of DLPNO-CCSD(T).

$$\mathrm{MP} + \mathrm{O_2} \longrightarrow \mathrm{MP(O_2)} \tag{6.1a}$$
$$\mathrm{MP(O_2)} + \mathrm{H^+} + \mathrm{e^-} \longrightarrow \mathrm{MP(OOH)} \tag{6.1b}$$
$$\mathrm{MP(OOH)} + \mathrm{H^+} + \mathrm{e^-} \longrightarrow \mathrm{MP(O)} + \mathrm{H_2O} \tag{6.1c}$$
$$\mathrm{MP(O)} + \mathrm{H^+} + \mathrm{e^-} \longrightarrow \mathrm{MP(OH)} \tag{6.1d}$$
$$\mathrm{MP(OH)} + \mathrm{H^+} + \mathrm{e^-} \longrightarrow \mathrm{MP} + \mathrm{H_2O} \tag{6.1e}$$

6.2.3 Computational Details

The free energies of reaction intermediates were calculated using the Computational Hydrogen Electrode (CHE).[5] A detailed description of the the thermodynamic, solvation,[66], and gas-phase O_2 corrections used and the procedure for calculating LFESRs is provided in Appendix E.1. All calculations were performed using ORCA 5.0.4.[67]

Multiplicities for Porphyrin Intermediates. The multiplicities used for the computation of LFESRs, relative energies of intermediates, and analysis of molecular geometries were kept consistent for all functionals and DLPNO-CCSD(T) and are listed in the "GS" column of Table 6.2. The multiplicity for each intermediate was assigned using reference values from experiment or *ab initio* calculations in the literature when available, or else the lowest-energy state from our own DLPNO-CCSD(T) calculations. Neither of these options were available for $NiP(O_2)$, but all tested DFT functionals predicted a triplet ground state, which we assumed to be accurate. Later, when assessing the variability of spin predictions for different functionals (Section 6.3.3), DFT predictions were determined via separate optimizations of low-, intermediate-, and high-spin structures.

DFT Calculation Details. The seven exchange-correlation functionals employed in the present study are described in Table 6.1. The chosen functionals encompass a range of theoretical approximations, from pure GGA to double-hybrid GGA. As the trends observed in the present study often coincide with the unofficial rungs of Jacob's ladder proposed by Perdew [68], we include them for ease of classification in the later discussion. Semi-empirical dispersion corrections have been demonstrated to significantly improve reaction energies for open-shell transition metal complexes computed across all rungs of Jacob's ladder.[56] Thus, Grimme's D3 dispersion correction with Becke-Johnson damping parameters [D3(BJ)][69, 70] was applied to all

functionals.

Table 6.1: Overview of the functionals used.

Functional	Class[a]	Rung[b]	%EXX[c]	%MP2[d]	Ref.
BP86	GGA	2	–	–	[71, 72]
PBE	GGA	2	–	–	[73]
TPSSh	Hybrid Meta-GGA	4	10	–	[74]
B3LYP	Hybrid GGA	4	20	–	[75]
PBE0	Hybrid GGA	4	25	–	[76]
B2PLYP	DH GGA	5	53	27	[77]
PWPB95	SOS DH Meta-GGA	5	50	27	[78]

[a] DH = Double-Hybrid. SOS = Spin-Opposite Scaled.
[b] Rung on the informal Jacob's ladder categorization of functionals.[68]
[c] Percentage of exact exchange included in the functional.
[d] Percentage of MP2 correlation included in the functional.

All structures were optimized using the def2-TZVP basis set using each of the first six functionals in Table 6.1. After optimization, single point calculations were performed using the def2-QZVPP basis set. Stability analysis was performed on the wavefunctions,[79] and where necessary, the calculations were restarted using rotated orbitals until stability was achieved.

In some cases, B2PLYP optimizations showed signs of instability, never reaching the force thresholds required for convergence. When the energies seemed sufficiently converged to make an assessment of ground state spin and geometry, the lowest energy structure along the optimization path was selected. These unconverged structures are indicated in the Table E.13. Because frequency calculations could not be performed on geometries that were not fully converged, B2PLYP was omitted from the construction of LFESRs and volcano plots.

DLPNO-CCSD(T) Calculations. DLPNO-CCSD(T) calculations were performed on TPSSh-optimized geometries. For all species, reference orbitals were quasi-restricted orbitals[80] generated from an unrestricted TPSSh calculation. By construction, these orbitals have no spin contamination, similar to a restricted open-shell reference. Thus, while spin contamination is discussed later as plaguing some of the DFT functionals, we found virtually no spin contamination in the final DLPNO-CCSD(T) wavefunctions (Table E.8). The iterative triples correction of Guo *et al.*[60] was employed, as it yields better relative energies for transition metal systems and other molecules with low-lying excited states.[81]. Due to the large disk-space demands of

this procedure, the cutoff for including triple natural orbitals (TCutTNO) was increased from 1.0×10^{-9} to 5.0×10^{-9}. This allowed all calculations to be performed on 2 TB of local disk space. Benchmarking illustrated that this change had minimal effect on the accuracy of the method (Appendix E.5), which is consistent with earlier benchmarking done by Guo *et al.*[81]

For calculations of reaction energies, two-point complete basis set (CBS) extrapolation was performed using the aug-cc-pVDZ and aug-cc-pVTZ basis sets on all atoms[82, 83, 84] using the procedure and fitting parameters of Neese and Valeev.[85] See Appendix E.4 for an analysis of basis set incompleteness errors. In addition, an extrapolation to the complete pair natural orbital space (CPS)[86] was performed using the CPS1 variant procedure described by Drosou *et al.*[49] In all cases, the NormalPNO setting was employed, though the TCutPNO setting was modified for the CPS extrapolation. For calculating the lowest energy spin states, the same CBS/CPS procedure was used. However, only the basis set of the metal atom was extrapolated, which improved efficiency while accurately treating the orbitals important for determining multiplicity. These calculations used the following basis sets: def2-SVP for H and C, def2-TZVP for N and O, and def2-TZVPP / def2-QZVPP for the metal.

CCSD(T) Calculations. CCSD(T) calculations were performed on H_2O, O_2, and H_2 as well as atomic O and H in order to benchmark density functional performance for the overall oxygen reduction reaction in Section 6.3.5. All calculations used B2PLYP geometries, a UHF reference, and a cc-pv6z basis. For free energy evaluations, the ZPE, thermal, and entropic corrections were taken from B2PLYP calculations.

A Note on Multireference Character. Near degeneracies among the 3d orbitals and strongly covalent bonds with some axial ligands are both potential sources of multiconfigurational character in metalloporphyrins.[87, 88] Where this character is mild, single reference coupled cluster should provide reference-level accuracy for reaction energies and spin-state energetics.[89, 87, 90, 56, 91] In fact, even in cases of moderate multiconfigurational character, CCSD(T) often provides only slightly diminished accuracy. [92, 93, 94, 88] To assess the degree of multiconfigurational character in the ground states of the presently studied complexes, we considered several metrics based on DLPNO-CCSD(T): T_1, the largest double excitation amplitudes, spin contamination, and %TAE[T]–the percentage of total atomization energy accounted for by the triples correction. These metrics (Table E.8) overwhelmingly fall within the thresholds established for well-behaved CC calculations.[95, 88] The weights of the

leading configurations and natural orbital occupation numbers from CASSCF calculations were also analyzed for all of the studied complexes (Tables E.9-E.12). These calculations revealed that some of the intermediates, notably all of the MP(O) species, exhibit moderate multiconfigurational character. Because of the differing multiconfigurational character along a reaction pathway, the accuracy of DLPNO-CCSD(T) may decrease to some degree. Still, we have no reason to doubt the general effectiveness of the method for the presently studied complexes and at any rate expect it to be a useful benchmark for the tested DFT functionals.

We note that DLPNO-CCSD(T) calculations were not performed for the $MP(O_2)$ intermediates, since both $FeP(O_2)$ and $CoP(O_2)$ exhibit antiferromagnetic coupling of electrons on the O_2 ligand and metal (Appendix E.8). These should be treated with a multireference method, or at least an unrestricted reference within CCSD(T) instead of quasi-restricted orbitals.

6.3 Results and Discussion

6.3.1 Linear Free Energy Scaling Relationships

LFESRs were found to exhibit significant dependence on the choice of functional, which impacts the derived volcano plots of catalyst activity. Figure 6.2 depicts the LFESRs between MP(O) and MP(OH) [Figure 6.2(a)] and MP(OOH) and MP(OH) [Figure 6.2(b)], calculated using all GGA and single-hybrid functionals. The relative energies of each intermediate, denoted ΔG_{O}, ΔG_{OH}, and ΔG_{OOH}, are defined in Appendix E.1.

The fitted scaling relationships depicted in Figure 6.2(a) and (b) show a monotonic decrease in slope and increase in intercept as the percentage of exact exchange in the functional increases (see Table 6.1). Thus, the fits for BP86 and PBE, which contain no exact exchange, are quite similar. Among the hybrid functionals, TPSSh shows the closest agreement with the pure GGAs, likely owing to its small amount of exact exchange. In contrast, the low slopes of the fits for B3LYP and PBE0 indicate significantly weaker binding of the OOH and O intermediates compared to the GGA predictions. This dependence on exact exchange is quite similar to that found by Busch et al. in the context of the water oxidation reaction on perfluoroporphyrins.[52] Finally, LFESRs constructed using BP86-optimized geometries and free energy cor-

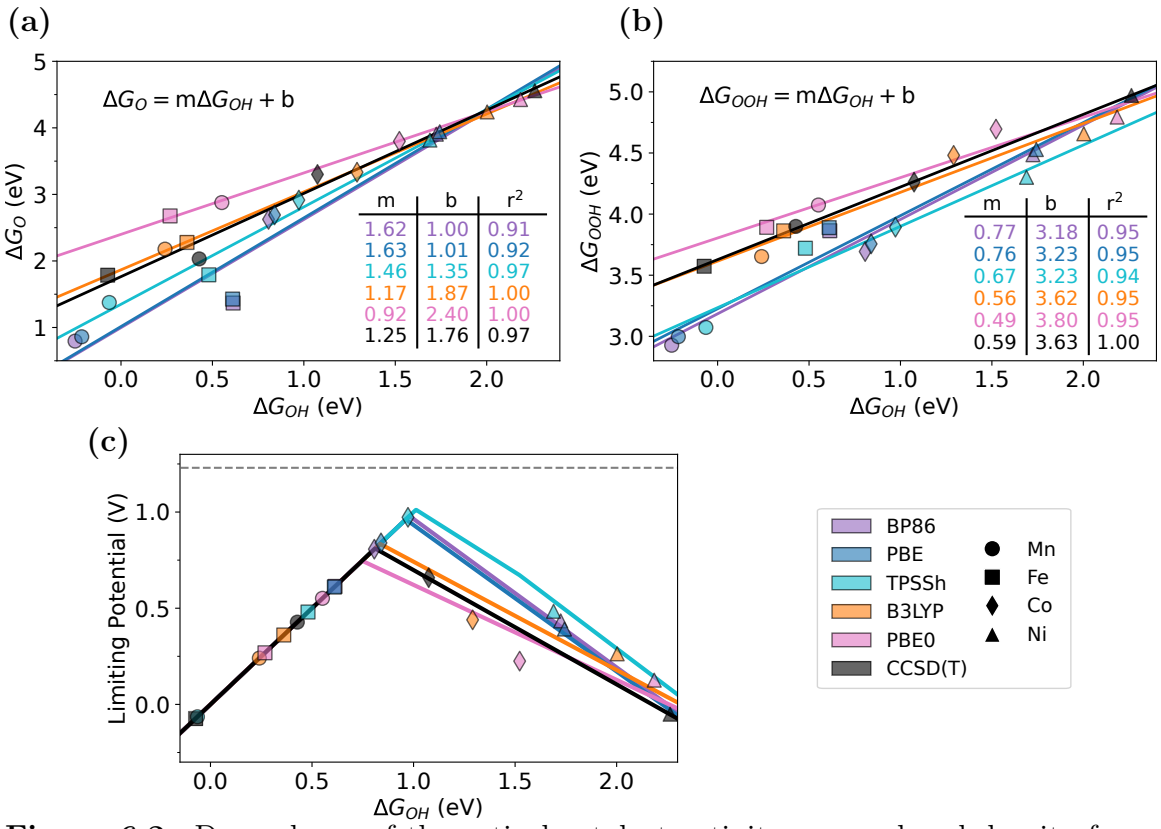

Figure 6.2: Dependence of theoretical catalyst activity on employed density functional. Linear free energy scaling relationships between the binding energies of **(a)** MP(O) and MP(OH) and **(b)** MP(OOH) and MP(OH). Parameters and r^2 values for the fit lines are shown as insets. Note that the different scale in **(b)** indicates a narrower range of energies for ΔG_{OOH}. **(c)** shows the resulting volcano plots derived from these scaling relationships. The theoretical ORR potential (1.23 V) is depicted as a dashed line above the volcano apex.

rections (Figure E.3) display the same trends and show that B2PLYP produces very similar fit lines to PBE0.

Based on electron-counting rules devised from adsorption on metal surfaces, one would expect the slope of the O/OH and OOH/OH LFESRs to be 2 and 1, respectively. [3, 96]. All functionals deviate significantly from this expectation. For GGA functionals, this discrepancy has previously been attributed to the lack of a flexible solvent model.[97] However, the much larger deviation for hybrid functionals cannot be dismissed so easily—indeed, such low slopes for the O/OH LFESR were seen to persist even under the application of an implicit solvent model in Ref [52]. Therefore, hybrid functionals, in particular those with greater than 10% exact exchange, do not support the commonly accepted assumption that the O ligand forms a double bond to the catalyst, whereas the OOH and OH ligands form single bonds.[96, 4] Instead,

these functionals predict that the M–O and M–OH bonds are rather similar in nature (this is reflected in the near-unity slope of the scaling relationship shown in Figure 6.2(a)), and that the M–OOH bond is weaker than the M–OH bond by about half (Figure 6.2(b)).

Combined, these effects mean that the hybrid functionals (other than TPSSh) predict a significantly less optimistic volcano plot than GGAs (Figure 6.2(c)), with minimum overpotentials of 0.39 V and 0.51 V for B3LYP and PBE0, respectively. Furthermore, the volcano plot is less symmetrical for these functionals. The right leg, corresponding to weak binding of OOH, is limiting for a broader range of OH binding strengths when using B3LYP and PBE0.

DLPNO-CCSD(T) electronic energies were corrected with TPSSh free energy terms to add reference lines to Figure 6.2. Fitted DLPNO-CCSD(T) LFESRs show remarkable agreement with B3LYP, even though individual data points do not show such a close accord between the two methods. The low slope of the O/OH scaling relation for DLPNO-CCSD(T) shows that PBE and BP86 cannot properly describe the relationship between these two intermediates. However, hybrid functionals do not universally remedy this situation, either, since there is a large variation in slope depending on the particular functional used. B3LYP seems to offer a fortuitous balance between TPSSh and PBE0, which seems to be linked to its intermediate proportion of exact exchange.

It should be noted that these LFESRs were calculated from only four catalysts per functional. Therefore, the coefficients of the best-fit lines should not be relied on as ironclad quantitative relationships. Nevertheless, the sampled MPs encompass a broad range of ΔG_{OH} values that are relevant to ORR, and the linear relationships show good fits to the data. Thus, the trends that emerge between functionals, which correlate well with the amount of exact exchange included in those functionals, represent real differences between functional predictions and not the effects of noise.

6.3.2 Benchmarking Relative Energies Against DLPNO-CCSD(T)

To determine which functional predicts the most accurate relative energies for constructing LFESRs, we calculated ΔE^{O}, ΔE_{OH}, and ΔE_{OOH} using DLPNO-CCSD(T) and compared against the DFT values. Due to the expense of computing vibrational energies with DLPNO-CCSD(T), only electronic energies are presented in Figure

6.3—otherwise, ΔE^{O}, ΔE_{OH}, and ΔE_{OOH} are defined analogously to ΔG^{O}, ΔG_{OH}, and ΔG_{OOH} (Appendix E.1). Unlike the LFESRs above, TPSSh/def2-TZVP geometries were used for all DFT and DLPNO-CCSD(T) single point calculations. An additional double-hybrid functional, the spin-opposite scaled PWPB95, which has performed well in recent benchmarking of transition metal reaction energies,[91, 56], was also included for comparison with B2PLYP.

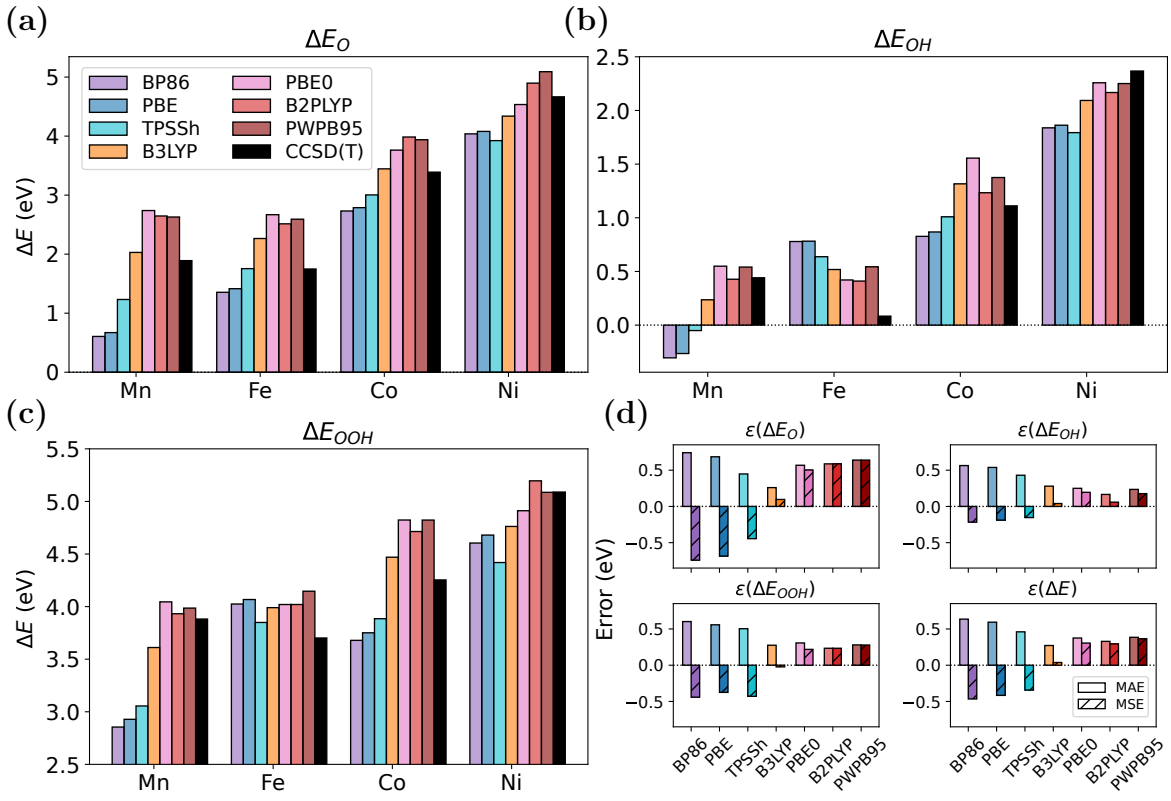

Figure 6.3: Benchmarking of relative energies of intermediates against DLPNO-CCSD(T). Panels **(a)**, **(b)**, and **(c)** show the relative energies of the bound O, OH, and OOH ligands, respectively. The plots in panel **(d)** show the Mean Absolute Error (MAE) and Mean Signed Error (MSE) of each functional relative to DLPNO-CCSD(T) for each of these ligands as well as the combined errors across all ligands ($\varepsilon(\Delta E)$).

As shown in Figure 6.3, BP86 and PBE usually significantly underestimate ΔE_{O}, ΔE_{OH}, and ΔE_{OOH} relative to DLPNO-CCSD(T), indicating overbinding of intermediates. Notably, FeP(OH) and FeP(OOH) are exceptions. This is likely due to both of these high spin sextet complexes being destabilized at the GGA level[98]—in fact, the GGAs predict a doublet ground state for both. TPSSh behaves similarly, albeit with a slightly lower Mean Absolute Error (MAE). In contrast, PBE0, B2PLYP, and

PWPB95 have lower MAEs but generally exhibit slight underbinding, summarized by their positive Mean Signed Errors (MSEs) for all intermediates in Figure 6.3(d). B3LYP falls between these two extremes, showing the lowest MAE across all functionals and a small MSE that points to minimal bias toward over- or underbinding. These results further reinforce the observation that increasing the proportion of exact exchange reduces the calculated binding strength of intermediates, with B3LYP striking the proper balance of exact exchange. They also indicate that while hybrid functionals offer a significant improvement over GGAs, there appears to be no benefit to using double-hybrid functionals.

MAEs across the three intermediates indicate that the bound O atom is treated less accurately than bound OH and OOH for nearly all functionals, but especially so for the GGA and double-hybrid functionals. GGAs are believed to provide a less accurate treatment of O-O double bonds than single[99], and it is possible that a similar effect is at play with the formally double-bound O atom here. The poor performance of B2PLYP and PWPB95 for O is somewhat surprising considering how well they perform on the other intermediates. It is likely that some of the difficulty stems from significant spin contamination in the MnP(O) doublet, FeP(O) triplet, and CoP(O) quartet states, which have values of $\langle S^2 \rangle_{\mathrm{B2PLYP}} - \langle S^2 \rangle_{\mathrm{exact}}$ of 0.64, 0.42, and 0.54, respectively (Figures E.4 and E.5). Such contamination is known to degrade the results of MP2.[100, 101] Interestingly, neither TPSSh nor B3LYP appear to suffer for MP(O), instead showing consistent accuracy across all intermediates.

6.3.3 Variation in Predicted Spin States

The correct prediction of the ground state spin multiplicities in the present study was an important problem that showed a large dependence on the chosen functional. At a fundamental level, the assignment of the correct ground state can provide mechanistic insights and even guide catalyst design to stabilize specific states with the desired reactivities. When experimental data are lacking, the spin multiplicities are often assumed from previous computational works, inferred based on theoretical arguments, or even calculated during geometry optimizations at lower levels of theory. Using an inappropriate spin state from one of these sources forces the reaction pathway through an excited state with an associated energetic penalty. Furthermore, the 3d transition metal porphyrins under study are known to contain low-lying excited states associated with both unoccupied metal and porphyrin orbitals, which make the proper deter-

mination of ground states challenging for DFT. Complicating the matter, different functionals tend to favor different spin states, albeit in a somewhat predictable way. In particular, including exact exchange in a functional preferentially stabilizes high-spin states in direct proportion to the percentage of exchange included.[102, 103, 104]. Figure E.6 confirms this trend for our systems and demonstrates that the effect is dampened by MP2 contributions in B2PLYP.

Table 6.2: Ground state multiplicities for metalloporphyrin intermediates.

Metal	Ligand	DFT[a]	CC[b]	GS[c]	Ref.	Metal	Ligand	DFT[a]	CC[b]	GS[c]	Ref.
Mn	–	6	6	6	6[d]	Co	–	2	2	2	2[d]
Mn	O_2	6	–	4	4[d,e]	Co	O_2	2	–	2	2[d]
Mn	OOH	5	5	5	–	Co	OOH	1	1	1	–
Mn	O	4	2[f]	2	–	Co	O	4	4	4	–
Mn	OH	5	5	5	–	Co	OH	1	1	1	–
Fe	–	3	5	3	3[d]	Ni	–	1	1	1	1[d]
Fe	O_2	1	–	1	1[d,e]	Ni	O_2	3	–	3	–
Fe	OOH	6	6	6	–	Ni	OOH	2	2	2	–
Fe	O	3	3	3	–	Ni	O	5	5	5	–
Fe	OH	6	6	6	6[e]	Ni	OH	2	2	2	–

[a] The most common spin predicted by the functionals studied (excluding PWPB95). Ties granted to the higher multiplicity.
[b] DLPNO-CCSD(T).
[c] Final assignment of the ground state multiplicity in the present work.
[d] Experimental. See Refs. [105, 106] for MnP, Ref. [107] for FeP, Ref. [108] for CoP, Refs. [109, 110, 111] for NiP, Refs. [112, 113] for $MnP(O_2)$, Refs. [114, 115] for $FeP(O_2)$, Ref. [116] for $CoP(O_2)$.
[e] *Ab initio* calculations. DMRG-CASPT2 for $MnP(O_2)$ and $FeP(O_2)$.[51] CASPT2 with CCSD(T) correction for 3s3p correlation[87, 90] and DLPNO-CCSD(T)[49] for FeP(OH).
[f] Splitting energy relative to quartet is less than 1 kcal/mol.

Table 6.2 shows the ground state multiplicities that we determined by DFT and DLPNO-CCSD(T) alongside those given by experiments and higher level calculations when available. At first glance, the DFT multiplicities, which were determined by taking the mode of the multiplicities predicted by all functionals, show excellent agreement with DLPNO-CCSD(T) and experimental results. However, this agreement belies the variability amongst the functionals (Table E.6). We compared the spin predictions of each functional against available reference data and our DLPNO-

CCSD(T) results (Figure 6.4(b)). Aside from the marginally best-performing B3LYP (17/20) and worst-performing B2PLYP (15/20), all functionals correctly predicted multiplicities for 16 of the 20 species. However, the erroneous species generally differed from functional to functional, and there was no obvious benefit from moving up rungs of Jacob's ladder. As a result, B2PLYP predicts different ground state spins than any of BP86, PBE, and TPSSh for a concerning 9 out of the 20 studied complexes (Figure E.6). Disagreements between functionals do appear to be tied strongly to the impact of exact exchange, with the functional with a higher proportion of exact exchange almost always predicting the higher multiplicity.

Table 6.2 also highlights in red what we might call poorly behaved intermediates, ones for which at least one functional misassigned the ground state spin. These intermediates tended to be concentrated in the earlier transition metal porphyrins, which exhibit strong binding of oxygen species (note more instances of disagreement in Mn and Fe than for Co and Ni). Cross-referencing with Figure 6.4(a), we see that pure GGAs and TPSSh tended to excel in determining spin ordering for weak-binding complexes (both later transition metal species and dioxygen species across all metals), while hybrid and double-hybrids improved predictions for stronger-binding complexes at the expense of some accuracy for the late transition metals.

It is important to note that despite the inconsistency among functionals, the DFT spin assignments for nine out of the eleven poorly behaved complexes were reconciled with available reference and DLPNO-CCSD(T) results simply by choosing the most commonly predicted multiplicity among all functionals. The two exceptions were $MnP(O_2)$, a notoriously challenging system with a low-lying sextet, and MnP(O), which DLPNO-CCSD(T) predicts to have a quartet less than 1 kcal/mol higher than the ground state doublet. For both of these systems, the six tested functionals were evenly split in their spin assignments, which highlights the difficulty that the Mn porphyrins pose for spin state ordering. Overall, these results show that outside of some exceptional cases, application of several functionals with a range of exact exchange can be a viable approach to determine ground state spins for metalloporphyrins when experimental data or higher-level calculations are unavailable or unfeasible.

Since the difficulty of ground state spin ordering arises largely because these systems have small spin splitting energies, one might assume that the energetic consequences of misassigning the ground state multiplicity would be rather small. Within our data set, when a functional incorrectly predicted the ground state, the true ground state was only 5.4 kcal/mol higher in energy than the incorrect state, on average (me-

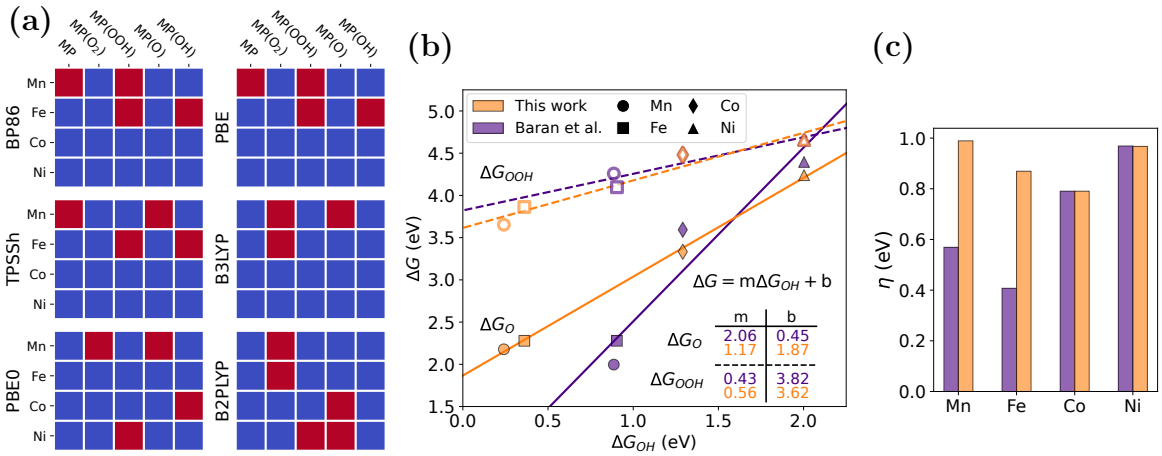

Figure 6.4: Dependence of ground state spin on employed density functional. **(a)** The correspondence between the GS spin predictions of each functional and the best guess for the true GS spin for each geometry. Blue and red indicate correct and incorrect prediction, respectively. **(b)** The OOH/OH and O/OH LFESRs calculated using B3LYP using either the ground state multiplicities from Ref [20] or from the present study. **(c)** The theoretical overpotentials calculated from these two sets of multiplicities using B3LYP.

dian 3.9 kcal/mol). To properly assess the impact of these spin splitting energies, we recalculated the LFESR for the best-performing B3LYP using the ground state spins determined by Baran *et al.* in a previous study using the pure GGA OLYP (See Table E.7).[20] Figure 6.4(b) shows that the O/OH scaling relation was most significantly affected, with the change driven primarily by changes in ΔG_{OH} for MnP and FeP. Recalculated overpotentials in Figure 6.4(c) tell a similar story, with the overpotentials for MnP and FeP dropping erroneously by roughly 0.4 eV while the remaining species are unchanged. Thus, while the average spin splitting energies for the metalloporphyrins are quite small, it only takes the reversal of spin ordering (or the use of an erroneous ground state spin calculated at a lower level theory) for a single larger gap intermediate to greatly impact theoretical overpotentials.

6.3.4 Variation in Predicted Geometries

Unlike spin state ordering, structural parameters are often assumed to be relatively insensitive to functional. We found that this assumption held true in general for metalloporphyrins but note some quite substantial outliers. Most notably, as has already been studied for FeP,[50, 117] metal-oxygen bond lengths were found to vary

directly and strongly with the amount of exact exchange in a functional for the dioxygen adducts of all but the most strongly binding MnP (Figure 6.5(a) and (c)). For $FeP(O_2)$ and $CoP(O_2)$, this variation is strongly linked to the degree of spin-symmetry breaking, with hybrid functionals tending to produce a greater degree of antiferromagnetic spin coupling between the metal center and dioxygen (Appendix E.8). A similar variation presented in the very weakly bound NiP(OOH), with GGA functionals preferring a configuration with an outward-facing hydrogen and the remaining functionals predicting hydrogen bond donation to the porphyrin nitrogen (Figure 6.5(d). Finally, the MP(O) intermediates showed moderate variations of about 0.1 Å in the metal-oxygen bond length depending on the functional used. On the whole, M–O bondlengths tend to correlate well within rungs of Jacob's ladder (Figure 6.5(b), even though most intermediates involved in electrocatalysis were fairly robust to changes in functional. Functional type and amount of exact exchange also correlated well with the amount that metal atoms were displaced from the porphyrin plane (Figure E.10) but less so with other geometrical parameters like metal-nitrogen bond lengths and the degree of ruffling and saddling of the macrocycle (Figures E.9, and E.11).

A natural question is whether the level of theory used for geometry optimization really matters energetically, for instance when computing catalyst activities. Figure 6.6(b) quantifies the energetic difference between each geometry optimized at the BP86 level and the energy of the re-optimized geometry for each other functional we tested. These relative energies are plotted against the RMSD for BP86 and re-optimized geometries as described in Figure 6.6(a) to understand how sensitive these systems are to small structural changes. For the most part, the structural and energetic differences remain small (< 0.1 Å and < 5 kcal/mol, respectively) across all intermediates for a given functional. This indicates that the relative energies of intermediates, and therefore computed catalyst activities, are only minimally affected by the functional used for geometry optimization. However, there are some notable exceptions. The weak-binding intermediates $FeP(O_2)$, $CoP(O_2)$, and NiP(OOH) all show intermediate to large RMSDs and large energy differences for at least one functional. These results suggest that caution should be taken when determining the structures of weak binding MP intermediates, though we note that this is rarely an issue for the determination of overpotentials since the dioxygen intermediate is not required for these.

These results also provide a strong warning against the use of double-hybrid functionals for metalloporphyrins. B2PLYP shows very large relative energies for

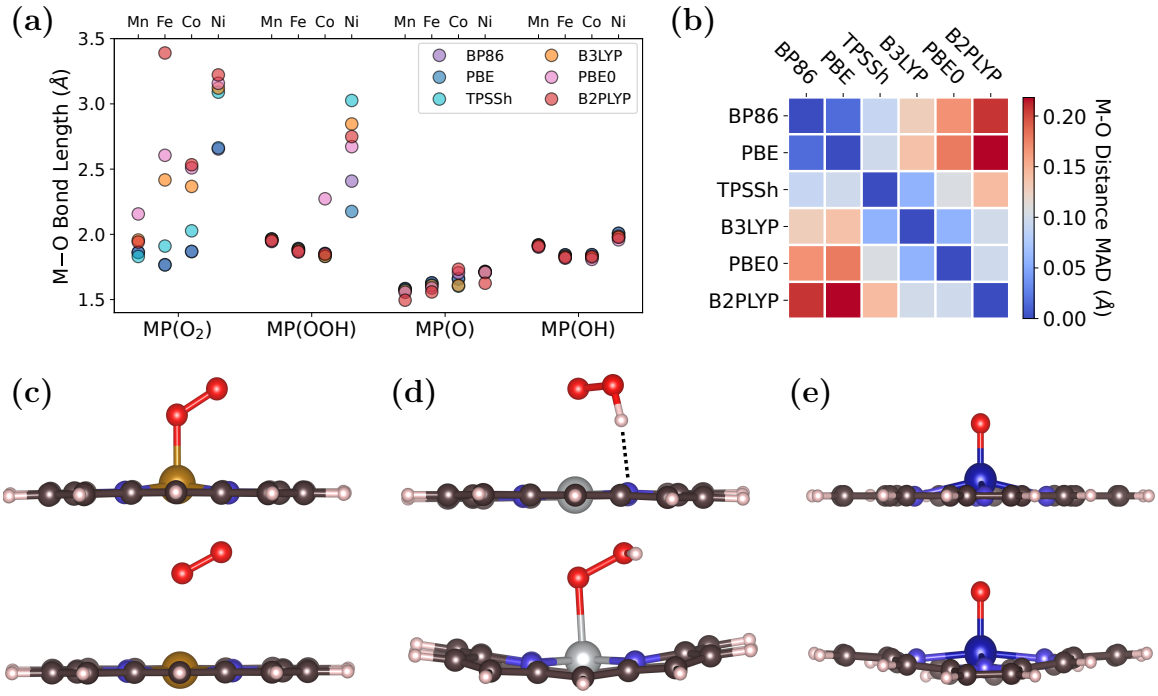

Figure 6.5: Dependence of geometries on employed density functional. Panel **(a)** shows the metal-oxygen bond lengths for all oxygen-containing intermediates computed with each functional. Panel **(b)** shows the Mean Absolute Deviation (MAD) of metal-oxygen bonds for pairs of functionals across all metalloporphyrin geometries and all tested multiplicities. Panel **(c)** shows BP86 (top) and PBE0 (bottom) structures of FeP(O_2) with multiplicity 1. Panel **(d)** shows B3LYP (top) and PBE (bottom) structures of NiP(OOH) with multiplicity 2. Panel **(e)** shows B3LYP (top) and PBE0 (bottom) structures of CoP(O) with multiplicity 4.

MnP(O), FeP(O), CoP(OOH) and NiP(OH) despite these intermediates having small RMSDs. When using B2PLYP for single-point calculations, all of these complexes showed large increases in spin-contamination at the BP86 geometry compared to the B2PLYP one. In addition, the geometries of FeP(O) and NiP(OH) would not converge fully when optimized with B2PLYP. It is well established that the Møller-Plesset perturbation series converges more slowly for spin-contaminated references [118, 100] and that MP2 fails dramatically in frequency calculations for geometries where spin contamination changes rapidly as a function of nuclear coordinates.[119] However, other work has argued that double-hybrids benefit from a cancellation of the energetic effects of spin contamination at the Hartree-Fock and MP2 levels.[120].

Our results, including comparison with resricted open-shell calculations (Figure E.4) suggest that the studied metalloporphyrins do not always benefit from this can-

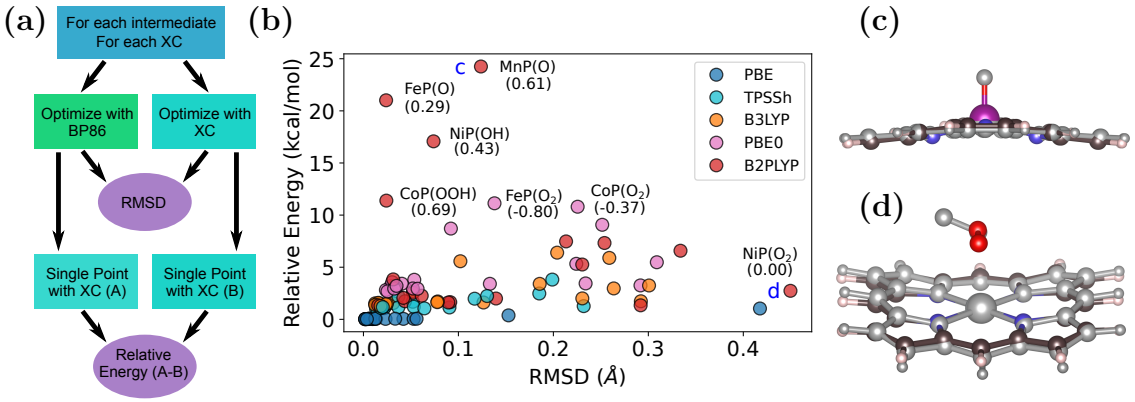

Figure 6.6: Comparison of geometries optimized by BP86 and other functionals. **(a)** Outline of the procedure for calculating the RMSD values and relative energies of BP86 geometries shown in Panel (b). **(b)** Energies of BP86-optimized geometries relative to the reoptimized geometries are plotted against the RMSD for these same two geometries for the ground states of all intermediates. Structures with large RMSD and relative energies have been labeled, with the change in spin contamination between the BP86 geometry and the reoptimized one ($\langle S^2 \rangle_{\mathrm{BP86}} - \langle S^2 \rangle_{\mathrm{XC}}$) indicated in brackets. **(c)** Overlay of the MnP(O) optimized at the BP86 (grey) and B2PLYP (color) levels. **(d)** Overlay of NiP(O_2) optimized at the BP86 (grey) and B2PLYP (color) levels.

cellation of errors. The reason for this requires further investigation, but it is likely that spin contamination will be a common issue for B2PLYP when computing low- and intermediate spin states of metalloporphyrins, even when static correlation is not a serious concern. Because the SCF component of B2PLYP has a high percentage of exact exchange, it will overstabilize high spin states relative to a low spin ground state, even flipping the state ordering in some cases to predict a high spin ground state. This leads to what Shee *et al.* have termed "variational collapse"[121] when calculating the low spin state—a mixing with the high spin ground state to variationally lower the total energy, which produces artificial spin contamination in the low spin state.

Furthermore, recent investigations have shown that even absent spin contamination, double-hybrids may be unreliable for metal-ligand bonds with multiple electron pairs, as in those with both σ- and π-bonding.[101, 121] Given these drawbacks and the lack of notable improvement over single hybrid functionals, we recommend against the use of double-hybrid functionals for metalloporphyrin and related systems without careful comparison against reference data.

6.3.5 Variation in $\Delta G^0_{\mathbf{ORR}}$ and Empirical O_2 Corrections

Finally, it is worth considering the extent to which the treatment of the gas-phase species H_2, H_2O, and O_2 by different functionals impacts calculated reaction pathways. To this end, we examine how the free energy of the overall 4-electron reduction of O_2 to water (Equation (E.2)) depends on the functional used and how empirical corrections to O_2 interact with this dependence.

The DFT reaction free energies were compared to the experimental value of -4.92 eV (-113.5 kcal/mol). Additionally, the atomization enthalpies of the involved molecules were calculated to pinpoint sources of error in the overall free energies. Table 6.3 shows these values and their errors, referenced against experimental results. Experimental values of $\Delta H^0_{\text{at}}(O_2)$ (118.876 kcal/mol) and $\Delta H^0_{\text{at}}(H_2)$ (104.154 kcal/mol) were taken from Luo [122] and $\Delta H^0_{\text{at}}(H_2O)$ (221.558 kcal/mol) from the NIST CCCBDB Database.[123]

Table 6.3: Theoretical ORR free energy and relevant atomization enthalpies.[a,b]

Method	$\Delta G(ORR)$	$\Delta H^0_{\text{at}}(O_2)$	$\Delta H^0_{\text{at}}(H_2)$	$\Delta H^0_{\text{at}}(H_2O)$
BP86	-101.2 (12.2)	138.5 (19.6)	106.5 (2.3)	227.5 (5.9)
PBE	-103.0 (10.5)	142.3 (23.4)	99.5 (-4.6)	223.3 (1.8)
TPSSh	-95.2 (18.3)	119.1 (0.2)	107.4 (3.2)	215.7 (-5.9)
B3LYP	-104.7 (8.8)	121.6 (2.7)	105.1 (0.9)	219.4 (-2.2)
PBE0	-107.8 (5.6)	122.9 (4.0)	99.1 (-5.0)	215.6 (-5.9)
B2PLYP	-108.1 (5.4)	122.0 (3.1)	103.4 (-0.8)	219.5 (-2.0)
CCSD(T)	-113.6 (-0.1)	117.8 (-1.1)	103.9 (-0.3)	220.7 (-0.8)

[a] Values in parentheses indicate errors relative to the reference values.
[b] All values in kcal/mol.

Moving from lower to higher runs of Jacob's ladder (top to bottom in Table 6.3) generally improves the predicted free energy of the ORR (the poor performance of TPSSh is a notable exception to this trend). Nevertheless, none of the tested functionals approach chemical accuracy (error $\leq$ 1 kcal/mol). Thus, semi-empirical corrections are important for the ORR. The poor treatment of O_2 atomization energies[124] and adsorption energies[125] relative to H_2 or H_2O by GGA functionals is typically used to justify an empirical correction to O_2 alone in order to bring calculated G^0_{ORR} values in line with experiment.[5, 126]. However, the errors associated with H_2 and H_2O have been shown to be important for some GGA functionals.[127, 128] Another recent study of the 2-electron ORR showed that for both GGA and hybrid functionals,

O_2-only corrections were insufficient in the face of similar order-of-magnitude errors in gas phase H_2O_2.[99] As a result, it is important to consider any similar magnitude gas-phase errors before applying an O_2-only correction.

In Table 6.3, the atomization energy of O_2 shows the expected large error for GGA functionals but a significantly reduced error for hybrid functionals and B2PLYP. For these higher-level functionals, these errors are of similar magnitude to those in the H_2 and H_2O atomization energies, leading us to believe that hybrid functionals treat all of these species with a comparable level of accuracy. Some caution is advised when using the accuracy of atomization energies to draw conclusions about a functional's accuracy for thermochemistry, as these do not correlate well in general.[129] For GGA functionals specifically, errors in atomization energies often derive more from a poor treatment of the spin polarized single atoms than from the treatment of molecules.[130] Bearing this in mind, we still believe that the uniformly small errors in atomization energies across all species for (double-) hybrid functionals indicates that the error associated with the O_2 molecule can no longer be considered *a priori* to be an order of magnitude worse than H_2O and H_2. This assertion is supported by recent work on $H_xN_yO_z$ molecules, which concluded that unlike with GGA functionals, corrections for O_2 were were unnecessary to produce accurate formation enthalpies when using B3LYP and PBE0.[131]

It thus seems likely that for (double-) hybrid functionals, residual errors in $\Delta G^0_{\mathrm{ORR}}$ have more to do with the incomplete cancellation of relatively small errors spread across all three species in the reaction than with a single error concentrated on O_2. Atomization energy errors in Table 6.3 suggest that lack of error cancellation is particularly to blame for the poor reaction free energy of TPSSh, while the relatively good free energy of PBE0 results from some fortuitous cancellation. If this is the case, merely shifting the O_2 free energy to correct the overall reaction free energy means that this O_2 energy absorbs the errors associated with H_2 and H_2O, introducing a bias that depends on the distribution of these errors, which is not systematic across functionals (Table 6.3).

Thus, while the proposal of an alternative gas-phase correction scheme is outside the scope of this work, we do think that the existing O_2 correction scheme does introduce a source of variability associated with the chosen functional. For hybrid functionals, this variability should be small in most cases, but perhaps not insignificant in light of the otherwise high accuracy of these functionals. Improved corrections may therefore be necessary to match the high performance of modern functionals without

introducing spurious errors.

6.4 Conclusions

In the present study, we evaluated the dependence of the theoretical activities and linear scaling relationships of metalloporphyrin catalysts on the particular functional used. Comparisons of the relative energies of intermediates with DLPNO-CCSD(T) showed that GGAs tended to overstabilize axial oxygen-containing ligands, double-hybrids understabilized them, and single hybrids stabilized them according to the amount of exact exchange in the functional. For the present systems, B3LYP, with its 20% exchange, produced the best accuracy while also minimizing bias toward over- or under-binding.

Breaking down the differences between functionals, we found that ground state spin state predictions were quite dependent on the presence of exact exchange in a functional and could have a significant impact on theoretical catalyst activities if not properly assigned. Pooling the predictions of functionals with different amounts of exchange, however, almost always generated an assignment in line with experiment and DLPNO-CCSD(T). On the other hand, geometries were generally resilient to the choice of functional. Exceptions included the metal-oxygen bonds of weakly bound intermediates and some striking difficulties with geometry convergence and poor energies for spin-contaminated wavefunctions when using B2PLYP, which highlight the potential pitfalls of using double-hybrid functionals for these systems. Finally, we believe the commonly used empirical O_2 correction could be an additional source of variation among functionals due to the different accuracy of GGAs and hybrids in treating O_2. This correction should be reassessed as hybrid functionals become more commonplace in theoretical catalysis studies.

The density functional dependence of catalyst activities and linear scaling relationships is important for the rational design of ORR catalysts. The binding strength of intermediates dictates the thermodynamically limiting electron transfer step and indicates whether key binding interactions need to be strengthened or weakened to increase catalyst activity. Thus, for catalysts with intermediate binding strengths, the choice of functional can have an immediate impact on catalyst design choices. We hope that the present work can guide the informed use of functionals for the study of porphyrins and other M-N-C catalysts for the ORR. Hybrid functionals, with the appropriate use of DLPNO-CCSD(T) for validation, represent a promising path for-

ward. We also note that further work is warranted to better understand the accuracy limits of DLPNO-CCSD(T) in the present context, given the moderate multiconfigurational character noted for some intermediates. This prospect will require a careful choice of multireference method and the selection of balanced active spaces across all reaction coordinates. These non-trivial challenges are are being made more approachable by the advent of algorithms for automatic active space selection and approximate CI solvers that allow the treatment of the large active spaces required.[132, 133]

Bibliography

[1] Brett Henderson, Sofia Donnecke, Scott N. Genin, Ilya G. Ryabinkin, and Irina Paci. Key role of density functional approximation in predicting m–n–c catalyst activities for oxygen reduction. *The Journal of Physical Chemistry C*, 128(38):15899–15911, September 2024.

[2] Yanghua He, Shengwen Liu, Cameron Priest, Qiurong Shi, and Gang Wu. Atomically dispersed metal-nitrogen-carbon catalysts for fuel cells: Advances in catalyst design, electrode performance, and durability improvement. *Chemical Society Reviews*, 49(11):3484–3524, 2020.

[3] F. Abild-Pedersen, J. Greeley, F. Studt, J. Rossmeisl, T. R. Munter, P. G. Moses, E. Skúlason, T. Bligaard, and J. K. Nørskov. Scaling properties of adsorption energies for hydrogen-containing molecules on transition-metal surfaces. *Physical Review Letters*, 99(1):016105, July 2007.

[4] Ambarish Kulkarni, Samira Siahrostami, Anjli Patel, and Jens K. Nørskov. Understanding catalytic activity trends in the oxygen reduction reaction. *Chemical Reviews*, 118(5):2302–2312, February 2018.

[5] J. K. Nørskov, J. Rossmeisl, A. Logadottir, L. Lindqvist, J. R. Kitchin, T. Bligaard, and H. Jónsson. Origin of the overpotential for oxygen reduction at a fuel-cell cathode. *The Journal of Physical Chemistry B*, 108(46):17886–17892, 2004.

[6] T. Bligaard, J.K. Nørskov, S. Dahl, J. Matthiesen, C.H. Christensen, and J. Sehested. The brønsted–evans–polanyi relation and the volcano curve in heterogeneous catalysis. *Journal of Catalysis*, 224(1):206–217, May 2004.

[7] Joseph H. Montoya, Linsey C. Seitz, Pongkarn Chakthranont, Aleksandra Vojvodic, Thomas F. Jaramillo, and Jens K. Nørskov. Materials for solar fuels and chemicals. *Nature Materials*, 16(1):70–81, December 2016.

[8] Michael Busch, Niels B. Halck, Ulrike I. Kramm, Samira Siahrostami, Petr Krtil, and Jan Rossmeisl. Beyond the top of the volcano? – a unified approach to electrocatalytic oxygen reduction and oxygen evolution. *Nano Energy*, 29:126–135, November 2016.

[9] Tyler Sours, Anjli Patel, Jens Nørskov, Samira Siahrostami, and Ambarish Kulkarni. Circumventing scaling relations in oxygen electrochemistry using metal–organic frameworks. *The Journal of Physical Chemistry Letters*, 11(23):10029–10036, November 2020.

[10] Aleksandra Vojvodic and Jens K. Nørskov. New design paradigm for heterogeneous catalysts. *National Science Review*, 2(2):140–143, April 2015.

[11] Javier Pérez-Ramírez and Núria López. Strategies to break linear scaling relationships. *Nature Catalysis*, 2(11):971–976, October 2019.

[12] Georgios Kyriakou, Matthew B. Boucher, April D. Jewell, Emily A. Lewis, Timothy J. Lawton, Ashleigh E. Baber, Heather L. Tierney, Maria Flytzani-Stephanopoulos, and E. Charles H. Sykes. Isolated metal atom geometries as a strategy for selective heterogeneous hydrogenations. *Science*, 335(6073):1209–1212, March 2012.

[13] Maximilian Moser, Izabela Czekaj, Núria López, and Javier Pérez-Ramírez. The virtue of defects: Stable bromine production by catalytic oxidation of hydrogen bromide on titanium oxide. *Angewandte Chemie*, 126(33):8772–8777, June 2014.

[14] Gianvito Vilé, Davide Albani, Maarten Nachtegaal, Zupeng Chen, Dariya Dontsova, Markus Antonietti, Núria López, and Javier Pérez-Ramírez. A stable single-site palladium catalyst for hydrogenations. *Angewandte Chemie International Edition*, 54(38):11265–11269, July 2015.

[15] Rodrigo García-Muelas, Federico Dattila, Tatsuya Shinagawa, Antonio J. Martín, Javier Pérez-Ramírez, and Núria López. Origin of the selective electroreduction of carbon dioxide to formate by chalcogen modified copper. *The Journal of Physical Chemistry Letters*, 9(24):7153–7159, December 2018.

[16] Thomas A.A. Batchelor, Jack K. Pedersen, Simon H. Winther, Ivano E. Castelli, Karsten W. Jacobsen, and Jan Rossmeisl. High-entropy alloys as a discovery platform for electrocatalysis. *Joule*, 3(3):834–845, March 2019.

[17] U. Heiz, A. Sanchez, S. Abbet, and W.-D. Schneider. Catalytic oxidation of carbon monoxide on monodispersed platinum clusters: Each atom counts. *Journal of the American Chemical Society*, 121(13):3214–3217, March 1999.

[18] Borna Zandkarimi and Anastassia N. Alexandrova. Dynamics of subnanometer pt clusters can break the scaling relationships in catalysis. *The Journal of Physical Chemistry Letters*, 10(3):460–467, January 2019.

[19] Zisheng Zhang, Borna Zandkarimi, Julen Munarriz, Claire E. Dickerson, and Anastassia N. Alexandrova. Fluxionality of subnano clusters reshapes the activity volcano of electrocatalysis. *ChemCatChem*, 14(15):e202200345, June 2022.

[20] Jakub D. Baran, Henrik Grönbeck, and Anders Hellman. Analysis of porphyrines as catalysts for electrochemical reduction of o2 and oxidation of h2o. *Journal of the American Chemical Society*, 136(4):1320–1326, January 2014.

[21] Giacomo M. Lari, Begoña Puértolas, Masoud Shahrokhi, Núria López, and Javier Pérez-Ramírez. Hybrid palladium nanoparticles for direct hydrogen peroxide synthesis: The key role of the ligand. *Angewandte Chemie*, 129(7):1801–1805, December 2016.

[22] Suljo Linic, Phillip Christopher, and David B. Ingram. Plasmonic-metal nanostructures for efficient conversion of solar to chemical energy. *Nature Materials*, 10(12):911–921, November 2011.

[23] Alireza Khorshidi, James Violet, Javad Hashemi, and Andrew A. Peterson. How strain can break the scaling relations of catalysis. *Nature Catalysis*, 1(4):263–268, April 2018.

[24] Felipe A. Garcés-Pineda, Marta Blasco-Ahicart, David Nieto-Castro, Núria López, and José Ramón Galán-Mascarós. Direct magnetic enhancement of electrocatalytic water oxidation in alkaline media. *Nature Energy*, 4(6):519–525, June 2019.

[25] Hoon T. Chung, David A. Cullen, Drew Higgins, Brian T. Sneed, Edward F. Holby, Karren L. More, and Piotr Zelenay. Direct atomic-level insight into the active sites of a high-performance pgm-free orr catalyst. *Science*, 357(6350):479–484, 8 2017.

[26] Michael L. Pegis, Catherine F. Wise, Daniel J. Martin, and James M. Mayer. Oxygen reduction by homogeneous molecular catalysts and electrocatalysts. *Chemical Reviews*, 118(5):2340–2391, February 2018.

[27] Bin Lv, Xialiang Li, Kai Guo, Jun Ma, Yanzhi Wang, Haitao Lei, Fang Wang, Xiaotong Jin, Qingxin Zhang, Wei Zhang, Ran Long, Yujie Xiong, Ulf-Peter Apfel, and Rui Cao. Controlling oxygen reduction selectivity through steric effects: Electrocatalytic two-electron and four-electron oxygen reduction with cobalt porphyrin atropisomers. *Angewandte Chemie International Edition*, 60(23):12742–12746, April 2021.

[28] Xialiang Li, Haitao Lei, Lisi Xie, Ni Wang, Wei Zhang, and Rui Cao. Metalloporphyrins as catalytic models for studying hydrogen and oxygen evolution and oxygen reduction reactions. *Accounts of Chemical Research*, 55(6):878–892, February 2022.

[29] Zuozhong Liang, Hongbo Guo, Guojun Zhou, Kai Guo, Bin Wang, Haitao Lei, Wei Zhang, Haoquan Zheng, Ulf-Peter Apfel, and Rui Cao. Metal–organic-framework-supported molecular electrocatalysis for the oxygen reduction reaction. *Angewandte Chemie International Edition*, 60(15):8472–8476, March 2021.

[30] Qin Wu, Guangjin Wang, and Mingjie Liu. On the sensitivity to density-functional approximations for co binding energies of single-atom catalysts in nitrogen-doped graphene. *ChemPhysChem*, 23(5):e202100787, February 2022.

[31] Lingmei Ni, Charlotte Gallenkamp, Stephan Wagner, Eckhard Bill, Vera Krewald, and Ulrike I. Kramm. Identification of the catalytically dominant iron environment in iron- and nitrogen-doped carbon catalysts for the oxygen reduction reaction. *Journal of the American Chemical Society*, 144(37):16827–16840, August 2022.

[32] Charlotte Gallenkamp, Ulrike I. Kramm, and Vera Krewald. Fen4 environments upon reduction: A computational analysis of spin states, spectroscopic properties, and active species. *JACS Au*, 4(3):940–950, February 2024.

[33] Edward F Holby, Gang Wu, Piotr Zelenay, and Christopher D Taylor. Structure of fe-nx-c defects in oxygen reduction reaction catalysts from first-principles modeling. *Journal of Physical Chemistry C*, 118:14388–14393, 2014.

[34] Edward F. Holby and Christopher D. Taylor. Activity of n-coordinated multi-metal-atom active site structures for pt-free oxygen reduction reaction catalysis: Role of oh ligands. *Scientific Reports*, 5:1–4, 2015.

[35] Alfred B. Anderson and Edward F. Holby. Pathways for O2 Electroreduction over Substitutional FeN4, HOFeN4, and OFeN4 in Graphene Bulk Sites: Critical Evaluation of Overpotential Predictions Using LGER and CHE Models. *Journal of Physical Chemistry C*, 123(30):18398–18409, 2019.

[36] Gerald Knizia and Garnet Kin-Lic Chan. Density matrix embedding: A simple alternative to dynamical mean-field theory. *Physical Review Letters*, 109(18):186404, November 2012.

[37] Gerald Knizia and Garnet Kin-Lic Chan. Density matrix embedding: A strong-coupling quantum embedding theory. *Journal of Chemical Theory and Computation*, 9(3):1428–1432, February 2013.

[38] Jincheng Lei and Tianyu Zhu. Impact of potential and active-site environment on single-iron-atom-catalyzed electrochemical co2 reduction from accurate quantum many-body simulations. *ACS Catalysis*, 14(6):3933–3942, February 2024.

[39] Robert H. Lavroff, Daniel Kats, Lorenzo Maschio, Nikolay Bogdanov, Ali Alavi, Anastassia N. Alexandrova, and Denis Usvyat. Aperiodic fragments in periodic solids: Eliminating the need for supercells and background charges in electronic structure calculations of defects. *arXiv*, 2024. arXiv:2406.03373v1 (accessed 2024-07-30).

[40] Abhishek Mitra, Matthew R. Hermes, Minsik Cho, Valay Agarawal, and Laura Gagliardi. Periodic density matrix embedding for co adsorption on the mgo(001)

surface. *The Journal of Physical Chemistry Letters*, 13(32):7483–7489, August 2022.

[41] Maristella Alessio, Denis Usvyat, and Joachim Sauer. Chemically accurate adsorption energies: Co and h2o on the mgo(001) surface. *Journal of Chemical Theory and Computation*, 15(2):1329–1344, December 2018.

[42] Francesca Fasulo, Abhishek Mitra, Ana B. Muñoz-García, Michele Pavone, and Laura Gagliardi. Unveiling the role of surface ir-oxo species in o2 evolution at iro2 electrocatalysts via embedded cluster multireference calculations. *The Journal of Physical Chemistry C*, 128(17):7343–7351, March 2024.

[43] Christopher Sheldon, Joachim Paier, Denis Usvyat, and Joachim Sauer. Hybrid rpa:dft approach for adsorption on transition metal surfaces: Methane and ethane on platinum (111). *Journal of Chemical Theory and Computation*, 20(5):2219–2227, February 2024.

[44] Elena Voloshina, Denis Usvyat, Martin Schütz, Yuriy Dedkov, and Beate Paulus. On the physisorption of water on graphene: a ccsd(t) study. *Physical Chemistry Chemical Physics*, 13(25):12041, 2011.

[45] Hong-Zhou Ye and Timothy C. Berkelbach. Adsorption and vibrational spectroscopy of co on the surface of mgo from periodic local coupled-cluster theory. *Faraday Discussions*, 2024. Article ASAP. DOI: 10.1039/d4fd00041b (accessed 2024-07-30).

[46] Thomas Mullan, Lorenzo Maschio, Peter Saalfrank, and Denis Usvyat. Reaction barriers on non-conducting surfaces beyond periodic local mp2: Diffusion of hydrogen on α-al2o3(0001) as a test case. *The Journal of Chemical Physics*, 156(7):074109, February 2022.

[47] Theodoros Tsatsoulis, Felix Hummel, Denis Usvyat, Martin Schütz, George H. Booth, Simon S. Binnie, Michael J. Gillan, Dario Alfè, Angelos Michaelides, and Andreas Grüneis. A comparison between quantum chemistry and quantum monte carlo techniques for the adsorption of water on the (001) lih surface. *The Journal of Chemical Physics*, 146(20):204108, May 2017.

[48] Björn Kirchhoff, Aleksei Ivanov, Egill Skúlason, Timo Jacob, Donato Fantauzzi, and Hannes Jónsson. Assessment of the accuracy of density functionals for

calculating oxygen reduction reaction on nitrogen-doped graphene. *J. Chem. Theory Comput.*, 17(10):6405–6415, October 2021.

[49] Maria Drosou, Christiana A. Mitsopoulou, and Dimitrios A. Pantazis. Reconciling local coupled cluster with multireference approaches for transition metal spin-state energetics. *Journal of Chemical Theory and Computation*, 18(6):3538–3548, May 2022.

[50] Mariusz Radoń and Kristine Pierloot. Binding of CO, NO, and o_2 to heme by density functional and multireference ab initio calculations. *The Journal of Physical Chemistry A*, 112(46):11824–11832, October 2008.

[51] Quan Manh Phung and Kristine Pierloot. The dioxygen adducts of iron and manganese porphyrins: electronic structure and binding energy. *Physical Chemistry Chemical Physics*, 20(25):17009–17019, 2018.

[52] Michael Busch, Alberto Fabrizio, Sandra Luber, Jürg Hutter, and Clemence Corminboeuf. Exploring the limitation of molecular water oxidation catalysts. *The Journal of Physical Chemistry C*, 122(23):12404–12412, May 2018.

[53] Anjli M. Patel, Stefan Ringe, Samira Siahrostami, Michal Bajdich, Jens K. Nørskov, and Ambarish R. Kulkarni. Theoretical approaches to describing the oxygen reduction reaction activity of single-atom catalysts. *The Journal of Physical Chemistry C*, 122(51):29307–29318, November 2018.

[54] Wanyi Jiang, Marie L. Laury, Mitchell Powell, and Angela K. Wilson. Comparative study of single and double hybrid density functionals for the prediction of 3d transition metal thermochemistry. *Journal of Chemical Theory and Computation*, 8(11):4102–4111, September 2012.

[55] Klaus A. Moltved and Kasper P. Kepp. Performance of density functional theory for transition metal oxygen bonds. *ChemPhysChem*, 20(23):3210–3220, October 2019.

[56] Leonard R. Maurer, Markus Bursch, Stefan Grimme, and Andreas Hansen. Assessing density functional theory for chemically relevant open-shell transition metal reactions. *Journal of Chemical Theory and Computation*, 17(10):6134–6151, September 2021.

[57] Fang Liu, Tzuhsiung Yang, Jing Yang, Eve Xu, Akash Bajaj, and Heather J. Kulik. Bridging the homogeneous-heterogeneous divide: Modeling spin for reactivity in single atom catalysis. *Frontiers in Chemistry*, 7:219, April 2019.

[58] Christoph Riplinger and Frank Neese. An efficient and near linear scaling pair natural orbital based local coupled cluster method. *The Journal of Chemical Physics*, 138(3), January 2013.

[59] Christoph Riplinger, Barbara Sandhoefer, Andreas Hansen, and Frank Neese. Natural triple excitations in local coupled cluster calculations with pair natural orbitals. *The Journal of Chemical Physics*, 139(13), October 2013.

[60] Yang Guo, Christoph Riplinger, Ute Becker, Dimitrios G. Liakos, Yury Minenkov, Luigi Cavallo, and Frank Neese. Communication: An improved linear scaling perturbative triples correction for the domain based local pair-natural orbital based singles and doubles coupled cluster method [DLPNO-CCSD(t)]. *The Journal of Chemical Physics*, 148(1):011101, January 2018.

[61] Nitish Govindarajan, Marc T. M. Koper, Evert Jan Meijer, and Federico Calle-Vallejo. Outlining the scaling-based and scaling-free optimization of electrocatalysts. *ACS Catalysis*, 9(5):4218–4225, March 2019.

[62] Hemjot Kaur and Neetu Goel. Tailoring the cobalt porphyrin for minimal overpotential in the electrochemical oxygen evolution/reduction reactions: A density functional study. *International Journal of Hydrogen Energy*, 48(81):31720–31733, September 2023.

[63] Tran Phuong Dung, Viorel Chihaia, and Do Ngoc Son. Effects of functional groups in iron porphyrin on the mechanism and activity of oxygen reduction reaction. *RSC Advances*, 13(13):8523–8534, 2023.

[64] Ibrahim Elghamry, Abdulrahman S. Alablan, Mohammed A. Alkhalifah, and Mamdouh E. Abdelsalam. High-performance organometallic catalyst based on nickel porphyrin/carbon fibre for the oxygen reduction reaction. *Journal of The Electrochemical Society*, 168(1):016510, January 2021.

[65] Michael L. Pegis, Bradley A. McKeown, Neeraj Kumar, Kai Lang, Derek J. Wasylenko, X. Peter Zhang, Simone Raugei, and James M. Mayer. Homogenous

electrocatalytic oxygen reduction rates correlate with reaction overpotential in acidic organic solutions. *ACS Central Science*, 2(11):850–856, October 2016.

[66] Federico Calle-Vallejo, José Ignacio Martínez, and Jan Rossmeisl. Density functional studies of functionalized graphitic materials with late transition metals for oxygen reduction reactions. *Physical Chemistry Chemical Physics*, 13(34):15639, 2011.

[67] Frank Neese, Frank Wennmohs, Ute Becker, and Christoph Riplinger. The ORCA quantum chemistry program package. *Journal of Chemical Physics*, 152(22):224108, jun 2020.

[68] John P. Perdew and Karla Schmidt. Jacob's ladder of density functional approximations for the exchange-correlation energy. *AIP Conference Proceedings*, 577(1):1–20, 07 2001.

[69] Stefan Grimme, Jens Antony, Stephan Ehrlich, and Helge Krieg. A consistent and accurate ab initio parametrization of density functional dispersion correction (DFT-D) for the 94 elements H-Pu. *J. Chem. Phys.*, 132(15):154104, April 2010.

[70] Stefan Grimme, Stephan Ehrlich, and Lars Goerigk. Effect of the damping function in dispersion corrected density functional theory. *J. Comput. Chem.*, 32(7):1456–1465, May 2011.

[71] A. D. Becke. Density-functional exchange-energy approximation with correct asymptotic behavior. *Physical Review A*, 38(6):3098–3100, September 1988.

[72] John P. Perdew. Density-functional approximation for the correlation energy of the inhomogeneous electron gas. *Physical Review B*, 33(12):8822–8824, June 1986.

[73] John P. Perdew, Kieron Burke, and Matthias Ernzerhof. Generalized gradient approximation made simple. *Physical Review Letters*, 77(18):3865–3868, October 1996.

[74] Viktor N. Staroverov, Gustavo E. Scuseria, Jianmin Tao, and John P. Perdew. Comparative assessment of a new nonempirical density functional: Molecules and hydrogen-bonded complexes. *The Journal of Chemical Physics*, 119(23):12129–12137, December 2003.

[75] Axel D. Becke. Density-functional thermochemistry. iii. the role of exact exchange. *The Journal of Chemical Physics*, 98(7):5648–5652, 1993.

[76] Carlo Adamo and Vincenzo Barone. Toward reliable density functional methods without adjustable parameters: The pbe0 model. *The Journal of Chemical Physics*, 110(13):6158–6170, April 1999.

[77] Stefan Grimme. Semiempirical hybrid density functional with perturbative second-order correlation. *Journal of Chemical Physics*, 124(3):034108, jan 2006.

[78] Lars Goerigk and Stefan Grimme. Efficient and accurate double-hybrid-meta-gga density functionals—evaluation with the extended gmtkn30 database for general main group thermochemistry, kinetics, and noncovalent interactions. *Journal of Chemical Theory and Computation*, 7(2):291–309, December 2010.

[79] Rüdiger Bauernschmitt and Reinhart Ahlrichs. Stability analysis for solutions of the closed shell kohn–sham equation. *The Journal of Chemical Physics*, 104(22):9047–9052, June 1996.

[80] Frank Neese. Importance of direct spin-spin coupling and spin-flip excitations for the zero-field splittings of transition metal complexes: A case study. *Journal of the American Chemical Society*, 128(31):10213–10222, aug 2006.

[81] Yang Guo, Christoph Riplinger, Dimitrios G. Liakos, Ute Becker, Masaaki Saitow, and Frank Neese. Linear scaling perturbative triples correction approximations for open-shell domain-based local pair natural orbital coupled cluster singles and doubles theory [DLPNO-CCSD(t/t)]. *The Journal of Chemical Physics*, 152(2):024116, January 2020.

[82] Rick A. Kendall, Thom H. Dunning, and Robert J. Harrison. Electron affinities of the first-row atoms revisited. systematic basis sets and wave functions. *The Journal of Chemical Physics*, 96(9):6796–6806, May 1992.

[83] Nikolai B. Balabanov and Kirk A. Peterson. Systematically convergent basis sets for transition metals. i. all-electron correlation consistent basis sets for the 3d elements sc–zn. *The Journal of Chemical Physics*, 123(6):064107, August 2005.

[84] Nikolai B. Balabanov and Kirk A. Peterson. Basis set limit electronic excitation energies, ionization potentials, and electron affinities for the 3d transition metal atoms: Coupled cluster and multireference methods. *The Journal of Chemical Physics*, 125(7):074110, August 2006.

[85] Frank Neese and Edward F. Valeev. Revisiting the atomic natural orbital approach for basis sets: Robust systematic basis sets for explicitly correlated and conventional correlated *ab initio* methods? *Journal of Chemical Theory and Computation*, 7(1):33–43, December 2010.

[86] Ahmet Altun, Frank Neese, and Giovanni Bistoni. Extrapolation to the limit of a complete pair natural orbital space in local coupled-cluster calculations. *Journal of Chemical Theory and Computation*, 16(10):6142–6149, September 2020.

[87] Kristine Pierloot, Quan Manh Phung, and Alex Domingo. Spin state energetics in first-row transition metal complexes: Contribution of (3s3p) correlation and its description by second-order perturbation theory. *Journal of Chemical Theory and Computation*, 13(2):537–553, January 2017.

[88] Milica Feldt and Quan Manh Phung. Ab initio methods in first-row transition metal chemistry. *European Journal of Inorganic Chemistry*, 2022(15):e202200014, April 2022.

[89] Mariusz Radoń. Spin-state energetics of heme-related models from dft and coupled cluster calculations. *Journal of Chemical Theory and Computation*, 10(6):2306–2321, May 2014.

[90] Quan Manh Phung, Milica Feldt, Jeremy N. Harvey, and Kristine Pierloot. Toward highly accurate spin state energetics in first-row transition metal complexes: A combined caspt2/cc approach. *Journal of Chemical Theory and Computation*, 14(5):2446–2455, April 2018.

[91] Sebastian Dohm, Andreas Hansen, Marc Steinmetz, Stefan Grimme, and Marek P. Checinski. Comprehensive thermochemical benchmark set of realistic closed-shell metal organic reactions. *Journal of Chemical Theory and Computation*, 14(5):2596–2608, March 2018.

[92] Mariusz Radoń. Benchmarking quantum chemistry methods for spin-state energetics of iron complexes against quantitative experimental data. *Physical Chemistry Chemical Physics*, 21(9):4854–4870, 2019.

[93] Gabriela Drabik, Janusz Szklarzewicz, and Mariusz Radoń. Spin-state energetics of metallocenes: How do best wave function and density functional theory results compare with the experimental data? *Physical Chemistry Chemical Physics*, 23(1):151–172, 2021.

[94] Hagen Neugebauer, Hung T. Vuong, John L. Weber, Richard A. Friesner, James Shee, and Andreas Hansen. Toward benchmark-quality ab initio predictions for 3d transition metal electrocatalysts: A comparison of ccsd(t) and ph-afqmc. *Journal of Chemical Theory and Computation*, 19(18):6208–6225, September 2023.

[95] Wanyi Jiang, Nathan J. DeYonker, and Angela K. Wilson. Multireference character for 3d transition-metal-containing molecules. *Journal of Chemical Theory and Computation*, 8(2):460–468, January 2012.

[96] F. Calle-Vallejo, J. I. Martínez, J. M. García-Lastra, J. Rossmeisl, and M. T. M. Koper. Physical and chemical nature of the scaling relations between adsorption energies of atoms on metal surfaces. *Physical Review Letters*, 108(11):116103, March 2012.

[97] Federico Calle-Vallejo, Alexander Krabbe, and Juan M. García-Lastra. How covalence breaks adsorption-energy scaling relations and solvation restores them. *Chemical Science*, 8(1):124–130, 2017.

[98] Mariusz Radoń. Revisiting the role of exact exchange in dft spin-state energetics of transition metal complexes. *Phys. Chem. Chem. Phys.*, 16(28):14479–14488, 2014.

[99] Michell O. Almeida, Manuel J. Kolb, Marcos R. V. Lanza, Francesc Illas, and Federico Calle-Vallejo. Gas-phase errors affect dft-based electrocatalysis models of oxygen reduction to hydrogen peroxide. *ChemElectroChem*, 9(12):e202200210, May 2022.

[100] Peter M. W. Gill, John A. Pople, Leo Radom, and Ross H. Nobes. Why does unrestricted møller–plesset perturbation theory converge so slowly for

spin-contaminated wave functions? *The Journal of Chemical Physics*, 89(12):7307–7314, December 1988.

[101] James Shee, Matthias Loipersberger, Adam Rettig, Joonho Lee, and Martin Head-Gordon. Regularized second-order møller–plesset theory: A more accurate alternative to conventional mp2 for noncovalent interactions and transition metal thermochemistry for the same computational cost. *The Journal of Physical Chemistry Letters*, 12(50):12084–12097, December 2021.

[102] Markus Reiher, Oliver Salomon, and Bernd Artur Hess. Reparameterization of hybrid functionals based on energy differences of states of different multiplicity. *Theoretical Chemistry Accounts: Theory, Computation, and Modeling (Theoretica Chimica Acta)*, 107(1):48–55, December 2001.

[103] Antony Fouqueau, Mark E. Casida, Latévi Max Lawson Daku, Andreas Hauser, and Frank Neese. Comparison of density functionals for energy and structural differences between the high- [5t2g:(t2g)4(eg)2] and low- [1a1g:(t2g)6(eg)] spin states of iron(ii) coordination compounds. ii. more functionals and the hexaminoferrous cation, [fe(nh3)6]2+. *The Journal of Chemical Physics*, 122(4):044110, January 2005.

[104] Frank Neese. Prediction of molecular properties and molecular spectroscopy with density functional theory: From fundamental theory to exchange-coupling. *Coordination Chemistry Reviews*, 253(5-6):526–563, March 2009.

[105] James P. Collman, J. L. Hoard, Nancy Kim, George Lang, and Christopher A. Reed. Synthesis, stereochemistry, and structure-related properties of .alpha., .beta., .gamma., .delta.-tetraphenylporphinatoiron(ii). *Journal of the American Chemical Society*, 97(10):2676–2681, May 1975.

[106] Harold Goff, Gerd N. La Mar, and Christopher A. Reed. Nuclear magnetic resonance investigation of magnetic and electronic properties of "intermediate spin" ferrous porphyrin complexes. *Journal of the American Chemical Society*, 99(11):3641–3646, May 1977.

[107] John F. Kirner, Christopher A. Reed, and W. Robert Scheidt. Stereochemistry of manganese porphyrins. 2. the toluene solvate of .alpha., .beta., .gamma., .delta.-tetraphenylporphinatomanganese(ii) at 20 and -175.degree.c. *Journal of the American Chemical Society*, 99(4):1093–1101, February 1977.

[108] Paul. Madura and W. Robert. Scheidt. Stereochemistry of low-spin cobalt porphyrins. 8. .alpha., .beta., .gamma., .delta.-tetraphenylporphinatocobalt(ii). *Inorganic Chemistry*, 15(12):3182–3184, December 1976.

[109] Linus Pauling and Charles D. Coryell. The magnetic properties and structure of the hemochromogens and related substances. *Proceedings of the National Academy of Sciences*, 22(3):159–163, March 1936.

[110] K.M. Smith. *Porphyrins and Metalloporphyrins: A New Edition Based on the Original Volume by J. E. Falk*. BBA Library. Elsevier Scientific Publishing Company, 1975.

[111] Florian Gutzeit, Marcel Dommaschk, Natalia Levin, Axel Buchholz, Eike Schaub, Winfried Plass, Christian Näther, and Rainer Herges. Structure and properties of a five-coordinate nickel(ii) porphyrin. *Inorganic Chemistry*, 58(19):12542–12546, March 2019.

[112] Brian M. Hoffman, Thomas Szymanski, Theodore G. Brown, and Fred Basolo. The dioxygen adducts of several manganese(ii) porphyrins. electron paramagnetic resonance studies. *Journal of the American Chemical Society*, 100(23):7253–7259, November 1978.

[113] Audrey T. Gallagher, Jung Yoon Lee, Venkatesan Kathiresan, John S. Anderson, Brian M. Hoffman, and T. David Harris. A structurally-characterized peroxomanganese(¡scp¿iv¡/scp¿) porphyrin from reversible o2 binding within a metal–organic framework. *Chemical Science*, 9(6):1596–1603, 2018.

[114] Lechoslaw Latos-Grazynski, Ru Jen Cheng, Gerd N. La Mar, and Alan L. Balch. Oxygenation patterns for substituted meso-tetraphenylporphyrin complexes of iron(ii). spectroscopic detection of dioxygen complexes in the absence of amines. *Journal of the American Chemical Society*, 104(22):5992–6000, November 1982.

[115] John S. Anderson, Audrey T. Gallagher, Jarad A. Mason, and T. David Harris. A five-coordinate heme dioxygen adduct isolated within a metal–organic framework. *Journal of the American Chemical Society*, 136(47):16489–16492, November 2014.

[116] Audrey T. Gallagher, Margaret L. Kelty, Jesse G. Park, John S. Anderson, Jarad A. Mason, James P. S. Walsh, Shenell L. Collins, and T. David Har-

ris. Dioxygen binding at a four-coordinate cobaltous porphyrin site in a metal–organic framework: structural, epr, and o2adsorption analysis. *Inorganic Chemistry Frontiers*, 3(4):536–540, 2016.

[117] Sebastian Ovalle and Cecile Malardier-Jugroot. Choice of functional for iron porphyrin density functional theory studies: Geometry, spin-state, and binding energy analysis. *Computational and Theoretical Chemistry*, 1213:113726, July 2022.

[118] N. C. Handy, P. J. Knowles, and K. Somasundram. On the convergence of the møller-plesset perturbation series. *Theoretica Chimica Acta*, 68(1):87–100, July 1985.

[119] Frank Jensen. A remarkable large effect of spin contamination on calculated vibrational frequencies. *Chemical Physics Letters*, 169(6):519–528, June 1990.

[120] Ambili S. Menon and Leo Radom. Consequences of spin contamination in unrestricted calculations on open-shell species: Effect of hartree-fock and møller-plesset contributions in hybrid and double-hybrid density functional theory approaches. *The Journal of Physical Chemistry A*, 112(50):13225–13230, August 2008.

[121] James Shee, Matthias Loipersberger, Diptarka Hait, Joonho Lee, and Martin Head-Gordon. Revealing the nature of electron correlation in transition metal complexes with symmetry breaking and chemical intuition. *The Journal of Chemical Physics*, 154(19):194109, May 2021.

[122] Yu-Ran Luo. *Comprehensive Handbook of Chemical Bond Energies*. CRC Press, March 2007.

[123] Nist computational chemistry comparison and benchmark database, 2022-05-22 2022. NIST Standard Reference Database Number 101.

[124] Stefan Kurth, John P. Perdew, and Peter Blaha. Molecular and solid-state tests of density functional approximations: Lsd, ggas, and meta-ggas. *International Journal of Quantum Chemistry*, 75(4–5):889–909, 1999.

[125] Jess Wellendorff, Trent L. Silbaugh, Delfina Garcia-Pintos, Jens K. Nørskov, Thomas Bligaard, Felix Studt, and Charles T. Campbell. A benchmark

database for adsorption bond energies to transition metal surfaces and comparison to selected dft functionals. *Surface Science*, 640:36–44, October 2015.

[126] Elizabeth Sargeant, Francesc Illas, Paramaconi Rodríguez, and Federico Calle-Vallejo. Importance of the gas-phase error correction for o2 when using dft to model the oxygen reduction and evolution reactions. *Journal of Electroanalytical Chemistry*, 896:115178, September 2021.

[127] Felix Studt, Malte Behrens, Edward L. Kunkes, Nygil Thomas, Stefan Zander, Andrey Tarasov, Julia Schumann, Elias Frei, Joel B. Varley, Frank Abild-Pedersen, Jens K. Nørskov, and Robert Schlögl. The mechanism of co and co2 hydrogenation to methanol over cu-based catalysts. *ChemCatChem*, 7(7):1105–1111, March 2015.

[128] Rune Christensen, Heine A. Hansen, Colin F. Dickens, Jens K. Nørskov, and Tejs Vegge. Functional independent scaling relation for orr/oer catalysts. *The Journal of Physical Chemistry C*, 120(43):24910–24916, October 2016.

[129] Johannes T. Margraf, Duminda S. Ranasinghe, and Rodney J. Bartlett. Automatic generation of reaction energy databases from highly accurate atomization energy benchmark sets. *Physical Chemistry Chemical Physics*, 19(15):9798–9805, 2017.

[130] John P. Perdew, Jianwei Sun, Adrienn Ruzsinszky, Pál D. Mezei, and Gábor István Csonka. Why density functionals should not be judged primarily by atomization energies. *Periodica Polytechnica Chemical Engineering*, 60(1):2–7, 2016.

[131] Ricardo Urrego-Ortiz, Santiago Builes, and Federico Calle-Vallejo. Impact of intrinsic density functional theory errors on the predictive power of nitrogen cycle electrocatalysis models. *ACS Catalysis*, 12(8):4784–4791, April 2022.

[132] Carlo Alberto Gaggioli, Samuel J. Stoneburner, Christopher J. Cramer, and Laura Gagliardi. Beyond density functional theory: The multiconfigurational approach to model heterogeneous catalysis. *ACS Catalysis*, 9(9):8481–8502, August 2019.

[133] Jenny G. Vitillo, Christopher J. Cramer, and Laura Gagliardi. Multireference methods are realistic and useful tools for modeling catalysis. *Israel Journal of Chemistry*, 62(1–2):e202100136, February 2022.

Chapter 7

Conclusions

Humanity faces an existential threat in its battle to keep global temperatures in check. At the same time, to meet the energy demands of a growing population, new devices for storing, controlling, and converting clean energy are essential. Nanostructured materials open the door to virtually endless possibilities for tailoring properties to specific applications. Nevertheless, to harness the potential of these materials, the relationships between nanostructure and function must be fundamentally understood. This dissertation has developed methods for elucidating the relationships between nanocomposite structure and dielectric permittivity, a key parameter in capacitive energy storage. Furthermore, this dissertation has evaluated existing electronic structure methods that are commonly applied to study the relationships between catalyst structure and activity toward the ORR, an efficiency-limiting reaction in hydrogen fuel cells. In the present chapter, we briefly review the major conclusions that can be drawn from each of these efforts and identify areas for future research.

7.1 Partitioning Nanodielectric Response

Chapter 3 refined and evaluated a real-space method for partitioning the dielectric response of matrix-inclusion nanocomposites. In particular, the displacements of Wannier centers were used to rationalize observed trends in permittivity with inclusion volume loading, inclusion aspect ratio, and matrix lattice strain by identifying the permittivity-enhancing tendencies of both the inclusion and the interfacial matrix ions. Other real-space descriptors—namely the spatial distribution of Born effective charges and maximally localized Wannier function spreads—supplemented the essen-

tially *descriptive* partitioning scheme in order to derive *mechanistic* explanations for the observed trends in the partitioned dielectric response.

Several important lessons crystallized from this work. First, we demonstrated that as long as the loading of inclusions is small, the enhancement factor α_{enh} introduced by [1] is a defining characteristic of the particular inclusion shape and the matrix into which it was introduced. Additionally, we showed that the impact of inclusion aspect ratio on permittivity involves a complex interplay between the polarization length and cross-section of the inclusion and the corresponding geometry of the interfacial matrix layers. While the inclusion geometry effects dominate the clamped ion response, the interfacial cross-section was identified as an important contributor to relaxed-ion permittivity. Finally, by considering different matrix oxides, we showed that the lattice mismatch between matrix and inclusion contributes to clamped- and relaxed-ion permittivity in generally opposing directions. While lattice strain in the matrix compresses the inclusion and limits its electronic polarizability, it also leads to matrix-driven increases in relaxed-ion polarization. The effects of inclusion aspect ratio and matrix lattice strain both point to the distinctions between inclusion and interface contributions to permittivity which should be considered in materials design, specifically with regards to different frequency ranges of operation.

The scope of Chapter 3 was limited to small (8 to 18-atom) silver inclusions embedded in rocksalt-structure alkaline earth metal oxide matrices. Thus, a potential extension of this work is to apply the same partitioning approach to different materials. Polymer nanodielectrics with either ceramic or metallic inclusions are an extremely important class of materials for energy storage with a plethora of experimental data available for comparison with theoretical results. While such materials are often modeled using classical mixing formulas based on empirical parameters, first principles studies could be used to deepen the understanding of the interfacial interactions between inclusion and matrix, especially when the inclusions are only nanometers in length. Furthermore, it would be useful to apply the partitioning method to substitutional defects in doped high-κ dielectrics, for example Zr-doped HfO_2[2], and other semicondonductor-processing-compatible oxides with nanocluster inclusions.

In addition to novel applications, the work of Chapter 3 could be fruitfully extended by improving the computational efficiency of the partitioning. In particular, convergence of Wannier function centers and spreads required careful attention and was more difficult in nanocomposites compared to pure bulk materials. Improving

the convergence properties of the algorithms for generating MLWFs in nanostructured materials would increase the practicality of the partitioning scheme. Beyond partitioning, further testing and improvement of the local permittivity method introduced at the conclusion of the chapter would be advantageous. In addition to the direct insights this local picture provides about the spatial distribution of electric fields and polarization, it also allows direct access to the local permittivity parameters required when building continuum models of nanodielectrics.

7.2 Continuum Model of Nanodielectric Response

Chapter 4 introduced a method for deriving continuum models for dielectric nanocomposite oxides by fitting to both the effective permittivity and local polarization in DFT calculations. The continuum approach relied conceptually on the scaling of nanocluster polarizability with Bader volume and the observation that the interfacial matrix atoms exhibit large polarizations that necessitate an explicit interfacial layer in the continuum model. Both the effective permittivity of the composite and the local polarization of the inclusion were used as variables for fitting physically meaningful continuum model parameters. The final model, produced only by fitting to spherical inclusions, was able to capture the qualitative trends in changing inclusion aspect ratio but was found to produce more accurate quantitative results for rod-like inclusions than disk-like ones.

The importance of this work lies in the demonstration that an appropriate continuum model can capture the relevant polarization phenomena in nanocomposite materials, even though such models have primarily been applied to composites with much larger-scale inclusions. The method that we developed for parameterizing such a model can be applied generally to link *ab initio* polarization response to continuum parameters. Moreover, the work further emphasized the importance of interfacial matrix ion mobility in the relaxed-ion permittivity and identified this as a difficult but important factor to capture heuristically in accurate continuum models

The developed continuum model was only fit to produce relaxed-ion permittivities. In high-frequency applications, however, the clamped-ion permittivity is also important. Thus, developing a continuum model for the electronic part of the permittivity could be a potential future direction for this research. Such an endeavor could lead to a deeper understanding of the differing role interfacial ions play in the electronic, versus ionic, polarization of the nanocomposites.

Furthermore, the continuum model was constrained to MgO/Ag nanocomposites. Thus, as with the partitioning method of Chapter 3, one of the most useful ways to extend the work of Chapter 4 would be to fit continuum models for different matrix-inclusion combinations. Such work would provide useful information about how transferrable the permittivities of an inclusion are between different matrices and how sensitive interfacial layer permittivities are to changes in the respective matrix and inclusion properties. A particularly salient research question would be what effect the covalency of bonding in the matrix—and between matrix and inclusion—has on the resulting interfacial permittivity and spatial extent of the interfacial properties. Understanding the relationships between structure and permittivity of the inclusion and interface could lead to analytical models for predicting the permittivities of these components in novel materials combinations based on their respective atomic and electronic structures. Such models, in turn, could be used to generate continuum model parameters and screen materials efficiently without the need for expensive *ab initio* calculations for each new marriage of inclusion and interface materials.

However, before this becomes a reality, *ab initio* computations are still necessary for deriving interfacial and inclusion parameters. Thus, deriving these parameters more efficiently from *ab initio* calculations (i.e. without the need to simulate multiple systems with different inclusion loadings) would improve the applicability of this approach. One path forward would be to circumvent the fitting procedure based on volume loading by deriving local permittivities directly from a single *ab initio* calculation, along the lines of the local permittivity procedure described at the end of Chapter 3. Using this more direct parameterizaton also has the advantage of providing information about the angular dependence of permittivity relative to the inclusion, information which may elucidate why the studied model performed less accurately for disk-shaped inclusions.

7.3 Inducible Atomic Dipole Modeling of Nanodielectric Response

After exploring a continuum approach to nanocomposite dielectrics, Chapter 5 investigated a classical inducible dipole approximation to compute the polarizability of composites. Since the previous chapters had indicated the need to account for the differences in electronic structure between matrix atoms at the interface and in

the bulk, a model of atomic polarizability was chosen that accounted partially for electronic structure by an empirical volume-scaling relationship. Such an approach is commonly used to define atomic polarizabilities in semiclassical dispersion corrections for DFT. The method was evaluated on a dataset of small molecules and several types of inorganic clusters.

Throughout this work, we developed a deeper understanding of the performance of the volume-scaled inducible atomic dipole model. First, we showed that the accuracy of the approach was impacted by the degree of charge transfer in the system and the anisotropy of the system's response. Moreover, we learned that modifying the short-range damping function used in the self-consistent determination of polarizability could be used to tune the anisotropy of the model's response. Although a strong correlation between response anisotropy and charge transfer was observed, it was shown that by adjusting the damping function used in the inducible dipole model, the anisotropy of the response could largely be recovered without having to include charge transfer terms explicitly in the model. Still, for very anisotropic silver nanorods, a simple Thole inducible dipole model performed better than the volume-scaled approach.

At the end of the chapter, an embedded core-shell cluster model was proposed for nanocomposites. The embedding scheme reduced spurious charge leakage associated with ionic cluster models while also providing a way to include a polarizable background to mimic a bulk material. The model thus represents a promising approach to studying the polarizability of inclusions in composites and isolated defects in materials.

Chapter 5 leaves open several avenues for future research. For one, while volume scaling did not improve the polarizability predictions over the Thole model for single-element silver nanorods, it is reasonable to assume that some accounting for the impact of the local chemical environment on atomic polarizability (beyond coupling to neighboring atomic dipoles) is important for descriptions of polarization at the interfaces within nanocomposites. This follows from the results of previous chapters indicating that interfacial layers not only experience high local fields but also have larger orbital spreads and greater ionic mobility, which make these layers inherently more polarizable than bulk. However, more work is needed to ascertain whether simple volume scaling is sufficient to account for these local chemical distinctions or whether more sophisticated descriptors of chemical environment are needed. Furthermore, descriptors of the local chemical environment need to be cheaply com-

putable. The present work required an electronic structure calculation in order to obtain atomic volumes, but this costly step is virtually antithetical to the idea of developing a classical dipole model in the first place. Thus, any classical dipole model of nanocomposites should be able to account for the local chemical environment using descriptors based solely on the atomic structure. Machine learning models predicting atomic volumes and other atomic descriptors present one path forward. In fact, such an approach is already used in calculating atomic polarizabilities in the Grimme D4 dispersion model.[3]

7.4 Real-Space Approaches to Nanodielectrics

Although the aforementioned chapters present three different approaches to understanding and predicting the dielectric behavior of nanocomposites, collectively they highlight the value of real-space descriptors of that behavior. The extended nature of solid dielectrics lends itself to the usual study of band structure and densities of states, both invaluable tools in solid-state physics. In the context of nanocomposites, understanding how the states introduced by inclusions affect the material band structure is certainly important, and various projections of electronic states onto localized atomic orbitals offer an ability to relate these changes to local atomic structure. However, direct inspection of the charge density and its change under the application of an electric field, the analysis of Wannier center displacements and spreads, and spatial mapping of Born effective charges offer a complementary toolset for studying the response in nanocomposites. This toolset offers concrete and intuitive insights about the origins of dielectric behavior of nanocomposites by directly reflecting the common sense picture of a composite's properties as being derived from the properties of multiple material domains and the interfaces between them. Additionally, these tools lend themselves well to the development of classical models, wherein the properties of different spatial domains in a continuum model or atomic properties in a classical dipole approach have a direct correspondence with the real-space properties derived from *ab initio* calculations.

7.5 Density Functionals for ORR Electrocatalysis

Chapter 6 delved into the second focus of this dissertation, computational modeling of M–N–C catalysts for the ORR. In particular, the goal was to assess the accuracy of

various density functionals in determining the overpotentials and intermediate binding energies for metalloporphyrin catalysts. Usurprisingly, the 3d metal porphyrins were highly sensitive to the density functional approximation used. In particular, the energy of different spin states and the bond lengths of loosely bound intermediates varied depending on the amount of exact exchange included in a functional. In turn, the computed overpotentials and binding energies were susceptible to significant changes depending on which spin state of different intermediates was taken to be the ground state, let alone which functional was used for computing the energetics.

Single reference diagnostics and analysis of CASSCF wavefunctions indicated that reaction intermediates exhibited low to moderate multiconfigurational character, with the oxo intermediate showing the largest deviation from a strictly single reference nature. In this regime, DLPNO-CCSD(T) is generally expected to provide good energetics, and so it was used to provide reference values for comparison with DFT. For the surveyed reaction mechanism, single hybrid functionals with low exact exchange, and in particular B3LYP, showed good agreement with the scaling relationships and overpotentials calculated with DLPNO-CCSD(T). On the other hand, double hybrid functionals displayed mixed performance, with quite consequential poor performance for oxo intermediates. Thus, double-hybrid functionals were not considered to be worth the extra computational effort.

The work of Chapter 6 is important for developing a set of best practices when studying M–N–C catalysts in particular, and to some extent single-atom catalysts more generally. Our results indicated that it is generally a good idea to evaluate M–N–C catalysts on a case-by-case basis for multiconfigurational effects, since they have complicated electronic structures dependent on their coordination geometry and bond characteristics. However, for computationally demanding systems where DFT is the most feasible approach, a good start involves using single hybrid functionals with varying levels of exact exchange to determine ground state spins. If low-exchange functionals exhibit significant symmetry breaking in a low-spin ground state, multi-reference methods should be considered; otherwise, these same low-exchange functionals are likely to provide good energetics.

In some sense, the complicated electronic structure that requires extra care when simulating M–N–C catalysts is the very quality that makes them attractive catalysts. Thus, in the design of next generation catalysts, it is critical that the applied computational methods are up to the task. One path forward is to stray from the simplicity and efficiency of single-reference methods. Along these lines, could one not bypass all

of the effort taken to ensure that single reference methods are appropriate by simply applying a multireference method from the start? Indeed, easy-to-apply and efficient multi-reference methods would be extremely useful in the study of M–N–C and other single-atom catalysts, provided an accurate treatment of dynamic correlation is included.

Quantum chemistry approaches to more efficient, and in some cases user-friendly multireference calculations are accelerating rapidly in the form of various embedding theories,[4] density-matrix renormalization group calculations,[5] and multiconfiguration pair-density functional theory[6] Quantum computing algorithms are a promising alternative approach to capturing correlation efficiently. For instance, iterative qubit coupled cluster (IQCC) is an algorithm that can be implemented on quantum devices or in specialized classical simulators, such as that of OTI Lumionics.[7] In fact, the present author and colleagues have begun to explore the application of this algorithm to small Nickel-oxygen complexes that show strong correlation. The promise of this method is its ability to handle extremely large active spaces. In the context of metalloporphyrin ORR catalysts, this means that metal, oxygen ligand, and important macrocycle orbitals can all be included in the correlation treatment. Thus, application of IQCC to metal macrocycles for ORR is a potential route forward for obtaining consistently accurate energies of 3d M–N–C catalysts.

However, beyond merely improving the computational efficiency of multireference approaches, another barrier to their wider adoption in the field of electrocatalysis is that they typically require significantly more specialized knowledge and user experience compared to the relatively straightforward application of DFT. Thus, while multireference approaches sidestep some of the challenges posed in the study of M–N–C catalysts, the algorithms need to reach a level of both efficiency and user-friendliness to make them broadly applicable to electrocatalytic studies.

7.6 Final Thoughts

The need to diversify technologies for energy storage and conversion is ongoing and urgent. Throughout this dissertation, we have discussed why nanostructured materials are promising for capacitive energy storage and electrocatalytic energy conversion applications. Computational approaches to materials design enable rapid and rational materials improvements to be made on the basis of causal links between the structure and properties of materials. However, the same nanostructured materials that will be

used to build a greener future also lay bare the currently necessary trade-offs between efficiency and transferability in materials simulations. This dissertation has proposed efficient coarse-grained models for nanocomposite dielectrics, which expand the range of nanostructure length scales that can be simulated in the development of improved capacitive energy storage materials. While efficient, these methods must be applied to the narrow range of materials types for which they were parameterized. In the context of the ORR, this dissertation expanded the scientific understanding of how different DFT approximations affect the predictions of catalyst activity. This work is critical to pushing forward the field of single-atom catalysis and avoiding common pitfalls in the application of DFT. At the same time, it highlighted that even quite versatile DFT functionals struggle with transferability in materials with complicated electronic structures.

A hopeful future is one in which the efficiency of highly transferable quantum mechanical methods continues improving, and with it the scope of quantum calculations. At the forefront of this push is the development of novel multireference algorithms that take advantage of effective approximations to improve efficiency. Even more radically, quantum computing algorithms with fundamentally better scaling with system size could offer truly paradigm-shifting approaches to the study of nanostructures with high fidelity. However, the development of improved algorithms, and in the case of quantum algorithms, the hardware to run them, takes precious time. Hardware design also relies on the same computational approaches that they hope to improve upon. Meanwhile, in the in-between, we must make the most efficient use of the computational resources we have. This dissertation has been an effort to do just that—developing and applying computationally efficient methods for the nanostructured materials that will be required to secure a sustainable energy future.

Bibliography

[1] David J. T. Hally and Irina Paci. Low-frequency polarization in molecular-scale noble-metal/metal–oxide nanocomposites. *Nanoscale*, 10(20):9583–9593, 2018.

[2] Writam Banerjee, Alireza Kashir, and Stanislav Kamba. Hafnium oxide (hfo2) – a multifunctional oxide: A review on the prospect and challenges of hafnium oxide in resistive switching and ferroelectric memories. *Small*, 18(23), May 2022.

[3] Eike Caldeweyher, Christoph Bannwarth, and Stefan Grimme. Extension of the D3 dispersion coefficient model. *Journal of Chemical Physics*, 147(3):0–7, 2017.

[4] Qiming Sun and Garnet Kin-Lic Chan. Quantum embedding theories. *Accounts of Chemical Research*, 49(12):2705–2712, November 2016.

[5] Leon Freitag and Markus Reiher. The density matrix renormalization group for strong correlation in ground and excited states, November 2020.

[6] Laura Gagliardi, Donald G. Truhlar, Giovanni Li Manni, Rebecca K. Carlson, Chad E. Hoyer, and Junwei Lucas Bao. Multiconfiguration pair-density functional theory: A new way to treat strongly correlated systems. *Accounts of Chemical Research*, 50(1):66–73, December 2016.

[7] Ilya G. Ryabinkin, Robert A. Lang, Scott N. Genin, and Artur F. Izmaylov. Iterative qubit coupled cluster approach with efficient screening of generators. *Journal of Chemical Theory and Computation*, 16(2):1055–1063, January 2020.

Appendix A

In Situ Characterization of Perovskite Quantum Dots via Finite Well Model

This Appendix briefly introduces a side project undertaken in support of collaborators at the University of Victoria and Queens University. The final work appeared as the article "Coupling Perovskite Quantum Dot Pairs in Solution using Nanoplasmonic Assembly" in the journal ACS Nanoletters.[1] Collaborators at the University of Victoria constructed an experimental setup known as a double-nanohole optical tweezer to trap $CsPbBr_3$ quantum dots (QDs) in a nanoscale aperture in a gold film. The emission spectra of the trapped QDs were recorded, and the size of the trapped QDs could be determined either by correlating the emission peak with calculations of the theoretical blueshift associated with small-size effects or through a calibrated linear relationship between thermal fluctuations and quantum dot size. Furthermore, it was demonstrated that two QDs could be simultaneously trapped, and that the emission spectrum of the trapped pair always showed a small redshift of approximately 1.1 meV relative to single trapped dots. Ultimately, the coupling and induced redshift was accounted for via Förster resonant energy transfer, with the theory for this mechanism being undertaken by researchers at Queen's University. The author byline from the article, in order and including affiliations, is reproduced on the following page for transparency.

Hao Zhang[1,2], Parinaz Moazzezi[1,2], Juanjuan Ren[5], Brett Henderson[3, 6], Cristina Cordoba[2, 4], Vishal Yeddu[2, 3], Arthur Blackburn[2, 4], Makhsud I. Saidaminov[1, 2, 3], Irina Paci[2, 3], Stephen Hughes[5], Reuven Gordon[1, 2]

[1] *Department of Electrical and Computer Engineering, University of Victoria, Victoria, British Columbia, Canada*

[2] *Centre for Advanced Materials & Related Technologies (CAMTEC), University of Victoria, Victoria, British Columbia, Canada*

[3] *Department of Chemistry, University of Victoria, Victoria, British Columbia, Canada*

[4] *Department of Physics and Astronomy, University of Victoria, Victoria, British Columbia, Canada*

[5] *Department of Physics, Engineering Physics and Astronomy, Queen's University, Kingston, Ontario, Canada*

[6] *Quantum Algorithms Institute, Surrey, British Columbia, Canada*

A.1 Statement of the Present Author's Contributions

My role in the above project was two-fold: (1) calculate the relationship between QD size and emission peak using a simple finite cubic well model, and (2) use double-well calculations to show whether or not the observed redshift of the coupled quantum dots could be accounted for by electron-tunneling between QDs. Thus, my work using theoretical blueshifts to help size QDs *in situ* remained useful. In the main text of the article, this contribution appeared as a short paragraph beginning with, "The size-dependence of the emission spectra of individual PQDs can be modeled by solving the Schrödinger equation under the effective mass approximation." I also contributed a write-up, including the calculated relationship between QD size and emission peak wavelength, in the supplemental information published alongside the article. Since an alternative mechanism was found to much better explain the coupled dot redshift, my modeling of double-wells was only used in a qualitative justification for ruling out tunneling as a mechanism, included in a short paragraph in the supplemental information. Thus, while my contributions represented only a minor addition to the final article, they are presented here in more detail. The procedures used fit nicely within the context of this dissertation as an application of a continuum approach, solved numerically via the Finite Element Method (FEM), to nanostructured materials.

A.2 Perovskite Quantum Dots: Background

The optical properties of QDs can be modulated by tuning the QD dimensions to take advantage of quantum confinement, making them useful materials in applications where specific wavelengths of light must be emitted or absorbed. Perovskite QDs, in particular, are excellent sources of coherent single photons[2] and efficient harvesters of solar energy in solar cells.[3] Additionally, the ability to couple multiple QDs opens the possibility of using them as qubits in quantum computation.[4] Because of the size-dependency of QD properties, synthesis or post-synthesis selection of monodisperse QDs is essential for many applications.

In the present project, the synthesized $CsPbBr_3$ QDs were viewed with a scanning transmission electron microscope (STEM) and observed to be cubic, with side lengths of 10.5 ± 0.5 nm. Moreover, the QDs were observed to remain separated by roughly 1.4 nm because of steric interactions between oleic acid capping ligands. Emission spectroscopy of trapped single QDs showed wavelengths of 520 nm, or 2.38 eV. This emission represents a blueshift relative to bulk $CsPbBr_3$, which has a band gap of 2.30 eV, due to an increased energy of excited electron-hole pairs associated with quantum confinement in the QD. Relating the size of this blueshift to QD side length allows the QDs to be sized spectroscopically in solution, without the need for STEM. Double-trapping of QDs produced a small but systematic redshift in this emission of 1.1 ± 0.6 meV.

A.3 Sizing QDs Using Emission Energy

The bandgap of a QD depends on the bandgap of the bulk material E_g^{bulk} and the gap-widening confinement energy of an excited electron-hole pair, E_c. Furthermore, the Coulombic attraction between a negatively charged electron and positively charged hole results in a stabilizing contribution that slightly narrows the gap, called the exciton binding energy E_b. The resulting QD band gap can be written

$$E_g = E_g^{\text{bulk}} + E_c - E_b. \tag{A.1}$$

The exciton in the QD has an exciton Bohr radius a_b defining the electron-hole separation, which in combination with the QD side length L can be used to define the degree of confinement. When $a_b \ll L$, the exciton is said to be weakly confined. For our QDs, we calculated the Bohr radius as $a_b = 4\pi\epsilon^{\infty}\epsilon_0\hbar^2/(e^2\mu)$, where ϵ^{∞} is

the optical permittivity inside the QD, ϵ_0 is the permittivity of free space, e is the elementary charge, and μ is the reduced effective mass of the exciton. Explicity, μ is given by $\mu = (m_e^* + m_h^*)/m_e^* m_h^*$, where m_e^* and m_h^* are the effective masses of the electron and hole, respectively. Using the parameters in Table A.1, we calculated the exciton Bohr radius in the QDs to be 3.9 nm. Since this is much smaller than the QD side length, an assumption of weak confinement was made. Under this assumption, the exciton binding energy can be approximated with[5]

$$E_b = \frac{\hbar^2}{2\mu a_b^2}. \tag{A.2}$$

Meanwhile, under the effective mass approximation,[6], the confinement energy can be estimated by the energy of the ground state solution of a particle in an infinite cubic well:[7]

$$E_C = \frac{3\hbar^2\pi^2}{2\mu L^2}. \tag{A.3}$$

A more accurate approach to calculating the confinement energy is to model the QD as a finite well, and calculate the lowest energy solution of the Schrödinger equation under the effective mass approximation for both the excited electron and associated hole.[7] Thus, we used the partial differential equation toolkit in MATLAB R2020a to find the lowest eigenvalue of the following equation using the FEM:

$$\left[\frac{-\hbar^2}{2m_c^*}\nabla^2 + V_c(\vec{r})\right]\psi_c(\vec{r}) = E_c\psi_c(\vec{r}). \tag{A.4}$$

Here, the subscript c indicates the carrier type (electron or hole), and V is the external potential. The external potential depends on the band offsets between the QD and its surroundings for each carrier type. For our calculations, we used the band offsets between $CsPbBr_3$ QDs and oleic acid ligands,[8] given in Table A.1 The total exciton confinement energy was found by adding the electron and hole confinement energies.

Table A.1: Effective Mass Approximation Parameters.

	E_g	ϵ^∞	$m_e^{*\mathrm{a}}$	$m_h^{*\mathrm{a}}$	V_e	V_h
Value	2.30 eV	4.8	0.134	0.128	3.14 eV	0.79 eV
Reference	[9]	[5]	[5]	[5]	[8]	[8]

[a] Relative to the mass of an electron.

The theoretical emission wavelengths of QDs with a range of side lengths were calculated using both an infinite and finite well. The model parameters are enumerated in Table A.1, and a diagram of the finite well band offsets is presented in Figure A.1(a). The results of both models are presented in Figure A.1(b). Because of the mellower confinement potential, the finite well model predicts smaller blueshifts for a given particle size. For an emission wavelength of 520 nm, the finite well model predicted a QD side length of between 10.5 and 11.0 nm, whereas the infinite well model predicted a larger side length between 11.5 and 12.0 nm. Thus, the finite well model correlated well with STEM measurements of the QDs (10.5 ± 0.5 nm).

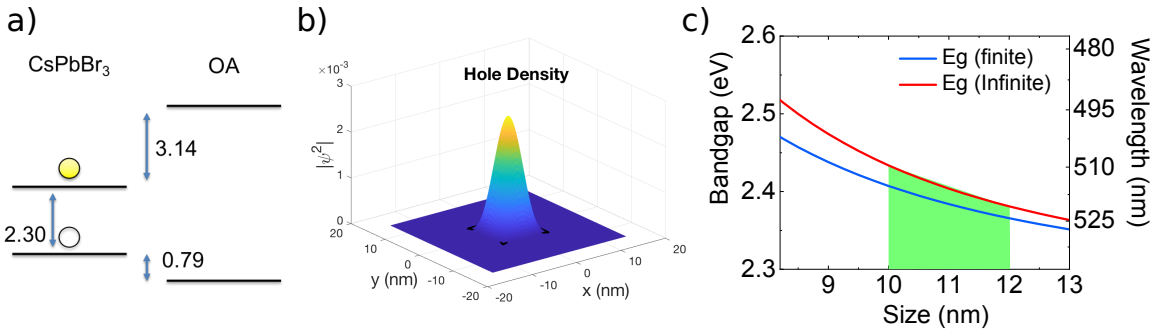

Figure A.1: Single QD finite well model. Panel **a)** shows a schematic of the band offsets (in eV) between the QD and oleic acid (OA) ligands. Panel **b)** shows a representative hole density, calculated using a 10 nm QD. Panel **c)** shows the bandgap dispersion with QD size (side length) from both the infinite and finite well models, taken from the supplemental information of Ref [1]. The plot was created by Hao Zhang using data provided by myself.

Modeling Coupled QDs

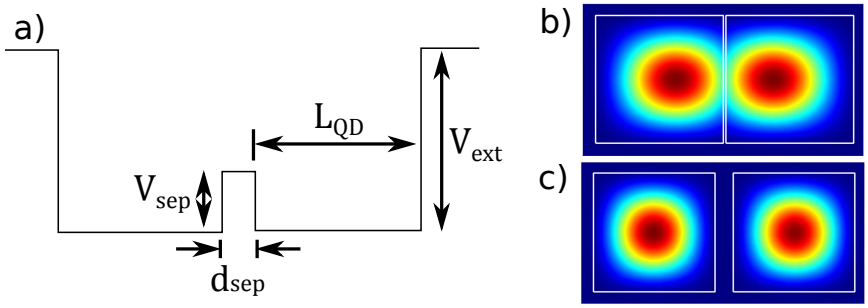

Figure A.2: Double-trapped QD finite well model. Panel **a)** shows a schematic of a general double-well potential. Panel **b)** shows a representative hole density, calculated for two 10 nm QDs with a separation of 2 Å. Panel **c)** shows the hole density for the same QDs but with a separation of 1.5 nm.

To model double-trapped, or coupled PQDs, we introduced a double-well potential where two finite cubic wells as described above were brought into close proximity. The general double-well potential is illustrated in Figure A.2(a). In our calculations, both the potential separating the wells and the external potential were set to the band offsets between $CsPbBr_3$ and oleic acid, as was done with the single QDs. Solving Equation (A.4) for the double well potential produces a lowest energy solution that is the symmetric combination of the solutions for single QDs. When the QDs were brought extremely close together, within less than 0.5 nm, significant carrier density was observed in the interstitial space betweeen the two QDs, indicative of carrier tunneling. However, for spacings of about 1.5 nm, which is on par with the separations observed in STEM images, the carrier density is almost entirely localized within the bounds of the two QDs.

The Coulombic binding energy of the exciton was neglected in calculations of the resulting redshifts. In theory, for a more complicated potential such as the double well, the binding energy can be calculated using a coupled Schrödinger-Poisson solver to give quantitative redshifts.[10] However, the redshifts that we calculated for experimental QD spacings were already much smaller than what had been observed experimentally. Since adding accurate Coulombic interactions should further localize carriers in order to increase overlap of the opposite charges,[10] we reasoned that doing so would only further decrease the computed redshifts. Thus, we concluded that tunneling, or delocalization of the exciton over coupled QDs, could not account for the observed redshift.

Bibliography

[1] Hao Zhang, Parinaz Moazzezi, Juanjuan Ren, Brett Henderson, Cristina Cordoba, Vishal Yeddu, Arthur M. Blackburn, Makhsud I. Saidaminov, Irina Paci, Stephen Hughes, and Reuven Gordon. Coupling perovskite quantum dot pairs in solution using a nanoplasmonic assembly. *Nano Letters*, 22(13):5287–5293, June 2022.

[2] Hendrik Utzat, Weiwei Sun, Alexander E. K. Kaplan, Franziska Krieg, Matthias Ginterseder, Boris Spokoyny, Nathan D. Klein, Katherine E. Shulenberger, Collin F. Perkinson, Maksym V. Kovalenko, and Moungi G. Bawendi. Coher-

ent single-photon emission from colloidal lead halide perovskite quantum dots. *Science*, 363(6431):1068–1072, March 2019.

[3] Seyeong Lim, Gyudong Lee, Sanghun Han, Jigeon Kim, Sunhee Yun, Jongchul Lim, Yong-Jin Pu, Min Jae Ko, Taiho Park, Jongmin Choi, and Younghoon Kim. Monodisperse perovskite colloidal quantum dots enable high-efficiency photovoltaics. *ACS Energy Letters*, 6(6):2229–2237, May 2021.

[4] Guido Burkard, Daniel Loss, and David P. DiVincenzo. Coupled quantum dots as quantum gates. *Physical Review B*, 59(3):2070–2078, January 1999.

[5] Michael A. Becker, Roman Vaxenburg, Georgian Nedelcu, Peter C. Sercel, Andrew Shabaev, Michael J. Mehl, John G. Michopoulos, Samuel G. Lambrakos, Noam Bernstein, John L. Lyons, Thilo Stöferle, Rainer F. Mahrt, Maksym V. Kovalenko, David J. Norris, Gabriele Rainò, and Alexander L. Efros. Bright triplet excitons in caesium lead halide perovskites. *Nature*, 553(7687):189–193, January 2018.

[6] Louis Brus. Electronic wave functions in semiconductor clusters: experiment and theory. *The Journal of Physical Chemistry*, 90(12):2555–2560, June 1986.

[7] Ruo Xi Yang and Liang Z Tan. Understanding size dependence of phase stability and band gap in cspbi3 perovskite nanocrystals. *The Journal of Chemical Physics*, 152(3):034702, 2020.

[8] Xiaochun Liu, Haifeng Zhao, Linfeng Wei, Xinjian Ren, Xinyang Zhang, Faming Li, Peng Zeng, and Mingzhen Liu. Ligand-modulated electron transfer rates from cspbbr3 nanocrystals to titanium dioxide. *Nanophotonics*, 10(8):1967–1975, 2020.

[9] Mohammed Ezzeldien, Samah Al-Qaisi, Z. A. Alrowaili, Meshal Alzaid, E. Maskar, A. Es-Smairi, Tuan V. Vu, and D. P. Rai. Electronic and optical properties of bulk and surface of CsPbBr3 inorganic halide perovskite a first principles DFT 1/2 approach. *Scientific Reports*, 11(1), October 2021.

[10] Jiabin Cui, Yossef E Panfil, Somnath Koley, Doaa Shamalia, Nir Waiskopf, Sergei Remennik, Inna Popov, Meirav Oded, and Uri Banin. Colloidal quantum dot molecules manifesting quantum coupling at room temperature. *Nature Communications*, 10(1):1–10, 2019.

Appendix B

Supporting Information for Chapter 3

This Appendix serves to supplement Chapter 3 by (1) supplying practical guidance for performing the calculations therein, and (2) providing details about the convergence of the methods used with respect to different simulation parameters. Regarding point (1), I found it somewhat tedious and confusing to determine a protocol for computing the centers of maximally-localized Wannier functions efficiently and reliably. The input scripts that I ultimately used are thus supplied in order to save others time and improve the reproducibility of my results. Moreover, an alternative method for obtaining Wannier centers is described along with its potential advantages in future work. With respect to point (2) above, we include some of the common benchmarking work (k-point sampling, plane wave cutoff) that proceeds many computational investigations. Here, we found it particularly important to probe the impact of sampling only the Gamma point, which is a feature of the CPMD code used throughout Chapter 3.

B.1 Input Files for Computing Wannier Centers

In order to compute the polarization change via the displacement of Wannier centers, we used the Car-Parrinello (CP) module of Quantum Espresso to evaluate the Wannier center positions under the conditions of a vanishing and finite applied electric field. First, the electronic energy was minimized using the normal CPMD protocol—namely, some steps of steepest descent minimization followed by damped electronic

dynamics. Following this, Wannierization was performed using an input file like the one below (note that atomic coordinates have been omitted to save space). The file instructs Quantum Espresso to read from a converged damped dynamics run saved in the *mgo_51.save* directory.

```
&CONTROL
  calculation = 'cp-wf',
  restart_mode = 'restart',
  ndr = 51,
  ndw = 52,
  nstep  = 1,
  iprint = 1,
  isave  = 1,
  dt    = 1,
  etot_conv_thr = 1.d-8,
  ekin_conv_thr = 1.d-10,
  prefix = "mgo",
  pseudo_dir = "./pbe_pseudos/"
  !verbosity = 'minimal'
/
&SYSTEM
    ibrav=1,
    A = 12.775387,
    nat=  216, ntyp= 3,
    ecutwfc = 70, ecutrho = 280,
    nr1b = 30, nr2b = 30, nr3b = 30,
/
&ELECTRONS
  emass = 300d0,
  emass_cutoff = 2.5d0,
  orthogonalization = 'ortho',
  ortho_max = 200
  electron_dynamics = 'damp',
  electron_damping = 0.05
/
```

```
&IONS
  ion_dynamics = 'none',
  ion_temperature = 'not_controlled',
/
&WANNIER
  wfsd = 3
  nit = 200,
  calwf = 3
/
ATOMIC_SPECIES
Mg    24.305    Mg.upf
O    15.999    O.upf
Ag    107.868    Ag.upf

ATOMIC_POSITIONS (angstrom)
...
```

The most critical lines of this input are `calculation = 'cp-wf'` in the `CONTROL` block, indicating that we are proceeding with a Wannier function calculation, and the lines within the `WANNIER` block. `wfsd = 3` performs Wannier function localization with the Jacobi algorithm, `nit = 200` requests 200 iterations of the localization, and `calwf = 3` is appropriate for starting with the CP wavefunction from a previous damped dynamics run and transforming it into the Wannier basis. For some systems, one may wish to use the conjugate gradients minimizer in the CPMD code instead of damped dynamics (we did this for the smallest 64-atom composite cell, for instance). In such a case, it is possible to use `calwf = 4`, which performs a single CP iteration before Wannierizing the Kohn-Sham orbitals. After running the input above, the coordinates of the resulting Wannier centers are printed in the `mgo_52.save/data-file-schema.xml` file, under the tag `<WANNIER_CENTERS>`.

To apply an electric field, the input was modified slightly. The line `tefield = .TRUE.` was added to the `CONTROL` block to indicate that a field was to be applied, and `efield = 0.001D0` and `epol = 3` were added to the `ELECTRONS` block to indicate electric field strength and direction. Moreover, `wf_efield = .TRUE.`, `wf\_switch = .FALSE.`, and `efz1 = 0.001D0` were added to the `WANNIER` block. These indicate that a field of 0.001 au should be applied in the z-direction, consistent

with the ELECTRONS block, and that the field should not be switched on adiabatically but rather be completely on from the start. This last option is appropriate since this Wannierization procedure read in the output from a damped electron dynamics calculation where the same electric field was already applied.

B.1.1 Alternative Approach to Computing Wannier Centers

Instead of using the CP module of Quantum Espresso, it is possible to use the PW module (the SCF code available via the pw.x executable) to compute the displacement of Wannier centers in external fields. This latter approach has the advantage that the PW code supports k-point sampling, whereas the CP code is a Gamma point code. Additionally, the PW code has more sophisticated iterative minimization algorithms that can produce quicker convergence than the damped-electronic dynamics in the CP code.

One downside of the PW code is that it cannot natively compute Wannier functions. Rather, it is interfaced to the external Wannier90 code. Practically speaking, we found that we were able to compute the displacement of Wannier centers with the PW/Wannier90 approach for simple systems. However, for nanocomposites, obtaining converged MLWFs in this way was difficult. In general, a good choice of initial projections onto atomic orbitals seemed critical for an efficient localization of Wannier functions. After the research appearing in Chapter 3 was conducted, we noticed that the use of automatic projections via the new selected columns of the density matrix (SCDM) algorithm[1] appeared to aid convergence of MLWFs in nanocomposites. Thus, we include here the inputs necessary to generate MLWFs via the PW/Wannier90 procedure using SCDM, as we think it could be a more flexible alternative to the CP procedure used in Chapter 3.

The process begins with a typical SCF run. Here, we show an input file pw.scf.in for a conventional unit cell of MgO:

```
&CONTROL
   calculation     = 'scf'
   restart_mode    = 'from_scratch'
   outdir          = './scf/'
   pseudo_dir      = '/home/pseudo_dojo/nc-sr-04_pbesol_standard_upf/'
   prefix          = 'mgo'
   lelfield        = .true.
```

```
   nberrycyc       = 1
/
&SYSTEM
   ibrav           = 1
   celldm(1)       = 7.88321387788
   nat             = 8
   ntyp            = 2
   ecutwfc         = 70
   ecutrho         = 280
   occupations     = 'fixed'
   nspin           = 1
   starting_charge(1) = 2
   starting_charge(2) = -2
/
&ELECTRONS
   electron_maxstep = 200
   conv_thr        = 1.D-10
   startingpot     = 'atomic'
   startingwfc     = 'atomic+random'
   mixing_mode     = 'plain'
   mixing_beta     = 0.7D0
   mixing_ndim     = 8
   diagonalization = 'david'
ATOMIC_SPECIES
   Mg  24.305   Mg.upf
    O  15.99900  O.upf
ATOMIC_POSITIONS crystal
Mg   0.25000   0.25000   0.25000
Mg   0.25000   0.75000   0.75000
Mg   0.75000   0.25000   0.75000
Mg   0.75000   0.75000   0.25000
 O   0.75000   0.75000   0.75000
 O   0.75000   0.25000   0.25000
 O   0.25000   0.75000   0.25000
 O   0.25000   0.25000   0.75000
```

```
K_POINTS automatic
  4 4 12   0 0 0
```

After running this input, we prepare the Kohn-Sham wavefunctions on the full k-point grid using the `open_grid.x` code distributed with Quantum Espresso. Note that Wannier90 requires the full grid, whereas the PW code often uses symmetry to reduce the number of k-points in the calculation. Using `open_grid.x` allows us to bypass the usual step of performing a non-SCF calculation before Wannier90. The input file for `open_grid.x`, which we name `pw.openg.in` is simply:

```
&inputpp
   outdir = './scf'
   prefix = 'mgo'
/
```

and is run with the command `open_grid.x < pw.openg.in > pw.openg.out` with optional parallelization via MPI.

For Wannierization, we use the following input to Wannier90, saved in the file `mgo.win`:

```
    num_wann        =  32
num_iter        = 200
#restart         = plot

auto_projections = .true.

begin atoms_frac
Mg   0.25000   0.25000   0.25000
Mg   0.25000   0.75000   0.75000
Mg   0.75000   0.25000   0.75000
Mg   0.75000   0.75000   0.25000
 O   0.75000   0.75000   0.75000
 O   0.75000   0.25000   0.25000
 O   0.25000   0.75000   0.25000
 O   0.25000   0.25000   0.75000
end atoms_frac
```

```
begin unit_cell_cart
4.1716174332 0.0 0.0
0.0 4.1716174332 0.0
0.0 0.0 4.1716174332
end unit_cell_cart

mp_grid : 4 4 12

begin kpoints
    0.00000000    0.00000000    0.00000000    0.00520833
    ...
end kpoints
```

Note that we have truncated the k-point list to save space, but the full list of points and weights, which are printed at the end of the `open_grid.x` output, should be included. Note also the use of the `auto_projections = .true.` option, which takes advantage of projections supplied by PW via the SCDM algorithm.

The interface between PW and Wannier90 is handled by the `pw2wan90.x` code, for which we create the input file `pw.pw2wan.in`:

```
&inputpp
   outdir = './scf'
   prefix = 'mgo_open'
   seedname = 'mgo'
   scdm_proj         = true
   scdm_entanglement = 'isolated'
   spin_component = 'none'
   write_mmn = .true.
   write_amn = .true.
   write_unk = .true.
/
```

Importantly, we have included the options to compute SCDM projections using procedure for isolated bands, which should be appropriate for finite gap insulators. Note also the use of the prefix `'mgo_open'`, since the `open_grid.x` code saves its results in a directory with the normal prefix appended with `_open`.

The preparation of the necessary integrals from PW and ultimately the Wannierization are performed with the following commands:

```
wannier90.x -pp mgo
srun pw2wannier90.x < pw.pw2wan.in > pw.pw2wan.out
srun wannier90.x mgo
```

The output of Wannier90 includes the Wannier center coordinates and their spreads. By obtaining the centers from both a zero-field and finite-field calculation and applying Equation (2.47) we compute the induced polarization. Then Equation (2.41) yields the permittivity. Additionally, displacements of individual Wannier centers can be used to partition the response when studying nanocomposites. Using the above input files, we computed a clamped-ion permittivity ϵ^{∞} of 3.32, which is reasonably close to the value of 3.19 computed with the standard Berry phase approach using the same k-point sampling and wavefunction cutoff (Table B.3).

As another demonstration of the PW/Wannier90 approach, we computed the decomposition of α_{enh} for the highest volume loading MgO/Ag_8 composite from Chapter 3 (Table 3.2). Recall that the unit cell for this composite consists of 64 atoms, with the central 8 oxide ions (4 Mg and 4 O) replaced by Ag. As this is just a demonstration, we computed the electronic structure with the PZ functional on a version of the unit cell symmetrized to the P-43m spacegroup to make the calculation more efficient. A 3×3×5 k-point grid was used and a 50 Ry plane wave energy cutoff for the wavefunctions, with a 400 Ry cutoff for the charge density. The calculation was referenced to a bulk calculation on a 2×2×2 MgO supercell with the previously determined bulk lattice constant of 4.240 Å, which used same k-point grid and cutoffs as the composite calculation.

The clamped-ion partitioning of α_{enh} is given in Table B.1, along with the partitioning calculated using the CP method in Chapter 3. Keeping in mind that the CP results are from a slightly different geometry and using the PBE functional, it is still apparent that the two methods are in reasonably close agreement. Certainly, both predict a clamped ion response that is dominated by the inclusion polarizability.

Table B.1: PW/Wannier90 calculation of clamped-ion α_{enh} for $(MgO)_{28}Ag_8$.

Method	ϵ_{bulk}	ϵ_{comp}	α_{inc}	α_{mat}	α_{cav}	α_{enh}
CP	2.87	5.25	768	218	-77	909
PW/W90	3.22	6.14	906	258	-91	1074

B.2 Convergence of Permittivity

B.2.1 With Functional and Cutoff Energy

As discussed in the main text, we used optimized norm-conserving Vanderbilt pseudopotentials from PseudoDojo. For most of the analysis, we used the PBE functional, but for the analysis of different oxides, we utilized PBESol. We examined the convergence of the permittivity with the wavefunction cutoff energy for different bulk alkaline earth oxides. We used the normal plane wave module of Quantum Espresso and studied conventional rocksalt unit cells of each oxide. The lattice constant of the unit cells were optimized using PBESol with a wavefunction cutoff of 70 Ry, a charge density cutoff of 280 Ry, and a 12×12×12 Monkhorst-Pack grid of k-points. Then, the clamped- and relaxed-ion permittivities were calculated using the finite field method with either the PBESol or PBE functionals. In these calculations, the wavefunction cutoff was varied between 60 and 120 Ry (between 50 Ry was also included for MgO with the PBESol functional), and the charge density cutoff was always 4 times this wavefunction cutoff. A 4×4×12 Monkhorst-Pack grid of k-points was used for all of the permittivity calculations. The results are given in Figure B.1.

First, we can see that the values of permittivity are already pretty well converged using a wavefunction cutoff of 60 Ry. Above this value, the clamped-ion permittivity only varies by about ±0.01 or less, and the relaxed-ion permittivity varies by a slightly larger but still acceptable value of about ±0.1. These ranges appear consistent across both functionals and all oxides. Furthermore, from the example of MgO using the PBESol functional and a 50 Ry cutoff, it is clear that reducing the cutoff below 60 Ry can cause dramatic changes in the computer permittivites. Thus, we chose a cutoff of 70 Ry for the wavefunction and 280 Ry for the charge density in order to balance efficiency and accuracy.

Using these values, we can also comment on the variation between functionals. PBESol universally predicts larger permittivity values than PBE. The difference between functionals is quite small (1-2%) for clamped-ion permittivity, but larger (up

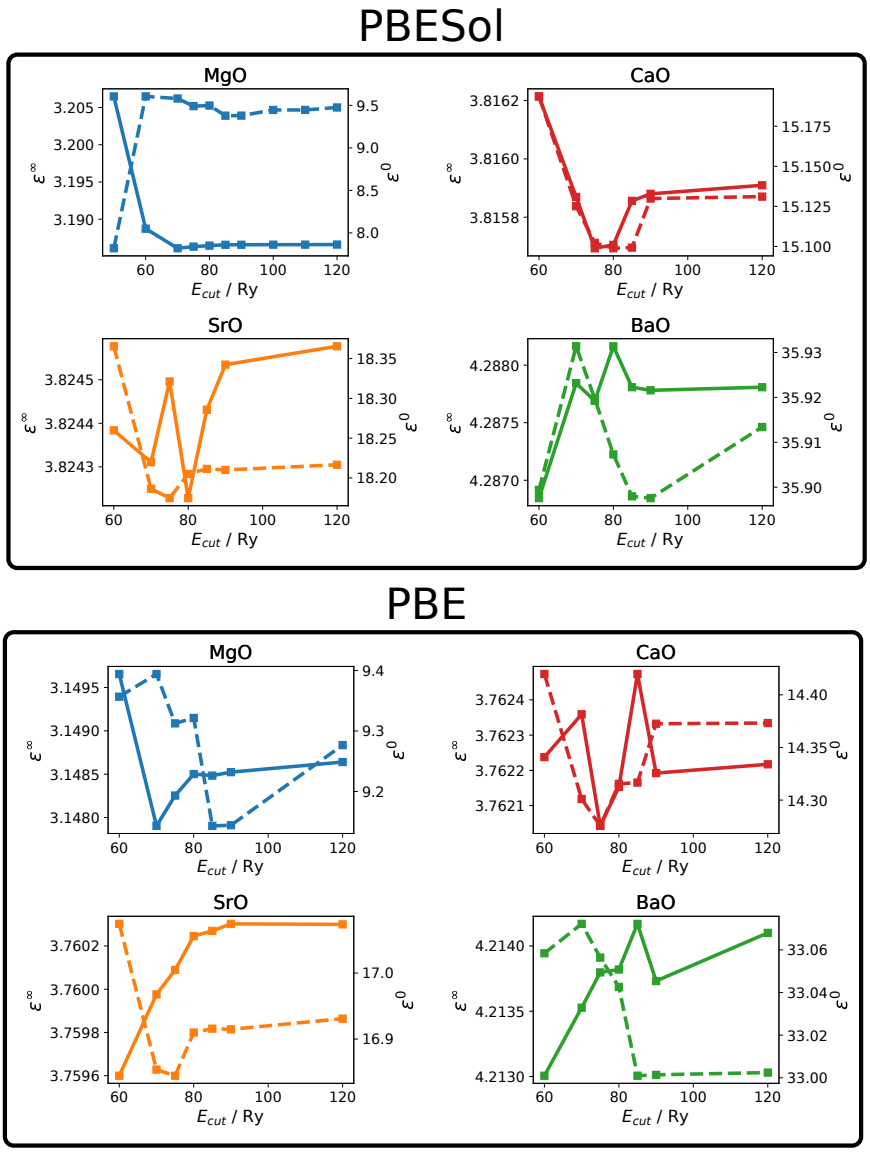

Figure B.1: Convergence of permittivity with plane wave energy cutoff E_{cut} using PBESol and PBE for each oxide. Solid lines show ϵ^{∞}, and dashed lines show ϵ^{0}.

to 8.6%) for relaxed-ion permittivity. Still, both functionals preserve the trend of increasing permittivity as the cation atomic number increases. They also are both consistent in predicting that SrO has the same clamped-ion permittivity as CaO but a larger relaxed-ion permittivity.

B.2.2 With k-Point Sampling

It is necessary to ensure that CPMD calculations, which were performed using a Gamma-point only sampling, produce sufficiently converged permittivities relative to calculations with a denser k-point grid. As discussed in Section 3.2, the permittivity computed using the Gamma point only should converge as $1/L^2$ for supercell length L.[2] We evaluated the effect of supercell size on both the computed lattice constants and permittivities of bulk oxides to better understand this convergence behavior for our systems. The calculations in this section all used the PBESol functional.

Table B.2 shows the lattice constants computed with both 2×2×2 and 3×3×3 supercells of the four alkaline earth oxides studied in Chapter 3 using CPMD. Additionally, the table includes the lattice constants calculated using the PW code with a conventional unit cell and a 12×12×12 Monkhorst-Pack grid of k-points. The lattice constants of the larger CPMD super cell seem well converged relative to the PW results. The lattice constants for the smaller CPMD supercell are also generally in good agreement with the PW results. CaO is the exception, with a lattice constant that is over 0.1 Å smaller when calculated with the small supercell in CPMD compared to the large one. The PBESol functional underestimates experimental lattice constants slightly for all of the studied oxides, by values ranging from 0.041 to 0.056 Å.

Table B.2: Convergence of bulk oxide lattice with k-point sampling.

Oxide	CP (2×2×2)	CP (3×3×3)	PW[a]	Expt.[b]
MgO	4.162	4.167	4.172	4.213
CaO	4.629	4.755	4.754	4.810
SrO	5.129	5.111	5.109	5.160
BaO	5.523	5.498	5.495	5.539

[a] Conventional unit cell with 12×12×12 Monkhorst-Pack grid.
[b] Computed from the densities in references [3, 4].

Table B.3 shows the clamped- and relaxed-ion permittivites calculated for the same supercells with CPMD and using the PW code with a 4×4×12 Monkhorst-Pack grid of k-points. The results show that the larger CPMD supercell produces significantly better-converged permittivities than the smaller supercell, when compared against the PW results. Still, there are noticeable discrepancies caused by the Gamma-point only sampling. In particular, the relaxed-ion permittivity of BaO is significantly too large, even in the larger CPMD cell, relative to the tighter k-point

grid. Nevertheless, the convergence in nearly all cases seems to be smooth, in that the large-supercell CPMD permittivities fall between the small-supercell CPMD values and the PW ones. The relaxed-ion permittivity of MgO is the sole exception in this regard. This smoothness is a good quality when it comes to the calculation of α_{enh} values in Chapter 3. Since we are computing the *enhancement* in permittivity relative to the bulk and not necessarily its absolute value, using a bulk reference permittivity computed using a supercell roughly the same size as the nanocomposite cell should cancel much of the error associated with finite k-point sampling. Thus, we adopt such a procedure in Chapter 3, as described in the following section.

Table B.3: Convergence of bulk oxide permittivity with k-point sampling.

	CP (2×2×2)		CP (3×3×3)		PW		Expt.	
Oxide	ϵ^∞	ϵ^0	ϵ^∞	ϵ^0	ϵ^∞	ϵ^0	ϵ^∞	ϵ^0
MgO	2.85	9.30	3.00	9.00	3.19	9.58	3.00[a]	9.78[b]
CaO	3.17	21.37	3.47	14.34	3.82	15.12	3.33[c]	11.1[c]
SrO	3.18	31.14	3.47	18.42	3.82	18.19	3.46[c]	13.1[c]
BaO	3.45	60.78	3.81	43.31	4.29	35.93	3.90[d]	34[e]

[a] Calculated from a refractive index of 1.733345 at 656.3 nm and 296.15 K.[5]
[b] From Ref [6] at 50K and zero pressure.
[c] Values from Ref [7].
[d] Calculated from a refractive index of 1.97571 at 623.8 nm and 296.15 K.[8]
[e] Value from Ref [9].

B.3 Permittivities of Bulk MgO Supercells

When dealing with anisotropic inclusions in non-cubic unit cells, there is a difference in k-point density along the different dimensions of the cell, which introduces errors of different magnitudes when calculating the permittivity along different inclusion directions. Thus, when computing reference bulk permittivities for α_{enh} calculations, we use bulk supercells that are not just of similar volume to the composite cell, but also similar shape, in order to best cancel k-point sampling errors. Specifically, when constructing a composite cell according to Figure 3.1, we replace a certain number of matrix ions in a bulk supercell with Ag atoms in order to create an inclusion of the desired aspect ratio. Then, this same bulk supercell is used as the reference in the α_{enh} calculation. Table B.4 provides the clamped- and relaxed-ion permittivities for

all the different reference supercells of MgO used in Chapter 3.

Table B.4: Bulk MgO reference permittivities.[a]

		PZ		PZ/PBE	
Supercell[b]	Composites	ϵ^∞	ϵ^0	ϵ^∞	ϵ^0
2×2×2	$(MgO)_{28}Ag_8$	2.853	9.227	2.870	9.291
3×3×3	$(MgO)_{104}Ag_8$	3.033	9.256	3.033	9.310
3×4×3	$(MgO)_{138}Ag_{12}$	3.035	9.276	3.038	9.330
	$(MgO)_{136}Ag_{16}$				
3×3×4	$(MgO)_{138}Ag_{12}$	3.118	9.330	3.107	9.375
	$(MgO)_{136}Ag_{16}$				
4×4×3	$(MgO)_{183}Ag_{18}$	3.034	9.287	3.035	9.340
4×3×4	$(MgO)_{183}Ag_{18}$	3.116	9.332	3.108	9.377
4×4×4	$(MgO)_{252}Ag_8$	3.114	9.331	3.107	9.376

[a] Permittivities calculated using a field and polarization in the z-direction (ϵ_{zz}).
[b] Multiples of conventional MgO unit cell in the x-, y-, and z-directions, respectively.

In all of the calculations in Table B.4, the bulk lattice constant for the supercells was held fixed at 4.23967 Å, the value calculated with the PZ functional in Ref [10]. As with the composites, the ionic positions were optimized in the presence of an external field using the PZ functional, and single point calculations were performed with the PBE functional to calculate the clamped and relaxed ion permittivities, as described in Section 3.2 of the main text. We refer to this combined method as PZ/PBE. Table B.4 provides the permittivities calculated with both PZ alone and PZ/PBE (only the PZ/PBE values were used for computing α_{enh} in the main text) for each supercell. The table also indicates which composites the given supercells correspond to. Note that a given bulk supercell can correspond to multiple composites, since Ag_{12} and Ag_{16} rods were both studied in 288-atom cells.

The convergence of the permittivity is seen to be primarily dependent upon the supercell length in the z-direction, since this is the direction along which the cells were polarized. Thus, the permittivity of the 3×3×4 cell is very similar to the 4×4×4 cell, despite being much smaller in volume. As the cell is lengthened in the $z-$direction, the clamped- and relaxed-ion permittivities both steadily increase toward converged values. Still, it should also be noted that most of the permittivities fall within a fairly narrow range despite the difference in cell sizes. The clamped-ion permittivity of the 2×2×2 cell is a bit of an outlier, being significantly smaller than that of the 3×3×3 cell. Finally, the PZ and PZ/PBE permittivities are remarkably similar.

Bibliography

[1] Valerio Vitale, Giovanni Pizzi, Antimo Marrazzo, Jonathan R. Yates, Nicola Marzari, and Arash A. Mostofi. Automated high-throughput wannierisation. *npj Computational Materials*, 6(1), June 2020.

[2] P. Umari and Alfredo Pasquarello. Polarizability and dielectric constant in density-functional supercell calculations with discrete k-point samplings. *Physical Review B*, 68(8), August 2003.

[3] Z P Chang and G R Barsch. Pressure dependence of the elastic constants of single-crystalline magnesium oxide. *J. Geophys. Res.*, 74(12):3291–3294, June 1969.

[4] Z.P. Chang and E.K. Graham. Elastic properties of oxides in the nacl-structure. *Journal of Physics and Chemistry of Solids*, 38(12):1355–1362, 1977.

[5] R.E. Stephens and I.H. Malitson. Index of refraction of magnesium oxide. *Journal of Research of the National Bureau of Standards*, 49(4):249, October 1952.

[6] R. A. Bartels and P. A. Smith. Pressure and temperature dependence of the static dielectric constants of kcl, nacl, lif, and mgo. *Physical Review B*, 7(8):3885–3892, April 1973.

[7] J.L. Jacobson and E.R. Nixon. Infrared dielectric response and lattice vibrations of calcium and strontium oxides. *Journal of Physics and Chemistry of Solids*, 29(6):967–976, June 1968.

[8] C. J. Anderson and E. B. Hensley. Index of refraction of barium oxide. *Journal of Applied Physics*, 46(1):443–443, January 1975.

[9] Renate S. Bever and Robert L. Sproull. The dielectric constant of barium oxide. *Physical Review*, 83(4):801–805, August 1951.

[10] David J.T. Hally and Irina Paci. Low-frequency polarization in molecular-scale noble-metal/metal-oxide nanocomposites. *Nanoscale*, 10(20):9583–9593, 2018.

Appendix C

Supporting Information for Chapter 4

C.1 Model Systems

Table C.1 presents structural information for the three supercells with Ag_8 inclusions, that were used to fit the continuum model. Lattice constants and relative permittivities were calculated using quantum dynamics, and band gaps were calculated with a single all-band SCF calculation in the PWSCF code within Quantum Espresso. All structures have non-zero band gap, despite the known underestimation of gap sizes by density functional theory.

Table C.1: Model systems used to fit the continuum model.

MgO Cell[a]	Ag (% at.)[b]	Lattice Constant (Å)	ϵ_∞	ϵ_r	Band gap (eV)
Bulk ($6 \times 6 \times 6$)	0	12.719[1]	3.0	9.3[1]	4.75
$8 \times 8 \times 8$	1.56	8.930	3.4	10.3	1.62
$6 \times 6 \times 6$	3.70	12.926 [1]	3.7	11.9[1]	1.40
$4 \times 4 \times 4$	12.5	17.077	5.5	34.6	0.50

[a] Indicates the number of MgO {100} planes included along each supercell direction.
[b] Eight Ag atoms replaced a cube of adjacent Mg and O atoms before relaxation.

C.1.1 Geometries and Interface Characteristics

The geometries of the three model systems of Table C.1 are shown in Figure C.1(a). The number of layers of MgO between image Ag inclusions increases from two to four

to six in going from the smallest (64 atoms) to the largest (512 atoms) supercells.

Bader analysis was performed using the Henkelman Group code [2] and the pseudo-charge density from Quantum Espresso CP runs. Although the use of pseudopotentials can sometimes lead to difficulties in finding density maxima at the atomic centers, no such problem was encountered for the MgO/Ag_8 systems. The analysis was also performed using the ground state charge density calculated using PBE/DZP in SIESTA, to provide additional validation for the data plotted in Figure C.1(b) and (c). The 216-atom geometry was used, and a reference density file with augmented core charges. No qualitative, and minimal quantitative differences, were found relative to the Quantum Espresso results, suggesting that the pseudo-charge density is sufficient to generate accurate Bader volumes and charges for these systems.

For all three systems, the inclusion was found to have a net Bader charge (charge of the nucleus plus core electrons minus the integrated charge of the electronic Bader volume) of approximately -2, indicating a transfer of electrons from the matrix. As shown in Figure C.1(b) and (c), this manifests as a slightly decreased volume and less negative net charge on the twelve oxygen atoms nearest the inclusion in each of the systems. The charge on the inclusion is mostly concentrated on the four silver atoms forming the inner tetrahedron, with each having net charge of approximately -0.75. In contrast, the outermost four silver atoms each have a net positive charge of approximately 0.2. The charges on oxygen atoms quickly normalize to net -2 values, as the distances from the inclusion increase, with 91-93 % of the charge transfer due to the twelve oxygen atoms nearest the inclusion. In the two larger systems, slight net oscillations in the oxygen charges are apparent as the distances from the inclusion increase. In the smallest system, the charge transfer is slightly more pronounced, and all oxygen atoms have somewhat fewer than eight electrons.

The layer of MgO adjacent to the inclusion has a qualitative difference in electronic structure relative to subsequent layers. In addition to trends identified by Hally and Paci,[1] such as larger Maximally Localized Wannier Function spreads near the inclusion, these results motivate the treatment of a thin layer of matrix as a separate interfacial layer in the continuum model.

C.1.2 Anisotropic Systems

Table C.2 describes the systems from [3] that were used to test the transferability of the FEM model to anisotropic composites. Each supercell geometry had at least

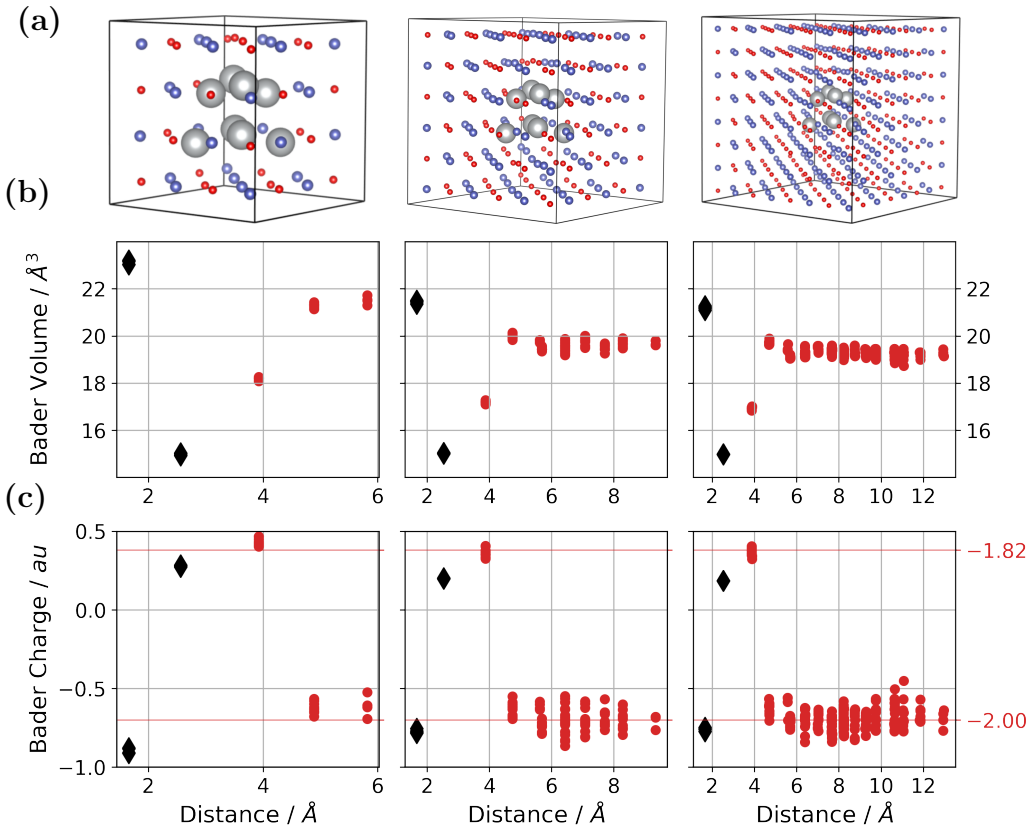

Figure C.1: Model system geometries and Bader Analysis of interface. (a) The 64, 216, and 512 atom composite geometries with eight-atom silver inclusions. The Bader volumes (b) and charges (c) of Ag and O atoms versus distance from the Ag particle centroid are also shown. Black diamonds and red circles represent Ag and O atoms, respectively.

four layers of MgO between inclusion images in every direction, resulting in atomic loadings between 3.7 and 5.6 %. We note that all inclusions are still quite small, falling around the 1 nm size regime.

Table C.2: Structural descriptors of anisotropic composites.

MgO Cell	Inclusion	Ag (% at.)	Inc. Length (nm)	Inc. Width (nm)
$6 \times 6 \times 8$	$2 \times 2 \times 3$	4.2	0.9	0.7
$6 \times 6 \times 8$	$2 \times 2 \times 4$	5.6	1.2	0.7
$6 \times 6 \times 10$	$2 \times 2 \times 5$	5.6	1.4	0.7
$8 \times 8 \times 6$	$3 \times 3 \times 2$	4.7	0.9	0.7
$10 \times 10 \times 8$	$4 \times 4 \times 2$	4.0	1.2	0.7

C.2 FEM Theory: Modeling a Parallel Plate Capacitor

In order to compute the permittivity of nanocomposites with the FEM, we modeled the composite as a representative volume element (RVE) between parallel plates and solved the electrostatic Laplace equation:

$$\nabla^2 \epsilon V = 0. \tag{C.1}$$

This equation yields the electrostatic potential V under the assumption that the material is a dielectric with a volume charge density of 0. To solve for V, we apply conditions to the boundaries of an RVE, $\partial\Omega$. We apply Dirichlet conditions on the top and bottom faces, setting the value of the potential for all points in space $\mathbf{r}$ on these faces such that

$$V(\mathbf{r}) = V_0 \quad \forall \mathbf{r} \in \partial\Omega_{\text{bottom}} \tag{C.2}$$

and

$$V(\mathbf{r}) = V_1 \quad \forall \mathbf{r} \in \partial\Omega_{\text{top}}. \tag{C.3}$$

Setting these conditions establishes the composite as a dielectric layer in a parallel plate capacitor. In addition, we enforce periodicity in the other two directions with Neumann boundary conditions on the remaining four sides of the RVE so that

$$\hat{\mathbf{n}} \cdot \nabla V(\mathbf{r}) = 0 \quad \forall \mathbf{r} \in \partial\Omega_{\text{side}}, \tag{C.4}$$

where $\hat{\mathbf{n}}$ is the boundary unit normal. This boundary condition amounts to specifying that the electric field be parallel to the RVE sides at those sides. These conditions establish the composite as an infinite-area capacitor dielectric, with a potential difference, $\Delta V = V_1 - V_0$, applied across its plates.

Once V is obtained, the energy U stored in the dielectric can be calculated as

$$U = \frac{1}{2} \int_\Omega \epsilon(\mathbf{r}) |\nabla V(\mathbf{r})|^2 d^3\mathbf{r}, \tag{C.5}$$

where $\epsilon(\mathbf{r})$ is the permittivity at each point in space. The energy stored in a parallel-

plate capacitor can also be written in terms of its capacitance C and its permittivity:

$$U = \frac{1}{2} C \Delta V^2, \tag{C.6}$$

where

$$C = \frac{\epsilon A}{d}, \tag{C.7}$$

A is the plate area, and d is the inter-plate distance. Solving for ϵ and then substituting the energy integral, yields an expression for the overall permittivity, that can be calculated via numerical integration from the finite element solution,

$$\epsilon = \frac{d \int_\Omega \epsilon(\mathbf{r}) |\nabla V(\mathbf{r})|^2 d^3\mathbf{r}}{A \Delta V^2}. \tag{C.8}$$

C.3 FEM Benchmarking

To validate our finite element approach, we computed the permittivities of serial and parallel composite geometries, which have known analytical solutions. The serial case consists of a two-phase laminar composite, with the electric field applied normal to the layers, and has a permittivity given by [4]

$$\frac{1}{\epsilon} = \frac{f_m}{\epsilon_m} + \frac{f_i}{\epsilon_i}, \tag{C.9}$$

where subscripts m, i and f denote the matrix, inclusion, and volume fraction, respectively. The parallel case is comprised of a two-phase composite for which all interfaces between the matrix and inclusion are strictly orthogonal to the applied field. This system has permittivity given by [4]

$$\epsilon = f_m \epsilon_m + f_i \epsilon_i. \tag{C.10}$$

Cubic meshes were generated with volume loadings of inclusion materials of between 5 % and 50 %. The matrix was assigned a relative permittivity of 1 and the inclusions a relative permittivity of 10, 20, or 30. In all cases, the FEM results matched analytical predictions to within floating point error (see Figure C.2). There were no significant mesh discretization errors.

For the parallel configuration, structures with cylindrical inclusions were also considered. For this case, the discretization of curved interfaces introduces errors. The

errors in the permittivities were found to be proportional to the volume discrepancies between ideal versus discretized cylinders. These errors were well suppressed by including a sufficient number of nodes per radian of curvature in the faces of the geometries. We used 20 elements per 2π radians for coarse grid searches of model parameters and 50 elements per 2π for single calculations on model geometries using optimal parameters.

C.3.1 Serial and Parallel Plates

Figure C.2 shows the serial and parallel configurations that were tested to validate the FEM. The geometries consisted of low-permittivity matrices, shown in blue, and a high-permittivity layer, shown in red. The relative permittivities were fixed at 1, and varied from 10 and 30, respectively. For both the serial and parallel configurations, the FEM results matched analytical predictions to within relative errors of 10^{-9}.

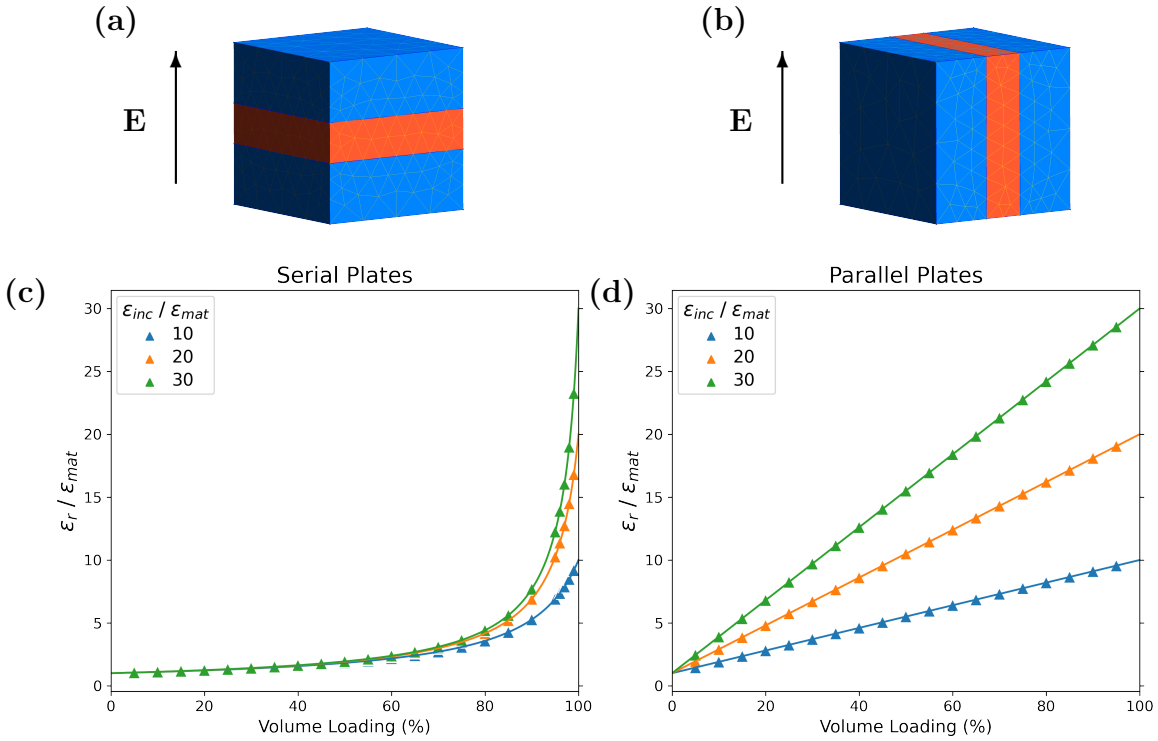

Figure C.2: FEM calculations of serial and parallel plate geometry permittivities and analytical solutions. Datapoints represent values calculated using the FEM, whereas the lines show the analytical solutions. Permittivities relative to the matrix permittivity are plotted in the figure.

C.3.2 Parallel Cylinders

The parallel configuration was also tested using cylindrical inclusions, as shown in Figure C.3 (a) and (b). This geometry has an exact analytical solution, but suffers from discretization errors from meshing when solved with the FEM. The discretization errors are due to differences between meshed and physical surfaces. Basis set error also occurs. Not all surfaces at the interface are parallel to the applied field, because of how the cylinder is discretized into tetrahedra. This leads to polarization and depolarization along the interface that cannot be described exactly by linear basis set elements. Comparisons between the analytical and FEM solutions can offer insight into the impact of these errors, which has implications for the ellipsoidal inclusions considered in this work. As shown in Figure C.3(c), the permittivity calculated via FEM closely matches the analytical solution, when the mesh is refined to have approximately 100 elements per 2π radians of curvature. Panel (d) demonstrates that the absolute error in relative permittivity, $\Delta\epsilon = \epsilon_{\text{analytical}} - \epsilon_{\text{FEM}}$, increases approximately linearly with volume loading. The error increases with the permittivity of the cylinder, and decreases with an inceased level of mesh refinement. Panel (e) demonstrates how the error is suppressed as the mesh is refined. Panel (f) shows that the relationship between the relative permittivity and discretization errors is approximately linear, the latter represented by the difference between meshed and ideal inclusion volumes. This result confirms that discretization is the primary source of error.

C.3.3 Symmetry Considerations

We restricted our analysis to spheres and ellipsoids with a rotational symmetry axis (disks and rods). We took advantage of symmetry to consider only 1/8 of each unit cell in FEM calculations. Specifically, we considered one of the rectangular prisms created by bisecting the simulation cell twice with orthogonal planes parallel to the cell sides. The boundary conditions remain the same, with the orthogonal electric field on the sides parallel to the applied electric field set equal to zero, and with the potential difference across the remaining two sides set to half of the total potential difference across the full cell. An example of a truncated cell for a disk is shown in Figure C.4.

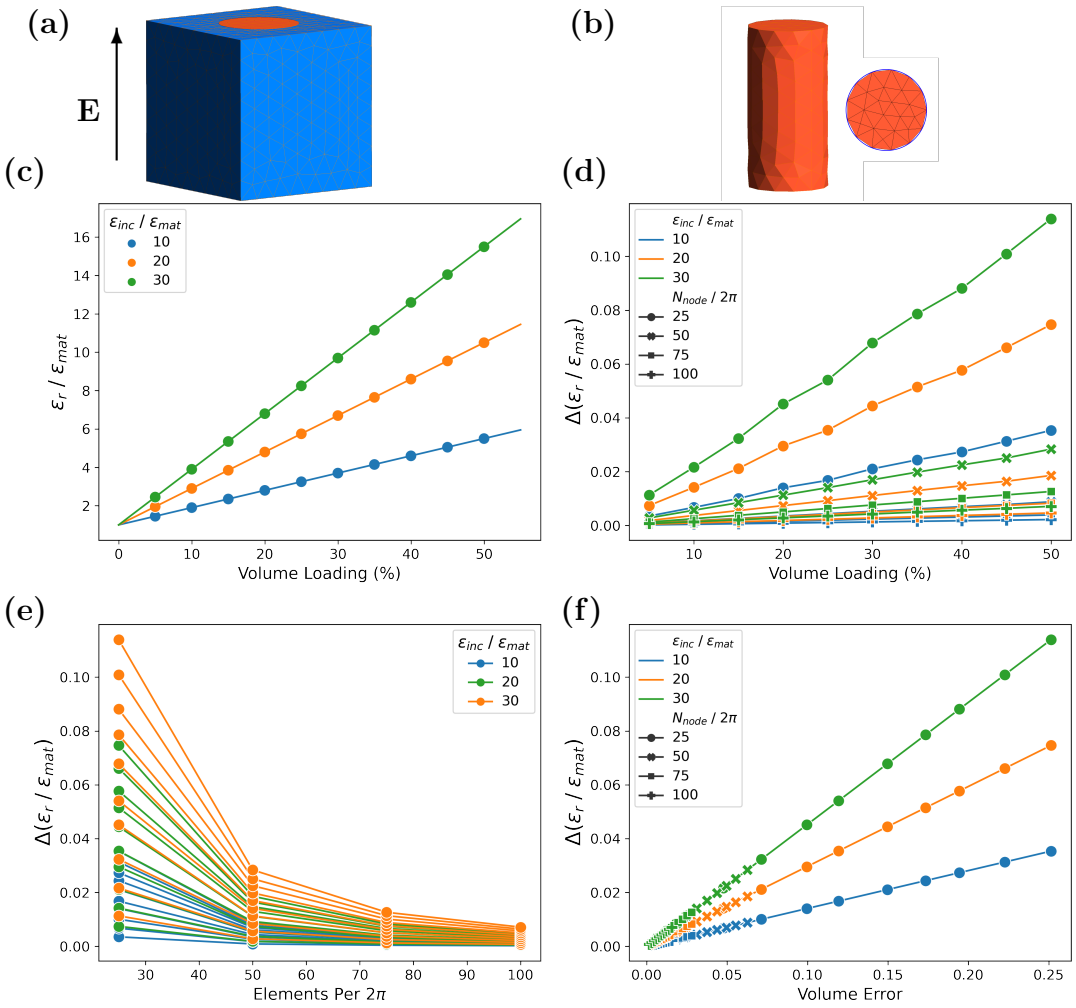

Figure C.3: FEM calculations of the permittivity of composites with cylindrical rods oriented parallel to the applied field. (a) The geometry and applied field direction, and (b) the mesh generated for the inclusion. (c) The permittivities calculated via the FEM with 100 elements per 2π radians of curvature (points), and analytical values (lines). The error in calculated relative permittivity varies with (d) volume loading, (e) mesh refinement and (f) discretization volume error. Permittivities plotted are relative to the matrix permittivity, as indicated by the axis labels.

C.3.4 Spheres Without an Interface

Spherical inclusions in cubic cells were also benchmarked for mesh convergence. Inclusions with volume loadings between 1 % and 50 % were studied. The sphere radius was 3.27 Å, which is the radius of a sphere with volume equal to the Bader volume of the Ag_8 inclusion in a 216 atom MgO supercell. The relative permittivity of the matrix was set to 9.26, and the relative permittivity of the inclusion was set to 10,

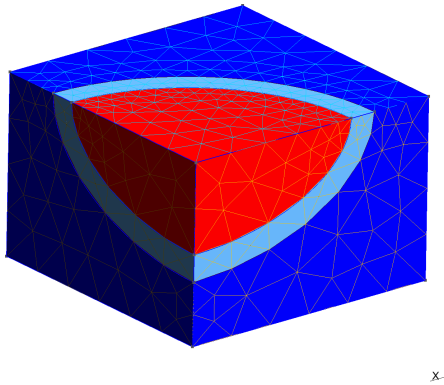

Figure C.4: Truncated simulation cell for a disk oriented with its long axes orthogonal to the z-axis.

100, 500, or 1000. The mesh was refined by varying the target number of nodes per 2π radians of curvature to between 10 and 80, while the coarse target mesh size at the supercell boundaries was held constant at 1.5 Å for a tetrahedral edge. The results are shown in Figure C.5. The level of mesh refinement has little impact for volume loadings below 25 %. For loadings nearing 50 %, refining of the mesh leads to a larger relative permittivity value, by as much as approximately 3 in the case of highest inclusion permittivity. However, for the loadings examined in this work, which were between 6.5 and 21.5 %, even a coarse mesh of 20 nodes per 2π radians would perform essentially equally well as a more refined mesh for these spherical inclusions. The difference would be negligible relative to the error inherent in the quantum dynamics method.

C.3.5 Spheres With an Interface

The impact of mesh refinement on geometries that include an inclusion interface was also investigated. Meshes were created for inclusion volume loadings between 2 and 25 % and interface thicknesses of 1, 2, and 3 Å. The inclusion radius was set to 3.27 Å and the matrix relative permittivity was fixed at 9.26. The inclusion and interface relative permittivities were set to either 100 or 500, resulting in four combinations. The meshes were refined by increasing the target number of nodes per 2π radians of geometry curvature from 10 to 80.

The presence of the interfaces causes a discontinuity or inflection point at the volume loading for which the interface first eclipsed the edge of the supercell. For an interface thickness of 1 Å, this occurred at an inclusion volume loading of 22 %, so we considered only loadings up to this value, which accounts for all loadings studied with

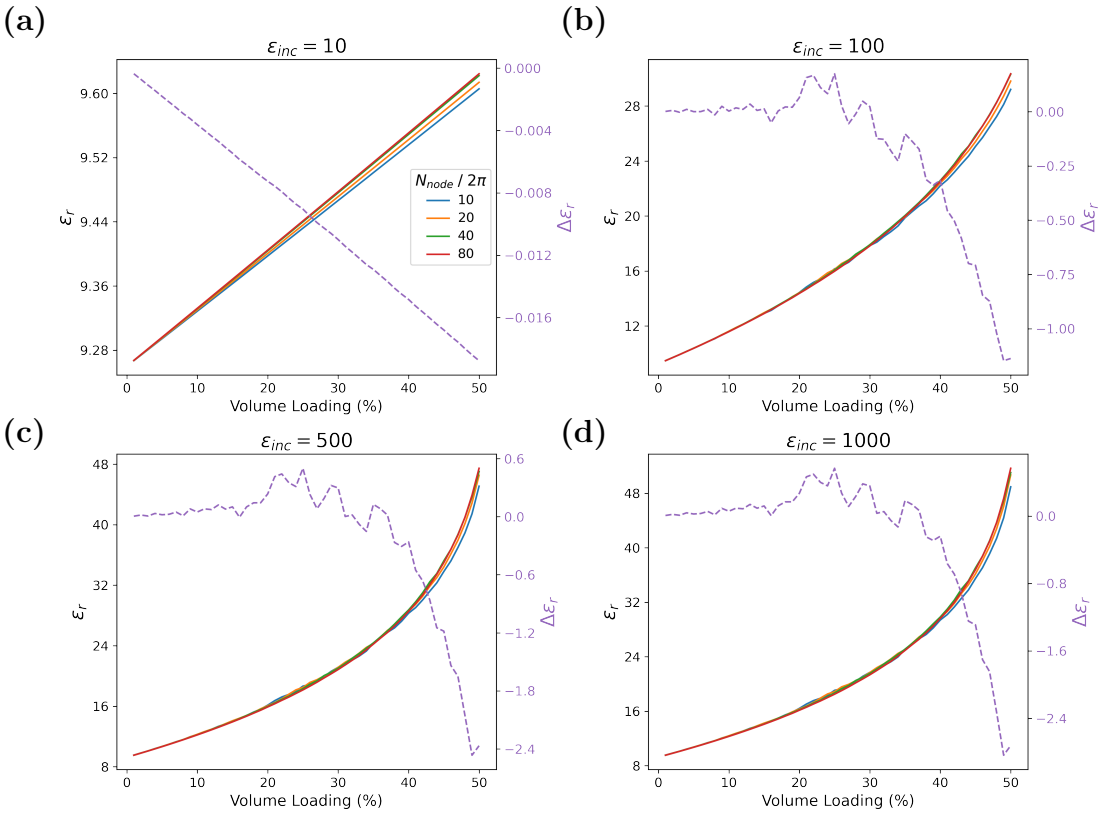

Figure C.5: Convergence of mesh size for spherical inclusions. Panels (a)-(d) show the FEM calculation of relative permittivity for an inclusion relative permittivity of 10, 100, 500, and 1000, respectively, each with 4 different levels of mesh refinement. The right-side ordinate axes and dashed purple lines show the difference between relative permittivity for the least refined and most refined meshes at each volume loading, $\Delta\epsilon_r$.

quantum dynamics. For interface layers thicker than 1 Å, the supercell boundaries impinge on this layer at even lower volume loadings, resulting in unphysical behaviour and difficulty modeling anything above relatively low loadings. Thus, we restricted our analysis to 1 Å interfaces.

As with the geometries lacking interfaces, the discrepancy between the refined and unrefined mesh was negligible at small volume loadings but was larger as the relative permittivity of the inclusion and interface increased. The interface permittivity had the largest effect on the discrepancy, as seen when comparing panels (b) and (c) in Figure C.6.

Taken together with the results for spherical inclusions lacking interfacial layers, these results reveal that for small volume loadings and thin interface layers below 1 Å, a mesh refinement parameter of 20 nodes per 2π radians should suffice for

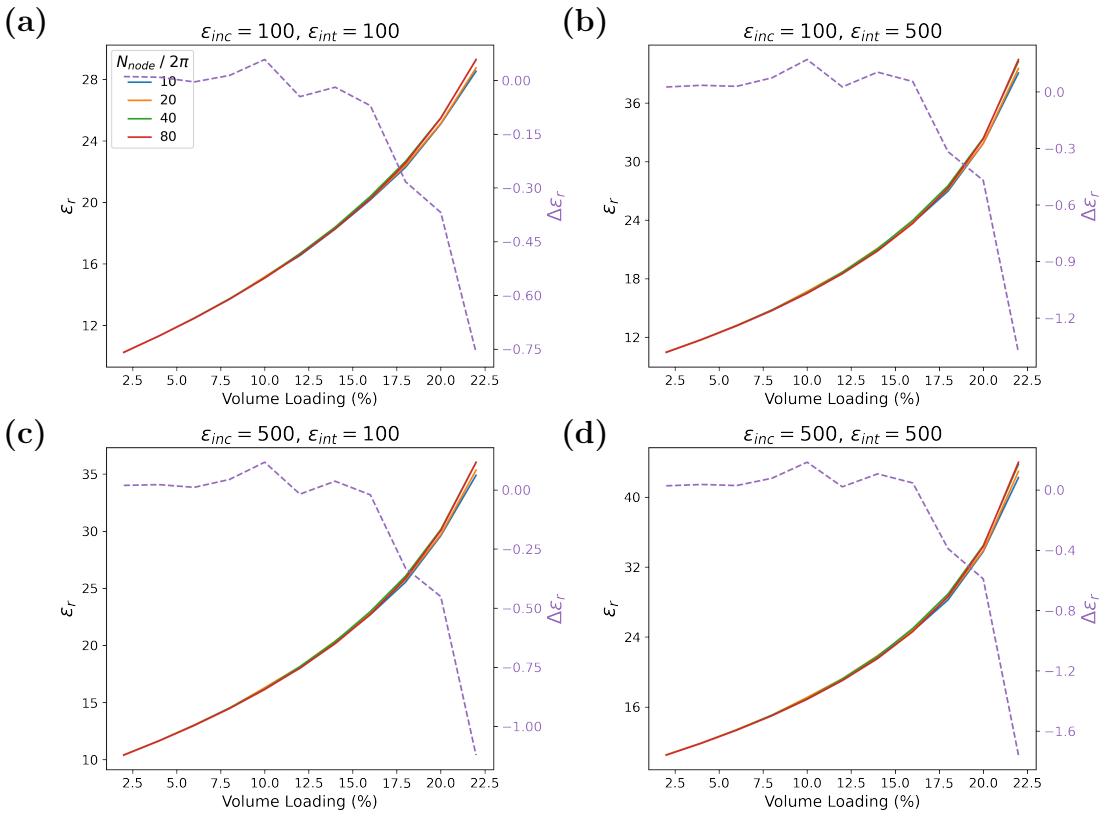

Figure C.6: Convergence of meshes with spherical inclusions and a 1 Å interface layer. Panels (a)-(d) show the FEM calculation of relative permittivity for an inclusion and interface relative permittivity of 100 or 500, with four different levels of mesh refinement, as solid lines. The right-hand ordinate axes and dashed purple lines show the difference between the relative permittivities of the least refined and most refined meshes at each volume loading, $\Delta\epsilon_r$.

searching the space of inclusion and interface permittivities. This relatively coarse mesh performs worse as volume loadings exceed 20 %, but may still be used in a coarse search for optimal inclusion and interface permittivites for all geometries considered in this work.

C.4 Mean Squared Displacements of Interface Ions for Ag_{12} and Ag_{18} Nanocomposites

Figure C.7 shows mean squared displacements of ions for Ag_{12} and Ag_{18} nanocomposites during molecular dynamics after equilibration at 400 K. There is an enhancement in the ionic displacement of Mg and O atoms at the interface with the inclusion rela-

tive to those ions in the bulk matrix. Furthermore, this effect seems to be localized to the ions closest to the inclusions, as ionic shells outside of immediate neighbors show a rapid return to bulk values. Finally, the ionic displacement is significantly larger in the disk-like Ag_{18} interface than in the rod-like Ag_{12} interface.

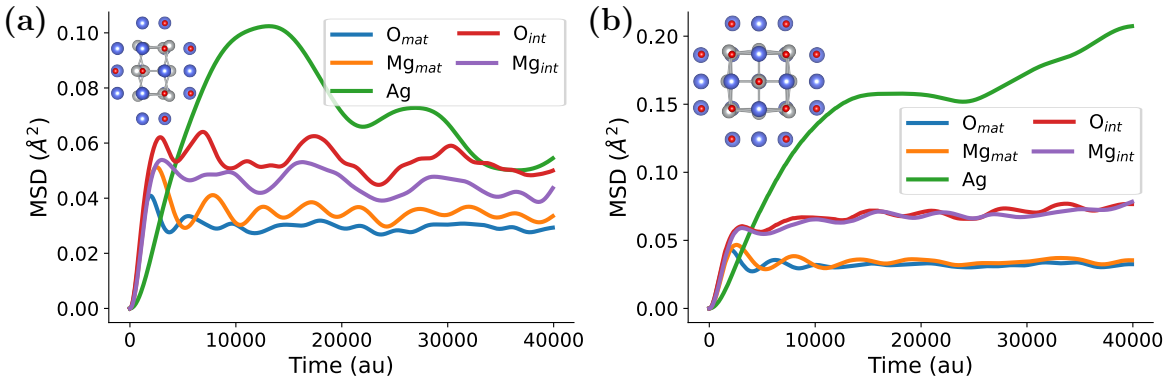

Figure C.7: Mean squared displacement of ions during *ab initio* molecular dynamics. Panel (a) shows the MSD of Mg, O, and Ag for a 288-atom nanocomposite cell with an Ag_{12} inclusion. MSD for ions neighboring Ag atoms are denoted with the "int" subscript, and atoms further from the inclusion with the "mat" subscript. The inset shows the inclusion plus ions denoted as "int". Panel (b) shows the corresponding MSDs for a 384-atom nanocomposite with an Ag_{18} inclusion.

C.5 Dipole Partitioning

C.5.1 Partitioning the Quantum Response

The response of a composite modeled using quantum dynamics can be partitioned using the polarization of Wannier centers within the composite as a heuristic mapping of the polarization strength of the inclusion, as distinct from the interface and matrix. Wannier centers were all found to be close to either oxygen or silver atom centers. The Mg atoms were fully ionized, with no remaining valence electrons in our pseudopotential approach with 10 core electrons per Mg atom. Thus, the centers could be unambiguously assigned to either the inclusion or specific matrix ions. The change in dipole moment of the simulation cell, Δp, can be calculated as

$$\Delta p = 2e \sum \Delta w_i + \sum Z_i \Delta R_i, \tag{C.11}$$

where Δw_i are the Wannier center displacements, e is the electron charge, and ΔR_i are ionic displacements with the corresponding charges Z_i. Δ refers to the difference between the finite and vanishing electric field states. For the inclusion, Δp can then be calculated as the sum of the ionic and electronic dipole moments over the silver ions alone and their associated Wannier functions:[1]

$$\Delta p_{\text{inc}} = 2e \sum_{\text{inc}} \Delta w_i + \sum_{\text{inc}} Z_i \Delta R_i. \tag{C.12}$$

Figure C.8 illustrates how the dipole moment was partitioned for the Ag_8 inclusion in a 216-atom supercell (left panels) and in the FEM model (right panels). In the quantum dynamics, the dipole moment of each atom is equal to the sum over the ionic dipole moment (a product of ionic charge and ionic displacement) and the polarization of the closest Wannier centers. These sums are depicted as vectors in the left-hand panels, with longer, red arrows indicating larger moments and shorter, blue arrows indicating smaller moments. Shells are used to depict how the dipole moments of groups of atoms were assigned to the inclusion (inner shell), interface (middle), and matrix (outer shell), with 24 Mg/O ions enclosed by the interfacial shell. The total dipole moment of each shell is the vector sum over the moments assigned to each atom in the shell. The right-hand panels depict the FEM model case. Here, vectors indicate the polarization density for a model with inclusion, interface, and matrix relative permittivities of 200, 50, and 9.26, respectively, and an applied potential of 0.5 V. The dipole moment of each shell is the numerical integral of the polarization density over its volume. The colorbars have arbitrary units and are meant as an indication of relative polarization magnitudes.

C.6 Polarizability of Dielectric Ellipsoids in Vacuum

Ellipsoids, like spheres, have uniform polarization in an uniform electric field. For an ellipsoid, the polarization density P_j for an external field E_{ext} applied along principal axis j is given in SI units by [5]

$$P_j = \frac{(\epsilon_r - 1)\epsilon_0}{1 + N_j(\epsilon_r - 1)} E_{\text{ext}}, \tag{C.13}$$

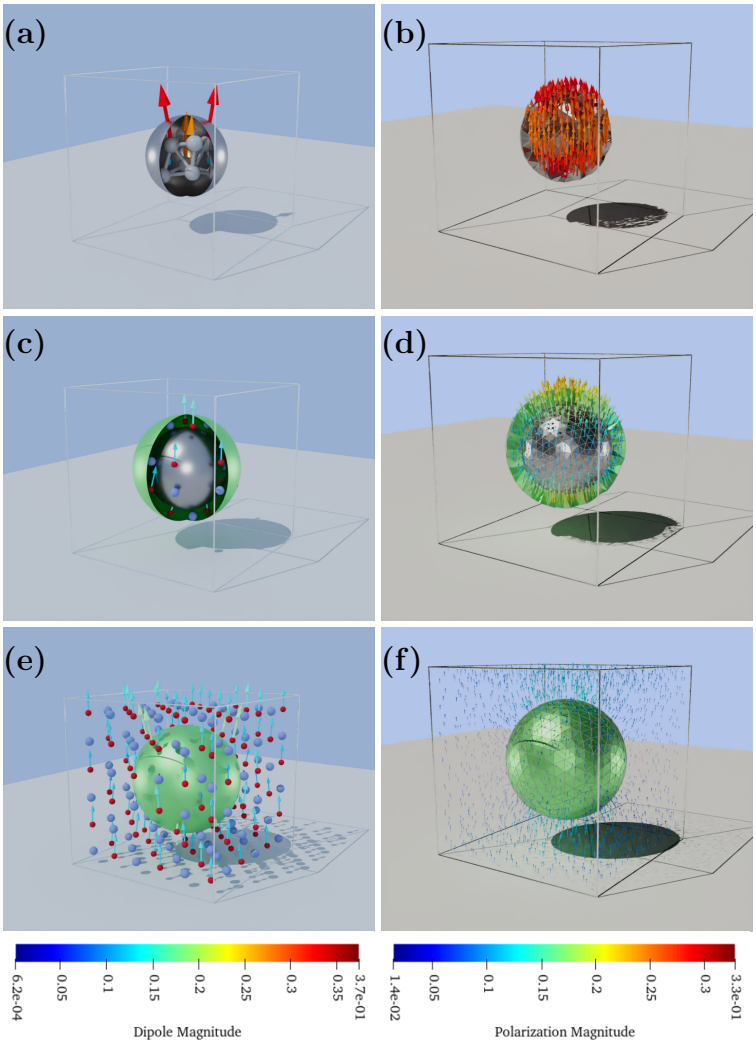

Figure C.8: Decomposition of the polarization response over a composite. Panels (a), (c), and (e) show the decomposition of the quantum dynamics response over the inclusion, interface, and matrix, respectively. Arrows indicate the change in dipole moment when an external field is applied. This change includes the ionic polarization (spatial displacement of ions) and the electronic polarization of the ions (the spatial displacement of the Wannier centers localized around that ion). Arrows are scaled and colored by dipole moment magnitude. Panels (b), (d), and (f) show the decomposition of the FEM response over the inclusion, interface, and matrix, respectively. Arrows indicate the polarization density.

where N_j is the depolarization factor along the axis j,

$$N_j = \frac{a_x a_y a_z}{2} \int_0^\infty \frac{ds}{(s+a_j^2)\sqrt{(s+a_x^2)(s+a_y^2)(s+a_z^2)}}, \tag{C.14}$$

and a_i is the inclusion semi-axis length in direction i. Note that the depolarization factor obeys the relationship $N_x + N_y + N_z = 1$, so that in the case of a sphere, $N_x = N_y = N_z = \frac{1}{3}$.

Multiplying this density by the volume of an ellipsoid, $\frac{4}{3}\pi a_x a_y a_z$, gives an expression for the dipole moment at a given field in terms of the ellipsoid relative permittivity,

$$d_j = \frac{4}{3}\pi a_x a_y a_z \frac{\epsilon_0(\epsilon_r - 1)}{1 + N_j(\epsilon_r - 1)} E_{\text{ext}}. \tag{C.15}$$

Since polarizability α is defined by $\alpha = \frac{d}{E}$, the polarizability of the ellipsoidal inclusion along principal axis j is

$$\alpha = \frac{4}{3}\pi a_x a_y a_z \frac{\epsilon_0(\epsilon_r - 1)}{1 + N_j(\epsilon_r - 1)}. \tag{C.16}$$

One can verify that plugging $N = \frac{1}{3}$ yields the expression for the polarizability of a sphere (see Equation (4.7) in main text).

Ellipsoid – External Field Misalignment. If the external field is not oriented along one of the ellipsoid axes, the polarization induced can be calculated as a superposition of the polarizations induced by the components of the field that do lie along each ellipsoid axis. That is, if we label the ellipsoid axes j', then

$$P_{j'} = \frac{(\epsilon_r - 1)\epsilon_0}{1 + N_{j'}(\epsilon_r - 1)} E_{\text{ext},j'}. \tag{C.17}$$

The three components $P_{j'}$ give the polarization density P' of the ellipsoid in the basis defined by its principal axes. Transforming these components back to the global coordinate system can then be used to find the polarizability of the inclusion along the direction of applied field.

The ellipsoid principal axes $a_{x'}$, $a_{y'}$, and $a_{z'}$, can be written as normalized column vectors $\hat{\mathbf{a}}_{x'}$, $\hat{\mathbf{a}}_{y'}$, and $\hat{\mathbf{a}}_{z'}$ in the global coordinate system. Together, these vectors form an orthonormal basis in real space. The matrix that transforms from the ellipsoidal to the global coordinate system is

$$\mathbf{A} = \begin{pmatrix} \hat{\mathbf{a}}_{x'} & \hat{\mathbf{a}}_{y'} & \hat{\mathbf{a}}_{z'} \end{pmatrix}. \tag{C.18}$$

Thus, to calculate the electric field in the global coordinate system $\mathbf{E}$ from the electric

field in the ellipsoidal coordinate system $\mathbf{E}'$, one would calculate

$$\mathbf{E} = \mathbf{A}\mathbf{E}', \tag{C.19}$$

and, similarly,

$$\mathbf{E}' = \mathbf{A}^{-1}\mathbf{E}. \tag{C.20}$$

Writing the equation above for the polarization of the ellipsoid as a vector equation in the ellipsoidal coordinate system, we have

$$\mathbf{P}' = \frac{(\epsilon_r - 1)\epsilon_0}{1 + \mathbf{N}'(\epsilon_r - 1)}\mathbf{E}'_{\text{ext}}, \tag{C.21}$$

where operations on the right-hand side are element-wise multiplication of the two vector quantities, and $\mathbf{E}'_{\text{ext}} = \mathbf{A}^{-1}\mathbf{E}_{\text{ext}}$. The polarization in the global coordinate system is

$$\mathbf{P} = \mathbf{A}\mathbf{P}' = \begin{pmatrix} P_x & P_y & P_z \end{pmatrix}^T. \tag{C.22}$$

Assuming the external field was applied along an axis of the global coordinate system, say z, then the polarizability of the inclusion in the j^{th} direction can be calculated as

$$\alpha_{jz} = \frac{4}{3}\pi a_x a_y a_z \frac{P_j}{E_z}. \tag{C.23}$$

C.7 Spherical and Ellipsoidal Models for Gold Nanoparticles

Gold particles with 4, 8, 13, 16, 26, and 55 atoms were modeled as dielectric ellipsoids in vacuum. As for silver, molecular dynamics based on forces from PBE/DZP calculations was performed at 500 K for 1 ps, followed by quenching, to obtain low-energy geometries. These geometries are not generally global minima, and all structures were compact, rather than cage-like. The polarizabilities of the particles were measured using PBE/DZP calculation under a 0.0001 a.u. electric field using finite differences. As shown in Figure 4.3 in the main text, the relationship between polarizability and volume is linear for silver particles. The concept of residuals is useful here, and they are defined as the difference in predicted polarizability between the polarizable ellipsoid and quantum models. Plotting the residuals in Figure C.9(b) confirms that the ellipsoidal model is a good fit, but does show a slight upward trend, indicating small

second order effects. Figure C.9(a) and (c) show that gold follows similar trends. The quality of fit is nearly identical to that for silver, but the average relative permittivity is 12.5, slightly smaller than the silver value (12.7).

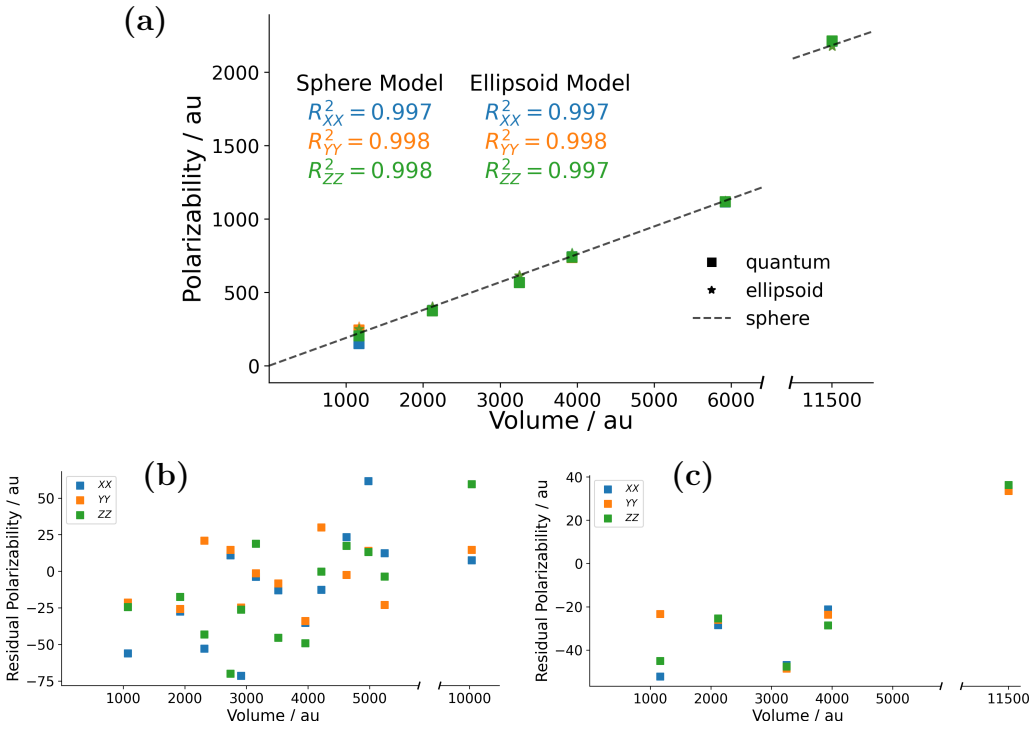

Figure C.9: (a) Ellipsoidal particle model for isolated Au Nanoparticles. Squares represent the polarizabilities along each Cartesian direction for a field applied in the same direction. The dashed line and stars depict the results of the spherical and ellipsoidal approximations, respectively. Panels (b) and (c) show the residuals from using the ellipsoid model for silver (model presented in the main text) and gold, respectively.

Because the gold particles were all roughly spherical or were oriented in such a way as to have nearly homogeneous polarizabilities, the same rod and disc configurations that were tested for silver were also examined. Conjugate gradient geometry optimizations were performed before measuring polarizabilities. A least squares method [6] was used to find the optimal representation of the electron delocalization volume, and the ellipsoid axes were scaled to match the volume of the 0.001 a.u. isosurface. The ellipsoidal model was then used to calculate the polarizabilities. Figure C.10 shows the comparison between the density functional theory calculations and the predictions of the ellipsoidal model. As for silver, ellipsoidal continuum particles accurately model the polarization anisotropy of gold. Prediction of the spherical model are also shown, and they provide the expected level of average agreement with the quantum mechanics.

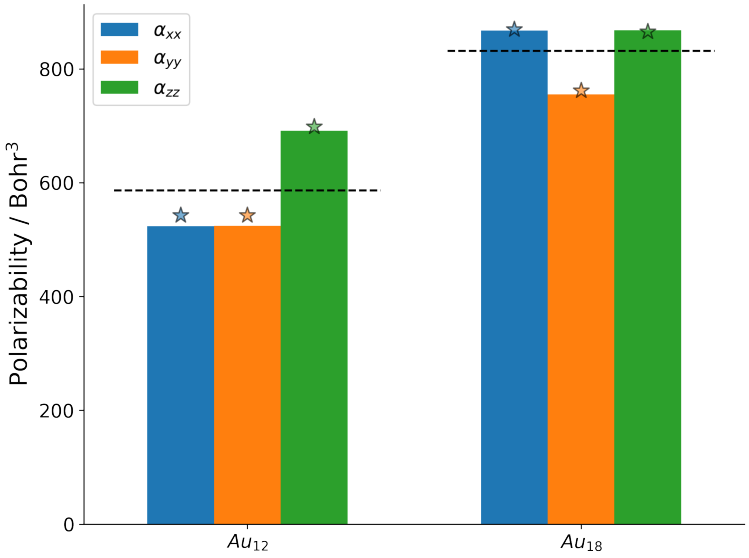

Figure C.10: Ellipsoidal model fits for rod- and disc-like gold particles in vacuum. Columns and stars depict the polarizabilities calculated using density functional theory and the predictions of the ellipsoidal model, respectively. The dotted lines depict spherical model results.

C.8 Adjusting Fitting Data

The performance of the model for rods and disks suggests that it might be tuned by adjusting the data used for parameterization. One could build a rod (disk)-specific model by fitting parameters to small rod (disk)-like inclusions. We built a second

ellipsoidal model with a smaller emphasis on interfacial polarizability and high loadings, by removing the highest loading geometry from the fitting set. Maintaining a 1 Å interface, we used a grid search and further Nelder-Mead optimization to obtain $\epsilon_{\text{inc}} = 32$ and $\epsilon_{\text{int}} = 63$. The model was tested on the same inclusions as in Table 4.1, and the results are shown in Table C.3.

Table C.3: Low-loading continuum model for rod- and disk-like inclusions.

Inclusion	$\epsilon_{\parallel,\, FEM}$	$\tau_{\parallel}$	$\epsilon_{\perp,\, FEM}$	$\tau_{\perp}$
$2 \times 2 \times 3$	12.1	-0.06	11.9	-0.02
$2 \times 2 \times 4$	13.4	-0.04	12.5	0.02
$2 \times 2 \times 5$	13.3	-0.11	12.4	-0.03
$3 \times 3 \times 2$	12.0	-0.20	11.8	-0.11
$4 \times 4 \times 2$	11.4	-0.33	10.9	-0.31

With the new model, we obtained accuracy within 11% (and typically much better) for the three rod-like inclusions. Performance for the disks was worse than the original model. This highlights the importance of careful selection of fitting geometries depending on the types of systems that are to be studied. It also highlights the differences between one-dimensional inclusions, which over low volume loadings follow the trends predicted by classical electrostatics, and two-dimensional inclusions, which exhibit large polarizations that prove more difficult to capture with the continuum model.

C.9 Rounded Prism Inclusion Model

While ellipsoids readily capture the anisotropy of gas phase nanoparticle polarizability and can be generalized to describe inclusions in nanocomposites, there are some cases where a cuboidal description of inclusions may be desirable. For instance, ellipsoids capture the shape of inclusions with small to moderate anisotropy. However, in some cases, a prism-shaped model with rounded edges may more closely approximate the geometry. We explored modeling our test composites as cuboidal inclusions, with rounded rectangular prisms for rods and disks. An example of a model mesh is shown in Figure C.11(a), with the geometry truncated to account for symmetry. We fit the model parameters of interface thickness, inclusion permittivity, and interface permittivity in the same manner as ellipsoidal inclusions. We set the fillet radius of

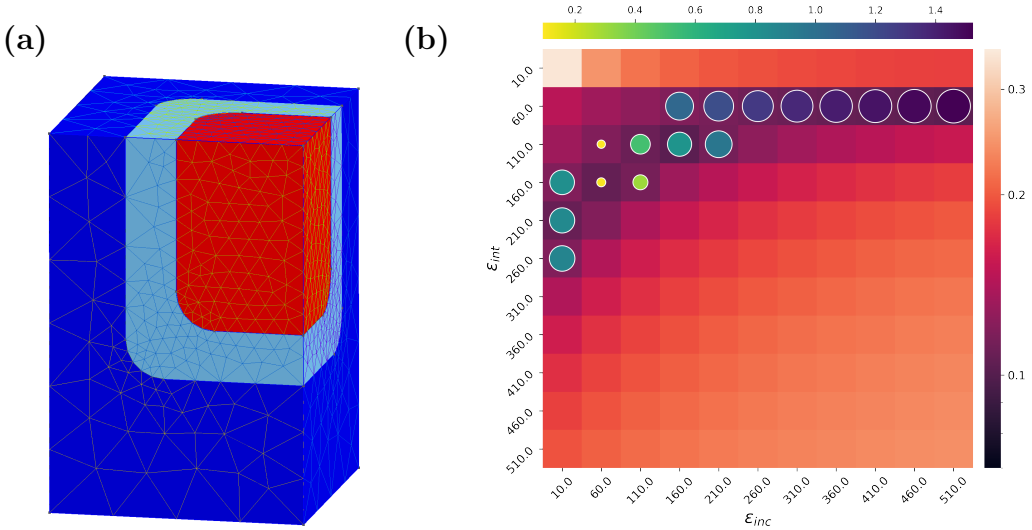

Figure C.11: Rounded prism inclusion model.

the rounded edges equal to 1.72 Å, approximately equal to the Van der Waals radius of Ag.[7] The results of the grid search over inclusion and interface permittivities is shown in Figure C.11(b). Finally, we used the parameters of 1 Å interface thickness, $\epsilon_{\text{inc}} = 60$, and $\epsilon_{\text{int}} = 160$, to estimate the permittivities of the same inclusions as Table 4.1. The results are shown in Table C.4.

Table C.4: Relative permittivities from a rounded prism continuum model.

Inclusion[a]	% At.	% Vol.	$\epsilon_{\parallel,\,\text{QD}}$[b]	$\epsilon_{\parallel,\,\text{FEM}}$	$\tau_{\parallel}$	$\epsilon_{\perp,\,\text{QD}}$[b]	$\epsilon_{\perp,\,\text{FEM}}$	$\tau_{\perp}$
$2 \times 2 \times 3$	4.2	7.6	12.9	14.4	0.12	12.2	14.2	0.16
$2 \times 2 \times 4$	5.6	10.0	13.9	17.0	0.23	12.3	15.2	0.24
$2 \times 2 \times 5$	5.6	10.0	14.9	16.5	0.11	12.8	14.9	0.16
$3 \times 3 \times 2$	4.7	8.3	15.0	14.3	-0.05	13.3	14.0	0.05
$4 \times 4 \times 2$	4	6.9	16.9	13.1	-0.22	15.9	12.1	-0.24

[a] Symbols $\parallel$ and $\perp$ indicate whether the inclusion has its long axis oriented parallel to the applied field and perpendicular to it, respectively. The field is oriented along z in each case, thus the $\parallel$ notation indicates that the rod or disk long axis was along z, whereas the $\perp$ notation indicates that the long axis was in the xy plane. τ is the permittivity error defined in Equation (4.8).
[b] Values from [3].

The results produced by the cuboidal representation are generally worse than those of the ellipsoidal model, predicting larger permittivities than the ellipsoidal model except in the case of the $2 \times 2 \times 5$ parallel rod and the $4 \times 4 \times 2$ disk in both

orientations. We suspect that this is due to the decrease in the depolarization field along the equator of these planar-faced rounded prisms relative to their ellipsoidal counterparts.

C.10 Modeling Larger Rods and Disks

To define continuum geometries for rod and disk inclusions, we used the Bader volume of the inclusions calculated from quantum dynamics. For the $2\times2\times3$ rods and $3\times3\times2$ disks, we applied the scaled bounding box described in Section 4.3.1 of the main text directly to the Bader volumes. However, for the other rods and disks, we extrapolated the dimensions from these smaller inclusions and their simulation cells rather than recalculating Bader volumes from a single point calculation. This mimics the scenario in which no quantum data is available. Cell side lengths were taken to be a linear extrapolation of the lengths for the cubic $2 \times 2 \times 2$ inclusion geometry, averaged with either the $2 \times 2 \times 3$ rod or $3 \times 3 \times 2$ disk for rods and disks, respectively. Inclusion axis dimensions were all defined relative to the Bader bounding box of either the $2 \times 2 \times 3$ rod or $3 \times 3 \times 2$ disk.

Rod Dimensions

The length of each additional segment added to the primary axis of the rod Δl was taken to be the difference between the length of the $2 \times 2 \times 3$ rod and the average of its other two dimensions l_0. Thus, the dimensions of a $2 \times 2 \times 4$ rod would be $l_0 \times l_0 \times (l_0 + 2\Delta l)$.

Rod Volumes

The volume of each additional segment added to a rod ΔV was taken to be the difference between the volumes of the $2 \times 2 \times 3$ rod and the $2 \times 2 \times 2$ "cube" V_0. Thus, the volume of a $2 \times 2 \times 4$ rod would be $V_0 + 2\Delta V$. The axes dimensions were then scaled to generate an ellipsoid with this volume.

Disk Dimensions

The length of each additional segment added to the long axes of a disk Δl was taken to be the difference between the average length of the $3 \times 3 \times 2$ disk long axes and the length of its short axis l_0. Thus, the dimensions of a $4 \times 4 \times 2$ disk would be $(l_0 + 2\Delta l) \times (l_0 + 2\Delta l) \times l_0$.

Disk Volumes

The total volume of a disk was defined as the sum of the volumes of its edge and face atoms. The volume of each edge atom in a disk V_e was taken to be the average

volume per atom in the $2 \times 2 \times 2$ "cube". The average volume of a face atom in a disk V_f was taken to be the total volume of the $3 \times 3 \times 2$ disk minus the volumes of the 16 edge atoms, divided by two, because there are two face atoms in the $3 \times 3 \times 2$ disk, i.e., $V_f = (V_{332} - 16V_e)/2$. Thus, the volume of a $4 \times 4 \times 2$ disk would be $24V_e + 8V_f$. The axes dimensions were then scaled to generate an ellipsoid with this volume.

Bibliography

[1] David J.T. Hally and Irina Paci. Low-frequency polarization in molecular-scale noble-metal/metal-oxide nanocomposites. *Nanoscale*, 10(20):9583–9593, 2018.

[2] W Tang, E Sanville, and G Henkelman. A grid-based bader analysis algorithm without lattice bias. *Journal of Physics: Condensed Matter*, 21(8):084204, January 2009.

[3] Archita N. S. Adluri, Brett Henderson, and Irina Paci. Tuning the dielectric response in a nanocomposite material through nanoparticle morphology. *RSC Adv.*, 12:10778–10787, 2022.

[4] Yugong Wu, Xuanhe Zhao, Fei Li, and Zhigang Fan. Evaluation of mixing rules for dielectric constants of composite dielectrics by MC-FEM calculation on 3d cubic lattice. *Journal of Electroceramics*, 11(3):227–239, December 2003.

[5] Charles Kittel. *Introduction to solid state physics*. Wiley, 8 edition, 2004.

[6] Yury. Ellipsoid fit (https://www.mathworks.com/matlabcentral/fileexchange/24693-ellipsoid-fit). MATLAB Central File Exchange, 2021. Retrieved September 5, 2021.

[7] A. Bondi. van der waals volumes and radii. *The Journal of Physical Chemistry*, 68(3):441–451, March 1964.

Appendix D

Supporting Information for Chapter 5

D.1 Polarizability of a System of Inducible Atomic Dipoles (IADs)

Applequist et al.[1] laid out the theory for calculating the molecular polarizability that results from a collection of IADs. Here, we review the mathematics of that theory in a notation consistent with Chapter 5.

When an external electric field is applied to these IADs, the dipole moment $\vec{\mu}_i$ of the i^{th} IAD can be calculated as

$$\boldsymbol{\mu}_i = \boldsymbol{\alpha}_\mathbf{i} \left[\mathbf{E}_i - \sum_{j \neq i} \mathbf{T}_{ij} \boldsymbol{\mu}_j \right]. \tag{D.1}$$

The term in square brackets on the RHS represents the total electric field acting on the i^{th} IAD, a superposition of the external field $\mathbf{E}_i$ at this position and the fields of all of the of the surrounding IADs. $\mathbf{T}_{ij}$ is the dipole field tensor, which describes the field at site i produced by the dipole at site j.

It is worth describing the somewhat unconventional notation in Equation (D.1) in more detail to avoid confusion. Note that $\boldsymbol{\mu}_i$ and $\mathbf{E}_i$ are each 3×1 column vectors, not scalars. For a collection of N IADs, the full vectors $\boldsymbol{\mu}$ and $\mathbf{E}$ are composed of the 3×1 column vectors describing the dipole and electric field at each site, appended end-to-end. Thus, $\boldsymbol{\mu}$ and $\mathbf{E}$ are each $3N \times 1$ column vectors, and the index i denotes the i^{th} 3-element block of each. Moreover, $\boldsymbol{\alpha}_i$ is the 3×3 polarizability tensor, and

$\mathbf{T}_{ij}$ is likewise a 3×3 tensor with a form described in Section 5.3.2. Thus, the full matrix $\mathbf{T}$ has dimensions $3N \times 3N$ and can be written as a block matrix:

$$\mathbf{T} = \begin{bmatrix} \mathbf{T}_{11} & \mathbf{T}_{12} & \dots \\ \vdots & \ddots & \\ \mathbf{T}_{N1} & & \mathbf{T}_{NN} \end{bmatrix}. \tag{D.2}$$

Equation (D.1) is usually rearranged as

$$\boldsymbol{\alpha}_i^{-1}\boldsymbol{\mu}_i + \sum_{j \neq i} \mathbf{T}_{ij}\boldsymbol{\mu}_j = \mathbf{E}_i. \tag{D.3}$$

This set of linear equations can be written in the matrix form

$$\mathbf{A}\boldsymbol{\mu} = \mathbf{E}, \tag{D.4}$$

where $\mathbf{A}$ is given by:

$$\mathbf{A} = \begin{bmatrix} \boldsymbol{\alpha}_{11}^{-1} & \mathbf{T}_{12} & \dots & \mathbf{T}_{1N} \\ \mathbf{T}_{21} & \boldsymbol{\alpha}_{22}^{-1} & \dots & \mathbf{T}_{2N} \\ \vdots & & \ddots & \vdots \\ \mathbf{T}_{N1} & \dots & & \boldsymbol{\alpha}_{NN}^{-1} \end{bmatrix}. \tag{D.5}$$

Thus, for a collection of N IADs, $\mathbf{A}$ will be a $3N \times 3N$ matrix, and $\boldsymbol{\mu}$ and $\mathbf{E}$ are column vectors with length $3N$ as described above. Equation (D.4) can be solved self-consistently to calculate the induced dipole moments on each IAD in the presence of external field $\mathbf{E}$.

In the context of IADs, it can be useful to rewrite Equation (D.4) so as to calculate "effective", or "self-consistently screened" (SCS) polarizabilities of each IAD. These screened polarizabilities $\boldsymbol{\alpha}_i^{\mathrm{SCS}}$ will include the mutual polarization effects of all surrounding IADs. Rewriting Equation (D.4) as

$$\boldsymbol{\mu} = \mathbf{A}^{-1}\mathbf{E}, \tag{D.6}$$

we see that it takes the form of the definition of polarizability, where the resulting dipole of each IAD is yielded from the multiplication of some matrix and the external field. To make this more explicit, Equation (D.6) now represents the set of linear equations

$$\boldsymbol{\mu}_i = \sum_j (\mathbf{A}^{-1})_{ij} \mathbf{E}_j. \tag{D.7}$$

To obtain the SCS polarizabilities, we consider a uniform external field. That is, the field $\mathbf{E}_j$ at all sites j is identical. Replacing $\mathbf{E}_j$ in Equation (D.7) with the uniform field $\boldsymbol{\mathcal{E}}$, we obtain

$$\boldsymbol{\mu}_i = \left[\sum_j (\mathbf{A}^{-1})_{ij} \right] \boldsymbol{\mathcal{E}} \tag{D.8}$$

$$\boldsymbol{\mu}_i = \boldsymbol{\alpha}_i^{\mathrm{SCS}} \boldsymbol{\mathcal{E}}. \tag{D.9}$$

Intuitively, $\boldsymbol{\alpha}_i^{\mathrm{SCS}}$ describes the response of site i to a uniform *external* field. This can be contrasted with what we might call the *intrinsic* polarizability of site i, given by $\boldsymbol{\alpha}_i$, which describes the response to the *local* field created by the superposition of the external field and the surrounding dipole fields (Equation (D.1)). Conveniently, the SCS polarizabilities are additive. That is, by summing the SCS polarizabilities over all sites, the molecular polarizability is obtained:

$$\boldsymbol{\mu}_{\mathrm{mol}} = \sum_i \boldsymbol{\mu}_i = \sum_i \left[\boldsymbol{\alpha}_i^{\mathrm{SCS}} \right] \boldsymbol{\mathcal{E}} \tag{D.10}$$

$$\boldsymbol{\alpha}_{\mathrm{mol}} = \sum_i \boldsymbol{\alpha}_i^{\mathrm{SCS}}. \tag{D.11}$$

As discussed in Chapter 5, the libMBD code solves for the SCS polarizability tensors $\boldsymbol{\alpha}_i^{\mathrm{SCS}}$ because these are important inputs to the many-body dispersion method.[2] The code does so by inversion and partial contraction of the matrix $\mathbf{A}$ as defined in Equation (D.5).

Bibliography

[1] Jon Applequist, James R. Carl, and Kwok-Kueng Fung. Atom dipole interaction model for molecular polarizability. application to polyatomic molecules and determination of atom polarizabilities. *Journal of the American Chemical Society*, 94(9):2952–2960, May 1972.

[2] Jan Hermann, Martin Stöhr, Szabolcs Góger, Shayantan Chaudhuri, Bálint Aradi, Reinhard J. Maurer, and Alexandre Tkatchenko. libmbd: A general-purpose package for scalable quantum many-body dispersion calculations. *The Journal of Chemical Physics*, 159(17), November 2023.

Appendix E

Supporting Information for Chapter 6

E.1 4-electron ORR / Computational Hydrogen Electrode

The 4-electron ORR can be written as

$$O_2(g) + 4(H^+ + e^-) \longrightarrow 2H_2O(l) \qquad \Delta G^0_{\mathrm{ORR}} = -4.92\mathrm{eV}. \tag{E.1}$$

The ORR was studied using the Computational Hydrogen Electrode (CHE).[1] Under the computational hydrogen electrode, the free energy of the proton-electron pair is equated to half that of gaseous H_2 [$\mathrm{G(H^+ + e^-)} = \frac{1}{2}\mathrm{G(H_2)}$]. This yields the alternative overall reaction:

$$O_2(g) + 2H_2(g) \longrightarrow 2H_2O(l) \qquad \Delta G^0_{\mathrm{ORR}} = -4.92\mathrm{eV}. \tag{E.2}$$

Free energies were calculated using the electronic energy (E_{el}), zero-point energy (ZPE), heat capacity corrections to the internal energy (E_{therm}), entropic effects ($-TS$), and solvation effects (E_{solv}):

$$G = E_{\mathrm{el}} + ZPE + E_{\mathrm{therm}} - TS + E_{\mathrm{solv}}. \tag{E.3}$$

For a given set of reaction intermediates, the free energy at electrode potential U was shifted by $-neU$, where n is the number of proton-electron pairs present in the

reactants of a given step of the balanced reaction, and e is the charge of an electron. All calculations correspond to pH = 0, and electric field effects were ignored.

Solvation Corrections. In this work, ΔE_{solv} is modeled by a solvation correction of -0.30 eV applied to the free energy of the MP(OH) and MP(OOH) intermediates, as implemented in previous works.[2, 3, 4] This correction is based on an estimation of the energy of hydrogen bonds formed between the OH and OOH adsorbates and surrounding water.[2] It is worth noting that although some have reported a close correspondence between this approximation and implicit solvation (Polarizable Continuum Model),[4] recent benchmarking has shown that such a constant correction may cause a relative underestimation of the solvation energy of the MP(O) intermediate for single-atom catalysts.[5, 6] On the other hand, implicit solvent models are functional dependent, and this dependence can obfuscate our understanding of how well different functionals treat the electronic structure of the ORR intermediates.

Thus, we chose a constant, functional-independent solvent model for two main reasons. First, we aimed in this study to better understand how different functionals treat the electronic structures of the ORR intermediates, not to produce reaction energies which could be compared directly to experiment. If implicit solvation were employed, it would either introduce additional dependence on functional, which we grant deserves attention but is outside the scope of this work, or as a recent ORR study suggests,[6] it would exhibit a relatively small dependence on functional. In the latter case, the comparisons between functionals made in the text would be unchanged.

Second, our choice obviates the need for further benchmarking of implicit solvation models in the present context. Several ORR adsorbates are capable of forming hydrogen bonds with the solvent that may not be well-described with implicit solvent.[7] On copper single-atom catalysts, implicit solvation from the VASPsol package[8] resulted in deviations of up to about 0.2 eV per intermediate from an explicit Thermodynamic Integration method of solvation.[6] Thus, the accuracy of such solvation models cannot be taken for granted. Additionally, one would need to establish how the accuracy of such solvent corrections varies between DFT and DLPNO-CC, since in the latter case solvation effects can be treated not just in the SCF but also in the coupled cluster iterations. Some early work suggests that DLPNO-CC solvation energies should be significantly more accurate than DFT ones, but the matter has only been studied in a small set of molecules.[9]

Thermodynamic Corrections. Thermal and entropic corrections were evaluated at 298.15 K. The pressure for entropic corrections was taken to be 1 bar, except

for the calculation of H_2O, which used a pressure of 0.035 bar. At this pressure, liquid and gaseous water are in equilibrium, allowing the free energy of the calculated gaseous water to be equated to that of liquid water as defined in the ORR half cell reaction.[1, 10, 11]

Empirical O_2 Correction. The free energy of O_2 was set such that the overall reaction free energy of the 4-electron pathway would match the theoretical value of 4.92 eV[12, 13], as is standard practice in ORR studies.[1, 11] A preliminary discussion on the efficacy of these corrections is presented in Section 6.3.5 of the main text.

Theoretical Overpotentials. Theoretical overpotentials were calculated as the difference between the theoretical half-cell potential for ORR (1.23 V) and the highest potential at which all steps in the free-energy pathway remained downhill.[1] For these calculations, binding of dioxygen (Equation (6.1)(a) in the main text) was not considered. Instead, steps (6.1)(a) and (b) in the main text were considered a single step, as is customary in the CHE.

Energies for Linear Scaling Relationships. The energies of intermediate species were calculated relative to the product energies following the convention of Nørskov *et al.*[1] Specifically, the relative free energies ΔG_{OOH}, ΔG_{O}, and ΔG_{OH} are calculated as the free energy changes of the following reactions, respectively:

$$\mathrm{MP} + 2\mathrm{H_2O} \longrightarrow \mathrm{MP(OOH)} + \frac{3}{2}\mathrm{H_2} \tag{E.4}$$

$$\mathrm{MP} + \mathrm{H_2O} \longrightarrow \mathrm{MP(O)} + \mathrm{H_2} \tag{E.5}$$

$$\mathrm{MP} + \mathrm{H_2O} \longrightarrow \mathrm{MP(OH)} + \frac{1}{2}\mathrm{H_2}. \tag{E.6}$$

Where only the electronic energies are considered, these relative energies are referred to as ΔE_{OOH}, ΔE_{O}, and ΔE_{OH}.

E.2 Constructing Volcano Plots

Construction of volcano plots has been reviewed elsewhere, for example in Ref [14], among many others. For completeness, we briefly describe the process here, using a notation consistent with the rest of the present work. To construct a volcano plot, we must derive the theoretical limiting potential for a range of binding energies using the fitted LFESRs. For the 4-step ORR represented in Equations (E.7) (the same as

Equations (6.1) in the main text with (a) and (b) combined), we label the free energy changes associated with each step as ΔG_1, ΔG_2, ΔG_3, and ΔG_4, respectively.

$$\mathrm{MP} + \mathrm{O_2} + \mathrm{H^+} + \mathrm{e^-} \longrightarrow \mathrm{MP(OOH)} \tag{E.7a}$$
$$\mathrm{MP(OOH)} + \mathrm{H^+} + \mathrm{e^-} \longrightarrow \mathrm{MP(O)} + \mathrm{H_2O} \tag{E.7b}$$
$$\mathrm{MP(O)} + \mathrm{H^+} + \mathrm{e^-} \longrightarrow \mathrm{MP(OH)} \tag{E.7c}$$
$$\mathrm{MP(OH)} + \mathrm{H^+} + \mathrm{e^-} \longrightarrow \mathrm{MP} + \mathrm{H_2O} \tag{E.7d}$$

The theoretical limiting potential U_{lim} corresponds to the energy change of least downhill step, which we call ΔG_{max} according to $U_{\mathrm{lim}} = -\Delta G_{\mathrm{max}}/e$. Written another way,

$$U_{\mathrm{lim}} = min\{-\Delta G_1, -\Delta G_2, -\Delta G_3, -\Delta G_4\}. \tag{E.8}$$

Using the above definitions of ΔG_{OOH}, ΔG_{O}, and ΔG_{OH} from Equations (E.4)-(E.6), we can redefine $\Delta G_{\{1-4\}}$ as:

$$\Delta G_1 = \Delta G_{\mathrm{OOH}} - 4.92 \tag{E.9a}$$
$$\Delta G_2 = \Delta G_{\mathrm{O}} - \Delta G_{\mathrm{OOH}} \tag{E.9b}$$
$$\Delta G_3 = \Delta G_{\mathrm{OH}} - \Delta G_{\mathrm{O}} \tag{E.9c}$$
$$\Delta G_4 = -\Delta G_{\mathrm{OH}}. \tag{E.9d}$$

Finally, we must use the fit LFESRs between ΔG_{OOH}, ΔG_{O}, and ΔG_{OH} to write Equations (E.9)(a)-(d) in terms of a single relative energy, which we choose as ΔG_{OH}. The LFESRs can be written as

$$\Delta G_{\mathrm{OOH}} = m_{\mathrm{OOH}} \Delta G_{\mathrm{OH}} + b_{\mathrm{OOH}} \tag{E.10a}$$
$$\Delta G_{\mathrm{O}} = m_{\mathrm{O}} \Delta G_{\mathrm{OH}} + b_{\mathrm{O}}. \tag{E.10b}$$

Here m_{OOH} and b_{OOH} are the slope and intercept, respectively, of the line fit to the plot of ΔG_{OOH} vs. ΔG_{OH}. Similarly, m_{O} and b_{O} are the slope and intercept of the line fit to the plot of ΔG_{O} vs. ΔG_{OH}. Substituting Equations (E.10) into Equations (E.9)

and then substituting that result into Equation (E.8) gives the following definition for the theoretical limiting potential over a range ΔG_{OH} values:

$$\begin{aligned} U_{\mathrm{lim}} = min\{&4.92 - b_{\mathrm{OOH}} - m_{\mathrm{OOH}}\Delta G_{\mathrm{OH}}, \\ &b_{\mathrm{OOH}} - b_{\mathrm{O}} + (m_{\mathrm{OOH}} - m_{\mathrm{O}})\Delta G_{\mathrm{OH}}, \\ &b_{\mathrm{O}} + (m_{\mathrm{O}} - 1)\Delta G_{\mathrm{OH}}, \\ &\Delta G_{\mathrm{OH}}\}. \end{aligned} \tag{E.11}$$

Figure E.1 shows the construction of U_{lim} defined in Equation (E.11) for the B3LYP and TPSSh functionals. The four lines in each plot correspond to each line of Equation (E.11), and in turn to the four steps of the reaction pathway. The resulting volcano plots are highlighted in light blue. All functionals other than TPSSh follow the pattern of the B3LYP plot. The left side of the volcano, known as the tight binding regime, is defined completely by the final reaction step, whereby OH is librated to form H_2O. Meanwhile, the right side of the plot, known as the weak binding regime, is defined by the first electrochemical step of the reaction, the formation of bound OOH.

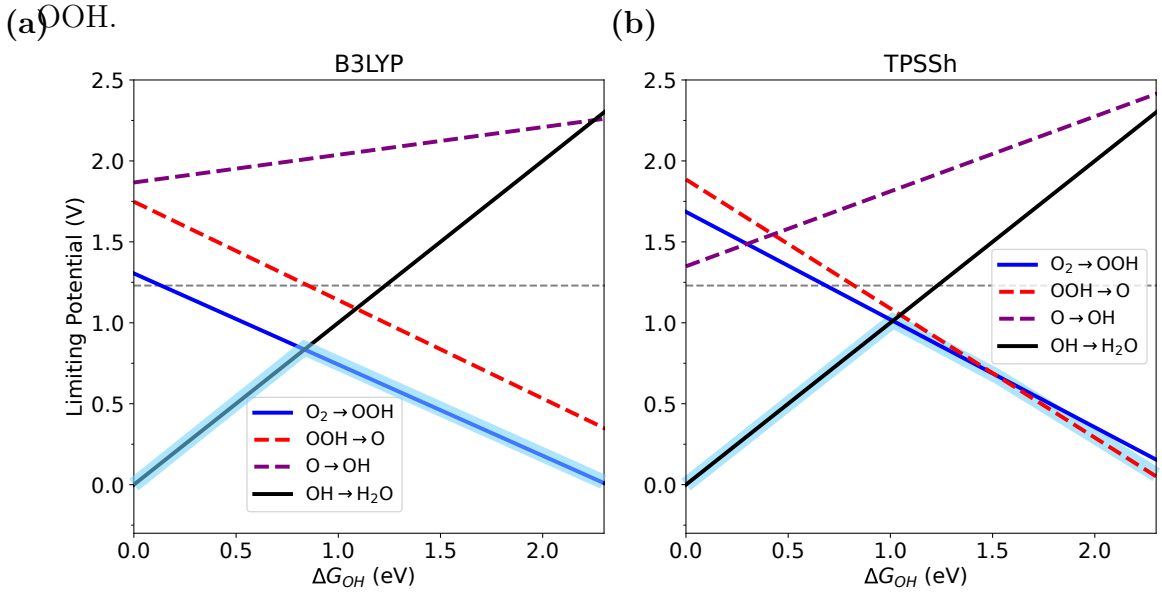

Figure E.1: Construction of theoretical limiting potential volcano plot for **(a)** B3LYP and **(b)** TPSSh functionals. The shape of the resulting volcano plot is highlighted in blue and is the minimum of all four plotted lines at each point.

In contrast, TPSSh shows a more complicated weak binding leg, where the far weak-binding regime is actually determined by the second reaction step, the formation

of the oxo (O) ligand. It is unclear if this behaviour of TPSSh would persist if fitting LFESRs to a larger number of catalysts or using a different solvation model which might stabilize MP(O) more.

E.3 Studies Benchmarking DFT Functionals for Transition Metal Complexes and the ORR

Table E.1 highlights several studied that evaluated the performance of different DFT functionals on transition metal systems. Some of these works are general in nature, using a broad dataset of transition metal complexes, while others specifically investigate performance for theoretical ORR catalysis. Colors group similar studies, with orange applied to studies of transition metals without consideration of the ORR, blue to studies of molecular systems associated with ORR, and green to studies of the ORR or the reverse process of water oxidation with catalysts similar to porphyrins. The following abbreviations are used throughout the table to denote density functional classes: LSDA = local spin density approximation, GGA = generalized gradient approximation, NGA: nonseparable gradient approximation, RS = range-separated, DH = Double-hybrid. BDEs denotes bond dissociation energies. MAE denotes Mean Absolute Error.

Table E.1: Studies benchmarking functionals on relevant transition metal systems.

Systems	Properties	Metals	functionals	Conclusions	Comments	Ref
3d Diatomics	BDEs	Metal: Sc–Zn, Ligand: H, N, O, F, S, Cl	GGA (5), Hybrid (5)	Hybrid functionals perform best. B97 (19% EXX) has lowest MAE (3.7 kcal/mol)	–	[15]

Continued on next page

Table E.1 – *Continued from previous page*

Systems	Properties	Metals	functionals	Conclusions	Comments	Ref
3d Diatomic oxides	BDEs	Sc–Zn, Y–Cd, La–Hg	LSDA (1), GGA (7), meta-GGA (2), meta-NGA (1), Hybrid GGA (9), Hybrid meta-GGA (5), Hybrid meta-NGA (1), RS-Hybrid (3), DH (1)	GGAs overestimate BDEs. Hybrids with 10-30% exact exchange and B2PLYP perform best (MAE $\sim$ 5 kcal/mol).	–	[16]
ccCA-TM/11: 3d TM complexes $\leq$31 atoms	ΔH_f	3d	Hybrid (4), RS-Hybrid (3), Hybrid meta-GGA (3), DH (3)	B97-1 and mPW2-PLYP perform best overall (MAE $\sim$ 7 kcal/mol). B97-1 is superior for open-shell and systems with multireference character.	No dispersion corrections used other than ωB97X-D.	[17]
MOR41: single reference, closed-shell TM complexes	Reaction energies	Ti, Cr-Ni, Mo, Ru-Pd, W, Ir, Pt	GGA (7), meta-GGA (3), Hybrid (14), DH (17), with D3 and nonlocal dispersion	Accuracy increases in order of GGA < meta-GGA < Hybrid < DH. PWPB95-D3(BJ) was the top performer (MAE 1.9 kcal/mol)	B3LYP was on the poor side among hybrids (MAE 4.9 kcal/mol with D3(BJ)). Dispersion was very important for B3LYP.	[18]
ROST61: single reference, open-shell TM complexes	Reaction energies	Sc-Cr, Co-Cu, Y-Ag, Ta, W, Os, Ir	GGA (5), meta-GGA (7), Hybrid (8), RS-Hybrid (2), DH (9), with D3, D4, and nonlocal dispersion	Double-hybrid PWPB95-D4 performed best, but single-hybrids with <30% exact exchange showed accuracy comparable to double-hybrids.	Mostly Cr and Ti complexes, with no Fe or Mn complexes. Dispersion corrections improved results.	[19]
Octahedral hexaqua and hexammonia complexes	Spin state splittings	Ti-Cu	Modified PBE0	Used CASPT2 to tune the %EXX of a PBE0-like functional for use on more realistic SACs. Found that higher exchange (40%) better reproduced CASPT2 results.	CASPT2 may overstabilize high spin. Transferrability of results to porphyrins unclear.	[20]
3d TM Phthalocyanines (Pc)	UV photoemission spectroscopy (UPS)	Mn, Fe, Co, Ni	PBE, B3LYP, PBE0, M06	All functionals predicted good geometries. PBE UPS spectra inferior to hybrid-GGAs.	MnPc and FePc show symmetry breaking and electronic structures very sensitive to functional.	[21, 22]

Continued on next page

Table E.1 – *Continued from previous page*

Systems	Properties	Metals	functionals	Conclusions	Comments	Ref
Iron porphyrin with and without axial imidazole ligand	spin states, geometries, O_2 binding energies	Fe	OLYP, BP86, B3LYP, PBE0	GGAs predict good geometries, but BP86 overestimates BDEs. OLYP gives good energetics. Hybrids overestimate Fe–O bond length and underestimate BDE.	Approximate correction applied for broken symmetry energies. No dispersion corrections. Unclear if results generalizable.	[23]
Iron porphyrin with axial imidazole ligand	spin states, geometries, O_2 binding energies	Fe	BP86, B97D, M3LYP, M06, TPSSh, ωB97XD	B97D (GGA + dispersion) predicts accurate geometries, spin states and binding energies. Other functionals fail in at least one respect.	Dispersion corrections not utilized outside of B97D and ωB97XD. Unclear if results generalizable.	[24]
MN_4 sites in graphene and graphene flakes	CO binding energy and S/T gap	Fe, Co, Ni	PBE, HSE, and modified PBE0	CO binding and S/T gaps are very sensitive to %EXX, and they show similar trends for %EXX < 30. Sensitivity varies from metal to metal.	–	[25]
FeN_4 sites in graphene	CORR and HER reaction energies	Fe	PBE, BEEF-vdW, RPBE+U (U = 2 eV), and HSE06	Functionals differ by $>$ 1eV in CO binding energies and none reproduce all reaction step energies to within 0.25 eV w.r.t. CCSD(T) embedding calculations.	Dispersion corrections were not applied to PBE, RPBE+U, or HSE06.	[25]
TM Corroles and perfluoroporphyrins	LFESRs for water oxidation	Mn, Co, Ru, Rh, Ir	20 GGA, meta-GGA, and hybrid GGA	Hybrids perform best but still generally underbind intermediates. Low exact exchange is preferred. LFESRs show very strong dependence on functional.	Small def2-SVP basis used for DFT and benchmark MR calculations. Dispersion corrections used in geometry optimizations but seemingly not for single point energies.	[26]
Copper-modified covalent triazene frameworks	ORR ligand binding energies	Cu	BEEF-vdW and D3(BJ)-corrected RPBE, PBE, B3LYP, PBE0, and HSE0	PBE0 and HSE06 perform best (MAE $\sim$0.1 eV) GGA functionals tend to overbind intermediates (MAE $\sim$ 0.6–0.7 eV).	Unclear whether these findings generalize to other metals and frameworks.	[6]
Bifunctional poprhyrin MOFs	Spin states, theoretical ORR overpotentials	Fe, Co	TPSSh, RPBE and HSE06 with D3(BJ) dispersion corrections.	TPSSh predicts accurate spin states and overpotentials. HSE06 underbinds intermediates, and RPBE overstabilizes low-spin states and overbinds intermediates.	Appears in the SI of a study on MOF-based catalysts. Only compared three functionals.	[27]

E.4 Benchmarking Basis Set Extrapolation for DLPNO-CCSD(T)

During the calculation of ΔE_{OOH}, ΔE_{O}, and ΔE_{OH}, aug-cc-pVNZ basis sets were used,[28, 29, 30] and an extrapolation using N=2,3 on all atoms was performed to estimate the complete basis set limit energies. This approach has been used previously to study single copper atom catalytic sites for the ORR.[6] While the DZ/TZ extrapolation is known to be less reliable than extrapolations with larger basis set cardinalities,[31] it represented the largest basis sets we found tractable using our computational resources. In particular, we made the choice to extrapolate the basis set of all atoms in the porphyrin macrocycle and include diffuse functions in order to limit effects of basis set superposition errors. This was not a consideration for the calculation of spin states, during which only the metal atom basis was extrapolated. However, it is more important for the calculation of ligand binding energies.

To quantify the impact of extrapolation error with these smaller basis sets, we examined the convergence of the DLPNO-CCSD(T) CBS-extrapolated energies ΔE_{OOH} and ΔE_{OH} for a small porphyrin mimic,[32, 33] [FeL_2], where L = $C_3N_2H_5$. The complexes were optimized at the TPSSh-D3(BJ)/Def2-TZVPP level, with the the metal and equatorial ligand atoms constrained in a planar configuration. We then performed DZ/TZ and TZ/QZ extrapolations using both the standard[34, 29, 30] and augmented[28, 29, 30] correlation consistent basis sets [(aug)-cc-pVNZ] on all atoms. The resulting energies are shown in Table E.2. As the results demonstrate, a small error of roughly 2-3 kcal/mol is introduced by the DZ/TZ extrapolation relative to the TZ/QZ one.

Table E.2: Extrapolated relative energies for [Fe(II)L_2].

Extrapolation	Augmented	ΔE_{OOH}	ΔE_{OH}
DZ/TZ	False	116.5137	39.0509
DZ/TZ	True	115.5065	38.3860
TZ/QZ	False	118.8523	40.1659
TZ/QZ	True	118.8462	40.4196

[a] All energies in kcal/mol.

E.5 Benchmarking Triples Cutoff for DLPNO-CCSD(T)

The TCutTNO parameter can be used to select the size of the Triples Natural Orbital (TNO) subspace used for the iterative triples calculations. This has a large impact on disk space requirements. When the iterative triples approximation was introduced, a default occupation threshold of 1.0E-9 was chosen for inclusion in the TNO space, based on convergence studies showing that this value was able to recover more than 99.9% of correlation energy relative to using a complete TNO subspace.[35] However, even larger TCutTNO thresholds were able to break this 99.9% barrier.[35] Due to limited disk space on the cluster used for these calculations and the need to efficiently perform many calculations for CBS/CPS extrapolations on all geometries, we compared results of a slightly looser TCutTNO thresholds with the default.

Table E.3: FeP Spin splitting calculation with two TCutTNO thresholds.[a]

			TCutTNO 1.0E-9			TCutTNO 5.0E-9		
	Basis	TCutPNO	CCSD	(T)	Total	CCSD	(T)	Total
M3	TZ	1.0E-6	-2248.1230	-0.2197	-2248.3427	-2248.1230	-0.2180	-2248.3411
	TZ	3.33E-7	-2248.1247	-0.2264	-2248.3510	-2248.1247	-0.2244	-2248.3491
	QZ	3.33E-7	-2248.1804	-0.2300	-2248.4104	-2248.1804	-0.2280	-2248.4084
	CBS	CPS	–	–	-2248.4512	–	–	-2248.4487
M5	TZ	1.0E-6	-2248.1543	-0.2070	-2248.3613	-2248.1543	-0.2057	-2248.3600
	TZ	3.33E-7	-2248.1529	-0.2131	-2248.3661	-2248.1529	-0.2116	-2248.3645
	QZ	3.33E-7	-2248.2077	-0.2162	-2248.4239	-2248.2077	-0.2146	-2248.4223
	CBS	CPS	–	–	-2248.4580	–	–	-2248.4560
Δ[b]	CBS	CPS	–	–	-0.0068	–	–	-0.0073

[a] All energies in Ha.
[b] M5 - M3.

Table E.3 shows the results of computing the triplet-quintet adiabatic spin splitting energy for FeP using TCutTNO thresholds of 5.0E-9 and 1.0E-9. The complete basis set / complete PNO space (CBS/CPS) extrapolation described in Section 6.2.3 of the main text was used. The tighter triples threshold typically reduces the triples energy [column (T) in Table E.3] by roughly 0.002 Ha. However, because this offset is relatively constant across all calculations, the resulting spin splitting energy changes by only 0.0005 Ha, or roughly 0.3 kcal/mol.

We also tested the sensitivity of spin splitting energies to the TCutTNO parameter using several complexes from Ref [33]. For these calculations, we performed

the same CBS/CPS extrapolation, but using a loose TCutTNO value of 1.0E-8. We also applied the Zero-Order Regular Approximation[36] for relativistic effects to be consistent with Ref [33]. Table E.4 compares our results to those in Ref [33], which used the default TCutTNO value, and to reference values obtained with CASPT2, corrected for semicore (3s3p) correlation using small-basis CCSD(T) calculations (CASPT2/CC).[37, 38, 39] Only one of the computed spin splittings varied by more than 1 kcal/mol from those computed with the tighter TCutTNO threshold. Moreover, the Mean Absolute Error (MAE) and Mean Signed Error (MSE) relative to CASPT2/CC results showed that loosening the TCutTNO threshold did not skew results relative to reference values.

Table E.4: Relative spin state energies of molecules from Ref [33].

Molecule	Spin-Splitting	Ref [33]	This Work	CASPT2/CC
$FeL_2(OH)$	HS 6 - IS 4	-6.3	-5.7	-4.6 [38]
$FeL_2(OH)$	HS 6 - LS 2	-4.9	-5.2	-6.6 [38]
$FeL_2(NH_3)(OH)$	HS 6 - IS 4	-11.0	-9.7	-9.6 [38]
$FeL_2(NH_3)(OH)$	HS 6 - LS 2	10.9	11.0	8.5 [38]
$[Fe(O)(NH_3)_5]^{2+}$	HS 5 - LS 3	3.1	2.0	0.4 [39]
FeP(OH)	HS 6 - IS 4	-11.3	-11.8	-9.7 [38]
	MAE[b]	1.9	1.5	
	MSE[b]	0.4	0.4	

[a] All energies in kcal/mol.
[b] Relative to CASPT2/CC.

In addition to spin-state energetics, which involve very minimal changes to the binding environment between optimized structures, we investigated how the change in binding energies depended on the chosen TCutTNO threshold. It is important in this context that bound and unbound intermediates exhibit a similar dependence upon TCutTNO, otherwise their relative energies might prove quite sensitive to TCutTNO. We used the same type of small models for porphyrin catalysts described above, namely $[FeL_2]$ and $[Co(II)L_2]$, where L = $C_3N_2H_5$. These complexes were optimized at the TPSSh-D3(BJ)/Def2-TZVPP level. The geometries optimized to a planar configuration; however, in order to prevent significant distortion of this configuration upon addition of an axial OH ligand, the ML_2 atoms were frozen in space during the optimization of $FeL_2(OH)$ and $CoL_2(OH)$. The optimized bound structures are shown as insets in Figures E.2(a) and (b).

CBS/CPS extrapolated DLPNO-CCSD(T) was performed, and E_{OH} was calculated for both models as the electronic energy change associated with Equation (E.6). In Figure E.2, ΔE_{OH} is plotted for both models using three different values for TCutTNO: 1.0E-8, 5.0E-9, and the default value of 1.0E-9. Both structures show a rather small dependence on the threshold value. For FeL_2, the binding energy only changes by 0.01 eV, or 0.23 kcal/mol, when decreasing TCutTNO from 5.0E-9 to 1.0E-9. CoL_2 shows a much smaller dependence still, as ΔE_{OH} only changes by 0.001 eV when TCutTNO is decreased from 1.0E-8 to 1.0E-9. Thus, while different porphyrins can be expected to to exhibit more or less of a dependence on this particular parameter, the dependence still seems to be rather small, and we expect increasing the threshold to 5.0E-9 to have minimal effect on binding-type relative energies.

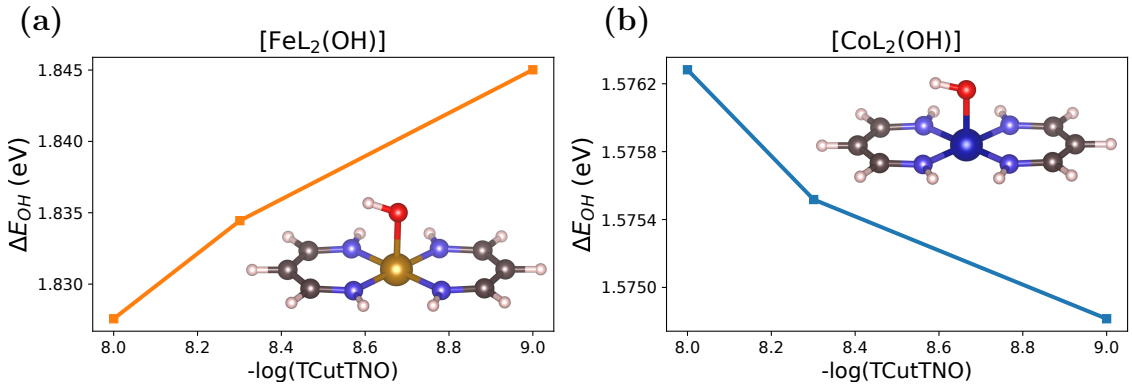

Figure E.2: Convergence of ΔE_{OH} with TCutTNO threshold for two model catalysts. Panel **(a)** shows $[FeL_2(OH)]$ and panel **(b)** shows $[CoL_2(OH)]$, where L = $C_3N_2H_5$.

Based on these results, we increased the TCutTNO threshold in our calculations to 0.5E-9. This was a threshold value that allowed us to perform all calculations with 2TB of scratch disc space while maintaining sufficient accuracy. The benchmarking performed indicates that the accuracy for the relative energies of spin states should not be reduced by more than about 1 kcal/mol relative to the tighter default threshold.

E.6 Binding Energies and LFESRs

E.6.1 LFESRs Using BP86-Optimized Geometries

To remove structural effects from the analysis and emulate many studies where geometries are optimized at the GGA level, we computed LFESRs with BP86-optimized

geometries. For each functional, single point energies were evaluated on these geometries. This contrasts with the LFESRs in Section 6.3.1 of the main text, where geometries were optimized separately with each functional. Figure E.3 shows the LFESRs computed for BP86-optimized geometries. B2PLYP is included among these LFESRs, with ZPEs and other thermochemical corrections calculated at the BP86 level.

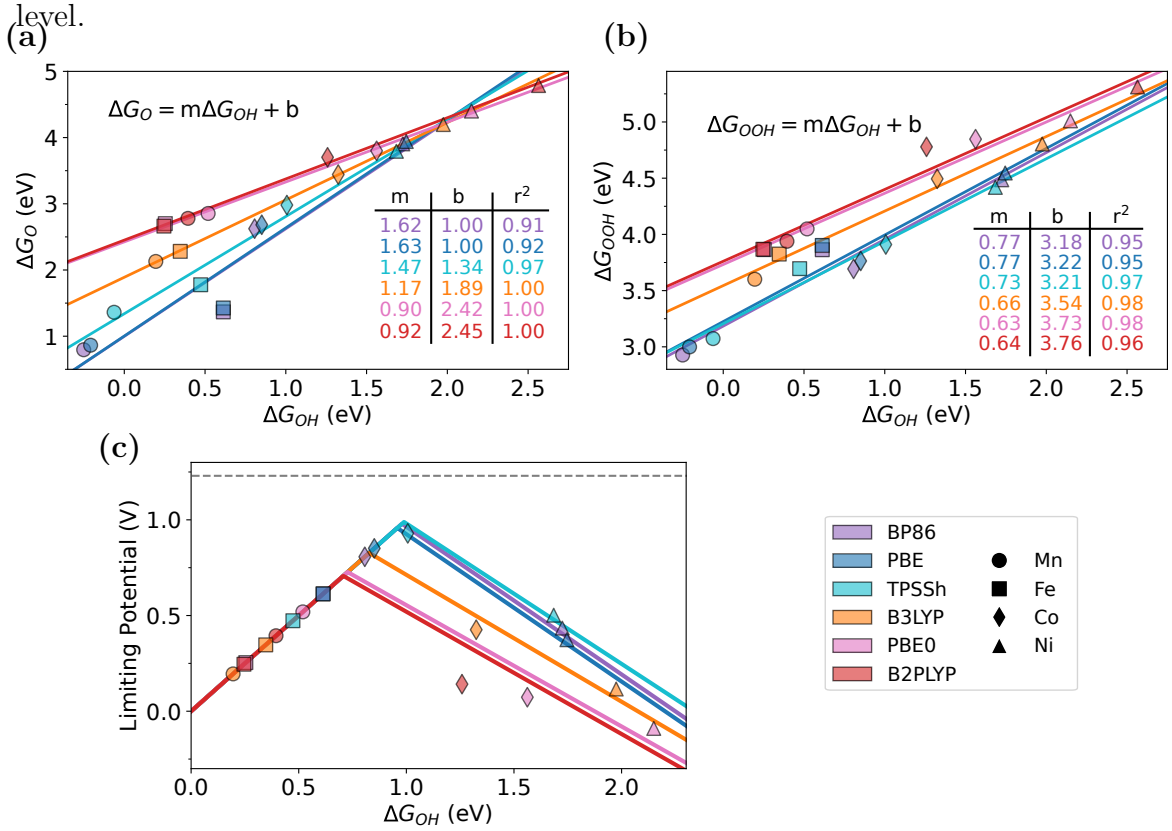

Figure E.3: Density functional dependence of catalyst activity calculated using BP86-optimized structures. LFESRs between the binding energies of MP(O) and MP(OH) [panel **(a)**] and between those of MP(OOH) and MP(OH) [panel **(b)**]. Note that the different scale in panel **(b)** indicates a narrower range of energies for ΔG_{OOH}. Panel **(c)** shows the volcano plots derived from the LFESRs. The theoretical ORR potential (1.23 V) is depicted as a dashed line above the volcano apex.

The LFESRs calculated in this way are not significantly different from those calculated with separate geometry optimizations, and the LFESRs of B2PLYP and PBE0 are quite similar.

E.6.2 Binding Energies with Restricted Open-Shell B2PLYP

For the double-hybrid B2PLYP, the degree of spin contamination had a large impact on the relative energies of intermediates. Figure E.4 shows ΔE_{O}, ΔE_{OH}, and ΔE_{OOH} calculated with Restricted Open-Shell B2PLYP (ROB2PLYP) alongside the other functionals used in the main text. By definition, ROB2PLYP does not suffer from spin contamination. Removing spin contamination reduces the MAE relative to DLPNO-CCSD(T) for both ΔE_{O} and ΔE_{OOH} and removes some of the weak binding bias of B2PLYP (as reflected in the overall MSE near 0). Even with these improvements, there appears to be no real benefit to using ROB2PLYP over the much more computationally efficient B3LYP.

Spin Contamination Observed for CoP(O) @ B2PLYP

In the calculation of ΔE_{O} for CoP(O), it was discovered that the additional spin symmetry-breaking introduced by the stability analysis in ORCA worsened the B2-PLYP energetics. By not performing a stability analysis on the SCF part of the B2PLYP wave function, the energy of the CoP(O) intermediate was reduced by 16.8 kcal/mol, and the error in ΔE_{O} was also reduced considerably. Therefore, the less spin-contaminated wave function (before stability analysis was performed) was used for the analysis in the main text. The explanation for the energetic discrepancy between the two wave functions lies in the different effects of spin contamination in the SCF and MP2 parts of B2PLYP calculations. Although additional spin symmetry breaking reduced the SCF energy, it significantly increased the MP2 portion of the B2PLYP energy. The failure of MP2 theory for very spin-contaminated wave functions is a known phenomenon.[40]

As in the main text, all of the relative energies in Figure E.4, including for CoP(O), were calculated with TPSSh geometries. However, spin contamination in the B2PLYP CoP(O) wave function was almost completely eliminated when the geometry was allowed to relax using B2PLYP. During relaxation, the porphyrin macrocycle lost its planarity, adopting a saddle configuration. This distortion removed the symmetry of the Co-N bonds by producing two longer and two shorter bonds. This appears to be a Jahn-Teller type distortion, removing the degeneracy of the partially filled d_{xz} and d_{yz} orbitals. Thus, the large breaking of spin symmetry when applying B2PLYP to the planar TPSSh geometry may result from the same breaking of orbital degeneracy that occurs when the geometry is allowed to relax. In any case, unrestricted B2PLYP

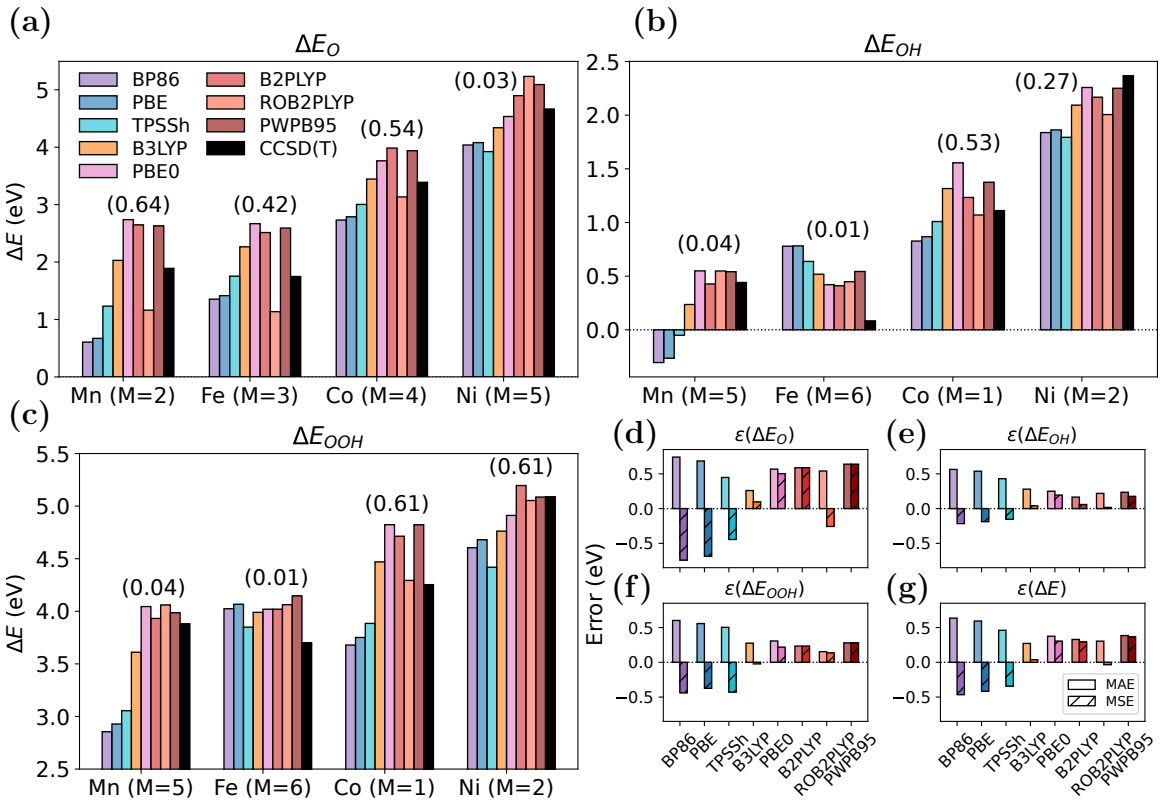

Figure E.4: Relative electronic energies of the bound O, OH, and OOH intermediates calculated using Restricted Open-Shell B2PLYP (ROB2PLYP), compared to DLPNO-CCSD(T) and the other functionals in the main text. Panel **(a)** shows ΔE_{O}, **(b)** shows ΔE_{OH}, and **(c)** shows ΔE_{OOH}. Values above the bars in parentheses indicate the spin contamination present in the unrestricted B2PLYP wave function, calculated as $\langle S^2 \rangle - S(S+1)$. Multiplicities for each structure are indicated on the x-axes. Panels **(d)**, **(e)**, **(f)**, and **(g)** show the Mean Absolute Error (MAE) and Mean Signed Error (MSE) relative to DLPNO-CCSD(T) for ΔE_{O}, ΔE_{OH}, ΔE_{OOH}, and all of these combined.

performs much better compared to the DLPNO-CCSD(T) reference when both are evaluated on the non spin contaminated saddle geometry.

Figure E.5 shows ΔE_{O} calculated on both the planar and saddle geometries using various flavors of B2PLYP. DLPNO-CCSD(T) energies for both geometries are included as reference.

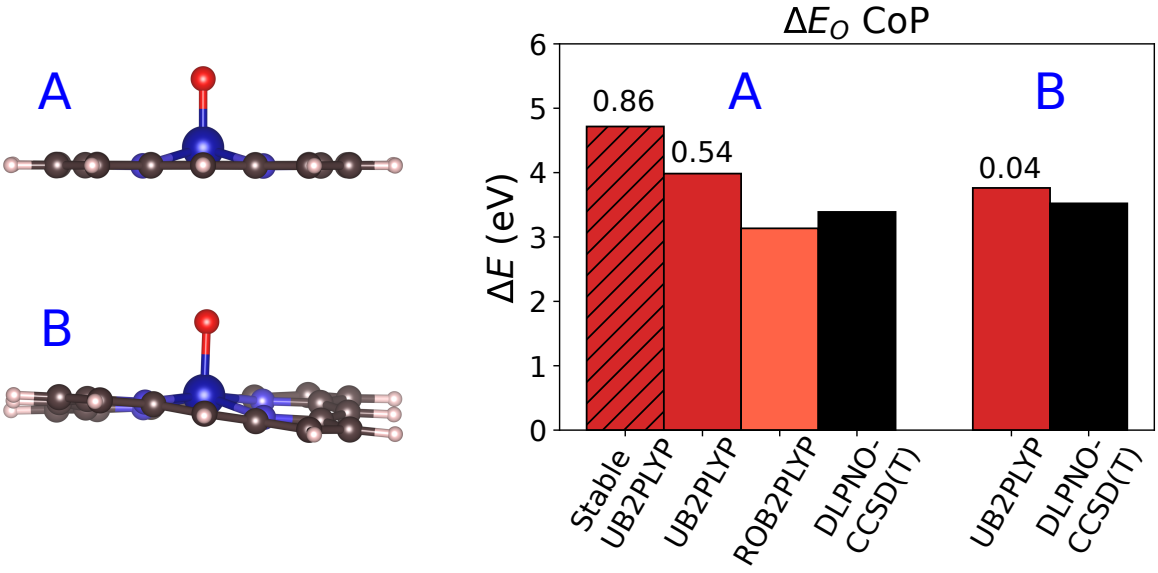

Figure E.5: CoP(O) relative energies (ΔE_{O}) calculated with several methods and geometries. Geometry A is the TPSSh-optimized geometry, and B is the B2PLYP-optimized geometry. The bars show ΔE_{O} calculated for structure A with unrestricted B2PLYP with and without a stable electronic structure, RO-B2PLYP, and DLPNO-CCSD(T). For structure B, unrestricted B2PLYP and DLPNO-CCSD(T) are shown. $\langle S^2 \rangle - S(S+1)$ is written above the bars showing unrestricted B2PLYP results.

E.7 Spin States

E.7.1 DLPNO-CCSD(T) Spin State Energy Splitting

Table E.5 shows the adiabatic (geometries optimized separately at each multiplicity using TPSSh) electronic spin splittings computed with DLPNO-CCSD(T) using both CBS and CPS extrapolation. As described in the main text, reference determinants were constructed from the quasi-restricted orbitals of the TPSSh ground state. No zero-point energy or other thermochemical corrections were applied.

Previous studies have estimated that the DLPNO-CCSD(T) method used here may overstabilize high-spin states by about 2 kcal/mol. Thus, the small energy splittings for MnP(O) and NiP(OOH) are likely closer to 3 kcal/mol in favor of the low-spin state. This bias does not fully account for the prediction of a quintet ground state in FeP, which is known experimentally to be a triplet. Using the tighter default TCutTNO threshold (see Methods in main text for details) very minimally reduced the spin splitting to 4.29 kcal/mol, and applying the Zero-Order Regular Approximation (ZORA) relativistic correction reduced the spin splitting to 3.67 kcal/mol.

Table E.5: DLPNO-CCSD(T) spin state energy splittings.

Metal	Ligand	Multiplicities	ΔE (kcal/mol)
Mn	N/A	$4-6$	17.72
Mn	MOOH	$3-5$	7.96
Mn	MO	$2-4$	-0.91
Mn	MOH	$3-5$	8.33
Fe	N/A	$3-5$	4.59
Fe	MOOH	$2-4$	-2.52
Fe	MOOH	$4-6$	8.86
Fe	MO	$3-5$	-9.28
Fe	MOH	$2-6$	15.53
Fe	MOH	$4-6$	11.10
Co	N/A	$2-4$	-7.25
Co	MO	$2-4$	3.19
Co	MOOH	$1-3$	-11.90
Co	MOH	$1-5$	-7.22
Co	MOH	$3-5$	0.56
Ni	N/A	$1-3$	-15.77
Ni	MO	$3-5$	5.23
Ni	MOH	$2-4$	-6.31
Ni	MOOH	$2-4$	-1.31

[a] All ΔE values are the energy of the lower spin minus that of the higher spin.

CASPT2 also generally overstabilizes the quintet and predicts it to be the ground state or essentially degenerate with the triplet.[38] However, full CCSD(T)-CBS has been shown to correctly predict a triplet ground state 3 kcal/mol lower than the quintet.[32] Therefore, FeP seems to be a system with a rather slow convergence with respect to the pair natural orbital space used, leading to an erroneous ground state prediction from our computational protocol.

E.7.2 Ground Spin State Determined by Each Functional

Table E.6 shows the ground state multiplicity predicted by each functional. As explained in the main text, the ground state was determined by optimizing the geometry of low, intermediate, and high spin structures and taking the structure with the lowest electronic energy (ZPE and entropic corrections were not considered, for consistency with DLPNO-CCSD(T) methodology). Separate geometry optimizations were per-

formed for each functional. The final column of Table E.6 shows the mode of the predicted multiplicities, with ties going to the higher multiplicity.

Table E.6: Ground state multiplicities determined by different functionals.

		GS Multiplicity						
Metal	Geometry	BP86	PBE	TPSSh	B3LYP	PBE0	B2PLYP	Mode
Mn	MP	4	4	4	6	6	6	6
Mn	MP(O_2)	4	4	4	6	6	6	6
Mn	MP(OOH)	3	3	5	5	5	5	5
Mn	MP(O)	2	2	4	4	4	2	4
Mn	MP(OH)	5	5	5	5	5	5	5
Fe	MP	3	3	3	3	3	3	3
Fe	MP(O_2)	1	1	1	5	1	5	1
Fe	MP(OOH)	2	2	2	6	6	6	6
Fe	MP(O)	3	3	3	3	3	3	3
Fe	MP(OH)	2	2	2	6	6	6	6
Co	MP	2	2	2	2	2	2	2
Co	MP(O_2)	2	2	2	2	2	2	2
Co	MP(OOH)	1	1	1	1	1	1	1
Co	MP(O)	4	4	4	4	4	2	4
Co	MP(OH)	1	1	1	1	5	1	1
Ni	MP	1	1	1	1	1	1	1
Ni	MP(O_2)	3	3	3	3	3	3	3
Ni	MP(OOH)	2	2	2	2	4	4	2
Ni	MP(O)	5	5	5	5	5	3	5
Ni	MP(OH)	2	2	2	2	2	2	2

E.7.3 Ground Spin States from Baran *et al.*

Table E.7 compares the ground state spins that we determined from a combination of literature values and DLPNO-CCSD(T) calculations with those determined using the GGA OLYP in Ref [4]. The spin predictions differ for 7 of the 16 total complexes compared, with OLYP always predicting the lower spin in these instances.

Table E.7: Ground state multiplicities from Ref [4] and the present study.

		GS Multiplicity	
Metal	Geometry	Ref [4]	Present Study
Mn	MP	4	6
Mn	MP(OOH)	1	5
Mn	MP(O)	2	2
Mn	MP(OH)	1	5
Fe	MP	3	3
Fe	MP(OOH)	2	6
Fe	MP(O)	3	3
Fe	MP(OH)	2	6
Co	MP	2	2
Co	MP(OOH)	1	1
Co	MP(O)	2	4
Co	MP(OH)	1	1
Ni	MP	1	1
Ni	MP(OOH)	2	2
Ni	MP(O)	3	5
Ni	MP(OH)	2	2

E.7.4 Differential Stabilization of Spin States by Functional

Figure E.6(a) shows the proportion of porphyrin intermediates where agreement was obtained on the ground state spin multiplicity between each pair of tested functionals. The "Actual" row/column represents our assignment of the true ground state spin multiplicity based on a combination collected data, including experimental results, *ab initio calculations* from previous studies (DMRG-CASPT2 for $MnP(O_2)$ and $FeP(O_2)$.[41] CASPT2/CC[37, 38] and DLPNO-CCSD(T)[33] for FeP(OH)), and our own DFT and DLPNO-CCSD(T) results. The tabulation of these assigned multiplicities is in Table 6.2 of the main text. Functionals in each row (column) are organized left-to-right (top-to-bottom) according to increasing rungs of Jacob's ladder, and among the hybrids, according to increasing exact exchange. There is a clear divide between low-exchange functionals (BP86, PBE, and TPSSh) and higher exact exchange functionals (B3LYP, PBE0, B2PLYP), with functionals within each of these two groups agreeing more often with each other than with functionals in the other group. In fact, the agreement among low-exchange functionals is noticeably better than among higher exchange ones.

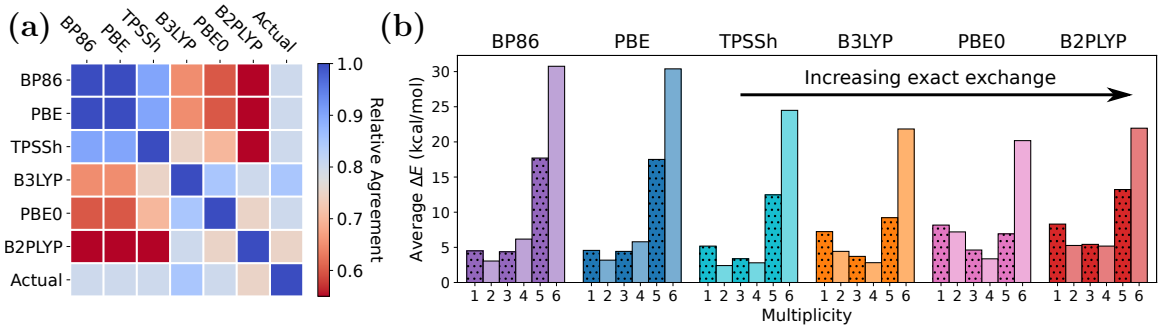

Figure E.6: The effect of functional on spin state and spin state energetics. Panel **(a)** shows the proportion of the 20 ORR intermediates studied for which each pair of functionals agreed in ground state spin predictions. Panel **(b)** shows the average energies of different spin states of all intermediates relative to the ground state energies of those intermediates for different functionals.

Figure E.6(b) shows how the amount of exact exchange in a functional affects the calculated relative energy of spin states across the studied porphyrins. As discussed in the main text, there is an expected linear relationship between the amount of exact exchange in a functional and the relative stability of high-spin states.[42, 43, 44]. Our data matches this expectation. Specifically, there is a marked decrease in the relative energy of high spin (quintet and sextet) states when even small amounts of exact exchange are included, and the stabilization of these states is seen to increase along the series TPSSh $\rightarrow$ B3LYP $\rightarrow$ PBE0. A relative destabilization of the low spin states is also seen across this series, though less pronounced. The introduction of MP2 correlation in B2PLYP counteracts this trend to some extent. Even though B2PLYP has more than double the proportion of exact exchange of PBE0, it shows a marked destabilization of high spin and, to a lesser extent, intermediate spin states relative to PBE0.

E.8 Spin Contamination

We found that several of the studied intermediates exhibited significant spin contamination in their ground states. The deviation of $\langle S^2 \rangle$ from its ideal value $S(S+1)$ is plotted in Figure E.7(a) for all metalloporphyrin complexes and functionals as an indication of spin contamination. Specifically, the figure illustrates the ground states of these intermediates, whose multiplicities are indicated in Table 6.2 in the main text. The most severe spin contamination is caused by antiferromagnetically coupled orbitals that produce broken-symmetry wave functions.[44]. This phenomenon is known to occur in the open shell singlet ground state of FeP(O_2), with a 1,1 coupling of electrons on the metal and O_2 seen for GGAs and a 2,2 coupling seen for hybrids.[23] We did observe such coupling in FeP(O_2), and we also observed 1,1 coupling between the metal atom and O_2 ligand in the quartet ground state of MnP(O_2) with B3LYP, PBE0, and B2PLYP and in doublet ground state of CoP(O_2) with all hybrid functionals. Finally, 1,1 coupling was observed in singlet CoP(OOH) with PBE0. To improve the accuracy of the treatment of such systems, spin projections such as those employed in Ref [23] may be necessary, though we did not employ such a scheme in this work.

Besides these instances, several other intermediates showed persistent spin contamination without the spatially separated α and β spin densities that indicate antiferromagnetic coupling. In particular, MnP(O), CoP(OOH), CoP(O), CoP(OH),

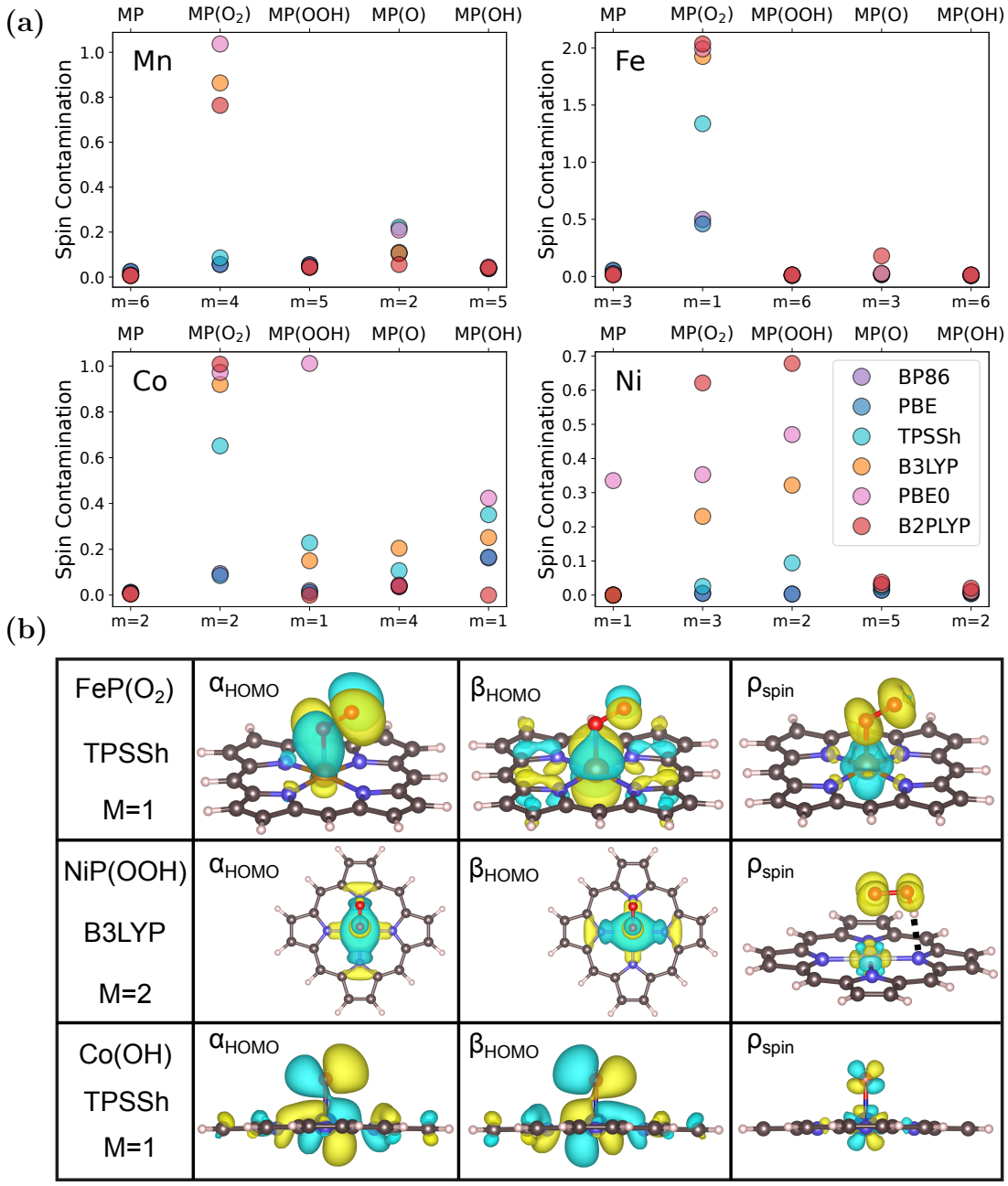

Figure E.7: Spin contamination in ground state wave functions. **(a)** Spin contamination, calculated as $\langle S^2 \rangle - S(S+1)$, for all intermediates and all tested functionals. The top horizontal axis labels the intermediate structures, while the bottom horizontal axis shows their multiplicity, calulated as $2S+1$. **(b)** Table of α and β corresponding orbitals (columns 2 and 3) and total spin densities (column 4) for $FeP(O_2)$, NiP(OOH), and CoP(OH). For spin densities, yellow isosurfaces show positive (α) spin and blue isosurfaces show negative (β) spin.

NiP(OOH) showed large values of $\langle S^2 \rangle - S(S+1)$ for multiple functionals. Hybrid functionals were more likely to exhibit serious spin contamination and antiferromagnetic coupling. Furthermore, spin contamination was only significant for low and intermediate spin states. These observations can be rationalized by the contaminated solutions resulting from the mixing of higher spin states into the nominally calculated spin state.[45, 46, 44] Thus, hybrid functionals are prone to this mixing since they incorporate some percentage of exact exchange, which favors higher spin states.[42] Meanwhile, high-spin states do not often exhibit such symmetry breaking because there are generally few low-lying higher spin states to be mixed in.

E.9 Assessment of Multireference Character

Table E.8 shows several diagnostics available from the aug-ccpVTZ DLPNO-CCSD(T) calculations in order to assess potential multireference character in the ground states of the studied porphyrins (for the additional states studied for the determination of spin splittings, the T_1, $|t_{2\max}|$, %TAE[T], and spin contamination metrics are available in the DLPNO_Spin_Splittings tab of the attached supporting_data.XLSX document). First, we tabulate spin contamination of the unrestricted Kohn-Sham orbitals that enter into the DLPNO-CCSD(T) procedure. It is worth noting that within the DLPNO-CCSD(T) scheme, canonical MOs are transformed into Quasi-Restricted Orbitals (QROs) before solving the coupled cluster equations. These QROs eliminate spin contamination in the reference entirely by construction. Still, a highly contaminated UKS wave function would mean that these QROs may not be a good reference and that the system may have multireference character.

In addition, we tabulate the smallest overlap value for the Unrestricted Corresponding Orbitals (UCOs). Small values of the UCO orbital overlap for the last doubly-occupied MO (values below about 0.85) can indicate spin coupled orbitals and static correlation. This type of correlation would indicate that DLPNO-CCSD(T) should not be applied.

Next, we tabulate properties of the DLPNO-CCSD(T) results. The spin contamination of the CCSD wave function will most likely be low based on the construction of the QRO reference; however, large values would indicate a problematic electronic structure. The T_1 diagnostic value (Frobenius norm of the single excitation amplitudes) is an indication of the degree of orbital relaxation during CCSD.[47] While it's use as an indicator of multireference character is dubious, large values (> 0.05) are

still indicative of a poor reference wave function.[48, 49] The largest double excitation amplitude $|t_{2\max}|$ has been suggested as a more reliable indicator of multireference character.[50] Typical values for single reference systems should be below 0.1,[48] while larger values strongly suggest that a multireference approach is warranted. The percent of total atomization energy that comes from triples excitations is another useful indicator of the quality of CCSD(T) energies, with %TAE[T] < 10 regarded as a practical criterion.[48] It is worth noting that these indicators have been investigated within the context of canonical cluster. Thus, diagnostic ranges should be similar for DLPNO-CCSD(T), but more investigation should be done to understand how these quantities change with such a local correlation method.[49]

Table E.8: Diagnostics for assessing potential multireference character.

Metal	Geometry	M[a]	$\mathrm{SSB}_{\mathrm{TPSSh}}$[b]	$\min\{S^{\mathrm{UCO}}_{\alpha,\beta}\}$	$\mathrm{SSB}_{\mathrm{CCSD}}$[b]	T_1	$\lvert t_{2\max}\rvert$	%TAE[T]
Mn	MP	6	0.0085	0.9985	0.0004	0.0153	0.0483	2.81
Mn	MP(OOH)	5	0.0444	0.9880	0.0033	0.0188	0.0937	3.19
Mn	MP(O)	2	0.2209	0.8866	0.0011	0.0148	0.0822	3.89
Mn	MP(OH)	5	0.0370	0.9875	0.0033	0.0177	0.0473	3.07
Fe	MP	3	0.0234	0.9951	0.0013	0.0153	0.0464	3.01
Fe	MP(OOH)	6	0.0098	0.9982	0.0009	0.0180	0.0941	3.05
Fe	MP(O)	3	0.0208	0.9970	0.0012	0.0150	0.0548	3.76
Fe	MP(OH)	6	0.0092	0.9984	0.0008	0.0176	0.0478	2.94
Co	MP	2	0.0081	0.9973	0.0004	0.0145	0.0482	3.05
Co	MP(OOH)	1	0.2181	0.8891	0.0000	0.0134	0.1084	3.54
Co	MP(O)	4	0.1066	0.9527	0.0073	0.0162	0.0580	3.63
Co	MP(OH)	1	0.3426	0.8128	0.0000	0.0132	0.0908	3.39
Ni	MP	1	0.0000	1.0000	0.0000	0.0142	0.0479	3.04
Ni	MP(OOH)	2	0.0886	0.9570	0.0001	0.0142	0.0483	3.12
Ni	MP(O)	5	0.0240	0.9964	0.0017	0.0171	0.1130	3.24
Ni	MP(OH)	2	0.0080	0.9980	0.0006	0.0132	0.0481	3.19

[a] Multiplicity $(2S+1)$.
[b] SSB indicates spin symmetry breaking (contamination), and is defined as $\langle S^2\rangle - S(S+1)$.

The studied molecules appear mostly well-behaved across the surveyed diagnostics. In particular, all fall well below the %TAE[T] = 10 threshold. Interestingly, triples appear to have the biggest contributions for the MP(O) species, but even all of these have %TAE[T] < 4. In addition, $T_1 < 0.02$ for all species, indicating that at least in terms of orbital rotation, the reference orbitals are reasonable. Spin contamination values of the TPSSh reference (before construction of QROs) indicate that MnP(O), CoP(OOH), CoP(O), CoP(OH), and NiP(OOH) should be examined carefully. However, the UCO overlap values for all species other than CoP(OH) clear them of suspected magnetic coupling. In the case of CoP(OH), the borderline UCO overlap

of 0.81 seems to indicate a case of strong spin polarization, and not magnetic coupling, as shown above in Figure E.7. After QRO construction and the coupled cluster iterations, no notable spin contamination persists for any of the species. Several species did show somewhat large maximum doubles amplitudes, with both CoP(OOH) and NiP(O) having $\max\{|\mathbf{t_2}|\} > 0.1$. In the case of NiP(O), these amplitudes correspond to excitations out of the Ni-O π bonding orbitals and into the π^* antibonding ones. In the case of CoP(OOH), the large amplitude belongs to a double excitation from the Co-O σ bonding orbital to the σ^* orbital of mostly $3dz^2$ character.

Based on the above metrics, the systems studied seem, on the whole, to be sufficiently single-reference in nature for the application of CCSD(T) as a reference method. It is, however, necessary to recognize some of these systems certainly are more multi-configurational than others. To further explore this, we also performed CASSCF calculations on the studied porphyrins and examined the dominant electron configurations. All calculations were performed using ORCA 5.0.4 using a def2-TZVP basis set on all atoms.

Active spaces were chosen to include metal 3d orbitals, the metal-nitrogen σ bonding orbital, and metal-oxygen bonding orbitals when present. In addition, a metal 4d doubleshell and a 3p oxygen doubleshell for oxygen bound to the metal atom was included. This procedure was similar to other studies on iron, manganese, and cobalt porphyrins[51, 52, 37] and follows general recommendations for transition metal complexes.[53] This resulted in an 11 orbital CAS for MP, 15 orbitals for MP(OH) and MP(OOH), and a 17 orbital CAS for MP(O). For all complexes with more than 15 active orbitals, the approximate Iterative-Configuration Expansion-Coniguration Interaction (ICE-CI) solver was used.[54, 55]

There are two exceptions to the active spaces described above. For MnP(O), the 4d doubleshell orbitals for the unoccupied $3d_{xz}$, $3d_{z^2}$, and $3d_{x^2-y^2}$ orbitals were minimally occupied and consistently rotated out of the active space, so they were omitted. Additionally, NiP(OOH) has very weak Ni–O bonding, and it was difficult to avoid the preparation of a CASSCF state with antiferromagnetically coupled electrons on the OOH ligand and Ni atom, despite the fact that we never observed such coupling for any DFT functionals. In order to prepare the desired state, with the radical located on the OOH ligand, we found it necessary to include the O–O σ and σ^* orbitals as well as the O–O π orbital that lies parallel to the porphyrin plane. Additionally, the Ni $4d_{x^2-y^2}$ orbital and the O 3p orbital parallel to the porphyrin plane were omitted due to their tendency to rotate out of the active space. Finally, we note that for

the NiP(OOH) species, the very weak metal oxygen bond meant there was minimal mixing between the orbitals of the OOH ligand and Ni atom. Thus, the orbitals labeled as M–O bonding orbitals in Table E.12 are essentially O–O π^* orbitals, and the antibonding orbitals are essentially of metal 3d character only.

It is worth noting that we did not include the porphyrin orbitals in the Gouterman set in our active spaces for reasons of computational efficiency. These orbitals are sometimes included in order to improve the accuracy of spin-state splitting energies[51, 52]—in reality many porphyrin π orbitals are typically necessary for accurate spin state energies. Excluding these porphyrin orbitals means that we are not able to describe the multiconfigurational character that arises from donation from the metal or axial ligand to the porphyrin ligand orbitals. In any case, their inclusion would result in at least some decrease in the weights of the leading configurations due to excitation between the occupied and unoccupied porphyrin π orbitals. The noninnocence of the porphyrin macrocycle would need to be explored further in a future study.

The computed ground states for all species are reported in Tables E.9 (bare metalloporphyrins), E.10 (MP(OH)), E.11 (MP(O)), and E.12 (MP(OOH)) with all configurations having weight greater than 0.02 reported.

Table E.9: CASSCF Ground States of bare metalloporphyrins.

Metal	$2S+1$	Weight	Principal Configurations	Natural Orbital Occupations					
				σ_{MN}	d_{xy}	d_{xz}	d_{yz}	d_{z^2}	$\mathrm{d}_{x^2-y^2}$
Mn	6	0.989	$(\sigma_{\mathrm{MN}})^2(\mathrm{d}_{xy})^1(\mathrm{d}_{xz})^1(\mathrm{d}_{yz})^1(\mathrm{d}_{z^2})^1(\mathrm{d}_{x^2-y^2})^1$	2.00	1.00	1.00	1.00	1.00	1.00
Fe	3	0.944	$(\sigma_{\mathrm{MN}})^2(\mathrm{d}_{xy})^2(\mathrm{d}_{xz})^1(\mathrm{d}_{yz})^1(\mathrm{d}_{z^2})^2(\mathrm{d}_{x^2-y^2})^0$	1.98	1.97	0.99	0.99	1.96	0.05
Co	2	0.944	$(\sigma_{\mathrm{MN}})^2(\mathrm{d}_{xy})^2(\mathrm{d}_{xz})^2(\mathrm{d}_{yz})^2(\mathrm{d}_{z^2})^1(\mathrm{d}_{x^2-y^2})^0$	1.99	1.98	1.96	1.96	1.00	0.05
Ni	1	0.925	$(\sigma_{\mathrm{MN}})^2(\mathrm{d}_{xy})^2(\mathrm{d}_{xz})^2(\mathrm{d}_{yz})^2(\mathrm{d}_{z^2})^2(\mathrm{d}_{x^2-y^2})^0$	1.98	1.99	1.97	1.97	1.95	0.09

Table E.10: CASSCF Ground States for MP(OH).

Metal	$2S+1$	Weight	Principal Configurations	Natural Orbital Occupations							
				σ_{MN}	σ_{MO}	π_{MO}	d_{xy}	π^*_{MO}	$\mathrm{d}_{xz/yz}$	σ^*_{MO}	$\mathrm{d}_{x^2-y^2}$
Mn	5	0.941	$(\sigma_{\mathrm{MN}})^2(\sigma_{\mathrm{MO}})^2(\pi_{\mathrm{MO}})^2(\mathrm{d}_{xy})^1(\pi^*_{\mathrm{MO}})^1(\mathrm{d}_{xz/yz})^1(\sigma^*_{\mathrm{MO}})^1(\mathrm{d}_{x^2-y^2})^0$	1.96	1.97	1.97	0.99	1.00	1.00	1.00	0.04
Fe	6	0.961	$(\sigma_{\mathrm{MN}})^2(\sigma_{\mathrm{MO}})^2(\pi_{\mathrm{MO}})^2(\mathrm{d}_{xy})^1(\pi^*_{\mathrm{MO}})^1(\mathrm{d}_{xz/yz})^1(\sigma^*_{\mathrm{MO}})^1(\mathrm{d}_{x^2-y^2})^1$	2.00	1.97	1.97	1.00	1.00	1.00	1.00	1.00
Co	1	0.865	$(\sigma_{\mathrm{MN}})^2(\sigma_{\mathrm{MO}})^2(\pi_{\mathrm{MO}})^2(\mathrm{d}_{xy})^2(\pi^*_{\mathrm{MO}})^2(\mathrm{d}_{xz/yz})^2(\sigma^*_{\mathrm{MO}})^0(\mathrm{d}_{x^2-y^2})^0$	1.97	1.85	1.98	1.97	1.96	1.97	0.016	0.06
		0.054	$(\sigma_{\mathrm{MN}})^2(\sigma_{\mathrm{MO}})^0(\pi_{\mathrm{MO}})^2(\mathrm{d}_{xy})^2(\pi^*_{\mathrm{MO}})^2(\mathrm{d}_{xz/yz})^2(\sigma^*_{\mathrm{MO}})^2(\mathrm{d}_{x^2-y^2})^0$								
Ni	2	0.885	$(\sigma_{\mathrm{MN}})^2(\sigma_{\mathrm{MO}})^2(\pi_{\mathrm{MO}})^2(\mathrm{d}_{xy})^2(\pi^*_{\mathrm{MO}})^2(\mathrm{d}_{xz/yz})^2(\sigma^*_{\mathrm{MO}})^1(\mathrm{d}_{x^2-y^2})^0$	1.94	1.93	1.98	1.98	1.97	1.97	1.03	0.10
		0.021	$(\sigma_{\mathrm{MN}})^1(\sigma_{\mathrm{MO}})^1(\pi_{\mathrm{MO}})^2(\mathrm{d}_{xy})^2(\pi^*_{\mathrm{MO}})^2(\mathrm{d}_{xz/yz})^2(\sigma^*_{\mathrm{MO}})^2(\mathrm{d}_{x^2-y^2})^1$								

Table E.11: CASSCF Ground States for MP(O).

Metal	$2S+1$	Weight	Principal Configurations[a]	Natural Orbital Occupations[b]							
				σ_{MO}	$\pi_{x,\mathrm{MO}}$	$\pi_{y,\mathrm{MO}}$	d_{xy}	$\pi^*_{x,\mathrm{MO}}$	$\pi^*_{y,\mathrm{MO}}$	σ^*_{MO}	$\mathrm{d}_{x^2-y^2}$
Mn	2	0.817	$(\sigma_{\mathrm{MO}})^2(\pi_{x,\mathrm{MO}})^2(\pi_{y,\mathrm{MO}})^2(\mathrm{d}_{xy})^2(\pi^*_{x,\mathrm{MO}})^0(\pi^*_{y,\mathrm{MO}})^1(\sigma^*_{\mathrm{MO}})^0(\mathrm{d}_{x^2-y^2})^0$	1.90	1.85	1.94	1.96	0.16	1.03	0.11	0.03
		0.029	$(\sigma_{\mathrm{MO}})^1(\pi_{x,\mathrm{MO}})^1(\pi_{y,\mathrm{MO}})^2(\mathrm{d}_{xy})^2(\pi^*_{x,\mathrm{MO}})^1(\pi^*_{y,\mathrm{MO}})^1(\sigma^*_{\mathrm{MO}})^1(\mathrm{d}_{x^2-y^2})^0$								
		0.029	$(\sigma_{\mathrm{MO}})^2(\pi_{x,\mathrm{MO}})^0(\pi_{y,\mathrm{MO}})^2(\mathrm{d}_{xy})^2(\pi^*_{x,\mathrm{MO}})^2(\pi^*_{y,\mathrm{MO}})^1(\sigma^*_{\mathrm{MO}})^0(\mathrm{d}_{x^2-y^2})^0$								
Fe	3	0.814	$(\sigma_{\mathrm{MO}})^2(\pi_{x,\mathrm{MO}})^2(\pi_{y,\mathrm{MO}})^2(\mathrm{d}_{xy})^2(\pi^*_{x,\mathrm{MO}})^1(\pi^*_{y,\mathrm{MO}})^1(\sigma^*_{\mathrm{MO}})^0(\mathrm{d}_{x^2-y^2})^0$	1.86	1.92	1.92	1.96	1.06	1.06	0.014	0.05
		0.024	$(\sigma_{\mathrm{MO}})^1(\pi_{x,\mathrm{MO}})^1(\pi_{y,\mathrm{MO}})^2(\mathrm{d}_{xy})^2(\pi^*_{x,\mathrm{MO}})^2(\pi^*_{y,\mathrm{MO}})^1(\sigma^*_{\mathrm{MO}})^1(\mathrm{d}_{x^2-y^2})^0$								
		0.024	$(\sigma_{\mathrm{MO}})^1(\pi_{x,\mathrm{MO}})^2(\pi_{y,\mathrm{MO}})^1(\mathrm{d}_{xy})^2(\pi^*_{x,\mathrm{MO}})^1(\pi^*_{y,\mathrm{MO}})^2(\sigma^*_{\mathrm{MO}})^1(\mathrm{d}_{x^2-y^2})^0$								
		0.021	$(\sigma_{\mathrm{MO}})^0(\pi_{x,\mathrm{MO}})^2(\pi_{y,\mathrm{MO}})^2(\mathrm{d}_{xy})^2(\pi^*_{x,\mathrm{MO}})^1(\pi^*_{y,\mathrm{MO}})^1(\sigma^*_{\mathrm{MO}})^2(\mathrm{d}_{x^2-y^2})^0$								
Co	4	0.798	$(\sigma_{\mathrm{MO}})^2(\pi_{x,\mathrm{MO}})^2(\pi_{y,\mathrm{MO}})^2(\mathrm{d}_{xy})^2(\pi^*_{x,\mathrm{MO}})^1(\pi^*_{y,\mathrm{MO}})^1(\sigma^*_{\mathrm{MO}})^0(\mathrm{d}_{x^2-y^2})^1$	1.82	1.91	1.91	1.97	1.07	1.07	0.019	1.00
		0.031	$(\sigma_{\mathrm{MO}})^1(\pi_{x,\mathrm{MO}})^1(\pi_{y,\mathrm{MO}})^2(\mathrm{d}_{xy})^2(\pi^*_{x,\mathrm{MO}})^2(\pi^*_{y,\mathrm{MO}})^1(\sigma^*_{\mathrm{MO}})^1(\mathrm{d}_{x^2-y^2})^1$								
		0.031	$(\sigma_{\mathrm{MO}})^1(\pi_{x,\mathrm{MO}})^2(\pi_{y,\mathrm{MO}})^1(\mathrm{d}_{xy})^2(\pi^*_{x,\mathrm{MO}})^1(\pi^*_{y,\mathrm{MO}})^2(\sigma^*_{\mathrm{MO}})^1(\mathrm{d}_{x^2-y^2})^1$								
		0.030	$(\sigma_{\mathrm{MO}})^0(\pi_{x,\mathrm{MO}})^2(\pi_{y,\mathrm{MO}})^2(\mathrm{d}_{xy})^2(\pi^*_{x,\mathrm{MO}})^1(\pi^*_{y,\mathrm{MO}})^1(\sigma^*_{\mathrm{MO}})^2(\mathrm{d}_{x^2-y^2})^1$								
Ni	5	0.834	$(\sigma_{\mathrm{MO}})^2(\pi_{x,\mathrm{MO}})^2(\pi_{y,\mathrm{MO}})^2(\mathrm{d}_{xy})^2(\pi^*_{x,\mathrm{MO}})^1(\pi^*_{y,\mathrm{MO}})^1(\sigma^*_{\mathrm{MO}})^1(\mathrm{d}_{x^2-y^2})^1$	1.91	1.90	1.90	1.98	1.08	1.08	1.07	1.01
		0.036	$(\sigma_{\mathrm{MO}})^2(\pi_{x,\mathrm{MO}})^1(\pi_{y,\mathrm{MO}})^1(\mathrm{d}_{xy})^1(\pi^*_{x,\mathrm{MO}})^2(\pi^*_{y,\mathrm{MO}})^2(\sigma^*_{\mathrm{MO}})^1(\mathrm{d}_{x^2-y^2})^0$								
		0.029	$(\sigma_{\mathrm{MO}})^1(\pi_{x,\mathrm{MO}})^1(\pi_{y,\mathrm{MO}})^2(\mathrm{d}_{xy})^1(\pi^*_{x,\mathrm{MO}})^2(\pi^*_{y,\mathrm{MO}})^1(\sigma^*_{\mathrm{MO}})^2(\mathrm{d}_{x^2-y^2})^0$								
		0.029	$(\sigma_{\mathrm{MO}})^1(\pi_{x,\mathrm{MO}})^2(\pi_{y,\mathrm{MO}})^1(\mathrm{d}_{xy})^1(\pi^*_{x,\mathrm{MO}})^1(\pi^*_{y,\mathrm{MO}})^2(\sigma^*_{\mathrm{MO}})^2(\mathrm{d}_{x^2-y^2})^0$								

[a] σ_{MN} is doubly occupied in all principal configurations and omitted to save space.
[b] σ_{MN} has an occupancy ≥ 1.97 for all species and is omitted to save space.

Table E.12: CASSCF Ground States for MP(OOH).

Metal	$2S+1$	Weight	Principal Configurations	Natural Orbital Occupations							
				σ_{MN}	σ_{MO}	π_{MO}	d_{xy}	π^*_{MO}	$\mathrm{d}_{xz/yz}$	σ^*_{MO}	$\mathrm{d}_{x^2-y^2}$
Mn	5	0.942	$(\sigma_{\mathrm{MN}})^2(\sigma_{\mathrm{MO}})^2(\pi_{\mathrm{MO}})^2(\mathrm{d}_{xy})^1(\pi^*_{\mathrm{MO}})^1(\mathrm{d}_{xz/yz})^1(\sigma^*_{\mathrm{MO}})^1(\mathrm{d}_{x^2-y^2})^0$	1.96	1.98	1.98	0.99	1.00	1.00	0.99	0.04
Fe	6	0.962	$(\sigma_{\mathrm{MN}})^2(\sigma_{\mathrm{MO}})^2(\pi_{\mathrm{MO}})^2(\mathrm{d}_{xy})^1(\pi^*_{\mathrm{MO}})^1(\mathrm{d}_{xz/yz})^1(\sigma^*_{\mathrm{MO}})^1(\mathrm{d}_{x^2-y^2})^1$	2.00	1.97	1.98	1.00	1.00	1.00	1.00	1.00
Co	1	0.867	$(\sigma_{\mathrm{MN}})^2(\sigma_{\mathrm{MO}})^2(\pi_{\mathrm{MO}})^2(\mathrm{d}_{xy})^2(\pi^*_{\mathrm{MO}})^2(\mathrm{d}_{xz/yz})^2(\sigma^*_{\mathrm{MO}})^0(\mathrm{d}_{x^2-y^2})^0$	1.98	1.84	1.99	1.98	1.97	1.97	0.17	0.05
		0.063	$(\sigma_{\mathrm{MN}})^2(\sigma_{\mathrm{MO}})^0(\pi_{\mathrm{MO}})^2(\mathrm{d}_{xy})^2(\pi^*_{\mathrm{MO}})^2(\mathrm{d}_{xz/yz})^2(\sigma^*_{\mathrm{MO}})^2(\mathrm{d}_{x^2-y^2})^0$								
Ni	2	0.897	$(\sigma_{\mathrm{MN}})^2(\sigma_{\mathrm{MO}})^2(\pi_{\mathrm{MO}})^1(\mathrm{d}_{xy})^2(\pi^*_{\mathrm{MO}})^2(\mathrm{d}_{xz/yz})^2(\sigma^*_{\mathrm{MO}})^2(\mathrm{d}_{x^2-y^2})^0$	1.99	1.99	1.02	1.99	1.97	1.97	1.96	0.07

Table E.9 shows that all of the bare metalloporphyrin ground states have leading configuration weights over 0.9, providing good support for them being single-reference and amenable to study with CCSD(T).

For the OH ligands (Table E.10), CoP(OH) and NiP(OH) show mild-to-moderate multiconfigurational character. In CoP(OH), this arises primarily from a double excitation from the metal-oxygen σ orbital to its antibonding counterpart. This type of correlation is typical for covalently bonded complexes.[53, 37] NiP(OH) is still largely single reference, but there is a non-trivial contribution from a single excitation from the metal-nitrogen σ bond to its antibonding counterpart.

The MP(O) complexes (Table E.11) all exhibit moderate multiconfigurational character. They are all dominated by a single configuration, but non-trivial contributions also come from excitations between metal-oxygen bonding and antibonding orbitals which results in a rather low weight for the leading configuration. The CoP(O) complex demonstrates the largest multiconfigurational character, which aligns with the difficulties we had with using double-hybrid functionals that are described in Sections 6.3.2 and 6.3.4 in the main text.

The MP(OOH) complexes (Table E.12) exhibit behavior very similar to MP(OH) complexes.

Based on a combination of the strong metrics derived from the DLPNO-CC wave functions and the weights of leading CASSCF configurations, we believe the application of DLPNO-CCSD(T) is an appropriate approach for benchmarking DFT functionals in the present study. In particular, we expect DLPNO-CCSD(T) to perform very well for the MP(OH) and MP(OOH) intermediates, where multiconfigurational character is generally mild. The MP(O) intermediates all show electronic structures dominated by single electronic configurations, albeit with somewhat low weights due to the presence of multiple additional configurations with small but non-negligible contributions. Thus, we still expect DLPNO-CC to perform well based on the strong performance of canonical coupled cluster for other systems in a similar correlation regime.[56, 57] Further study on the multiconfigurational character of these systems could be beneficial in a future contribution.

E.10 Geometric Parameters

As noted in the main text, B2PLYP exhibited some difficulty converging a handful of geometries. Generally, when these geometries were useful for the assessment of a

ground state spin and seemed close to a converged structure, we included them in our analysis by picking the lowest energy structure along the optimization trajectory. Table E.13 lists these structures which were used despite not being fully converged.

Table E.13: List of B2PLYP geometries that were included in our analysis but did not reach force convergence thresholds and showed small energy oscillations.

Metal	Ligand	Multiplicity
Co	O	2
Co	O_2	2
Co	O_2	4
Co	OOH	3
Fe	O	1
Fe	O	3
Ni	O	3
Ni	OH	2
Ni	OH	4
Ni	OH	6

In addition, the $CoP(O_2)$ structure with multiplicity 6 would not converge for most functionals, and for these functionals, it was excluded from our analysis. Two additional B2PLYP structures also would not converge. As they were not relevant for the assignment of the ground state spin multiplicity, we also omitted them from our analysis. All structures which were omitted from analysis because they would not converge are listed in Table E.14.

Table E.14: List of geometries that were not included in any analysis because they did not converge and had energies well above the ground state.

Metal	Ligand	Multiplicity	Functional
Co	O	6	B2PLYP
Co	O_2	6	B3LYP
Co	O_2	6	BP86
Co	O_2	6	PBE
Co	O_2	6	PBE0
Co	O_2	6	TPSSh
Mn	O	6	B2PLYP

E.10.1 Metal–Oxygen Bonds

Figure E.8 shows how metal-oxygen bond lengths varied with different functionals across all intermediates. For the $MP(O_2)$ and MP(OOH) intermediates, the shortest metal-oxygen interatomic distance is reported.

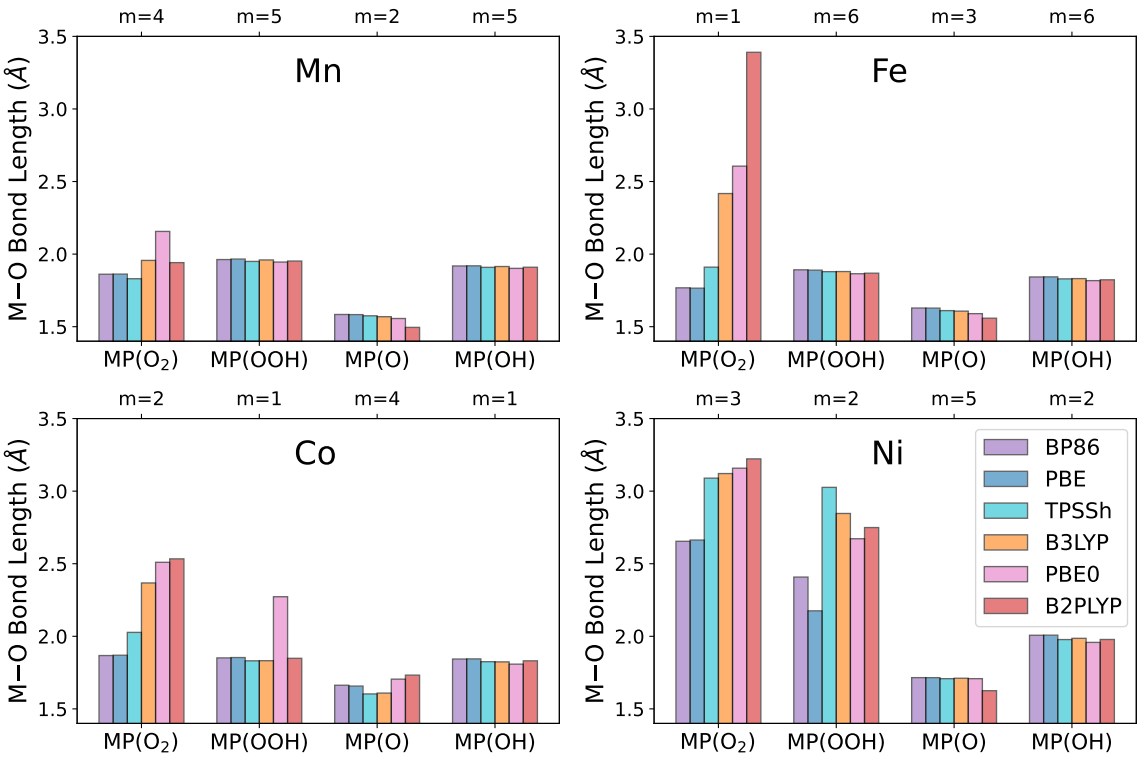

Figure E.8: Metal-Oxygen bond lengths for ground state structures computed with each functional.

E.10.2 Metal–Nitrogen Bonds

Figure E.9 shows how metal-nitrogen bond lengths varied with different functionals across all intermediates. The mean of all four metal-nitrogen bonds is reported for each structure.

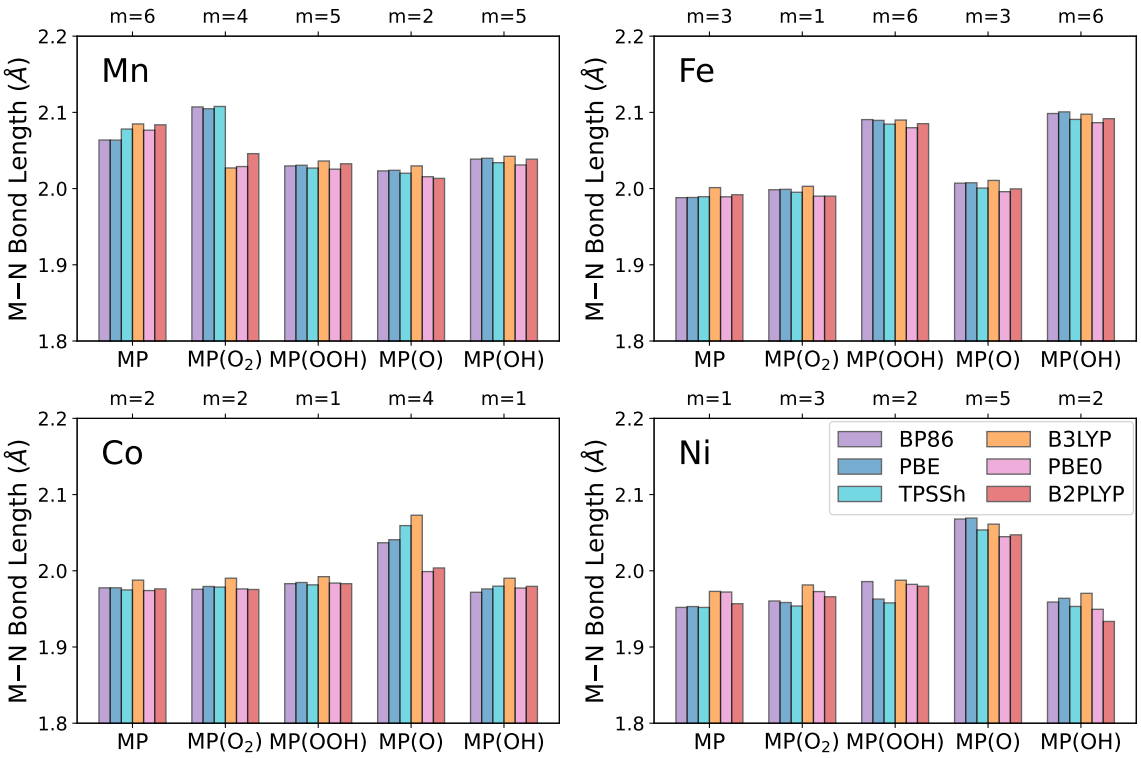

Figure E.9: Metal-Nitrogen bond lengths for ground state structures computed with each functional.

E.10.3 Distance from Metal To the Porphyrin Plane

For some intermediates, the metal atom lifts out of the plane formed by the coordinating nitrogens, toward the bound oxygen. We quantified this displacement by finding the plane that best fits the four nitrogen atoms through least squares fitting and finding the distance from the metal to this fit plane.

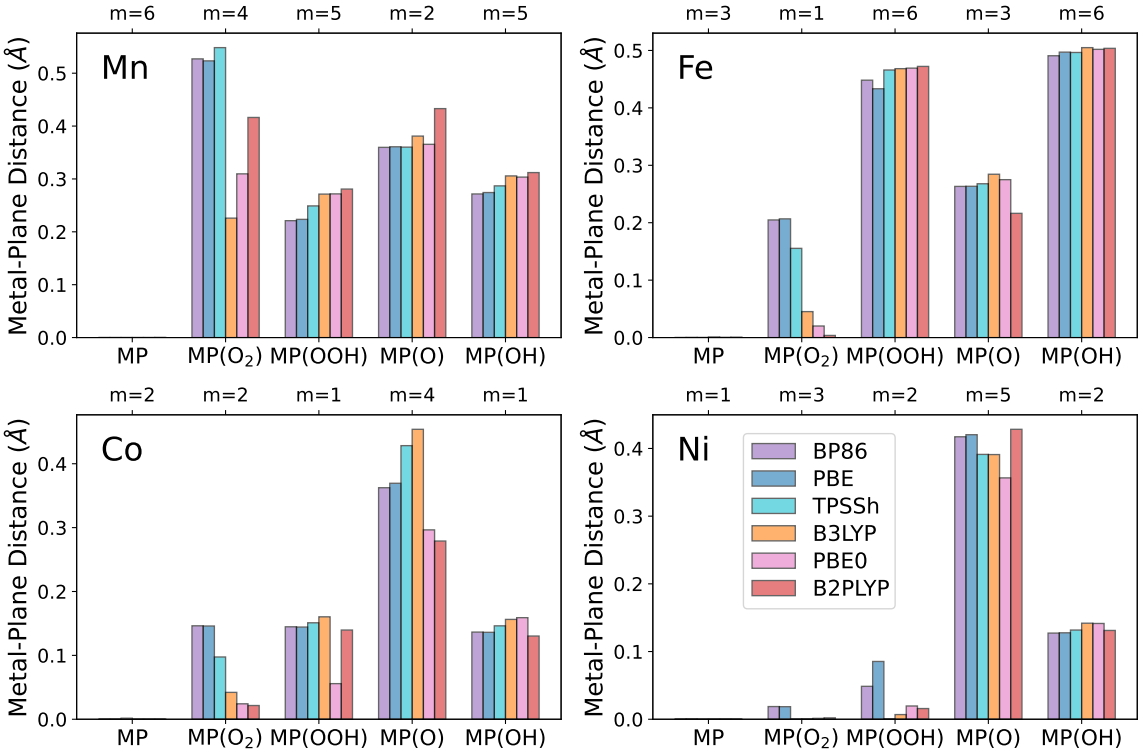

Figure E.10: Metal displacement from nitrogen plane for ground state structures computed with each functional.

E.10.4 Nonplanarity of the Carbon Macrocycle

Some porphyrin intermediates are saddle-shaped rather than planar. In order to quantify the deviation from ideal planarity, we fit a plane to the 20 carbon atoms in the porphyrin macrocycle using least squares fitting. The mean absolute displacement of the carbon atoms from this plane is used as a measure of nonplanarity.

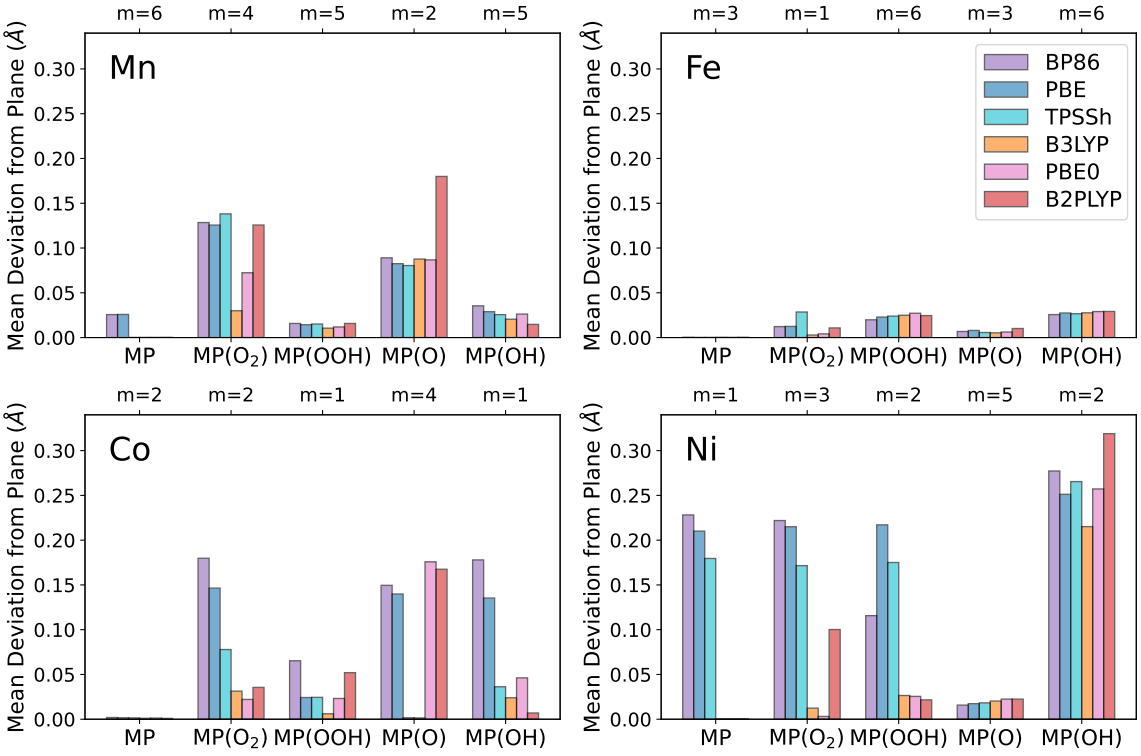

Figure E.11: Nonplanarity of the carbon macrocycle for ground state structures computed with each functional.

E.10.5 Pairwise Agreement Between Functionals for Geometrical Parameters

For each of the geometrical parameters mentioned above (M–O bond length, M–N bond length, metal–porphyrin plane distance, and Nonplanarity of the porphyrin), we calculated the Mean Absolute Deviation (MAD) between the predictions of all pairs of functionals across all intermediates and tested spin states (Figure E.12).

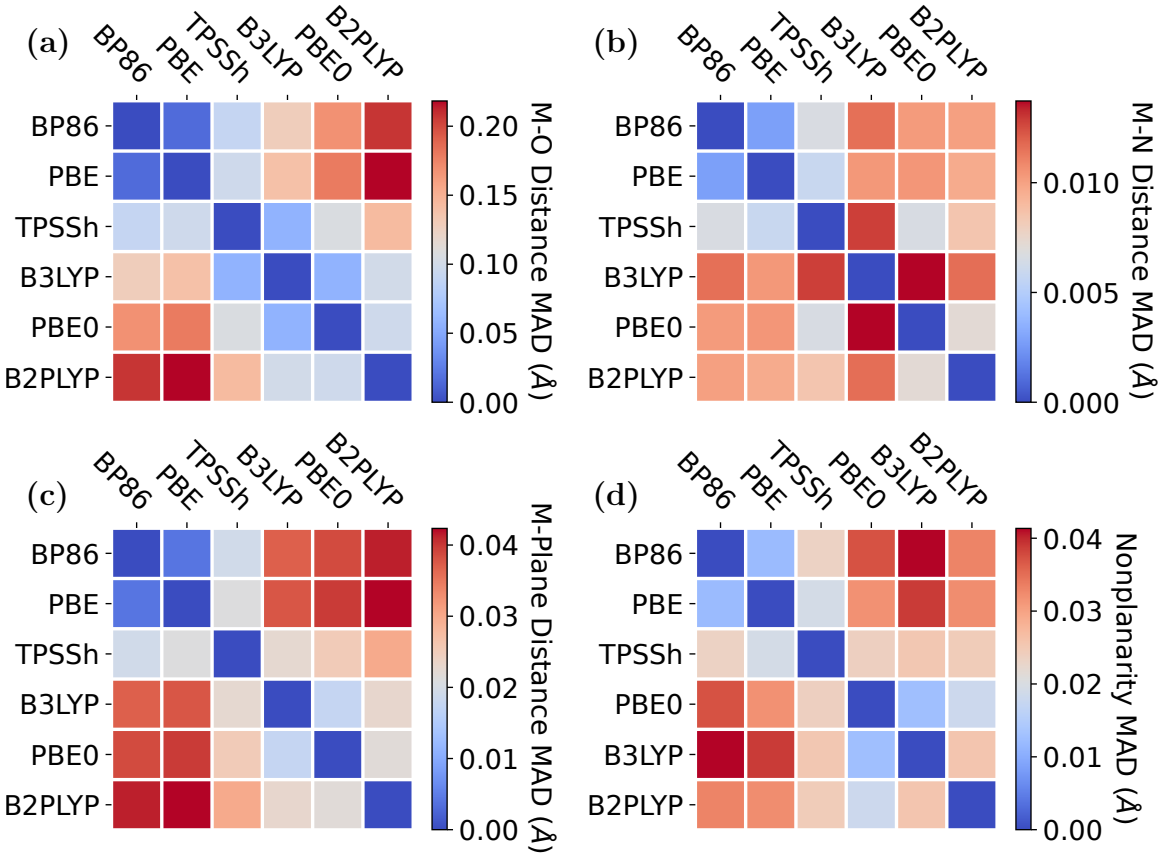

Figure E.12: Agreement between pairs of functionals for different geometrical parameters. Mean absolute Deviation (MAD) between pairs of functionals across all applicable intermediates and spin states for **(a)** M–O bond length, **(b)** M–N bond length, **(c)** Metal displacement from porphyrin plane, and **(d)** Nonplanarity of porphyrin.

M–O bond distance displace both the most variability between functionals in terms of MAD and the most obvious agreement within rungs of Jacob's ladder. For instance, PBE and B2PLYP predict M-O bond lengths that differ by an average of about 0.2 Å. However, MADs between pairs of GGA functionals (and TPSSh) or pairs of hybrid

functionals tend to be significantly lower than this (a blue block in the upper left of the plot and another block of blue in the middle of the plot). For the other geometric parameters, the agreement between PBE and BP86 tends to be strong across the board. However, the *relative* agreement between hybrid functionals is lower than in the M–O case. We emphasize *relative* agreement because these parameters tend to have less absolute variability than M–O bond lengths (note the smaller range of color scales for Figure E.12 (b)-(d)).

E.11 Vibrational Contributions

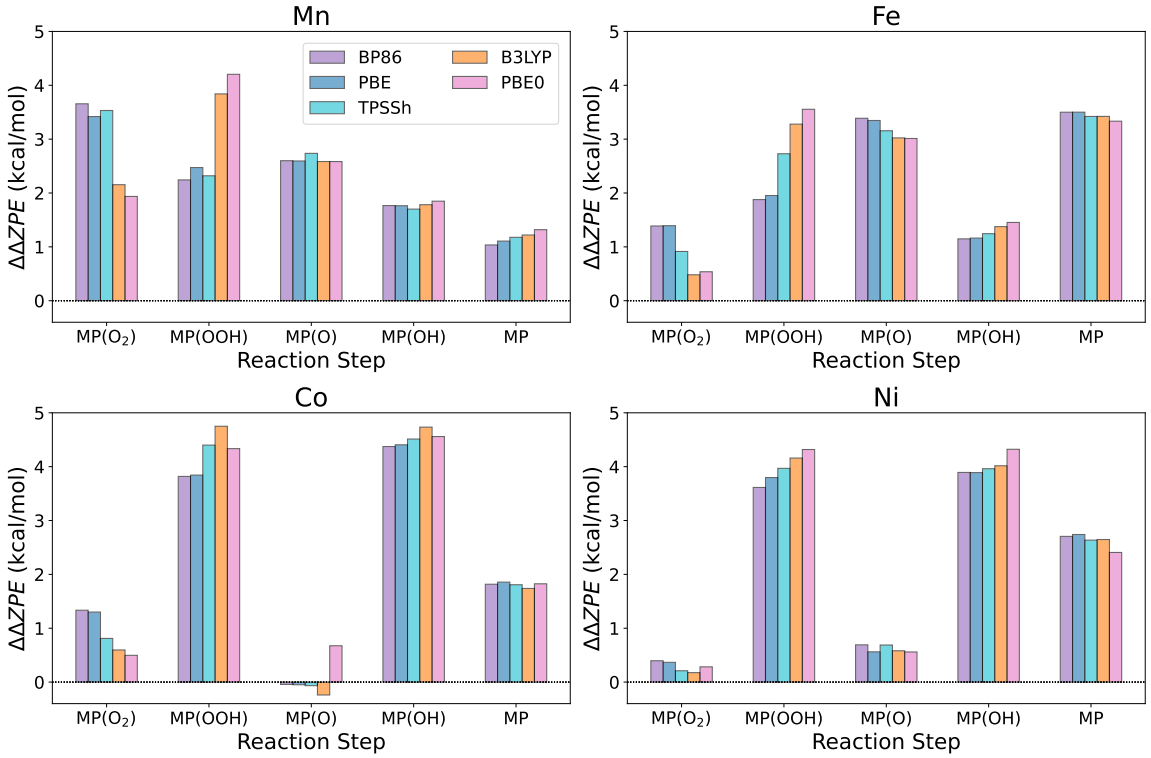

Figure E.13: $\Delta\Delta ZPE$ values for the steps of the 4-electron ORR pathway with with Mn-, Fe-, Co-, and Ni-porphyrins. Steps are labeled by the porphyrin intermediate formed as a product in that step. Geometries are optimized separately for each functional and the multiplicities are the ground state multiplicities from Table 6.2 in the main text.

The common assumption that the vibrational energies will be largely unaffected by the choice of functional holds true for the present catalysts. The change in zero point energies for each reaction step ($\Delta\Delta$ZPE) in Equations (6.1)(a)-(6.1)(e) of the

main text are plotted in Figure E.13. Even with differences in predicted geometries (i.e. using the structures optimized for each functional), the zero point corrections for reaction steps only varied by about 2 kcal / mol (0.09 eV) between functionals in the worst cases. Typical discrepancies were significantly lower. As a result, we do not consider ZPE a major contributor to the dependence of theoretical overpotentials on functional in the present context.

E.12 ORCA Calculation Parameters and Example Input Files

All DFT calculations were performed using the RIJCOSX approximation, which uses the resolution of identity approximation to calculate coulomb integrals and COSX numerical integration for exchange integrals (when exact exchange is included). The Weigend auxiliary basis sets (def2/J) were used for coulomb fitting. B2PLYP and PWPB95 calculations also used the resolution of identity for approximating MP2 correlation integrals (RI-B2PLYP in ORCA nomenclature), using the auxiliary basis set corresponding to the primary basis set (e.g. def2-TZVP/C when def2-TZVP was used). The frozen core approximation was used for MP2 calculations, which is the default in ORCA. Optimizations were performed with TighTSCF and TightOPT thresholds.

E.12.1 OPT / FREQ Input File

```
!UKS B3LYP D3BJ RIJCOSX def2-tzvp def2/J TightSCF TIGHTOPT FREQ
%maxcore 3500
%scf
  MaxIter 300
end
*xyzfile 0 6 input.xyz
%PAL
  NPROCS 28
END
```

E.12.2 DFT Single Point Input File

```
!UKS B3LYP D3BJ RIJCOSX def2-qzvpp def2/J TightSCF UNO UCO MOREAD
%moinp "guess.gbw"
%maxcore 3500
%scf
  MaxIter 300
  StabPerform True
end
*xyzfile 0 6 input.xyz
%PAL
  NPROCS 28
END
```

E.12.3 RO-B2PLYP Single Point Input File

```
!ROKS RI-B2PLYP D3BJ RIJONX def2-qzvpp def2/J def2-QZVPP/C
!TightSCF MOREAD
%maxcore 3500
%moinp "guess.gbw"
%scf
  MaxIter 300
end
*xyzfile 0 6 input.xyz
%PAL
  NPROCS 28
END
```

E.12.4 DLPNO-CCSD(T) Spin Splitting

Metal with QZ Basis

```
!UKS TPSSh NORI DLPNO-CCSD(T1) def2-svp def2-svp/C
!VeryTightSCF NormalPNO MOREAD
%moinp "guess.gbw"
%base "ccsdt"
%maxcore 20000
```

```
%basis
 newgto O "def2-TZVP" end
 newgto N "def2-TZVP" end
 newgto Fe "def2-QZVPP" end
 newauxcgto Fe "def2-QZVPP/C" end
 newauxcgto O "def2-TZVP/C" end
 newauxcgto N "def2-TZVP/C" end
end
%scf
  MaxIter 300
  DIISMaxEq 10
  StabPerform True
end
%mdci
  UseQROs true
  TCutTNO 5.0e-9
end
*xyzfile 0 6 input.xyz
%PAL
  NPROCS 8
END
```

Metal with TZ Basis

```
!UKS TPSSh NORI DLPNO-CCSD(T1) def2-svp def2-svp/C
!VeryTightSCF NormalPNO MOREAD
%moinp "guess.gbw"
%base "ccsdt"
%maxcore 20000
%basis
 newgto O "def2-TZVP" end
 newgto N "def2-TZVP" end
 newgto Fe "def2-TZVPP" end
 newauxcgto Fe "def2-TZVPP/C" end
 newauxcgto O "def2-TZVP/C" end
```

```
 newauxcgto N "def2-TZVP/C" end
end
%scf
  MaxIter 300
  DIISMaxEq 10
  StabPerform True
end
%mdci
  UseQROs true
  TCutTNO 5.0e-9
end
*xyzfile 0 6 input.xyz
%PAL
  NPROCS 8
END
```

Metal with TZ Basis and Loose TCutPNO Threshold

```
!UKS TPSSh NORI DLPNO-CCSD(T1) def2-svp def2-svp/C
!VeryTightSCF NormalPNO MOREAD
%moinp "guess.gbw"
%base "ccsdt"
%maxcore 20000
%basis
 newgto O "def2-TZVP" end
 newgto N "def2-TZVP" end
 newgto Fe "def2-TZVPP" end
 newauxcgto Fe "def2-TZVPP/C" end
 newauxcgto O "def2-TZVP/C" end
 newauxcgto N "def2-TZVP/C" end
end
%scf
  MaxIter 300
  DIISMaxEq 10
  StabPerform True
```

```
end
%mdci
  UseQROs true
  TCutTNO 5.0e-9
  TCutPNO 1.0e-6
end
*xyzfile 0 6 input.xyz
%PAL
  NPROCS 8
END
```

E.12.5 DLPNO-CCSD(T) Binding Energy

Metal with DZ Basis

```
!UKS NORI TPSSh DLPNO-CCSD(T1) aug-cc-pvdz
!VeryTightSCF aug-cc-pvdz/C NormalPNO UNO UCO  MOREAD
%moinp "guess.gbw"
%base "ccsdt"
%maxcore 12000
%basis
newauxcgto Fe "AutoAux" end
end
%mdci
  MaxIter 150
  UseQROs true
  TCutTNO 5e-9
end
*xyzfile 0 6 input.xyz
%PAL
  NPROCS 16
END
```

Metal with TZ Basis

```
!UKS NORI TPSSh DLPNO-CCSD(T1) aug-cc-pvtz
```

```
!VeryTightSCF aug-cc-pvtz/C NormalPNO UNO UCO MOREAD
%moinp "guess.gbw"
%base "ccsdt"
%maxcore 12000
%scf
  MaxIter 300
  DIISMaxEq 10
  StabPerform True
end
%mdci
  UseQROs true
  TCutTNO 5e-9
end
*xyzfile 0 6 input.xyz
%PAL
  NPROCS 16
END
```

Metal with TZ Basis and Loose TCutPNO Threshold

```
!UKS NORI TPSSh DLPNO-CCSD(T1) aug-cc-pvtz
!VeryTightSCF aug-cc-pvtz/C NormalPNO UNO UCO MOREAD
%moinp "guess.gbw"
%base "ccsdt"
%maxcore 12000
%scf
  MaxIter 300
  DIISMaxEq 10
  StabPerform True
end
%mdci
  UseQROs true
  TCutTNO 5e-9
  TCutPNO 1.0e-6
end
```

```
*xyzfile 0 6 input.xyz
%PAL
  NPROCS 16
END
```

Bibliography

[1] J. K. Nørskov, J. Rossmeisl, A. Logadottir, L. Lindqvist, J. R. Kitchin, T. Bligaard, and H. Jónsson. Origin of the overpotential for oxygen reduction at a fuel-cell cathode. *The Journal of Physical Chemistry B*, 108(46):17886–17892, 2004.

[2] Federico Calle-Vallejo, José Ignacio Martínez, and Jan Rossmeisl. Density functional studies of functionalized graphitic materials with late transition metals for oxygen reduction reactions. *Physical Chemistry Chemical Physics*, 13(34):15639, 2011.

[3] F. Calle-Vallejo, J.I. Martínez, J.M. García-Lastra, E. Abad, and M.T.M. Koper. Oxygen reduction and evolution at single-metal active sites: Comparison between functionalized graphitic materials and protoporphyrins. *Surface Science*, 607:47–53, January 2013.

[4] Jakub D. Baran, Henrik Grönbeck, and Anders Hellman. Analysis of porphyrines as catalysts for electrochemical reduction of o2 and oxidation of h2o. *Journal of the American Chemical Society*, 136(4):1320–1326, January 2014.

[5] Federico Calle-Vallejo, Alexander Krabbe, and Juan M. García-Lastra. How covalence breaks adsorption-energy scaling relations and solvation restores them. *Chemical Science*, 8(1):124–130, 2017.

[6] Anjli M. Patel, Stefan Ringe, Samira Siahrostami, Michal Bajdich, Jens K. Nørskov, and Ambarish R. Kulkarni. Theoretical approaches to describing the oxygen reduction reaction activity of single-atom catalysts. *The Journal of Physical Chemistry C*, 122(51):29307–29318, November 2018.

[7] Qiang Zhang and Aravind Asthagiri. Solvation effects on dft predictions of orr activity on metal surfaces. *Catalysis Today*, 323:35–43, February 2019.

[8] Kiran Mathew, Ravishankar Sundararaman, Kendra Letchworth-Weaver, T. A. Arias, and Richard G. Hennig. Implicit solvation model for density-functional study of nanocrystal surfaces and reaction pathways. *The Journal of Chemical Physics*, 140(8), February 2014.

[9] Miquel Garcia-Ratés, Ute Becker, and Frank Neese. Implicit solvation in domain based pair natural orbital coupled cluster (dlpno-ccsd) theory. *Journal of Computational Chemistry*, 42(27):1959–1973, August 2021.

[10] Ruguang Ma, Gaoxin Lin, Yao Zhou, Qian Liu, Tao Zhang, Guangcun Shan, Minghui Yang, and Jiacheng Wang. A review of oxygen reduction mechanisms for metal-free carbon-based electrocatalysts. *npj Computational Materials*, 5(1), July 2019.

[11] Elizabeth Sargeant, Francesc Illas, Paramaconi Rodríguez, and Federico Calle-Vallejo. Importance of the gas-phase error correction for o2 when using dft to model the oxygen reduction and evolution reactions. *Journal of Electroanalytical Chemistry*, 896:115178, September 2021.

[12] Brian E. Conway, John O'M. Bockris, Ernest Yeager, Shahed U. M. Khan, and Ralph E. White, editors. *Comprehensive Treatise of Electrochemistry*, volume 7. Springer New York, NY, 1983.

[13] Steven G. Bratsch. Standard electrode potentials and temperature coefficients in water at 298.15 k. *Journal of Physical and Chemical Reference Data*, 18(1):1–21, January 1989.

[14] Ambarish Kulkarni, Samira Siahrostami, Anjli Patel, and Jens K. Nørskov. Understanding catalytic activity trends in the oxygen reduction reaction. *Chemical Reviews*, 118(5):2302–2312, February 2018.

[15] James Shee, Benjamin Rudshteyn, Evan J. Arthur, Shiwei Zhang, David R. Reichman, and Richard A. Friesner. On achieving high accuracy in quantum chemical calculations of 3d transition metal-containing systems: A comparison of auxiliary-field quantum monte carlo with coupled cluster, density functional theory, and experiment for diatomic molecules. *Journal of Chemical Theory and Computation*, 15(4):2346–2358, March 2019.

[16] Klaus A. Moltved and Kasper P. Kepp. Performance of density functional theory for transition metal oxygen bonds. *ChemPhysChem*, 20(23):3210–3220, October 2019.

[17] Wanyi Jiang, Marie L. Laury, Mitchell Powell, and Angela K. Wilson. Comparative study of single and double hybrid density functionals for the prediction of 3d transition metal thermochemistry. *Journal of Chemical Theory and Computation*, 8(11):4102–4111, September 2012.

[18] Sebastian Dohm, Andreas Hansen, Marc Steinmetz, Stefan Grimme, and Marek P. Checinski. Comprehensive thermochemical benchmark set of realistic closed-shell metal organic reactions. *Journal of Chemical Theory and Computation*, 14(5):2596–2608, March 2018.

[19] Leonard R. Maurer, Markus Bursch, Stefan Grimme, and Andreas Hansen. Assessing density functional theory for chemically relevant open-shell transition metal reactions. *Journal of Chemical Theory and Computation*, 17(10):6134–6151, September 2021.

[20] Fang Liu, Tzuhsiung Yang, Jing Yang, Eve Xu, Akash Bajaj, and Heather J. Kulik. Bridging the homogeneous-heterogeneous divide: Modeling spin for reactivity in single atom catalysis. *Frontiers in Chemistry*, 7:219, April 2019.

[21] Noa Marom and Leeor Kronik. Density functional theory of transition metal phthalocyanines, i: electronic structure of nipc and copc—self-interaction effects. *Applied Physics A*, 95(1):159–163, April 2009.

[22] Noa Marom and Leeor Kronik. Density functional theory of transition metal phthalocyanines, ii: electronic structure of mnpc and fepc—symmetry and symmetry breaking. *Applied Physics A*, 95(1):165–172, April 2009.

[23] Mariusz Radoń and Kristine Pierloot. Binding of CO, NO, and o_2 to heme by density functional and multireference ab initio calculations. *The Journal of Physical Chemistry A*, 112(46):11824–11832, October 2008.

[24] Sebastian Ovalle and Cecile Malardier-Jugroot. Choice of functional for iron porphyrin density functional theory studies: Geometry, spin-state, and binding energy analysis. *Computational and Theoretical Chemistry*, 1213:113726, July 2022.

[25] Qin Wu, Guangjin Wang, and Mingjie Liu. On the sensitivity to density-functional approximations for co binding energies of single-atom catalysts in nitrogen-doped graphene. *ChemPhysChem*, 23(5):e202100787, February 2022.

[26] Michael Busch, Alberto Fabrizio, Sandra Luber, Jürg Hutter, and Clemence Corminboeuf. Exploring the limitation of molecular water oxidation catalysts. *The Journal of Physical Chemistry C*, 122(23):12404–12412, May 2018.

[27] Tyler Sours, Anjli Patel, Jens Nørskov, Samira Siahrostami, and Ambarish Kulkarni. Circumventing scaling relations in oxygen electrochemistry using metal–organic frameworks. *The Journal of Physical Chemistry Letters*, 11(23):10029–10036, November 2020.

[28] Rick A. Kendall, Thom H. Dunning, and Robert J. Harrison. Electron affinities of the first-row atoms revisited. systematic basis sets and wave functions. *The Journal of Chemical Physics*, 96(9):6796–6806, May 1992.

[29] Nikolai B. Balabanov and Kirk A. Peterson. Systematically convergent basis sets for transition metals. i. all-electron correlation consistent basis sets for the 3d elements sc–zn. *The Journal of Chemical Physics*, 123(6):064107, August 2005.

[30] Nikolai B. Balabanov and Kirk A. Peterson. Basis set limit electronic excitation energies, ionization potentials, and electron affinities for the 3d transition metal atoms: Coupled cluster and multireference methods. *The Journal of Chemical Physics*, 125(7):074110, August 2006.

[31] Frank Neese and Edward F. Valeev. Revisiting the atomic natural orbital approach for basis sets: Robust systematic basis sets for explicitly correlated and conventional correlated *ab initio* methods? *Journal of Chemical Theory and Computation*, 7(1):33–43, December 2010.

[32] Mariusz Radoń. Spin-state energetics of heme-related models from dft and coupled cluster calculations. *Journal of Chemical Theory and Computation*, 10(6):2306–2321, May 2014.

[33] Maria Drosou, Christiana A. Mitsopoulou, and Dimitrios A. Pantazis. Reconciling local coupled cluster with multireference approaches for transition metal spin-state energetics. *Journal of Chemical Theory and Computation*, 18(6):3538–3548, May 2022.

[34] Thom H. Dunning. Gaussian basis sets for use in correlated molecular calculations. i. the atoms boron through neon and hydrogen. *The Journal of Chemical Physics*, 90(2):1007–1023, January 1989.

[35] Yang Guo, Christoph Riplinger, Dimitrios G. Liakos, Ute Becker, Masaaki Saitow, and Frank Neese. Linear scaling perturbative triples correction approximations for open-shell domain-based local pair natural orbital coupled cluster singles and doubles theory [DLPNO-CCSD(t/t)]. *The Journal of Chemical Physics*, 152(2):024116, January 2020.

[36] E. van Lenthe, J. G. Snijders, and E. J. Baerends. The zero-order regular approximation for relativistic effects: The effect of spin–orbit coupling in closed shell molecules. *The Journal of Chemical Physics*, 105(15):6505–6516, October 1996.

[37] Kristine Pierloot, Quan Manh Phung, and Alex Domingo. Spin state energetics in first-row transition metal complexes: Contribution of (3s3p) correlation and its description by second-order perturbation theory. *Journal of Chemical Theory and Computation*, 13(2):537–553, January 2017.

[38] Quan Manh Phung, Milica Feldt, Jeremy N. Harvey, and Kristine Pierloot. Toward highly accurate spin state energetics in first-row transition metal complexes: A combined caspt2/cc approach. *Journal of Chemical Theory and Computation*, 14(5):2446–2455, April 2018.

[39] Quan Manh Phung, Carlos Martín-Fernández, Jeremy N. Harvey, and Milica Feldt. Ab initio calculations for spin-gaps of non-heme iron complexes. *Journal of Chemical Theory and Computation*, 15(8):4297–4304, July 2019.

[40] James Shee, Matthias Loipersberger, Adam Rettig, Joonho Lee, and Martin Head-Gordon. Regularized second-order møller–plesset theory: A more accurate alternative to conventional mp2 for noncovalent interactions and transition metal thermochemistry for the same computational cost. *The Journal of Physical Chemistry Letters*, 12(50):12084–12097, December 2021.

[41] Quan Manh Phung and Kristine Pierloot. The dioxygen adducts of iron and manganese porphyrins: electronic structure and binding energy. *Physical Chemistry Chemical Physics*, 20(25):17009–17019, 2018.

[42] Markus Reiher, Oliver Salomon, and Bernd Artur Hess. Reparameterization of hybrid functionals based on energy differences of states of different multiplicity. *Theoretical Chemistry Accounts: Theory, Computation, and Modeling (Theoretica Chimica Acta)*, 107(1):48–55, December 2001.

[43] Antony Fouqueau, Mark E. Casida, Latévi Max Lawson Daku, Andreas Hauser, and Frank Neese. Comparison of density functionals for energy and structural differences between the high- [5t2g:(t2g)4(eg)2] and low- [1a1g:(t2g)6(eg)] spin states of iron(ii) coordination compounds. ii. more functionals and the hexaminoferrous cation, [fe(nh3)6]2+. *The Journal of Chemical Physics*, 122(4):044110, January 2005.

[44] Frank Neese. Prediction of molecular properties and molecular spectroscopy with density functional theory: From fundamental theory to exchange-coupling. *Coordination Chemistry Reviews*, 253(5-6):526–563, March 2009.

[45] Frank Jensen. A remarkable large effect of spin contamination on calculated vibrational frequencies. *Chemical Physics Letters*, 169(6):519–528, June 1990.

[46] Frank Neese. Definition of corresponding orbitals and the diradical character in broken symmetry DFT calculations on spin coupled systems. *Journal of Physics and Chemistry of Solids*, 65(4):781–785, April 2004.

[47] Timothy J. Lee and Peter R. Taylor. A diagnostic for determining the quality of single-reference electron correlation methods. *International Journal of Quantum Chemistry*, 36(23 S):199–207, apr 1989.

[48] Wanyi Jiang, Nathan J. DeYonker, and Angela K. Wilson. Multireference character for 3d transition-metal-containing molecules. *Journal of Chemical Theory and Computation*, 8(2):460–468, January 2012.

[49] Milica Feldt and Quan Manh Phung. Ab initio methods in first-row transition metal chemistry. *European Journal of Inorganic Chemistry*, 2022(15):e202200014, April 2022.

[50] Dimitrios G. Liakos and Frank Neese. Interplay of correlation and relativistic effects in correlated calculations on transition-metal complexes: The (cu2o2)2+ core revisited. *Journal of Chemical Theory and Computation*, 7(5):1511–1523, April 2011.

[51] Mariusz Radoń, Ewa Broclawik, and Kristine Pierloot. Dft and ab initio study of iron-oxo porphyrins: May they have a low-lying iron(v)-oxo electromer? *Journal of Chemical Theory and Computation*, 7(4):898–908, March 2011.

[52] Sergio Augusto Venturinelli Jannuzzi, Quan Manh Phung, Alex Domingo, André Luiz Barboza Formiga, and Kristine Pierloot. Spin state energetics and oxyl character of mn-oxo porphyrins by multiconfigurational ab initio calculations: Implications on reactivity. *Inorganic Chemistry*, 55(11):5168–5179, February 2016.

[53] Kristine Pierloot. The caspt2 method in inorganic electronic spectroscopy: from ionic transition metal to covalent actinide complexes*. *Molecular Physics*, 101(13):2083–2094, July 2003.

[54] Vijay Gopal Chilkuri and Frank Neese. Comparison of many-particle representations for selected-ci i: A tree based approach. *Journal of Computational Chemistry*, 42(14):982–1005, March 2021.

[55] Vijay Gopal Chilkuri and Frank Neese. Comparison of many-particle representations for selected configuration interaction: Ii. numerical benchmark calculations. *Journal of Chemical Theory and Computation*, 17(5):2868–2885, April 2021.

[56] Hagen Neugebauer, Hung T. Vuong, John L. Weber, Richard A. Friesner, James Shee, and Andreas Hansen. Toward benchmark-quality ab initio predictions for 3d transition metal electrocatalysts: A comparison of ccsd(t) and ph-afqmc. *Journal of Chemical Theory and Computation*, 19(18):6208–6225, September 2023.

[57] Gabriela Drabik, Janusz Szklarzewicz, and Mariusz Radoń. Spin-state energetics of metallocenes: How do best wave function and density functional theory results compare with the experimental data? *Physical Chemistry Chemical Physics*, 23(1):151–172, 2021.

Appendix F

Accessible Chemistry Web Tools

Throughout my time as a PhD student, I have been fortunate to work alongside members of the McIndoe group at the University of Victoria in helping them build accessible web tools for visualization and kinetics analysis. In these collaborations, I primarily took on the role of a software developer and not a chemist. Thus, I will provide only a brief overview of the three projects I have worked on in this capacity and point to references where the tools are more lengthily described.

F.1 Catacycle

Catacycle is a web tool conceived of by Prof. Scott McIndoe for encoding reaction rate information visually in the depiction of catalytic cycles. Based on an analogy to water flowing more freely through larger pipes, increasing arrow thickness for a step in the catalytic cycle drawing was proposed as a way to indicate larger rate constants for a given step. Aside from enabling the visual encoding of rate constants, the project aimed to make drawing catalytic cycles easier and more repeatable, without the need to fuss over arrow alignment or install any software on the user's computer.

James McFarlane led the initial development of a set of python modules for drawing customizable catalytic cycles, wherein users could specify rate constants that would be reflected in the resulting arrow thicknesses. I was then tasked with extending this codebase to allow further user control over the aesthetics of the resulting arrows and with continuing James' work of building a lightweight web application with Flask to allow users to generate catalytic cycles via a purely graphical interface. Sofia Dönnecke assisted with ideation, testing, and code development along

the way. The resulting website is freely available to the public at `catacycle.com`, and the python modules for generating cycles programmatically are available at `https://github.com/brettrhenderson/Catacycle`. Additionally, Scott McIndoe contributed the editorial "An Information-Rich Graphical Representation of Catalytic Cycles" to *Organometallics* detailing the use of the tool and discussing best practices for encoding rate constant information when, for example, different steps in the cycle have different order rate laws.[1] Figure F.1

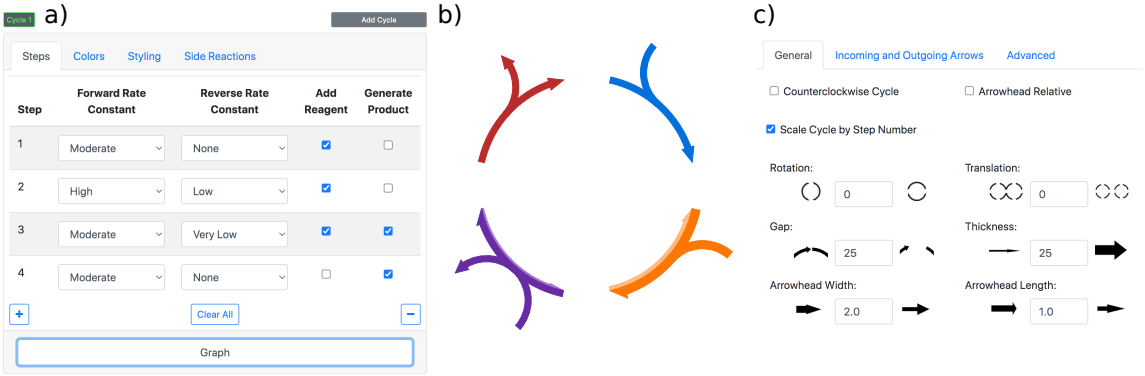

Figure F.1: Snapshot of the catacycle.com interface. Users input information about step rate, reversibility, and presence of ingoing or outgoing reagents in a web form (Panel **a)**). Note that users can also generate interlocking cycles via the "Add Cycle" button. The program generates a vector image of the cycle (Panel **b)**), which can be downloaded and decorated with molecular drawings of reagent. Panel **c)** shows some additional handles available for tweaking cycle appearance.

.

F.2 Continuous Addition Kinetic Elucidation

In a second project with the McIndoe group, I built a web-interface for a novel kinetic analysis methodology developed by Peter J.H. Williams, David Harrington, and Scott McIndoe. The methodology, called Continuous Addition Kinetic Elucidation (CAKE) uses a syringe pump to continuously add one species, typically a catalyst, to a reaction mixture. Continuous monitoring of the reaction progress results in reaction trace shapes that are characteristic of a given reactant and catalyst order. Thus, the rate law for the reaction can be extracted from a single experiment, instead of requiring multiple experiments with different concentrations of catalyst and reactant. For reactions with a single yield-limiting reactant and catalyst, the CAKE curves can

be fit to analytically forms. Williams also implemented a CAKE analysis software in python which uses non-linear least-squares regression to fit experimental CAKE data to simulated CAKE experiments to determine the reactant and catalyst order as well as the rate constant. Moreover, the code is able to determine the amount of irreversible catalyst poisoning. The methodology was published in the article "Continuous addition kinetic elucidation: catalyst and reactant order, rate constant, and poisoning from a single experiment" in *Chemical Science*,[2]

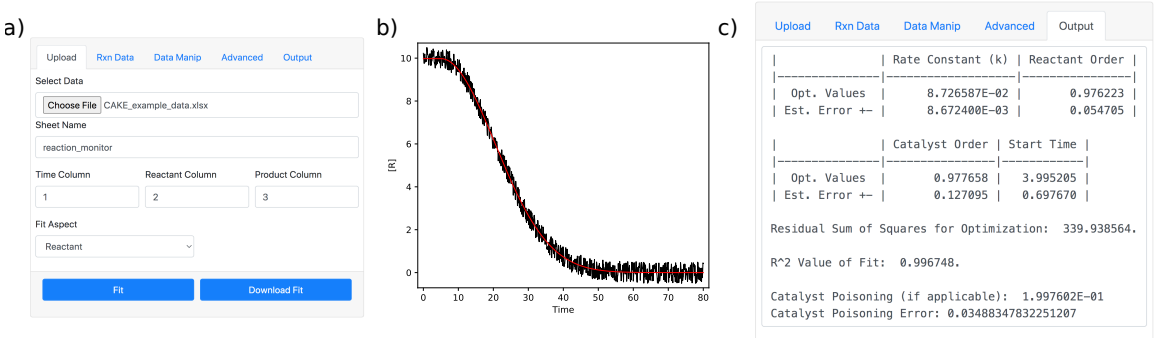

Figure F.2: Snapshot of the CAKE web interface. Users input information about the CAKE experiment in a web form (Panel **a)**). The program generates a best-fit to the experimental data (Panel **b)**, from which the rate constant and catalyst and reactant orders can be extracted (Panel **c)**). The fit in this figure is generated from the simulated data provided at `https://mcindoe.pythonanywhere.com/user-guide`. The fit plots in **b)** show simulated reactant concentrations in black, with the best-fit curves in red.

I was tasked with building a lightweight Flask application to make the CAKE analysis code (`https://github.com/peterjhw07/cake`) more accessible (it should be noted that I did not participate in the development of the method itself nor the writing of the article introducing it). The resulting application exposes most of the methods available in the python code via a fully graphical interface. The interface was chosen to be very similar to that of Catacycle. Users upload pre-formatted CAKE reaction data in an Excel sheet and then populate a web form with information about the reactants and catalyst as well as different parameters for smoothing and fitting the CAKE curves. The code then outputs the fitted curves and fit parameters, as shown in Figure F.2. The CAKE code and web interface also allow users to simulate CAKE reactions, which can be useful for planning the catalyst infusion rates and sampling timescales required to collect nice-looking experimental data. The version of the web that was available at the time of publishing Ref [2] is freely available

at `https://mcindoe.pythonanywhere.com/cake_old`. This version allows a single reactant and catalyst order and catalyst poisoning to be fit, as discussed in the original CAKE article. A development version with support for fitting orders of multiple reactants, is available at `catacycle.com/cake`.

F.3 Automated Variable Time Normalization Analysis

In this final project with the McIndoe group, I worked alongside Sofia Dönnecke to develop a python-based tool for automating the popular graphical kinetic analysis method known as Variable Time Normalization Analysis.[3] Much of the work was undertaken in 2021, but it was eventually sidelined in favor of development of the novel CAKE methodology and was never published. In recent months, two reports of other automated VTNA tools have appeared in the literature.[4, 5] Thus, while our implementation of an automated VTNA tool will likely remain in development limbo, this section will report briefly on its status. The knowledge gained in its development may aid in future contributions to the other published automated VTNA implementations (`https://gitlab.com/heingroup/kinalite` and `https://github.com/ddalland/Auto-VTNA`.

VTNA was proposed as a user-friendly method to minimize the number of experiments needed to derive reaction rate laws in an age where sophisticated reaction monitoring techniques allow the extraction of detailed reaction profiles. In VTNA, reaction profiles obtained using two different concentrations of a given reagent R are plotted on the same graph. The time axis of the graph is "normalized" by taking it to be the following time integral

$$\int_{t=0}^{n} [R]^{\alpha} dt \approx \sum_{i=1}^{n} \left(\frac{[R]_i + [R]_{i-1}}{2} \right)^{\alpha} (t_i - t_{i-1}), \tag{F.1}$$

where the right-hand side is the discretized version of the integral obtained from the trapezoidal rule. When α is chosen to be the correct order of reagent R in the rate law, the two reaction profiles will overlay. Furthermore, when all reagents have been properly normalized in this way, the reactant and product traces become linear, with a slope equal to either the observed rate constant k_{obs} (products) or $-k_{\text{obs}}$ (reactants). Figure F.3 shows this procedure for the simulated reaction $2A + B \longrightarrow 2C$ with

rate law rate = $k_{obs}[A]^2[B]$. The reaction was simulated with two different starting concentrations of A, allowing a sequential normalization to find the order of A that overlays the plots of $[B]$ and $[C]$ for the two reactions and then the order of B that linearizes the traces.

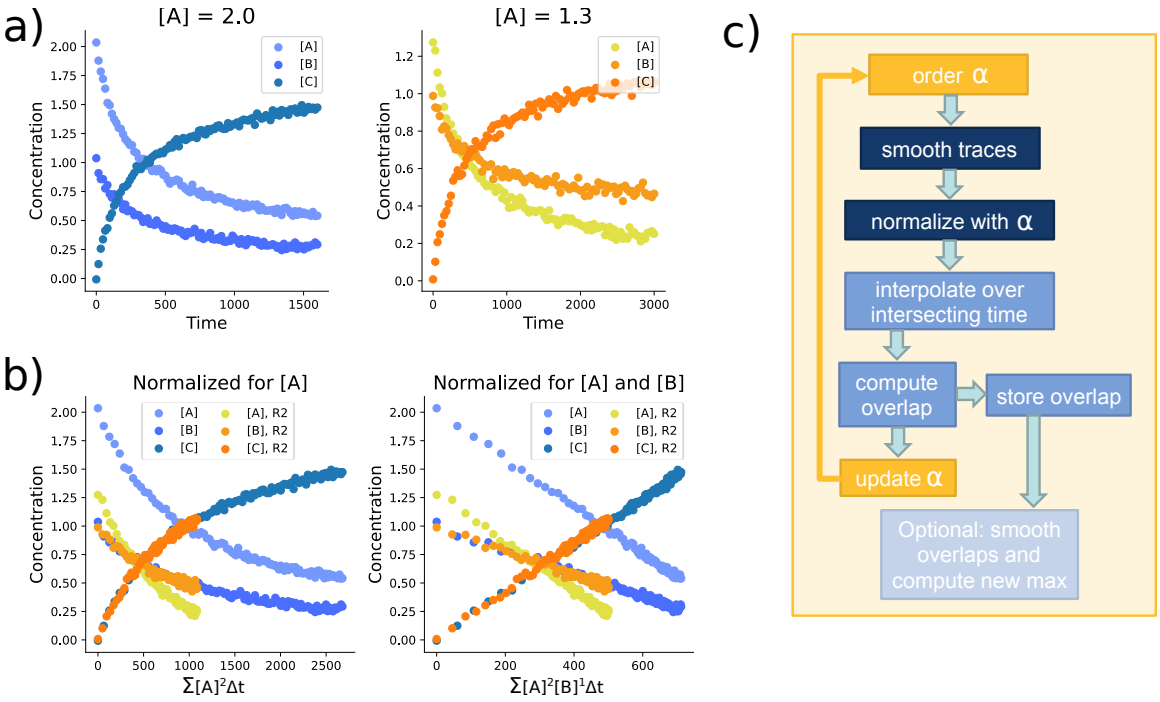

Figure F.3: Example of VTNA on simulated reaction data. Panel **a)** shows the original traces of all three species for two different starting values of $[A]$. Panel **b)** shows the traces once the time axis has been normalized to second order in $[A]$ (left) and once the time axis has been normalized to to second order in $[A]$ and first order in $[B]$. Panel **c)** shows the flow of the algorithm used to automate the first normalization which leads to trace overlays.

The procedure outlined above can be automated if suitable metrics are defined to score the overlap between two curbs and the linearity of a given curve. First, to find the order for a reactant whose concentration was varied between two experiments, we implemented an algorithm that followed the basic steps depicted in Figure F.3 in order to overlay two reaction traces. The time axis is repeatedly normalized using different orders α, and the overlap between two corresponding traces is computed for each α. The traces chosen for computing overlap may be product or reactant traces depending on what the user is able to most easily monitor over the course of the reaction.

Traces can be optionally smoothed before this procedure, and for each value of α, the trace with the greater number of samples over the interval on which the two traces overlap is downsampled to match the normalized time values of the points on the other trace. The overlap metric can be chosen among the root mean square deviation (RMSD), mean absolute deviation (MAD), or the Pearson correlation coefficient between the two traces, though we found in early testing that RMSD seemed to produce the best reaction orders. Finally, α can be varied using a simple grid search, which results in an informative plot of the overlap vs. α (Figure F.4). We found that smoothing this resulting plot before taking its maximum tended to improve the resulting order. We note that this procedure is slightly different from what is implemented in the newer Auto-VTNA package, which fits each trace to a monotonic polynomial function before evaluating the overlap between them.[5]

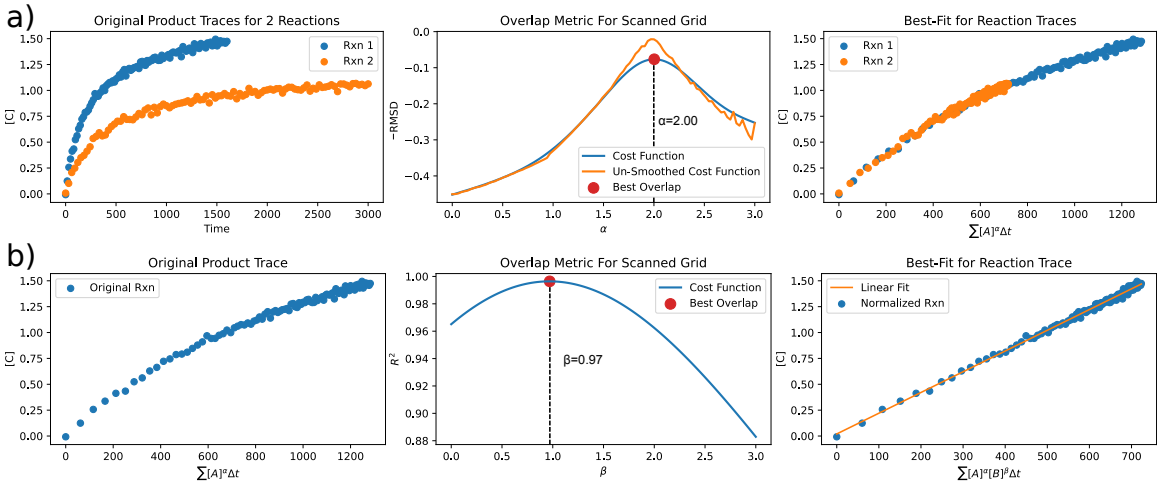

Figure F.4: Graphical output of our automated VTNA tool. Panel **a)** shows the output for overlapping two traces, with the original traces (left), the overlap metric and smoothed overlap metric over many values of reactant order α (center) and the final overlaid traces (right). Panel **b)** shows the output from finding the final reagent order and linearizing the trace. The reaction traces are from the same simulated reaction shown in Figure F.3.

When the time axis has been normalized by all but one of the reagents in the rate law, the order of the final reagent can be determined to be the order β for that reagent such that when the trace is additionally normalized by this reagent, it becomes linear. Thus, the value of β is varied, and a linearity metric is evaluated for each β to find its optimal value. We took the linearity metric to be the squared correlation coefficient (r^2) for a linear least squares fit to the trace. The procedure is shown for the simulated

reaction data in Figure F.4(b). We also note that besides a grid search over a range of possible orders, we also enabled the use of Scipy[6] optimization functions to speed the process for both single trace linearization and two trace overlay. However, the grid search with subsequent smoothing of the overlap function seemed less susceptible to noise than these faster optimizers.

The original VTNA method can also be extended to model catalyst activation and deactivation processes that can sometimes confound kinetic analyses.[7] In our implementation, we include a method for fitting one type of catalyst deactivation: rapid and irreversible catalyst poisoning. In this scenario, the concentration of catalyst in the reaction mixture is assumed to remain constant over the course of the reaction, but is lower than the nominal catalyst concentration by some amount p. We denote the actual concentration of catalyst after poisoning $[catalyst - p]$. The catalyst poisoning functionality in our implementation is limited, but it is able to fit the poisoning when the order in the catalyst is already known. Work toward simultaneous fitting of poisoning and order is ongoing. An example of determining the amount of poisoning is given in Figure F.5 for a simulated catalyzed reaction $A \longrightarrow B$ with a rate that is first order in catalyst concentration and some amount of initial poisoning. Given two product traces obtained with different initial catalyst concentrations (but assumed to have the same poisoning), the traces are overlaid by normalizing with respect to $[catalyst - p]^1$ using the known catalyst order of 1. The value of p is varied in order to maximize the overlap of the two traces.

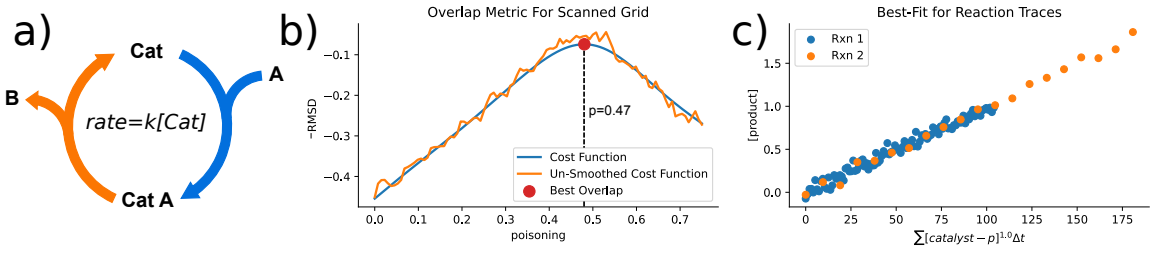

Figure F.5: Automatic fitting of irreversible catalyst poisining. Panel **a)** shows the simulated reaction and rate law. Panel **b)** shows the raw and smoothed overlap metric for a range of poisoning values. In this case the optimal poisoning was found to be 0.47 mmol, just off from the value of 0.5 mmol used to simulate the reaction traces. Panel **c)** shows the final product traces overlaid.

Several important bridges needed to be crossed before our implementation of automated VTNA could have been released. Most importantly, significantly more testing

was needed, on both real and simulated data, to evaluate its performance. In particular, most of our tests had been performed on high-data-density reaction traces. However, depending on the technique used for reaction monitoring, many fewer data points might be available. Additionally, for experiments run with different starting concentrations, the number of data points for one trace might be many more than the other. Further testing would assess how our automated fitting performs in situations with low data density and mismatched data densities between traces. The recently published Auto-VTNA method in particular found that curve fitting before computing overlaps, which we did not implement, improved performance for mismatched-density data.[5] Besides extensive testing of order fitting, further improvements could also be made to the poisoning fitting methods in our implementation, in particular determining the conditions under which robust fitting of both order and poisoning can be done simultaneously. Although development of our tool is unlikely to continue due to the recently published alternatives, this area of catalyst poisoning is one feature that does not appear to have been incorporated in the original releases of these alternative codes and could be an avenue by which we could contribute to these codebases in the future.

Bibliography

[1] James McFarlane, Brett Henderson, Sofia Donnecke, and J. Scott McIndoe. An information-rich graphical representation of catalytic cycles. *Organometallics*, 38(21):4051–4053, October 2019.

[2] Peter J. H. Williams, Charles Killeen, Ian C. Chagunda, Brett Henderson, Sofia Donnecke, Wil Munro, Jaspreet Sidhu, Denaisha Kraft, David A. Harrington, and J. Scott McIndoe. Continuous addition kinetic elucidation: catalyst and reactant order, rate constant, and poisoning from a single experiment. *Chemical Science*, 14(36):9970–9977, 2023.

[3] Jordi Burés. Variable time normalization analysis: General graphical elucidation of reaction orders from concentration profiles. *Angewandte Chemie International Edition*, 55(52):16084–16087, November 2016.

[4] Finn Bork, Sean Clark, Peter Burland, David Sale, and Jason Hein. Kinalite — a user-friendly online tool for automated variable time normalization analysis (vtna). *ChemRxiv*, March 2024.

[5] Daniel Dalland, Linden Schrecker, and King Kuok (Mimi) Hii. Auto-vtna: an automatic vtna platform for determination of global rate laws. *Digital Discovery*, 2024.

[6] Pauli Virtanen, Ralf Gommers, Travis E. Oliphant, Matt Haberland, Tyler Reddy, David Cournapeau, Evgeni Burovski, Pearu Peterson, Warren Weckesser, Jonathan Bright, Stéfan J. van der Walt, Matthew Brett, Joshua Wilson, K. Jarrod Millman, Nikolay Mayorov, Andrew R. J. Nelson, Eric Jones, Robert Kern, Eric Larson, C J Carey, İlhan Polat, Yu Feng, Eric W. Moore, Jake VanderPlas, Denis Laxalde, Josef Perktold, Robert Cimrman, Ian Henriksen, E. A. Quintero, Charles R. Harris, Anne M. Archibald, Antônio H. Ribeiro, Fabian Pedregosa, Paul van Mulbregt, and SciPy 1.0 Contributors. SciPy 1.0: Fundamental Algorithms for Scientific Computing in Python. *Nature Methods*, 17:261–272, 2020.

[7] Alicia Martínez-Carrión, Michael G. Howlett, Carla Alamillo-Ferrer, Adam D. Clayton, Richard A. Bourne, Anna Codina, Anton Vidal-Ferran, Ralph W. Adams, and Jordi Burés. Kinetic treatments for catalyst activation and deactivation processes based on variable time normalization analysis. *Angewandte Chemie International Edition*, 58(30):10189–10193, June 2019.

Appendix G

Python Scripts and Programs

G.1 Python Born Effective Charge Package

I created a small Python package for performing much of the analysis in Chapters 3 and 7.2. The package is called PyBEC and is available on the python package index. It can be installed in python3 virtual environments with `pip install pybec`. Additionally, the code, including example usage is available at `https://github.com/brettrhenderson/PyBEC`. Note that the name PyBEC comes from the fact that the code was originally written to compute Born effective charges (BECs) and plot them in various ways that are useful for interpreting polarization in nanocomposites. I also ended up using it as a more general tool for parsing the CPMD outputs of Quantum Espresso.

G.2 Permittivity from CPMD

I used a python script for calculating the effective permittivity from CPMD calculations as well as monitoring the progress of these calculations. It is available at in the repository `https://github.com/Paci-Group/eps-calculator`. The script needs three CPMD output files: 1) a zero field Berry Phase calculation (`zero_field.out`), 2) a finite field clamped-ion calculation (`clamped_ion.out`), and 3) a finite field relaxed-ion calculation (`relaxed_ion.out`). Note that the field is expected to be applied in the z-direction. The script automatically corrects for jumps by a quantum of polarization during the polarization process and can plot the polarization over the course of the relaxation for inspection. For finite field calculations with an electric

field of 0.001 au, the script can be run as:

```
python calculate_eps_cpmd.py zero_field.out \
-c clamped_ion.out relaxed_ion.out\
--efield 0.001 --plot
```

The script produces minimal output, giving the quantum of polarization (pq), zero-field polarization (p_i), clamped-ion polarization (p_ci), relaxed-ion polarization (p_f), unit cell volume (vol), and applied electric field (efield). Then, it gives the high frequency (ϵ^{∞}) and low frequency (ϵ^{0}) permittivity. For a calculation on SrO, this looks like:

```
pq = 28.978, p_i = 0.000, p_ci = 4.779, p_f = 4.761,
vol=24333.099, efield = 0.0010

Dielectric Constants:

|  High Frequency   |  Low Frequency   |
|-------------------|------------------|
|        3.468      |       18.424     |
```

The plot produced compares the evolution of the cell dipole moment (polarization multiplied by the cell volume) that is output by Quantum Espresso with the values that have been corrected for jumps by multiples of a quantum of polarization (Figure G.1).

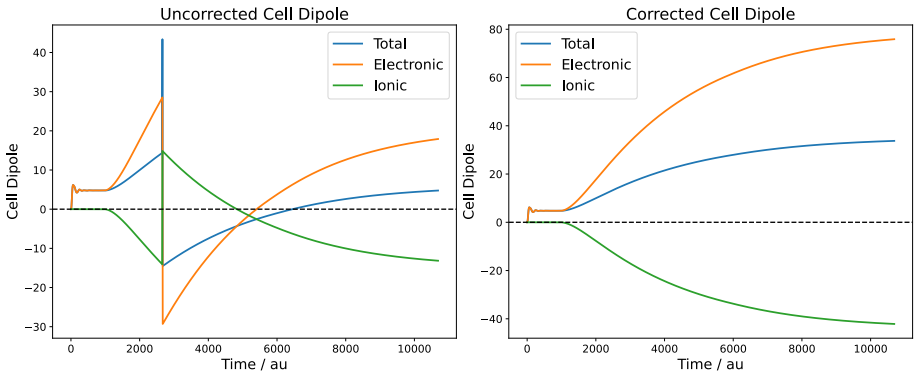

Figure G.1: Cell dipole as a function of simulation time for bulk SrO

G.3 Permittivity from PW

An additional script was used for calculating the permittivity from the output of the PW module of Quantum Espresso (used mostly in validating the CPMD approach in Appendix B). This script is stored in the repository `https://github.com/Paci-Group/PW_Epsilon_Parser`. The script requires three output files: 1) a zero field Berry Phase calculation, 2) a finite field clamped-ion calculation, and 3) a finite field relaxed-ion calculation. Note that the field is expected to be applied in the z-direction. The script produces a formatted output with the clamped- and relaxed-ion permittivities as well as the Born effective charges. Below is an example output for a conventional unit cell of BaO:

```
1. Zero Field Berry Phase Output:
BerryPhase(Efield=[0. 0. 0.],
           Edipole=[1.73410341e-09 4.76154358e-08 4.44577535e-08],
           Idipole=[234.97256031 234.97256031 234.97256031],
           NBerry=1,
           Volume (au)=1119.8156,
           Alat (au)=10.3844,
           Cell=[1. 1. 1.])

2. Clamped-Ion Berry Phase Output:
BerryPhase(Efield=[0.    0.    0.002],
           Edipole=[-1.50651791e-07 -4.30106724e-07  5.72780476e-01],
           Idipole=[234.97256031 234.97256031 234.97256031],
           NBerry=3,
           Volume (au)=1119.8156,
           Alat (au)=10.3844,
           Cell=[1. 1. 1.])

3. Relaxed-Ion Berry Phase Output:
BerryPhase(Efield=[0.    0.    0.002],
           Edipole=[2.73580565e-06 7.03115875e-06 2.00320271e+00],
           Idipole=[234.97256844 234.97258118 238.68012693],
           NBerry=3,
           Volume (au)=1119.8156,
```

```
            Alat (au)=10.3844,
            Cell=[1. 1. 1.])

Epsilon_infinity (e_xz, e_yz, e_zz): 1.000, 1.000, 4.214
Epsilon_0 (e_xz, e_yz, e_zz): 1.000, 1.000, 33.043
Born Effective Charges: (Symbol, X, Y, Z, Z_xz, Z_yz, Z_zz)
    Ba      0.000000  0.000000  0.000000   0.000  -0.000   2.771
    O       2.747599  2.747599  2.747599  -0.000  -0.000  -2.771
    Ba      0.000000  2.747599  2.747599   0.000   0.000   2.771
    Ba      2.747599  0.000000  2.747599  -0.000  -0.000   2.771
    Ba      2.747599  2.747599  0.000000  -0.000   0.000   2.771
    O       2.747599  0.000000  0.000000  -0.000   0.000  -2.771
    O       0.000000  2.747599  0.000000   0.000  -0.000  -2.771
    O       0.000000  0.000000  2.747599   0.000   0.000  -2.771
```

G.4 Wannier Decomposition of Permittivity

I used several scripts and Quantum Espresso input files to compute the decomposition of the permittivity enhancement from Wannier functions as described in Chapter 3.2. Some of the input files have already been described in Appendix B.1. The repository `https://github.com/Paci-Group/CP-Wannier` contains Quantum Espresso input templates and two sets of scripts for setting up and analyzing the Quantum Espresso calculations. While both sets of scripts use the CP module of Quantum Espresso, one works using the normal Car-Parrinello solver (`setup_cp.py`, `analyze_cp.py`), and the other set uses the conjugate gradients solver (`setup_cg.py`, `analyze_cg.py`). The analysis scripts compute the permittivity using both the Berry phase and Wannier center methods and then proceed to decompose the response of the nanocomposite into matrix and inclusion contributions. An example of the output, calculated using a system with an MgO matrix and Ag_{12} rod with polarization along the rod's long axis, is shown below:

```
CHECKING CONVERGENCE:
    CLAMPED ION ZERO FIELD CONVERGED: True
    CLAMPED ION EFIELD CONVERGED    : True
    RELAXED ION ZERO FIELD CONVERGED: True
    RELAXED ION EFIELD CONVERGED    : True
```

```
EPSILON CALCULATIONS:
    EPSILON INFINITY BERRY PHASE:   4.2201
    EPSILON INFINITY WANNIER    :   4.1037
    EPSILON RELAXED  BERRY PHASE:  12.8998
    EPSILON RELAXED  WANNIER    :  12.8350

NOW PERFORMING MORE IN DEPTH WANNIER DECOMPOSITION...

CLAMPED ION DECOMPOSITION:

Ensure Wannier Partitioning is as expected:
  Number of WCs per element:
    Init:
      Ag: 114        Mg: 552        O: 552
    Final:
      Ag: 114        Mg: 552        O: 552


Displaying the polarization components in the Z direction:

    ELEMENTS    ELECTRONIC  IONIC       TOTAL
    Ag          1.3896      0.0000      1.3896
    Mg          0.1077      0.0000      0.1077
    O           3.3308      0.0000      3.3308
    ALL         4.8281      0.0000      4.8281

CLAMPED ION PERMITTIVITY VECTOR (exz, eyz, ezz) FROM WANNIER CENTERS:
      0.9902,   0.9967,   4.1037

RELAXED ION DECOMPOSITION:

Ensure Wannier Partitioning is as expected:
  Number of WCs per element:
    Init:
      Ag: 114        Mg: 552        O: 552
    Final:
      Ag: 114        Mg: 552        O: 552


Displaying the polarization components in the Z direction:
```

```
    ELEMENTS    ELECTRONIC  IONIC       TOTAL
    Ag          -13.4564    16.8532     3.3967
    Mg          0.9887      -0.9278     0.0609
    O           49.9979     -35.0450    14.9529
    ALL         37.5301     -19.1195    18.4106

RELAXED ION PERMITTIVITY VECTOR (exz, eyz, ezz) FROM WANNIER CENTERS:
      0.9898,   0.9840,  12.8350

NOW PERFORMING HALLY, PACI (2018) ALPHA ENHANCEMENT DECOMPOSITION...

FIRST PERFORMED USING EPS VALUES FROM WANNIER SUMMATION:
POL TYPE   EPS_BULK   EPS_COMP   ALPH_INC   ALPH_MAT   ALPH_CAV   ALPH_ENH
CLAMPED     3.1070     4.1037     1389.6      290.1     -129.3     1550.4
RELAXED     9.3750    12.8350     3396.7     2499.8     -514.1     5382.4

NEXT PERFORMED USING EPS VALUES FROM WANNIER SUMMATION, SCALED TO BERRY PHASE POL:
POL TYPE   EPS_BULK   EPS_COMP   ALPH_INC   ALPH_MAT   ALPH_CAV   ALPH_ENH
CLAMPED     3.1070     4.1037     1441.8      419.1     -129.3     1731.5
RELAXED     9.3750    12.8350     3415.3     2582.0     -514.1     5483.2

NOW PERFORMED USING EPS VALUES FROM BERRY PHASE (AS IN HALLY, PACI 2018):
POL TYPE   EPS_BULK   EPS_COMP   ALPH_INC   ALPH_MAT   ALPH_CAV   ALPH_ENH
CLAMPED     3.1070     4.2201     1389.6      471.2     -129.3     1731.5
RELAXED     9.3750    12.8998     3396.7     2600.5     -514.1     5483.2
```

G.5 Continuum Models of Nanocomposites

The input files for GMsh and GetDP used to calculate the permittivities of continuum models of nanocomposite using the finite element method are stored at `https://github.com/Paci-Group/NanoComposite_FEM`. That repository also has a set of input scripts needed to calculate the permittivity using the CPMD module of Quantum Espresso located in the directory `quantum_espresso_input_example`.

G.6 Inducible Atomic Dipole Models

I used several python scripts to perform the inducible atomic dipole modeling in Chapter 5, all of which are housed in the repository `https://github.com/Paci-Group/iad-models`. The scripts rely on a slightly modified version of the liMBD package.

In particular, the following function must be added to the file `src/pymbd/pymbd.py`:

```
def screening_aim(coords, alpha_0, C6, R_vdw, beta, lattice=None, nfreq=15):
    r"""Screen atomic polarizabilities.

    :param array-like coords: (a.u.) atom coordinates in rows
    :param array-like alpha_0: (a.u.) atomic polarizabilities
    :param array-like C6: (a.u.) atomic :math:`C_6` coefficients
    :param array-like R_vdw: (a.u.) atomic vdW radii
    :param float beta: MBD damping parameter :math:`\beta`
    :param array-like lattice: (a.u.) lattice vectors in rows
    :param int nfreq: number of grid points for frequency quadrature

    Returns static polarizabilities (isotropic), static atomic polarizability tensors,
    static molecular polarizability tensor, :math:`C_6` coefficients, and
    :math:`R_\mathrm{vdw}` coefficients (a.u.).
    """
    nqho = len(alpha_0)
    freq, freq_w = freq_grid(nfreq)
    omega = 4 / 3 * C6 / alpha_0**2
    alpha_dyn = [alpha_0 / (1 + (u / omega) ** 2) for u in freq]
    alpha_dyn_rsscs = []
    alpha_dyn_rsscs_aniso = []
    alpha_dyn_rsscs_mol = []
    for a in alpha_dyn:
        sigma = (np.sqrt(2 / np.pi) * a / 3) ** (1 / 3)
        dipmat = dipole_matrix(
            coords, 'fermi,dip,gg', sigma=sigma, R_vdw=R_vdw, beta=beta, lattice=lattice
        )
        a_nlc = np.linalg.inv(np.diag(np.repeat(1 / a, 3)) + dipmat)

        # atomic polarizability tensors (sum 3x3 blocks for each 3 rows)
        a_nlc_block = np.stack(np.split(np.stack(np.split(a_nlc, nqho, axis=0), axis=0), nqho, axis=2), axis=1)
        a_atomic = a_nlc_block.sum(axis=1)
        alpha_dyn_rsscs_aniso.append(a_atomic)

```

```
        # molecular polarizability tensor (full contraction over 3x3 blocks)
        a_molecular = a_atomic.sum(axis=0)
        alpha_dyn_rsscs_mol.append(a_molecular)

        a_contr = sum(np.sum(a_nlc[i::3, i::3], 1) for i in range(3)) / 3
        alpha_dyn_rsscs.append(a_contr)

    alpha_dyn_rsscs = np.stack(alpha_dyn_rsscs)
    C6_rsscs = 3 / np.pi * np.sum(freq_w[:, None] * alpha_dyn_rsscs**2, 0)
    R_vdw_rsscs = R_vdw * (alpha_dyn_rsscs[0, :] / alpha_0) ** (1 / 3)
    return alpha_dyn_rsscs[0], alpha_dyn_rsscs_aniso[0], alpha_dyn_rsscs_mol[0], C6_rsscs, R_vdw_rsscs
```

This function is very similar to the `screening` function already in pymbd. However, in addition to returning the isotropic screened atomic polarizabilities, it also returns the full screened atomic polarizability tensors and the full molecular polarizability tensor. In order to have this function available when pymbd is imported, two lines must be also be changed in the file `src/pymbd/__init__.py`. The import line and the definition of the `__all__` variable should be replaced with:

```
from .pymbd import ang, from_volumes, mbd_energy, mbd_energy_species, screening, screening_aim
__all__ = ['mbd_energy', 'mbd_energy_species', 'screening', 'ang', 'from_volumes', 'screening_aim']
```

Once these changes have been made and pymbd installed locally, one of the analysis scripts can be run. They use atomic basins that have been caclulated previously to model a molecule using the self-consistent screening approach described in Appendix D. Note that the output gives the full polarizability tensor for each atom in a molecule. Sample output is given from the `ts_fi_horton_analysis.py` script for the BH_3 molecule:

```
    *** Using the MBIS AIM Basins
    ---------------------------------------------


  +++ Using the Manz CCSD(T) reference polarizabilities
    ---------------------------------------------
```

```
Coordinates (Bohr) and Supplied AIM polarizabilities (a.u.):
   B      0.00000000    0.00000000    0.00000000   11.53246327
   H      0.00000000    2.24877393    0.00000000    3.44094092
   H      1.94755160   -1.12438696    0.00000000    3.44185616
   H     -1.94755160   -1.12438696    0.00000000    3.44488482

Isotropic Molecular Polarizability from TS-vdW:   21.86014517

Coordinates (Bohr) and Isotropic AIM polarizabilities (a.u.)
Calculated using TS+SCS Method:
   B      0.00000000    0.00000000    0.00000000   11.92324068
   H      0.00000000    2.24877393    0.00000000    2.70285778
   H      1.94755160   -1.12438696    0.00000000    2.70367765
   H     -1.94755160   -1.12438696    0.00000000    2.70607662

Coordinates (Bohr) and Anisotropic AIM polarizabilities (a.u.)
Calculated using TS+SCS Method:
   B      0.00000000    0.00000000    0.00000000
    ---------------------------------------------
         13.76897059    0.00069922    0.00000000
          0.00069921   13.76733756    0.00000000
          0.00000000    0.00000000    8.23341390
     - Isotropic Polarizability (Tr(alpha) / 3):   11.92324068

   H      0.00000000    2.24877393    0.00000000
    ---------------------------------------------
          0.93285343   -0.00001191    0.00000000
          0.00038150    5.46191866    0.00000000
          0.00000000    0.00000000    1.71380125
     - Isotropic Polarizability (Tr(alpha) / 3):    2.70285778

   H      1.94755160   -1.12438696    0.00000000
    ---------------------------------------------
```

```
          4.33102864   -1.96109735    0.00000000
         -1.96162384    2.06560552    0.00000000
          0.00000000    0.00000000    1.71439879
      - Isotropic Polarizability (Tr(alpha) / 3):    2.70367765

  H     -1.94755160   -1.12438696    0.00000000
   -------------------------------------------
          4.33428907    1.96259811    0.00000000
          1.96273120    2.06778685    0.00000000
          0.00000000    0.00000000    1.71615392
      - Isotropic Polarizability (Tr(alpha) / 3):    2.70607662


Molecular Polarizability Tensor from TS+SCS:
         23.36714173    0.00218808    0.00000000
          0.00218808   23.36264860    0.00000000
          0.00000000    0.00000000   13.37776787
      - Isotropic Polarizability (Tr(alpha) / 3):   20.03585273

Isotropic Molecular Polarizability from TS+SCS:   20.03585273
```

G.7 Partitioning Polarizability into Charge Transfer and Local Dipole Components

Scripts for partitioning the polarizability into charge transfer and local dipole components can also be found in the repository `https://github.com/Paci-Group/iad-models`, within the `decomposition` directory. In particular, the script `get_decomposed_polarizabilities_zero_centered.py` performs the decomposition for a set of clusters. The script parses the output from ORCA to get both the analytically and numerically calculated polarizability tensors. Then, it parses the output from Critic2 to compute the atomic contributions to the polarizability tensor. Finally, the atomic contributions are summed to give the origin-independent molecular charge transfer and local dipole polarizability tensors. An example of the output for the $(TiO_2)_2$ cluster is presented below. Note that in the summed atomic

polarizability tensors, there is some numerical noise from the integration of QTAIM basins that makes the tensors not perfectly symmetric.

```
    * Analyzing Cluster tio2_2
-------------------------------------------------
  - Extracting cluster polarizabilities from analytical and finite
  difference calculations.

    Analytical Polarizability Tensor
    -------------------------------------------------
    91.45992    -0.02270    -24.20988
    -0.02270    53.61619    -0.00500
    -24.20988    -0.00500    56.03076

    Diagonalized Analytical Polarizability
    -------------------------------------------------
    43.74658    53.61620    103.74409

    Isotropic Analytical Polarizability: 67.03563

    Numerical Polarizability Tensor
    -------------------------------------------------
    91.46000    -0.02000    -24.21000
    -0.02000    53.61000    -0.00500
    -24.21000    -0.00000    56.03000

    Diagonalized Numerical Polarizability
    -------------------------------------------------
    43.74590    53.61001    103.74409

    Isotropic Numerical Polarizability: 67.03333

  - Extracting site-specific polarizabilities from Bader analysis.

    +++ reporting only the diagonal elements of the polarizability
```

```
tensors for each atom
* Atomic Positions (in Bohr)
  -2.55001    -0.00463    0.01587
  2.54944    -0.00286    -0.01442
  -0.00112    2.34912    -0.00279
  0.00056    -2.35662    0.00424
  4.21262    -0.00609    -2.56647
  -4.21319    -0.00141    2.56792
* Local Dipole Polarizabilities (Bohr ^3)
  2.27622    1.99721    2.52181
  2.27604    1.99726    2.52191
  6.00632    6.95710    6.88790
  6.00621    6.95687    6.88785
  8.62463    7.30105    6.19071
  8.62413    7.30099    6.19081
* Charge Transfer Polarizabilities (Bohr ^3)
  3.47706    0.00000    -0.04078
  3.47490    0.00001    -0.04077
  0.00000    10.55252    0.00002
  0.00000    10.55301    0.00002
  25.32090    0.00001    12.43657
  25.32268    0.00001    12.43509
* Total Polarizabilities (Bohr ^3)
  5.75328    1.99722    2.48103
  5.75094    1.99727    2.48115
  6.00632    17.50962    6.88793
  6.00621    17.50988    6.88788
  33.94553    7.30106    18.62728
  33.94682    7.30100    18.62589

+++ Summing over atomic polarizabilities to obtain
decomposed cluster polarizabilities.
Summed Atomic Dipole Polarizability Tensor
-------------------------------------------------
33.81355    0.00509    2.89871
```

```
0.01051    32.51048    -0.00077
6.70727    0.00006    31.20099

Diagonalized Summed Atomic Dipole Polarizability
-------------------------------------------------
27.90849    32.51048    37.10606

Summed Atomic Charge Transfer Polarizability Tensor
-------------------------------------------------
57.59554    -0.02149    -27.08464
-0.03391    21.10556    -0.00387
-30.90171    -0.00581    24.79016

Diagonalized Summed Atomic Charge Transfer Polarizability
-------------------------------------------------
7.93610    21.10558    74.44959

Total Summed Atomic Tensor
-------------------------------------------------
91.40910    -0.01640    -24.18593
-0.02340    53.61604    -0.00464
-24.19444    -0.00574    55.99115

Diagonalized Total Summed Atomic Polarizability
-------------------------------------------------
43.72057    53.61605    103.67966

Isotropic Summed Atomic Dipole Polarizability: 32.50834
Isotropic Summed Atomic Charge Transfer Polarizability: 34.49709
Isotropic Total Summed Atomic Polarizability: 67.00543
```